A FRAMEWORK FOR THE OPTIMIZATION OF DOCTRINE AND SYSTEMS IN ARMY AIR DEFENSE UNITS USING PREDICTIVE MODELS OF STOCHASTIC COMPUTER SIMULATIONS

A Dissertation
Presented to
The Academic Faculty

by

Brian M. Wade

In Partial Fulfillment
of the Requirements for the Degree
Doctor of Philosophy in the
School of Aerospace Engineering

Georgia Institute of Technology
May 2017

A FRAMEWORK FOR THE OPTIMIZATION OF DOCTRINE AND SYSTEMS IN ARMY AIR DEFENSE UNITS USING PREDICTIVE MODELS OF STOCHASTIC COMPUTER SIMULATIONS

Approved by:

Dr. Daniel Schrage, Advisor
School of Aerospace Engineering
Georgia Institute of Technology

Dr. Dimitri Mavris
School of Aerospace Engineering
Georgia Institute of Technology

Dr. Lakshmi Sankar
School of Aerospace Engineering
Georgia Institute of Technology

Dr. Apinut Sirirojvisuth
School of Aerospace Engineering
Georgia Institute of Technology

Dr. David Knudson
Center for Army Analysis
United States Army

Date Approved: 16 March 2017

ACKNOWLEDGEMENTS

First and foremost, I want to thank my wife, Joanna, for her unwavering support. I cannot put into words how fortunate I am to have her in my life. She has been my cheerleader and relentless editor. She took on the burden of running our family alone, allowing me to concentrate on school. She made it possible for me to complete this degree and I am eternally grateful to her for it.

I am also deeply indebted to my two daughters, Hailey and Zoe, for their sacrifice during the long path to completing this dissertation. I have missed countless adventures, dinners, and bedtimes because "Daddy is working on the computer again." I hope that this can be an example to them of what you can do if you put your mind to it.

I would also like to thank my parents for their guidance and support during my early years. My father was my coach, spiritual leader, and counselor. He is my role model now that I am a father. He taught me perseverance, dedication, and humility. He left this world too early, but in that time he passed on a legacy that I hope to continue for my family. To my mother, the teacher, household manager, and glue of our family. She showed me the beauty of math. Growing up, she spent endless hours at the kitchen table helping me with math, spelling, and homework. She believed in me, which paved the path to make this achievement possible.

Finally, I would like to thank my advisor, Dr. Daniel Schrage. He has provided me invaluable mentorship and advice. He showed me that it is possible to be both a Soldier and a scholar. I could not have made it without his support.

TABLE OF CONTENTS

LIST OF TABLES

LIST OF FIGURES

LIST OF SYMBOLS AND ABBREVIATIONS

ABT	Air Breathing Threat
AC	Aircraft
AC1	Aircraft Type 1
AC2	Aircraft Type 2
AC3	Aircraft Type 3
ADA	Air Defense Artillery
ADOSO	ADA Doctrine, Organization, and Systems Optimization
AGL	Above Ground Level
AHP	Analytical Hierarchy Process
AMD	Air and Missile Defense
AMSAA	Army Material Systems Analysis Activity
ANN	Artificial Neural Net
ANOVA	Analysis of Variance
ASCM	Anti-Ship Cruise Missile
ATACMS	Army Tactical Missile System
AVG	Average
BDA	Battle Damage Assessment
BM	Ballistic Missile
BMD	Ballistic Missile Defense
BMOA	Ballistic Missile Operations Area
C2	Command and Control

CBA	Capabilities Based Assessment
CDF	Cumulative Density Function
CEP	Circular Error Probable
CM	Cruise Missile
CMF	Cumulative Mass Function
COG	Catastrophic Kill on Ground
CONOPS	Concept of the Operations
COSAGE	Combat Sample Generator
CPI	Coherent Processing Interval
CRH	Caliber Radius Head
csv	Comma Separated Values
dB	Decibels
DCR	DOTmLPF Change Request
DEB	Deflection Error Probable
DOB	Depth of Burst or Depth of Burial
DoD	Department of Defense
DOE	Design of Experiments
DOF	Degrees of Freedom
DOTmLPF	Doctrine, Organization, Training, Material, Leadership, Education, Personnel, and Facilities
DPS	Defense Planning Scenarios
EADSIM	Extended Air Defense Simulation
EEW	Equivalent Explosive Weight (to TNT)

EM	Electro-Magnetic
FAA	Functional Area Analysis
FLT	Flight
FNA	Functional Needs Analysis
FSA	Functional Solutions Analysis
FOV	Field of View
FY	Fiscal Year
GEM	Guidance System Enhanced Missile
GPS	Global Positioning System
HPC	High-Performance Computing
IAMD	Integrated Air and Missile Defense
ICBM	Intercontinental Ballistic Missile
ICD	Initial Capabilities Document
IFF	Identify Friend or Foe
Inf	Infrastructure
Int	Interceptor
IRBM	Intermediate Range Ballistic Missile
IRL	Interface Readiness Level
ISR	Intelligence Surveillance and Reconnaissance
JCIDS	Joint Capabilities Integration Development System
JICM	Joint Integrated Campaign Model
JWS	Joint Weaponeering System
LACM	Land Attack Cruise Missile

LT	Lower Tier Air Defense Artillery System
LTA	Lower Tier Interceptor Type A
LTB	Lower Tier Interceptor Type B
LTC	Lower Tier Interceptor Type C
LHD	Latin Hypercube Design
MADM	Multi-Attribute Decision Making
MDA	Missile Defense Agency
MDD	Material Development Decision
MFE	Model Fit Error
MLE	Maximum Likelihood Estimate
MRE	Model Representation Error
MOS	Minimum Operating Strip
MRBM	Medium Range Ballistic Missile
MS	Mile Stone
MSE	Missile Seeker Enhanced
MSL	Mean Sea Level
MTCR	Missile Technology Control Regime
NDRC	National Defense Research Council
NGPP	Non-Graphical Post Processor (of EADSIM)
NN	Neural Net
NOE	Nap of the Earth
ODE	Ordinary Differential Equation
Pd	Probability of Detection

PDF	Probability Density Function
Pk	Probability of Kill
PMF	Probability Mass Function
POL	Petroleum, Oil, and Lubrication Site
P-P	Probability-Probability Plot
PRF	Pulse-Repetition Frequency
PRI	Pulse-Repetition Interval
PT	Point Defense Air Defense Artillery System
PTO4	Prevent Take Off For 4-Hours
Q-Q	Quantile-Quantile Plot
R	Correlation Coefficient
R^2	Coefficient of Determination
RCS	Radar Cross Section
REP	Range Error Probable
RISTA	Reconnaissance, Intelligence, Surveillance, Targeting, and Acquisition
RMSE	Root Mean Squared Error
RRE	Radar Range Equation
RSE	Response Surface Equation
RSS	Residual Sum of Squares
RV	Reentry Vehicle
SLS	Shoot-Look-Shoot
SNR	Signal to Noise Ratio
SRBM	Short Range Ballistic Missile

SSE	Sum of Squares of the Error
SSL	Shoot-Shoot-Look
SSPK	Single Shot Probability of Kill
STD	Standard Deviation
STORM	Synthetic Theater Operations Research Model
STRATCOM	Strategic Command
TBE	Teledyne Brown Engineering
TBM	Theater Ballistic Missile
TBM1	Theater Ballistic Missile Type 1
TBM2	Theater Ballistic Missile Type 2
TBM3	Theater Ballistic Missile Type 3
TEL	Transporter-Erector-Launcher
THAAD	Terminal High Altitude Area Defense
TOPSIS	Technique for Order of Preference By Similarity to Ideal Solution
TRL	Technology Readiness Level
TTP	Tactics, Techniques, and Procedures
UAS	Unmanned Aerial System
UAV	Unmanned Air Vehicle
US	United States
UT	Upper Tier Air Defense Artillery System
WGS84	World Geodetic System 1984
WMDs	Weapons of Mass Destruction

SUMMARY

Proliferation of missile technology has increased in recent years. Today, almost every military force in the world maintains an arsenal of Theater Ballistic Missiles (TBMs) and Cruise Missiles (CMs). These technologies are less expensive to acquire and maintain than a conventional air force, but offer many of the same advantages, such as precision strike and deep shaping operations. This proliferation is advancing much faster than the Air Defensive Artillery (ADA) system's capabilities, since the cost of counter-missile systems is much greater than the ballistic or cruise missiles that they target. Additionally, much of the ADA system's tactics were developed on past battlefields, with small and uniform raids made up of only a limited number of TBMs or CMs. Today, the ADA systems face raids composed of a large number of systems made of combinations of different types of TBMs and CMs.

This dissertation presents a new methodology that can be used to address large-scale, complex raids made up of different types TBMs and CMs that attempt to overwhelm the ADA systems at a particular location. This method will allow for technology gap identification, but the primary focus will be on how existing ADA systems can adjust their tactics in order to minimize the damage caused by threats that are not shot down and impact friendly forces.

Nearly all the literature to date optimizes systems and tactics to reduce the number of leakers — threats not shot down — that impact the ground. However, simply counting the number of leakers does not adequately describe the effects to friendly forces. Instead, the first part of this work combines existing methods for external ballistics, concrete penetration, explosive cratering, and weapon blast and fragmentation damage in

order to create an integrated program that can describe the damage to an airfield runway, infrastructure, and parked aircraft. The second part of this work focuses on modeling the ADA missile engagements using an accredited Department of Defense ADA simulation model called the Extended Air Defense Simulation (EADSIM).

Both the airfield damage model and ADA simulation have run times ranging from minutes to hours. They are also stochastic; so a large number of runs are required for each input vector in order to properly understand the output range. In order to reduce the computation time to allow for later optimization, the methods of Design of Experiments and Machine Learning, such as Neural Networks and Gaussian Process Models, were used to create fast running models that predict the outputs of these simulations.

The final part of this work uses these prediction algorithms to first optimize the enemy fire plan, then optimize the ADA defense tactics, and finally optimize the ADA defense tactics with a new interceptor missile system. Initially, the enemy attack plan must be optimized in order to discover combinations of the different types of TBMs and CMs that cause the most damage to different areas of the airfield. This analysis produces a frontier of non-dominated solutions that maximize different effects, such as damage to the runway, aircraft, or fuel points. Given this set of optimized fire plans, the friendly ADA tactics are optimized in order to minimize the damage to friendly assets for the lowest cost. A multi-attribute decision making tool is then used to select a specific set of tactics and these tactics are then compared to the base case.

1. INTRODUCTION

"They may vex us with shot, or with assault. To intercept this inconvenience, a piece of ordnance 'gainst it I have placed."

- Shakespeare, *Henry IV*

The threat of attack from Theater Ballistic Missiles (TBMs) and Cruise Missiles (CMs) is not new to the Army. Since the first V-2 Rockets were launched from Germany into England during World War II, countries have strived to find defensive measures from their devastating effects. The dawn of the Cold War ushered in renewed emphasis once Ballistic Missile (BM) technology progressed far enough to allow nuclear weapons to be delivered across oceans in a matter of minutes. Unfortunately, BM defense has progressed much slower than the BM technology itself. This is not unusual since BM and CM defense technology has been equated to trying to hit a bullet with another bullet. A more accurate analogy for today's modern battlefield with its many threat types such as TBMs, CMs, and unmanned aerial systems (UASs), would be trying to find many different bullets, birds, and mosquitos and shooting all with three with different types of guns and bullets.

Almost every modern military force in the world today has some type of TBM and CM arsenal. These technologies are less expensive to maintain than a conventional air force and many times much cheaper to acquire as well. They offer many of the same advantages as a manned air force such as precision strike, deep shaping operations, and air interdiction at a fraction of the price. As a result, countries are investing millions of dollars into the development of TBM and CM technology in order to counter the advantages of advanced military's manned air forces. The advances in these technologies and their proliferation are progressing much faster than the defensive systems.

The defensive systems against TBMs and CMs originated from systems designed to defend against manned aircraft (helicopters or airplanes). Now, these systems are collectively known as Air and Missile Defense (AMD) systems or Air Defense Artillery (ADA) systems, and target a collection of threats ranging from TBMs, CMs, UASs, and manned aircraft. The heart of AMD systems is their radar. The radar is what allows the AMD systems to detect targets and allow weapon systems to track and hone-in on a target (refer to appendix A for an overview of radar technology). TBMs and CMs generally carry a lethal payload while UASs are generally used for surveillance. For the foreseeable future, the most modern militaries will maintain air dominance, or at least air parity, in almost any conflict. This means that the threat from manned aircraft will be small. Most countries understand this and do not invest in a manned air force. Instead they invest in TBMs and CMs in order to deliver lethal effects. Thus, this work will concentrate on defense from TBMs and CMs.

1.1. TBM and CM Definition

1.1.1. Theater Ballistic Missiles (TBMs)

A TBM is a sub-class of BMs. A BM is a missile that follows a ballistic flight path [1]. This means that it spends a significant portion of its flight subject to only the forces of drag and weight. A ballistic trajectory is the same as a ball being thrown into the air. Once the main engine cuts off shortly after liftoff, usually 1-8 minutes later, the missile is in free-flight. BMs are categorized according to their maximum range as shown in Table 1 below [1, 2].

Table 1: Ballistic Missile Categories

Missile Type	Abbreviation	Maximum Range (Km)
Intercontinental Ballistic Missile	ICBM	Over 5500
Intermediate-Range Ballistic Missile	IRBM	3000 – 5500
Medium-Range Ballistic Missiles	MRBM	1000 – 3000
Short-Range Ballistic Missiles	SRBM	Up to 1000

TBMs are either Short-Range Ballistic Missiles (SRBMs) or Medium-Range Ballistic Missiles (MRBMs). Army ADA systems are generally used against TBMs while National Level Defenses are used against longer range BMs. The accuracy of a TBM is given by its Circular Error Probability (CEP). This is the radius of a circle where 50% of the TBMs are expected to impact within. Generally, a TBM's CEP is about 1% of its range for low cost systems [3]. There are some systems, however, with advanced guidance systems that can achieve a CEP of 35-50 meters [3]. Examples of US TBM systems are the MGM-140 Army Tactical Missile System (ATACMS) missile or the Multiple Launch Rocket System (MLRS) rocket system.

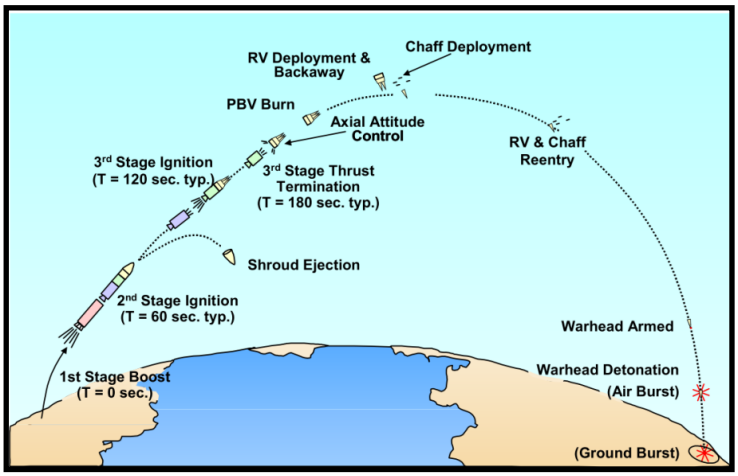

Figure 1: Ballistic Missile Stages (Image From [4])

1.1.2. Cruise Missiles (CMs)

A Cruise Missile (CM) is a missile that is self-propelled, guided, and sustains flight through aerodynamic forces such as lift for most of its flight and whose mission is

to deliver ordnance onto a target [5]. In essence, a CM is like what we think of as a UAS today, but whose mission is to impact a target in order to cause damage. CMs are generally categorized by their mission and launch mode. The two broadest categories are Land-Attack Cruise Missiles (LACMs) and Anti-Ship Cruise Missiles (ASCM). Either type can be launched from a ground based launcher, an aircraft, a ship, or a submarine [6]. An example of a US CM is the Tomahawk missile (shown below in Figure 2). This missile is either a ship or a sub-launched LACM.

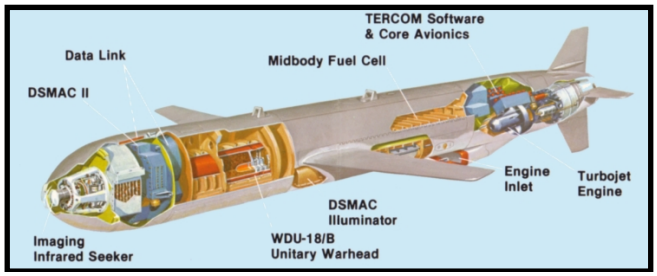

Figure 2: General Dynamics AGM-109H/L Cruise Missile (Image From[7])

1.2. TBM and CM Proliferation

TBMs and CMs were first used in WWII when Germany terrorized England by launching the V-1 and VM-2 rockets at population centers. The V-1 operated more like a cruise missile, while the V-2 operated more like a TBM. Since that time, most large and modern militaries have acquired ballistic missile technology. The proliferation, however, has been increasing in recent years with the spread of the internet. More and more countries are gaining know-how and physical systems that allow them to not only maintain a robust TBM and CM force, but also to aim them accurately. The spread of UASs is also giving these countries a new and efficient means to aim these TBMs and CMs accurately and then to assess the damage they inflict after the attack. This threat will assuredly increase with time. As guidance and electronic systems become less

expensive, the proliferation of CMs and TBMs will increase and those systems will become the predominate threat to military forces. In modern warfare against an enemy that posses TBMs and CMs, the military must be prepared to operate in an environment where critical infrastructure and forces are under constant threat from these systems.

1.2.1. Theater Ballistic Missile Proliferation

TBM acquisition has traditionally been tempered by an international treaty that limits the export of technology and sale of BMs and their sub-systems. This treaty, known as the Missile Technology Control Regime (MTCR), was founded in 1987 by the G8 partners. The MTCR is politically binding, but not legally binding, and restricts the proliferation of rockets and missiles capable of carrying a payload of at least 500 kg for at least 300 km [8, 9]. This treaty limits the proliferation of TBM technology; however, many smaller non-signature countries are beginning to acquire the technology and are exporting them heavily, unregulated by the MTCR. In 2012, over 31 countries (23 of whom are not part of the MTCR) had BM systems and that number is growing [2]. Some of these countries, such as North Korea, are avid exporters of the technology [10]. While others, such as China, have large Research and Development Programs [11]. Figure 3 below shows a map of countries and the TBM names and types they are suspected to operate.

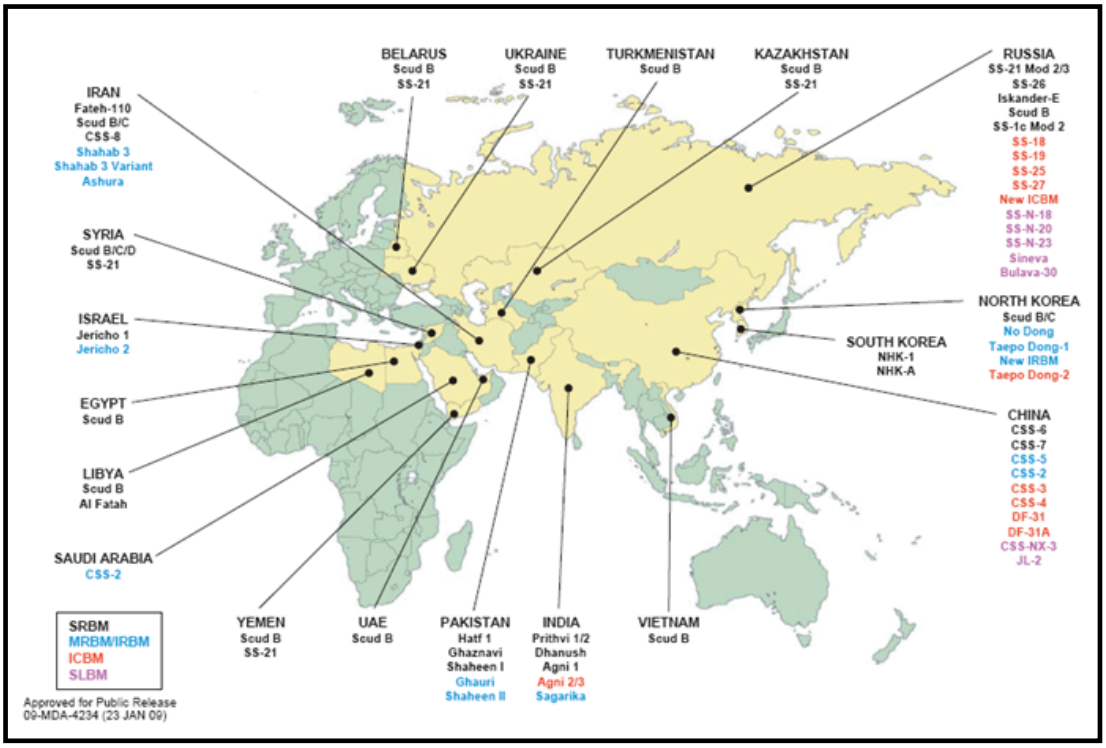

Figure 3: Ballistic Missile Proliferation (Image From [12])

1.2.2. Cruise Missile Proliferation

As Dennis Gormley so elegantly states: "CMs traditionally fly under the radar literally and figuratively" [13]. Their proliferation has only just begun to accelerate and as a result they are typically overlooked in favor of TBMs. CMs will not supplant TBMs, but when deployed together, they can overwhelm even the best ADA systems [13]. In fact, a Defense Science Board concluded that within 5-10 years, America's ability to defend and deter aggressors in regional conflicts could be severely challenged due to the threat of CM proliferation [14]. There are approximately 75 different countries that operate over 130 different types of CMs today [14, 15]. A majority of these are short range ASCMs. Only about 12 countries are known to produce LACMs, however, many experts expect this number to increase due to the availability of lower price technology [15, 16], and due to new systems that allow ASCMs to be converted to potent LACMs

[17]. When compared to TBMs, CMs are generally more accurate (by a factor of at least 10), cost about half as much, are easier to maintain and transport, and can be launched from a variety of platforms including land, air and sea based systems [13]. All of these advantages have fueled their spread in recent years.

LACM are also restricted by the MTCR, however, their restriction is much harder to enforce than that of BMs. Most countries agree that TBM should be limited, but there is no consensus about CMs and their closely related cousin, the UAS. There are also exemptions in the treaty for civilian and military aircraft that create loopholes for dual-use sub-systems like autopilot guidance systems and gyro stabilization systems. Finally, the modularity of CMs allows technology to fall under the regulation limits but then be installed on larger systems [8]. Traditionally, CMs have been extremely expensive and highly technical thus limiting their proliferation. The most challenging aspect was the auto-pilot and internal guidance system. The invention of the GPS constellation along with advances in guidance systems has offset these technological challenges [8, 18, 19]. Today, the US Army estimates that with a $50 million investment, a country could acquire over 100 CMs, which could be outfitted to fire from any vehicle, ship, or aircraft. An equal investment in TBMs would only acquire 15 missiles with three transporter-erector-launcher (TEL) platforms [14]. Perhaps even more alarming, in 2003 a New Zealand engineer documented how to build a CM for under $5,000 in response to US experts who challenged his claim that it could be done [17]. The alarming drop in the cost of technology will fuel the spread and use of CMs in future conflicts.

1.3. A Poor Man's Air Force

As the combat power from modern military's air forces continues to grow, many countries will come to the conclusion that they cannot directly confront those militaries in an air-to-air engagement. They will look for other ways to gain the same capabilities, avoiding an air-to-air confrontation. This is known as an asymmetric approach. An enemy avoids direct confrontation against a strength, and instead seeks to counter with systems that target a weakness. TBMs and CMs offer a way to balance the threat of an advanced manned air force since they provide many of the advantages of a manned air force. Traditionally, an air force has looked to shape the "deep fight" attacking strategic targets such as Command and Control (C2) nodes, large tank or troop formations, choke points in supply routes, or logistic staging areas. These deep-shaping operations can also be accomplished by TBM or CM raids. The Army recognized this trend in its FY98 Air and Missile Defense Master Plan. A graphic from this plan is shown below in Figure 4. This figure shows how TBMs and CMs are effective against the US for the least amount of difficulty.

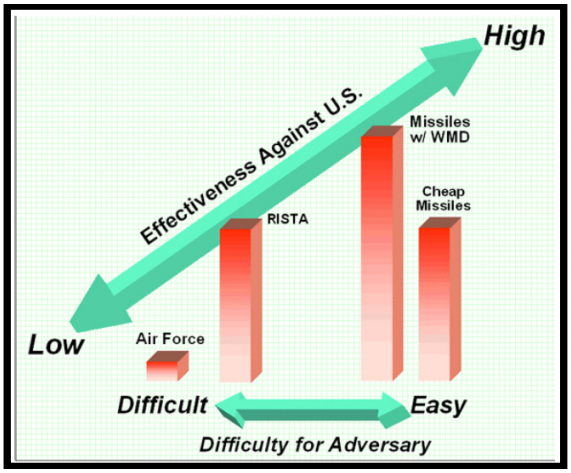

Figure 4: Adversary's Missiles v. Air Force (Image From [3])

In addition, a manned air force provides precision strike and air interdiction against high valued targets. As guidance systems and GPS technology have come down in price, CMs are now able to accurately strike targets many miles away through heavily defended areas. This is why the US Air Force and Navy fire the Tomahawk CM into enemy ADA positions before sending in manned fighters.

TBMs and CMs are much cheaper to operate and maintain compared to a manned air force. The life-cycle cost of a system is dominated mainly by its operations and maintenance costs. Fuel, maintenance, and pilot training are traditionally the largest component of a manned air force's budget. In contrast, a missile force needs minimal maintenance and crew training. Advanced TBMs and CMs vary in cost and some are more expensive to initially purchase than a manned fighter, but many are less expensive and the cost is falling every day. Taken in the context of reduced operations cost, it is easy to see why many countries have opted for a missile force as opposed to a manned air force. In fact, US Air Force Lt Col David Nicholls showed that as long as CMs were shot down at a rate less than 80% in a raid, then CMs are more cost effective than a manned air force [17].

2. THE NEED FOR A NEW METHOD

"Our scientific power has outrun our spiritual power. We have guided missiles and misguided men."

- Martin Luther King, Jr.

The previous section discussed the evolution and spread of TBMs and CMs. This proliferation has increased exponentially in the last few years, particularly with CMs. This next section will show that historically the largest threat has been mainly from small raids of TBMs. Looking to the future, the trend will be to a mix of TBMs and CMs in larger sized raids. The current ADA systems and tactics are unprepared to handle large-scale attacks from a mix of these threat systems.

2.1. Historical Trends

The use of TBMs and CMs in modern war is relatively new. Due to their high expense, they were usually reserved as a strategic weapon. In modern war, advanced TBMs have only seen large-scale use in the Iran-Iraq War, the Afghan Civil War, and the two Gulf Wars. In the eight year Iran-Iraq war, a total of 189 TBMs were launched and 135 of them landed on their intended target, the city of Tehran [20]. Over the span of the 13 year Afghanistan civil war and subsequent Russian invasion, almost 2,000 TBMs were launched [20]. This is a much larger number compared to the Iran-Iraq war, but still only equates to an average of less than 13 missiles per month, and the USSR was a global super-power at the time.

Looking at more recent wars with US involvement, TBMs have seen very limited use and in very small raids. In the first Gulf war, 39 TBMs were fired at Israel. Of these 39, 27 occurred when the Patriot missile system was operational and that system achieved

a 40% success rate [20]. The 2003 Gulf War saw more variety and variability in the attacks. The diffusion of technology allowed Iraq to acquire more varied and accurate systems. In the war, Iraq launched 18 TBMs, 5 CMs, and 2 ultralight aircraft at the US and allied forces [17]. These attacks and their results are enumerated in Table 2.

The important thing to note from Table 2 is that systems other than TBMs were used. UAS technology was still in its infancy, but the success of the ultralight aircraft shows that small non-metallic aircraft can evade even the most sophisticated radar. Also note that none of the CM strikes were detected or intercepted. These CMs, flying at a low altitude or as close to the terrain as possible in a flight mode called Nap of the Earth (NOE), hid the missile in the clutter of the ground. They also indirectly caused three friendly fire incidents. The radar operators knew that CMs were a threat and that their signatures would look very much like an aircraft. These CMs were slightly smaller than the coalition aircraft operating in the region, but they have similar radar cross sections (RCSs) (see appendix A for a discussion on RCS). The CMs also flew at the same altitude and airspeed as the aircraft. Thus, when the operators saw a signature on their radar that looked like a CM and did not respond to the standard Identify Friend or Foe (IFF) interrogations, they assumed that they were CMs. This unfortunately resulted in the destruction of one radar, the downing of two aircraft, and the tragic loss of three pilots. Thus, for the first time CMs and TBMs were used to create synergetic effects. This highly complex attack is what the future of modern warfare will look like.

Table 2: Missile Threat and Response From 2003 Iraq War (Reproduced From [17])

Date / Time (z)	Threat Number + type	Apparent Targets	Response
20 March 0718	1 CM: Seersucker	Marine Camp Commando	No detection indicated, nor missile interception attempted.
20 march 0924	1 unknown missile	TAA Thunder	Missile was detected by USS *Higgins* and intercepted after three GEM missiles fired.
20 March 1030	1 BM: Ababil-100	Camp Commando and Camp Doha	Missile was detected by Air and Missile Defense Workstation (AMDWS) and intercepted after two PAC-3 missiles were fired.
20 March 2100-2200	2 BM: Ababil-100, al-Samound		Missiles not intercepted, fell into Persian Gulf.
20 March 2320	1 BM: Ababil-100	Camp Udari	Missile intercepted after one GEM and one PAC-2 were fired.
21 March 1001	1 BM: Ababil-100	TAA Fox, AlJahra	Missile was detected by AMDWS and intercepted after Kuwaiti Patriot battery fired two GEM missiles.
23 March 1547	Friendly Fire: British Tornado GR-4	Somewhere in Northern Kuwait	US Patriot PAC-2 battery misidentified friendly aircraft as a missile threat and destroyed the aircraft, killing the two pilots.
23 March	1 BM: al-Samound	Camp New Jersey	Missile was intercepted after US Patriot battery fired one PAC-2 and one GEM missile.
24 March 1035	1 BM: al-Samound	Camp Virginia and Camp New Jersey	Missile was intercepted after three GEM-Plus missiles were fired.
24 march 1342	1 BM: Ababil-100	Camp Doha	Missile was not intercepted, fell into Kuwaiti desert.
25 March 1248	1 BM: Ababil-100	Camp Commando	Missile was intercepted by Kuwaiti Patriot battery.
26 March 1250	Friendly Fire – US F-16 CJ	Patriot battery forward- to protect 3rd Infantry Division	Mistaking the F-16 for a missile threat, the Patriot's radar "painted" the F-16, which in turn fired on the radar, damaging it. The Patriot battery, reportedly, was operating on automatic.
26 March 1658	1 BM: Ababil-100		Missile blew up shortly after launch without causing damage.
27 March 0831	1 BM: Ababil-100	Coalition Forces Land Component Headquarters	Missile was intercepted by US and Kuwaiti batteries after four GEM missiles were fired.
27 March 2056	1 BM: Ababil-100 or FROG-7	Northern Iraq	Missile was not intercepted and landed in the desert.
28 March 2250	1 CM: Seersucker	Struck shopping mall outside Kuwait City	Press reports indicate no detection and no interception.
28 March	2 manned ultralights	US Army encampment South of Baghdad	No detection until two penetrating aircraft were directly over encampment. Tracked by avengers, but no interception attempted due to delay in execution authority.
29 March 1500	1 BM: FROG-7	Northern Kuwait	Missile was not intercepted, fell into desert.
1 April 0603	1 BM: al-Samound	Forced in LSA Bushmaster	US Patriot battery intercepted the missile with one PAC-3 interceptor.
1 April	1 unknown missile		Missile was not intercepted.
1 April	3 CM: Seersucker		Missiles were not intercepted, landed near Iraq-Kuwait border.
2 April	Friendly Fire – US F/A-18C	Near Karbala	A US Patriot battery misidentified the F/A-18 as a threatening missile and destroyed the aircraft, killing the pilot.
3 April	3BM: FROG-7		Missiles were not intercepted, landed in An Najaf.

2.2. The Future and the Threat of a Complex Attack

A complex attack is an attack from more than one threat system. In the context of the ADA systems, this is an attack from one or more types of systems: TBMs, CMs, UAVs, and aircraft. Typically the raids will consist of TBMs and CMs since these are the less expensive to maintain than a manned air force, and UAVs typically carry a very small payload and are used for surveillance. Note that within each of these types there can also be several different categories. The TBMs can include a mix of SRBMs and MRBMs. Each of these will approach the target at a different angle and speed.

For a ballistic missile, at the normal intercept attitudes (0-60 km), these speeds can range from 2-3 km/s at sea level, or Mach 5.8 to 8.7 [21]. See Figure 5 below, which shows the re-entry velocity v. altitude of various reentry vehicles (RVs) at different TBM coefficients (β). The TBM coefficient is roughly equivalent to a flat plate drag index. The approach angle, as measured from the horizon, is typically 45-90 degrees.

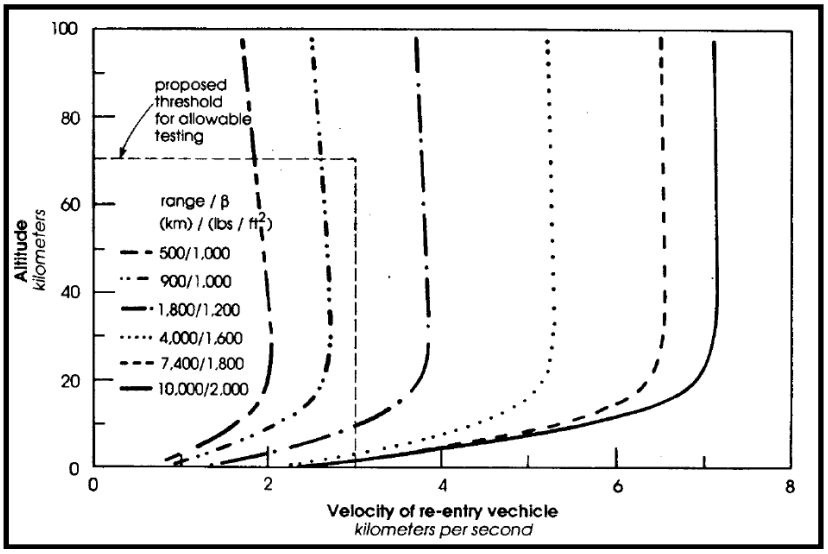

Figure 5: Reentry Vehicle Speeds for Ballistic Missiles (Image From [21])

A CM is typically sub-sonic although new variants are being designed for supersonic or even hypersonic cruise [22]. The approach angle for these is much less

than that of a TBM, typically 0-20 degrees. CMs have the added advantage of being able to use aerodynamic forces to bank and turn. This means that CMs can approach a target from many angles including directly behind the ADA radar systems.

The TBM and CM threats will be timed to all arrive at the same time, but at various speeds, altitudes, and directions. Each of these systems will also have very different RCS values (see appendix A), which mean they will be detected at different ranges. The difference in attack profiles, speed, and size is what makes defeating these complex attacks much harder than an attack from TBMs only.

The results of these attacks also vary significantly from system to system. Typically, TBMs carry a larger payload than CMs. This means that the TBMs are able to deliver larger blast and fragmentation damage than CMs [23]. Although they deliver a smaller payload, CMs are more maneuverable and generally more accurate than TBMs. This is due to advanced avionics, the ability to update its position in flight, and the slower speed allows for more advanced seekers. This makes CMs more accurate than TBMs [24].

The large diversity in the speed and RCS of TBMs and CMs also affects the ADA system's engagement window. This is the time or distance from where the ADA system can begin engaging the threat to the time it must stop. The start of the engagement window is generally limited to either the maximum range of the weapon or the maximum range at which the radar can reliably detect the target. The minimum engagement range is generally limited to either the minimum range of the weapon or the time/distance where the ADA system stops the engagements because the target is handed off to another system. Because the TBMs generally have a smaller RCS and travel faster than the CM,

they will have a smaller engagement window than CMs [25]. These characteristics are summarized in Table 3 below.

Table 3: TBM and CM Characteristics

Characteristic		TBM	CM
Explosive Payload		Large	Small
Accuracy		Low	High
Engagement Window	Speed	Fast	Slow
	RCS	Small	Large
	Resulting Engagement Window	Short	Long

To date, most academic analysis involving ADA has focused almost exclusively on TBMs only [26-38]. Large TBMs were the main threat, especially to the mainland US, during the Cold War. Only recently has the technology proliferated to allow many countries to operate a sizable CM force [17]. As a result, most ADA systems were designed to face a TBM threat, not necessarily a CM threat, and definitely not a combined threat from both TBMs and CMs arriving simultaneously. A raid made up of TBMs and CMs will have systems with vastly different RCS values, so detection of all targets simultaneously is not guaranteed. Only a few recent studies have considered the detection aspect of the missile defense problem along with the target allocation problem. A majority of these studies involved TBMs only, and did not consider a complex raid that included CMs [39-46].

The increased difficulty of combating a complex attack creates a capability gap for many military force's ADA units. The ADA systems were designed to defeat smaller uniform raids, but not necessarily the larger mixed raids that can be expected in the future. In order to close this capability gap, military planners and leaders must consider both material and non-material solutions.

2.3. JCIDS and the DOTMLPF Solutions

Within the DoD, the Joint Capabilities Integration Development Systems (JCIDS) process helps planners and leaders understand the solution space for a given problem or capability gap. This solution space can involve any combination of available resources: Doctrine, Organization, Training, Material, Leadership and Education, Personnel, and Facilities (DOTMLPF) [47]. Sometimes Policy is also included (DOTMLPF-P). If policy is not included, then it is assumed to be part of Leadership and Education. These elements of the solution space are abbreviated DOTMLPF, but lately the DoD has changed the abbreviation to DOTmLPF with a "little m" to emphasize that a material solution should be considered only after all other elements have been shown incapable of closing the capability gap [48].

The JCIDS process is shown below in Figure 6. In this diagram, once a capability gap is identified, it must first be vetted against all the areas of DOTmLPF and if a solution is found, it is documented in a DOTmLPF Change Request (DCR) of the Capabilities Based Assessment (CBA). Only after all non-material solutions are exhausted is a material acquisition process started with the Initial Capabilities Document (ICD) and the Material Development Decision (MDD).

The material acquisition process then proceeds through milestone (MS) A-C. MS A decision is the initial investment decision. This is a decision on whether to pursue product or design concepts and commit resources (human and monetary) to the maturation of the concept both technologically and conceptually [49]. MS B is the development decision that commits resources to award contracts in order to develop and produce prototypes of the system for testing [49]. MS B initiates an acquisition program

[50]. MS C is the initial production decision to enter low-rate initial production of the system [49]. Reference [48] contains more information on the JCIDS process, the acquisition process, and how each fits into the larger joint force analysis.

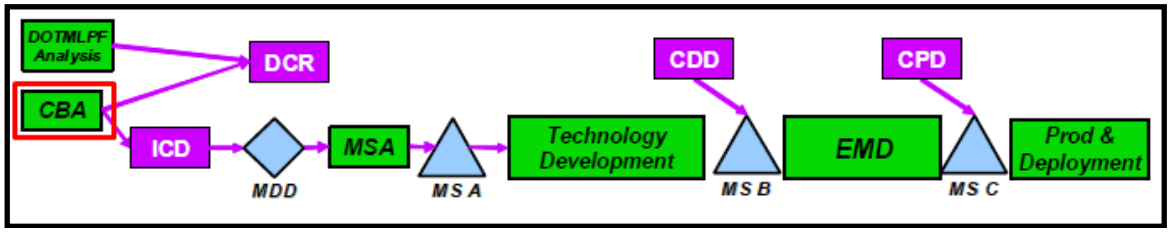

Figure 6: DoD Acquisition / JCIDS Process (Image From [51])

The emphasis of this process is to force leaders and planners to look at non-material solutions first. The material solution was often the first thing people turned to in order to close a capability gap, but that solution is generally more expensive compared with other DOTmLPF solutions. Most other solutions involve changing the organizational structure or leveraging other already available resources to fix a problem.

Going straight to a material solution is recognized throughout the Army and DoD as a problem. Lieutenant General David Mann, the head of Army Space and Missile Command, stated that "we will never heave enough interceptors, we need to add a level of sophistication to the way we look at the threat [52]." The late Major General John Rossi, the former commander of the Army Fires Center of Excellence, stated the problem even more precisely when he said: "I get a lot of offers to consider tools and technology. I get less on, 'Here's a concept on how to employ what you have in a different way to gain some advantages,' because when there's limited resources, you're not going to get a whole lot more [52]." The proliferation of missile technology and the threat of a complex attack have caused a capability gap in many country's ADA forces. Only a relatively few studies in the literature have considered the cost along with the optimization of the

defense [29, 53, 54]. In this era of shrinking defense budgets, this capability gap needs to be addressed by changes in our tactics or organization before a new ADA system is developed, and in both cases the cost of the defense must be considered.

2.4. ADA System Analysis Simulation: EADSIM

In the CBA shown in Figure 6, as well as the analysis supporting each MS decision, is conducted with the use of computer simulations. ADA systems and their interceptors are very expensive. Typically, only a small number of tests are conducted each year with actual systems. A majority of the testing of tactics and the evaluation of new systems is done digitally through computer simulations [46]. One of the primary computer simulations used throughout DoD is the Extended Air Defense Simulation (EADSIM). Teledyne Brown Engineering (TBE) maintains EADSIM and the Missile Defense Agency (MDA) is the executive agent for the program. EADSIM is the accredited ADA simulation program for DoD, meaning that it has been validated and verified. Within the DoD, the users of the program include: the Center for Army Analysis, the Army Fires Center of Excellence, the Office of the Secretary of Defense (OSD) Simulation Analysis Center (SAC), Air Force A9, Navy N81, US Central Command (CENTCOM), US Strategic Command (STRATCOM), and the Missile Defense Agency (MDA). It is also used by over 350 agencies in over 31 countries. The model is continuously updated by TBE based on user requests and funding in order to ensure that it is up to date with the latest innovations and remains useful for emerging threats. The framework of the EADSIM program is summarized in Figure 7 below.

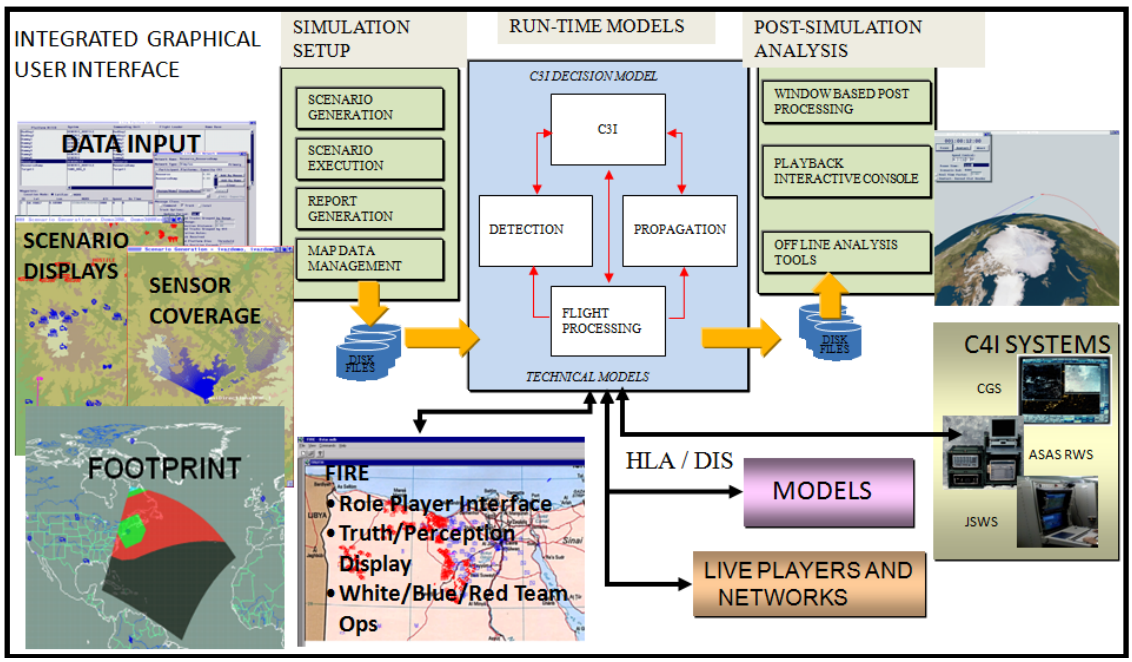

Figure 7: EADSIM Program Framework (Image From [55])

Systems within EADSIM are modeled as a collection of individual elements with a rule set that the user modifies to fit the role of the individual system. Each aircraft, missile, and ground system is individually modeled and tracked within the simulation environment [55].

The main advantages of EADSIM are that it has an advanced radar model and flight dynamics model built into the program. This allows for targets to be dynamically detected and tracked. EADSIM also has the ability to account for target RCS fluctuations and degradations. Swerling models (see appendix A) can be used to model target RCS fluctuations and additional detection degradations can be used to account for terrain and range or speed ambiguities. The different Swerling models and RCSs used for TBMs and CMs will mean that each individual missile will be detected at different ranges. EADSIM also has the capability to dynamically model the Pk of a system based on the target-shooter pair, range to the target, and altitude of the target. In addition, it is also

able to model the communications between systems and is able to allow a simulated commander to dynamically allocate targets among his subordinate systems.

The main disadvantages of EADSIM are its long the run time and storage requirements. EADSIM is a stochastic simulation. Therefore, many Monte Carlo runs are required for each simulation input vector. A single simulation run on a standard desktop can take anywhere from minutes for simple models to hours for complex campaign length scenarios. This means that a 30 run Monte Carlo can take hours to days to complete. The storage requirements are also very large. A 30 Monte Carlo run for a campaign length scenario can produce 2-3 gigabytes of data. These files must be post-processed in order to extract the information relevant for a particular study and analysis question.

Due to all of its advantages, and because it is the DoD accredited model, EADSIM is the simulation software that is used to support the analysis in the CBA and MS decisions illustrated in Figure 6. However, due to its disadvantages in setup and run time, only a handful of cases are typically developed and simulated. Additionally, the JCIDS process specifies that an approved concept of the operations (CONOPS) must be used [48]. Because the entire decision space cannot be simulated, the tactics tested are limited and typically based on the currently accepted tactics. With a new system or a new threat, these tactics may not remain optimal.

2.5. The Enemy Fire Plan and Damage from Leakers

In most higher fidelity ADA simulations like EADSIM, the enemy missile fire plan is pre-scripted. The missile fire plan is the number, type, launch location, launch time, and target set of the TBMs and CMs that the ADA systems will try to defend

against. In most of these simulations, the ADA system's results and demonstrated capability are highly dependent on that initial fire plan. In most analyses, however, only one fire plan is tested. Many times it is not known if this fire plan represents the maximum capabilities of the enemy force or if it is optimized to achieve a desired effect. Even in the literature there are relatively few studies that have considered the optimization of the enemy fire plan along with the optimization of the ADA defense [30, 56].

A single fire plan is typically used for two main reasons. First, the JCIDS process specifies that the CBA should use the Defense Planning Scenarios (DPS) for long-term scenarios, or developed operations plans (OPLAN) for near-term scenarios [50, 57]. The time horizon for the development of a new system typically dictates a long-term scenario, so the DPS are typically used over the OPLANs. Many times only a single fire plan is specified in the DPS, and there is little justification given for why that one particular fire plan is included. Second, there is no established model to articulate why one fire plan may be more optimal than another. This is because the DoD does not have a large-scale accredited damage effects model that will specify the damage to a large target made up of small and different individual targets such as an airfield, port, or assembly area from an enemy missile attack. The Joint Weaponeering System is the accredited weapons effects model used by the DoD, but typically it only models the damage against a single target or small target group with similar characteristics [58, 59].

Because there is no model to describe the effects, most analyses simply try to minimize the number of leakers – the threats that are not shot down and impact the target area. In the past, minimizing the number of leakers was sufficient because with small

and uniform raids, the damage was highly correlated to the number of leakers. In the future, this may not be the case due to the differences in the speed, accuracy, engagement window, and payload of TBMs and CMs as expressed in Table 3. This diversity means that the capability of the ADA system to defend against each missile type is different and the effects of leakers from each missile type are different.

Using a single fire plan or a fire plan that is assigned without prior analysis and forethought ignores the differences in the capabilities of different types of TBMs and CMs. Because the outcome of an ADA simulation is so highly dependent on the initial fire plan, without the proper analysis of the fire plan, the overall analysis of the ADA system may not be optimal. This will be demonstrated in the next chapter.

3. MOTIVATING EXAMPLE

"As you know, you go to war with the Army you have. They're not the Army you might want or wish to have at a later time."

- Donald Rumsfeld, former US Secretary of Defense

The previous chapter showed that the systems and doctrine of the ADA forces has been developed to face small raids composed of TBMs only due to the fact that this was the historical threat. The rapid advancement and proliferation of both TBM and CM technology means that in the future, that same ADA force will face larger raids made up of both TBMs and CMs. This creates a capability gap in the ADA force. To solve this, the JCIDS process demands that analysts consider all aspects of the DOTmLPF framework and look at non-material solutions before deciding that a new material approach is needed.

The testing of these DOTmLPF solutions will be conducted with high fidelity ADA simulations, such as the DoD accredited simulation program EADSIM, due to the high costs of live tests. Within EADSIM, the enemy fire plan is pre-scripted, so considerable thought must be placed into the development of that fire plan. This chapter will show how changes in the ADA system's tactics and enemy fire plan can result in large changes in the number of missiles that are not intercepted and impact the ground – commonly called leakers. Using this example, it will then summarize the current problems with the existing methodology.

3.1. ADA Doctrine Example

Three of the most common ADA tactics that are examined include the firing doctrine, the interceptor-target pairing, and the hand-off altitudes or ranges. The firing

doctrine is the number of missiles that are simultaneously shot at a target in a salvo. The interceptor-target pairing is the selection of the interceptor to use against each incoming target [60]. For ADA systems that can engage both TBMs and CMs, the hand-off altitude is the altitude where the systems stop engaging TBMs and shift their focus to CMs.

The most commonly varied ADA tactic in the literature is the firing doctrine. The ADA system can use a shoot-look-shoot (SLS) doctrine, sometimes referred to as a shoot-1 doctrine, or a shoot-shoot-look (SSL) doctrine, sometimes referred to as a shoot-2 doctrine. The SLS doctrine means that one interceptor is shot at a given incoming missile and the operator then waits to see what the result of that intercept is before deciding on the next action. If the missile is not destroyed, then the operator can attempt to shoot another interceptor if there is time. The SSL fire doctrine means that two interceptors are fired in a salvo and the operator looks to see the effect of both of these interceptors. If both are not successful and the incoming missile is not destroyed, then the operator can shoot two more interceptors if there is time [61].

The advantage of the SSL fire doctrine is that by shooting two interceptors the combined probability of kill (Pk) is larger than a single interceptor's Pk. This assumes that one interceptor hit is sufficient. In essence, both interceptors have to miss in order for the missile to survive. Thus, for a given number of interceptors, *n*, the combined Pk is given by [38]:

$$Pk_{combined} = 1 - (1 - Pk)^n$$

This equation simply says that the combined Pk is one minus the probability of all interceptors missing. Traditionally, ADA systems have used SLS for CM

engagements and SSL for TBM engagements, except when the cost of the interceptor is very high. If this is the case, then some ADA systems will use a SLS strategy against TBMs.

The interceptor-target pairing is important because many ADA systems have a number of different interceptors available to shoot at each target. These interceptors have their own unique advantages and disadvantages, as well as different costs and inventory levels. An interceptor that is optimized to engage TBMs at a great distance may have its own internal seeker. This allows the interceptor to find the target without the aid of the ground-based radar, since radar detection power decreases as distance to the fourth power (see appendix A). This would increase the Pk of the interceptor against certain TBMs. However, the advanced technology of an internal seeker will typically make the interceptor more expensive than one that relies on the ground-based radar for guidance.

The hand-off altitude determines the engagement window for the TBMs and CMs (see section 2.2 for a description of the engagement window). A higher hand-off altitude will shrink the engagement window against TBMs, but increase the engagement window against CMs. A lower hand-off altitude will do the opposite. A smaller engagement window means that there are fewer opportunities to engage all threats. With a large number of threats, too small of an engagement window might also mean that some threats cannot be engaged, since the ADA system is typically limited in the number of interceptors it can control in flight simultaneously. Finally, if an interceptor does not hit its target, too small of an engagement window can also mean that the target cannot be reengaged a subsequent time.

To illustrate just how these three tactical options can change the number of leakers and the number of interceptors fired, a 300 run Monte Carlo simulation was conducted in EADSIM. This test scenario was for an attack with 10 TBMs and 10 CMs arriving simultaneously against a target that is being defended by a single ADA system with 40 interceptors of one type (Interceptor A) and 40 interceptors of another type (Interceptor B).

Using this test scenario for all cases, the effects of a change in shot doctrine and interceptor selection are shown below in Figure 8. The first and second rows of the figure show histograms of the number of cases with different quantities of TBM and CM leakers. The third row shows a histogram of the cases with different quantities of interceptors fired. The left column corresponds to a SSL shot doctrine while the middle column corresponds to a SLS shot doctrine. The right column is a SLS fire doctrine with a different interceptor choice.

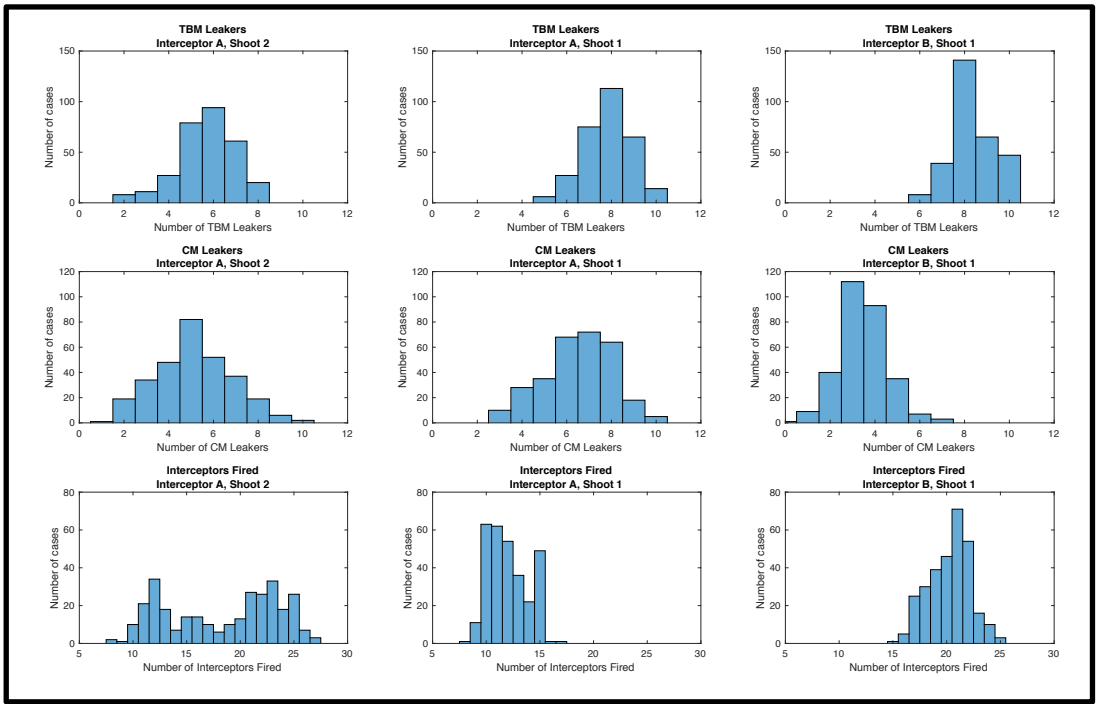

Figure 8: Test Case for Change in ADA Shot Doctrine and Interceptor Choice

Looking at the first two columns of Figure 8, a change in shot doctrine from SSL (left column) to SLS (middle column) resulted in an increase in TBM and CM leakers, but a large decrease in the number of interceptors fired. Likewise, looking at the two right columns, a change from Interceptor A (middle column) to Interceptor B (right column) resulted in a decrease in the number of CM leakers with a slight increase in the number of TBM leakers. The number of interceptors fired, however, increased substantially.

These results beg the question of whether or not the change in the number of leakers results in significantly more or less damage. Section 2.2 showed that TBMs are less accurate than CMs, but deliver more explosive power. Does the decrease in TBM leakers with a SSL doctrine result in significantly less damage? Is this enough to justify the large increase in the number, and therefore the cost, of the interceptors fired? Likewise, does the decrease in the number of CM leakers and increase in TBM leakers with a change from Interceptor A to Interceptor B significantly change the damage resulting from the attack? Does this change in tactics offset the cost change from the increase in the number of interceptors fired? Without a damage effects model, an analyst cannot accurately express the results for each attack. This is especially true since one set of tactics decreases the number of TBM leakers, while another decreases the number of CM leakers. Which leakers are more dangerous and at what point does the damage become statistically different or unacceptable to the commander? With a large attack made up of two or more dissimilar weapons, simply minimizing the number of leakers is no longer sufficient. The analyst must be able to express the resulting damage from those leakers.

A similar analysis can be conducted for a change in the hand-off altitude. In this test case, the ADA system has a TBM engagement window from 10,000-20,000 meters. Figure 9 below shows the results from changing the hand-off altitude from 18,000 meters (high hand-off altitude) to 12,000 meters (low hand-off altitude). The first and second rows show histograms of the number of cases with a given number of TBM or CM leakers. The third row is a histogram of the number of interceptors fired.

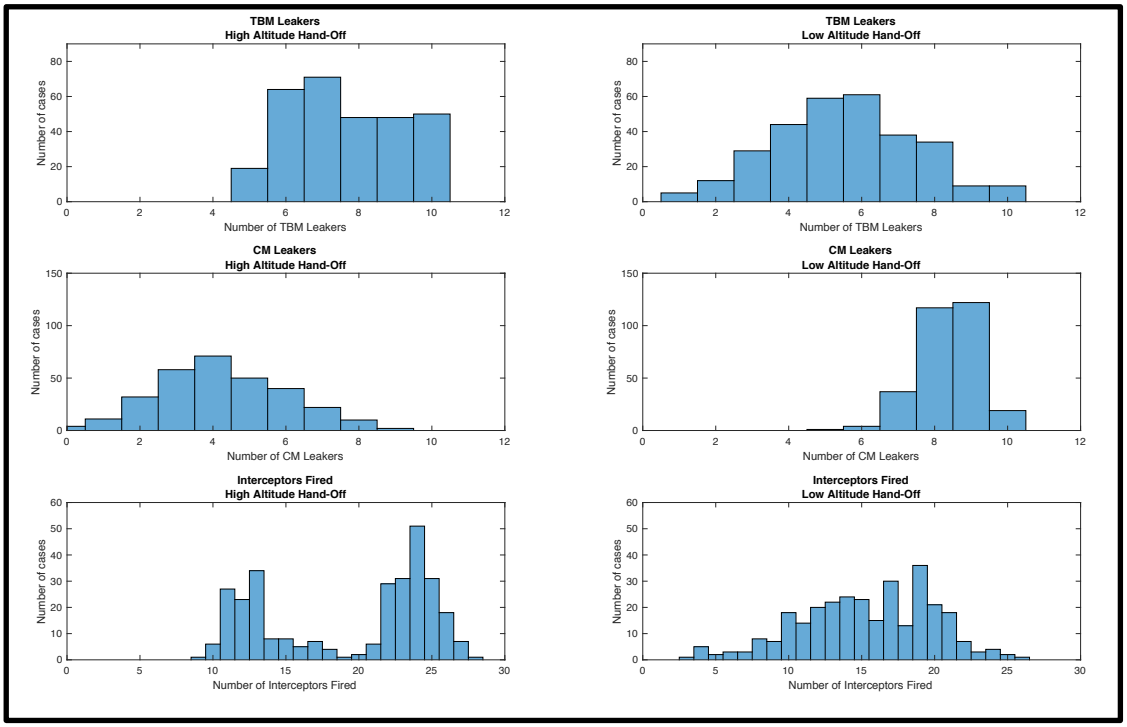

Figure 9: Test Case for a Change in Hand-Off Altitude

As expected, the higher hand-off altitude (left column) shows a greater number of TBM leakers with a small number of CMs leakers. This is because the higher hand-off altitude increases the engagement window against CMs at the expense of the engagement window against TBMs. The lower hand-off altitude (right column) shows the opposite. The average number of interceptors fired in each case is about equal, but the higher hand-off altitude shows a bi-model distribution likely due to the SSL shot doctrine used against

the TBMs. If the radar detected the TBMs early, the engagement window was sometimes large enough to allow a small number of reengagements against TBMs that were missed during their first engagement.

Once again, these results show the need for a damage effects model. The hand-off altitude directly affects the number of TBM and CM leakers. Changing the hand-off altitude increases one type of leakers while decreasing the other. Without knowing which of these missiles causes more damage, the analyst might conclude that a mid-range altitude is best, so that no one missile type has a larger number of leakers. The flaw in this logic is that the damage caused by the two missile types is not necessarily equal (as per Table 3). The question that must be answered is does a greater number of TBM leakers cause more damage than a greater number of CM leakers?

These two case studies also highlight the dilemma in optimizing the ADA doctrine. A change in fire doctrine, interceptor-target pairing, or hand-off altitude causes different amounts of TBM and CM leakers and different amounts, and therefore cost, of interceptors fired. This simple example did not include the complexity of a multi-layered defense, which is what most ADA forces maintain. In a multi-layer defense the analyst must also consider the hand-off altitude between layers, as well as the fire doctrine and weapon-target pairing of each system. Without a structured and fast running simulation, the resulting large design space cannot adequately be explored and the analyst is left to rely on historical data and tactics, or simple deviations from the historical tactics.

3.2. Enemy Fire Plan Example

The number of leakers is also highly sensitive to the initial enemy fire plan. The enemy fire plan is the number, type, launch location, launch time, and target set of the

TBMs and CMs. The number of leakers is highly correlated to the number of initial missiles fired. Typically, a greater number of incoming missiles results in a greater number of leakers. However, even for equally sized raids, the type of TBMs or CMs in a raid can affect the number of leakers. Each TBM and CM has a different trajectory, flight pattern, and RCS. This means that each one will be detected at a different time and the time from interceptor launch to interceptor impact will vary for each missile. Each TBM and CM also has different susceptibility to a given interceptor, which results in a different Pk for each interceptor-target pairing. A good overview of the Pk and damage from a weapon's impact, blast, or shrapnel is given by Driels [62].

In order to illustrate this point, Figure 10 shows the results of a 300 run Monte Carlo simulation with EADSIM for three test cases of raids made up of 10 total TBMs and 10 total CMs. Two different types of TBMs were used in this scenario. TBM1 had a high and fast trajectory, while TBM2 had a shallow and relatively slow trajectory. There were also two different types of CMs. CM1 was a slower and larger CM, while CM2 was a faster and smaller CM. The first column shows histograms for the number of runs that had a given number of TBM leakers (top row) and a given number of CM leakers (bottom row) for a raid made up of 10 TBM1 missiles and 10 CM1 missiles. The second column shows the histograms the number of cases that had a given number of leakers for a raid made up of 10 TBM2 missiles and 10 CM2 missiles using the same ADA tactics from the first column.

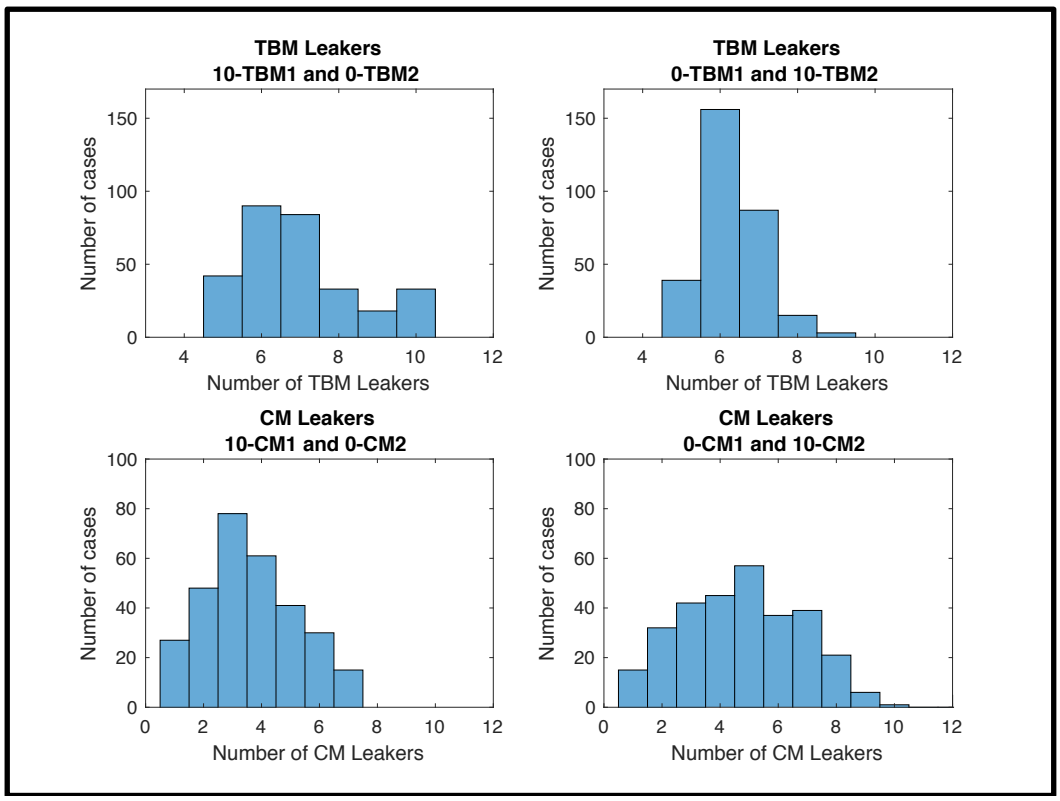

Figure 10: Test Case for Different TBMs and CMs Used in Similarly Sized Raids

These results show that even for a similarly sized raid, the number of leakers is dependent on the type of inbound missile. Looking first at TBM leakers (first row), a raid made up of only TBM2 missiles tended to have a smaller number of leakers and a smaller variation in the number of leakers, than a raid made up of TBM1 missiles. The second row shows that a raid made up of CM2 missiles was likely to have more leakers and a larger variation in the number of leakers, than a raid made up for CM1 missiles.

This analysis did not consider the cost or inventory of each missile. The enemy missile commander must balance the cost and inventory with the damage he or she hopes to create. TBMs and CMs are used to enable other actions on the battlefield. For an attack on an airfield, the purpose of the TBMs and CMs may be to shut down the airfield long enough to stop aircraft from interfering with a main effort attack. Likewise, an

attack on a port could be meant to stop the flow of supplies long enough to halt an enemy advance. Without a weapons effects model it is difficult to know how many TBM and CM leakers are required to ensure a high probability of success for either of these two actions. The enemy fire plan should fire just enough missiles of each type to ensure a high probability of success in order to preserve the limited missile inventory for other targets throughout the campaign. In wartime, the enemy missile force will likely conduct this pre-mission analysis, so the ADA analyst must do the same before optimizing the ADA tactics.

A similar tradeoff can also be shown for the release altitude of submunitions from a missile. TBMs and CMs typically carry two different types of warheads: unitary and submunitions. A unitary warhead contains all the explosive power in a single container. This delivers a larger amount of damage to a single impact point. A submunition warhead releases many smaller bomblets at a given release altitude. These bomblets then spread out as they fall from the release point to the ground. This delivers a large number of small blasts over an area. The spread of the submunitions is directly correlated to the release altitude [63]. In addition, most ADA interceptors cannot defeat the submunitions once they are released from the TBM or CM. This means that the higher the submunition release altitude, the lower the likelihood that the TBM will be intercepted before it can drop its bomblets. For CMs, however, a higher release altitude means that the CM must cruise to the target at a higher altitude. This means that the CM crosses the radar horizon sooner and is more susceptible to being detected and destroyed.

The effect of different submunition release altitudes is illustrated in Figure 11. This figure shows the results from a 300 run Monte Carlo simulation in EADSIM for a

raid made up of 10 TBMs and 10 CMs each carrying submunitions. The left column shows the histograms for the number of cases that had a given number of TBM leakers (top row) and CM leakers (bottom row) for a low altitude submunition release (12,000 meters for TBMs and 20 meters for CMs). The second column shows the same histograms for a high altitude submunition release (18,000 meters for TBMs and 170 meters for CMs).

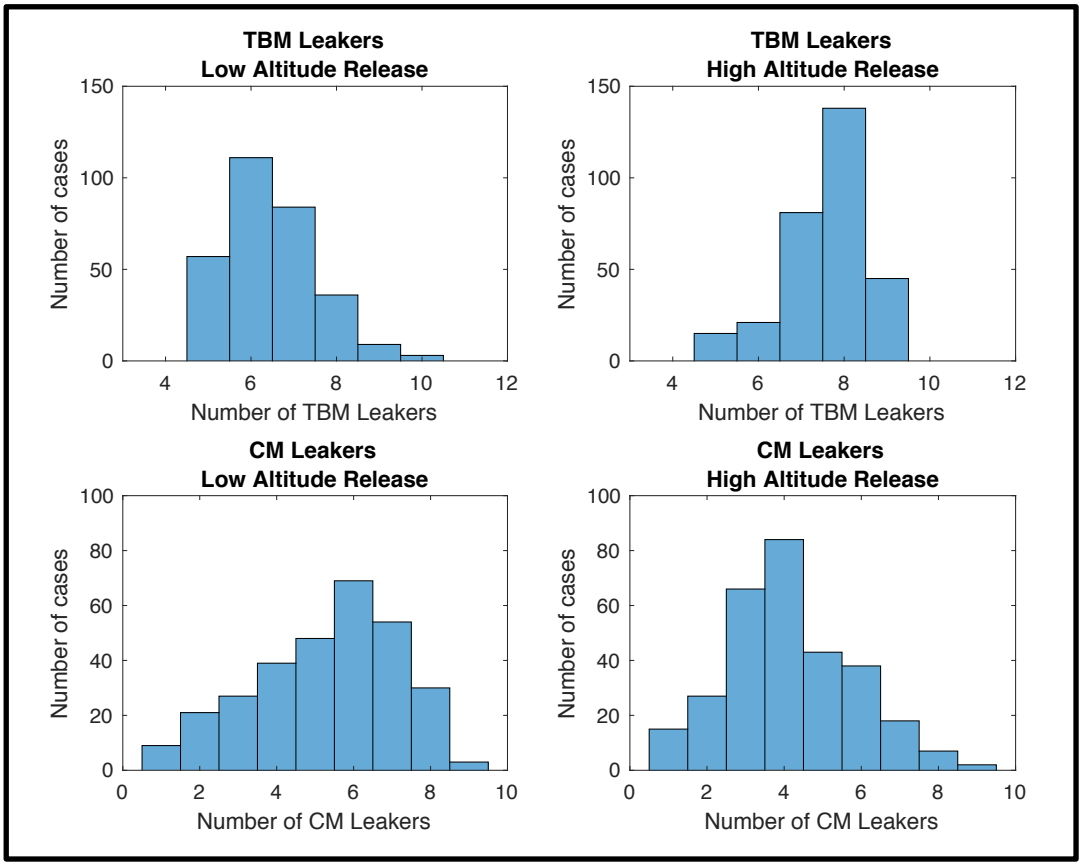

Figure 11: Test Cast for Different Submunition Release Altitudes of TBMs and CMs

As expected, the lower release altitude resulted in less TBM leakers than the higher TBM release altitude. The effect was the opposite for CMs. A higher release altitude resulted in less CM leakers due to the increased susceptibility of the CM at the higher cruise altitude. Looking at only these results, an analyst might conclude that

TBMs should release their submunitions as high as possible and CMs should release their submunitions as low as possible. However, this ignores the spread of those submunitions and the resulting damage. If released too high, the submunitions from a TBM might disperse so far that the resulting damage does not achieve the desired effect. A weapons' damage effects model coupled to an ADA model is needed to balance the Pk change from a higher release altitude with the spread and damage from the submunitions.

A weapons' damage effects model coupled to the ADA model can ensure that the enemy fire plan is optimized to maximize the damage resulting from submunition and unitary warheads delivered by different TBM and CM types. Due to competing demands to cause damage to different target sets, there will likely be many optimal fire plans depending on the enemy forces commander's goals for maximizing damage, minimizing the number of missiles in a raid to keep inventory levels high, and minimizing the cost of the missiles fired.

3.3. Problem Statement

The proliferation of TBM and CM technology is accelerating. The cost of these systems is decreasing, allowing more and more countries to purchase them in large quantities. The threat from a large complex attack of TBMs and CMs is an emerging threat that creates a capability gap in most ADA forces.

The JCIDS process demands that non-material solutions be considered before any new material solution, so there is an immediate need to use the current ADA systems in a more effective manner. The ADA simulations that are used to test these systems have enough fidelity to reliably test different tactics or systems, but their long run times and setup times, coupled with their large data storage needs makes them too cumbersome for

this task. In addition, the absence of a damage effects model means that analysts cannot adequately express the effects of leakers in order to ensure that the initial enemy fire plan is optimized. The lack of a damage effects model also means that analysts cannot show how a change in ADA tactics or organization results in a change to the damage that leakers cause to the defended assets. These challenges can be categorized into three general problem statements:

- Problem 1: There is no established method or model to either describe the damage to a target from missiles that leak through the ADA defenses or to optimize the enemy fire plan to achieve certain effects against a target.
    - Problem 1.a: Historically, analyses relied on minimizing the number of leakers, but the diversity of a complex threat means that the greatest number of leakers may not represent the largest amount of damage to specific area of the target.
    - Problem 1.b: ADA system's analysis is highly sensitive to the initial enemy fire plan. If this plan is not optimized first, then the resulting ADA system's optimization may not be correct.
- Problem 2: New tactics are needed against large complex raids made up of both TBMs and CMs that enables the ADA systems to minimize the damage to the defended asset for the lowest cost.
    - Problem 2.a: There is no historical framework for a large complex raid composed of many different missile types.

- Problem 2.b: The current fiscal environment and the JCIDS process demand that non-material solutions be considered before the development of a new ADA system.

- Problem 3: Due to the high cost of ADA systems and their interceptors, testing is typically done in high fidelity computer simulations. These high fidelity models are difficult to use in trade-studies due to their long run times and storage requirements. These models also only count the number of leakers and do not estimate the damage from those leakers.
  - Problem 3.a: A new simulation method is needed that maintains close to the same level of accuracy as the high fidelity simulations, but runs at least an order of magnitude faster, so that it can be used in trade studies.
  - Problem 3.b: This new simulation should link the ADA simulations to the damage effects models.

4. RESEARCH OBJECTIVES, QUESTIONS, AND HYPOTHESIS

"No problem can withstand the assault of sustained thinking."
- Voltaire, French writer and philosopher

The premise of this research is twofold. First, there is not an integrated ADA model that will allow for rapid trade studies of different tactics, organization structures, or systems while still maintaining a level of accuracy comparable to higher fidelity simulations. Secondly, there is also not an established simulation to assess the damage and effects of a missile attack on a large target set, such an airbase or seaport. As a result, the changes in ADA doctrine or organization cannot be mapped to changes in the damage done to friendly assets, and the enemy fire plan cannot be optimized to achieve damage to these different areas of the target set.

The first problem creates a gap in ADA systems because historically conflicts involving missiles have used small raids of TBMs, thus the ADA doctrine has been optimized to fight this legacy threat. However, the rapid proliferation of missile technology may lead to future conflicts that involve large raids made up of a mixture of these systems. A new method is needed to test doctrine of the current ADA systems and trade doctrine with system capabilities in order to meet this new threat.

In most of the recent literature, the studies look at only a single threat type, and a vast majority of the studies deal with TBMs only. A small percentage of the studies look at defense against aircraft, but virtually none have examined the optimal defense against CMs. The current ADA systems and doctrine were designed around small raids of mostly TBMs. The doctrine is not designed to handle large raids of TBMs and CMs together. In addition, the doctrine is not optimized to maximize the defense while

minimizing the cost. The JCIDS process demands all non-material solutions be explored before new system capabilities. There is no simulation or analytical tool that exists to rapidly explore the effects of changes in doctrine with system capabilities.

The second problem creates an issue with ADA analysis in general. Because there is no model that allows analysts determine what are the effects of the threats that "leak" through the friendly defenses, analysts attempt to minimize the number of leakers. The number of leakers is not nearly as important as the effects those leakers have on friendly operations. A weapons effect models will also allow an analyst to develop a good enemy fire plan. Most studies in the literature do not have a good analytical underpinning to the number of enemy missiles used in the analysis.

In order to address these problems, this research will have three major objectives. The first objective is to develop a tool for analyzing the effects of leakers. This tool is needed in order to optimize the enemy fire plan and to express how changes in the ADA systems' tactics and organization translate to damage done to the defended asset. Once created, it can then be used to test the theory that minimization of the aggregate number of leakers equates to minimization of the damage to the defended asset.

Objective 1: Determine a method to merge existing tools for ballistics, cratering in concrete, and weapons effects to create a program that will optimize the enemy fire plan to create the most damage to runways, POL sites, and aircraft for a set number of cruise and ballistic missiles as opposed to simply maximizing the number of leakers.

Research Question 1: Will a fire plan optimized to achieve a given effect (destruction of aircraft, POL sites, or runway) be the fire plan with the greatest number of leakers?

Hypothesis 1: A fire plan weighted with CMs, as opposed to TBMs, will destroy more point targets such as POL sites and aircraft. A fire plan weighted with TBMs, as opposed to CMs, will destroy more area targets, such as the runway. These will not necessarily be the fire plans with the most leakers.

The second objective is to create a framework that will guide analysts through optimization of the enemy fire plan, then investigating non-material changes in the ADA system in order to close any capability gaps, before examining potential material solutions. The solutions from this methodology must also include the cost of the defense, since ADA systems are generally one of the highest costing systems in a military force. In a protracted conflict, the ADA system's interceptors will have to be used in a manner that will give an adequate level of protection to the defended asset while preserving the number of interceptors so that they are available throughout the length of the campaign. This framework should be based on higher fidelity simulations and the results reproducible in these simulations. These higher fidelity simulations are the agreed upon method for analysis since actual testing of ADA systems is generally too expensive.

Objective 2: Determine a method to close existing ADA capability gaps through changes to organization and/or doctrine against a given set of complex threats, at a given location, and for a given a set of ADA systems, that will optimize the defense at the lowest cost.

Research Question 2: Will the proposed method allow for rapid optimization tactics against a complex attack that is reproducible in the higher fidelity simulation?

Hypothesis 2: When the optimized result from the proposed method is tested in the higher fidelity simulations there will be a reduced amount of damage to the airfield for an equal or lower cost as compared to the base case, with a 95% confidence level.

The final objective is to determine a method to reproduce the results of the higher fidelity ADA simulation and damage effects model proposed in objective one, but in a much more rapid manner. The higher fidelity simulations take minutes to hours for a single run of the input vector and because they are stochastic, many runs are required to understand the output range. In most cases, the large design space in these simulations cannot be proven to be convex, so gradient-based optimization methods cannot be used to find the global optimum. This means that a stochastic optimization method is required. Stochastic optimization methods require many function calls, so their use necessitates a faster running model. This last objective and research question will attempt to show that the outputs from these simulations can be modeled with known distributions and the

shape parameters of these distributions can be predicted with machine learning techniques. Once trained, the machine learning techniques can predict an output in fractions of a second. If these outputs are the shape factors of a known distribution, then the entire output space can rapidly be described.

Objective 3: Determine a method that combines ADA simulations and weapons effect simulations such that the method maintains the same accuracy as high fidelity models, but runs at least an order of magnitude faster.

Research Question 3: Can machine learning accurately predict stochastic high fidelity air defense and weapons effects simulation outputs?

Hypothesis 3: Space filling designs of experiments coupled with predictive models will be able to predict the shape factors for the distributions of the outputs of higher fidelity models. They will be able to do this to such an extent that more than 95% of validation cases pass the chi-squared test at a 99% confidence level and will run at least an order of magnitude faster.

5. PROPOSED FRAMEWORK AND MODELS

"I think that only daring speculations can lead us further and not the accumulation of facts."

- Albert Einstein

In order to address the problems and objectives outlined in the previous two chapters, a new framework if needed for ADA analysis. This new framework should link ADA simulation tools to analytically based damage effects models. This new framework should also maintain the robustness and accuracy of large scale vetted models, but should allow different tactics and organization to be rapidly tested. These tactics should minimize cost while simultaneously maximizing the defense of the defended assets. Finally, this new framework should allow rapid tradeoffs between system capabilities and tactics in order to close capability gaps. The framework developed in this dissertation to meet all these goals is called the ADA doctrine, organization, and systems optimization (ADOSO) framework

5.1. New Framework: ADOSO

The general methodology for the new framework, ADOSO, is shown in Figure 12. The process starts with the rectangle on the top, labeled "Develop Enemy Fire Plan Based on Effects." This is the first major goal of the process. For any given effect and enemy missile set, there are numerous combinations of munitions that will achieve the tactical effect that is mapped to the desired operational or strategic level effect; however, not every combination of weapons will be optimal. The goal of this first step is optimize the enemy fire plan to achieve different outcomes. These fire plans are then are carried through to the following steps.

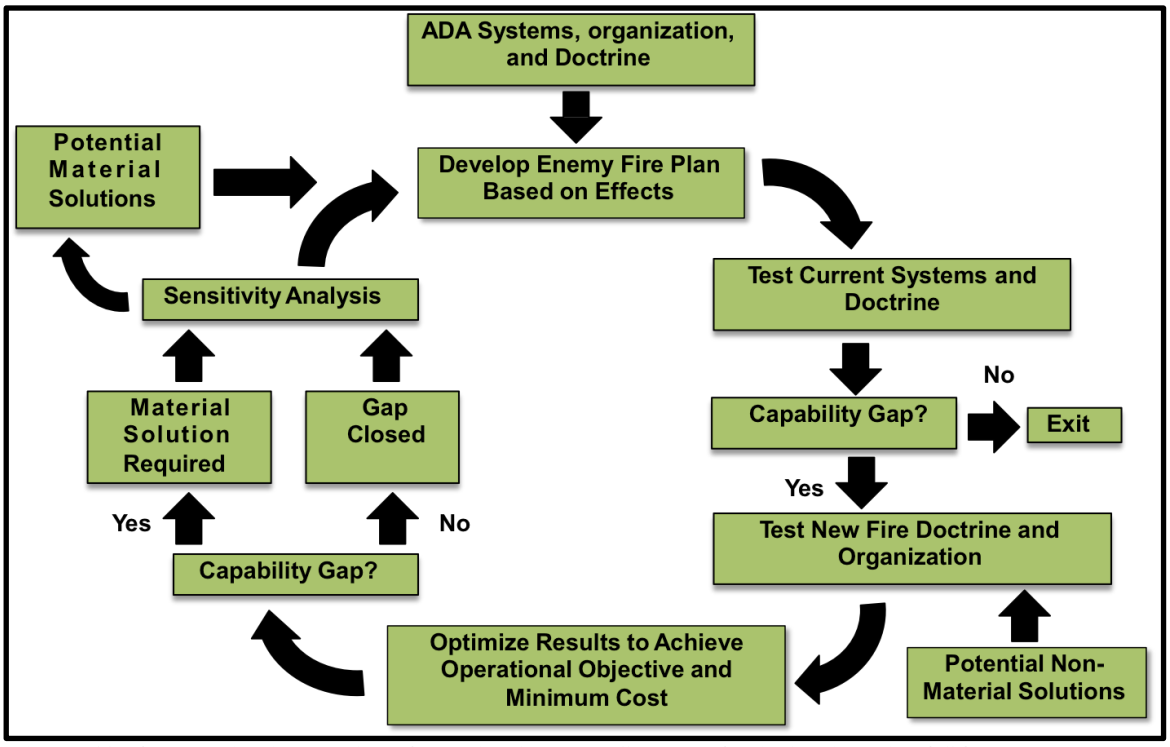

Figure 12: Overall ADA Doctrine, Organization, and Systems Optimization (ADOSO) Framework

Once these fire plans are created, the process continues clockwise where the current systems and current doctrine are tested against those fire plans to determine if a capability gap exists. This capability gap is quantified by a significant departure from the commander's desired protection levels and tactical requirements. For example, if the commander states that the longest an airport can be closed due to a missile attack is one hour, than an aggregate mean across all the attack plans that is longer than this requirement would be a capability gap.

Assuming that a capability gap does exit, ADOSO initially examines non-material solutions in accordance with the DOTmLPF framework. In this problem, the non-material DOTmLPF solutions will be either doctrine and/or organization. In order to close the capability gap, a range of cases for different firing doctrine and different organizational structures is established and tested against a range of enemy fire plans.

These cases are then optimized. This optimization takes place at the bottom of Figure 12. Again, if the aggregate mean of the effect is still significantly deviated from the commander's objective then the capability gap still exists. If this is not the case, then the gap can be closed through a non-material solution.

In both cases, if the capability gap is closed or still remains open, a sensitivity analysis is needed to highlight the robustness of the proposed solution. If the gap is closed, then the sensitivity analysis will show how sensitive the outcome is to the doctrine, organization, and fire plan so that the commander can factor this into his or her risk analysis. If the gap cannot be closed and a material solution is required, this sensitivity analysis will show the types of capabilities the new product will require and the risk associated with each level of capability.

5.2. Integration of the New Framework into the JCIDS Process

The CBA of the JCIDS process shown in Figure 6 is comprised of three separate steps: the functional area analysis (FAA), functional needs analysis (FNA), and functional solutions analysis (FSA) [50, 64]. These steps are sequential and are shown below in Figure 13.

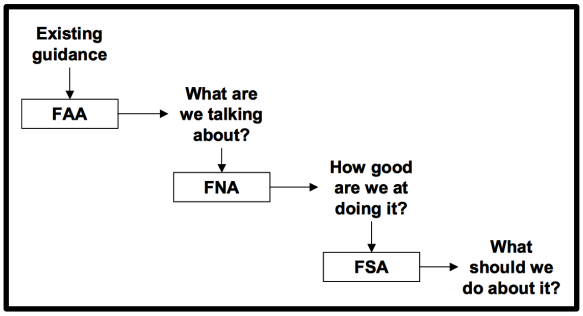

Figure 13: Capability Based Assessment (CBA) Steps (Image From [64])

The FAA examines the operational environment by synthesizing presidential and DoD guidance and specifies the problem and scenario to be studied. The FNA then determines how well existing and programmed capabilities, structure, and doctrine can address the problem defined by the FAA. The output of the FAA is a set of capability gaps that must be addressed. The FSA then examines the DOTmLPF solutions for these capability gaps [50, 64]. A good solution should not only close the capability gap, but should also be affordable (cost), feasible (technologically and policy), and strategically responsive (delivers solutions when needed against the entire threat identified in the FAA) [64]. The steps of the FSA as well as the overall breakdown of the FAA, FNA, and FSA within the CBA are shown below in Figure 14.

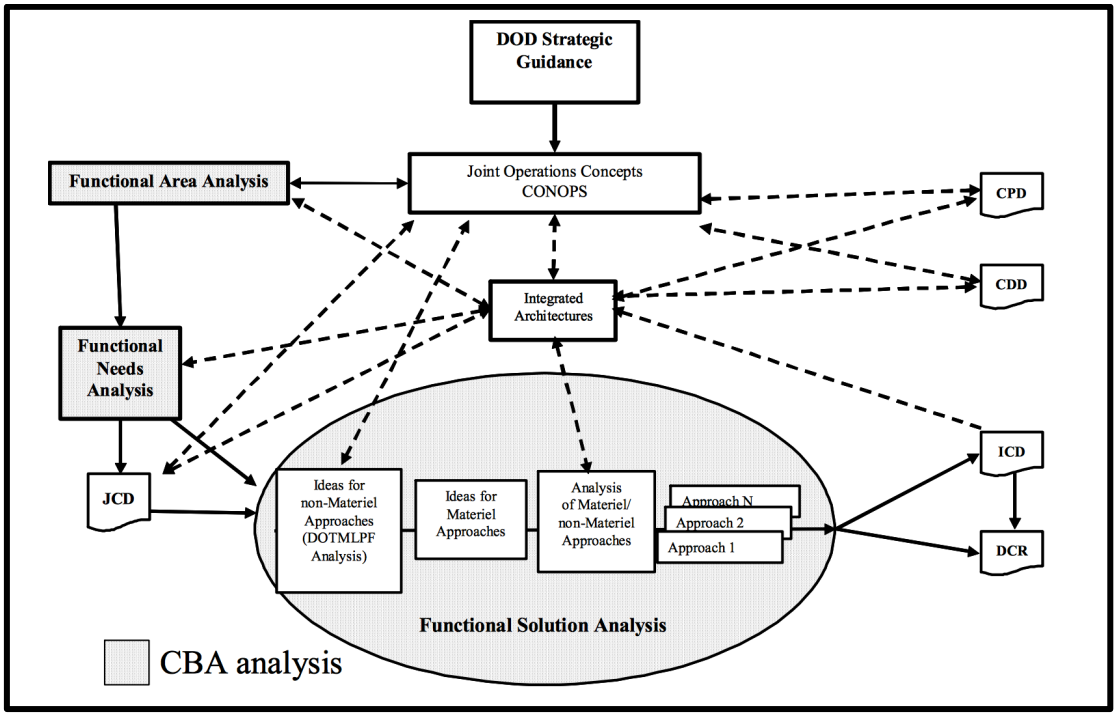

Figure 14: Steps of the Capability Based Analysis (Image From [64])

The ADOSO methodology proposed in Figure 12 facilitates the FSA process by first examining the non-material solutions and then examining material solutions only if

the gap is not closed with a non-material solution. In addition, by first optimizing the enemy fire plan, it ensures that the solution is strategically responsive against the missile force of the threat. If a cost model is also included, then the new methodology meets all the requirements of the FSA: affordability, feasibility, and strategically responsive. The complete integration of the new method within the CBA and FSA is shown below in Figure 15.

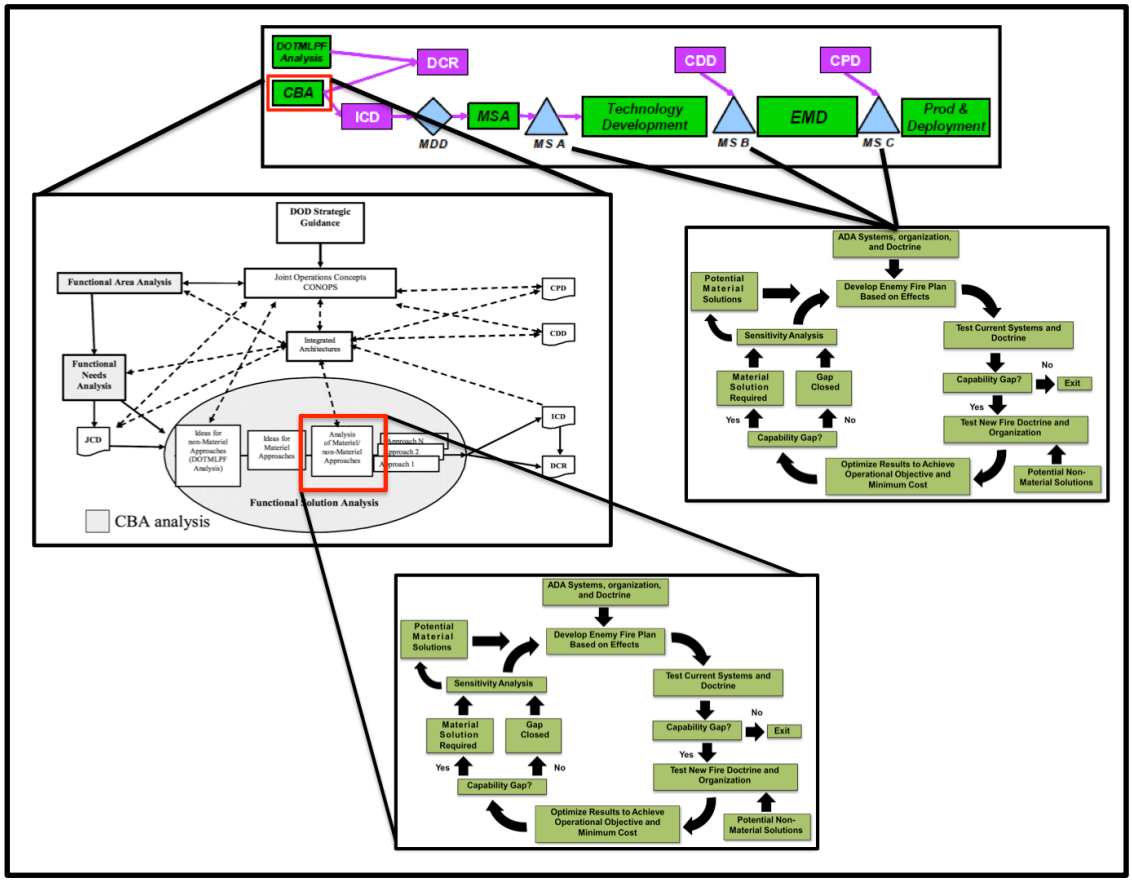

Figure 15: ADOSO Methodology Within the JCIDS Framework

In addition to being used in the FSA, the new framework also facilitates MS decisions. These are the blue triangles in Figure 15. Each MS decision determines whether to continue the program to the next phase, modify the program, or terminate it. Each of these MS decisions involves a review of the merits and costs of the system.

Because ADA systems are typically too expensive to conduct large-scale testing, a majority of the testing is done in simulation and hardware in the loop tests. These tests lead to greater understanding of the capabilities of the new system.

The increased knowledge of the system's capabilities necessitates that previous analysis is revisited and analyzed to determine if the initial assumptions for the capability of a new system are different than what the current testing shows. If this is the case, then the ADOSO framework can be used to optimize the enemy fire plan again to account for the new capability. Once this is complete, the doctrine and organization of the ADA forces can be re-optimized to ensure that the new system still meets the feasibility, affordability, and strategic responsiveness criteria.

5.3. The Use of Surrogate Models in the New Framework

The ADOSO framework is iterative. It loops back upon itself because the enemy force will constantly adjust their methods, systems, and doctrine to what they perceive as the tactics that the ADA system will employ. Thus, as soon as a new material or non-material solution is implemented, then the fire plan used to create and test that solution is no longer valid. Instead, the enemy fire plan model must be re-optimized and the new solutions tested against the newly optimized enemy fire plan. Because many simulation runs are needed for this process, a method is needed to replicate the results of higher fidelity simulations at a much faster pace, while still maintaining the same level of accuracy. This is realized through the use of designs of experiments (DOEs) and surrogate models. An overview of DOEs and surrogate models is given in Appendix B and C. Their application to the fire plan is explained in section 6.3 and 6.5, and their application to the ADA simulation is explained in section 7.7.

6. AIRFIELD AND RUNWAY DAMAGE MODELS

"I think frugality drives innovation, just like other constraints do. One of the only ways to get out of a tight box is to invent your way out."
- Jeff Bezos, founder and CEO, Amazon.com

The first step of the new ADOSO methodology is to optimize the enemy fire plan. As explored and stated previously, most analysis of missile defense uses the number of leakers, or missiles that are not shot down, as the measure of effectiveness. When raids were small, uniform, and composed primarily of ballistic missiles, this measure worked reasonably well since the expected damage could be easily calculated from a known missile quantity and type. Now that most raids are expected to consist of a mixture of cruise and ballistic missiles, this measure is no longer sufficient [25]. The measures of effectives must include the direct effect on friendly forces. It must show how the operations of the friendly forces are disrupted through either the destruction of combat assets or the destruction of enabling assets.

6.1. Scenario, Model, and Weapons Selections

The proliferation of CMs and UASs means that the US ADA systems will face large-scale complex attacks in future conflicts. There are no historical examples of such attacks because this proliferation has just begun to accelerate. A new analytical method is needed to generate feasible and realistic fire plans.

When a rational enemy decides to launch a combination of TBMs, CMs, and UASs, they are hoping to achieve some effect for the least amount of resources expended and at the smallest risk to their own force. TBMs and CMs are not inexpensive weapons and their use comes with risk. TBMs must be launched from a Transporter, Erector, and

Launcher (TEL) vehicle. CMs must be launched from a ground vehicle, ship, or aircraft. When launching either of these weapons the weapons themselves as well as the launch platform is subject to enemy fire. The loss of a TEL or CM launch platform obviously means that platform cannot be used in future missions.

The enemy must balance the payoff, or the benefit, of the attack with the risks and constraints or limitations. Whenever a TEL is moving or setting up for a launch it is at risk of being detected and destroyed. Limitations can range from the maximum number of TBMs or CMs an enemy can launch at a single time to the time and distance constraints to get the launch platform in position.

The benefit the enemy wants to achieve is best measured by the effects they want to see after the attack. This is known as effects based targeting. Instead of deciding to launch ten CMs from two aircraft and ten TBMs from ten TELs, the enemy will ask what effect they want to achieve and then look at multiple methods to achieve that effect. This is a subtle change in thinking, from platforms to effects, but the efficiency it brings is enormous.

For a given effect, say the destruction of a friendly asset, the enemy force first determines all ways to achieve that effect. If those ways are kinetic and involve TBMs and CMs, the enemy must determine how many assets of each type to fire in order to ensure that the desired number hit the target. Not all the missiles shot will hit the target. In addition to missing the target, some will be intercepted by friendly ADA units. Therefore, the number required must be scaled up to account for misses and intercept losses. The amount of increase due to accuracy and intercept losses is based on the accuracy of the missiles and the lethality of the defending ADA units. These are both

probabilistic in nature, so there are many options that achieve the desired effect within a given certainty.

6.1.1. Scenario Selection

The missile force is an enabler on the battlefield. The effects from a missile attack are used to enable other decisive action in the campaign. This effect will vary from target to target and across time over the campaign. These effects can also be non-material or non-military force related such as using missiles as a terror weapon or for attention grabs in the media. These effects are harder to quantify in simulation, so the effects against material and military operations will be the focus of this work. Some of the typical effects an enemy may want are listed below in Table 4. This table shows how an operational effect is mapped to a tactical effect at a given target.

Table 4: Example Target and Desired Effects from Missile Attack

Target	Desired Tactical Effect	Operational Effect
Airport	Damage Runway, fuel, or support infrastructure to prevent all takeoffs/landings for two hours. Damage aircraft to prevent use in war effort.	Degrade enemy capability to generate close air support (CAS) sorties during an operation.
Port	Damage pier structure to prevent ship unloading for six hours.	Slow the flow of forces arriving into theater via ship in order to complete an operation to secure key terrain.
Command and Control Node	Disrupt communications in order to cause a temporary halt of enemy formation.	Disrupt enemy offense long enough to allow units to establish defensive fortifications and positions.
Enemy Formation	Destroy 20% of vehicles in a defensive formation.	Degrade enemy forces prior to an attack.

The above targets and effects are just a brief example, but it shows how an enemy force has a certain operational effect it hopes to achieve by using its missile force. The enemy must calculate which tactical effect will cause the desired operational effect, then

determine what mix of capabilities will achieve the tactical effect. In this work, the attack on an airport (the first row of Table 4) will be used as the test case.

In the airbase attack, the enemy forces want to damage the runway to such an extent that they cause it to be unusable for takeoffs and landings for a certain period of time or limit the number of takeoffs and landings to an acceptable level to meet other operational goals that those aircraft might impact. Likewise, they might also choose to damage the support infrastructure such as the Petroleum, Oil, and Lubrication (POL) points to achieve the same type of degradation. Finally, they may choose to directly target the aircraft on the ground in order to destroy them before they can be used in the campaign. The friendly forces want to maintain the takeoff and landing operations on the runway, facilities at the airport, and aircraft on the ramp, so that they can launch enough aircraft at a given time to meet the needs of the Joint Force Commander. These objectives are summarized in Figure 16.

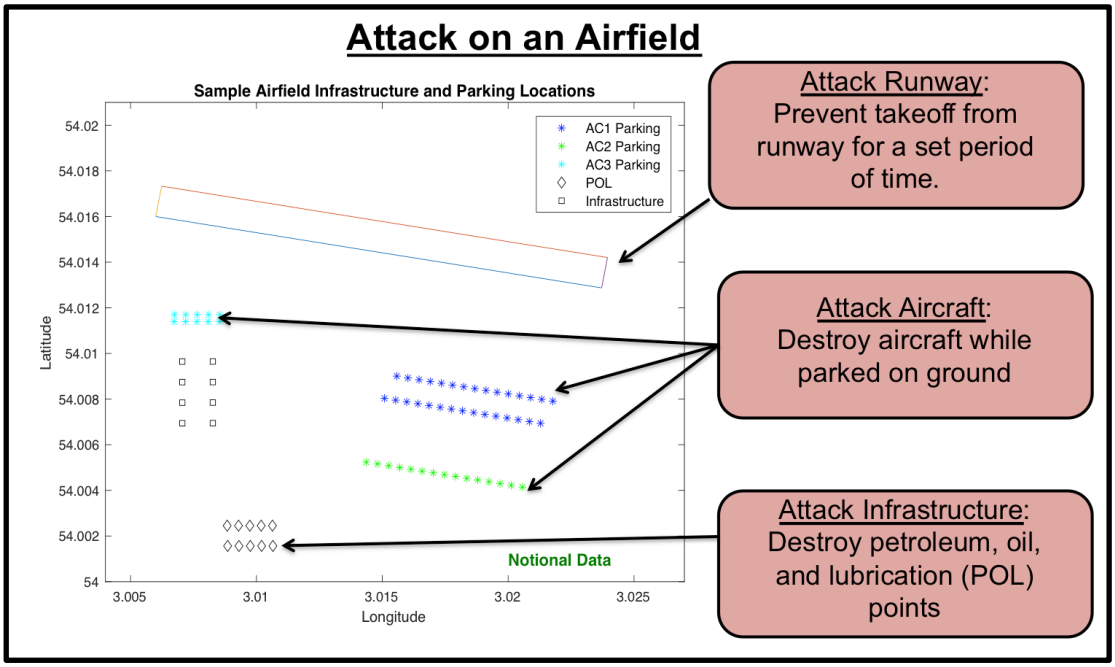

Figure 16: Attack on Airfield Enemy Objectives

Typically runways are much larger than what a single aircraft needs to take off or land. The smallest continuous and undamaged area of the runway needed for a given aircraft to takeoff and land is called the Minimum Operating Strip (MOS). Therefore, the enemy forces are attempting to damage the runway through impact craters such that the number of MOSs are below a given threshold. The friendly forces are trying to ensure that a minimum number of MOSs remain available to accomplish their missions. Note that these objectives are temporary because the friendly forces will begin repair of the runway as soon as the attack is over. This struggle is illustrated below in Figure 17.

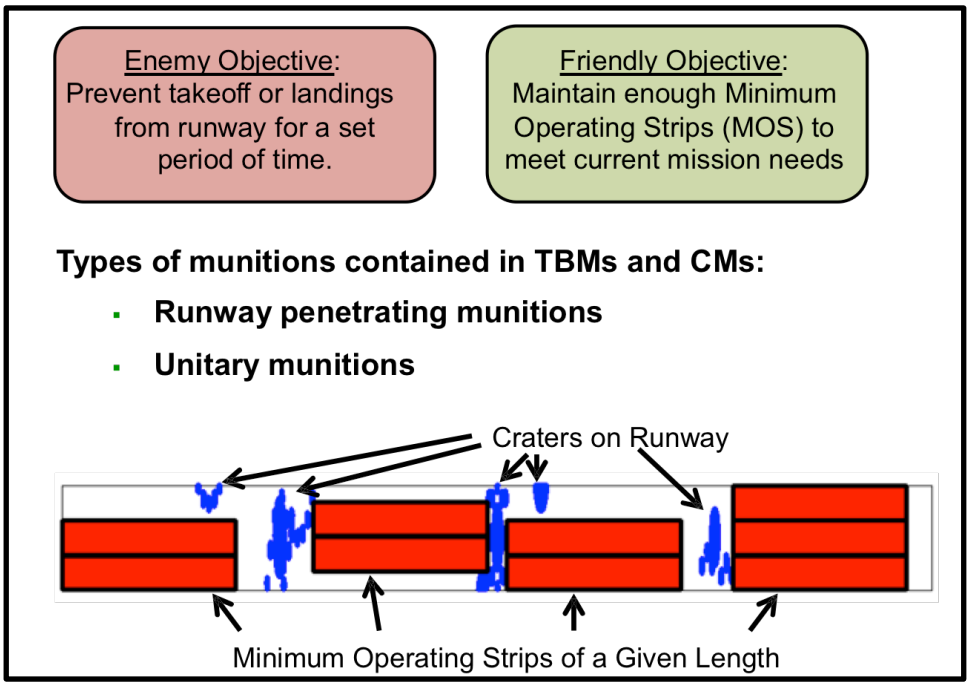

Figure 17: Attack on a Friendly Airfield Scenario: Runway Attack

The POL points and hangars are fixed based on the airfield original construction, so they are typically easier to target because they are stationary and the enemy force can use the time before hostilities to develop location and targeting data on them. Additionally, there are typically more hangars and POL points than what is needed to maintain operations for a short period of time. The hangars typically house the

maintenance facilities, parts, personnel, and equipment, and the POL points are needed to fuel the aircraft between each mission. If enough POL points or hangars are destroyed, the remaining facilities can form a bottleneck of aircraft trying to get through these facilities or if they are all destroyed then operations on the airfield will decrease or cease. The enemy forces are attempting to destroy enough hangars and POL points to reduce operations below a specific threshold for a specific amount of time. The friendly forces are trying to maintain enough of these facilities to keep operations at a level required by the Joint Forces Commander.

The last method for attacking an airfield, attacking the aircraft directly, is much more straightforward. The enemy forces recognize that it is more advantageous to destroy the aircraft on the ground than in the air. Therefore, the enemy forces wish to destroy as many aircraft as possible and the friendly forces want to minimize the number of aircraft destroyed. Unlike the fixed hangars and POL points, however, the aircraft are always moving on the airfield and airfield personnel attempt to minimize damage to them by parking them in a fashion that maximizes the minimum distance between aircraft. In this way, a single missile has a reduced chance of damaging more than one aircraft. These objectives, including the objectives for the POL and infrastructure attacks are summarized in Figure 18.

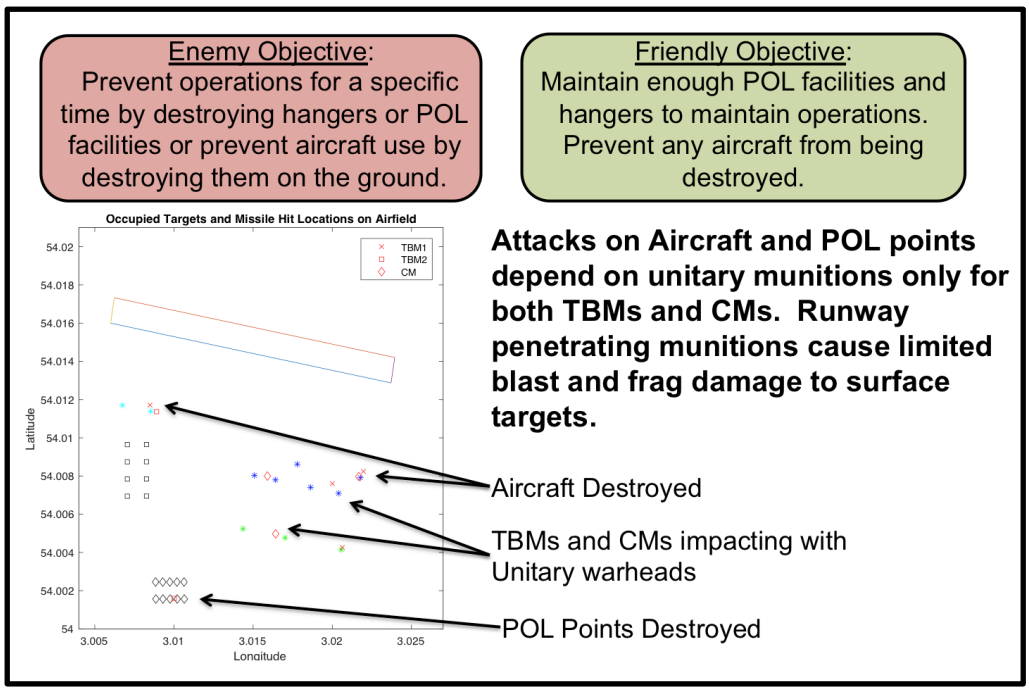

Figure 18: Attack on a Friendly Airfield Scenario: Airfield Infrastructure and Aircraft

6.1.2. Weapons Damage and Effects Model Selection

The DoD maintains several different damage models. One of the primary models used for blast and fragmentation damage is the Joint Weaponeering System (JWS) [62]. The JWS model also has modules for concrete and soil penetration. This would have made JWS an effective tool for this research, unfortunately, it is based on single engagements. The detailed setup and execution of the JWS model allows it to be used only for a single engagement against a single target of server targets close together and in a known formation. The research in this study requires a model that can estimate the damage across an entire airfield with many weapons and target pairings. Luckily, the methodology for most of the models in JWS is summarized in the book, Weaponeering: Conventional Weapon System Effectiveness by Morris Driels [62]. This dissertation will leverage the methods described in this book as well as other supporting research to

develop damage effects models that can be applied to the larger simulations with many different weapons effects happening simultaneously.

6.1.3. Scenario Weapon Selection

The enemy force has a set of missiles to use in its attack on the airfield. Each missile system has unique capabilities and weaknesses. These were enumerated in Table 3. A TBM arrives at a high rate of speed, so the AMD engagement window against it is small. They carry a large amount of explosives, but the TBMs are not very accurate. The CMs travel at a slowed speed and are usually detected from further away making the engagement window large. However, CMs are generally more accurate due to their more advanced seekers and internal guidance systems but carry a smaller sized payload.

Typically TBMs and CMs have two distinct warhead categories: unitary and submunitions. A unitary warhead has a single large explosive payload, typically tied to a point or a proximity fuse. These warheads deliver a large amount of explosive power to a single location on the ground. These types of munitions are primarily used to target the aircraft and airfield infrastructure such as the hangars and POL points, but can also cause damage to the runway.

The submunition warheads dispense many smaller "bomblets" that disperse as they fall to the ground. These smaller bomblets each have a small warhead tied to a proximity or point-detonating fuse. This type of warhead delivers a smaller amount of explosive power dispersed over a large area. In an attack on a runway, a specific type of submunition is often used called a runway-penetrating munition. In order to create a large crater in concrete, the detonation of the explosive should be within or below the pavement layer. Therefore, these munitions are designed to maintain a higher velocity as

they fall and are shaped to burrow into the concrete on impact. A delay fuse is used to delay the detonation until the munitions penetrates into the concrete layer to a certain depth (defined by a time after impact with the surface). Because the detonation is subsurface there is generally only a small amount of damage to surface targets since most of the overpressure and fragmentation is contained by the earth.

In order to properly model both a unitary and a runway-penetrating warhead, several sub-models will be required. These models include a flight dynamics model, a concrete penetration model, and a cratering model. An overall illustration of these models for each type of munition is shown below in Figure 19.

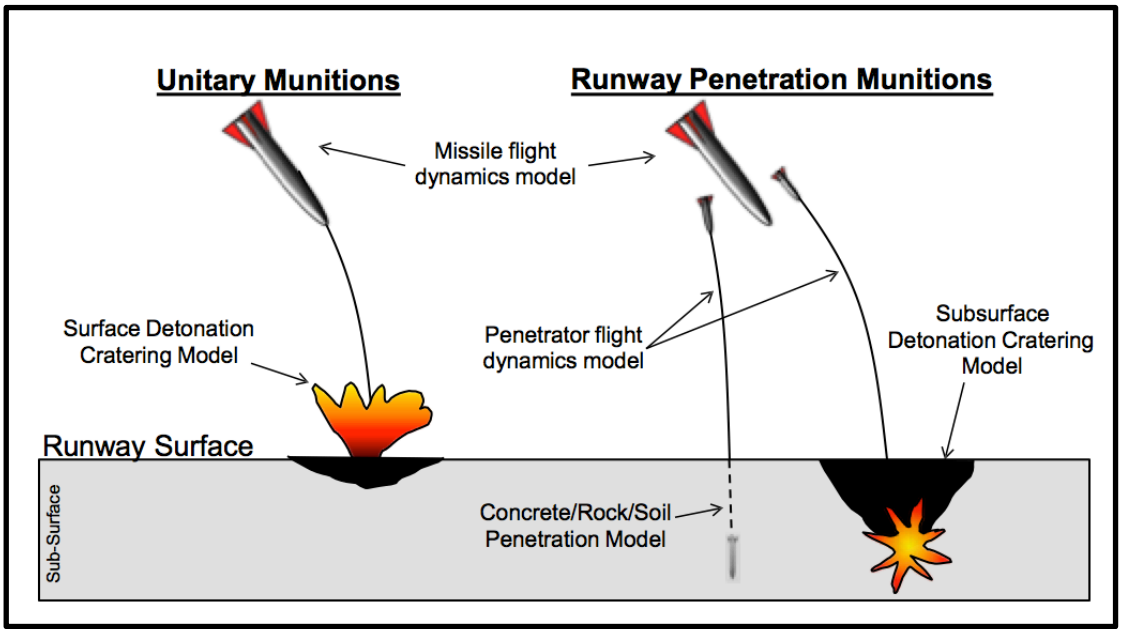

Figure 19: Airfield Effects Model for the Different Warhead Types

6.2. Runway Damage Effects Model

The overall damage to a runway caused from a series of TBM and CM attacks with different warheads can be calculated with an Airfield Effects Model. This model is composed of five main parts: the missile flight propagation model, the penetrator flight propagation model, the concrete penetration model, the cratering model, and finally, the

runway availability model. These models apply to both TBMs and CMs and for both unitary and penetrator submunition warheads; however, the unitary warhead does not use the penetrator flight or the penetrator penetration models. Also, the CMs do not use the missile flight model. A short description of each is described below, followed by a detailed explanation of the methodology. A diagram illustrating the submodels and the overall methodology is illustrated in Figure 20.

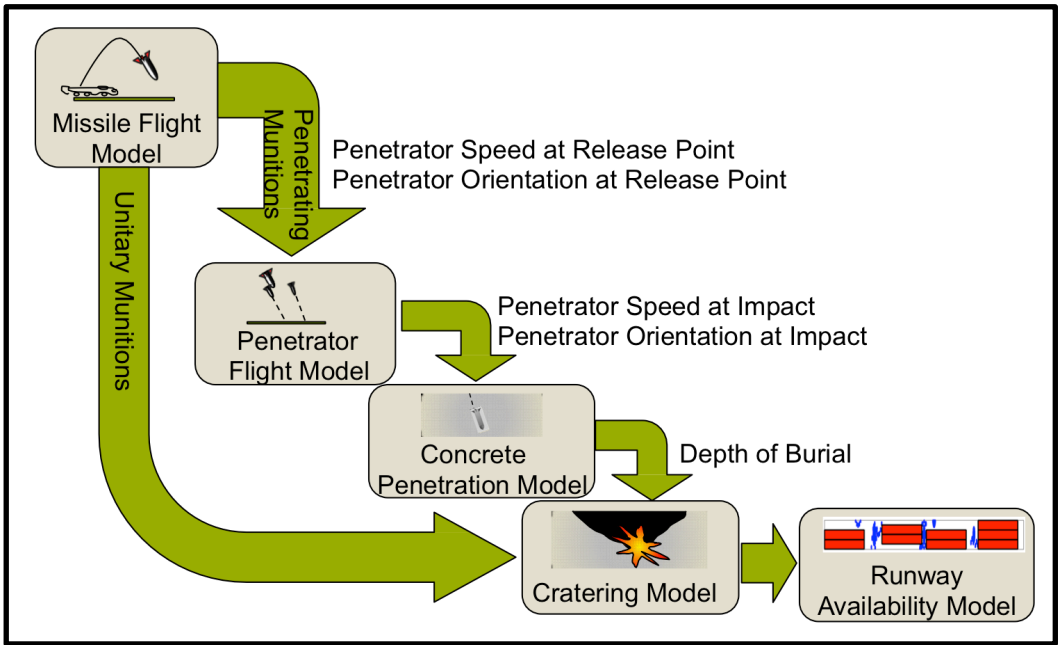

Figure 20: Runway Damage Model with Submodels and Links

The flight propagation model is a three-degrees of freedom (3-DOF) model for TBMs that propagates the TBMs from launch to impact. This is needed to determine the orientation and speed of the TBM submunition at the release point of the submunitions for penetrator warheads or at the impact point for unitary warheads. A 3-DOF model was used because the TBM reentry vehicles (RVs) are typically axisymmetric aligned to the velocity vector with little to no yaw perturbations. This means that the roll axis is inconsequential and the pitch and yaw can be determined from the angle of the velocity

vector. The main input for this model is from the EADSIM fight propagation model. For CMs, the missiles are assumed to pitch to a 45-degree downward angle when they release their submunitions.

The penetrator flight model is a six-degrees of freedom (6-DOF) model that calculates the speed and orientation of each submission from its release point to the ground. The additional three degrees of freedom (pitch, roll, and yaw) are needed, beyond the 3-DOF model used in the flight propagation model, because the runway penetration model is highly sensitive to the initial angle and velocity and impact. The additional accuracy of the 6-DOF model ensures that the follow-on concrete penetration model is accurate.

The concrete penetration model determines the depth that the submunition burrows into the concrete of the runway given its impact velocity and orientation. This model has additional modules for penetration into the rock/aggregate layer below the concrete and the soil layer below the rock. This model is important because the cratering model is highly sensitive to the depth of the explosion.

The concrete cratering model determines the size of the crater from either a detonation on the surface, for a unitary munitions, or from a detonation at a given depth, for a penetration munitions. This model describes the depth and width of a crater that is formed in the concrete from the size of the warhead, the weight of explosive, and depth of explosion.

Finally, the runway availability model uses the above models to predict the impact locations of a given set of inbound missiles. If there are runway penetrator submunitions, it then calculates the submunitions' impact points, given the carrier TBMs

impact points. Next, it determines the crater size for each impact and projects the crater outline polygons onto the larger runway rectangle. Finally, it determines the maximum number of MOS sized rectangles that can be fit fully within the overall runway rectangle without any MOS rectangle overlaying on top of another MOS rectangle or a crater polygon.

6.2.1. Runway Damage Effects Model: Missile Flight Sub-Model

A TBM motor can be fueled by either solid or liquid propellant. Typically the propellant used in liquid propelled TBMs is very caustic, so the propellant must be drained from the TBM when it is in storage. Therefore, a solid propellant TBM is easier to handle because it does not need to be fueled before the mission limiting the exposure of personnel and missile components to the fuel. This means, however, that the amount of fuel and the amount of resulting thrust that the TBM motor will produce is set at the time of manufacturing. A liquid propelled TBM can be fueled with different amounts of fuel to control the burn time. Due to the simplified handling procedures, most TBMs (SRBMs and MRBMs) are solid propelled motors. This analysis will focus on these types of missiles. Because the burn time is set, the range is controlled by the vertical launch angle. A close-range target requires a very step launch angle while a long-range target requires a relatively low launch angle. This is illustrated in Figure 21 below.

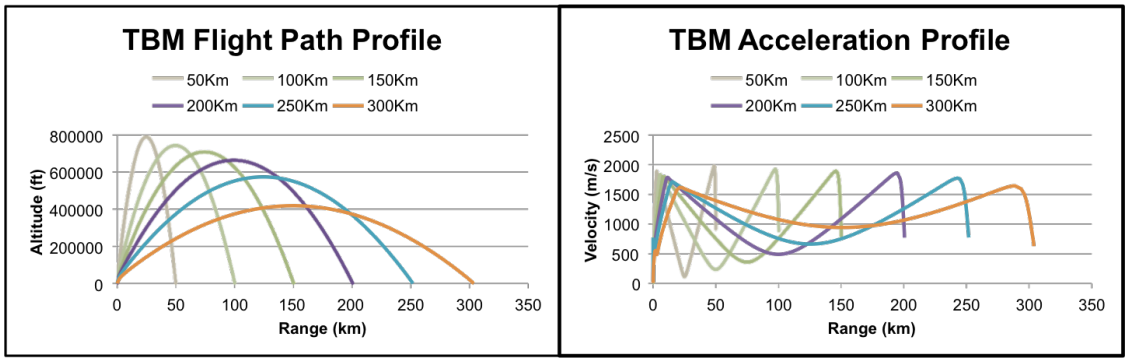

Figure 21: Solid Propellant TBM Altitude and Velocity as a Function of Target Range

The missile flight model propagates a TBM from its launch point to its impact point using a 3-DOF model. The purpose of this model is to determine the impact velocity and orientation for unitary warhead munitions or the velocity and orientation of the TBM at the release altitude for submunition warheads. For a given TBM, the orientation and velocity of that TBM at the release altitude depends on the distance from the launch point to the impact point and the release altitude. This is illustrated below in Figure 22.

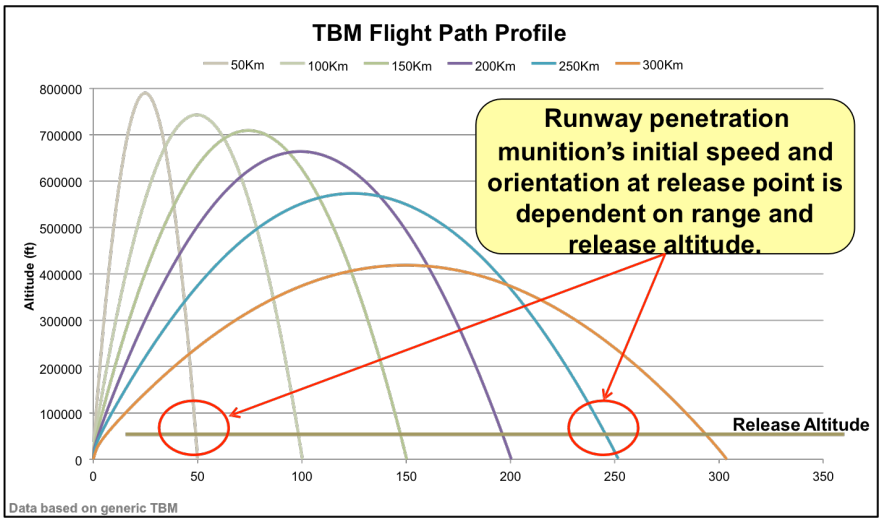

Figure 22: TBM Flight Profiles for Different Ranges

In the model selection section, EADSIM was determined as the best model for an air defense simulation. EADSIM has a built-in and validated 3-DOF missile flight

module. This research will make use of this model. Details from the EADSIM flight model are available from the playback section using the report called a trajectory report [65]. In order to produce the trajectory report, the TBM and the target must be created in a scenario, the scenario run through the EADSIM compiler, and then the scenario "played back" through the playback window. This means that to develop a set of velocity and orientation statistics for a large set of TBM ranges (distance from TBM launch point to impact point), each range will need to be run through the EADSIM scenario. Because this study uses DOEs where the range of the TBM is an input, a method was required to allow the author to quickly populate in EADSIM the TBMs at the ranges given in the DOE and then extract the relevant data for use in evaluating the surrogate models.

In order to create an instance of a TBM in EADSIM, or a platform as it is called inside the program, at a minimum that platform requires a system type (TBM type), an initial location, a target, and a launch time. The initial location must be specified in a latitude and longitude (decimal degrees) format [65]. Therefore, for a given range specified in the DOE, the latitude and longitude of the TBM must be calculated. This calculation depends on the earth model being used in EADSIM. EADSIM has the capability to use both a spherical earth and the earth model specified in the WGS84 model [55, 65].

For a spherical earth model, the haversine formula, or the spherical law of cosines, are simple formulas to find the arc length between two points of longitude and latitude [66-68]. The haversine formula is well conditioned even for small distances and is extremely accurate even for use on the actual earth. The haversine formula is given as:

$$a = sin^2\left(\frac{LatA - LatB}{2}\right) + \cos(LatA) * \cos(LatB) * sin\left(\frac{LongA - LongB}{2}\right)$$

$$c = 2 * atan2\left(\sqrt{a}, \sqrt{1-a}\right)$$

$$d = R * c$$

In this formula, the locations of the two points are given in latitude (Lat) and longitude (Long), and d is the distance between them. The spherical law of cosines is a slightly simpler version of the haversine formula and with the numerical precision of modern computers it will generally be as accurate as the haversine formula [66]. The spherical law of cosines is also easier to manipulate into other useable forms such as finding the location of a point along a bearing from a known point. Therefore, in this work, the spherical law of cosines will be used over the haversine formula. Using the spherical law of cosines, the latitude and longitude of a point along a distance and bearing from a known point can be calculated as:

$$Lat2 = \text{asin}\left(\sin(lat1) * \cos\left(\frac{d}{R}\right) + \cos(lat1) * \sin\left(\frac{d}{R}\right) * \cos(brg)\right)$$

$$Lon2 = lon1 + ATAN2\left(\sin(brg) * \sin\left(\frac{d}{R}\right) * \cos(lat1), \cos\left(\frac{d}{R}\right) - \sin(lat1) * \sin(lat2)\right)$$

In the above equations, *lat1* and *lon1* are the latitude and longitude of the start point in radians. *R* is the average radius of the earth commonly given as 6,371.22 km [66, 67]. The variable *brg* is the direction of travel from the known start point (*lat1*, *lon1*) in radians and *d* is the distance to travel along that direction. Also note that the latitude and longitude calculated for the new point (*lat2*, *lon2*) will be in radians so the answer must be converted back to decimal degrees [66].

For the WGS84 model (or any ellipsoid), the Vicenty's algorithm can be used to calculate the latitude and longitude of a point on a sphere given a starting point and an azimuth and distance (arc length) [67]. Unlike the direct formula of the spherical law of cosines, the Vicenty algorithm must be solved iteratively and requires the use of a

computer program capable of using conditional loops. The major equations of this algorithm are listed below:

Known values [69]:

a: major semiaxis of the ellipsoid (6,378.137 km for WGS84)

b: minor semiaxis of ellipsoid (6,356.752315 km for WGS84)

Vicenty Formulas [67, 69]:

$$f = \frac{a-b}{a}$$

$$u^2 = \frac{cos^2\alpha(a^2 - b^2)}{b^2}$$

$$U = \tan^{-1}\big((1-f) * \tan(lat1\big)$$

$$\tan\sigma_1 = \frac{\tan(U)}{\cos(\alpha)}$$

$$A = 1 + \frac{u^2}{16384}[4096 + u^2(-768 + u^2(320 - 175u^2))]$$

$$B = \frac{u^2}{1024}[256 + u^2(-128 + u^2(74 - 47u^2))]$$

The next three equations are solved iteratively until the difference between σ values calculated in two consecutive iterations is less than an acceptable tolerance. The initial guess for σ is: $\sigma = \frac{dis}{bA}$

$$2\sigma_m = 2\sigma_1 + \sigma$$

$$\Delta\sigma = Bsin\sigma\left[cos2\sigma_m + \frac{1}{4}B(\cos\sigma(-1 + 2cos^2 2\sigma_m)\right.$$

$$\left. - \frac{1}{6}Bcos2\sigma_m(-3 + 4sin^2\sigma)(-3 + 4cos^2 2\sigma_m))\right]$$

$$\sigma = \frac{dis}{bA} + \Delta\sigma$$

Once σ has converged, the process continue with:

$$Lat2 = ATAN2\,(\sin Ucos\sigma + cosUsin\sigma\cos(brg)\,,(1$$

$$-f)[sin^2\alpha + (sinUsin\sigma - cosUcos\sigma cos\alpha)^2]^{\frac{1}{2}})$$

$$\lambda = ATAN2\,(\sin\sigma\sin(brg)\,,cosUcos\sigma - sinUsin\sigma\cos\,(brg))$$

$$C = \frac{f}{16}cos^2\alpha[4 + f(4 - 3cos^2\alpha]$$

$$L = \lambda - (1 - C)fsin\alpha\left[\sigma + Csin\sigma[cos2\sigma_m + Ccos\sigma(-1 + 2cos^2 2\sigma_m)]\right]$$

$$Lon2 = lon1 + L$$

In the above equations, the known variables are given below. The others specified above are intermediate variables. For a description of these variables and the Vicenti algorithm see Vicenty, 1975 [70].

$lat1$	Starting point latitude in radians.	$lon1$	Starting point longitude in radians.
dis	Distance to move along the given bearing	α	Bearing from initial point in radians
$lat2$	Ending point latitude in radians.	$lon2$	Ending point longitude in radians.

Using one of the two formulas given above for either a spherical or ellipsoid earth model (whichever one is currently set to be used in EADSIM) a set of latitude and longitude points can be developed for a given set of distances from a known point as specified in the DOE.

Once the initial set of latitude and longitude points are created, the platforms can be rapidly generated in EADSIM using the "Converlay" tool. This tool comes with the normal EADSIM package and uses a csv file to rapidly generate TBM and CM platforms. Using the latitude the longitude points calculated above, each TBM was coded with the convertlay tool and established in an EADSIM scenario. For this initial run of the DOE,

terrain should not play a role in the TBM's flight calculations. The terrain will be taken into account in later modeling, but this initial DOE should ignore the effects of terrain, therefore the EADSIM model and the initial point (target) can be chosen outside of any map and terrain data loaded into the EADSIM program. A screen shot from one of the author's DOE creation runs is shown in Figure 23. This shows the TEL icons in a north-south line at the distances from a target (shown in blue to the South) specified from the DOE.

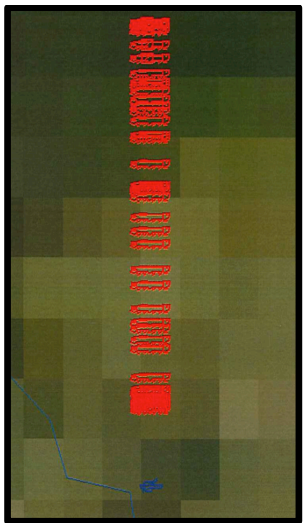

Figure 23: Screen Shot of EADSIM Range Runs

Once the EADSIM platforms are created and the simulation is run through the EADSIM compiler, the trajectory report can be generated for all the missiles shot in the simulation using the trajectory extractor report. The critical data needed out of this report is the missile position, velocity, altitude (in MSL or AGL since they will be equal with no terrain data), heading, and orientation. EADSIM is also capable of producing other data, but the data listed will be used later in subsequent calculations. A screenshot of the trajectory report generation tool is shown below in Figure 24.

The trajectory report that is generated will be saved to the disk in a ".txt" format. On occasion, EADSIM will fail to "fly" certain missiles. This only happens occasionally

and when it does happen it is usually just one or two missiles out of several hundred. It is not known why this occurs and calls to Teledyne Brown Engineering could not solve the phenomenon. To help catch this, the author generated a MATALB code that checks for missing flight data. When this occurs, one can go back into the scenario generation and move the TEL by 0.00001 degrees of latitude and rerun the scenario. This typically solves the mysterious no-fly problem.

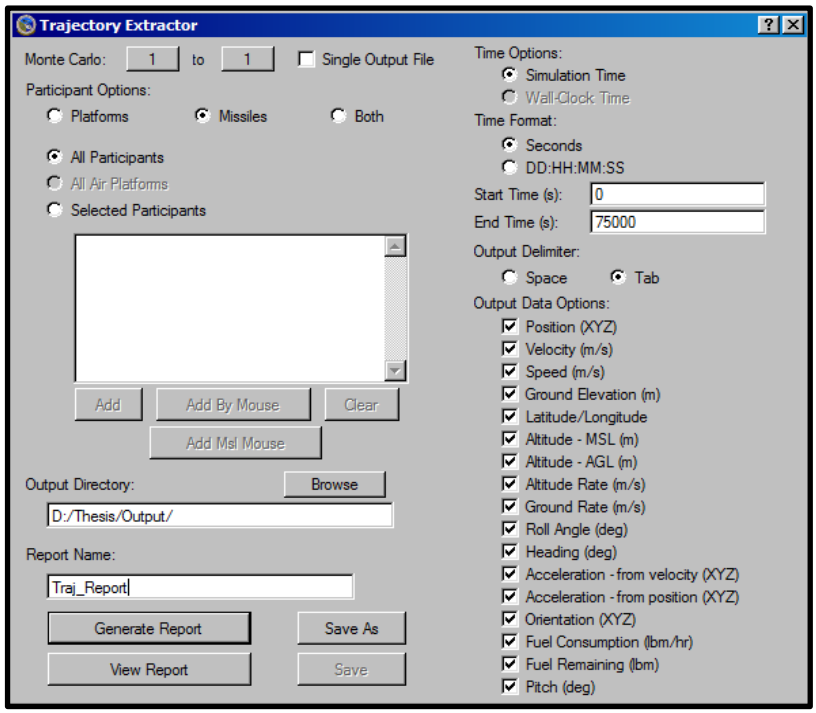

Figure 24: EADSIM Trajectory Report Generation Tool

For submunition warheads, the DOE will also specify a release altitude. Once the trajectory report is saved to a disk, it can be analyzed to calculate the velocity and orientation at a given release altitude. From the inertial from, a the body frame is established where the x-axis is coincident with the axis of symmetry of the TBM reentry vehicle (RV), the y-axis is parallel to the y-axis of the inertial frame and the z-axis is

perpendicular to these two axis. From the inertial frame, the vertical and horizontal velocity can be calculated as:

$$V_{vert} = \frac{z_2 - z_1}{t_2 - t_1}$$

$$V_{horz} = \frac{d_2 - d_1}{t_2 - t_1}$$

Where *z* is the MSL or AGL altitude (both equal with no terrain data), *t* is the simulation time, and *d* is the horizontal distance from the launch point. Initially, the time step just before the release point is found from interpolation of the altitude data. This time point and its associated altitude and distance, as well as the time, distance, and altitude of the time point immediately following are then used in equations 12 and 13. The total velocity is then found by: $V_{total}=(V_{vert}^2+V_{horz}^2)^{0.5}$. The orientation of TBM RV at the release altitude is found from the orientation of the body frame. The body frame is inline with the line of flight of the TBM RV, so there is no yaw angle and the pitch is found by $\text{atan}(V_{vert}/V_{horz})$.

6.2.2. Runway Damage Effects Model: Penetrator Flight Sub-Model

The Penetrator flight model is a 6-DOF-ballistics model. This model uses small time steps to propagate a penetrator to the ground from its release points. At each time step it calculates the gravity and aerodynamic forces and moments on the body based on its current velocity and orientation and uses those forces and moments to calculate the velocity and orientation at the next time step. The initial conditions for the penetrators released from the TBM RV are the RV speed and orientation calculated in the last section.

The ballistics model used in the analysis is given in Robert McCoy's Book [71-73] and is explained below. The 120mm mortar was chosen as a good representative runway penetrator given its size and weight. A diagram of the 120mm mortar is shown below.

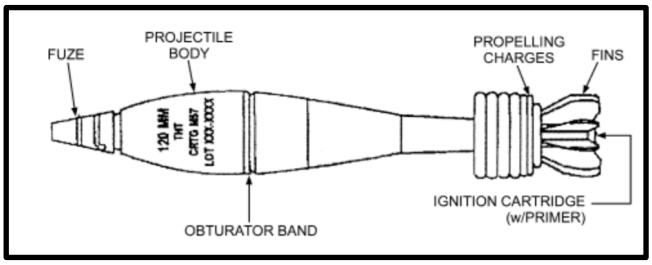

Figure 25: 120 mm Mortar (Image From [74])

McCoy's book also has additional tables and values that specify the aerodynamic characteristics of a 120mm mortar [71, 75]. The 120mm is normally a sub-sonic munitions. The runway penetrators are deployed from the TBM at supersonic speed, so the author had to extend the aerodynamic coefficient trends into the supersonic regime. The extensions were based on other supersonic munitions found in McCoy's book and are shown below in Figure 26.

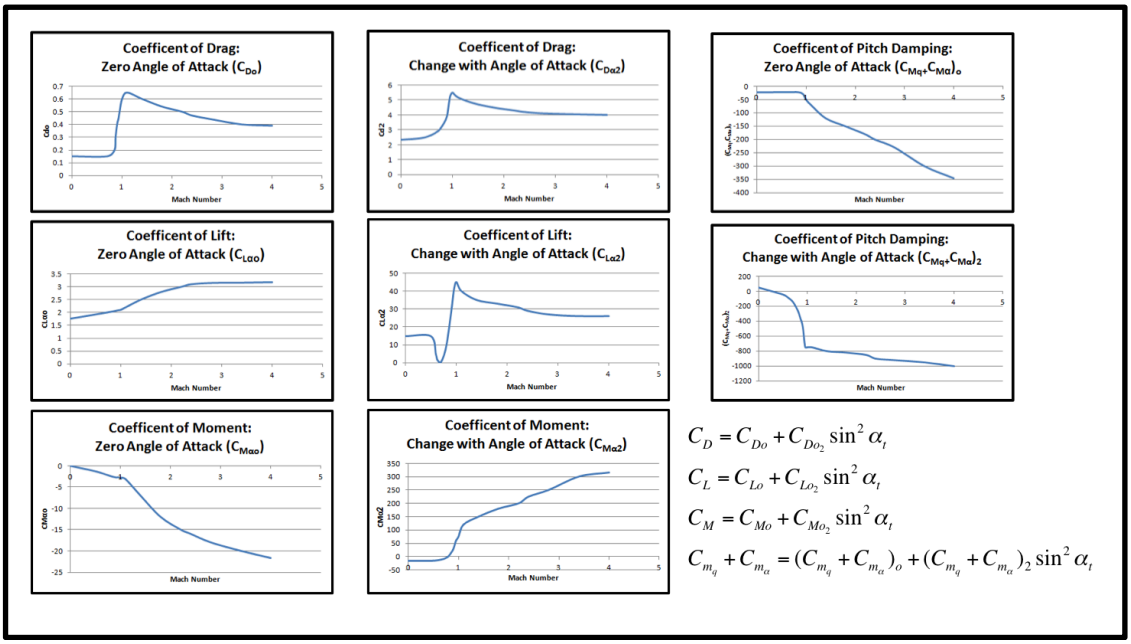

Figure 26: Extended Aerodynamic Coefficients for a 120mm Mortar (Data From [71])

In the 6DOF-ballistics model, the ordinary differential equations (ODEs) that describe the time rate of change of the munitions' speed in the inertial x, y, and z frames, as well as the angular velocity of the body frame's x, y, and z axes are shown below. These equations reference the frames of reference shown below in Figure 27. They are derived from Newtons's equation that the time rate of change of the linear or angular velocity is proportional to the mass (or mass moment of inertia) and the resultant sum of the forces (or moments) on acting on the body. The equations are transformed from the inertial frame to the body frame through the Euler angles. For addition information on transformations through the Euler angles please see Harkins, 2003 [76].

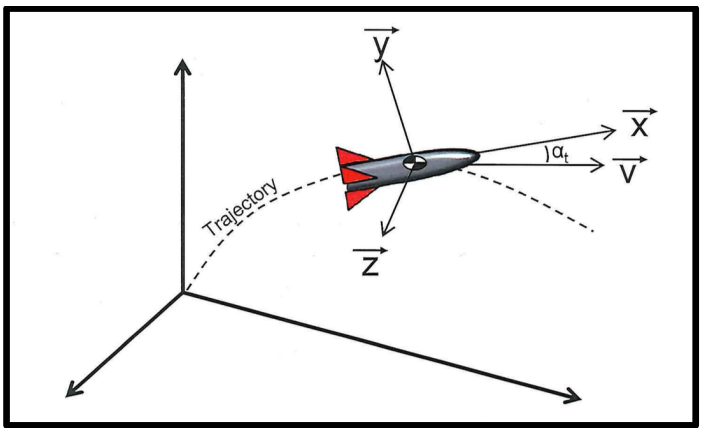

Figure 27: 6-DOF Frames of Reference

In these equations, several assumptions were made. Because the runway penetrators do not have a motor (they are in free-fall flight), the thrusting terms for the ballistic equations are not shown [71-73]. It was also assumed that there was no wind so the wind components have been neglected and because this analysis did not assume a launch location to Coriolis accelerations have been neglected. Normally, neglecting both the wind and Coriolis acceleration would lead to large aiming errors in an actual scenario, however, this analysis is seeking to find the general orientation of the TBM RV for any given launch condition. Wind will extend or reduce the range of the TBM RV for a given launch angle. Additionally, the Coriolis forces will cause the flight path to appear to curve along the surface of the earth. This will have the effect to reducing the range. Therefore, for an actual scenario, the user should first calculate the theoretical range assuming no wind or Coriolis acceleration. Then use the calculations in the Missile Flight Section to find the orientation. Finally, calculate the actual range, but continue using this orientation throughout further analysis. The equations used in the 6-DOF ballistics model are shown below. Here axis 1, 2, and 3 are the x, y, and z-axis respectively.

The first equations describe the acceleration of the projectiles center of mass relative to the initial frame. The next three equations describe the angular acceleration of the projectile about its center of mass relative to the body frame. The next three equations describe the orientation of the unit vector through the rounds center of gravity and pointed along the axis of symmetry. These equations are relative to the inertial frame. Finally the last three equations describe the rounds distance traveled relative to the initial frame.

$$\dot{V}_1 = -\tilde{C}_D v_1 + \tilde{C}_{L_\alpha}(v^2 x_1 - v v_1 cos\alpha_t) - \tilde{C}_{N_{p\alpha}}(x_2 v_3 - x_3 v_2) + \tilde{C}_{N_q}(h_2 x_3 - h_3 x_2) + g_1 + \Lambda_1$$

$$\dot{V}_2 = -\tilde{C}_D v_2 + \tilde{C}_{L_\alpha}(v^2 x_2 - v v_2 cos\alpha_t) - \tilde{C}_{N_{p\alpha}}(x_3 v_1 - x_1 v_3) + \tilde{C}_{N_q}(h_3 x_1 - h_1 x_3) + g_2 + \Lambda_2$$

$$\dot{V}_3 = -\tilde{C}_D v_3 + \tilde{C}_{L_\alpha}(v^2 x_3 - v v_3 cos\alpha_t) - \tilde{C}_{N_{p\alpha}}(x_1 v_2 - x_2 v_1) + \tilde{C}_{N_q}(h_1 x_2 - h_2 x_1) + g_3 + \Lambda_3$$

$$\dot{h}_1 = \left(\tilde{C}_{l_p} + \tilde{C}_{l_\delta}\right) x_1 + \tilde{C}_{M_\alpha}(v_2 x_3 - v_3 x_2) + \tilde{C}_{M_{p\alpha}}(v_1 - v x_1 cos\alpha_t) + \tilde{C}_{M_q}\left(h_1 - \frac{I_x P}{I_y} x_1\right)$$

$$\dot{h}_2 = \left(\tilde{C}_{l_p} + \tilde{C}_{l_\delta}\right) x_2 + \tilde{C}_{M_\alpha}(v_3 x_1 - v_1 x_3) + \tilde{C}_{M_{p\alpha}}(v_2 - v x_2 cos\alpha_t) + \tilde{C}_{M_q}\left(h_2 - \frac{I_x P}{I_y} x_2\right)$$

$$\dot{h}_3 = \left(\tilde{C}_{l_p} + \tilde{C}_{l_\delta}\right) x_3 + \tilde{C}_{M_\alpha}(v_1 x_2 - v_2 x_1) + \tilde{C}_{M_{p\alpha}}(v_3 - v x_3 cos\alpha_t) + \tilde{C}_{M_q}\left(h_3 - \frac{I_x P}{I_y} x_3\right)$$

$$\dot{x}_1 = (h_2 x_3 - h_3 x_2)$$

$$\dot{x}_2 = (h_3 x_1 - h_1 x_3)$$

$$\dot{x}_3 = (h_1 x_2 - h_2 x_1)$$

$$x_1 = v_1 dt$$

$$x_2 = v_2 dt$$

$$x_3 = v_3 dt$$

Where:

$\vec{V}$	Velocity vector with respect to (wrt) the inertial frame.	$\vec{h}$	Angular momentum divided by the transverse moment of inertia

$\vec{x}$	Unit vector along the projectiles rotational axis	t	time
ρ	Air density	d	Projectile reference diameter
S	Projectile reference area	m	Projectile mass
I_x	Projectile axial moment of inertia	I_y	Projectile transverse moment of inertia
C_D	Coefficient of drag	$C_{L\alpha}$	Coefficient of lift
C_{Npa}	Magnus force coefficient	$(C_{Nq}+ C_{Na})$	Pitch damping force coefficient
C_{lp}	Spin damping moment coefficient	$C_{l\delta}$	Rolling moment due to fin cant
C_{Ma}	Pitching moment coefficient	C_{Mpa}	Magnus moment coefficient
$(C_{Mq}+ C_{Ma})$	Pitch damping moment coefficient	Λ	Coriolis acceleration
α_t	Angle between the velocity vector and the body x-axis	g	Gravity vector

In these equations, the Euler angles of pitch, role, and yaw were used to transfer between the inertial frame and the body frame. In these equations, the pitch (α) is used in several trimetric terms. Specifically, many of the terms have a cos α that can become numerically unstable at high angles of attack, typically beyond +/- 89.5 degree. The advantage of the Euler angles is their ease of use and interpretation, but one must be cautious of the pitch term instability. Another method that does not have this singularity, but is more difficult to implement and interpret is a transformation via quaternions. An excellent summary of quaternions and their use to develop the equations of motion is available in Siouris's book [77]. In the analysis used in this dissertation, the Euler angles were used, but the author continuously checked the pitch value to ensure it did not increase beyond 89.5 degrees.

The twelve-coupled ballistic equations of motion ODEs explained above need to be solved simultaneously. In MATLAB, this is best done with the ODE45 algorithm. A good introduction and example of the ODE45 are found in [78, 79]. The overall initial conditions for the 6-DOF model is the speed and orientation of the TBM RV at the penetrator release altitude as calculated in the last section. When released, not all penetrators are released at the same angle in order to ensure a fairly uniform spread of the resulting craters. Therefore, in the 6-DOF model, the initial orientation of the penetrator was formed from the orientation of the RV plus a release angle. This release angle was specified in the DOE as a value between 0 and a maximum release angle of 10 degrees. The penetrator was then propagated to the ground using the 6DOF equations specified above. The impact time was found through interpolation of the altitude to find the time step when impact occurred. The impact angle and speed could then be interpolated using this impact time. In addition to the impact speed and orientation, a spread radius was also calculated. This was the horizontal ground distance from the impact point of the projectile at the given release angle to the impact point of a projectile with a release angle of zero. This would later allow the author to use the output "spread radius" from this program as a regression input for the cratering program.

The results of this analysis are shown below for two different test cases each with 40 penetrators for six different ranges from 50km to 300km with a constant release angle. The first test case has a release altitude from the TBM of 30,000 ft above ground level (AGL) and the second has a release altitude of 10,000 ft AGL. Figure 28 and Figure 29 shows a close in view of the impact pattern for these test cases. Because the release angle was constant, the impact pattern in each case was circular. For a normal TBM the release

angle is not constant. Note that the impact angle increases as the range increases and as the release altitude decreases. Looking left to right of each release altitude case, the impact angle decreases as the range increases. Note that the effect is more exaggerated for the lower release altitude, 10,000 ft, than the higher release altitude, 30,000 ft.

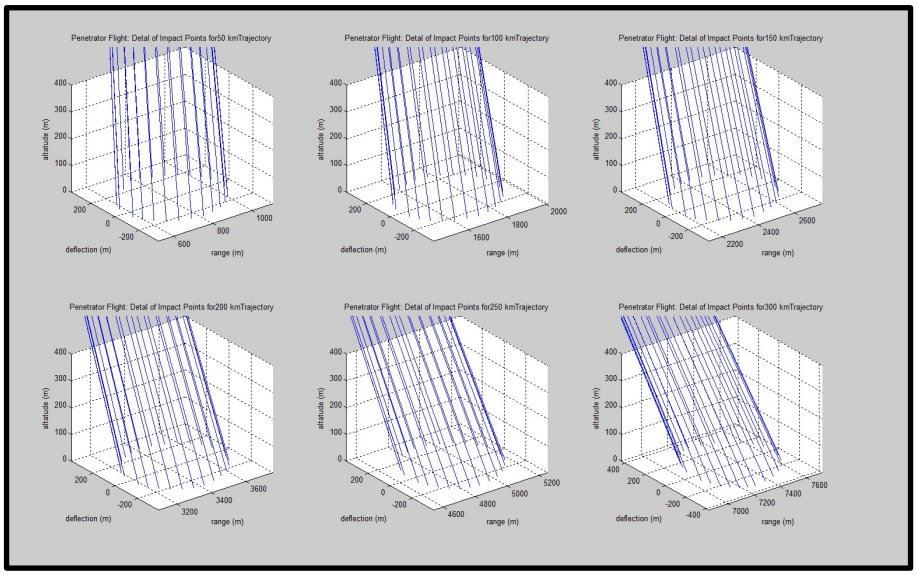

Figure 28: 6DOF Model Output for 30,000 ft Test Case: Zoomed to Impact

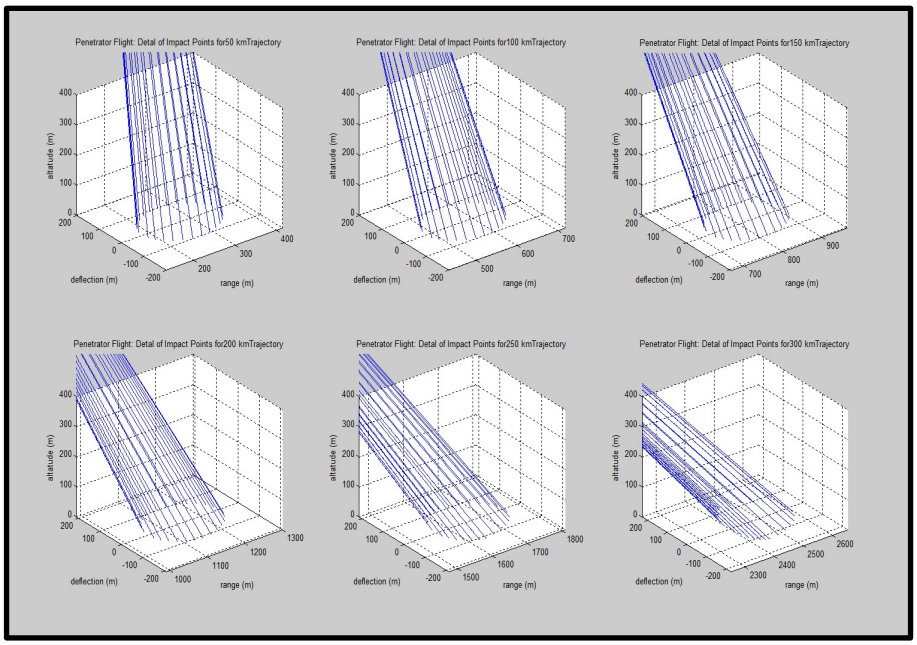

Figure 29: 6DOF Model Output for 10,000 ft Test Case: Zoomed to Impact

This same 6DOF model was also used for a CM releasing penetrators. Here it is assumed that the CM pitches to 45 degrees down angle and releases the penetrators at 100 ft AGL. These results are shown below in Figure 30. Again, this test case was conducted with a set release angle resulting in a circular impact pattern on the ground. In reality and in subsequent analysis in this dissertation, the release angle will vary between zero and a set maximum release angle.

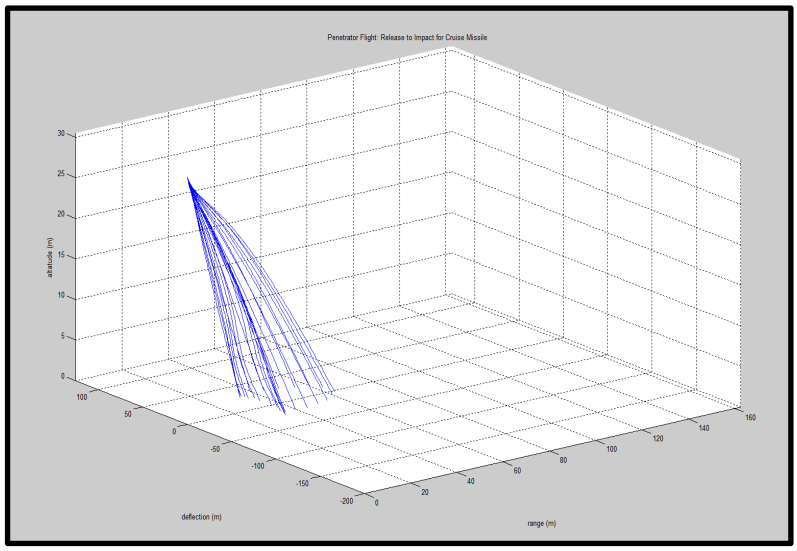

Figure 30: 6DOF Model Output for CM Test Case: Overall Flight

6.2.3. Runway Damage Effects Model: Penetration Sub-Model

Once the penetrators reach the ground, the impact force initiates a time delay on the fuse. In addition, the body shape and material allows the penetrator to use the impact energy to begin to penetrate into and possibly through the concrete layer. If they penetrate through the concrete layer they will continue onto the next layer, typically crushed and compacted aggregate rock, and finally into the semi-infinite soil layer below. A side view of a typical runway construction with these layers is shown below in Figure 31. Once the penetrator loses all its energy from the impact it will come to rest inside one of these runway layers. If the time delay fuse detonates before the penetrator has

come to rest then the penetrator will explode at whatever depth it currently is within a layer.

Figure 31: Typical Runway Construction Layers

There is significant amount of ongoing research into concrete penetration theories and to a slightly lesser extent into soil and rock penetration. An excellent summary of the current work is from Li, et al. [80]. The most active research in concrete penetration is from the nuclear engineering field. These scientists are concerned about penetration of critical shielding around nuclear reactors. The penetrators in these cases can range from weapons like bullets and fragments, to objects that might be thrown in a natural disaster such as metal pieces, glass, and wood, to objects that would be ejected from a mechanical failure inside the power plant such as turbine blades and shaft components [81].

Most research in the last ten years has been into numerical simulation of concrete penetration. This is because concrete has a complicated non-linear response to impact loading [82, 83]. As a result, there is not a closed form solution to the penetration depth for any penetrator into any concrete structure. Most modern research uses computational structures codes, such as ABAQUAS, AUTODYN, and LS-DYNA [83]. These computational studies are applicable to a wide range of impact situations from shallow to deep penetration and deformable penetrators and is a good tool to help extend the applicability of existing empirical equations [84-87]. Although numerical simulation is superior to empirical formulas for many cases, in this research empirical formulas will be

used. There are several reasons for this. First, most empirical codes have been shown to match experimental data especially for cases that are present in this dissertation: specifically high speed strikes on concrete with ogive-nose shaped projectiles. Also, the penetration depths needed to be solved for any general case of impact depth and speed, because the penetration code is run in sequence with the 6-DOF flight model. The penetration code is passed impact speed and angles values from the 6-DOF model code, and it would be difficult setup a numerical simulation that would capture the wide range of impact conditions and target conditions [88].

Because of this wide range of projectiles and speeds there are many empirical forms of penetration equations. The selection of the correct empirical equation depends on the speed of the projectile, the size of the projectile compared to the target, and the material of the target and projectile. For low velocity impacts (200-300 mps) the most common formulas are: CEA-EDF formula, UKAEA formula, Degan Formula, Chang Formula, and Adeli-Amin Formula [80, 89]. For penetration of concrete due to explosively formed fragments, the Ammann and Whitney Formula and the Whiffen Formula are good choices [80]. For this application of penetrator rods into concrete the most commonly used formulas are the Modified National Defense Research Council (NDRC) formula, the Haldar formula, and the Sandia Equations. In fact, these formulas are even recommended by various Army and Air Force Manuals [84].

The three penetration equations all deal with high-speed impacts (200-1500 fps) with non-deformable missiles. These types of impacts are generally called “Hard” impacts. In reality, all missiles that impact at that speed will deform to varying degrees. The deformation has the effect of reducing the actual depth of penetration; however, the

missile must deform to at least 40% of the calculated non-deformable penetration depth before the deformation effects become significant [90]. In the analysis conducted in this dissertation, the penetrators typically did not penetrate deep enough for this effect to become significant. For the hard, non-deforming penetrator, the penetration path is typically a straight line. Therefore the vertical depth that the round penetrates is a factor of its impact angle and its penetration length as see below in Figure 32.

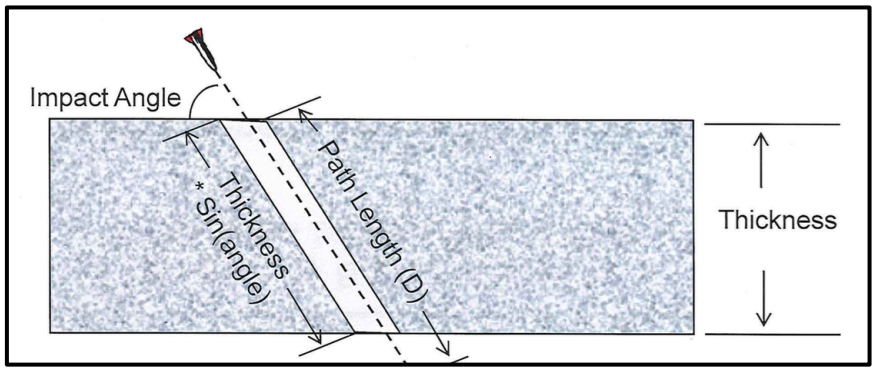

Figure 32: Straight Line Penetration Through Concrete

6.2.3.1. Modified NDRC Formulas

The Modified NDRC formula was developed in 1946 and put forward by a committee in the National Defense Research Council [91]. The original formulations for the Modified NDRC formulas came from the Ballistics Research Laboratory (BRL) in 1941. The equations were later modified by the Army Corps of Engineers (ACE) to fit the latest test data at that time in 1943. Although an older formula, it is still applicable today because it is based on an actual theory of penetration for non-deforming missiles [92]. Because the model is based on a theory of penetration and is not a simple curve fit to data, the model can be expanded beyond its original test data with confidence. The main assumptions of the theory that the contact force between the target medium and the projectile increased linearly to a maximum value. The theory also assumes that the

penetrator does not deform, is cylindrical, and that the target concrete is semi-infinite. The semi-infinite assumption means that the theory does not consider spalling or cracking effects on the opposite side of the target. The original NDRC equations were extended by Kennedy to account for the "K" term [90]. It is these new equations that are collectively known as the Modified NDRC Formulas. Kar extended the Modified NDRC formulas to account for other types of penetrator materials other than steel, but for this analysis with steel projectiles, his equations simplify back to the original modified NDRC formulas [93]. The Modified NDRC equations are given below [80, 90-92].

$$x = \left[4KNW_d\left(\frac{V_0}{1000d}\right)^{1.8}\right]^{1/2} \quad for\ \frac{x}{d} \leq 2.0$$

$$x = \left[KNW_d\left(\frac{V_0}{1000d}\right)^{1.8} + d\right] \quad for\ \frac{x}{d} \geq 2.0$$

$$k = \frac{180}{\sqrt{f_c}}$$

where:

x	Penetration depth (in)	W	Penetrator Weight (lbs)
Vo	Impact velocity (ft/s)	d	Penetrator Diameter (in)
fc	Concrete Compressive Strength (psi)	N	Nose Factor = 0.72 for Flat-Nosed 0.84 for Blunt-Nosed 1.0 for Spherical-Ended 1.14 for Sharp-Nosed

6.2.3.2. Haldar Formulas

Haldar and Hamieh used the Modified NDRC formulas as a baseline, but expanded them because they saw variations from experimental data for larger types of penetrators [82]. Unlike the modified NDRC formulas, they did not use a penetration

theory, but instead an empirical curve fit the data. They did, however, non-dimensionalize the data with a new impact factor, I. This non-dimensionalization makes their formula unit independent (any consistent set of units can be used) which is a significant improvement over many other empirical formulas mainly because the units give undo importance to some factors over others mainly due to their relative magnitude that results from the units chosen [82, 84]. Similar to the Modified NDRC, the Haldar equations assume a cylindrical and non-deforming penetrator and because it is based on empirically fitted data, it is only valid for impact factors between 0.3 and 455. The Haldar equations is given as [80-82]:

$$x = d(-0.0308 + 0.2251 * I) \quad for\ 0.3 \leq I \leq 4.0$$

$$x = d(0.6740 + 0.0567 * I) \quad for\ 0.4 < I \leq 21.0$$

$$x = d(1.1875 + 0.0299 * I) \quad for\ 21.0 < I \leq 455$$

$$I = \frac{WNV^2}{gd^3 f_c}$$

where:

x	Penetration depth	W	Penetrator Weight
V	Impact velocity	d	Penetrator Diameter
fc	Concrete Compressive Strength	N	Nose Factor = 0.72 for Flat-Nosed 0.84 for Blunt-Nosed 1.0 for Spherical-Ended 1.14 for Sharp-Nosed

6.2.3.3. Sandia Formulas

The Sandia equations were developed at the Sandia National Laboratory. The original formulation was derived in 1967, but later modified in 1972, 1988, and most recently in 1997 by C.W. Young [94]. The Sandia equations are empirical curve fits

similar to the Haldar equations, but unlike Haldar's they are not completely based on non-dimensional factors. This does give them the same disadvantage that the Modified NDRC equations have, in that the units tend to give undue importance to certain factors. Unlike the other two formulations, however, the Sandia equations are based on thousands of test cases and accounts for factors that the others do not, such as the amount and strength of reinforcement, cure time, and finite target thickness. The Sandia equations also apply to soil and rock as well as to concrete. The equations have also been combined and used with other penetration equations of more complicated formula beyond the scope of this research into an elaborate penetration code called the Simplified Analytical Model of Penetration with Lateral Loading (SAMPLL) [94]. The SAMPLL code is used today by the US Army. The Sandia equations have been shown to be within 10-15% accurate of true penetration depth. This is typically within the spread range of repeated measurements in experiential data [86]. The main assumptions of the Sandia Equations are that the penetrator weighs more than 5 lbs for soil or 10 lbs for rock and concrete and remains intact following a stable trajectory, impact velocity is less than 4,000 fps, and the penetration depth is more than three calibers. The Sandia Penetration Equations are given below [62, 94]:

For concrete and Rock:

$$x = 0.3 * K_h * S * N * \left(\frac{W}{A}\right)^{0.7} \ln(1 + 2V^2 * 10^{-5}) \quad for\ V < 200\ fps$$

$$x = 0.00178 * K_h * S * N * \left(\frac{W}{A}\right)^{0.7} (V - 100) \quad for\ 200 \leq V \leq 4000\ fps$$

where:

x	Penetration depth (ft)	W	Penetrator Weight (lbs)

V	Impact velocity (fps)	A	Penetrator Cross Sectional Area (in^2)
S	Target Material S-Number (Explained Below)	N	Nose Factor (Explained Below)
K_h	Lightweight Penetrator Factor (Explained Below)		

For concrete and rock, the Lightweight Penetrator Factor can be calculated as:

$$K_h = 0.4 * W^{0.15} \quad for\ W < 400\ lbs$$

$$K_h = 1 \quad f\ or\ W \geq 400\ lbs$$

In the Sandia Equations, the target material S-Number plays a critical role. The S-number equations given in the Sandia report are as follows. These S-numbers are estimated to be within 10% accuracy which is the typical scatter spread of most test data [94].

For concrete:

$$S = 0.085 * K_e * (11 - P)(t_c T_c)^{-0.06} \left(\frac{5000}{f_c}\right)^{0.3}$$

For Rock:

$$S = 12(f_c Q)^{-0.3}$$

where:

P	Volumetric Percent Rebar (%)	t_c	Concrete Cure Time (yrs). If $t_c > 1$ then $t_c = 1$
T_c	Target Thickness (calibers). If $T_c > 6$ then $T_c = 6$	f_c	Concrete/Rock compressive strength (psi)
K_h	Edge Correction Factor (Explained Below)	Q	Rock Quality (dimensionless)

The Edge correction factor, K_h can be found for reinforced (F=20) and unreinforced (F=30) concrete as:

$$K_e = \left(\frac{F}{W_1}\right)^{0.3} \quad for\ W_1 < F$$

$$K_e = 1 \quad for\ W_1 \geq F$$

Where W_1 is the target thickness in calibers of the penetrator. The rock quality, Q, in the rock S-Number equation is a dimensionless factor that varies between 0 and 1. It is 0 for very loose and low quality rock and 0.9 for massive, high quality rock.

Finally, the Nose Factor in the penetration distance equations can be found for any projectile by measuring its Caliber-Radius-Head (CRH). The CRH is a dimensionless number that describes a rounds ballistic length to the radius of curvature of its nose. CRH number for most munitions is formally shown as a dual number such as 3/4 crh where the first number is the ballistic length and the second number is the radius of curvature; however, it is many times abbreviated to just the second number such as 4crh [95]. The radius of curvature is the length of the radius, centered at point E, for the arc that forms the nose cone shape as seen in Figure 33.

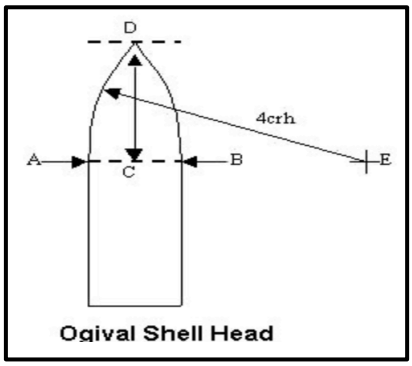

Figure 33: Caliber Radius Head (CRH) (Image From [95])

The formula for the simplified CRH is given below where *r* is the radius of curvature of the shell and *d* is the caliber or diameter [96].

$$CRH = \frac{r}{d}$$

For a given penetrator the nose factor can be found as:

$$N = 0.18 * (CRH - 0.25)^{0.5} + 0.56$$

6.2.3.4. Comparison of the Concrete Penetration Equations

The last few sections explained the three most common penetration equations for hard penetrators hitting concrete targets at high velocities: the Modified NDRC Formulas, the Haldar Formulas, and the Sandia Equations. Each of these equations is empirical in nature. They were modeled and adjusted based on the best test data available at their creation. In order to validate which one to use, they each need to be tested against new, modern penetration data that was not used in their creation. Test data from Forrestal, et al, and Cargile, J.D., and Canfield and Clator will be used for this validation [97-99]. These experiments used hard, ogive-nosed projectiles with a CRH of either 2 or 3 fired into concrete with compressive strengths ranging from 34 MPa to 63 MPa. The six plots in Figure 34 show the results of the test data (blue stars) compared to the three penetration models: Sandia (red solid line), NDRC (dashed red line), and Haldar (dotted red line).

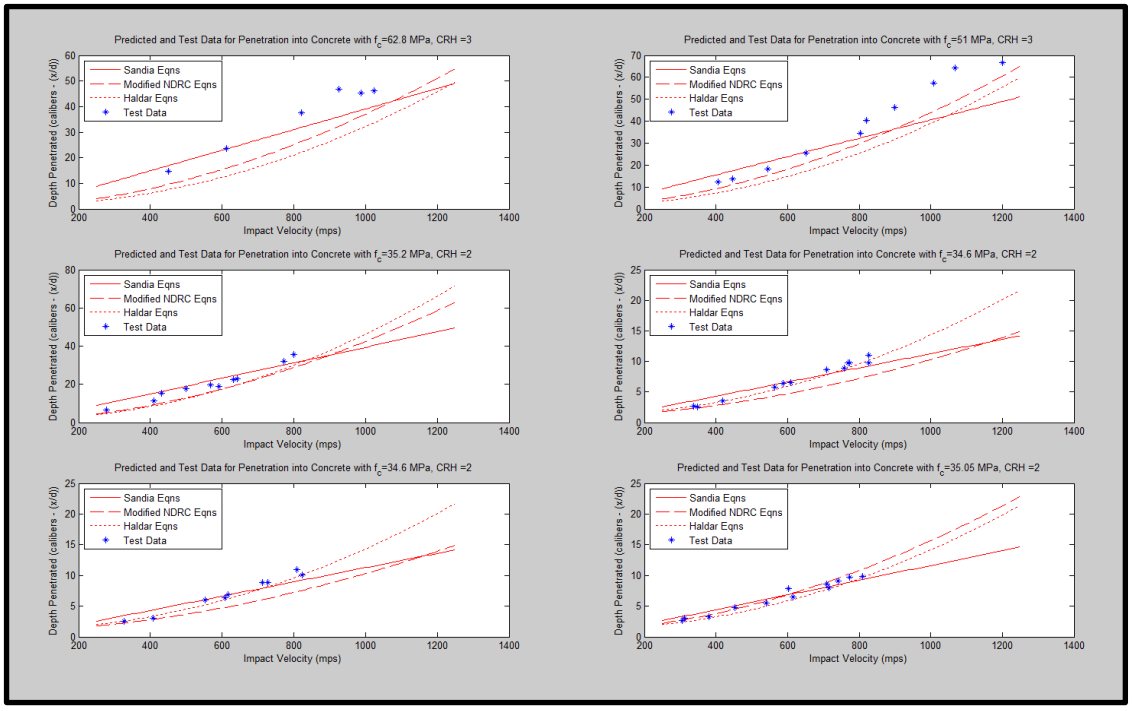

Figure 34: Penetration Model Comparison to Test Data

The results show good agreement in all cases below 800 mps (2,625 fps). The two top graphs used hard concrete (f_c=62.8 MPa and 51 MPa). For these two cases, all three equations have large errors beyond the 800 mps. Looking at the residuals shown in Figure 35, the difference between the predicted and actual penetration values, Modified NDRC (middle graph) and the Haldar (lower graph) both under predict the penetration depth. These two graphs show consistent positive residual values. The Sandia has a more consistent prediction interval. When the R-Squared values are compared in Table 5, the Sandia also shows a better correlation with the test data. Therefore, the Sandia penetration equations will be used for the penetration model in this dissertation.

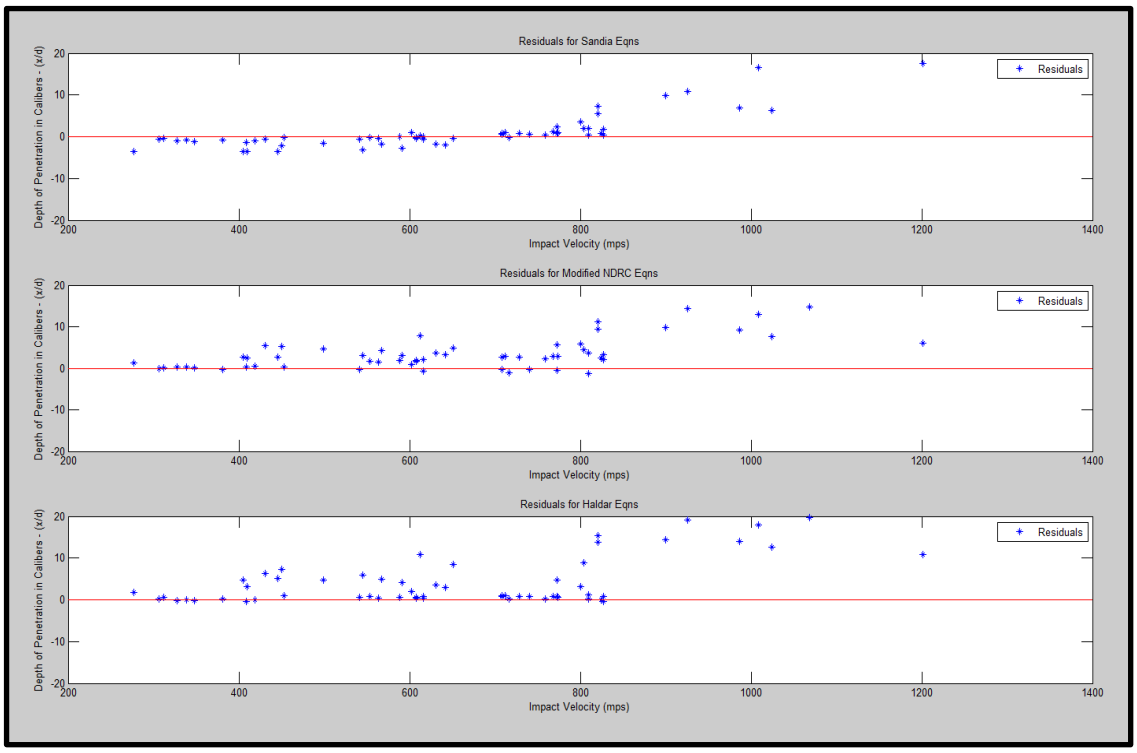

Figure 35: Residuals of Test Data to Predicted Penetration Depth

Table 5: R^2 Values for Penetration Equations Compared to Test Data

Test Case	R^2 Values		
	Sandia	NDRC	Haldar
1	**0.7404**	0.3831	0.2257
2	**0.9753**	0.9592	0.8882
3	**0.9453**	0.8755	0.8279
4	**0.9354**	0.5451	0.9731
5	**0.9138**	0.4140	0.9486
6	**0.9761**	0.9556	0.9693

6.2.3.5. Penetration through Soil

The Sandia equations also have application in soil; however, it is possible to derive a more physics based model. The soil penetration model is developed by Driels and is based on decelerating viscous forces on the round as it moves through the soil [62]. These equations are solved in a sequential fashion where one first calculates the acceleration based on the current velocity and then uses that acceleration to find a new

velocity. Using that velocity and a given time step to move the round further into the soil. The equations for penetration through soil are below [62].

The deceleration force on the round is:

$$F = -\pi r^2(\gamma_{sl} + \beta_{sl}V^2)$$

This force causes an acceleration:

$$a = \frac{dv}{dt} = \frac{V(t+dt) - v(t)}{dt}$$

The velocity at the next time step is:

$$V(t+dt) = v(t) - \left(\frac{\pi r^2}{m}\right)(\gamma_{sl} + \beta_{sl}V^2)$$

The position at the next time step is:

$$x(t+dt) = x(t) + \frac{V(t+dt) + V(t)}{2}dt$$

These equations are solved iteratively until the velocity goes to zero. In the above equations γ_{sl} is the soils static soil constant and β_{sl} is the dynamic soil constant. Driels recommends the following values for these terms [62]:

Table 6: Soil Constants (Data From [62])

Soil Type	Example	γ_{sl} (psi)	B_{sl} (lb-s^2)/in^4
Hard (S<6)	Hard, Dense, Clay or Permafrost soil	750	0.0000824
Medium (6<S<12)	Loose dry or moist sandy soil	350	0.0000689
Soft (S>12)	Wet, Soft, Clay, Tidal mud flats	160	0.0000592

6.2.4. Runway Damage Effects Model: Cratering Sub-Model

Referring back to Figure 19 and Figure 20, the cratering model is applicable to both unitary (surface burst) weapons as well as penetration weapons. For the penetration munitions, the round will tunnel through the concrete, rock, or soil until it comes to rest or the timed delay fuse detonates after a pre-determined time from the initial impact with

the surface. Therefore, there are five distinct regions where the detonation can take place: a detonation on the surface of the concrete runway, a detonation within the concrete layer, a detonation under the concrete in either the rock or soil layer, a detonation on the surface of the soil off the runway, or a detonation within the soil off the runway. Because this analysis is meant to inform the runway availability model, it will only consider the first three cases: detonation on, within, or below the runway concrete layer.

6.2.4.1. Cratering From Explosions on or Within Concrete and Soil

When measuring the size of explosively formed craters there are normally two measurements given for every dimension: the apparent and true dimension. This is because material from the medium in which the explosion took place is initially ejected upwards and then some will fall back into the crater. The true and apparent dimensions are shown in Figure 36.

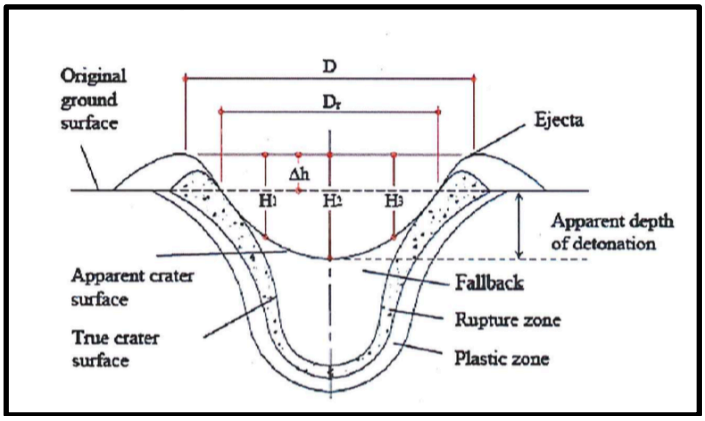

Figure 36: Apparent and True Measurements of a Crater (Image From [100])

For surface bursts or shallow depths of burst, most of the material is ejected outward and very little will fall back into the crater. In these types of craters, the apparent and true measurements are nearly equal. As the depth of burst increases, more

and more material is deflected vertically and subsequently falls back into the crater. This increases the true dimensions and reduces the apparent dimensions. As the depth increases, more and more of the medium falls back into the crater resulting in a very small apparent dimension [101, 102]. This phenomenon is illustrated in Figure 37.

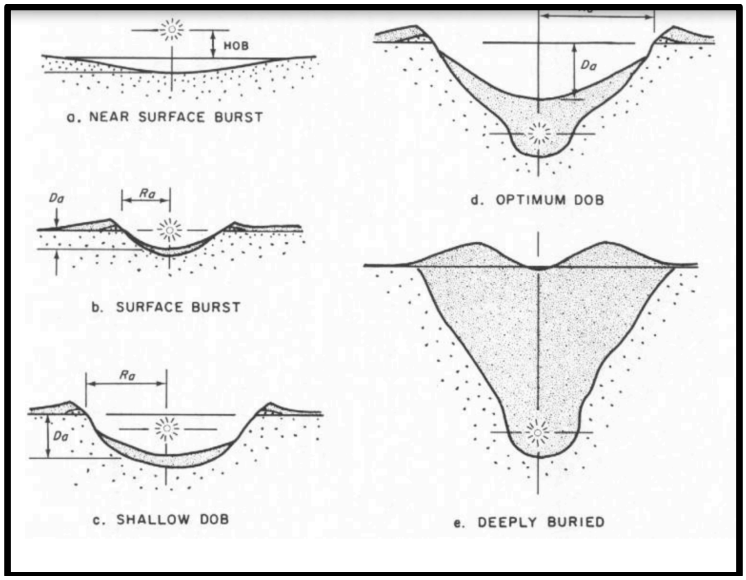

Figure 37: Apparent and True Crater Size as a Function of Depth of Burst (DOB) (Image From [103])

The two critical factors in crater formation are the explosive weight or mass and the depth of burst. For a given amount of explosive, the true size of the crater will increase with depth of burst until a certain point where most of the energy is absorbed by the medium between the explosive and the surface. Beyond that depth, the explosive will form a buried cavern called a camouflet. When a camouflet is formed, there is a small entry hole with possible blast damage, but a majority of the crater is buried below the surface [104, 105]. In addition, if the explosion takes place below a layer of concrete, the explosive force can cause parts of the concrete layer above to deform or "heave." The various types of craters are shown below in an image adopted from [62]. The time and effort to repair the crater is a function of the size as well as the type of crater. A spall

crater can normally be fixed with some fill material and a cap. A blowout or standard crater will require the crater to be filled and a patch applied over the hole. A crater with heave will require the heaved portion be cut out before the hole can be filled and patched [106].

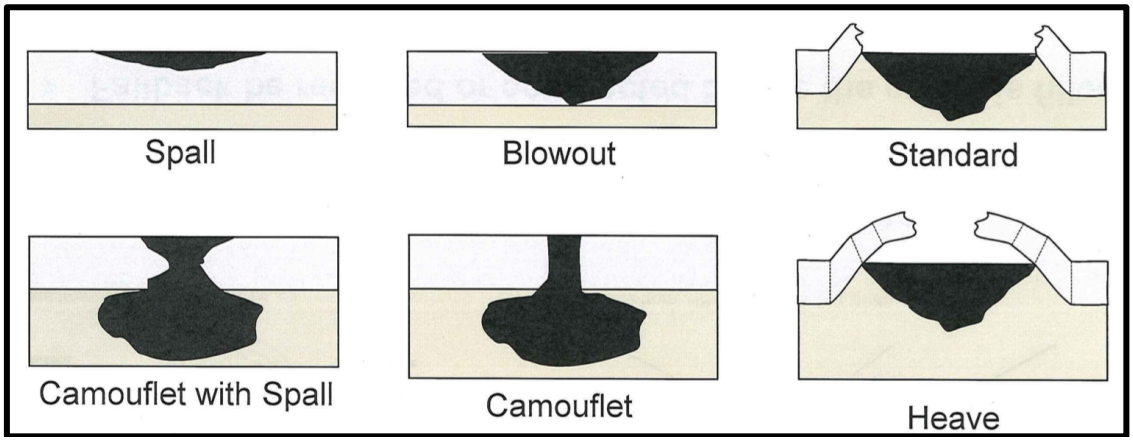

Figure 38: Types of Craters (Adopted From Image in [62])

Because the main factors that affect the size of a crater are the amount of explosive and the depth of burst, cratering equations typically used a scaled depth of burst defined as [62]:

$$Z = \frac{Z_c}{W^n}$$

Where Z is the scaled depth of burst, Z_c is the actual depth of burst, W is the explosive weight, and n is an exponential factor. The original value proposed for n was 1/3 by Hopkinson in 1915 [107]. Hopkinson postulated that the blast waves from two different charges would be identical at some scaled distance from either charge [108]. The 1/3 scaling exponent was proposed because the characteristic length in cratering studies was the radius of the spherical charge. This radius is proportional to the cube-root of the spherical charge's mass. Lampson [109] and Morrey et al [110] later confirmed the 1/3 scaling for crater radius for crater depth and radius based on experimentation.

Other researchers have suggested scaling exponents of 3/10, 7/24, and 5/16 [62]. Many of these alternatives are based on observations of craters in various materials by different charge masses. For smaller explosions of less than 10 lbs of TNT equivalent explosive, Chabai found that the 1/3 scaling factor was adequate [111]. Because the runway penetrating bomblets used in this study each contain 5-10 lbs of TNT equivalent weight, the 1/3 scaling will be used in this work.

For any real explosive, the chemical charge is encased in some protective shell. In the case of the penetrating munition used in this study, this shell is the metal of the penetrator. Because this shell must be strong enough to maintain its shape during the impact and tunneling through the concrete, it will absorb a significant portion of the energy of the explosive detonation. The amount of energy that is absorbed is described by the Modified Fano Equation [62]:

$$W_e = W(EEW)\left(0.6 + \frac{0.4}{1 + 2\frac{M}{C}}\right)$$

Where W is the explosive weight, W_e is the equivalent weight of uncased explosive available after the case fracture, EEW is the equivalent explosive weight factor, M is the case mass, and C is the charge mass. The original Fano equation appeared in a Navy Report in 1953. The original equation contained the constants 0.2 and 0.8, and the EEW factor was not included, but these constants were later modified to the 0.6 and 0.4 seen in the above equation and the EEW factor added to account for different types of explosives [112]. This factor scales different explosives to an equivalent weight of TNT, upon which the Fano equation is based. The EEW factors for several common explosives is shown below in Table 7. These EEW factors are from Driels [62]. A more extensive

list of EEW factors can be found in Maienschein [113] and a third list with the derivation of EEW can be found in [114].

Table 7: Equivalent Explosive Factors (Data From [62])

Explosive	EEW Multiplier
TNT	1.00
H-6	1.35
Tritonol	1.07
Comp B	1.11
Comp A3	1.07
Comp C4	1.30
Explosive D	0.92
HBX-1	1.17
HBX-3	1.14
Minol II	1.20

The current form presented above is called the Modified Fano equation and is in wide-spread use for a variety of applications; however, its use is best limited to steel and stronger materials. Other lighter and weaker materials show poor correlation with the Modified Fano Equation [115]. In this application, the runway penetrators are made of a strong steel-like material in order to maintain their shape after impact. Therefore, the Modified Fano Equation is appropriate. A plot of the Modified Fano equation appears below in Figure 39 for increasing case mass to charge mass (M/C) ratios. This plot was constructed to model a similar plot in both Bulson and Needham [112, 115]. From this chart it is apparent that the fraction of available energy quickly decays as the case mass is increased and approaches a limiting fraction of 60% of the energy available for large case masses.

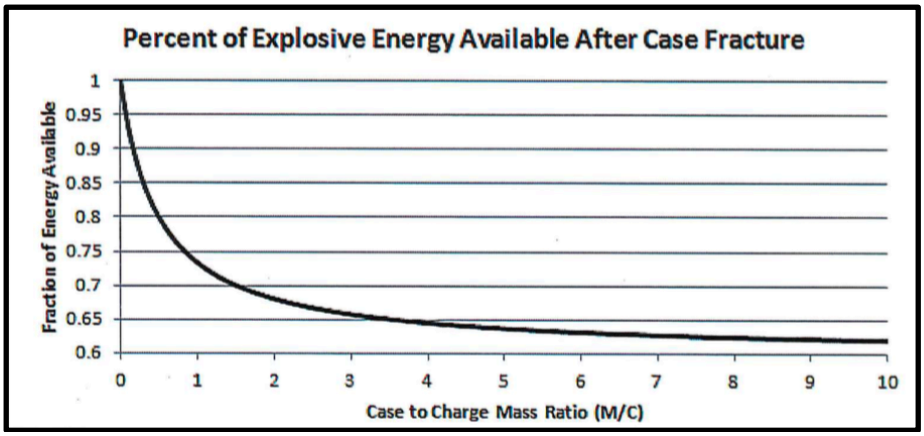

Figure 39: Portion of Explosive Energy Absorbed by Case Material (Adopted From Image in [112])

Referring back to the Hopkinson scaling equation, the discussion above showed that 1/3 is an appropriate scaling exponent and the weight used in the equations should be the equivalent explosive weight after the case fracture as descried by the Modified Fano equation. This means that the crater radius and depth are given by:

$$r = \frac{r_c}{W_e^{1/3}}$$

$$d = \frac{d_c}{W_e^{1/3}}$$

Where r and d are the scaled radius and depth of the crater, r_c and d_c are the actual radius and depth of the crater and W_e is the equivalent weight of explosive available after case fracture. These dimensions are based on the depth of burst (DOB) that is also scaled as:

$$DOB = \frac{DOB_c}{W_e^{1/3}}$$

Where DOB is the scaled depth of burst, DOB_c is the actual depth of burst, and W_e is the equivalent explosive charge after case fracture. Using these scaling terms, the US Army conducted a series of tests and developed a 90% confidence band for the size of a

crater on the surface and within concrete. Some of these tests are publicly available such as the test by Chabai [116]. Other tests were conducted and not publically published. The end result from these several hundred tests were charts of scaled depth of burst vs scaled diameter and depth as shown by Kiger and Balsara [117]. The author digitized this diagram, as well as the diagram in Driels [62] using the iOS application called Graph Click. This produces a series of points that fall along the curves in these graphs. These curves are then fitted with a polynomial using the MATLAB polyfit function. The result is a polynomial equation that described the scaled diameter and depth vs scaled depth of burst. These results are plotted below in Figure 40.

For any given explosion by an explosive charge with a known case mass to charge ratio at a given depth, the polynomials plotted below allow the calculation of the depth and diameter of the resulting crater. For each set of curves, the diameter and depth, the top curve is for unreinforced concrete and the bottom curve is for reinforced concrete. These lines represent the boundaries of a 90% experimental data fit. This means that for reinforced concrete, 90% of the test data fell above the bottom curve and below the midpoint between the top and bottom curve. For unreinforced concrete, 90% of the test data fell below the top curve and above the midpoint between the top and bottom curve.

As can be seen from the plot in Figure 40, the diameter and depth initially increase as depth increases until a maximum value of 0.6 to 0.8 $m/kg^{1/3}$ then decreases until the resulting crater is a camulflet when the scaled depth of burst is greater than about 1.2 $m/kg^{1/3}$. For detonations in soil, a similar graph along with the coefficients for a 6-degree polynomial fit are given in Driels [62].

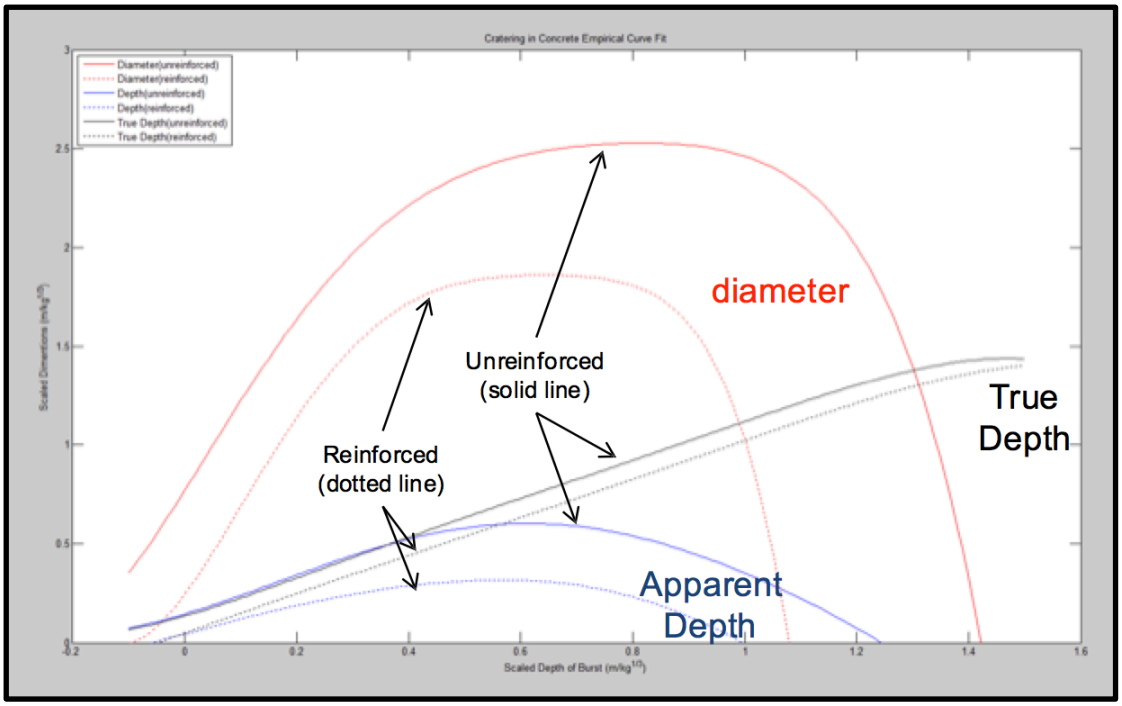

Figure 40: Crater Scaled Diameter and Depth as a Function of Scaled Explosive Depth of Burst (Created Based on Image in [117])

The optimal scaled depth of burst of 0.6 to 0.8 m/kg$^{1/3}$ results in a true depth of burst that is relative to the explosive and case weight as can be seen from the depth of burst equation and energy absorbed in the fracturing of the case described by the modified Fano equation. For a given case weight, as the amount of explosive is increased, the equivalent weight of the explosive increase and the true optimal depth of bust increases in depth. This relationship is summarized for a case-mass to charge ratio of 5 in a steel case and increasing explosive weights in Table 8. The highlighted areas show the optimal scaled depth of burst (0.6 to 0.8 m/kg$^{1/3}$) and the top line of the table shows the true depth of burst for that explosive weight. This graph shows that for a 1.5 lb explosive charge encased in a 7.5 lb container (case-mass to charge ratio of five) the optimal depth of burst is 18-23 inches below the surface.

Table 8: Optimal Depth of Burst for a Steel Shell with Case Mass to Charge Ratio of 5

Scaled Crater Diameter (m/kg^(1/3))															
Explosive Wt (lbs)	Explosive Mass (kg)	Equivalent Exp Wt (kg)	True Depth of Burst (in)												
			18	19	20	21	22	23	24	25	26	27	28	29	30
1.5	0.68	0.43	0.604	0.638	0.671	0.705	0.738	0.772	0.806	0.839	0.873	0.906	0.940	0.973	1.007
1.6	0.73	0.46	0.591	0.624	0.657	0.690	0.723	0.756	0.788	0.821	0.854	0.887	0.920	0.953	0.986
1.7	0.77	0.49	0.579	0.612	0.644	0.676	0.708	0.740	0.773	0.805	0.837	0.869	0.901	0.934	0.966
1.8	0.82	0.52	0.569	0.600	0.632	0.663	0.695	0.726	0.758	0.790	0.821	0.853	0.884	0.916	0.948
1.9	0.86	0.55	0.558	0.589	0.620	0.651	0.682	0.713	0.745	0.776	0.807	0.838	0.869	0.900	0.931
2	0.91	0.58	0.549	0.579	0.610	0.640	0.671	0.701	0.732	0.762	0.793	0.823	0.854	0.884	0.915
2.1	0.95	0.61	0.540	0.570	0.600	0.630	0.660	0.690	0.720	0.750	0.780	0.810	0.840	0.870	0.900
2.2	1.00	0.64	0.532	0.561	0.591	0.620	0.650	0.679	0.709	0.739	0.768	0.798	0.827	0.857	0.886
2.3	1.04	0.66	0.524	0.553	0.582	0.611	0.640	0.669	0.699	0.728	0.757	0.786	0.815	0.844	0.873
2.4	1.09	0.69	0.517	0.545	0.574	0.603	0.631	0.660	0.689	0.717	0.746	0.775	0.804	0.832	0.861
2.5	1.14	0.72	0.510	0.538	0.566	0.595	0.623	0.651	0.679	0.708	0.736	0.764	0.793	0.821	0.849
2.6	1.18	0.75	0.503	0.531	0.559	0.587	0.615	0.643	0.671	0.699	0.726	0.754	0.782	0.810	0.838
2.7	1.23	0.78	0.497	0.524	0.552	0.579	0.607	0.635	0.662	0.690	0.717	0.745	0.773	0.800	0.828
2.8	1.27	0.81	0.491	0.518	0.545	0.572	0.600	0.627	0.654	0.682	0.709	0.736	0.763	0.791	0.818
2.9	1.32	0.84	0.485	0.512	0.539	0.566	0.593	0.620	0.647	0.674	0.701	0.727	0.754	0.781	0.808
3	1.36	0.87	0.480	0.506	0.533	0.559	0.586	0.613	0.639	0.666	0.693	0.719	0.746	0.773	0.799
3.1	1.41	0.90	0.474	0.501	0.527	0.553	0.580	0.606	0.632	0.659	0.685	0.711	0.738	0.764	0.791
3.2	1.45	0.92	0.469	0.495	0.521	0.548	0.574	0.600	0.626	0.652	0.678	0.704	0.730	0.756	0.782
3.3	1.50	0.95	0.465	0.490	0.516	0.542	0.568	0.594	0.619	0.645	0.671	0.697	0.723	0.748	0.774
3.4	1.54	0.98	0.460	0.485	0.511	0.537	0.562	0.588	0.613	0.639	0.664	0.690	0.715	0.741	0.767
3.5	1.59	1.01	0.456	0.481	0.506	0.531	0.557	0.582	0.607	0.633	0.658	0.683	0.709	0.734	0.759
3.6	1.63	1.04	0.451	0.476	0.501	0.526	0.552	0.577	0.602	0.627	0.652	0.677	0.702	0.727	0.752
3.7	1.68	1.07	0.447	0.472	0.497	0.522	0.547	0.571	0.596	0.621	0.646	0.671	0.696	0.720	0.745
3.8	1.73	1.10	0.443	0.468	0.492	0.517	0.542	0.566	0.591	0.616	0.640	0.665	0.689	0.714	0.739
3.9	1.77	1.13	0.439	0.464	0.488	0.513	0.537	0.561	0.586	0.610	0.635	0.659	0.683	0.708	0.732
4	1.82	1.16	0.436	0.460	0.484	0.508	0.532	0.557	0.581	0.605	0.629	0.654	0.678	0.702	0.726

In most cases, a delay fuse timer will control the depth of burst. The detonation of the fuse is delayed from the initial impact by several fractions of a second to allow the shell to penetrate to the desired depth assuming that the shell is able to penetrate to that depth. The fuse delay is normally controlled by time and not depth and normally has some variability to it. Therefore in this work, the fuse deploy was modeled as a uniform distribution centered at the optimal depth for the given explosive weight and with end points two inches above and below that depth. During the simulations, the depth of penetration was initially calculated without regard to the fuse (assumed infinite time fuse). This was then compared to a random draw for the fuse depth [U(d-2,d+2)] where d is the optimal depth. If the penetration equations showed that the round was able to penetrate beyond that depth, then the round detonated at the depth specified by the random draw. If the penetration equations showed that the round was not able to penetrate to the optimal depth, then the round detonated at the depth specified by the penetration equations.

6.2.4.2. Cratering From Explosions on or Above the Surface of Concrete

A surface-burst explosion is an explosion where the depth of penetration is zero. This would occur from a point-detonating fuse or a fuse that detonates the main explosive as soon as it makes contact with a solid surface. A point-detonating fuse is the easiest and most inexpensive type of fuse. Many TBMs and CMs will use this type of fuse. The size of the crater that a surface burst munition would crater can be calculated from Figure 40. Here, the scaled depth of burst is zero. Because point-detonating fuses are the least expensive and least complicated of the fuse types, they are used in a variety of weapons used in a variety of roles. The crater that point detonating fuses make will be larger than an airburst munition of the same explosive weight, but less than that of one with a time-delay penetrating type of fuse.

An above surface explosion is caused from a proximity charge. These charges have a device that senses how far above the surface the munitions is at and then initiates the detonation at a pre-determined altitude above the surface. The main types of proximity fuses used in ground attack munitions have either a radar altimeter or a barometric altimeter. The radar altimeter activates after the munition reaches apogee or when it is released from the carrier vehicle for sub-munition type of munition. It sends out an electro-magnetic pulse and then receives the reflected pulse that bounces off the surface. From the time delay between the sent signal and the received signal, the radar altimeter can determine its altitude above the ground. The barometric altimeter uses the increasing barometric pressure compared to a reference pressure (the pre-set static atmospheric pressure at the surface) to determine its altitude. With either type of fuse, the weapon detonates at a certain height above the ground.

An above surface burst will produce a very shallow and wide crater as seen in Figure 37. The main purpose of an above surface burst is to damage material and personnel with blast waves and fragmentation. As the altitude increases, the depth of the crater decreases. The size of the crater that an above surface detonation causes can again be calculated from Figure 40, but for an above surface detonation, the scaled depth of burst will be negative. From Figure 40, it is evident that a scaled depth of burst of above -0.2 kg/m^3 will result in a crater depth and radius of zero.

6.2.4.3. Cratering from Explosions Below Concrete

The polynomials plotted in Figure 40 allow the author to calculate the actual diameter and depth of a crater from a detonation on top of or within a concrete layer. For detonations that occur below a concrete layer, a different method is used. In a majority of cases in the work of this dissertation, the explosives detonated on or within the concrete due to the time-delayed fuse of the munition. The only cases where the munitions detonated below the concrete was in some of the early screening tests where the concrete was very thin. This section is shown mainly for completeness.

The method for calculating the size of a crater from detonations below a concrete layer was derived by Ross and Rosengren [118] and is elaborated on by Driels [62]. In general, their method calculates the impulse force below the concrete resulting from a stress function created by the explosive charge. It then calculates the critical impulse needed to shear a concrete plug directly above the explosive charge of a given radius. The size of the crater can be found by slowly increasing the radius of the plug until the critical shear impulse matches the applied impulse. This is illustrated below in Figure 41.

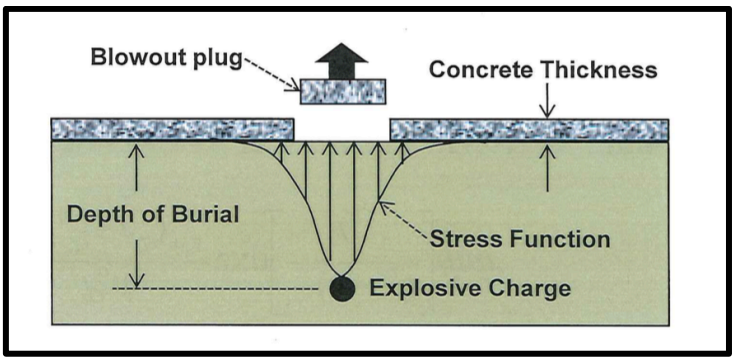

Figure 41: Method for Calculating Crater Size From Detonation Below Concrete (Adopted From Image in [62])

The critical impulse needed to shear the concrete can be found from the following equation [62, 118]:

$$I_{cr} = \frac{2\sqrt{2}}{3} h\sqrt{[(1-q)\rho_c + q\rho_r][(1-q)\sigma_c + q\sigma_r]}$$

Where I_{cr} is the critical impulse, h is the concrete thickness, q is the volumetric percent rebar in the concrete, ρ_r and ρ_c are the densities of the rebar and concrete, and σ_r and σ_c are the tensile strengths of the rebar and concrete. The concrete thickness and volumetric percentage rebar were variables that were previously used in the penetration equations. The tensile strength of the concrete and rebar and the density of the rebar are new. The penetration equations used the compressive strength of the concrete. Concrete compressive strength estimations can be calculated from the equations found in [119] or estimated from general numbers found in [120]. The tensile strength for concrete can be estimated from the compressive strength from the equations derived by Oluokun [121]:

$$f_{ct} = 1.38(f_c')^{0.69}$$

Where f_{ct} is the concrete tensile strength and f_c' is the concrete compressive strength. Continuing with other properties in the critical impulse formula, concrete density can be

estimated from [122]. The density of standard rebar types is found in [123] and the tensile strengths of rebar can be found from [124].

The critical impulse is the amount of impulse needed to shear a concrete cylindrical plug from the overall concrete layer. The detonation below the plug produces an impulse stress function that peaks directly above the explosive and decays radially outward as shown in Figure 41. The method for calculating the amount of impulse that results from this stress function at a given radius on the concrete face away from the point directly above the explosive center can be found with the following equation [62, 118]:

$$I = \frac{4}{\pi h^2} \int_0^R \int_{t_a}^{t_p} \frac{P_0 d_b}{(d_b^2 + r^2)^{4/3}} e^{\left[\frac{-(t-t_a)}{t_a}\right]} dt dr$$

Where I is the impulse imparted, h is the concrete thickness, r is the radius of the plug, P_0 is the peak incident overpressure when the wave arrives at the plug surface, d_b is the depth of the center of mass of the explosive, t_a is the arrival time of the blast wave and t_p is the positive pressure duration. This equation is a modification of the Friedlander's equation [108]. The peak detonation pressure can be found for various explosive compounds from [125] in table 1.2 or estimated from [126].

6.2.5. Runway Damage Effects Model: Runway Availability Sub-Model

The last several sections outlined the process used to determine the crater size that resulted from either a runway penetrating type of munition of a unitary type munition where the fuse type was either a point-detonating fuse or a proximity fuse. The next step is to determine the effect of creating a series of craters on a runway, or in other words, how many useable strips of runway remain after an attack that causes multiple craters on a runway.

6.2.5.1. Minimum Operating Strip (MOS)

Aircraft typically do not need the entire width and length of a runway to takeoff and land. The smallest strip of runway that an aircraft needs to either takeoff or land is called a minimum operating strip (MOS). A MOS is rectangular in shape and its dimensions are different for different aircraft, operating conditions, and loading [127, 128]. Typically the landing distance is longer than the takeoff distance for a given airplane, but both are dependent on the stall speed, which is dependent on the aircraft weight, and the pavement conditions (wet, dry, ice, etc.). A MOS sized for the takeoff distance would include the distance to accelerate from a standstill to the lift off velocity. This lift off velocity is typically about ten percent over the stall speed [129]. A MOS that is sized for landing would include the distance from touchdown, which typically occurs slightly above stall speed, to the point at which the aircraft fully stops. In some cases, the takeoff MOS may also be sized to allow for accelerate-stop. This is the total distance for the aircraft to accelerate from a stand still to decision speed, called V1, and then apply full breaking force until it comes to a stand still. For most Air Force fighter aircraft, with the exception of the A-10, the MOS will typically be at least 3,000 ft [130] but depending on conditions it could be larger. The A-10 has a slower stall speed and could have a MOS as small as 1,500 ft [175].

Whichever MOS is used, the MOS must be completely clear or all craters and debris for its full length and width and the MOS must completely lie within the bounds of the runway. The MOS, however, does not have to start or end at the beginning or end of the runway. Any area of the runway that is completely clear of craters over the full area of the MOS can be used. The immediate goal following and attack is to have the

requisite number of MOSs of a given size opened as soon as possible. Again, the size of the MOS is dependent on the aircraft, its load, and the conditions. The number of MOSs are dependent on the number of near simultaneous launches or landings that are required at the airport. After an attack, an airfield damage repair team will scout the full length of the runway looking for available MOSs that can be immediately used. They will also look for areas where an MOS could be quickly formed by repairing the fewest or the smallest craters [106, 128, 131]. If a repair is needed to a crater site, the repair could consist of simply refilling the crater hole with cement for small craters or filling in the hole and placing a large repair sheet on top for larger craters [106, 132]. An example of MOSs along a runway following an attack that produced a certain number of craters of various sizes on the runway is shown below in Figure 42.

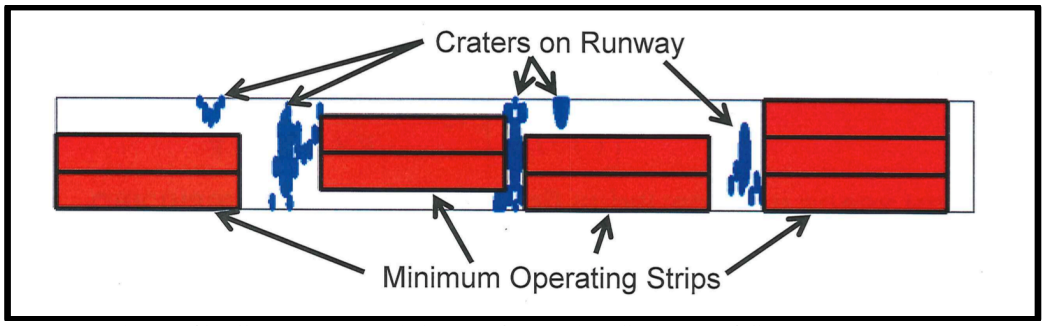

Figure 42: Craters and Minimum Operating Strips (MOSs) on a Runway

6.2.5.2. Aim Point Distribution Across and Along the Runway

When an enemy force is targeting the runway with a set of accurate weapons, they will attempt to disperse those weapons along the length of the runway in order to close as many MOSs as possible. But, when targeting with a relatively inaccurate weapon they will spread those aim points out much less in an attempt to aim more at the center of the runway. In this work, it is assumed that for CMs there are eight aim points along the length of the runway and three aim points at each of these eight across the width of the

runway. Each of these aim points is evenly distributed across the length and width. This is illustrated below in Figure 43. For less accurate TBMs, it is assumed that there are three aim points along the length of the runway and these aim points are all at the center-line of the runway. When shooting at the runway with multiple weapons, the aim points are randomly chosen without replacement until the number of weapons exceeds the number of aim points that have not yet been targeted. Once that happens, all aim points are coded as available and the process continues selecting random aim points without replacement.

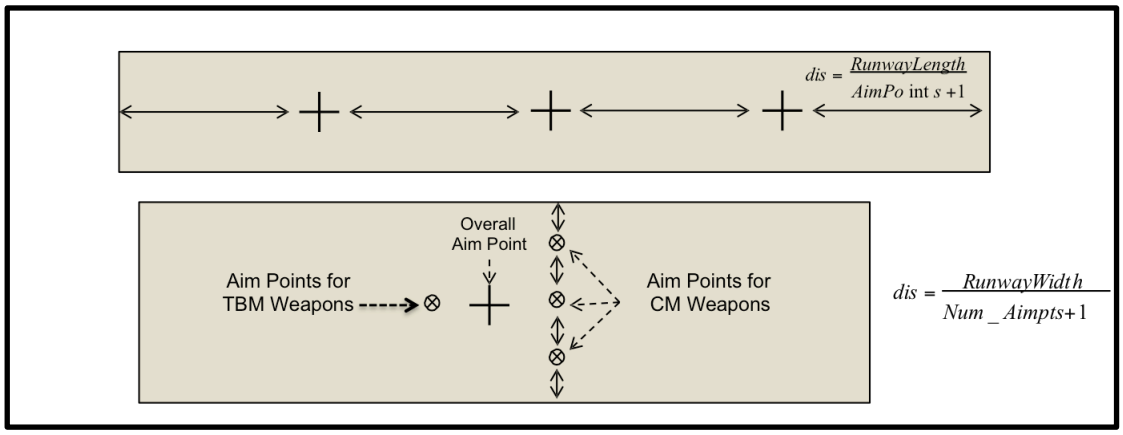

Figure 43: Aim Point Distribution Along the Runway and Across the Runway

6.2.5.3. Unguided Weapons' Impact Error

While the enemy force may equally distribute the weapons along and across the runway, the weapons do not necessary hit their exact target. The accuracy of a ballistic or cruise missile is quantified by its circular error probable (CEP). The CEP is the radius of a circle, centered at the aim point, in which 50% of the weapons are expected to land [62]. The impact error can also be broken down into range and deflection errors. The range-direction is normally parallel to the gun-line, or a line drawn from the launch point to the aim point. The deflection-direction is perpendicular to the gun-target line. A

weapon shot at an aim point can miss in both the range and deflection direction. The range error probable (REP) or the deflection error probable (DEP) is the distance from the aim point to a pair of equidistant parallel lines in which 50% of the impacts will occur [62]. The definition CEP, REP, and DEP are shown below in graphical form.

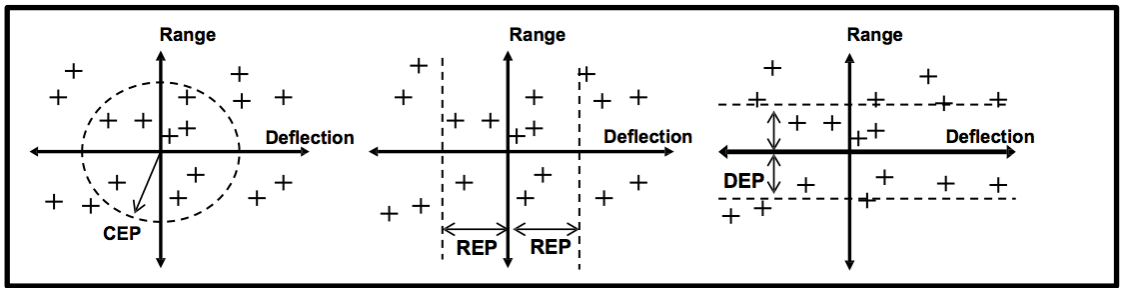

Figure 44: Circular, Range, and Deflection Error Probable (CEP, REP, DEP)

In testing, the CEP is normally calculated from the observed REP and DEP. Most weapons will miss in a fashion that forms a normal distribution of impact points around the aim point [62]. In testing, this normality assumption can be verified with the Chi-squared test [133]. If the weapon is not biased to miss in any given direction, then the mean of the impact points will be the aim point. Thus, the range or deflection error can be described as $N(0,\sigma_r)$ or $N(0,\sigma_d)$ where N stands for the normal distribution and $N(\mu,\sigma)$ is the mean and standard deviation of that normal distribution. For a given test, an experimenter can determine the standard deviation in both the range and deflection direction as:

$$\sigma = \sqrt{\frac{\sum_1^n (x_n - \mu)^2}{n-1}}$$

where n is the number of observations, x_n is the range or deflection error of the n^{th} observation, and μ is the mean range of deflection error of those observations. Because the range and deflection errors are normally distributed, and by definition, 50% of the

impacts lie within the REP or DEP perimeter, the REP and DEP can be found with the standard normal tables. Referring to Figure 45, the REP or DEP enclose 25% of the area to each side of the mean in the normal distribution. Using a single tail normal distribution table, this means that 75% of the area under the normal distribution lies to the left of the right most REP or DEP line. The 75% area z-score is 0.6745. Therefore, the REP and DEP can then be calculated as [62]:

$$REP = 0.6745\sigma_r \ \ and \ \ DEP = 0.6745\sigma_d$$

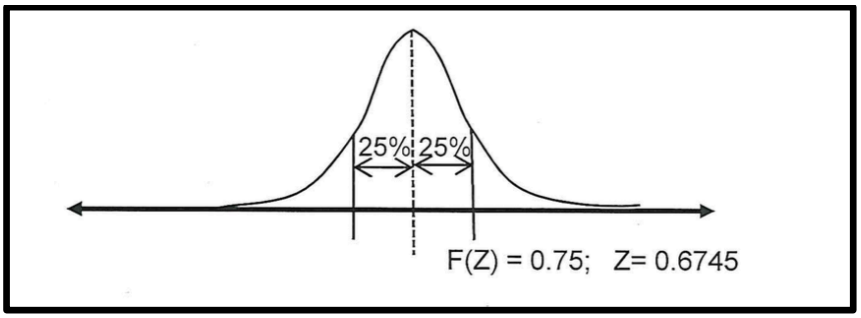

Figure 45: Normal Distribution for REP or DEP

When the range and deflection errors are combined they create a two dimensional error. Both range and deflection errors are normally distributed and two perpendicular normal distributions are described by the bivariate distribution. The probability density function (PDF) of the bivariate distribution is given as:

$$f(x,y) = \frac{1}{2\pi\sigma_x\sigma_y\sqrt{1-p^2}} exp - \left[\frac{1}{2(1-p^2)}\left\{\frac{(x-\mu_x)^2}{2\sigma_x^2} + \frac{(y-\mu_y)^2}{2\sigma_y^2} - 2p\frac{(x-\mu_x)}{2\sigma_x}\frac{(y-\mu_y)}{2\sigma_y}\right\}\right]$$

where μ is the mean of either x or y, σ is the standard deviation, and p is the correlation between x and y given as $V_{xy}/(\sigma_x\sigma_y)$ where V_{xy} is the covariance. If x and y are independent, meaning that the weapon is equally likely to miss in both the range and deflection direction, then the covariance is zero and the bivariate distribution PDF equation reduces to:

$$f(x,y) = \frac{1}{2\pi\sigma_x\sigma_y\sqrt{1-p^2}} exp - \left[\frac{(x-\mu_x)^2}{2\sigma_x^2} + \frac{(y-\mu_y)^2}{2\sigma_y^2}\right]$$

In addition to being uncorrelated, a further special case of the bivariate distribution is if the means or both variables are equal to zero and the standard deviations are equal. This occurs when the weapon is equally likely to miss in either range or deflection, meaning the REP and DEP is uncorrelated, the REP and DEP both have a mean of zero, meaning the weapon is not biased in one direction over another and the weapon misses an equal amount in both range and deflection, meaning the standard deviations are equal. When this happens, the impact distribution can be described by the Rayleigh distribution [62]. It is important to note that even though the range and deflection errors are normally distributed with equal variance and each with a mean of zero (N(0,σ)), the radius, given by $r=(x^2+y^2)^{0.5}$, is Rayleigh distributed [62]. The PDF of the Rayleigh distribution is given as:

$$f(r) = \frac{r}{\sigma^2} exp\left[\frac{-r^2}{2\sigma^2}\right]$$

where r is the radius to the impact point from the aim point and σ is the standard deviation (equal in both range and deflection). The cumulative distribution function (CDF) of the Rayleigh distribution is given as:

$$F(r) = 1 - exp\left[\frac{-r^2}{2\sigma^2}\right]$$

Referring back to the definition of CEP, the CEP is the radius where we expect 50% of the weapons to fall within. So, for a Rayleigh distributed impact set, the CEP is found from the standard deviation of the impacts using the CDF. The probability of an impact landing within a given radius band is found with the CDF as [62]:

$$P(r_1 < r < r_2) = F(r_2) - F(r_1) = exp\left[\frac{-r_1^2}{2\sigma^2}\right] - exp\left[\frac{-r_2^2}{2\sigma^2}\right]$$

so setting r_1 to zero and r_2 to the CEP and P(r<CEP) to 50% (0.5), the CDF of the Rayleigh distribution reduces to [62]:

$$CEP = 1.1774\sigma$$

This form of the CEP is easier to work with in simulation, because it is easiest to calculate a miss distance in both x and y (range and deflection) and use those for calculating the impact point as shown in Figure 46. Most literature sources will report the error of a weapon in the form of a CEP. Likewise, many weapons satisfy the Rayleigh assumptions, so the standard deviation of the range and deflection (x and y) error are equal and each error can be described by the normal distribution N(o,σ) [62]. For a given CEP, this standard deviation is found with the above.

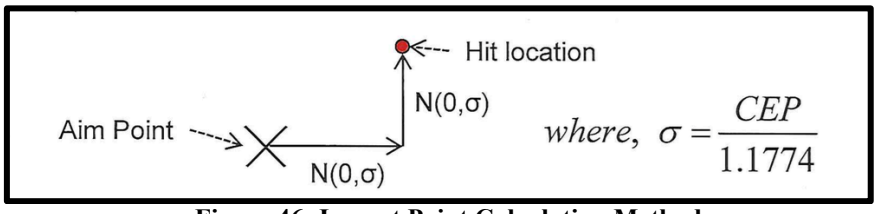

Figure 46: Impact Point Calculation Method

6.2.5.4. Guided Weapons' Impact Error

Guided weapons typically have a suite of sensors on board to identify where the weapon is relative to its pre-programmed flight path. These sensors could consist of a global position system (GPS), an inertial navigation system, a terrestrial navigation system, a look ahead and look down terrain following radar, or a combination of these. It will have some sort of guidance algorithm that will actuate control surfaces in order to correct for any deviations from its planned flight path. Most guided weapons will also have a terminal guidance sensor that hones in on its intended target. These sensors could

be radar based, electro optical or infrared based, or a combination of these. A special class of guided weapons is anti-radiation weapons. These weapons sense the electromagnetic energy that radars radiate and hone in on the source.

The final result of a guided weapons flight and terminal guidance phase will fall into one of three categories: direct hit, near miss, or gross error [62]. A direct hit is when all guidance systems function as they are supposed to and the weapon hits the exact location that it was aimed at. A gross error occurs when either the flight guidance system or the terminal guidance systems fail in a catastrophic manner and the weapon lands very far from its intended aim point. Typically, any impact more than 4 standard deviations from the aim point is considered a gross error [62].

A near miss occurs when the weapon's flight or terminal guidance system is functioning properly, but environmental conditions or the target geometry prevent the weapon from fully correcting its course and it lands near its intended aim point. Most weapons' near miss patterns exhibit a normal distribution, N(0,σ) [62]. Each of these outcomes will have a probability associated with them that is based on testing or modeling and simulation. Because the outcome from the engagement with a guided weapon must fall into one of these three categories, their sum must add to one [62]:

$$P_{direct\ hit} + P_{near\ miss} + P_{gross\ error} = 1$$

Typically, most CEP number for guided weapons are reported for their near misses with the gross error and a number of the direct hits removed [62]. Thus, from a testing perspective, after a set of samples, the standard deviation is calculated for the entire data set and any sample that is more than 4σ from the mean is removed and considered a gross error. The probability of a gross error is calculated as the total number

of points removed from the data set (because they were >4σ) divided by the total sample set. Next, a chi-squared test is performed on the remaining data (direct hits and near misses). If the chi-squared test fails because the direct hits bin creates too much kurtosis, some of the direct hits are removed and the test repeated. Also any points that now fall outside the 4σ limit are removed and counted as gross errors. This process is repeated until the remaining data set is approximately Gaussian. As more and more direct hits are removed, the chi-squared test would improve and then begin to degrade. The optimal point of the chi-squared test is generally used in order to determine the number of direct hits to remove [62]. From this normal distribution a standard deviation, σ, can be calculated and from that standard deviation, using the Rayleigh distribution described in the previous section, the CEP is calculated as [62]:

$$CEP = 1.1774\sigma$$

The above equation can be used to calculate the standard deviation from a known CEP of a weapon. In simulation, in order to determine the impact location of a guided weapon relative to its aim point, a random draw is conducted relative to the uniform distribution, U(0,1) to determine the guidance outcome: direct hit, near miss, or gross error. Referring to Figure 47, if the U(0,1) draw is less than the probability of a gross error, then the weapon will impact at +/- 4σ in both range and deflection from the aim point. If the U(0,1) draw is greater than the probability of a gross error but less than the probability of a gross error plus the probability of a near miss, then two more random draws from the N(0,σ) are conducted to determine the error in range and deflection. If the U(0,1) random draw is greater than the probability of a gross error plus the probability of a near miss, then the result is a direct hit [62].

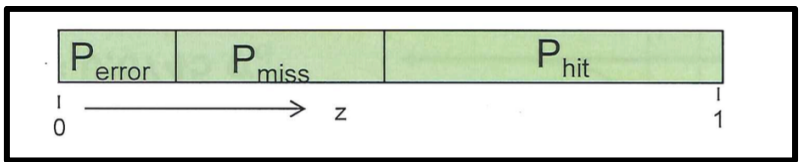

Figure 47: Guidance Results for a Guided Weapon

6.2.5.5. Runway Penetrating Sub-munitions' Impact Pattern

Calculations for the mean impact point for both unguided and guided weapons relative to their aim points has been previously discussed. For unitary munitions, the impact would occur at this location and the crater size determined as explained in the cratering section for a depth of burial (DOB) of zero. For runway penetrating submunitions, the previous two sections describe how to calculate the mean impact point of the cluster. Next, it is necessary to investigate the individual impact point of each penetration munitions relative to this mean impact point.

A submunition is released from its carrier vehicle at a predetermined point in that carrier vehicle's flight. This is typically based on altitude and speed sensed via a barometric or radar altimeter, but it could also be based on data from a terminal type senor described in the last section. The submunition can be expelled from the carrier vehicle via a push mechanism, an explosive charge, or centrifugal force for rotating carrier vehicles. Whatever the mechanism that is used to expel the submunition, its initial flight conditions (speed, altitude, rotation, etc.) upon release are a function of the carrier vehicle's flight conditions. In other words, its initial speed will be the carrier vehicle's speed plus the exit velocity. Its initial pitch will be that of the carrier vehicles plus the additional pitch provided from the exit mechanism.

Most weapons are designed to provide various amounts of additional energy to each submunition such that the submunitions are carried to the ground and land in a

uniformly distributed manner [134]. Because the submunitions land in a uniform distribution about the main impact point, all that is needed to calculate their impact location is the maximum distance they can land from the mean impact point. Then a uniform random draw can determine how far between the mean impact location and this maximum distance each penetrator lands relative to the mean impact location.

In order to determine the maximum spread possible for a submunition, the 6DOF flight model described earlier is used, with a specified the release altitude and speed of the carrier vehicle, and at the maximum possible release angle. Referring back to Figure 22, the penetrator's initial speed and angle is dependent on the release altitude and the range from the launch point to the impact point. Therefore, for a given range and release altitude, the initial speed is that of the carrier vehicle at the release altitude and the initial pitch is that of the carrier vehicle plus the maximum possible pitch that can be imparted from the release mechanism. Using these initial conditions, the 6-DOF model can then propagate the submunition to the ground. Its impact point, relative to that of a submunition with a zero release angle, determines the maximum spread of the uniformly distributed impacts.

Most weapons will exhibit a circular uniform impact pattern on the ground. For these weapons the impact of each weapon is determined with radial coordinates as described by Figure 48. Here, the angular distance between each weapon is 360 degrees divided by the number of penetrators. The radial distance is based on a uniform distribution and is equal to the max spread distance times U(0,1). For those weapons that exhibit a square impact pattern. The range and deflection distance from the mean impact

point for each weapon is found from the uniform distribution from -1 to 1: the range or deflection error is the max spread times U(-1,1).

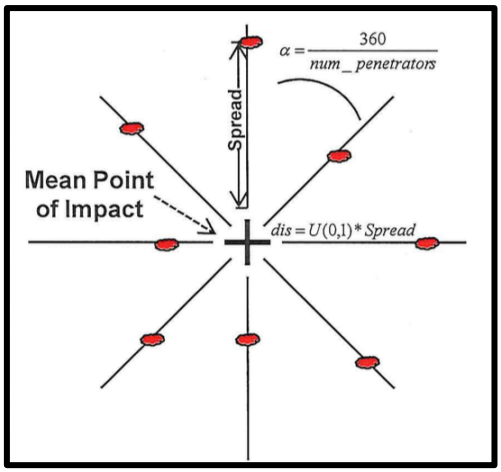

Figure 48: Circular Uniform Submunition Impact Pattern

6.2.5.6. Runway Minimum Operating Strip (MOS) Selection Algorithm

The last several sections explained how to calculate the impact locations for unguided and guided weapons and how to calculate the impact location for submunition types of weapons. Once the impact locations are known, the first several sections in this chapter explain how to calculate their crater size based on either a surface burst explosion or from that a penetrating type munitions. For a given attack with a series of different weapons, these methods are applied to each weapon to determine the resulting crater pattern on the runway. Once the pattern is known (location and size of each crater) the final step is to determine how many minimum operating strips (MOSs) remain on the undamaged portions of the runway.

The most logical search pattern is to start at one end of the runway and work along the length to the opposite end. So, for a cratering pattern such as that shown in Figure 49, the MOS search starts at the bottom left of the runway and progresses initially, bottom to top and then left to right.

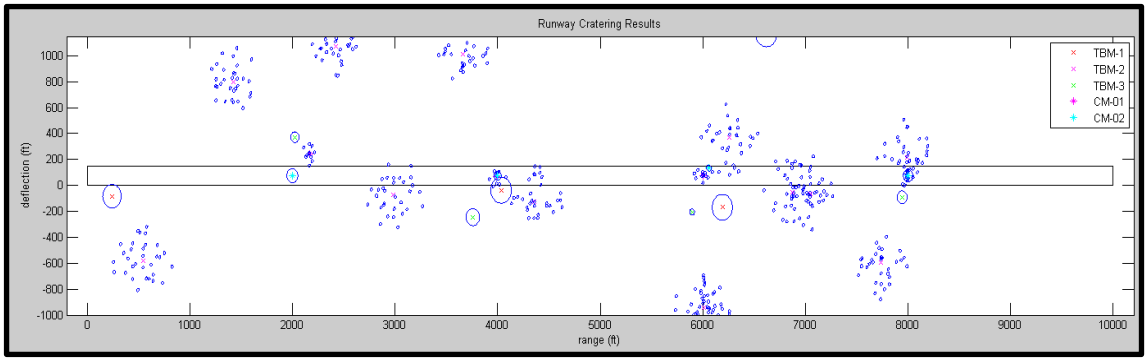

Figure 49: Sample Crater Pattern on a Runway

At the start location, the program places a MOS rectangle of the given size at the lower left corner of the runway. The program then looks inside the MOS to determine if there are any craters or preexisting MOSs that lie within the bounds of the proposed MOS. If there are not any craters or other portions of another MOS, then that MOS location is good and the program moves to the top of that MOS and repeats the process. If there are craters within the proposed MOS location, the program finds the top of each crater and moves to the top of the crater furthest from the bottom edge of proposed MOS location and repeats the process. If there is a preexisting MOS that falls within the boundaries of the proposed MOS, the program moves to the top of the preexisting MOS and repeats the process. If there are both craters and MOSs within the proposed MOS location, the program moves to either the top of the crater furthest from the bottom of the proposed MOS location or the top of the preexisting MOS, whichever is further away from the bottom of the proposed MOS location. This process is repeated until the program reaches the top edge of the runway.

Once at the top edge of the runway, the program must select how far to move in the horizontal direction along the length of the runway. The program looks at all craters and preexisting MOSs that it found during its vertical search. It then finds the right edge

of each crater and preexisting MOS. The program then moves to the right edge of the crater or preexisting MOS that is closest to the current proposed MOS start location and repeats the vertical process. The reason the program only moves to the next closest crater or MOS location is because other MOSs may be able to be stacked above or below that location. This process of searching vertically and then horizontally continues until the program reaches the far end of the runway. Once complete, the MOSs are counted.

This method produces a set of MOSs that are anchored at the lower left corner of an available space. The MOSs could move up or right until they encounter another MOS or crater as illustrated below in Figure 50. However, there is not enough room either above or to the right of the MOSs to place another entire MOS of the given size.

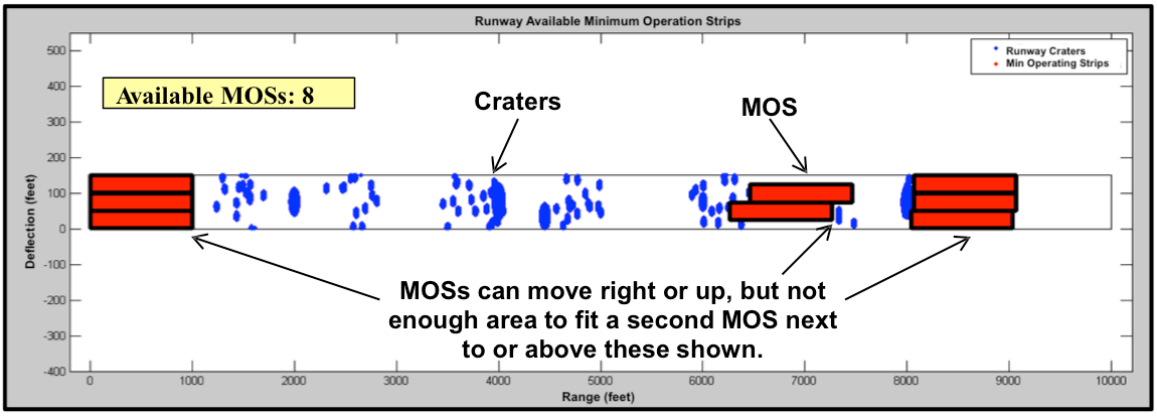

Figure 50: Sample Results from MOS Selection Program

6.3. Runway Damage Effects Model Surrogate Model

Using the methods descried in sections 6.2-6.2.4, a MATLAB code was created to calculate the impact location and crater size for an attack from TBMs and CMs. The program then uses the MOS selection algorithm described in section 6.2.5 to determine the number of MOSs of a given size remained following the attack. On the author's two core 3.0 GHz computer, the 6-DOF flight model takes an average of 30 minutes to propagate rounds to the ground. The runway cratering model and MOS selection

program takes 2-10 minute to run depending on the number of munitions and craters. In addition, the runway availability model is stochastic, so many Mote Carlo runs are required to create meaningful distributions.

These run times are too long for direct use in later sections of this dissertation. These later sections will examine the effectiveness of an AMD laydown based on the number of MOSs that remain. In essence the effectiveness is based on the outcome or the effects of the attack. Therefore, the calculations and determination of the number of MOSs available had to be sped up. This increase in speed is realized with surrogate models, also known as metamodels. Metamodels (also known as surrogate models) are models of a model. The process of design of experiments and the creation of these metamodels is described in appendix B and C. This section will describe the process of creating the specific metamodel of the airfield effects model.

6.3.1. Spread and Crater Size Surrogate Models for TBMs and CMs

The airfield effects metamodel requires two separate surrogate models: one for the maximum spread of the submunitions and a second that predicts the crater depth from each submunition. The maximum spread metamodel will predict the radius of the submunition impacts assuming that all submunitions were ejected at the maximum allowable release angle. As stated earlier, observed cluster munitions impact patterns appear uniformly distributed [63]. Once this maximum distance is known, a uniform random number can be drawn for each submunition to determine its impact radius. This impact radius is then used with other factors to predict penetration distance and the minimum and maximum possible size of the crater. The process of creating these metamodels is summarized in Figure 51.

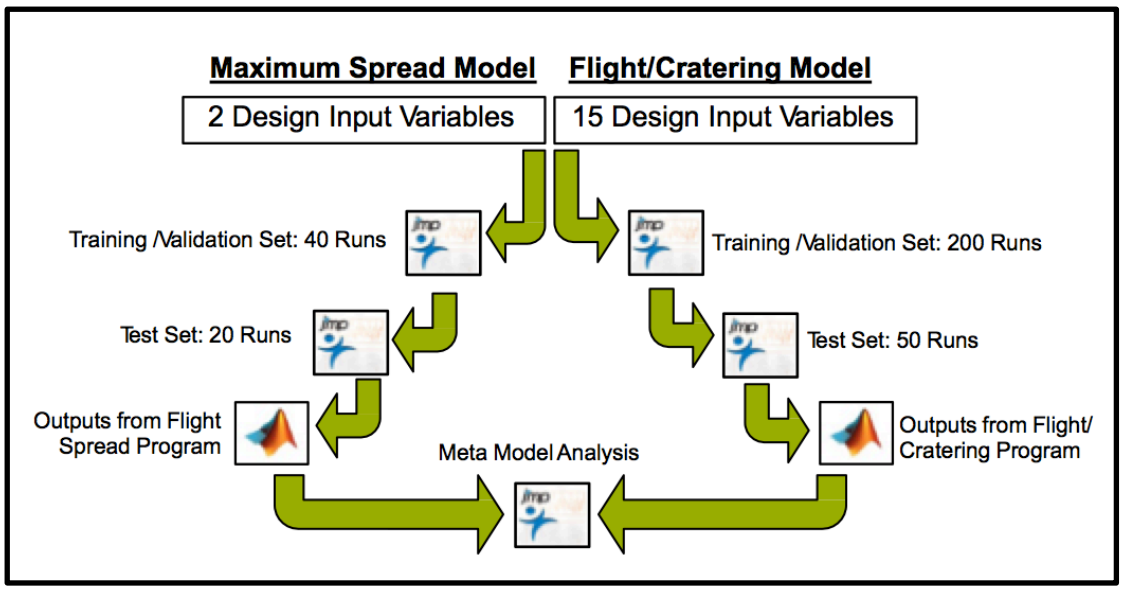

Figure 51: Airfield Attack Effects TBM Metamodel Setup

Each metamodel requires two data sets as explained in appendix C, a training and validation set and a test set. The rule of thumb for the smallest number of test points, or runs, in the training and validation set is at least 10 runs per design variable and at least 20% of the training set for the validation set [135, 136]. In both the spread and cratering metamodel, more design points than the ten per rule of thumb were used to help ensure a good model fit and ensures a smaller degree of error. This was needed because these predictive models will be used later with other predictive models of the surface-to-air engagements and any prediction errors will compound together.

The training and test sets for each model were created in JMP using the Latin hypercube design. This design was chosen because it helps to spread the points in the design space, but ensures that the set can be projected into a smaller dimensional space without overlap of the points [137-140]. This was especially valuable in the cratering metamodel since the same design set was used to predict the minimum and maximum crater size and there was no guarantee that the two models would use the same design

variables. In both cases the validation set was also created in JMP using the augment design feature. This allowed additional points to be populated into the original design ensuring that those validation points were spread as far from the training points and each other as possible. Because the points end up being spread through the design space, if they show a good validation fit then that increases confidence in the predictive ability of the metamodel.

6.3.1.1. TBM Max Spread Metamodel Results

The maximum spread metamodel predicts the maximum radius that could result from a submunition released at the given release altitude and speed at the maximum possible release angle of five degrees. The simulation uses the flight propagation model from EADSIM (see section 6.2.1) to fly the TEL from the launch point to the release point and then releases two submunitions at the given release altitude: one at a release angle of zero degrees and one at the maximum angle of five degrees. It then propagates each to the ground in a six degree-of-freedom model (see section 6.2.2). After that, it measures the distance between the two impact points. The input variables for the maximum spread model are the TEL launcher distance and the release altitude. The launcher distance plays a role in the TBM angle at release as well as the release speed. The release altitude is important because the submunitions will spread more at a higher release altitude. A summary of the inputs and outputs from this analysis is shown below in Figure 52.

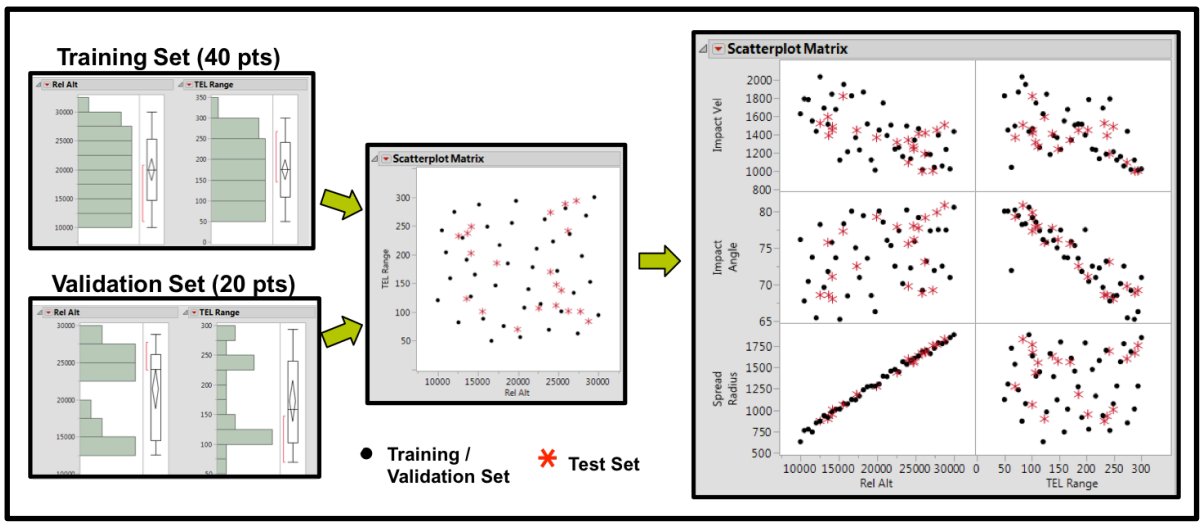

Figure 52: TBM Max Spread Model DOE Inputs and Outputs Diagram

In Figure 52, the black circles are the model fit set and the red stars are the validation points (these were excluded from the fitting process and used later to validate the fit). The results are also summarized in histogram format in Figure 53.

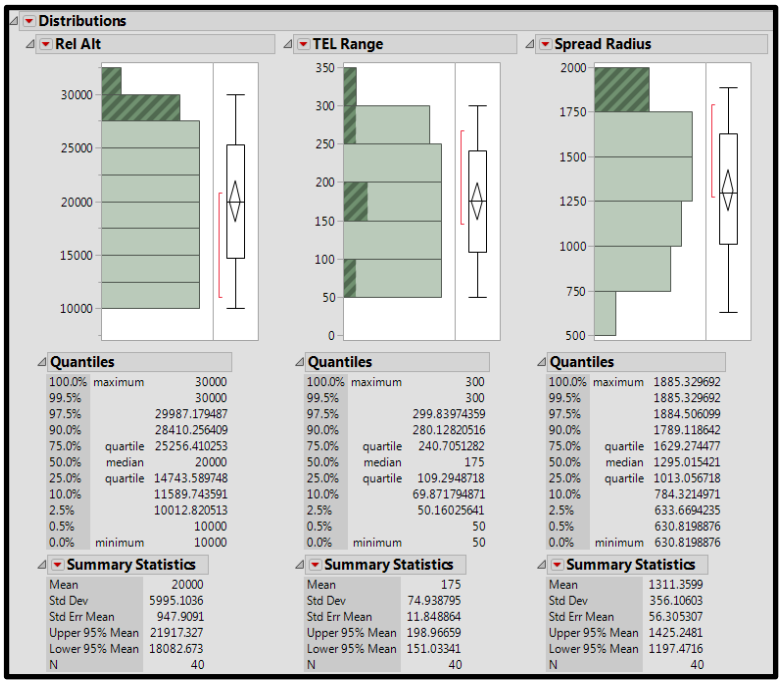

Figure 53: TBM Max Spread Model DOE Input and Outputs Histogram

The maximum spread observed was 1,885 ft and the minimum spread was 631 feet. This means that the spread varied over a range of about 1,254 feet. Figure 53 also highlights the intuitive fact that the largest spread resulted from the highest release angles. Using these outputs, two metamodels of the maximum spread radius were created: a response surface (RSM) and a neural net with 20 hidden nodes each with a hyperbolic tangent activation function (NN20). Both of these models were evaluated with the techniques described in appendix C. The actual v. predicted graph for these two models is shown below along with their associated R^2 and root mean squared error (RMSE).

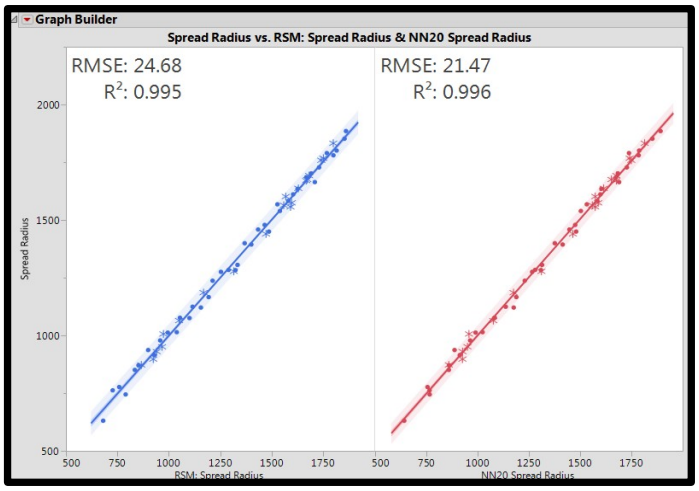

Figure 54: TBM Max Spread Metamodel Actual by Predicted

Each model was very good at predicting the maximum spread. Each had an R^2 over 0.99 and each had low RMSEs. The residual plot of each, shown below in Figure 55, also showed no issue for either model.

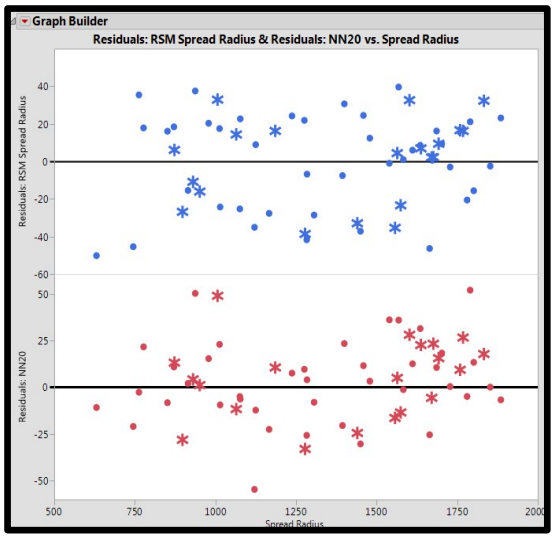

Figure 55: TBM Max Spread Metamodel Residuals

A good model must not only predict well, but it should also be unbiased. In order to ensure that the model was unbiased, a histogram of the residuals was also plotted and the histogram tested verse the normal distribution using the Sharprio-Wilk test for normality. These results are shown below.

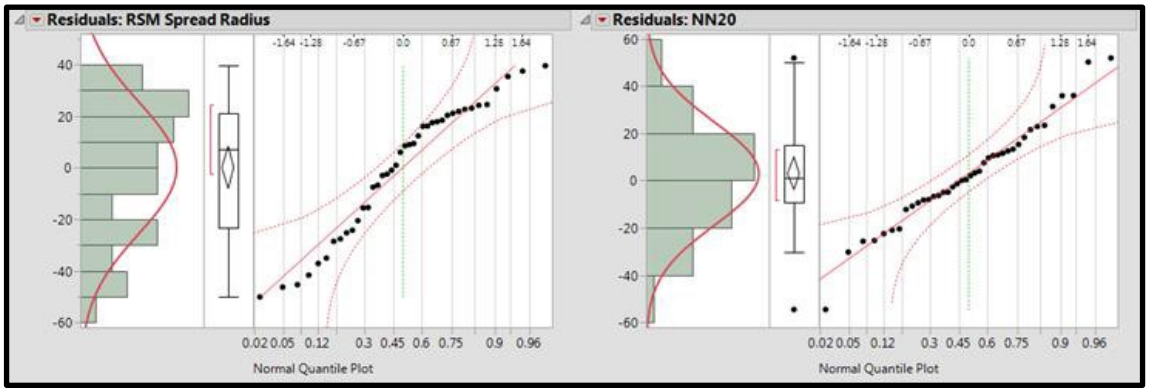

Figure 56: Histogram of Residuals and Normal Quantile Plot for TBM Max Spread Models

Table 9: Shaprio-Wilk Test Results for TBM Max Spread Model Residuals

Shaprio-Wilk Test	P-Value
Response Surface Eqn	0.0336
Neural Net	0.8279

The response surface equation appears to deviate more from the normal distribution than the neural net. This is confirmed by the Sharprio-Wilk p-value less than 0.05 for the response surface model. Therefore, the neural net was chosen as the best metamodel for the max spread distance of the TBM. This model will be used in future sections to help predict the impact point for each submunission as explained earlier in section 6.2.5.5.

6.3.1.2. TBM Crater Size Metamodel Results

The cratering model for the TBMs used all parts of the process explained in sections 6.2 through 6.2.4.3. The TBM was initially propagated to the release point using the EADSIM flight program. At the given release altitude, a penetrator was ejected at the given release angle and propagated to the ground using the six degree of freedom model. Once it impacted, the penetration equations used the impact velocity and angle to determine the penetration depth. Once the round exploded, the cratering model predicted the min and max crater size that would result from an explosion at that depth. Because the cratering model used all these other models the input set was the set for all the inputs of all the models. There were 15 input variables in the cratering metamodel. These were described in various parts in sections 6.2 through 6.2.5 and are summarized in Table 10 below.

Table 10: DOE Inputs for TBM Cratering Metamodel

Input	Min	Max	Units
Penetrator Release Altitude	10,000	30,000	ft
Number of Penetrators	10	40	number
Launcher Range	50	300	km
Penetrator Release Angle	0	5	degree
Delay Fuse Max Depth	6	36	in
Explosive Weight	1	15	lb
Runway Width	50	1000	ft
Concrete Thickness	12	42	in
Percent Rebar	0	5	%
Concrete Compressive Strength	2,000	3,500	psi
Density of Concrete	125	175	lbf/ft^3
Tensile Strength of Rebar	70,000	90,000	psi
Rock Thickness	6	24	in
Rock Unconfined Compressive Strength	3,000	4,000	psi
Rock Quality	0.5	0.9	none

These fifteen factors were used in JMP to produce a 200-design point training and fitting set and a 50-point validation set. The training set was a Latin hypercube design and the validation set was produced from a space filling augmentation to ensure that it sampled evenly throughout the design space and away from any points already in the training and fit set. The same training and validation set were used to create both the minimum and maximum crater size prediction model. The Latin hypercube design was used because the same factors may not play a role in both the min and max size models and the Latin hypercube can project into smaller dimensional spaces without loss of points. A summary of the training set and validation set is shown in Figure 57, along with the factor ranges in brackets and the associated units of that factor in parenthesis.

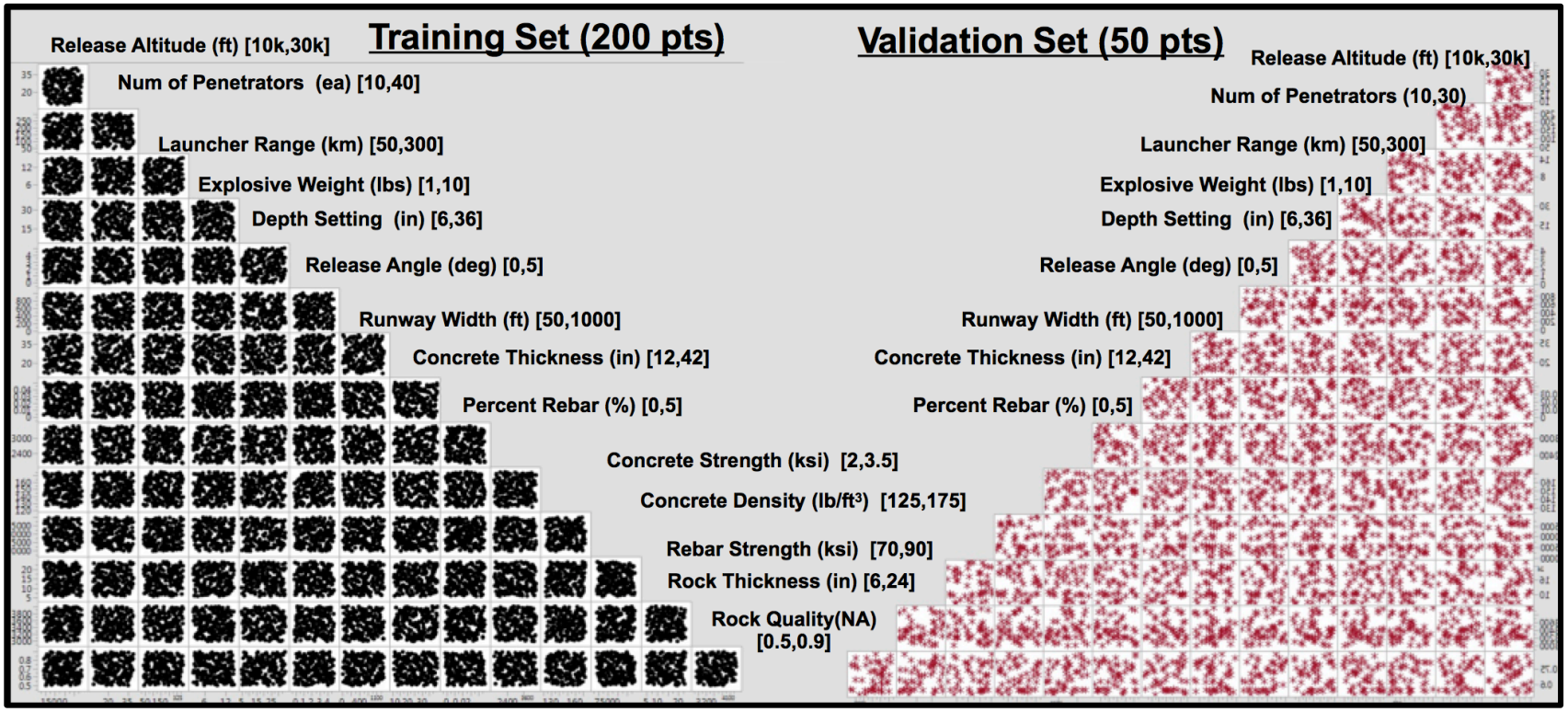

Figure 57: TBM Flight and Cratering Model DOE Distribution

The first step after the DOE run was to validate the assumptions identified about the use of the Sandia equation and the six-degree of freedom model from sections 6.2.2 and 6.2.3.4. The impact speed should be less than 4,000 feet per second and the impact angle less than 89.5 degrees. To validate these two assumptions, all results from both the training set and validation set were plotted in a histogram. This histogram is shown in Figure 58. From the data below each histogram it can be seen that the maximum impact speed was 2,159 feet per second and the maximum impact angle was 87.4 degrees. Both of these values are less than the maximum allowable values.

Figure 58 also shows the results for the minimum and maximum crater diameter size. It should be noted that both the minimum and maximum distributions show a range of about 10.5 feet from their respective minimum to maximum values. The maximum crater diameter ranged from 5.62 feet to 16.53 feet (10.91 foot range), and the minimum crater diameter ranged from 4.07 feet to 14.20 feet (10.13 foot range). The results for both the training and validation sets are also plotted against each input factor in Figure 59. In Figure 59 the black dots are the training set and the red stars are the validation set. The results show that the cater size is dominated by the max depth setting and the explosive weight and the other factors play a smaller role.

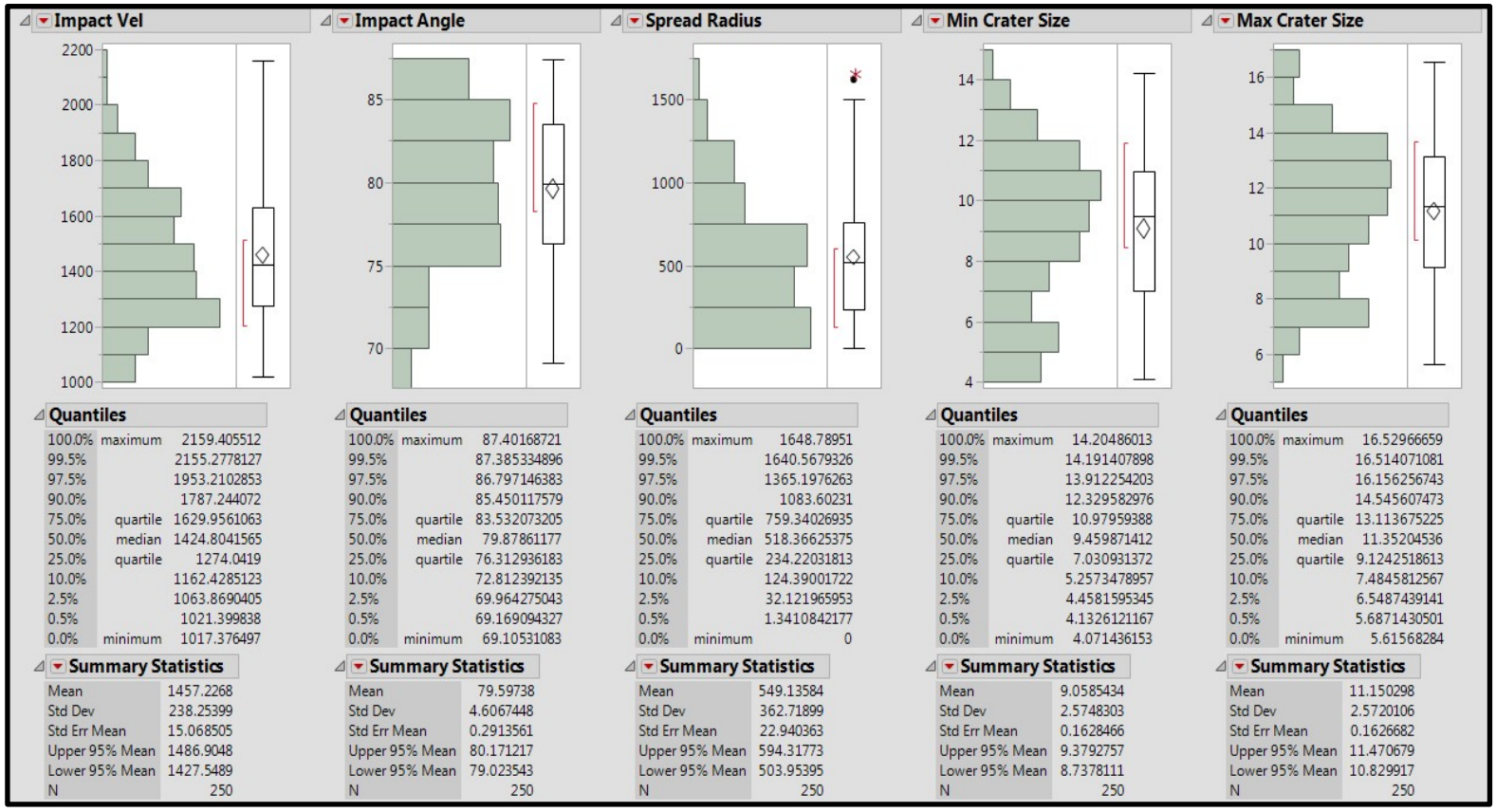

Figure 58: TBM Flight and Crater Assumptions Validation

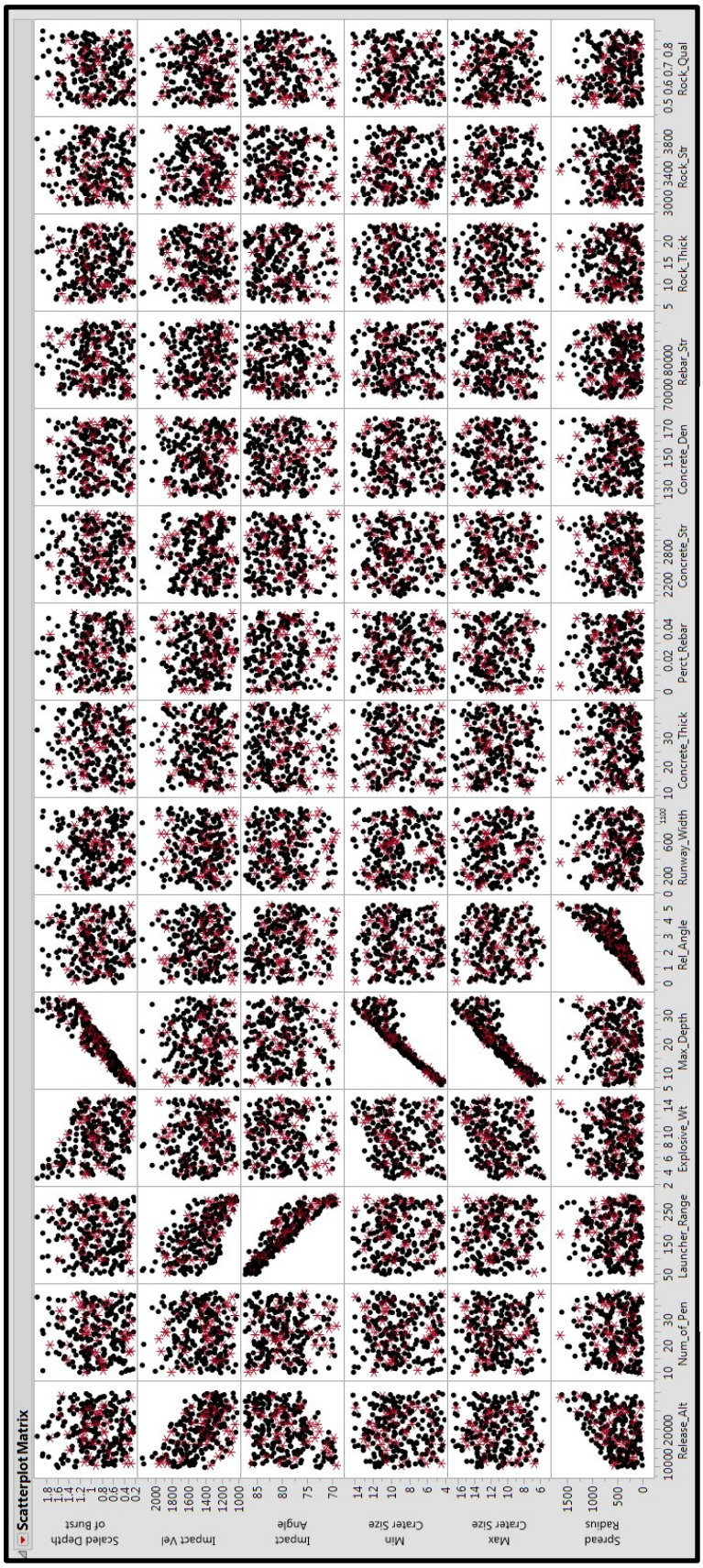

Figure 59: TBM Flight and Crater Size Results Plotted Against Inputs

For both the minimum and maximum crater size, multiple models were created and compared to each other in order to select the best one. Starting with the minimum crater size, the following models were created: a response surface model, a response surface model of a box-cox transform, three different neural net models with 7, 10, and 15 hidden nodes, each with a hyperbolic tangent activation function, a neural net with 10 hidden nodes for the box-cox transform, and finally, a Gaussian kriging model.

The results of fitting all these models are shown in Figure 60. This figure shows the actual v. predicted plots for both the training and validation data sets along with each models root mean squared error (RMSE) and R^2 value. The training data set models are shown on the left and the validation set data models are shown on the right. When selecting a model, the ability to predict is the most important characteristic. Therefore, the actual v. predicted, RMSE, and R^2 values of the validation set should be considered above those of the training set since the validation set was not used to create the model. The validation set is a test of the models predictive power. A summary of the RMSE of the validation set is shown below in Table 11

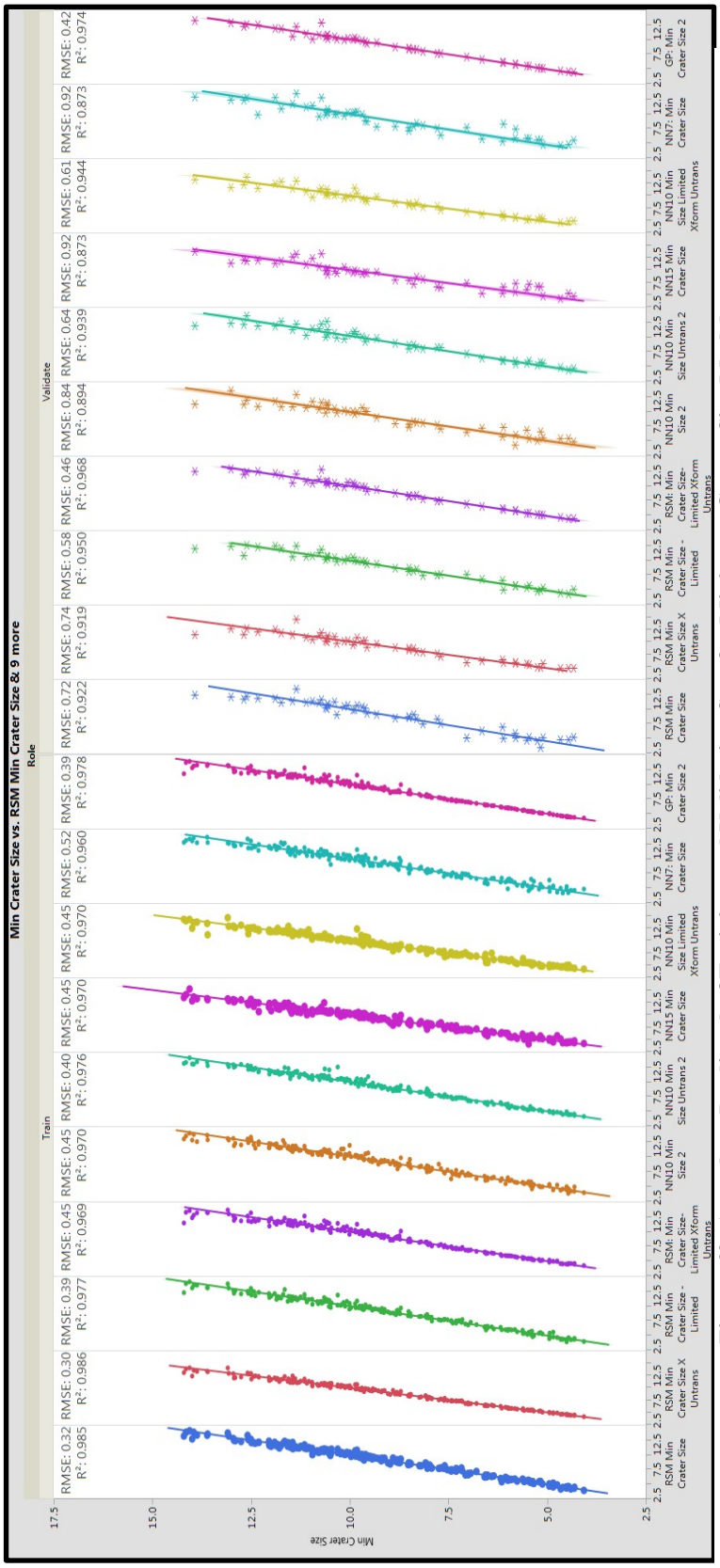

Figure 60: Actual vs. Predicted of Training and Validation Sets for Minimum Crater Size Models

Table 11: Error for Each Model of the Minimum Crater Size Using the Validation Set

Model	RMSE	%Error
RSM	0.72	7.11
RSM (Box-Cox Xform)	0.74	7.30
RSM (Stepwise)	0.58	5.72
RSM (Stepwise Xform)	0.46	4.54
NN (10 Node)	0.84	7.99
NN (10 Node with Xform)	0.64	6.32
NN (15 Node)	0.92	9.08
NN (7 Node)	0.61	6.02
NN (10 Node with Stepwise)	0.92	9.08
Gaussian Kriging (Process)	0.42	4.15

Table 11 shows that the Gaussian kriging model performed the best in terms of prediction capability, but the residuals also must be considered in the model selection. While the response surface models must have random distributions of the error, the neural nets and kriging models do not necessarily have to have this feature, but it is desirable. A plot of the residuals for each model is shown below in Figure 61 and the summary statistics for each model is organized in Table 12. The table shows the statistics for the training set on top (model fit error) and the validation set on the bottom (model representation error). Most models showed an increase in the residuals at a crater size around 10 feet. Overall, the Gaussian kriging model, the model with the lowest RSME of the validation set, did not have a poor residual plot. This is confirmed in the residual histogram and normal quantile plot of Figure 62. The main deviations from normal were the results of two points.

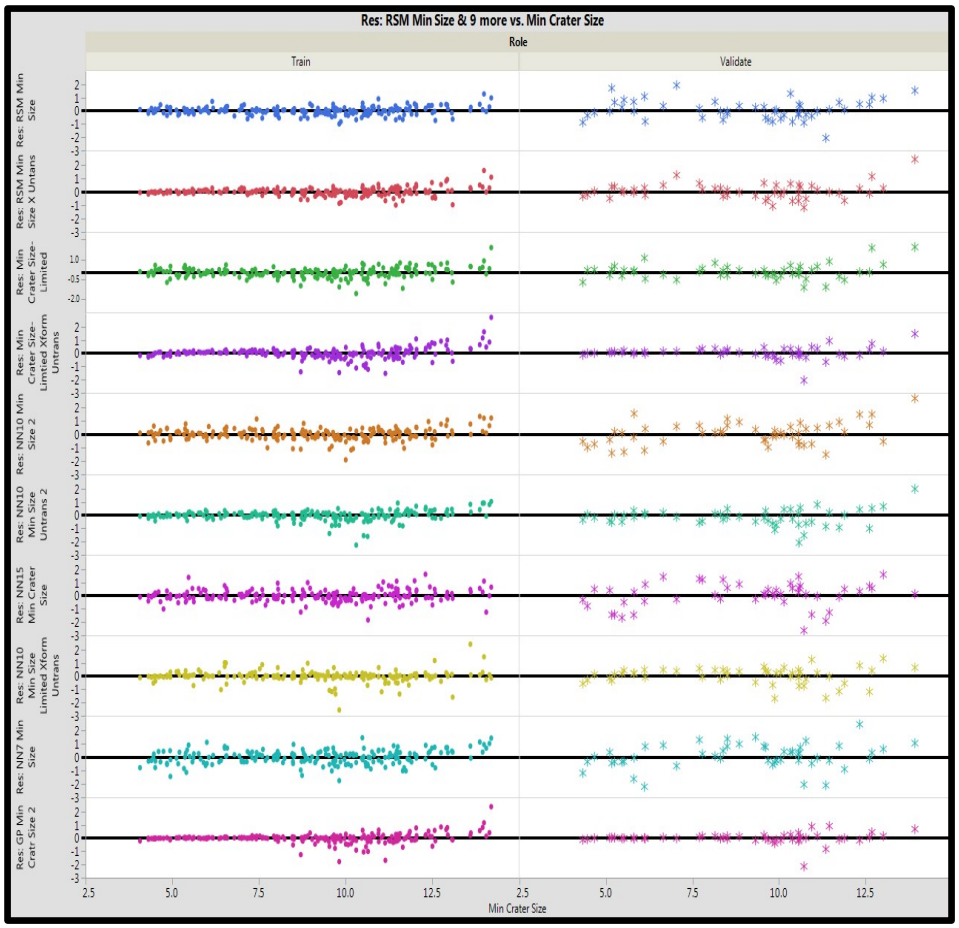

Figure 61: Residuals of Minimum Crater Size Models for Training and Validation Sets

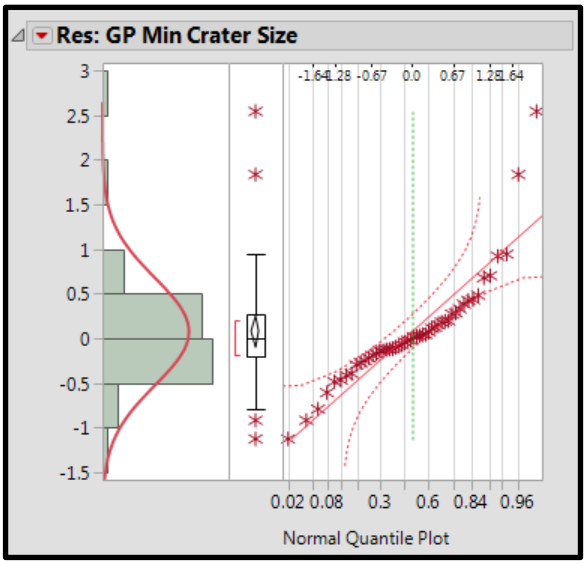

Figure 62: Residual Histogram and Normal Quantile Plot of Residuals from Minimum Crater Size kriging Model

Table 12: Residual Summary Statistics for Minimum Crater Size Models

	Model	Residuals				
		Mean	Std Dev	Min	Max	SW P-Value
Model Fit Error	RSM	1.44E-16	0.316	-0.985	1.273	0.0037
	RSM (Box-Cox Xform)	5.04E-3	0.303	-0.993	1.583	0.0001
	RSM (Stepwise)	1.42E-16	0.393	-1.570	1.900	0.001
	RSM (Stepwise Xform)	8.75E-3	0.453	-1.523	2.711	0.001
	NN (10 Node)	-1.12E-2	0.448	-1.909	1.329	0.002
	NN (10 Node with Xform)	-2.54E-2	0.397	-2.257	1.035	0.001
	NN (15 Node)	-2.56E-3	0.452	-1.833	1.614	0.002
	NN (7 Node)	-1..41E-3	0.515	-1.753	1.446	0.622
	NN (10 Node)	-2.12E-2	0.455	-2.556	2.411	0.001
	Gaussian Process	5.71E-13	0.384	-1.776	2.373	0.001
Model Representation Error	RSM	9.70E-2	0.747	-2.055	1.932	0.512
	RSM (Box-Cox Xform)	-1.14E-2	0.758	-3.276	2.425	0.001
	RSM (Stepwise)	8.94E-2	0.575	-1.104	1.942	0.002
	RSM (Stepwise Xform)	4.08E-2	0.462	-2.049	1.462	0.001
	NN (10 Node)	6.00E-2	0.834	-1.517	2.675	0.420
	NN (10 Node with Xform)	-1.65E-1	0.639	-2.079	1.989	0.070
	NN (15 Node)	4.40E-2	0.928	-2.625	1.589	0.018
	NN (7 Node)	7.36E-2	0.919	-2.204	2.446	0.103
	NN (10 Node)	4.14E-2	0.624	-1.691	1.337	0.010
	Gaussian Process	7.7E-2	0.600	-1.123	2.539	0.001

The maximum crater size metamodel was prepared the same way as the minimum crater size model. For the maximum crater size, the following models were created: Response surface equations, a response surface equation with a stepwise regression that only chose certain factors, a response surface equation of the Box-Cox transform, two different neural nets one with 10 and the other with 7 hidden nodes with a hyperbolic tangent activation function, a neural net with 7 hidden nodes on the Box-Cox transformed results, and finally, a Gaussian kriging model.

The results of fitting all these models are shown in Figure 63. This figure shows the actual v. predicted plots for both the training and validation data sets along with each models root mean squared error (RMSE) and R^2 value. Just as in the minimum crater

size section, the training data set models are shown on the left and the validation set data models are shown on the right. The prediction capability of the model is demonstrated by the validation set so those results should be weighted more than the training set. A summary of the RMSE of the validation set is shown below in Table 13.

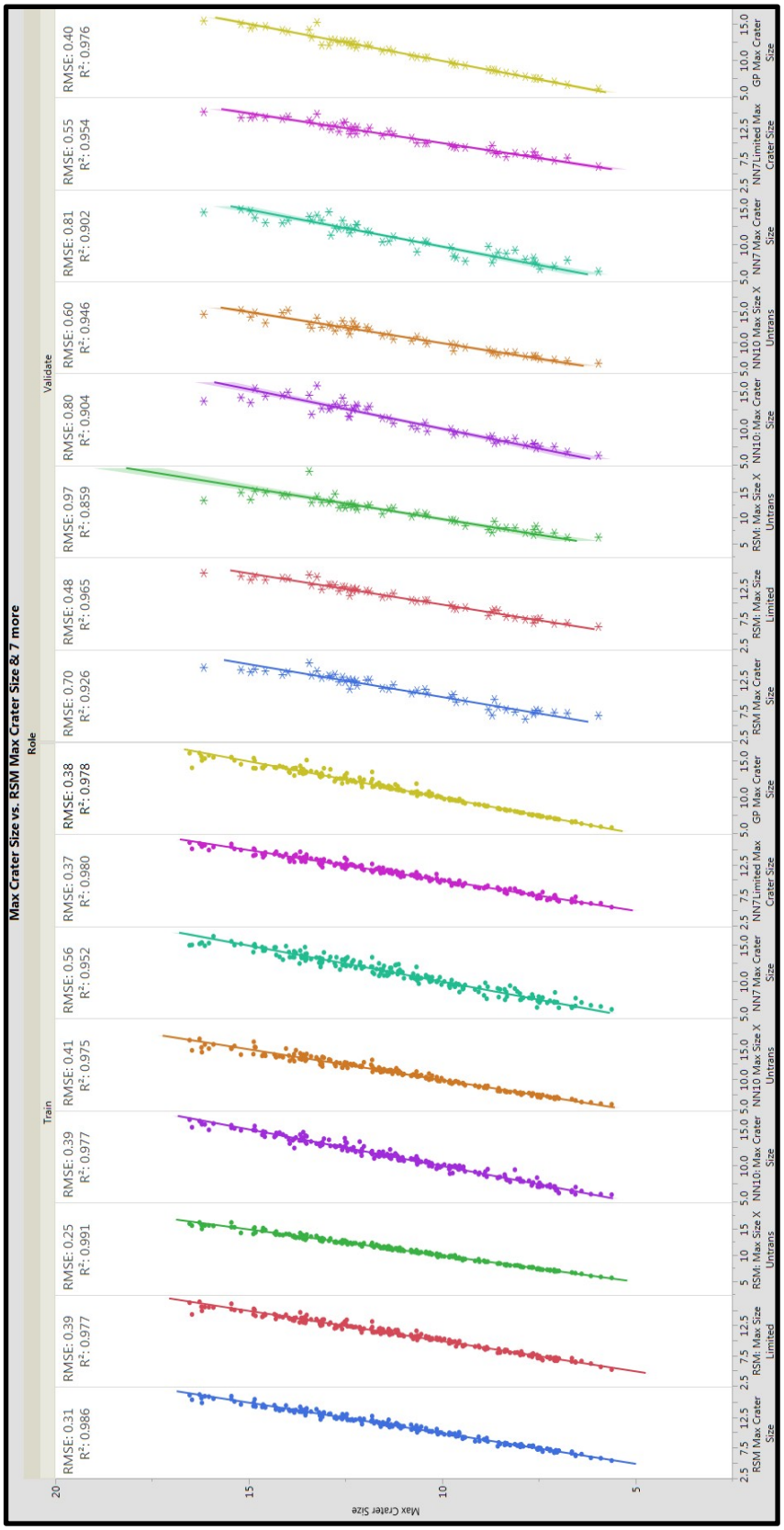

Figure 63: Actual vs. Predicted for the Training and Validation Sets of the Maximum Crater Size

Table 13: Error for Each Model of the Maximum Crater Size Using the Validation Set

Model	RMSE	%Error
RSM	0.70	6.41
RSM (Stepwise)	0.48	4.40
RSM (Box-Cox Xform)	0.97	8.89
NN (10 Node)	0.80	7.33
NN (10 Node with Xform)	0.60	5.50
NN (7 Node)	0.81	7.42
NN (7 Node with Stepwise)	0.55	5.04
Gaussian Process	0.40	3.67

Table 13 shows that the Gaussian kriging model performed the best in terms of prediction capability, but the response surface equation also performed well. In order to determine which to use, the residuals are to be considered. A plot of the residuals for each model is shown below in Figure 64 and the summary statistics for each model's residuals is organized in Table 14. The residual histogram and normal quantile plot for both the Gaussian Kriging model (left) and the Response Surface Model (right) are shown in Figure 62. The normal quantile plot shows a strong non-linear shape for the kriging model while the response surface is more linear. This indicates that the response surface model has a more normal distribution of the residuals. Overall, the prediction capability of the response surface model and kriging model are similar, but the more even distribution of the errors of the response surface model indicates that it is a better predictor of the maximum crater size.

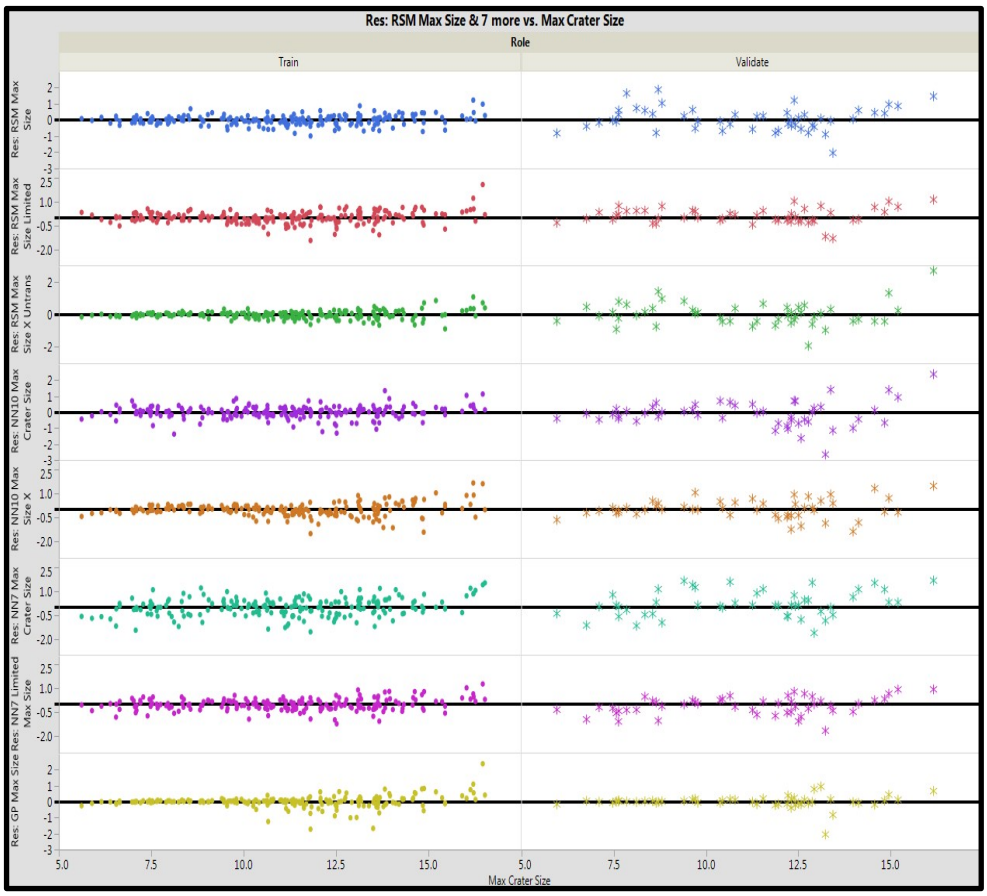

Figure 64: Residuals of Maximum Crater Size Models for Training and Validation Sets

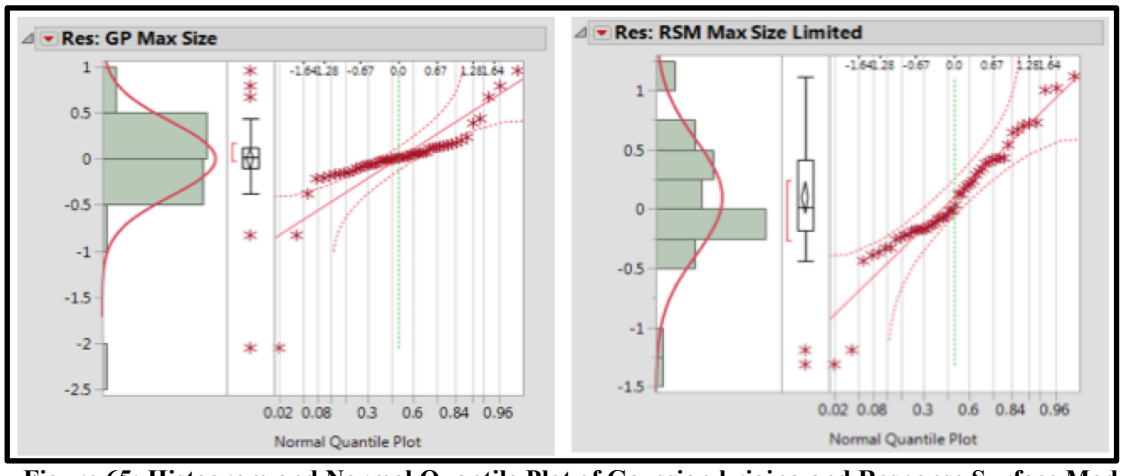

Figure 65: Histogram and Normal Quantile Plot of Gaussian kriging and Response Surface Model for Maximum Crater Size

Table 14: Residual Summary Statistics for Maximum Crater Size Models

	Model	Residuals				
		Mean	Std Dev	Min	Max	SW P-Value
Model Fit Error	RSM	-8.0E-16	0.309	-0.984	1.238	0.002
	RSM (Stepwise)	4.93E-16	0.391	-1.434	2.061	0.001
	RSM (Box-Cox Xform)	3.20E-3	0.248	-0.870	1.109	0.001
	NN (10 Node)	-5.60E-3	0.391	-1.372	1.346	0.001
	NN (10 Node with Xform)	-1.01E-2	0.410	-1.491	1.649	0.001
	NN (7 Node)	-8.01E-3	0.564	-1.559	-1.506	0.718
	NN (7 Node with Stepwise)	-1.03E-2	0.365	-1.207	1.259	0.019
	Gaussian Process	9.46E-13	0.380	-1.724	2.374	0.001
Model Representation Error	RSM	8.59E-2	0.724	-2.036	1.885	0.459
	RSM (Stepwise)	9.57E-2	0.482	-1.314	1.119	0.043
	RSM (Box-Cox Xform)	-5.83E-2	1.075	-5.614	2.730	0.001
	NN (10 Node)	-9.55E-2	0.810	-2.647	2.384	0.140
	NN (10 Node with Xform)	4.44E-2	0.598	-1.358	1.469	0.831
	NN (7 Node)	2.02E-1	0.801	-1.626	1.659	0.217
	NN (7 Node with Stepwise)	-9.35E-2	0.548	-1.637	0.925	0.702
	Gaussian Process	-1.70E-3	0.402	-2.051	0.954	0.001

6.3.2. Airfield Damage Effects Surrogate Models for CMs

The damage effects model creation for cruise missile (CMs) was done in a similar manner than that of the theater ballistic missile (TBMs) models explained the in the last few sections. The CM metamodel also requires two separate surrogate models: one for the maximum spread of the submunitions and a second that predicts the crater depth from each submunition. The maximum spread metamodel will predict the radius of the submunition impacts. Then using a uniform distribution the actual impact location for each submunition can be calculated between that of a zero release angle and that of a release angle at the maximum value. This impact radius is then used with other factors to predict penetration distance and the minimum and maximum possible size of the crater.

For the training and test sets for both the max spread and crater size models, a Latin hyper cube design created in JMP, was used. Just as in the TBM models explained in the last section, the Latin hypercube design helps to spread the points in the design space, but ensures that the set can be projected into a smaller dimensional space without overlap of the points [137-140], since the same design set was used to predict the minimum and maximum crater size and there was no guarantee that the two models would use the same design variables. Again, just as in the TBM models, the validation sets were also created in JMP using the augment design feature. This allowed additional points to be populated into the original design ensuring that those validation points were spread as far from the training points and each other as possible.

6.3.2.1. CM Max Spread Metamodel Results

The maximum spread metamodel predicts the maximum radius that could result from a submunition released from the cruise missile at the given release altitude and speed at the maximum possible release angle of ten degrees. Unlike the TBM max spread model, this simulation did not need the flight propagation model from EADSIM. Instead, it was assumed that the CM traveled to the release point and then pitched down at a 45-degree angle. At this nose down orientation it then released two submunitions at the given release altitude: one at a release angle of zero degrees and one at the maximum angle of ten degrees. It then propagated each to the ground in a six degree-of-freedom model (see section 6.2.2). Finally, it measured the distance between the two impact points. The input variables for the maximum spread model were the cruise missile speed and the release altitude. The release altitude varied from 20 feet above ground to 500 feet above ground and the cruise speed varied from 100 meters per second to 500 meters per

second. A summary of the inputs and outputs from this analysis is shown below in Figure 66.

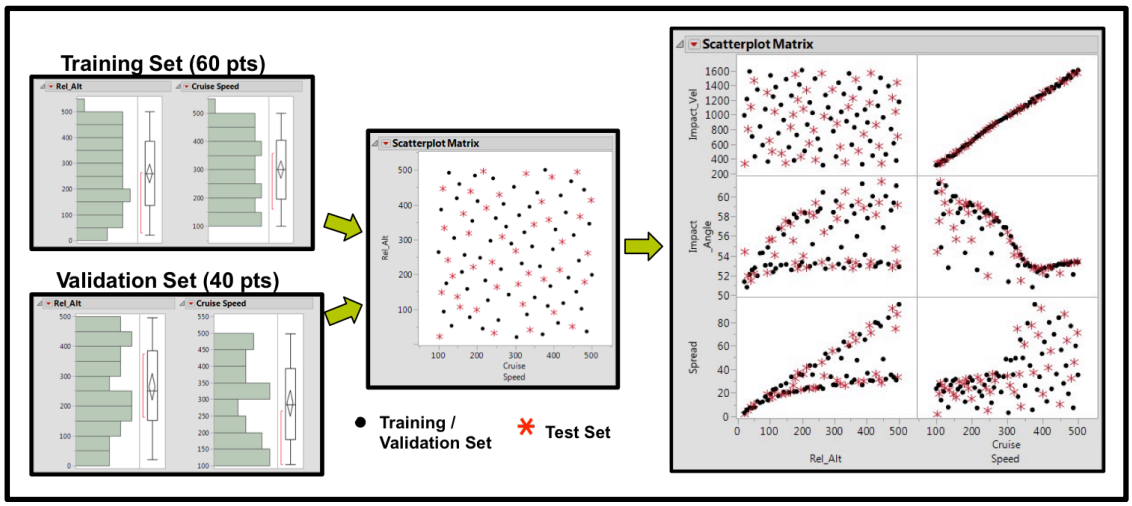

Figure 66: CM Max Spread Model DOE Inputs and Outputs Diagram

In Figure 66, the black circles are the training points and the red stars are the validation points. In order to ensure a good fit, thirty times the number of inputs (sixty total) were used in the training set and 40 points (40%) were used in the validation set. The results are also summarized in histogram format in Figure 67.

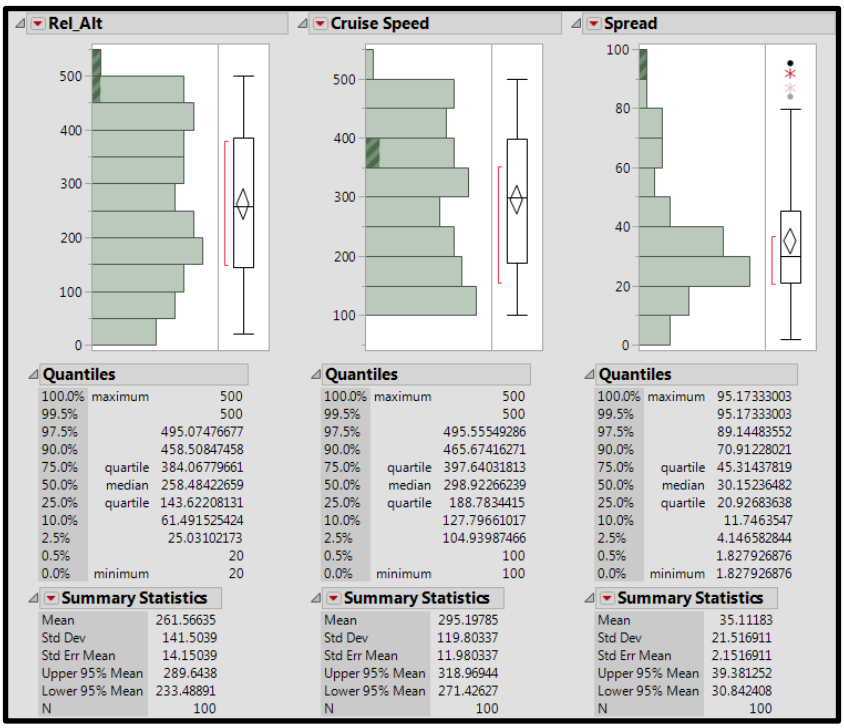

Figure 67: CM Max Spread Model DOE Inputs and Outputs Histogram

The maximum spread observed was 95.2 ft and the minimum spread was 1.9 feet. This means that the spread varied over a range of about 93 feet. Figure 67 also highlights that the largest spread was from a high release altitude at a speed around 350 mps (about mach 1). Using these outputs, five metamodels of the maximum spread radius were created: a response surface model (RSM), a response surface model of the Box-Cox transform, two neural nets, one with 5 hidden nodes and another with 10 hidden nodes each with a hyperbolic tangent activation function, and a Gaussian kirging model. All of these models were evaluated with the techniques described in appendix C. The actual v. predicted graph for these two models is shown below along with their associated R^2 and root mean squared error (RMSE).

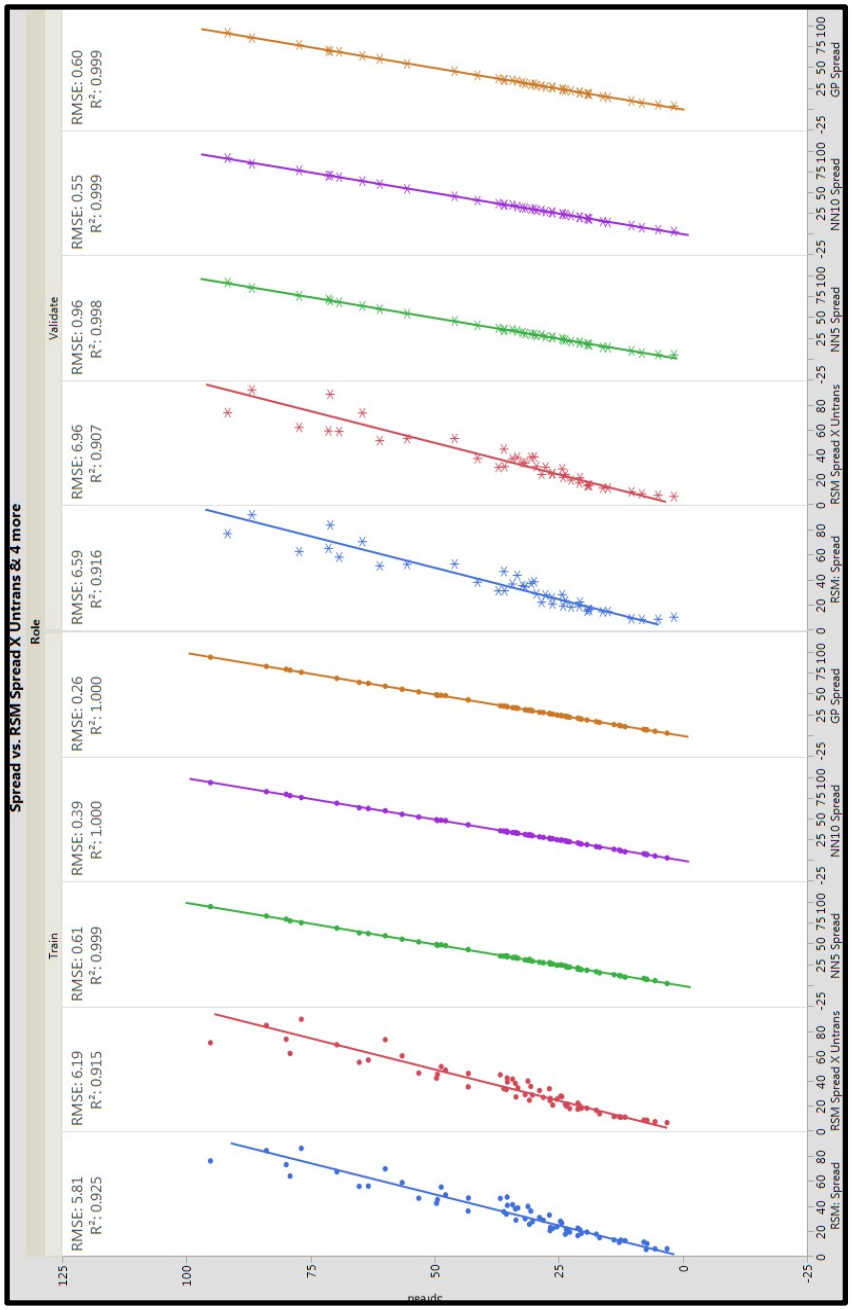

Figure 68: Actual v. Predicted for Training and Validation Sets of CM Max Spread Models

In Figure 68, the training set is shown on the left and the validation set is shown on the right. All models performed well, but the best models in terms of their RMSE and R^2 values were the neural net with 10 nodes and the Gaussian kriging model. The RMSE and R^2 values are summarized in the table below.

Table 15: Error for Each Model of the Maximum Spread for CMs Using the Validation Set

Model	RMSE	%Error
RSM	6.59	7.06
RSM (Box-Cox Xform)	6.96	7.46
NN (5 Node)	0.96	1.03
NN (10 Node)	0.55	0.59
Gaussian kriging	0.60	0.43

A plot of the residuals for the best performing models, the two neural nets and the Gaussian kriging model, is shown below in Figure 70. Each model shows a fairly random distribution of the error. The histogram of the residuals and the normal quantile plot for the two best modes, the neural net with 10 nodes and the Gaussian kriging models is shown in Figure 69 and a summary of the residual statistics is shown in Table 17. Both of the models show a good distribution of the residuals, but the neural net seems just a little more linear. This is confirmed by the Sharprio-Wilk test in Table 16. Therefore, the neural net with 10 nodes was chosen as the model for the CM max spread.

Table 16: Shaprio-Wilk Test for CM Max Spread Models' Residuals

Shaprio-Wilk Test	P-Value
NN 10 Node	0.4924
Guassian kriging	0.0002

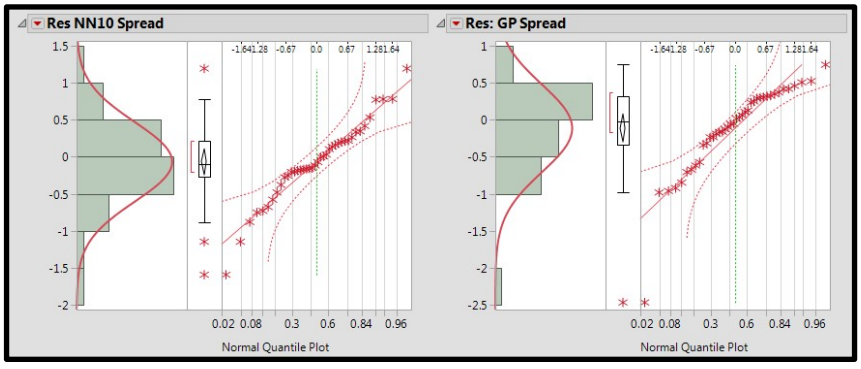

Figure 69: Histogram and Normal Quantile Plot for CM Max Spread Models

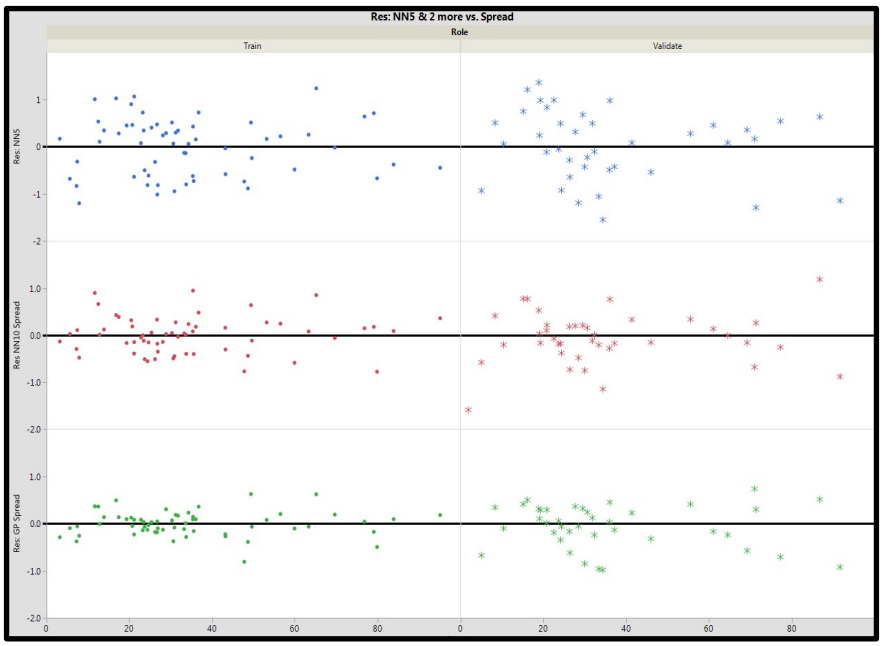

Figure 70: Residuals of Training and Validation Set for CM Max Spread Models

Table 17: Residual Summary Statistics for CM Max Spread Models

	Model	Residuals				
		Mean	Std Dev	Min	Max	SW P-Value
Model Fit Error	RSM	2.61E-15	5.76	-12.44	18.28	0.2642
	RSM (Box-Cox Xform)	2.16E-1	6.14	-14.11	23.57	0.0040
	NN (5 Node)	-3.35E-3	0.61	-1.20	1.25	0.1136
	NN (10 Node)	4.95E-4	0.39	-0.78	0.95	0.3608
	Gaussian kriging	1.92E-12	0.26	-0.81	0.63	0.3393
Model Representation Error	RSM	2.58E-2	6.51	-13.43	14.12	0.7742
	RSM (Box-Cox Xform)	2.39E-1	6.89	-18.48	17.10	0.6249
	NN (5 Node)	-6.65E-2	0.95	-3.78	1.37	0.0014
	NN (10 Node)	-6.66E-2	0.54	-1.59	1.19	0.4924
	Gaussian kriging	-1.14E-1	0.59	-2.47	0.74	0.0002

6.3.2.2. CM Crater Size Metamodel Results

Unlike the TBM crater size model, the CM crater size model did not use the EADSIM flight propagation model. Instead, it was assumed that the CM arrived to their target at the altitude designated in the DOE and then pitched nose down at a 45 degree angle

before releasing the runway penetrators at the release angle specified in the DOE. The penetrators were then propagated to the ground using the six-degree of freedom model. Once the penetrators impacted, the penetration equations used the impact velocity and angle to determine the penetration depth. The round then tunneled to the minimum of the penetration depth calculated in the penetration equations or the penetration depth set in the DOE. It then exploded and the cratering model predicted the min and max crater size that would result from an explosion at that depth.

Because the CMs were traveling at a much slower speed than the TBMs, there was no way for the CM penetrators to tunnel through both the concrete and the rock layer. Therefore, in the CM input DOE, the inputs having to do with the rock layer were neglected. Additionally, it was assumed that the number of penetrators was fixed in the smaller confines of the CM and the max release angle increased to 10 degrees to spread the penetrators out more at the lower release altitudes. This meant that there were 10 input variables in the cratering metamodel. These were described in various parts in sections 6.2 through 6.2.5 and are summarized in Table 18.

Table 18: DOE Inputs for CM Cratering Metamodel

Input	Min	Max	Units
Penetrator Release Altitude	10	500	ft
Penetrator Release Angle	0	10	degree
Delay Fuse Max Depth	6	36	in
Explosive Weight	1	10	lb
Runway Width	50	1000	ft
Concrete Thickness	12	42	in
Percent Rebar	0	5	%
Concrete Compressive Strength	2,000	3,500	psi
Density of Concrete	125	175	lbf/ft^3
Tensile Strength of Rebar	70,000	90,000	psi

These ten factors were used in JMP to produce a 220-design point training and fitting set and a 55-point validation set. The training set was a Latin hypercube design and the validation set was produced from a space filling augmentation to ensure that it sampled evenly throughout the design space and away from any points already in the training and fit set. A summary of the training set and validation set is shown in Figure 71 along with the factor ranges in brackets and the associated units of that factor in parenthesis.

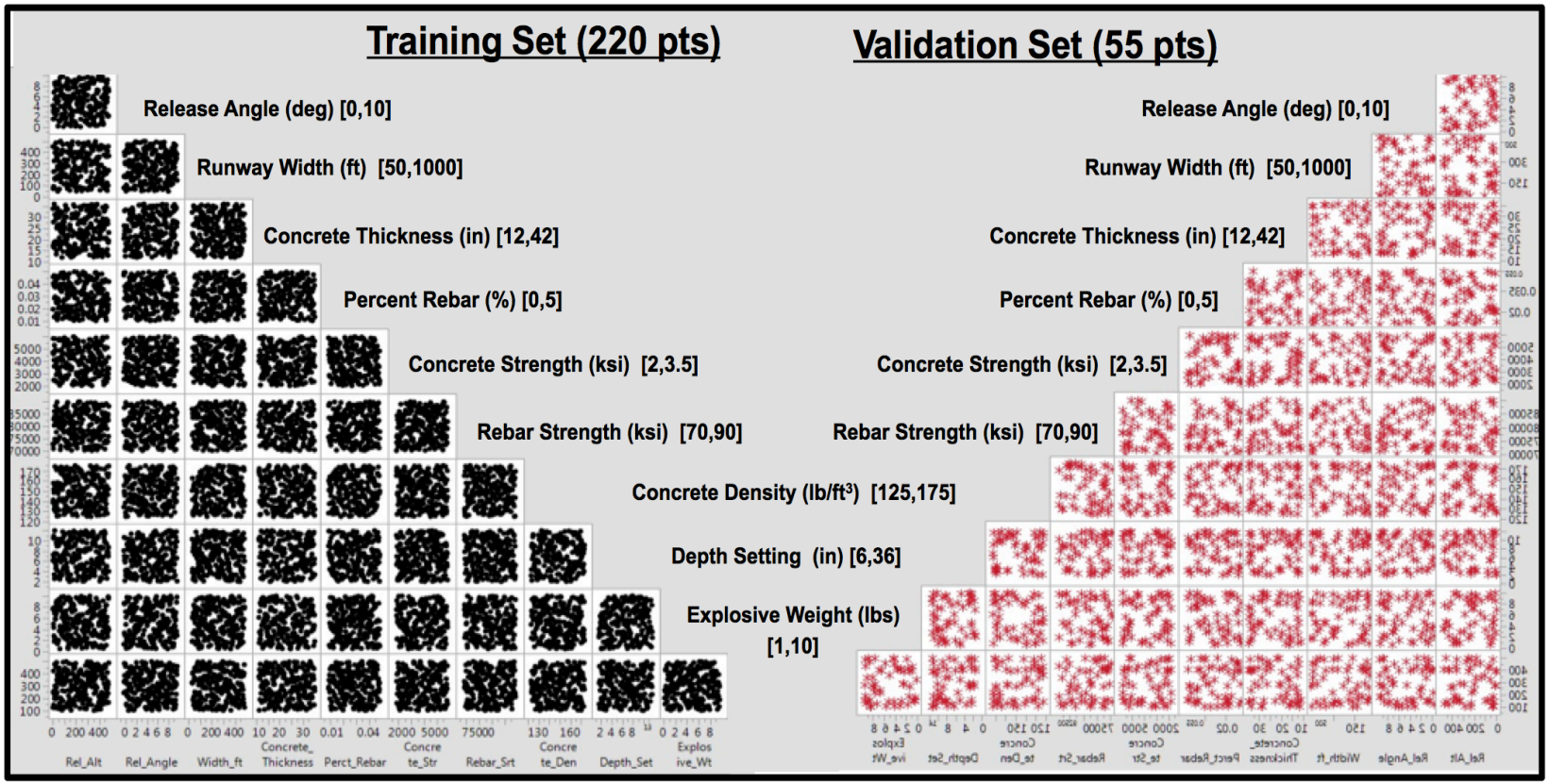

Figure 71: CM Flight and Cratering DOE Distributions for Training and Validation Sets

Just as in the TBM case, the first step after the DOE run was to validate the assumptions identified about the use of the Sandia equation and the six-degree of freedom model from sections 6.2.2 and 6.2.3.4 restated here as: the impact speed should be less than 4,000 feet per second and the impact angle less than 89.5 degrees. To validate these two assumptions, all results from both the training set and validation set were plotted in a histogram, shown in Figure 72. From the data below each histogram, it can be seen that the maximum impact speed was 1,619 feet per second and the maximum impact angle was 62.3 degrees. Both of these values are less than the maximum allowable values.

Figure 72 also shows the results for the minimum and maximum crater diameter size. The maximum crater diameter ranged from 2.19 feet to 7.60 feet (5.41 foot range), and the minimum crater diameter ranged from 1.42 feet to 5.59 feet (7.17 foot range). The results for both the training and validation sets are also plotted against each input factor in Figure 73. The black dots are the training set and the red stars are the validation set. The results show that the cater size is dominated by the maximum depth setting, the explosive weight, and the speed of the CM. The other factors play a much smaller role in the outputs.

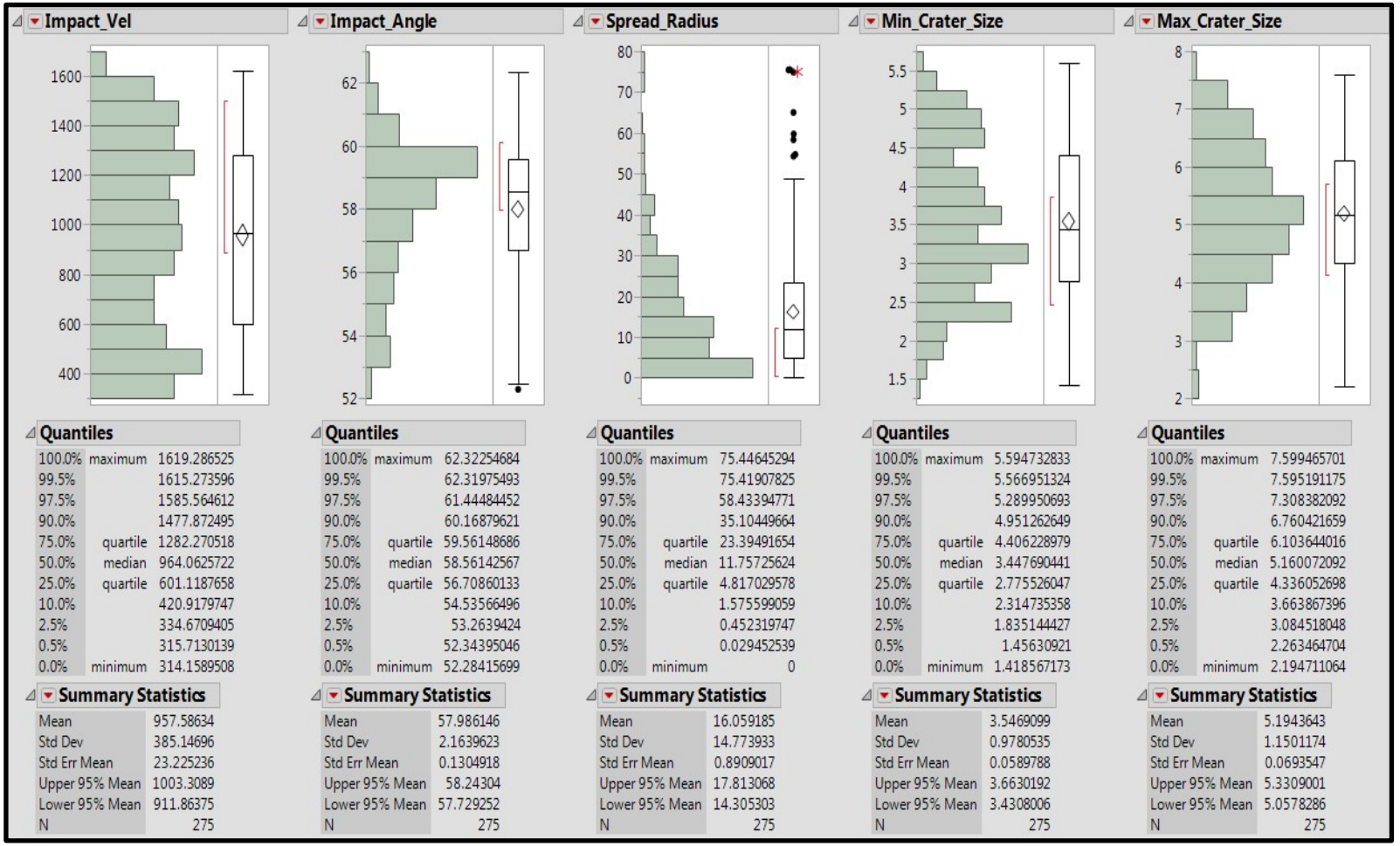

Impact_Vel Quantiles		
100.0%	maximum	1619.286525
99.5%		1615.273596
97.5%		1585.564612
90.0%		1477.872495
75.0%	quartile	1282.270518
50.0%	median	964.0625722
25.0%	quartile	601.1187658
10.0%		420.9179747
2.5%		334.6709405
0.5%		315.7130139
0.0%	minimum	314.1589508

Impact_Vel Summary Statistics	
Mean	957.58634
Std Dev	385.14696
Std Err Mean	23.225236
Upper 95% Mean	1003.3089
Lower 95% Mean	911.86375
N	275

Impact_Angle Quantiles		
100.0%	maximum	62.32254684
99.5%		62.31975493
97.5%		61.44484452
90.0%		60.16879621
75.0%	quartile	59.56148686
50.0%	median	58.56142567
25.0%	quartile	56.70860133
10.0%		54.53566496
2.5%		53.2639424
0.5%		52.34395046
0.0%	minimum	52.28415699

Impact_Angle Summary Statistics	
Mean	57.986146
Std Dev	2.1639623
Std Err Mean	0.1304918
Upper 95% Mean	58.24304
Lower 95% Mean	57.729252
N	275

Spread_Radius Quantiles		
100.0%	maximum	75.44645294
99.5%		75.41907825
97.5%		58.43394771
90.0%		35.10449664
75.0%	quartile	23.39491654
50.0%	median	11.75725624
25.0%	quartile	4.817029578
10.0%		1.575599059
2.5%		0.452319747
0.5%		0.029452539
0.0%	minimum	0

Spread_Radius Summary Statistics	
Mean	16.059185
Std Dev	14.773933
Std Err Mean	0.8909017
Upper 95% Mean	17.813068
Lower 95% Mean	14.305303
N	275

Min_Crater_Size Quantiles		
100.0%	maximum	5.594732833
99.5%		5.566951324
97.5%		5.289950693
90.0%		4.951262649
75.0%	quartile	4.406228979
50.0%	median	3.447690441
25.0%	quartile	2.775526047
10.0%		2.314735358
2.5%		1.835144427
0.5%		1.45630921
0.0%	minimum	1.418567173

Min_Crater_Size Summary Statistics	
Mean	3.5469099
Std Dev	0.9780535
Std Err Mean	0.0589788
Upper 95% Mean	3.6630192
Lower 95% Mean	3.4308006
N	275

Max_Crater_Size Quantiles		
100.0%	maximum	7.599465701
99.5%		7.595191175
97.5%		7.308382092
90.0%		6.760421659
75.0%	quartile	6.103644016
50.0%	median	5.160072092
25.0%	quartile	4.336052698
10.0%		3.663867396
2.5%		3.084518048
0.5%		2.263464704
0.0%	minimum	2.194711064

Max_Crater_Size Summary Statistics	
Mean	5.1943643
Std Dev	1.1501174
Std Err Mean	0.0693547
Upper 95% Mean	5.3309001
Lower 95% Mean	5.0578286
N	275

Figure 72: CM Flight and Cratering DOE Results for Assumptions Validation

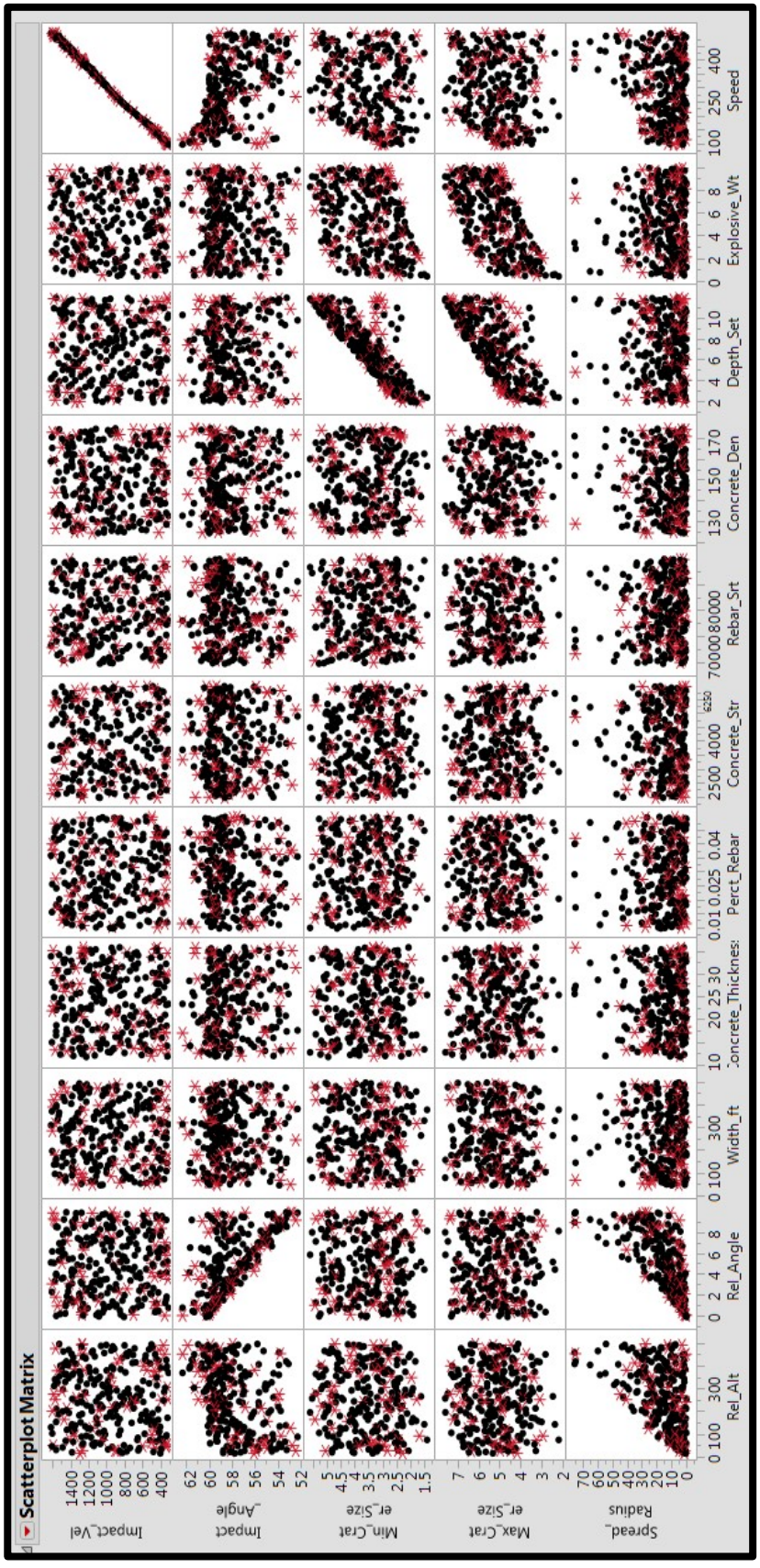

Figure 73: CM DOE Output as a function of Inputs

Just as in the TBM case, for both the minimum and maximum crater size, multiple models were created and compared to each other in order to select the best one. Starting with the minimum crater size, the following models were created: a response surface model, a response surface model of a box-cox transform, a response surface model with a stepwise regression, three different neural net models with 5, 10, and 15 hidden nodes each with a hyperbolic tangent activation function (the neural net with 15 nodes was done on only the factors identified in the stepwise regression), and finally, two Gaussian kriging models, one on all factors and the second on only the factors identified in the stepwise regression.

The results of fitting all these models are shown in Figure 74. This figure shows the actual v. predicted plots for both the training and validation data sets along with each models root mean squared error (RMSE) and R^2 value. The training data set models are shown on the left and the validation set data models are shown on the right. When selection a model, the ability to predict is the most important characteristic. Therefore, the actual vs. predicted, RMSE, and R^2 values of the validation set should be considered above those of the training set since the validation set was not used to create the model. The validation set is a test of the models predictive power. A summary of the RMSE of the validation set is shown below in Table 19.

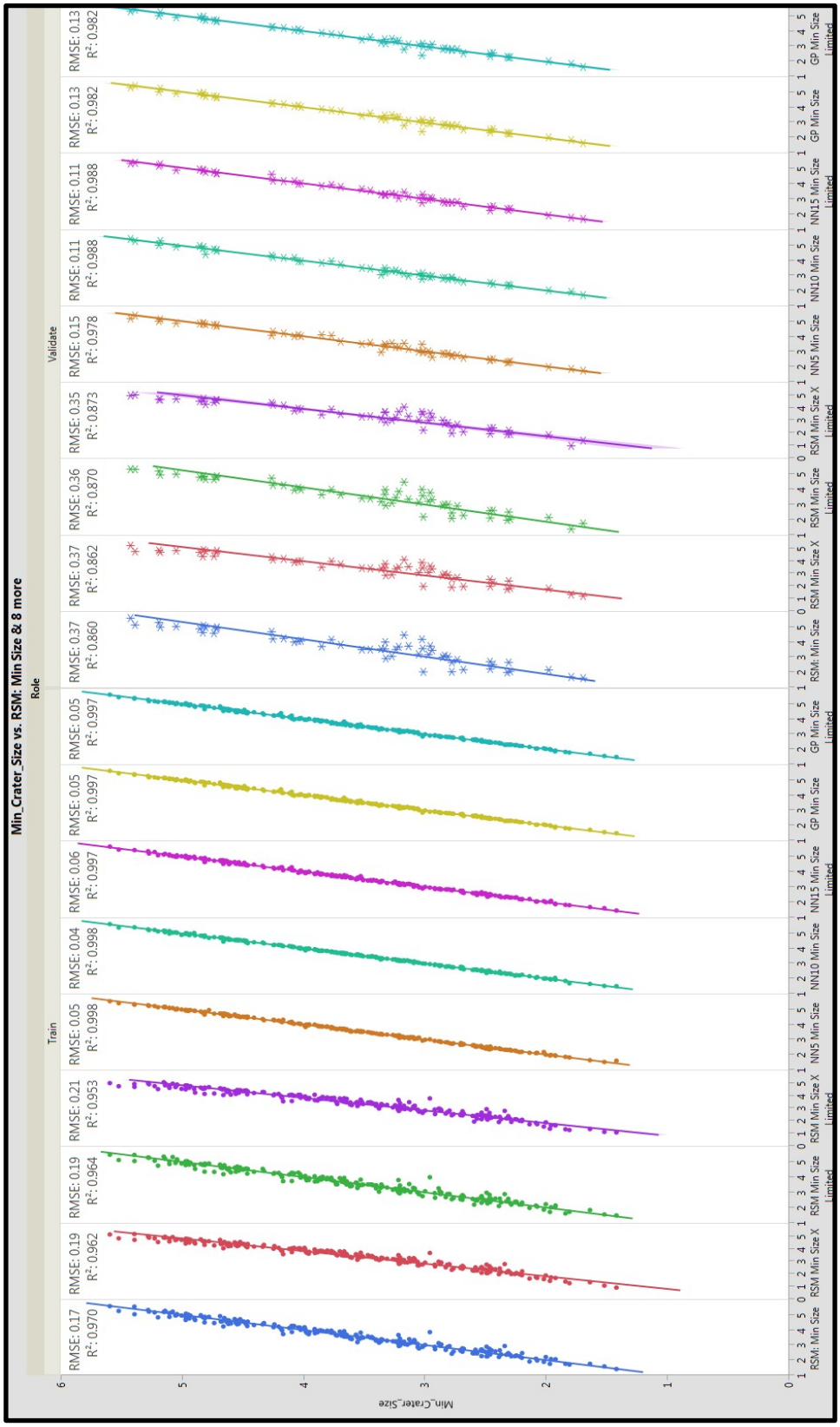

Figure 74: Actual vs. Predicted for Training and Validation Sets of CM Minimum Crater Size

Table 19: Error for Each Model of the Minimum Crater Size for CMs Using the Validation Set

Model	RMSE	%Error
RSM	0.37	8.87
RSM (Box-Cox Xform)	0.37	8.87
RSM (Stepwise)	0.36	8.63
RSM (Stepwise Xform)	0.35	8.39
NN (5 Node)	0.15	3.60
NN (10 Node)	0.11	2.64
NN (15 Node with Stepwise)	0.11	2.64
Gaussian kriging	0.13	3.12
Gaussian kriging (with Stepwise)	0.13	3.12

Table 19 shows that the Neural Nets and the Gaussian kriging model performed the best in terms of prediction capability, but the residuals also must be considered in the model selection. A plot of the residuals for each model is shown below in Figure 75, and the summary statistics for each model is organized in Table 20. The table shows the statistics for the training set on top (model fit error) and the validation set on the bottom (model representation error).

Overall, each of the neural net models' and each of the Gaussian models' residuals look good. The models with the smallest error are the neural net 10 node and neural net 15 node. The residual histogram and normal quantile plot of these two models is shown in Figure 76. Both models exhibit a fairly linear plot on the normal quantile plot. In general, a neural net with more hidden nodes will perform better than a neural net with less hidden nodes, all else being equal. So in this case, the neural net with 15 nodes was chosen as the CM minimum crater size model.

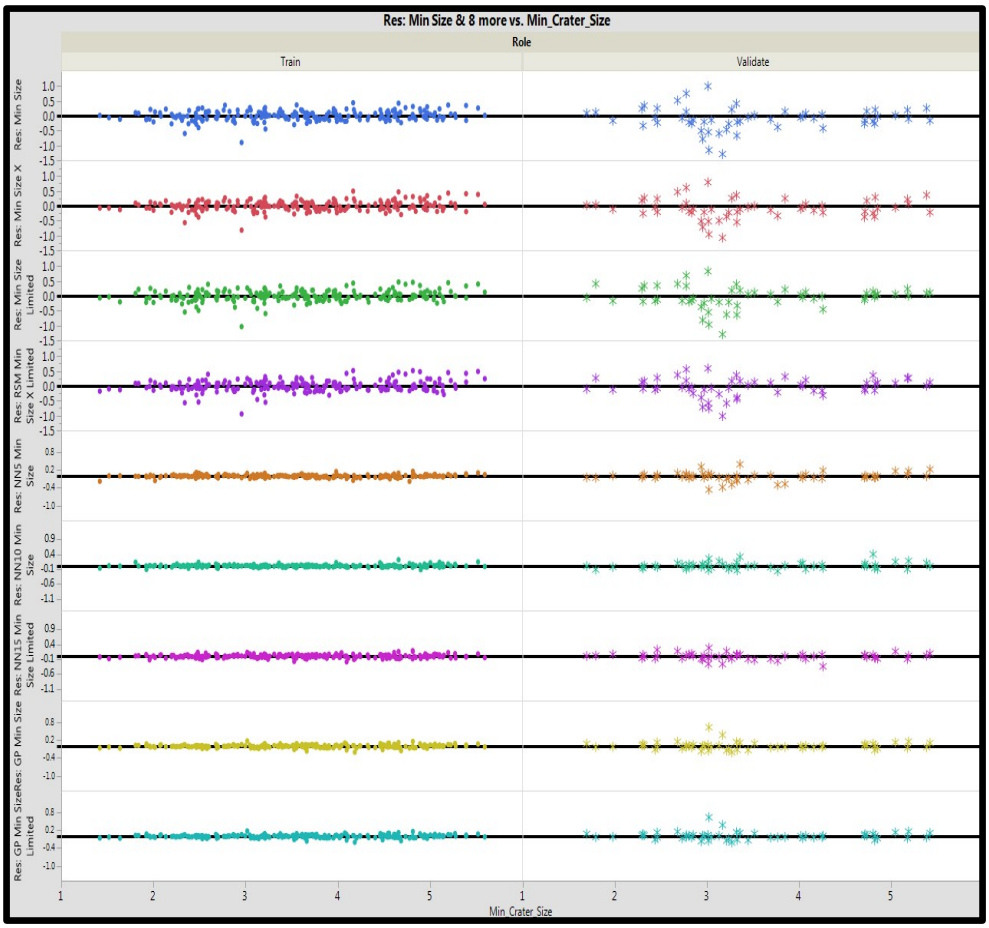

Figure 75: Residuals for Training and Validation Sets for CM Minimum Crater Size

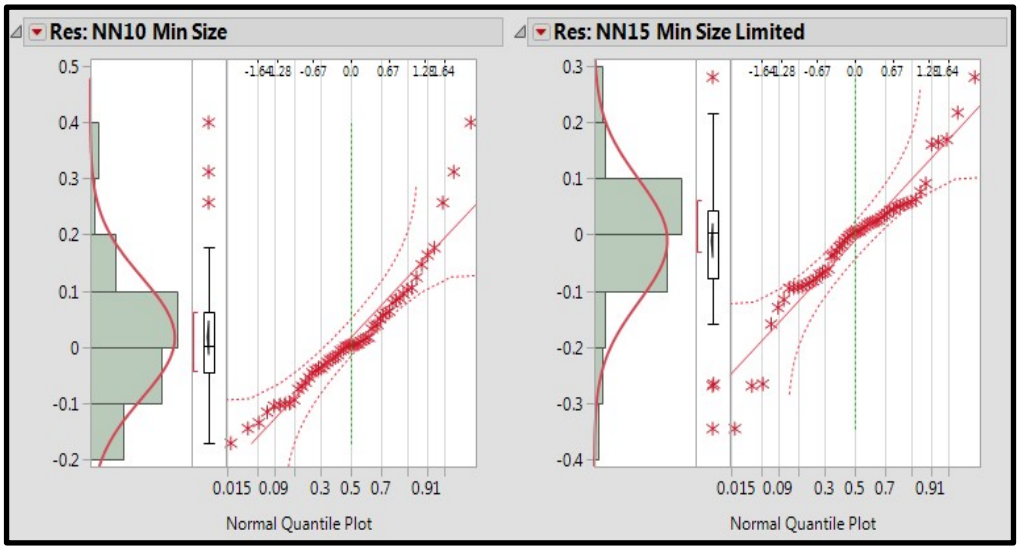

Figure 76: Histogram of Residuals and Normal Quantile Plot for Top Two Minimum Crater Size Models

Table 20: Summary Statistics for Residuals of CM Minimum Crater Size Models

	Model	Residuals				
		Mean	Std Dev	Min	Max	SW P-Value
Model Fit Error	RSM	-6.06E-18	0.170	-0.90	0.44	0.0001
	RSM (Box-Cox Xform)	2.43E-3	0.167	-0.82	0.50	0.0001
	RSM (Stepwise)	4.24E-17	0.187	-1.03	0.47	0.0001
	RSM (Stepwise Xform)	3.15E-3	0.191	-0.94	0.52	0.0001
	NN (5 Node)	-9.59E-4	0.047	-0.18	0.16	0.0001
	NN (10 Node)	8.24E-3	0.041	-0.12	0.21	0.0001
	NN (15 Node with Stepwise)	-8.14E-4	0.055	-0.19	0.18	0.0321
	Gaussian kriging	-1.36E-13	0.049	-0.20	0.18	0.0001
	Gaussian kriging (with Stepwise)	-2.31E-13	0.049	-0.20	0.18	0.0001
Model Representation Error	RSM	-1.02E-1	0.391	-1.29	1.00	0.0368
	RSM (Box-Cox Xform)	-9.29E-2	0.342	-1.07	0.80	0.2364
	RSM (Stepwise)	-5.18E-2	0.371	-1.29	0.83	0.0137
	RSM (Stepwise Xform)	-3.93E-2	0.316	-1.01	0.59	0.0693
	NN (5 Node)	-1.61E-2	0.144	-0.46	0.40	0.0005
	NN (10 Node)	1.65E-2	0.108	-0.17	0.40	0.0017
	NN (15 Node with Stepwise)	-1.08E-2	0.11	-0.35	0.28	0.0170
	Gaussian Process	1.30E-2	0.13	-0.21	0.64	0.0001
	Gaussian Process (with Stepwise)	1.13E-2	0.13	-0.21	0.64	0.0001

The maximum crater size metamodel was prepared the same way as the minimum crater size model. For the maximum crater size, the following models were created: Response surface model, a response surface model with a stepwise regression that only chose certain factors, a response surface equation of the Box-Cox transform, two different neural nets of all factors: one with 7 and the other with 10 hidden nodes with a hyperbolic tangent activation function, two different neural nets on only the factors identified in the stepwise regression: one with 7 hidden nodes and the other with 10 hidden nodes, and finally, a Gaussian kriging model.

The results of fitting all these models are shown in Figure 77. This figure shows the actual v. predicted plots for both the training and validation data sets along with each

model's root mean squared error (RMSE) and R^2 value. Just as in the minimum crater size section, the training data set models are shown on the left and the validation set data models are shown on the right. The prediction capability of the model is demonstrated by the validation set so those results should be weighted more than the training set. A summary of the RMSE of the validation set is shown below in Table 13.

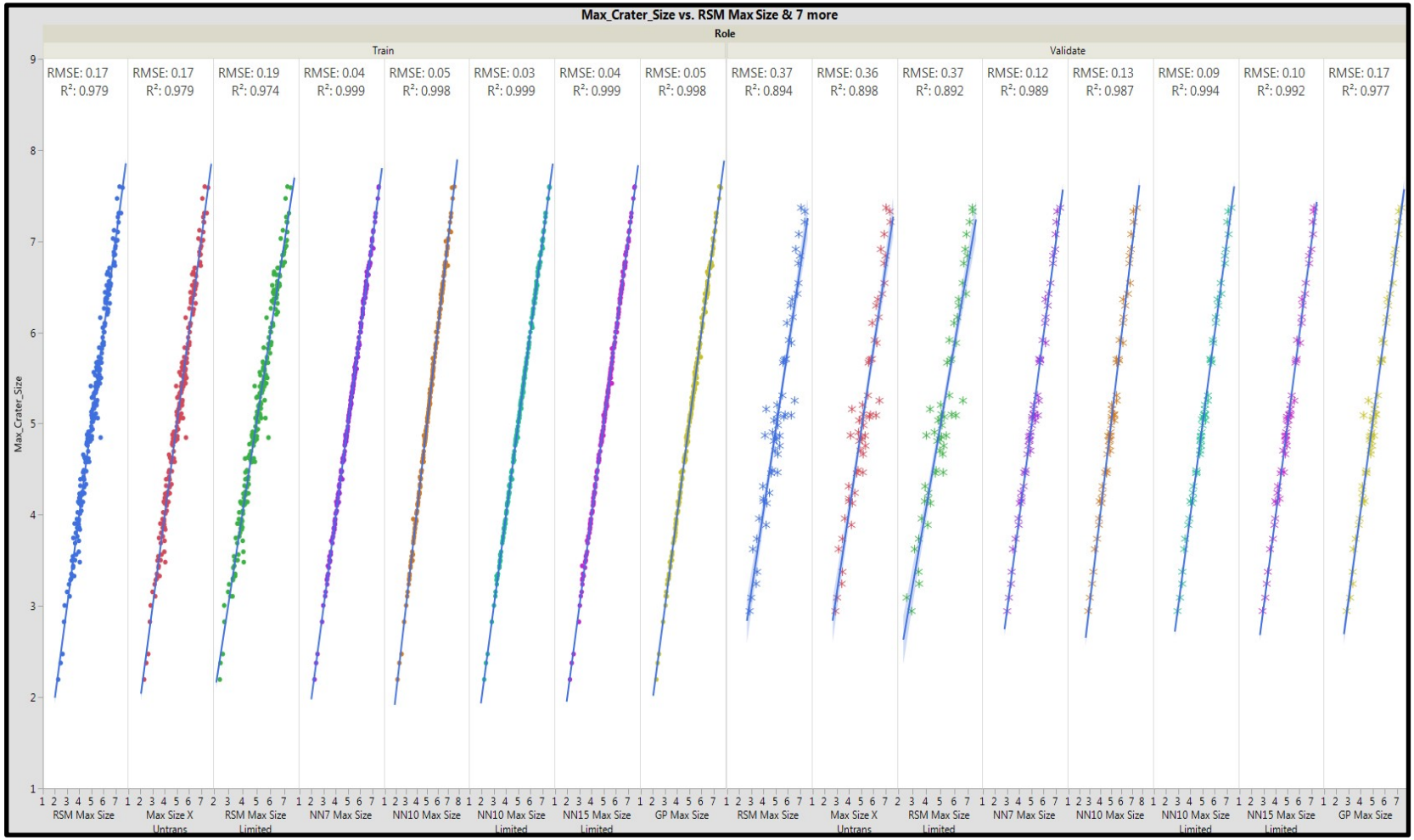

Figure 77: Actual v. Predicted for Training and Validation Sets of CM Maximum Crater Size

Table 21: Error for Each Model of the Maximum Crater Size for CMs Using the Validation Set

Model	RMSE	%Error
RSM	0.37	6.84
RSM (Box-Cox Xform)	0.36	6.65
RSM (Stepwise)	0.37	6.84
NN (7 Node)	0.12	2.22
NN (10 Node)	0.13	2.40
NN (10 Node with Stepwise)	0.09	1.66
NN (15 Node with Stepwise)	0.10	1.85
Gaussian Process	0.17	3.14

Table 21 shows that the Neural Net models performed the best in terms of prediction capability. Again, the residuals also must be considered in the model selection. A plot of the residuals for each model is shown below in Figure 78 and the summary statistics for each model is organized in Table 22. The table shows the statistics for the training set on top (model fit error) and the validation set on the bottom (model representation error).

Overall, each of the neural net models' residuals looks randomly distributed. The models with the smallest error were the neural net 10 node and neural net 15 node. The residual histogram and normal quantile plot of these two models is shown in Figure 79. Both models exhibit a fairly linear plot on the normal quantile plot. Just as in the minimum crater size, generally the neural net with more hidden nodes will be a better predictor. So, the neural net with 15 nodes was chosen as the CM maximum crater size model.

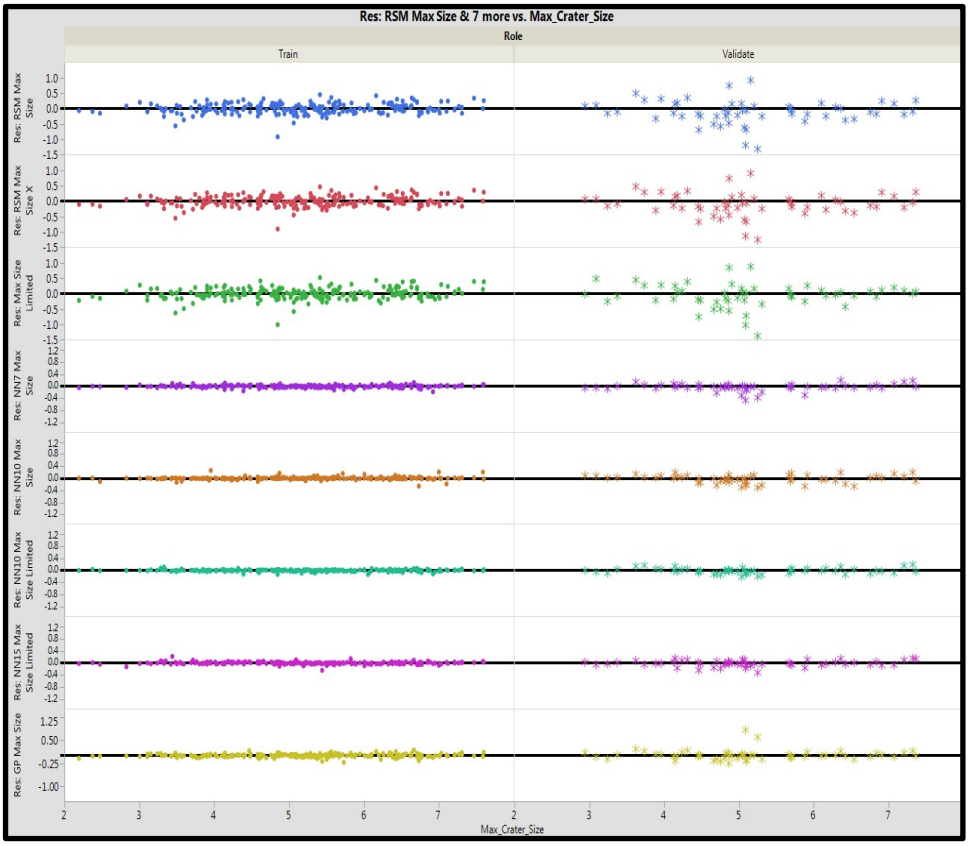

Figure 78: Residuals for CM Maximum Crater Size Models

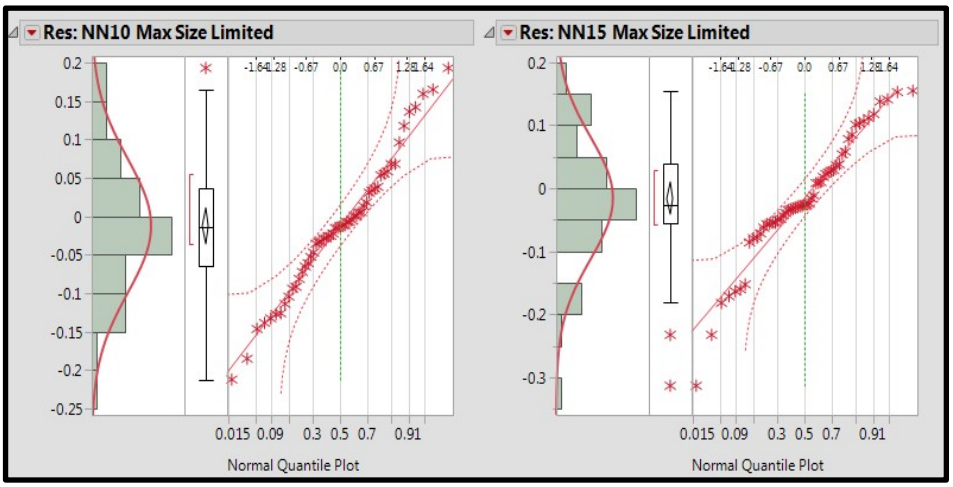

Figure 79: Histogram and Normal Quantile Plot of Best Maximum Crater Size Models

Table 22: Summary Statistics for CM Maximum Crater Size Residuals

	Model	Residuals				
		Mean	Std Dev	Min	Max	SW P-Value
Model Fit Error	RSM	3.61E-16	0.169	-0.93	0.46	0.0001
	RSM (Box-Cox Xform)	5.76E-4	0.169	-0.91	0.47	0.0001
	RSM (Stepwise)	-1.64E-16	0.186	-1.01	0.53	0.0001
	NN (7 Node)	-3.98E-3	0.042	-0.18	0.12	0.0001
	NN (10 Node)	3.08E-3	0.048	-0.26	0.26	0.0001
	NN (10 Node with Stepwise)	-2.97E-3	0.032	-0.13	0.11	0.0001
	NN (15 Node with Stepwise)	-4.84E-5	0.039	-0.24	0.22	0.0001
	Gaussian kriging	-5.73E-13	0.052	-0.22	0.18	0.0001
Model Representation Error	RSM	-1.10E-1	0.391	-1.32	0.93	0.0304
	RSM (Box-Cox Xform)	-1.08E-1	0.381	-1.26	0.91	0.0531
	RSM (Stepwise)	-5.84E-2	0.390	-1.38	0.88	0.0118
	NN (7 Node)	-3.31E-2	0.119	-0.46	0.20	0.0001
	NN (10 Node)	-2.11E-2	0.130	-0.30	0.20	0.1008
	NN (10 Node with Stepwise)	-1.23E-2	0.087	-0.21	0.19	0.5822
	NN (15 Node with Stepwise)	-1.53E-2	0.097	-0.31	0.15	0.0520
	Gaussian kriging	1.87E-2	0.170	-0.25	0.84	0.0001

6.3.3. Runway Cratering Simulation

This next section describes how the surrogate models of the last section were used to develop an overall runway cratering and MOS availability model and how the number of required Monte Carlo simulations was calculated. These surrogate models were needed because the 6-DOF model that propagated the submunitions to the ground takes an average of 30-45 minutes per munition on a 3.0 GHz computer. With missiles that have 30 submunitions per missile and simulation runs with10 missiles inbound, the computations would require days for a single run. This is prohibitive because due to the random nature of the impact and crater size, many Monte Carlo runs will be required in this next section. The surrogate models from the last section will help to realize this required speed-up in computations.

The runway MOS availability model process was described earlier in section 6.2.5. That section outlined the process to determine the aim points along the runway for the CMs and TBMs, the process to determine the impact location relative to the aim point for both guided and unguided weapons, the process to determine the spread of submunitions around the mean impact points, and finally, the process to determine the number of MOSs available once the crater size for each impact was determined. Following the process from section 6.2.5, once the mean impact point was determined for submunition carrying missiles, the max spread metamodels shown in sections 6.3.1.1 (for TBMs) and 6.3.2.1 (for CMs) were used to determine the maximum possible circular radius that a submunition could land from the mean impact point. Because observations show that submunitions typically land in a relatively uniform pattern [63], the impact location for each submunition is calculated by uniformly distributing the impact location radially around the mean impact point and uniformly between the mean impact point and the maximum spread radius. This process was described in section 6.2.5.5. For each impact the minimum and maximum crater size is then calculated from sections 6.3.1.2 for TBMs and 6.3.2.2 for CMs. The actual crater size is then a uniform random draw between these two extremes. Once each crater size is determined, the number of undamaged MOSs can be calculated with the procedure described in section 6.2.5.6.

A MATLAB code was created to perform the steps listed above and the process repeated many times, in a Monte Carlo fashion, for each design point in a DOE. This DOE was created using a Latin hypercube design with the variable values given in Table 23 below.

A Latin Hypercube was used to ensure that the DOE maintained its sampling properties even if some of the variables were found to be unimportant for a given output and the DOE collapsed into a lower dimensional space. This design is shown in Figure 80.

Table 23: Input DOE Values for Runway Cratering Model

Input	Min	Max	Units
TBM 1 – Number	0	10	ea
TBM 2 – Number	0	10	ea
TBM 3 – Number	0	10	ea
CM 1 – Number	0	10	ea
CM 2 – Number	0	10	ea
TBM Launch Distance	50	300	Km
TBM Penetrator Release Altitude	10,000	30,000	ft
CM Penetrator Release Altitude	50	500	ft

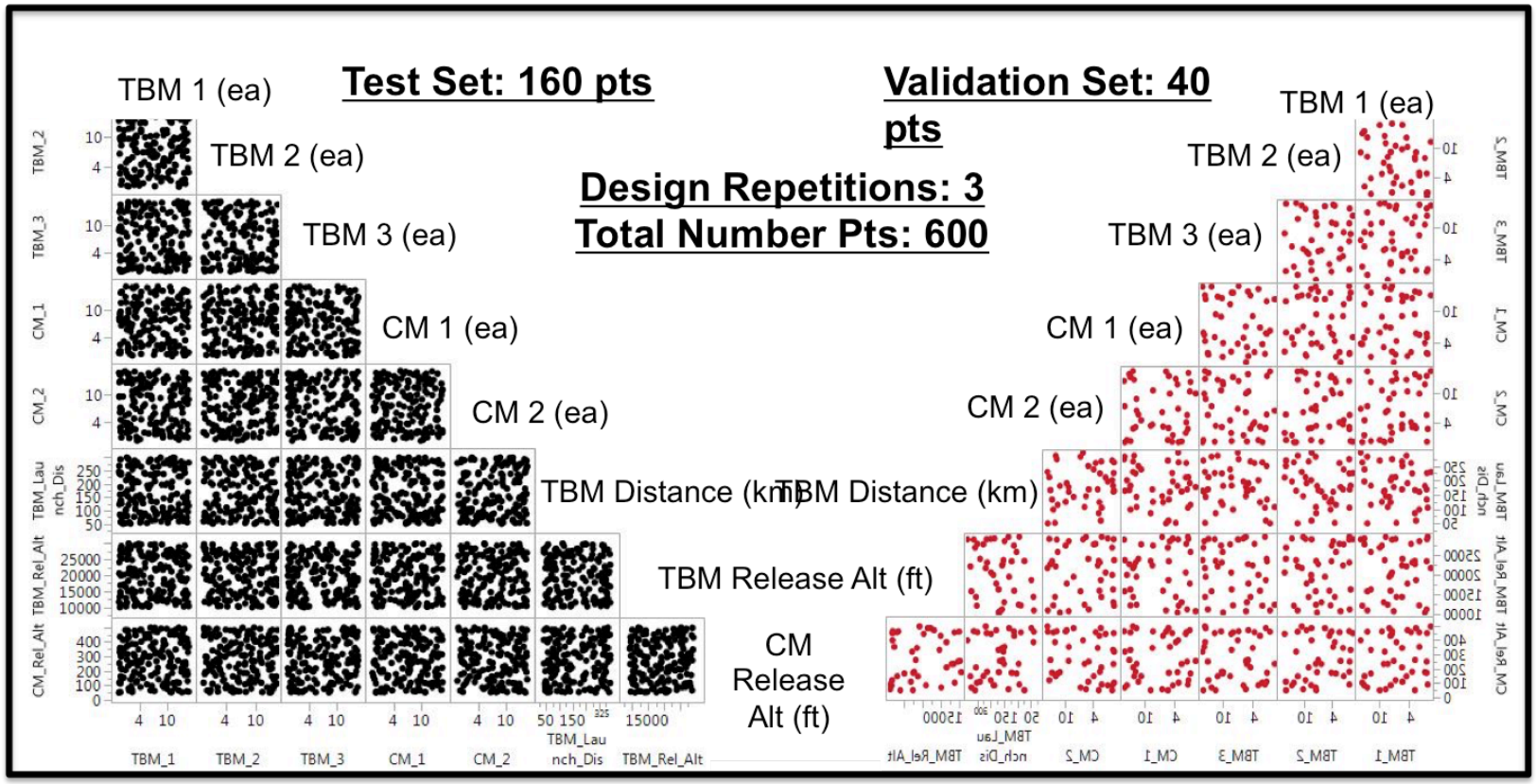

Figure 80: Runway Cratering Simulation DOE

Other variable values for elements described in section 6.2 were held constant. These are shown in Table 24 with their set values. The variables in this table are set at the time of the airfield construction or missile design and cannot be changed. These values for the airfield pavement were set based off US Federal Aviation Administration (FAA) airfield standards outlined in reference [141]. Values for the missile speed and pitch are based off reasonable inputs selected by the author.

Table 24: Inputs Held Constant in Runway Cratering Model

Inputs Held Constant	Min	Units
Concrete Thickness	30	in
Concrete Strength	3000	psi
Percent Rebar	1	%
Concrete Density	145	lbf/ft^3
Rebar Strength	90	Ksi
Cruise Missile Speed	245	mps
Cruise Missile Pitch Angle at Release	45	deg
Min Operating Strip (MOS) Width	100	ft
Min Operating Strip (MOS) Length	2000	ft
Runway Width	200	ft
Runway Length	10000	ft
Cruise Missile Speed at Release	245	Mps
Cruise Missile Pitch Angle at Release	- 45	deg
Number of Aim Points	8	ea

6.3.3.1. Enemy Missile Parameters

In this simulation, two distinct types of TBMs and two distinct types of CMs were used. TBM1 and TBM2 are variants of each other that have the same flight profile, but

TBM1 is a unitary warhead and TBM2 has a submunition warhead. TBM3 has different design and missile parameters. Likewise, CM1 and CM2 were two different missiles with different flight profiles. Critical design inputs for each of these missiles are listed below in Table 25 for the TBMs and Table 26 for the CMs.

Table 25: TBM Missile Design Parameters

Missile	Mass (kg)		Specific Impulse (s)	Reference Area (m^2)	Axial Thrust (kN)	RCS (m^2)
	Dry	Fuel				
TBM 1/2	2600	2447	400	150	150	1.8
TBM 3	2000	2500	290	150	150	0.7

Table 26: CM Missile Design Parameters

Missile	Max G Load	Weight (lbs)		Thrust (lbs)	Wing Area (ft^2)	RCS (m^2)
		Empty	Fuel			
CM 1	10	1200	600	950	20.4	1.1
CM 2	15	1565	935	1300	16	0.5

These design parameters allowed the missiles to operate over a wide range of distances and altitudes. The critical flight envelope values for these missiles are shown below in Table 27 and Table 28.

Table 27: TBM Critical Flight Profile Values

Missile	Apogee		Max Range	
	Range (km)	Altitude (km)	Range (km)	Impact Time (s)
TBM1/2	246.3	124.2	497.2	376
TBM3	154.7	91.8	306.3	311

Table 28: CM Critical Flight Profile Values

Missile	Speed (kts)		Cruise	
	Min	Max	Altitude (m)	Speed (kts)
CM 1	115	600	300	500
CM 2	115	950	300	625

On board each of these missiles are different styles of warheads. TBM 1 and 2 are both the same missile body but TBM1 carries a unitary warhead and TBM 2 carries a

submunition warhead with runway penetrating munitions. TBM 3 is a different missile body and carries a unitary warhead. Weapon parameters for the unitary weapons are shown in Table 29 and for the submunition weapons in Table 30. TBM missile explosive parameters for unitary warheads were based on values found in the following references [23, 142].

Table 29: Unitary Warhead Parameters

Missile	Explosive Weight (lbs)	Case Mass to Charge Mass Ratio	Equivalent Explosive Multiplier (EEW)
TBM 1	365	5	1
TBM 3	100	5	1
CM 2	60	5	1

Table 30: Runway Penetrating Submunitions Parameters

Missile	Submunitions				
	Number	Explosive Weight (lbs)	Case Mass to Charge Ratio	Depth Range (in)	Release Altitude (ft)
TBM 2	70	3	5	24-28	10,000-30,000
CM 1	40	1.5	5	18-22	50-500

The guidance system on the missile body helps to guide the warhead to the correct target. There are two types of guidance systems, precision and non-precision. The differences between these guidance systems as well as the methodology used to calculate the probability of hit and hit location relative to the aim point were explained in sections 6.2.5.3 and 6.2.5.4. For this work, the guidance system parameters were developed by the author to approximate reasonable values. These are listed below in Table 31. TBM1 and TBM2 represent legacy inaccurate, but large warhead weapons. TBM3 represents an upgraded precision guided missile that is small to minimize its radar cross section. Likewise, CM1 is an advanced fast, small, and accurate CM while CM2 is a slower, legacy model. In Table 31, each missile guidance type and CEP is explained. The

probability of direct hit is the chance that the missile impacts its intended aim point with no error. The probability of failure is the chance that there is a catastrophic fault in the guidance system and the missile misses by more than four standard deviations (as explained in section 6.2.5.4). The remaining probability after the probabilities of direct hit and failure are accounted for is the probability of a near miss. The method for calculating the impact point of a near miss is outlined in section 6.2.5.4.

Table 31: Missile Guidance Parameters

Missile	Precision / Nonprecision	CEP (m)	Probability of Direct Hit	Probability of Failure
TBM1 / 2	Nonprecision	200	NA	NA
TBM 3	Nonprecision	50	NA	NA
CM 1	Precision	20	50%	5%
CM 2	Precision	20	70%	3%

6.3.3.2. Number Monte Carlo Iterations

The complete code for the runway cratering simulation and MOS availability was written in MATLAB using the methodology and weapon parameters described in section 6.3.3. In this simulation, there are many parameters that are based on random draws including the impact location of each weapon and submunition and the size of the crater. This meant that every time the simulation was run, different results were obtained depending on the random numbers that were drawn. If these results are placed in bins of increasing number of MOSs available, as in the case of Figure 82, then a distribution of outputs can be estimated. This begs the question of how many simulations are necessary in order to be satisfied with the resulting distribution. During the first couple of iterations, the resulting distribution not only grows and takes shape, but it also shifts along the x-axis (number line) as the average of the results changes. It is possible to

calculate the number of iterations required such that the observed average value of the number of MOSs available is within 10% of the true mean with a 95% confidence [143, 144]. The procedure for calculating this is iterative. First, make a certain number of iterations to develop an initial mean and confidence interval half-length given by:

$$\delta(n,\alpha) = t_{n-1,1-\alpha/2}\sqrt{\frac{S^2(n)}{n}}$$

where n is the number of iterations, t is the student-t statistic for the given confidence level, α. This is then used in the following equations. The first is to calculate the relative error, i.e. a percent error of the true and estimated value, and the second is the absolute error, i.e. the difference between the true and estimated value. Typically, relative error is used for mean values greater than 1 and absolute error for mean values between 0 and 1.

$$\delta(n,\alpha)/\left|\bar{X}(n)\right| \le \gamma' = \gamma/(1+\gamma) \quad \text{For relative error}$$

$$\delta(n,\alpha) \le \gamma' = \gamma/(1+\gamma) \quad \text{For absolute error}$$

If the above statement is true, then the appropriate number of iterations have been completed. If not, the user should complete another Monte Carlo iteration and check again. This process continues until the statement is true or a specified maximum number of iterations are completed.

Initially, it is important to determine the correct initial number of iterations to complete. For many simulations, the mean and standard deviations used in the above equations will vary dramatically over the first few iterations. In order to investigate this, the author ran 1,000 iterations for three test cases and observed the fluctuation of the

calculation for the minimum number of iterations to ensure that true mean was within 10% of the actual mean with a 95% confidence. These test cases were:

1) Small Attack: 2x TBM2 and 2x CM2
2) Medium Attack: 6x TBM1, 6x TBM2, 3x TBM3, 6x CM1, 6x CM2
3) Large Attack: 12x TBM1, 12x TBM2, 12x TBM3, 28x CM1, 28x CM2

For all cases, the number of iterations required stabilized around 300 iterations, but was the largest for case 3, the large attack. The results from case 3 are shown below in Figure 81. This means that during each iteration of the DOE described in section 6.3.3.1, the simulation will be run for 300 iterations before the number of actual iterations required to be within 10% of the true mean with a 95% confidence level is calculated.

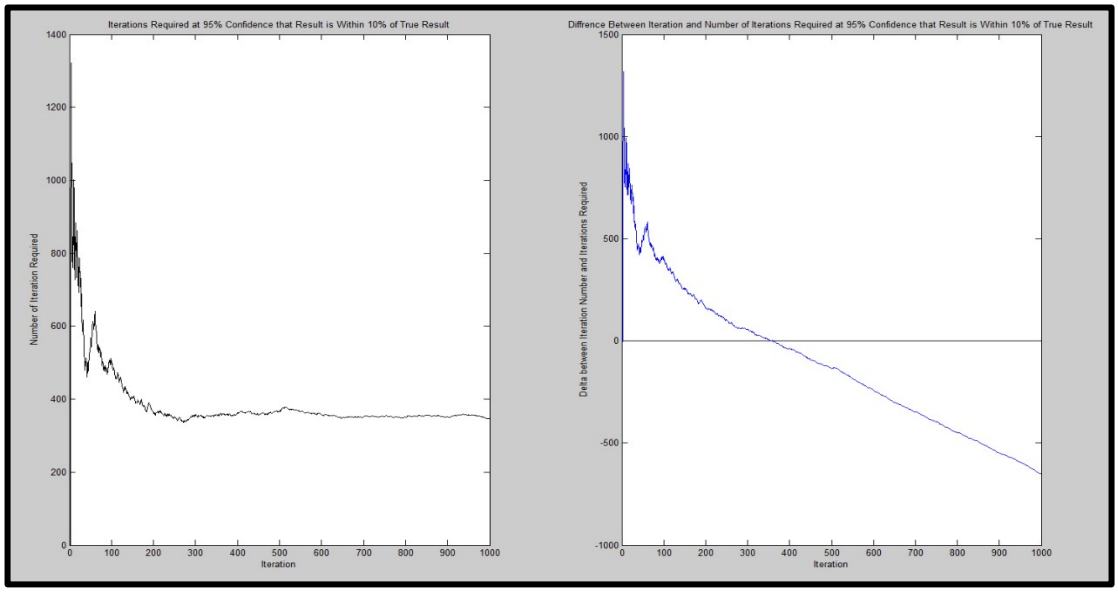

Figure 81: Case 3 - Number of Iterations Required for Large Attack, So that the Average Number of MOSs is Within 10% of the True Mean With 95% Confidence

For the above case, the number of MOSs available from each iteration are shown in a histogram below in Figure 82. These results make intuitive sense for a large attack where most cases result in zero MOSs available because most of the runway is damaged from the large number of missiles, but in rare cases there are a few MOSs available due

to bad targeting and guidance in the missiles. This figure also demonstrates how a distribution can be created for a given number of Monte Carlo runs around a single design point. This will be elaborated on further in the next section.

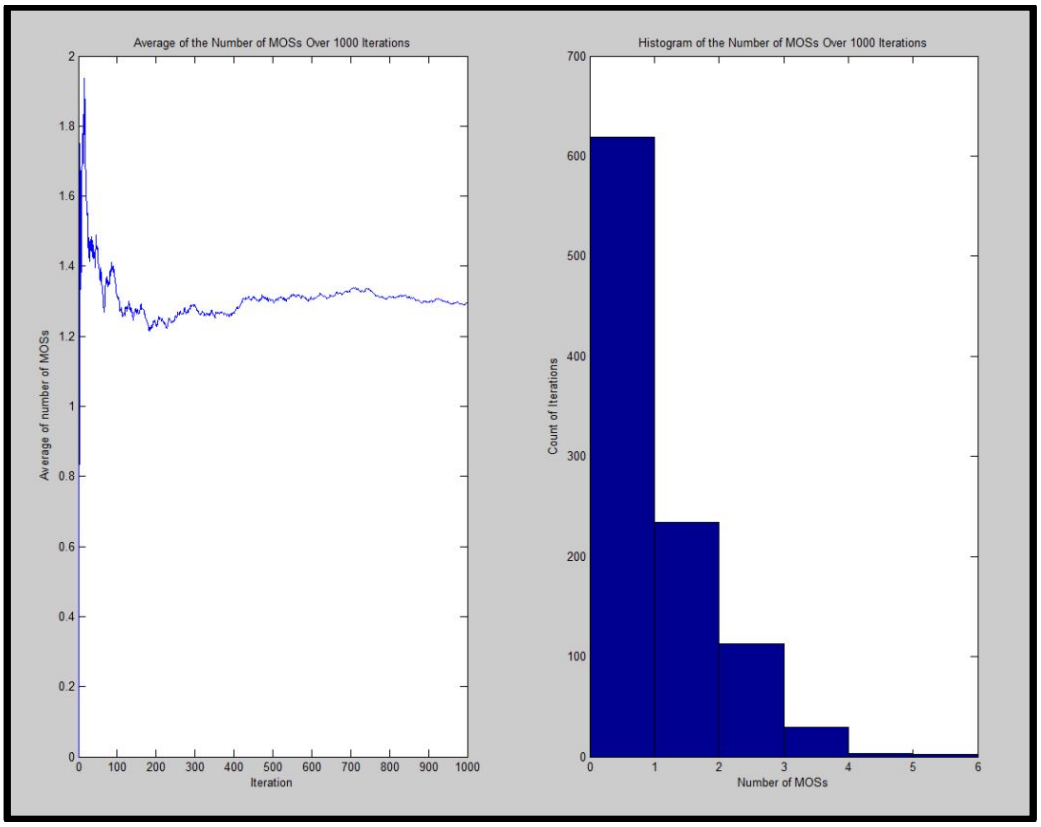

Figure 82: Case 3 - Number of Minimum Operating Stripe (MOS) Available from Large Attack After 1,000 Iterations.

6.3.3.3. Output Distribution Selection

Figure 82 demonstrates how for a fixed set of input values, a simulation that depends on random number draws will result in different values. In this simulation, each Monte Carlo run resulted in a different number of whole number MOSs available. Because there was only whole number of possible results, a discrete distribution is needed to describe the resulting output. The most common discrete distributions are the binomial, geometric, and the Poisson distribution. These are explained below and tested for the sample population.

Two other common discrete distributions, the hypergeometric and negative binomial distribution were not considered due to their nature. The hypergeometric distribution describes the probability of selecting a given number of successes from a set population of n where the total number of successes is known [202, 203]. In this case, the total number of successes (MOSs being available) is not known for every case. The negative binomial distribution describes the number of trials necessary in a Bernoulli trial such that a certain number of successes are observed. This is the opposite of the binomial distribution where the number of trials is set and the distribution describes the number of successes. In this model, the number of possible MOSs is set by the runway area and MOS area, so the negative binomial distribution is not appropriate.

6.3.3.4. Binomial Distribution

The binomial distribution describes the number of successes in a given number of independent Bernoulli (success – fail) trials where each has a probability success of p. A process can be described by a binomial distribution if the following four criteria are met [145, 146]:

1: The number of observations n is fixed.

2: Each observation is independent.

3: Each observation represents one of two outcomes ("success" or "failure").

4: The probability of "success" p is the same for each outcome.

In the case of the Runway Availability program, there is a fixed set of MOSs that can exist based on the size of the runway and the MOS (each MOS has the same size). Each MOS on the runway will be either available or not available after the attack depending if it contains cratering within its bounds. The trials are independent because

the existence of craters in one MOS does not mean that another MOS will also have craters.

The binomial distribution has a probability mass function described by the following equation [133, 143, 146]:

$$p(x) = \begin{cases} \binom{nn}{x} p^x (1-p)^{nn-x} & if\ x \in (0,1,2 \ldots, nn) \\ 0 & otherwise \end{cases}$$

This probability mass function is shown below in Figure 83 for different values of p (probability of success) and nn (number of observations).

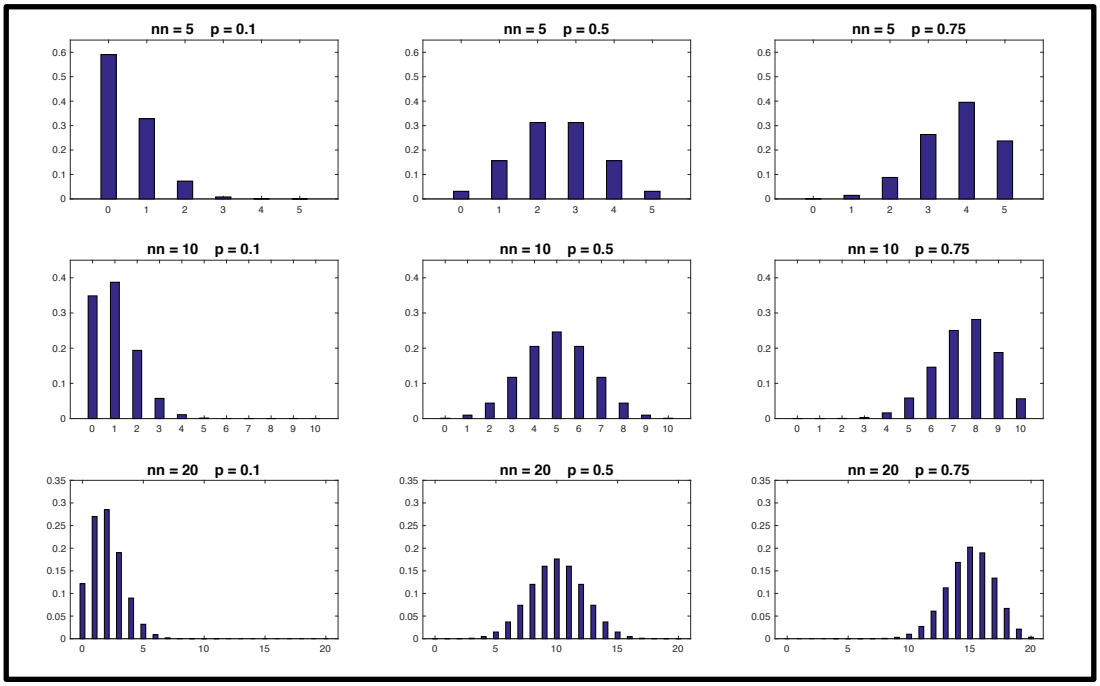

Figure 83: Effects of Different Parameters on the Binomial PMF

6.3.3.5. Geometric Distribution

The geometric distribution describes the number of trials until the first observed success for a given number of independent Bernoulli (success – fail) trials where each has a probability success of p [145, 146]. The distribution has one parameter, p, which describes the probability of success in the Bernoulli trials. The PMF is given as:

$$p(x) = \begin{cases} p(1-p)^x & if\ x \in (0,1,2 \ldots, nn) \\ 0 & otherwise \end{cases}$$

6.3.3.6. Poisson Distribution

The Poisson distribution describes the number of occurrences of an event within a particular interval of time, or the number of items within a batch of random size. In this case, it describes the number of available MOSs from a set of all available MOSs. The PMF is given as:

$$p(x) = \begin{cases} \dfrac{e^{-\lambda}\lambda^x}{x!} & if\ x \in (0,1,2 \ldots, nn) \\ 0 & otherwise \end{cases}$$

6.3.3.7. Sensitivity of the Binomial Distribution to Parameters

During the fitting process, the value of nn is set by the number of possible successes. For the runway cratering case, nn is the number of possible MOSs that can fit onto the undamaged runway. For an aircraft destruction case, it is the number of aircraft present at the time of the attack. Thus, nn is set by the scenario and the fitting process is primarily concerned with the value of p, the probability of success. This then begs the question of how sensitive is p to a starting value of nn. A test case for this is shown below in Figure 84. Here, a small change (5%) in the value of p is plotted for two different levels of nn for both a case of a low p value (.05) and a case of a higher p value (0.7). As can be seen in the figure, when nn is small (nn=5), the distributions for both the high and low value of p changes slightly but does not shift position. The location of the maximum value of the PMF does not change when p is increased by 5%. This is not the case for the bottom two graphs in the figure when nn is 30. Here, the same 5% increase in p causes a greater change in shape (especially in the low number of trials in the left

graph) and it also causes the entire PMF to shift right. In the bottom left graphs, a p value of 0.05 has a maximum PMF at a value of 1, while a value of p of 0.1 has its maximum PMF at 4. This same shift is seen in the lower right hand graph where the case of p=0.7 has a maximum PMF at 21 and the case of p=0.75 has a maximum PMF at 24.

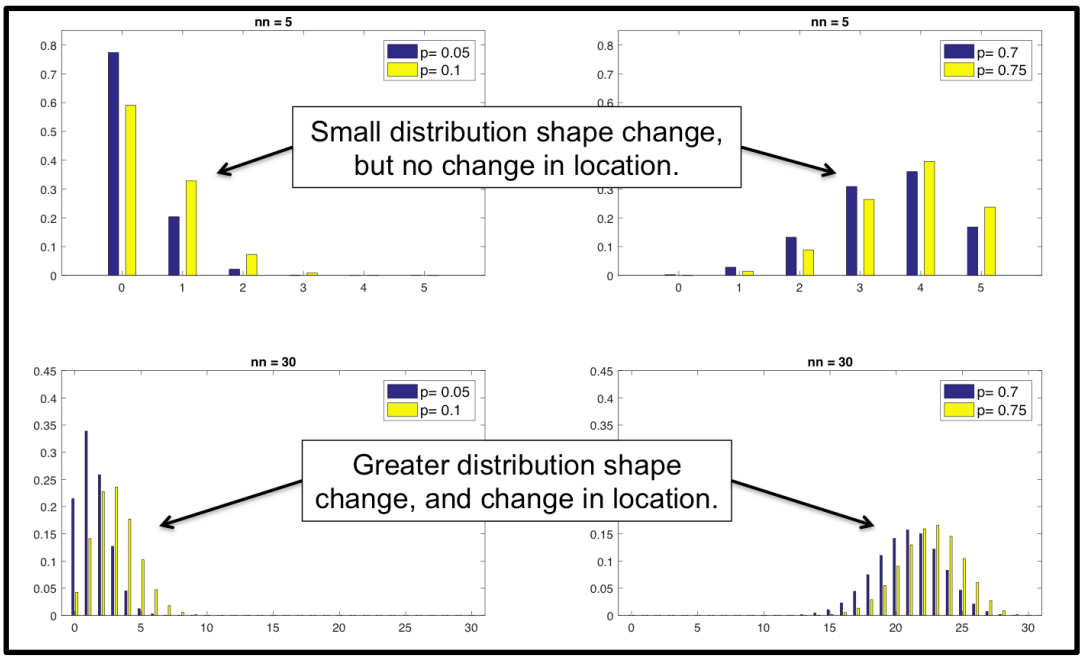

Figure 84: Parameter Sensitivity of Binomial Distribution

6.3.3.8. Maximum Likelihood Estimate

The first step in fitting all the design points for the DOE with one of the discrete distributions (binomial, geometric, or Poisson) was to determine which distribution was appropriate for each response. The appropriate distribution would be the one that fit the "best" for the most number of test cases. The best fit is the one that results in the lowest residual sum squared error (RSS). This is expressed as:

$$RSS = \sum_{i=1}^{n} (y_i - f(x_i))^2$$

The first term in the above equation is the observed output and the second is the estimated output from the distribution. Thus, the shape parameters of the distribution must first be established. This was accomplished with method of maximum likelihood estimate (MLE). This method finds the unknown parameter of the distribution, θ, in order to maximize the likelihood function, L(θ). The likelihood function is given by:

$$L(\theta) = f(x_1, \theta) f(x_2, \theta) \dots f(x_n, \theta)$$

where $f(x_n,\theta)$ is the output of the distribution at x_n given the shape parameter is θ. The method of MLE finds the value of θ to maximize the likelihood function. This effectively means that it finds an estimate of the unknown shape parameter such that it maximizes the likelihood of observing the given values.

6.3.3.9. Distribution Selection for the Runway Availability Model

The shape parameters for each of the discrete distribution, binomial, geometric, and Poisson, were estimated using the MLE for the observed 200 DOE cases. The RSS was then calculated for each case against the 200 DOE trials. The results of this analysis are summarized below in Table 32. This table shows the number and percent of the 200 DOE cases where the RSS was lowest for the given distribution. This table shows that the binomial distribution resulted in the lowest RSS for all 200 DOE cases.

Table 32: Maximum Likelihood Results for Runway Availability Models

Distribution	Number of Cases with Lowest RSS	Percent of Cases with Lowest RSS
Binomial	200	100%
Geometric	0	0
Poisson	0	0

6.3.3.10. Testing the Goodness of Fit: The P-P and Q-Q Plot

In statistics, how well a specified distribution fits the observed data can be visualized with the quantile-quantile (Q-Q) plot and the probability-probability (P-P) plots. These plots are useful to compare how closely a specified cumulative distribution function (CDF) fits the CDF of the observed values [143]. Because most distributions have an S-shaped pattern, it can be difficult to assess how close the two CDFs match each other. The P-P and Q-Q plot differences between the two CDFs on a straight line in a way that is much easier to inspect.

The Q-Q plot is a graph of a given quantile of the empirical CDF plotted against the same quantile of the theoretical CDF. If the two CDFs are from the same theoretical distribution, then the plotted line should have an intercept of 0 and a slope of 1. If there are differences in the quantiles, then the plots will deviate from this straight line. Similarly, a P-P plot is a plot of a given probability of one CDF versus the same probability of the second distribution. Again, if the two distributions are approximately the same, the graph of the points will fall along a line of y=x. The definition of the P-P and Q-Q plot is illustrated in Figure 85.

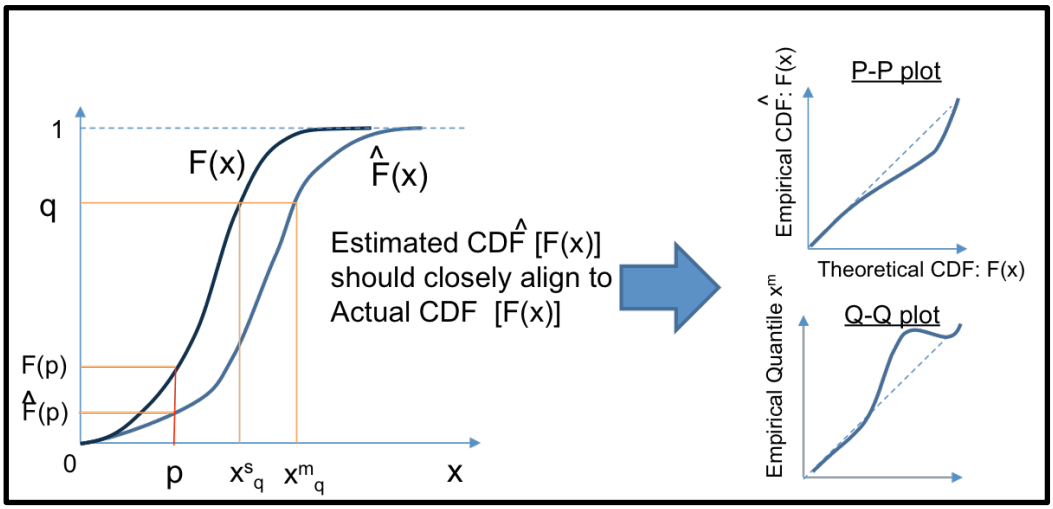

Figure 85: P-P and Q-Q Plot Description

6.3.3.11. Testing the Goodness of Fit: Chi-Square Test

For discrete data such as is used in this study, the methods to statistically test the goodness of fit are limited. The Kolomogrov-Smirnov Test is probably the most widely used test, but this can only be used or continuous distributions. Another common test, the Anderson-Darling Test is only good for a subset of continuous distributions [143]. The best test for discrete distributions is the oldest hypothesis test, the Chi-Square test. This test is a formal comparison of the theoretical and observed histogram [143]. First, the range of data is divided into k adjacent intervals: $[a_0,a_1)$, $[a_1,a_2)$, … ,$[a_{k-1},a_k)$. Then the number of observations that fall into each of these bins is summed. Next, the expected proportion of the X_j that are expected to fall into each bin is calculated. For discrete distributions, this is found as follows [143, 146]:

$$np_j = \sum_{a_{j-1} \le x_j \le a_j} \hat{p}(x_i)$$

where p-hat is the probability mass function of the fitted distribution. This is then used to calculate the test statistic:

$$\aleph^2 = \sum_{j=1}^{k} \frac{(N_j - np_j)^2}{np_j} = \sum_{all\ cells} \frac{(observed - expected)^2}{expected}$$

The p-value is then found by comparing this test statistic to chi-squared tables or curves. In this test the null hypothesis is that the tests come from the same distribution and the alternative hypothesis is that they are not from the same distribution. The value of χ^2 is compared to the test statistic $\chi_{\alpha,k-1}$ where α is the significance and k is the number of observations. It is also important to note that to use the chi-squared test, the observations should be independent from the distribution shape parameters. This means that it is only valid to compare the validation points to the expected distribution defined

by the model created with the test points. This is because the validation points were kept completely separate from any model fitting process.

6.3.3.12. Binomial Fitting Program

The purpose of this work is to produce predictive models for the shape parameters of distributions given only an input vector. In order to ensure a good fit of the predicted data, the prediction models need to be trained with existing data. To ensure a high quality prediction, the training data should be as accurate as possible. That means for any given input vector, the fitted values of the beta distribution should be adjusted until the fitted distribution matches as close as possible to the actual distribution. This is especially true given the large number of observations that this work is making for each input vector (see section 6.3.3.2).

To facilitate this high accuracy matching, a MATLAB program was created to adjust the shape parameter of the beta distribution (p-value) using a combination of the Augmented LaGrange Method and Sequential Unconstrained Minimization (SUMT) [147]. This program minimized the differences between the actual and observed CDFs similar to the work by AbouRizk [148]. In essence, the program tried to reduce the deviations from the line y=x in both the Q-Q and P-P plots. Formally, the objective function that was minimized was:

$$F(\vec{X}) = \sum_{i=1}^{n} \left(F_q(\vec{X}_i) - \hat{F}_q(\vec{X}i) \right)^2 + \sum_{i=1}^{n} \left(F_p(\vec{X}_i) - \hat{F}_p(\vec{X}_i) \right)^2$$

Subject to: $0<p<1$

where F-hat is the CDF created from a bin(p,nn) distribution, nn is the total possible successes, n is the number of observations, *Fq* is the actual and estimated quantitles, and

Fp is the actual and estimated probabilities (see section 0). The structure of the program followed the flow charts given in Vanderplaats book [147].

1. Calculate nn from the equation: floor (Area Runway/Area of one MOS)
2. Estimate p with most likely estimators (MLE) as a start point.
3. Use Augmented Lagrange Multiple Method (ALM) to minimize constrained problem and form a series of Sequential Unconstrained Minimizations.
    -- For each unconstrained minimization, use Broyden-Fleetcher-Goldfarb-Shanno (BFSG) method.
        -- For each one-dimensional search within BFSG:
            1. Find bounds on minimum
            2. Refine bounds with golden section method
            3. Use polynomial approximation to find 1-D minimum.
        -- Repeat BFSG until converged:
            - Small absolute change in pseudo-objective function.
            - Small relative change in pseudo-objective function.
            - Kuhn-Tucker (KT) Conditions met.
4. Repeat ALM method until the convergence criteria outlined above are met.

This program is fast running. On a 3.0 GHz computer it takes about 2 minutes per design point. This program was used to fit all binomial distributions in the following sections.

To test the program and ensure that it was fitting the binomial distribution correctly, a series of tests were conducted using distributions generated with known parameters and with a known working program (MATLABs binornd program). A total

of nine tests were conducted using a low, medium and high setting for each the probability of success (p) and the number of trails (nn).

Each trial was tested both visually and with a chi-squared test. The visual tests included plotting both the PMF and CMF from the distribution generated with set parameters and a distribution generated with the parameters fitted with the binomial fitting program. Using the CMF, a P-P and Q-Q plot was also generated. To pass these visual tests, the estimated parameters (p and nn) should be about the same, the PMFs and CDFs should overlap to a high degree and the P-P and Q-Q plots should lie on a 45-degree line. The Chi-squared test was conducted with a 99% confidence level using 1,000 randomly generated points. To pass this test, the test had to fail to reject the null hypothesis that the distributions were from the same overall distribution. The results of these nine tests are shown below in Figure 86 for a p value of 0.2, Figure 87 for a p-value of 0.5 and Figure 88 for a p value of 0.9.

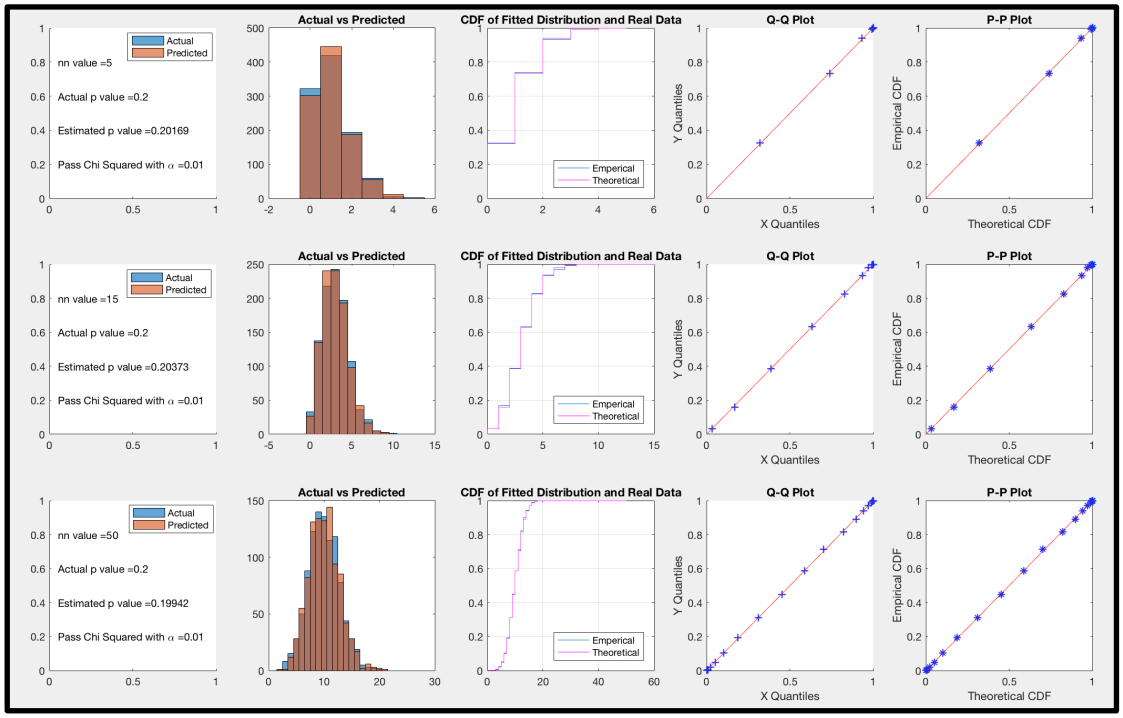

Figure 86: Binomial Fitting Program Test for P=0.2

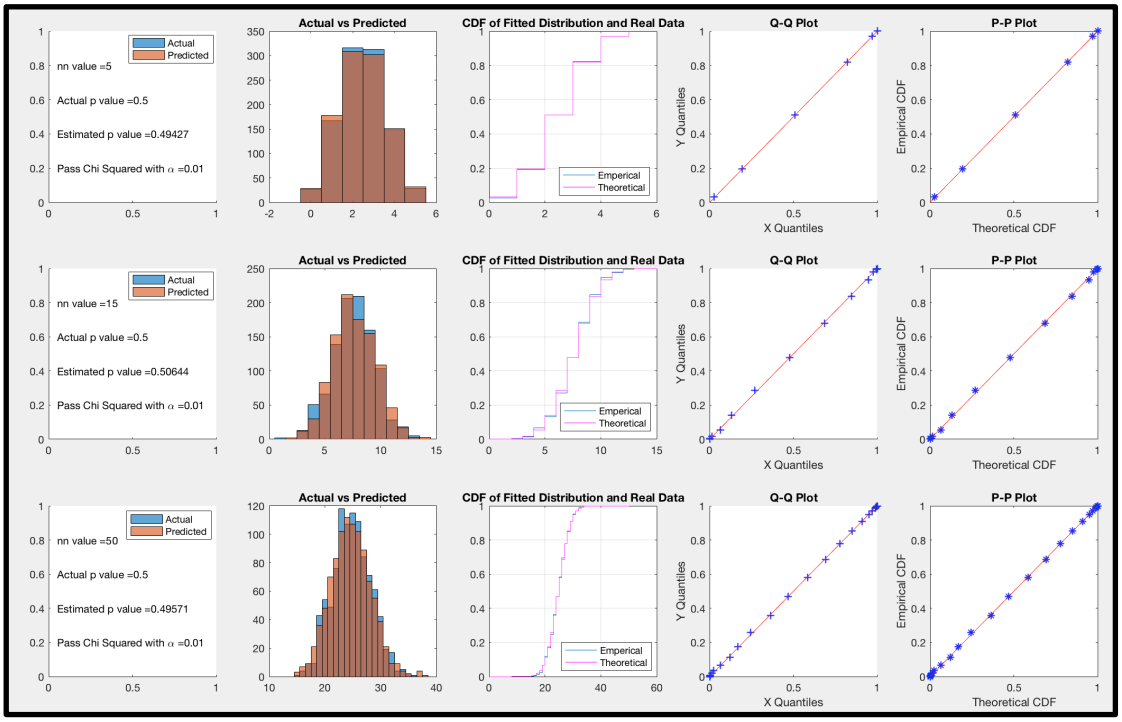

Figure 87: Binomial Fitting Program Test for P=0.5

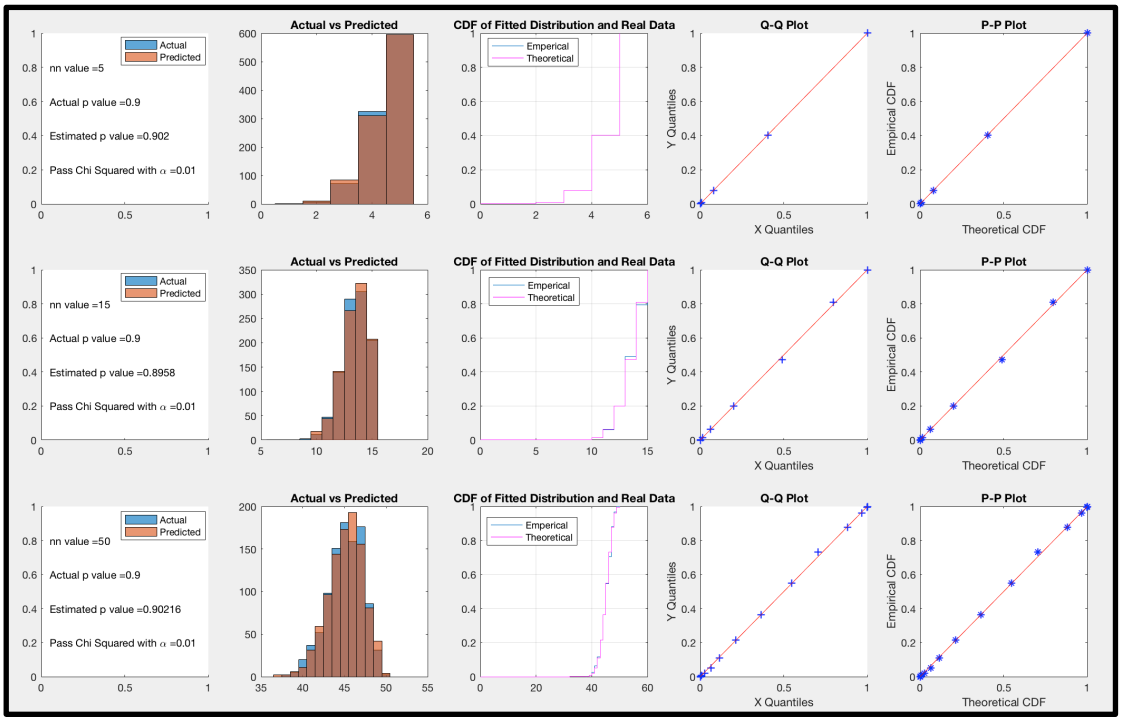

Figure 88: Binomial Fitting Program Test for P=0.9

6.3.3.13. Runway Cratering Metamodel Fit

The goal of this section is to create a metamodel able to predict the shape parameters of the output distributions from the Runway Cratering Program described in the previous sections. As explained in section 6.3.3.4, the binomial distribution is a good discrete distribution to describe the MOS available program. Each MOS that exists on the runway is either available or not available at the end of the attack and each MOS is independent of the other.

The shape parameter, p-value, for each distribution was calculated using the program described in section 6.3.3.12 for the number of Monte Carlo runs prescribed by the process in section 6.3.3.2. In the binomial distribution fitting process, the number of possible successes, nn, was based on the runway and MOS parameters. The total number of possible MOSs that could exist on the runway is given by:

nn = Number of MOSs that could exist = floor (Runway Area / MOS area)

With the runway and MOS parameters given in Table 24, the total number of possible MOSs is 10. Using this number of possible MOSs, the fitting program adjusted the p-value of the binomial distribution until the divergences in the P-P and Q-Q plot were minimized. These p-values are summarized in Figure 89. This figure shows that the p-value parameter does not have any strong trends in any set of the variables or any controlling variables.

A neural net model, described in appendix C, was used to predict the probability of success (P-value) of any MOS becoming non-available. Determining the optimal number of hidden nodes in a neural net is an area of active research and is typically chosen from a rule-of-thumb [149, 150]. In this work, the number of nodes in the hidden

layer was determined by gradually adding nodes until a divergence between the test and verification set's R^2 values was observed. Additionally, because the data being estimated was noisy since it was produced for a set of observations of a random process, multiple networks were built and the results averaged together.

During this process, each time a net is built, the points are randomly cast into a training and validation set. In order to ensure that a group of points remained completely independent, initially 20% of the points were randomly chosen and cast into an Overall Validation set. This set was withheld from all the training. The remaining 80% of the points were then used in the fitting process. The 20% of initial validation points were then used to test the generalized prediction capability of the neural net. This process was used in all the neural net fitting processes described below and in further sections.

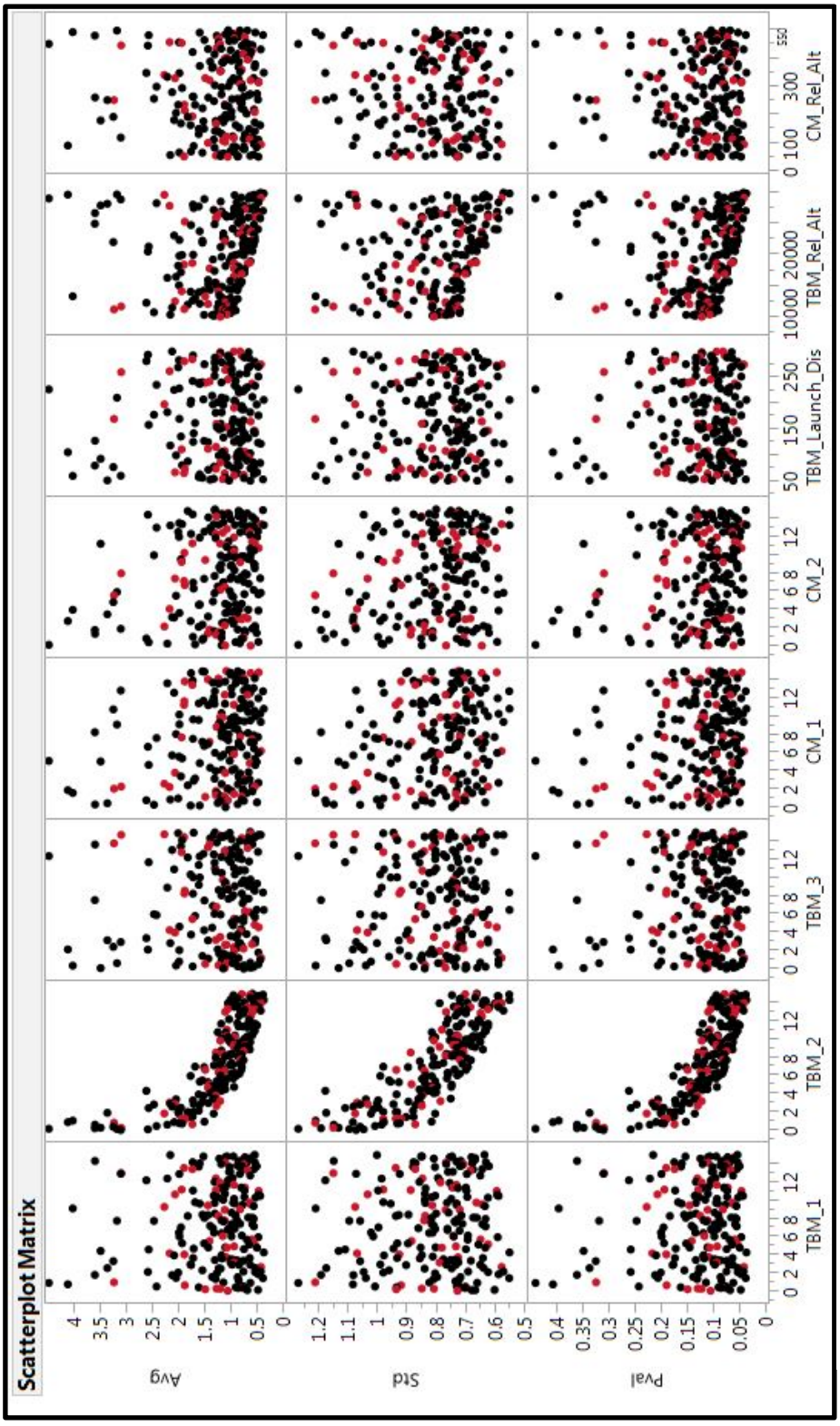

Figure 89: Results from Runway Cratering Program

Using the process described above of adding hidden nodes until a divergence is observed between the training and validation sets, a hidden layer size of 10 nodes was chosen for the p-value prediction NN model. Additionally, a square-root transformation was used to stabilize the variance [151]. Due to the large amount of noise, 5 nets were developed and the average number of predicted MOSs was carried forward. The results are shown below in Figure 90 and the residual distributions are shown in Figure 91. Note that the Validation set shown in the table on the bottom right represents the original 20% of the Overall Validation points that were reserved from the fitting process. This is different than the validation set shown in the graph in the upper right, which was the validation set from the 80% of the points used in fitting.

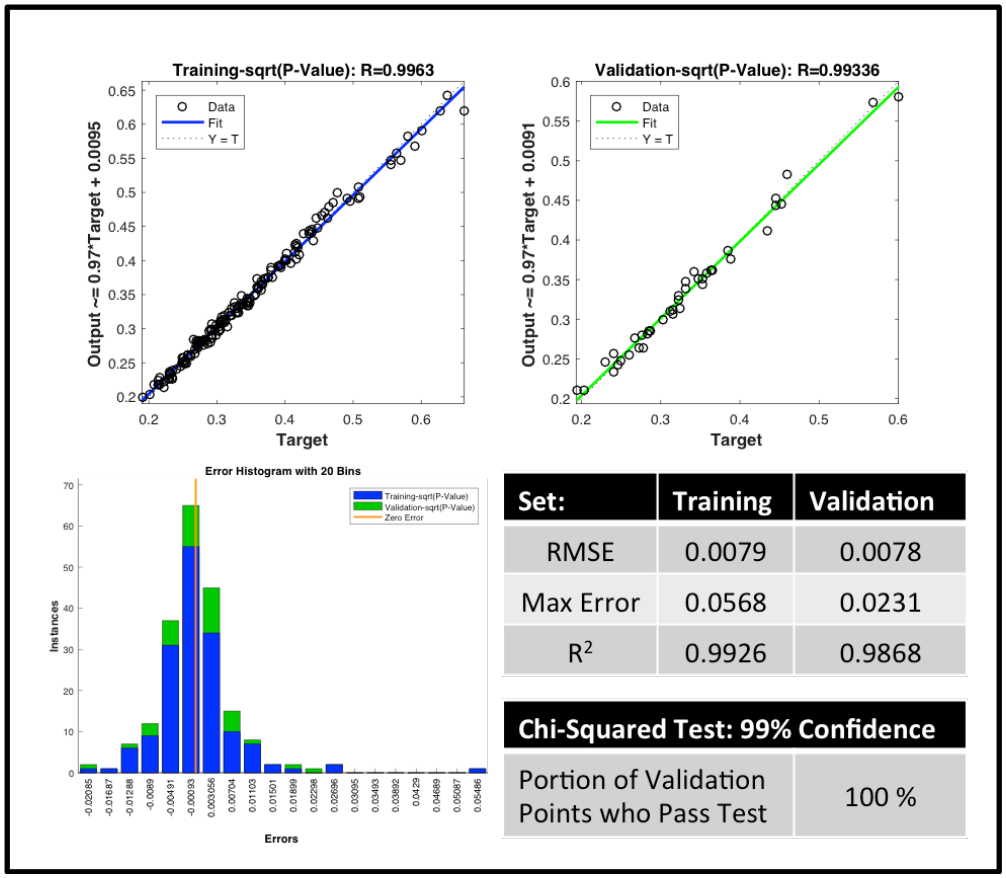

Figure 90: Results of the probability of MOS not being available (P-value)

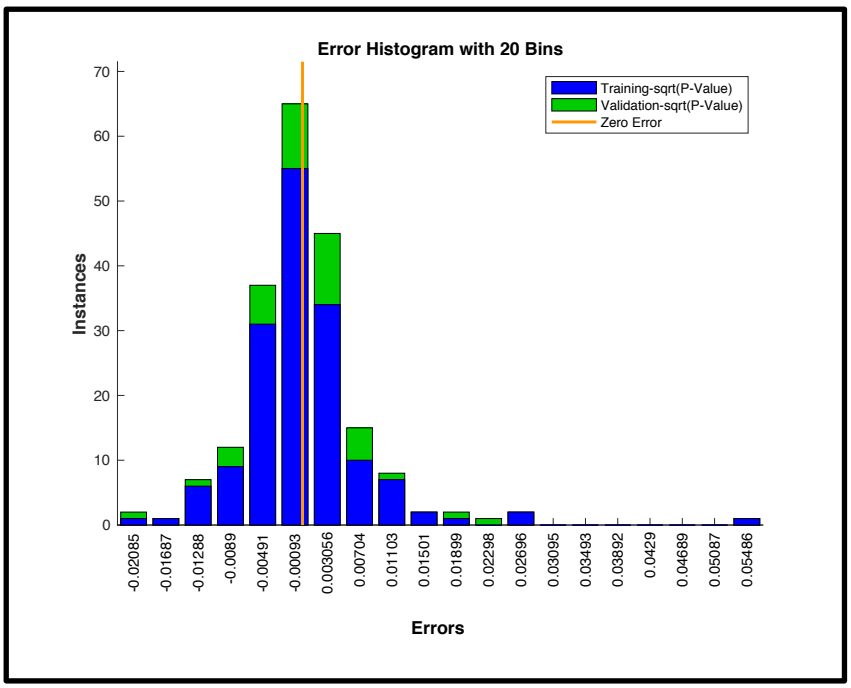

Figure 91: Residual Distribution from Probability of MOS not Being Available (P-value)

In general, the NN produced a good prediction of the binomial p-value. For the Overall Validation points, the model has a general root mean squared error (RMSE) of 0.0078. This means that the average error in the p-value, the percent chance that any one MOS is available has a prediction error of 1%. The maximum observed prediction error was 5.7%, but as seen in Figure 91, this rarely occurred and 95% of the DOE points had an error less than 2.5% for the binomial p-value.

The predicted p-value was then used to generate random points from the associate binomial distribution. This distribution was compared to the observed distribution using the chi-squared test. The number of points in the random distribution was the same as the number of points in the observed distribution. When all the distributions are compared, 100% of the validation distributions pass the test with a confidence level of 99%. This means that the chi-squared test fails to reject the null hypothesis, that the two distributions are the same, with a 99% confidence level.

This helps to answer research question number 3. This question asked if the metamodels would be as accurate as the true models. The hypothesis was that the metamodels would maintain enough accuracy such that over 95% of the validation points would pass the chi-squared test with a 99% confidence level. This was shown to be true for the MOS model.

As an additional check, the author produced plots of the actual v. predicted PMFs, CMFs, Q-Q and P-P plots for both the training and Overall Validation sets. These points were chosen at random from within each set. While not an exhaustive test of the prediction capability, they do offer an additional sanity check of the results. These results are seen below in Figure 92 and Figure 93 for the test cases, and Figure 94 and Figure 95 for the validation cases.

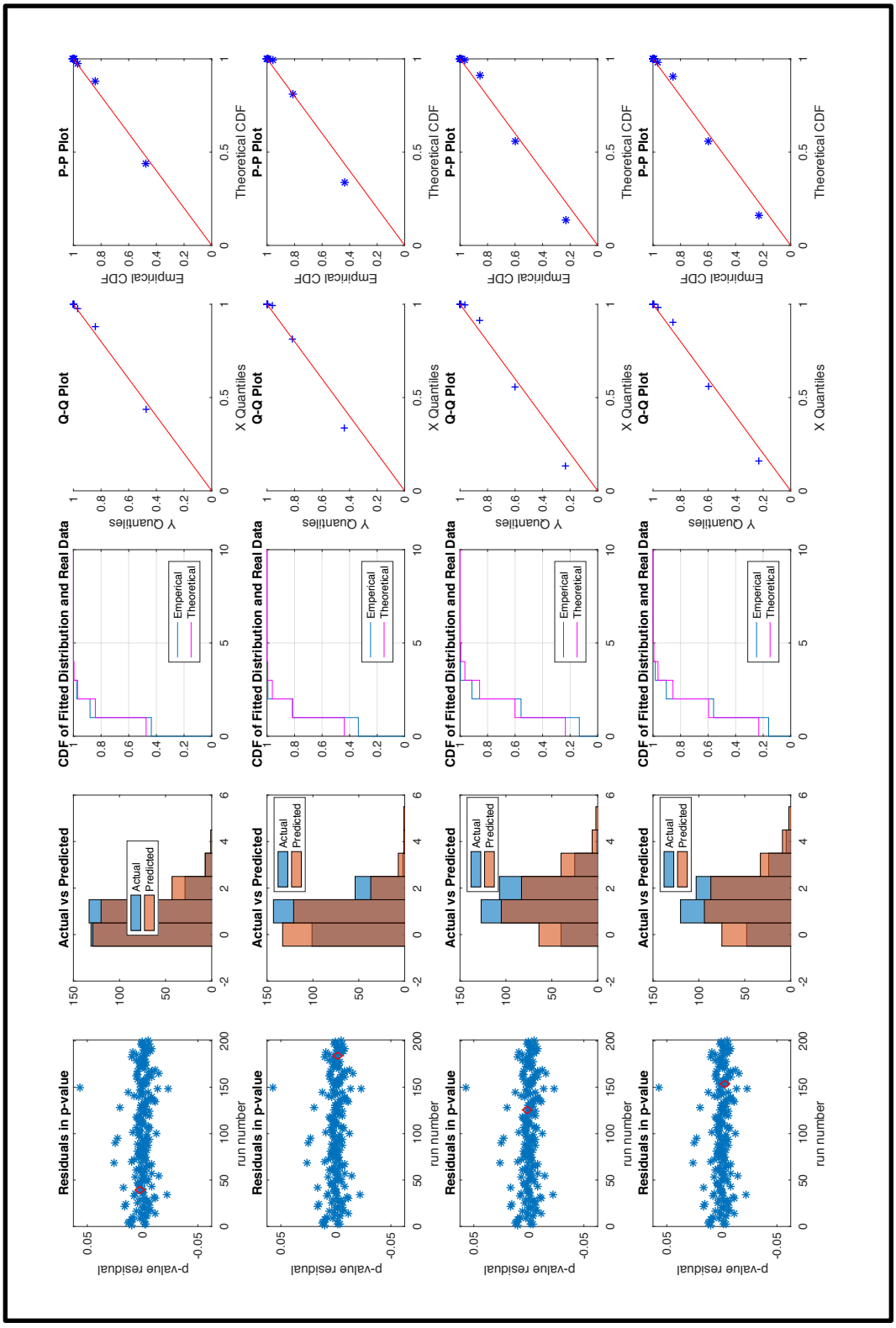

Figure 92: Binomial distribution prediction sample results - Test Set - 1 of 2

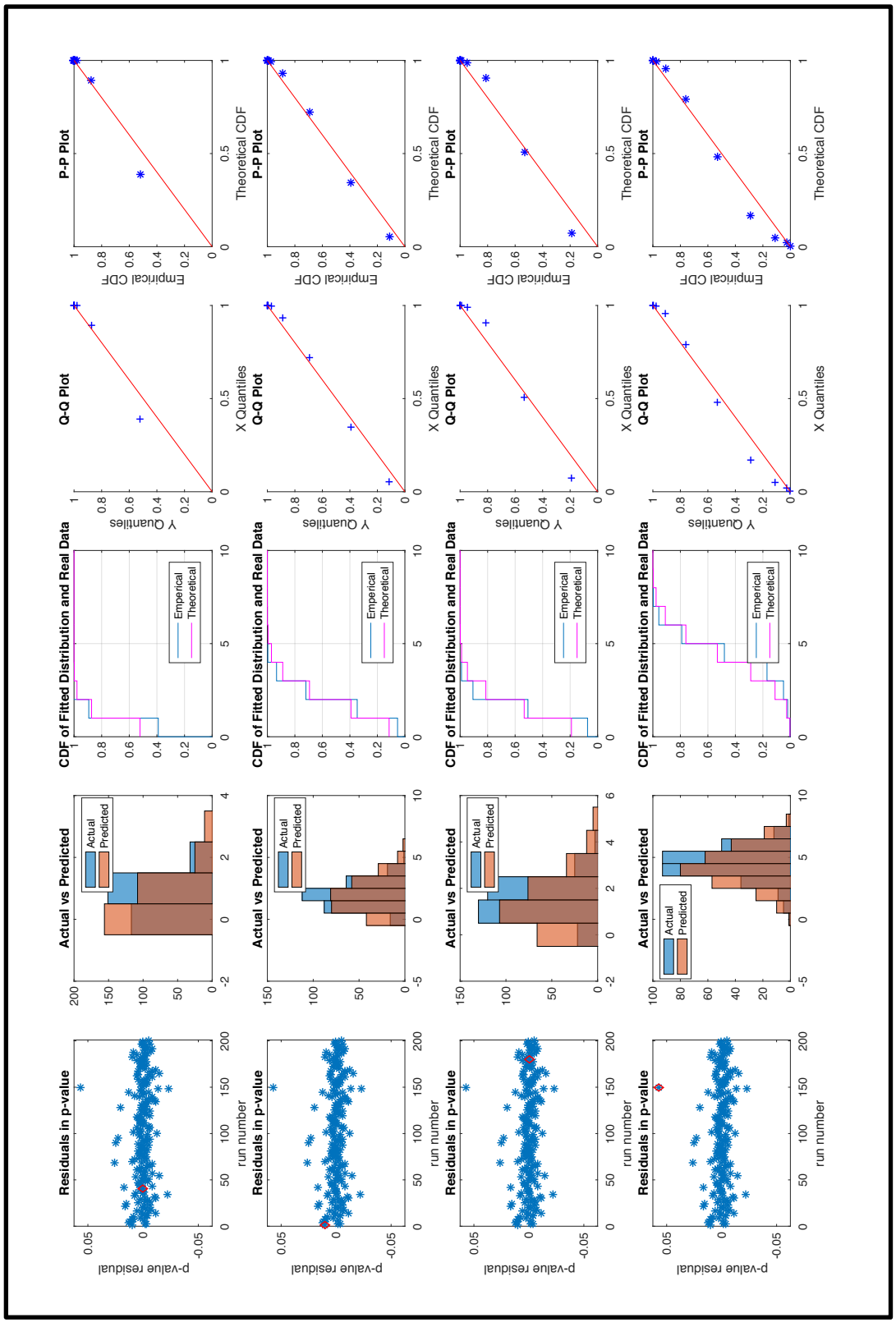

Figure 93: Binomial distribution prediction sample results - Test Set - 2 of 2

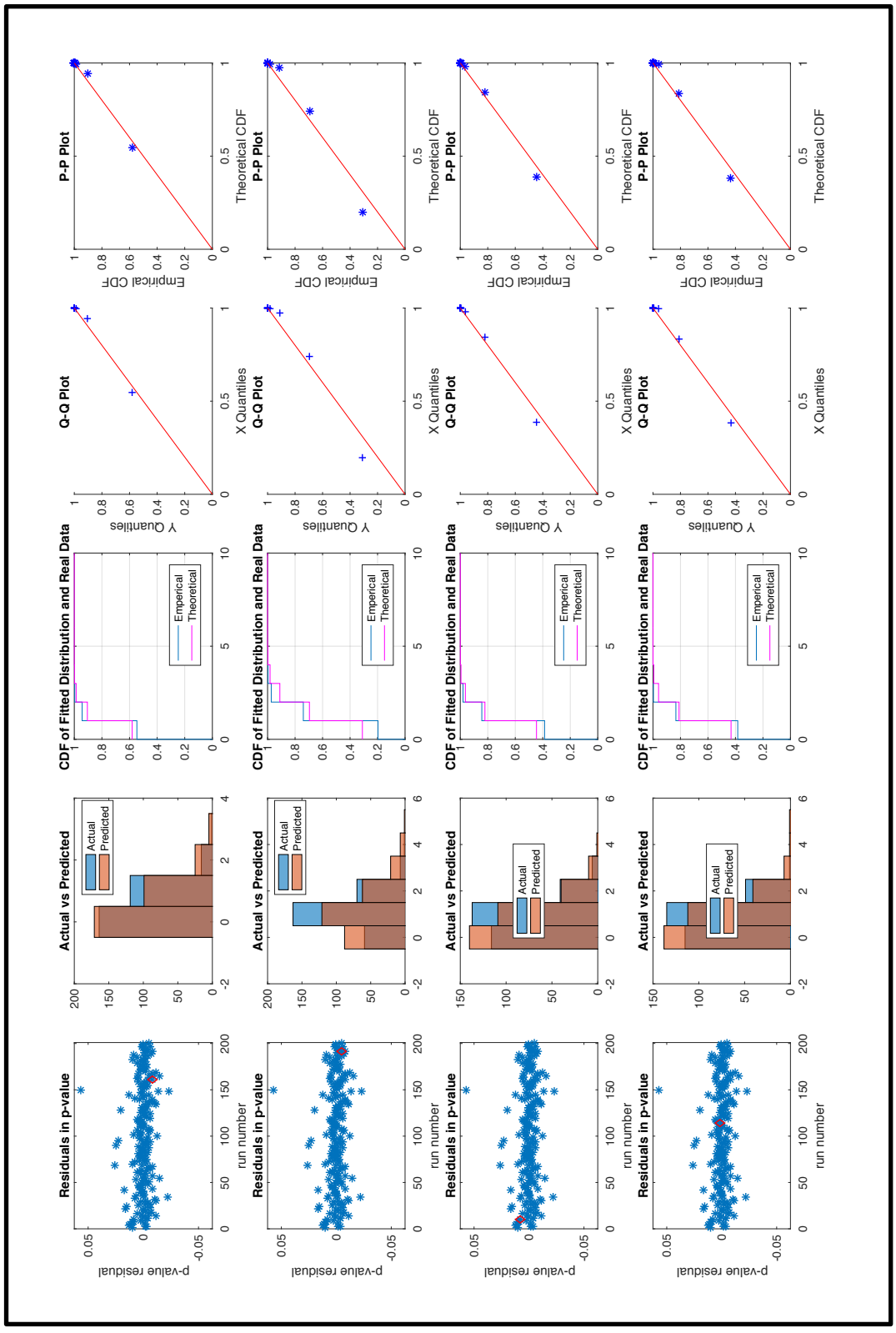

Figure 94: Binomial distribution prediction sample results – Validation Set - 1 of 2

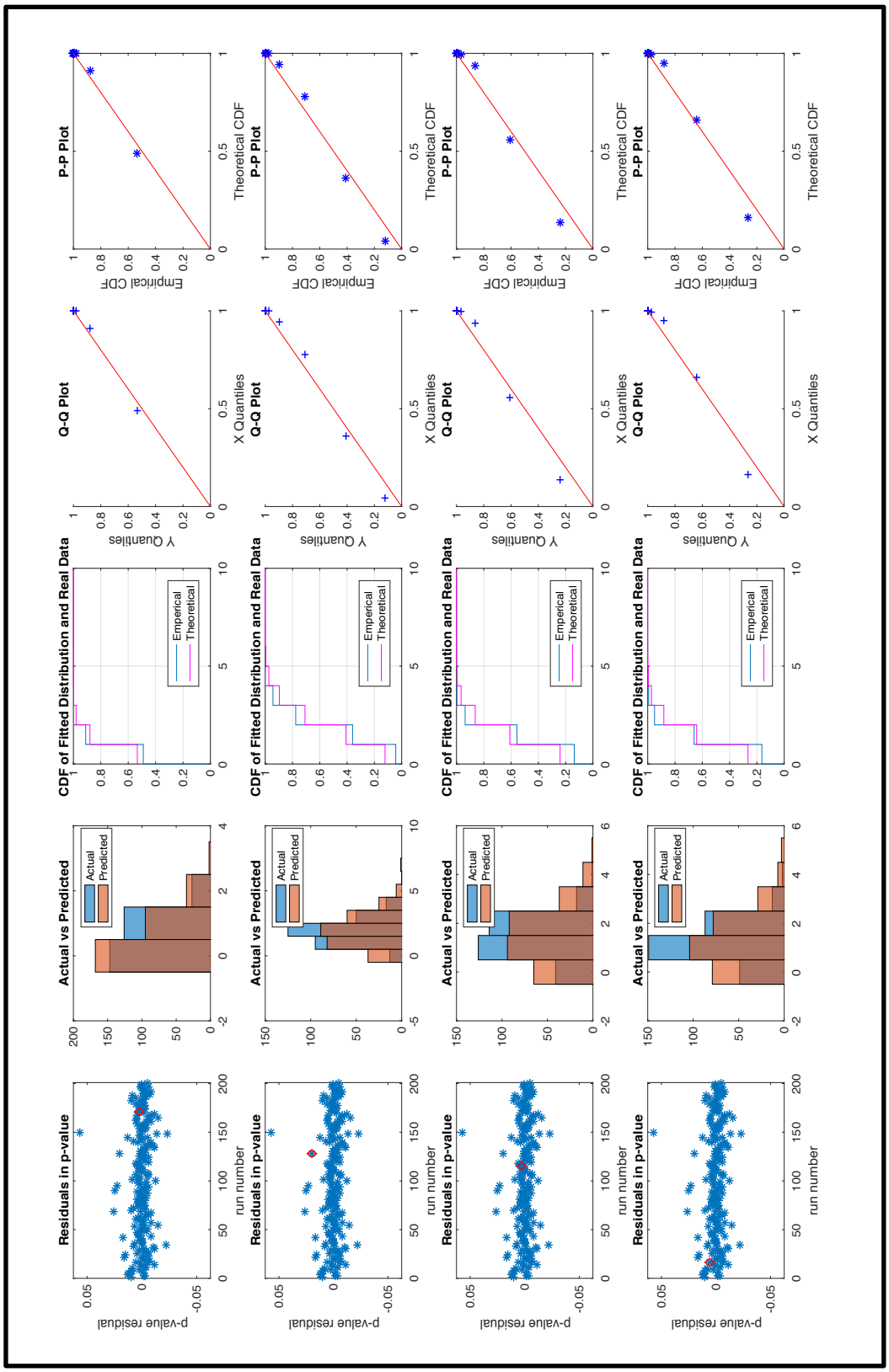

Figure 95: Binomial distribution prediction sample results – Validation Set - 2 of 2

6.4. Airfield Damage Simulation

The previous several sections outlined the process to predict the damage done to a runway and the number of undamaged MOSs that would remain after an enemy missile attack. This section will examine the damage done to the rest of the airfield to include the aircraft parked on ramps, hangar and repair infrastructure, and refuel points commonly called Petroleum, Oil, and Lubrication (POL) points. These are shown as the highlighted areas in Figure 96.

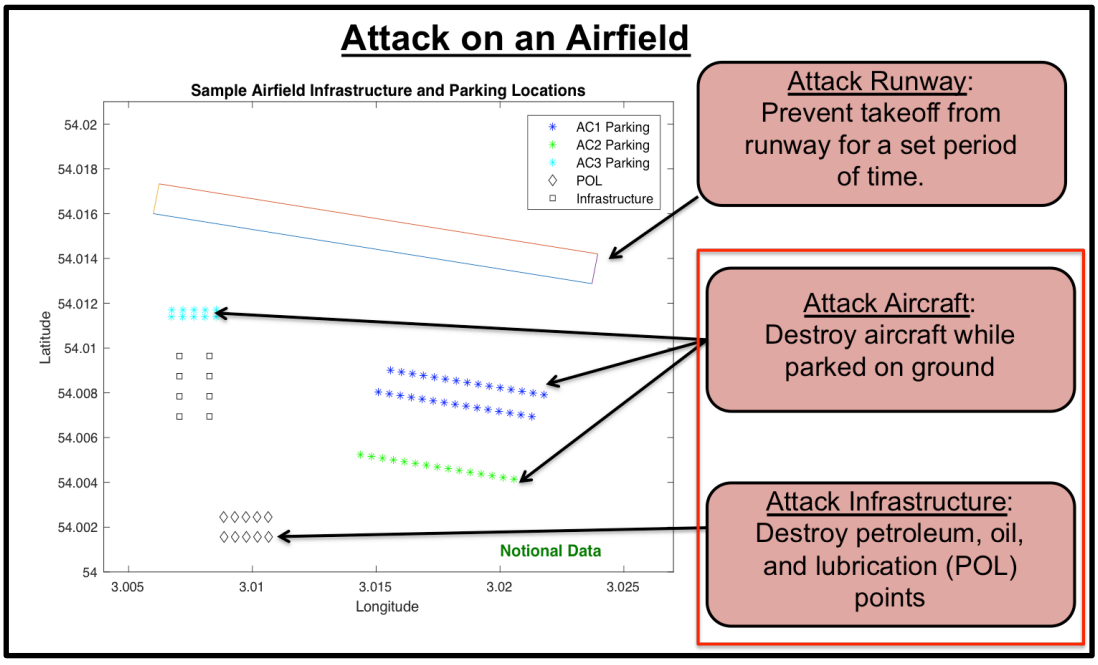

Figure 96: Enemy Goals for Attack on Airfield Portions Off Runway

An attack on the runway has the goal of damaging it to an extent that takeoffs and landings are prevented until the runway is repaired. This temporarily shuts down operations on the airfield. The goal of an attack on the infrastructure to include the repair hangars or POL points is also to damage critical portions to temporarily shut down operations. Destruction of POL points will shut down operations due to a lack of fuel or cause a bottleneck for aircraft trying to use the remaining undamaged POL points.

Likewise, destruction of critical repair assets slows or halts the repair and inspection of aircraft between missions.

An attack on the aircraft parked on the ramp is different in that it will permanently remove those aircraft from the campaign. While this is more advantageous than temporarily slowing or halting operations, it is more difficult to do because the aircraft are always operating and repositioning on the airfield. The runway, POL points, and hangars are fixed locations that are easier to target. Additionally, the previous section showed the advantage of using runway-penetrating munitions to damage and crater the runway. These munitions delay their explosion until they burrow into the concrete to a certain depth. This limits the damage they cause on the surface from blast and fragmentation. Thus, attacks on the airfield hangars, POL points, and aircraft should be done with unitary warheads with surface or proximity fuses. Thus, in this study, damage caused from TBM2 or CM1, each carrying runway-penetrating submunitions will be neglected for surface targets.

The methodology for the airfield attack simulation is very similar to the runway cratering simulation presented in section 6.2, especially in terms of determining where missiles impact relative to their aim points. For any given airfield, the location of hangars and POL points remains relatively fixed. These locations are recorded for use later. The aircraft on the airfield, however, are mobile. A smart airfield commander will maximize the distance between these aircraft so that a single missile has a reduced chance of damaging multiple aircraft. This means that the first step in the simulation is to determine the location of the aircraft parked on the ramp. Then determine the aim points relative to the targets on the airfield. The enemy force will then apportion the attack to

each target set (hangars, POL, and aircraft). During the attack, the impact location for each missile relative to the aim point is found in a similar manner to that explained in sections 6.2.5.3 and 6.2.5.4. Finally, the damage that results from the blast and fragmentation of the missiles is calculated for nearby targets. This process is summarized in Figure 97 below and explained in detail in the following sections.

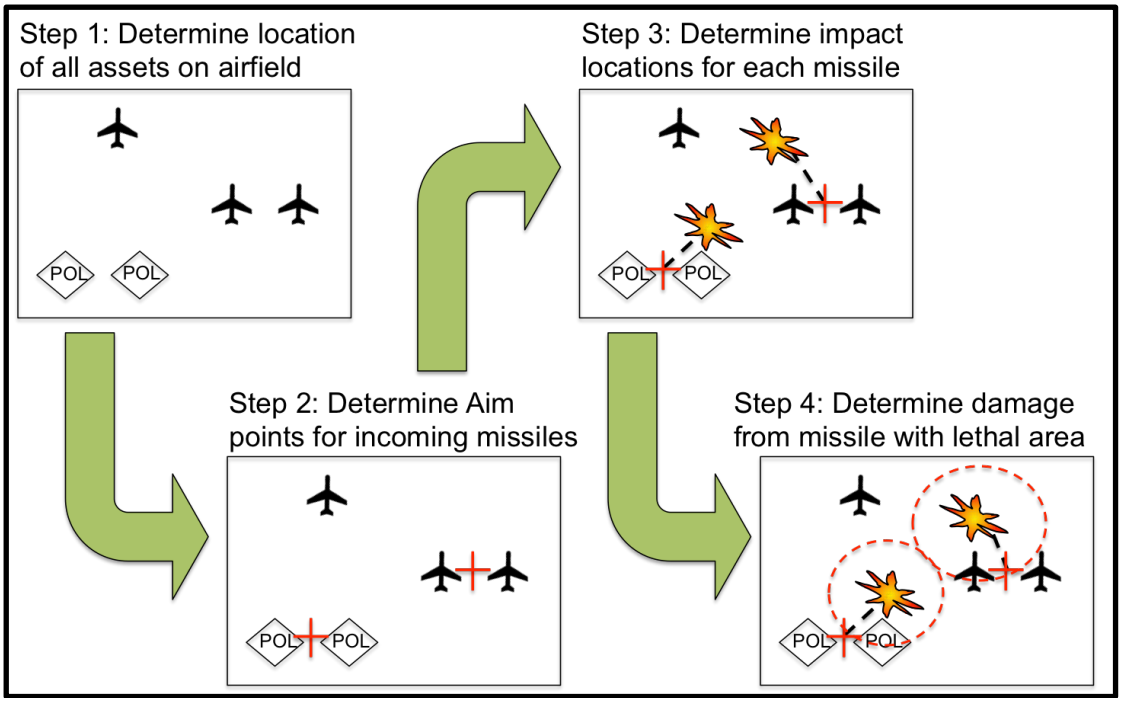

Figure 97: Airfield Damage Model Process

6.4.1. Airfield Attack Simulation: Step 1 – Location of Assets

As mentioned above, typically hangars and POL points are fixed locations. The location (latitude and longitude) for these can be obtained from mapping software. In addition, while the aircraft can be moved, the parking locations can be assumed to remain fixed. These locations can be obtained from mapping software as well. In this simulation, for a test case, a hypothetical airfield was created using latitude and longitude points in the middle of the Atlantic Ocean. This hypothetical airfield has eight POL points spaced 50 meters apart in two east-west rows of four. It also has ten hangars each

spaced 100 meters between buildings arranged in two north-south rows. For the aircraft parking, it was assumed the airfield supported three different types of aircraft, AC1, AC2, and AC3. The parking for each aircraft type was arranged together and was 50 meters apart. Aircraft type 1 was arranged in two rows of 15 parking spots angled parallel to the runway. Aircraft type two was set further south of the parking for aircraft type 1 in a single row of 15 spots. The parking for aircraft type 3 was set just north of the hangars in two east-west rows of six parking spots each. This notional airfield is shown in Figure 98.

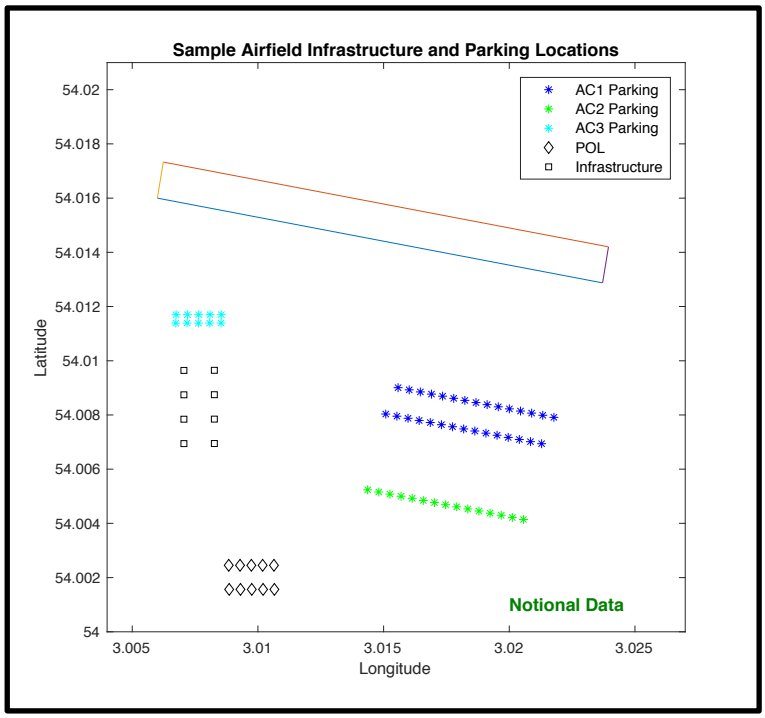

Figure 98: Notional Airfield with Asset Locations Marked

When selecting the location for aircraft to park in these parking locations, most airfield commanders will want to spread the aircraft as far apart as possible in order to minimize the damage to the aircraft. Generally, however, aircraft of the same type are kept in their assigned parking locations in order to facilitate maintenance and inspections. Thus, when placing a given number of aircraft of each type on the airfield, the simulation

would randomly place the first aircraft into a parking location for its assigned type. Subsequent aircraft were then placed in parking locations for their type such that the minimum distance between all aircraft was maximized. If an aircraft type had more aircraft present than assigned parking locations, it was assigned a parking spot of any type such that the minimum distance between all aircraft was maximized. This is demonstrated in Figure 99 for six aircraft of type AC1, three aircraft of type AC2, and two aircraft of type AC3.

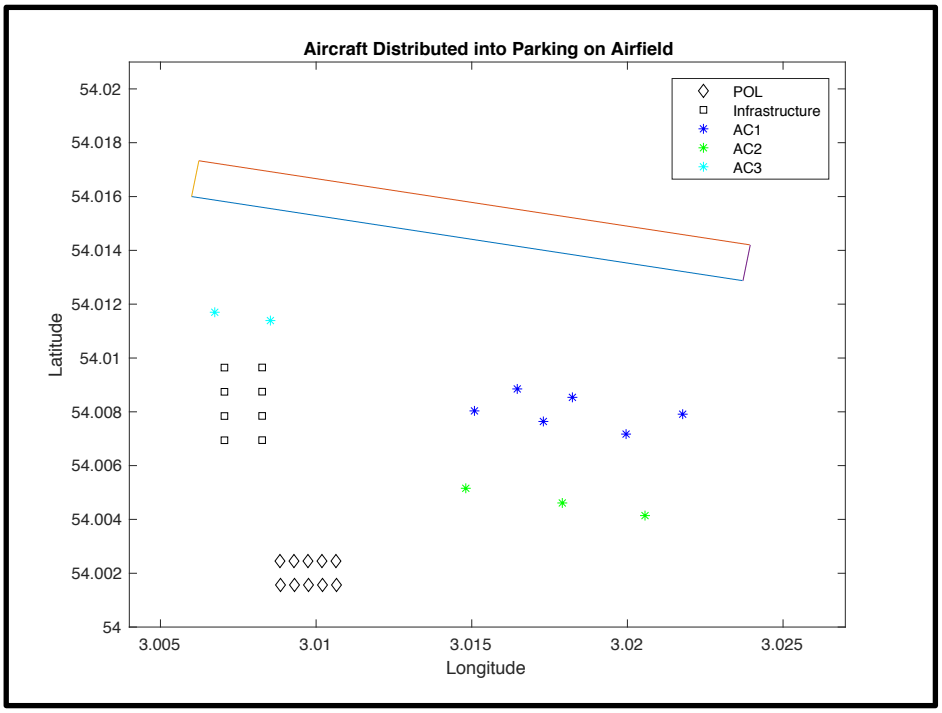

Figure 99: Aircraft Distributed into Parking to Maximize the Minimum Distance Between Aircraft

6.4.2. Airfield Attack Simulation: Step 2 – Location of Aim Points

The second step in the process is to plot the aim points. It can be assumed that the enemy force will have relatively good intelligence and will know the locations of hangars, POL points and all aircraft parking spots. What they will not know is which parking spots are being used at the time of the attack. This is mainly due to the delay in what is called the "kill chain." This is the total set of processes from the gathering of

intelligence to the release of the missile. For even modern militaries with advanced communications and intelligence gathering equipment this can be several hours long. During this delay the aircraft can be moved and repositioned due to normal operations or due to deliberate attempts to confuse enemy targeting.

Aim points are chosen to cover the POL points, hangars, and general parking locations, without consideration of aircraft locations. In this work, aim points were generally distributed with 150 meters between aim points for aircraft parking locations, 100 meters between aim points for POL targets, and for hangars there was one aim point per hangar. This distribution was a compromise between number of target and the damage radius for each missile. The damage radius will be explained further in the next section. A plot of the aim points relative to the infrastructure and parking locations is shown below in Figure 100.

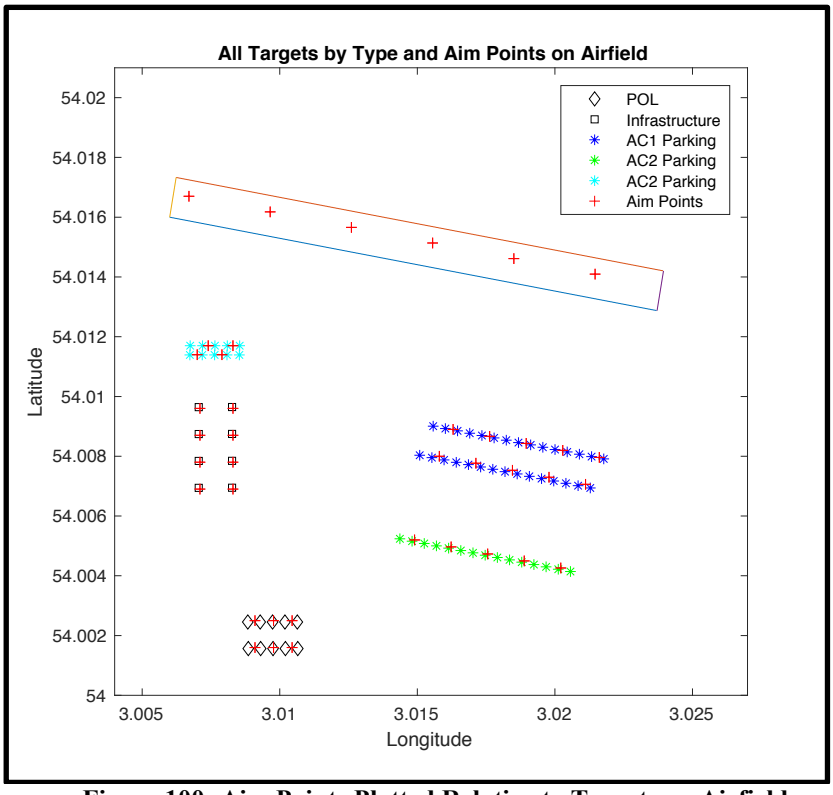

Figure 100: Aim Points Plotted Relative to Targets on Airfield

6.4.3. Airfield Attack Simulation: Step 3 – Impact Locations

The third step is to determine the impact location for each missile. The attack is setup to shoot a proportion of the total number of each missile type at a given target set: aircraft, hangars, POL, or runway. It was assumed that the missiles that leak through the defenses and impact the airfield maintain the same distribution. This means that the missiles that are shot down are randomly distributed in the same proportion as what was originally shot. Thus, for each leaker, a random draw was conducted against the initial target distribution to determine its aim point set: aircraft, hangars, POL, or runway. Then a uniform random draw was conducted, without replacement, to determine the individual aim point for that missile within the aim point set.

Once the individual aim point is chosen, it is possible to calculate the impact location relative to that aim point using the methods described in section 6.2.5.3 for unguided missiles or section 6.2.5.4 for guided missiles in reference [62] which summarizes the entire weaponeering process. For unguided missiles the impact location is Rayleigh distributed according to the missile's CEP [62]. This is described below in Figure 101. This picture shows how the range and deflection error relative to the missiles flight path are both normally distributed with a mean of zero and equal standard deviations derived from the missile's CEP.

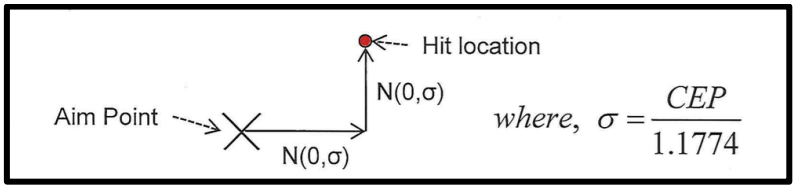

Figure 101: Impact Location Calculations Relative to Aim Point for Unguided Weapons

For guided missiles, the impact point is located by first determining the accuracy of the guidance system. A guided missiles can either directly impact the target, have

small errors that accumulate in the guidance logic that cause it to have a near miss, or the guidance system can experience a catastrophic error [62]. These probabilities for the missiles used in this study are summarized in Table 31 in section 6.2.5.4. To determine the type of impact, a uniform random draw is conducted between 0 and 1. This number is then compared to the probabilities found in Figure 102 below.

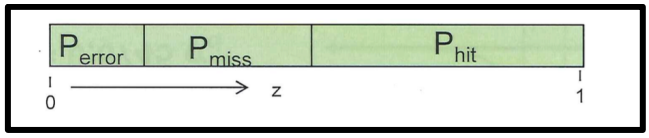

Figure 102: Guided Missiles Type of Miss

If the uniform draw falls into the probability of a direct hit region (P_{hit}), then the impact location is the same as that of the aim point. If the uniform draw falls into the probability of a near miss region (P_{miss}), then the impact location relative to the aim point is calculated the same as in Figure 101 except that the range and deflection errors are each given by (error distance)=t*σ where t=N(0,1) and σ is the same as expressed in Figure 101. If the uniform draw falls into the probability of a catastrophic error region (P_{error}) then the range and deflection errors are each given by (error distance)=4*σ.

The above process for both guided and unguided missiles is repeated for each individual leaker to determine its impact latitude and longitude. These are then plotted with all existing targets on the airfield so that the damage can be calculated according to the process in the following section. An example of this for an attack made up of four TBM1 missiles, two TBM3 missiles, and three CM2 missiles against the sample airfield with a missiles distribution of 60% aircraft, 20% POL, and 20% hangars is shown below in Figure 103.

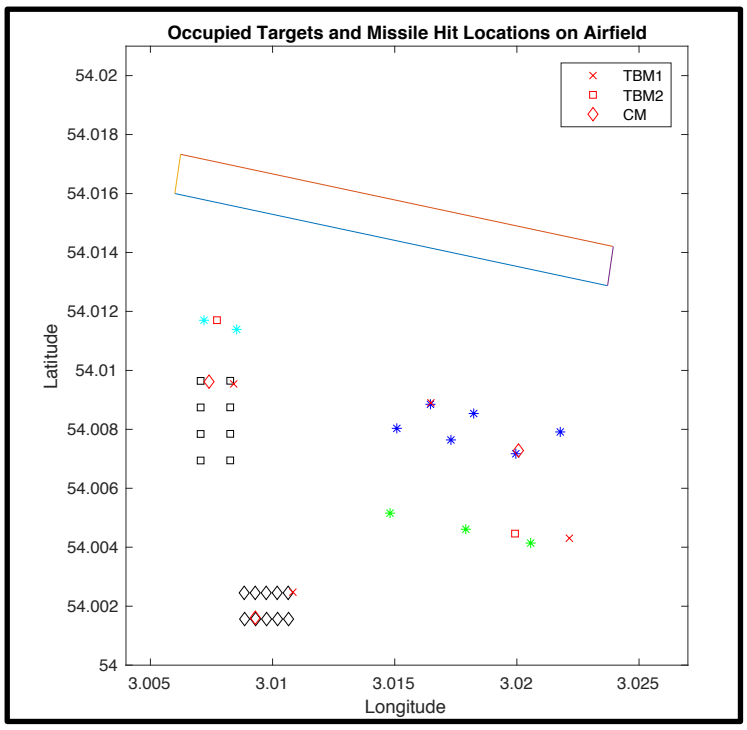

Figure 103: Sample Results Showing Impact Locations Relative to Targets on an Airfield

6.4.4. Airfield Attack Simulation: Step 4 – Damage from Impacts

Determining the lethal area of a weapon is an area within weaponeering that has received much study and is well documented [58, 152-155]. Reference [62] is one of the definitive resources on the topic and devotes several chapters to the subject of weapon effectiveness. Within the Department of Defense (DoD), the Army Material Research and Analysis Activity (AMSAA) is the proponent for weapons effectiveness. They maintain a large database of weapon-target pairings that give the lethal area based on numerous parameters such as angle of fall and target orientation. AMSAA also regularly updates the database with the Joint Weaponeering System (JWS), a computer system used to determine the probability of kill for different weapon attack patterns and munition types against arrays of targets.

Because this area is so well researched, this work will make use of notional, and thus unclassified, lethal areas for all weapon-target pairs. The notional lethal areas used in this work are summarized in Table 33. Note that these are the catastrophic-kill-on ground (COG) radiuses. The author only tracked these kills and not repairable damage that is sometimes tracked in other studies, i.e. prevent takeoff for four hours (PTO4).

Table 33: Lethal Radius for Missile-Target Pairs

Missile	Lethal Radius (m)				
	AC 1	AC 2	AC 3	POL	Hangar
TBM 1	80	100	30	30	15
TBM 3	60	80	20	20	10
CM 2	40	50	20	15	5

Given the impact location latitude and longitude found in the previous section, all nearby targets of a given category are checked against the lethal radiuses in the above table using the distance equations found in section 6.2.1. Any target that falls within this lethal radius is considered destroyed. This is shown in Figure 104 below. The picture on the left shows the general locations of aircraft parking, infrastructure locations, and aim points. The picture on the right shows the impact location relative to the targets present at the time of the attack. Finally, the summary below both pictures shows the number of aircraft and infrastructure damaged or destroyed during the attack.

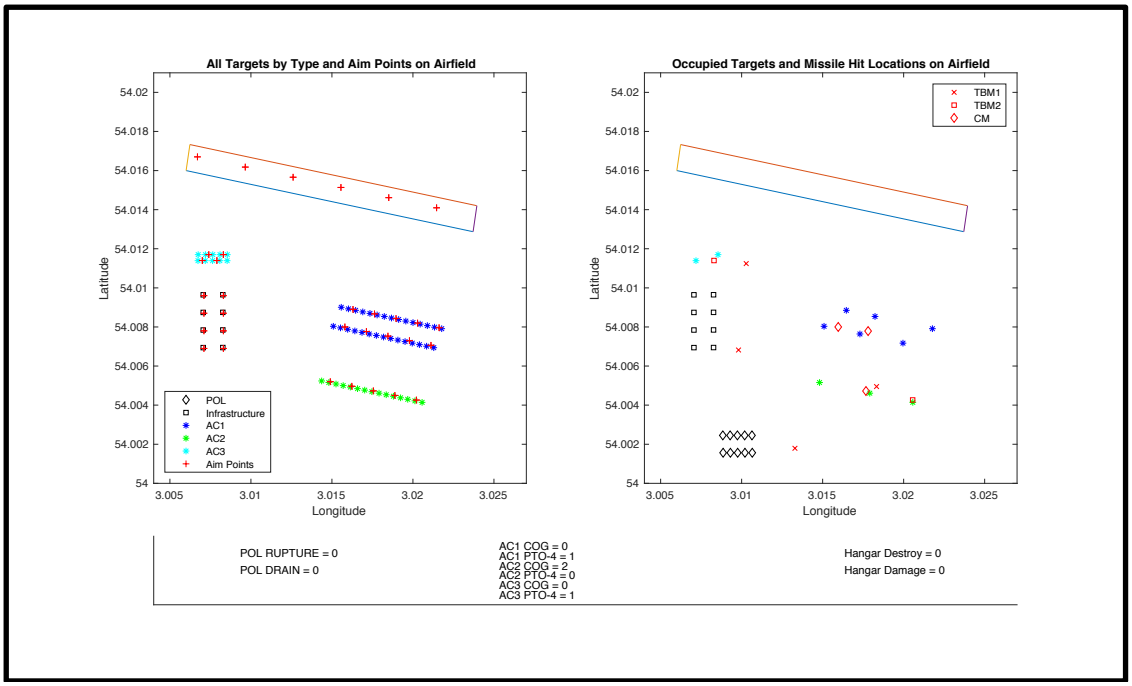

Figure 104: Sample Results for Damage to Aircraft and Infrastructure for an Attack on an Airfield

6.5. Airfield Damage Surrogate Model

The airfield damage model described in the last section is stochastic. Each run of the model will produce different numbers of aircraft and infrastructure destroyed even with the same inputs due to the large number of random draws involved in the model. This means that if the model is run a large number of times using the same inputs (Monte Carlo simulation), a distribution of possible outputs can be created. Just as in the runway cratering models described in section 6.3.3, the author wanted to create a predictive model that would accurately forecast the shape parameters for that resulting distribution given the vector of input parameters.

6.5.1. Number of Iterations Required

The first step in this process is to determine the number of iterations for each Monte Carlo series given the inputs. This was done similar to the method outlined in

section 6.3.3.2. The test cases used for the minimum number of Monte Carlo simulations in order to calculate the number of iterations required such that the estimated average is within 10% of the true average with a 95% confidence is summarized below. These test cases all included the same number of fixed assets: ten POL points and eight hangar buildings and each case was run for 1,000 iterations.

Table 34: Test Cases for Number of Iterations Required for Airfield Simulation

Test Case	Number of Aircraft	Size of Attack	Aircraft			Missiles		
			AC1	AC2	AC3	TBM1	TBM2	CM2
1	Medium	Medium	6	6	5	5	5	5
2	Large	Small	12	12	10	1	1	1
3	Small	Large	1	1	1	10	10	10

The largest number of iterations was required by case 2: Large number of aircraft and small attack size for the prediction of the number of aircraft destroyed. These results are shown below in Figure 105. In this figure, the graphs on the left show the calculations for the number of iterations required until the estimate of the average number of items destroyed is within 10% of the true mean with 95% confidence. The graphs on the right show the difference between that estimate and the current number iterations. The graphs from top to bottom show the calculations for the number of aircraft destroyed, POL points destroyed, and hangars destroyed.

Note that initially the number iterations required fluctuated rapidly, but in all cases, it stabilized after about 300 iterations. Therefore, in the analysis in the next section, all Monte Carlo trials were run for at least 300 iterations before the number of iterations required was calculated. This calculation was then made on subsequent iterations until the current number of iterations was greater than this calculated number. The histogram of results from the 1,000 Monte Carlo iterations is shown in Figure 106.

These results show how the binomial distribution will most likely be a good distribution to model the results of the simulation.

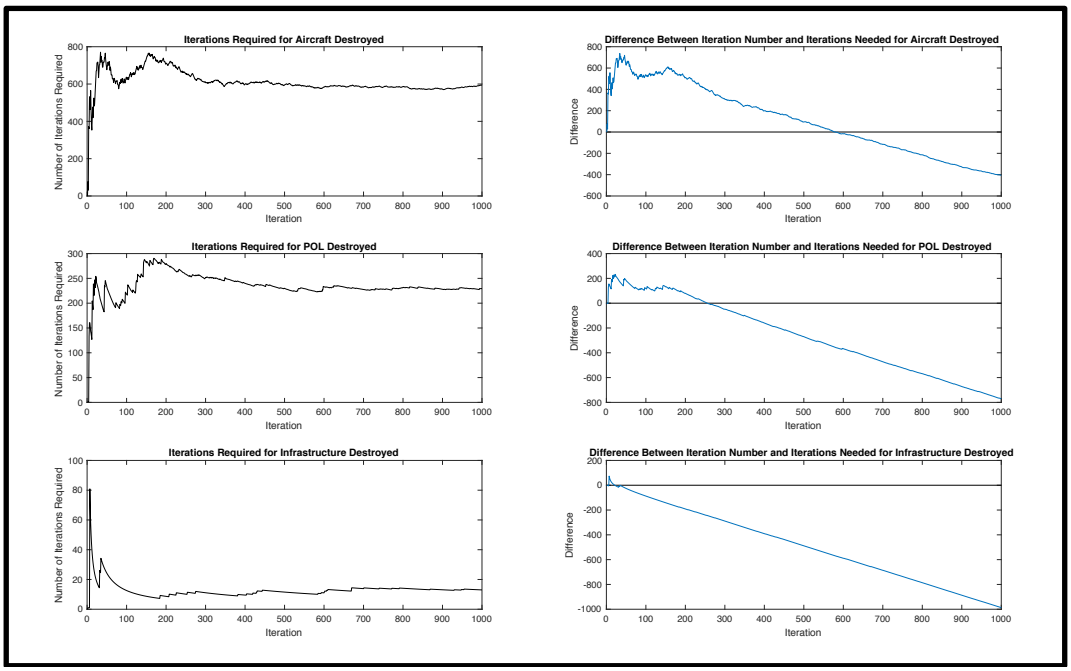

Figure 105: Number of Iterations Required for the Mean to be Within 10% of the True Mean With 95% Confidence for the Airfield Damage Simulation: Case 2

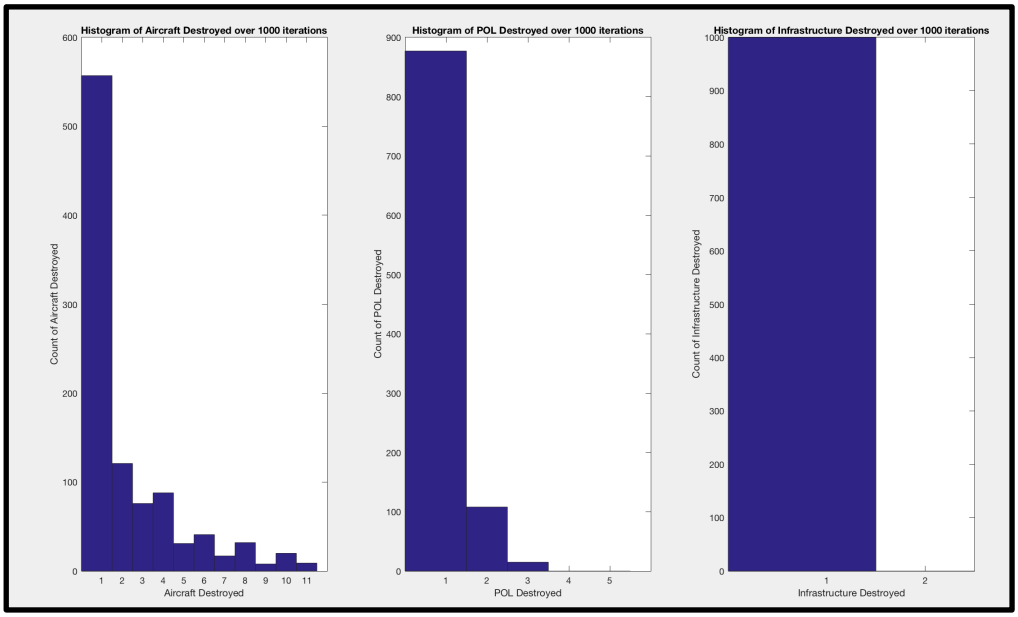

Figure 106: Histograms of Results for Case 2 of Number of Iterations Required for Airfield Attack Simulation

Case 1: Medium attack and a Medium Number of Aircraft and Case 3: Large attack and small number of aircraft showed a similar number of iterations required to ensure that the calculated mean was within 10% of the true mean with 95% confidence. These results are shown below in Figure 107 for case 3 and Figure 109 for case 1. Here it is observed that the number of iterations required stabilized after about 175-200 iterations. The histograms of results are also shown in Figure 108 for case 3 and Figure 110 for case 1. These results show that the binomial distribution will be a good approximation of the results.

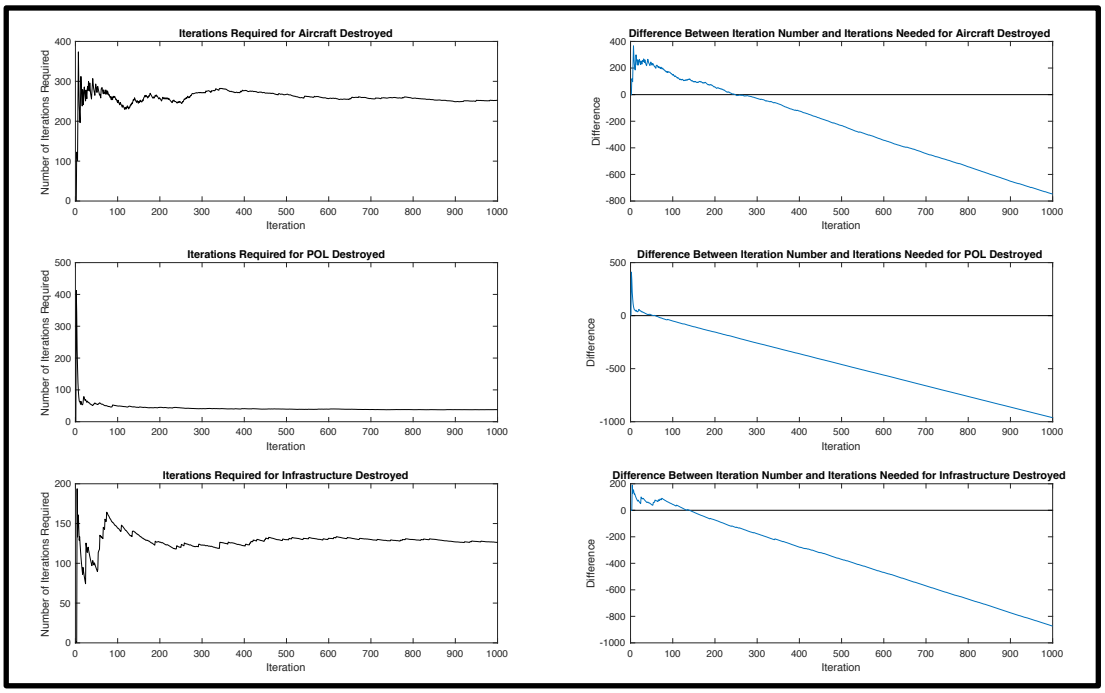

Figure 107: Number of Iterations Required for the Mean to be Within 10% of the True Mean With 95% Confidence for the Airfield Damage Simulation: Case 3

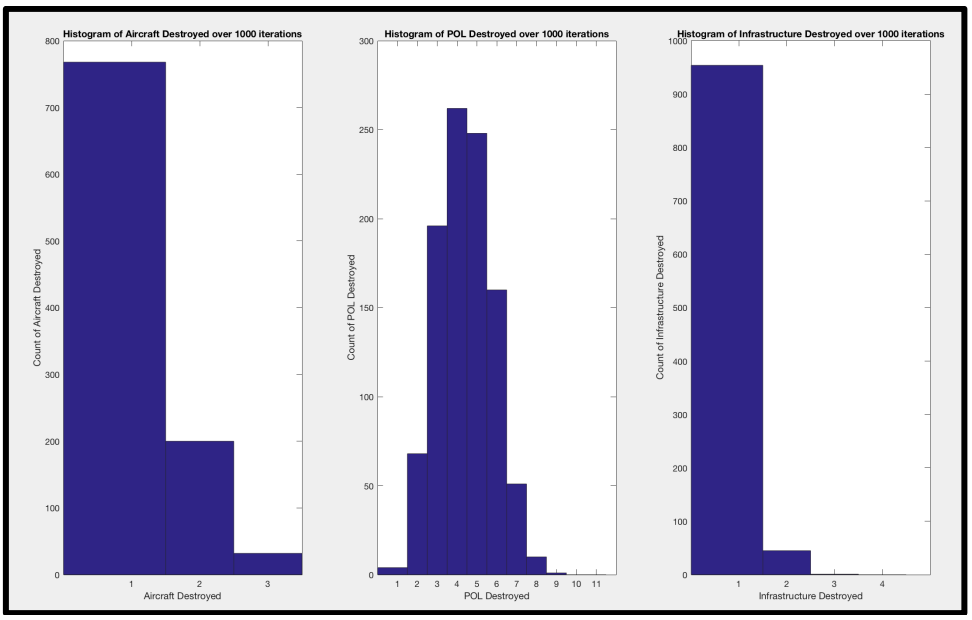

Figure 108: Histograms of Results for Case 3 of Number of Iterations Required for Airfield Attack Simulation

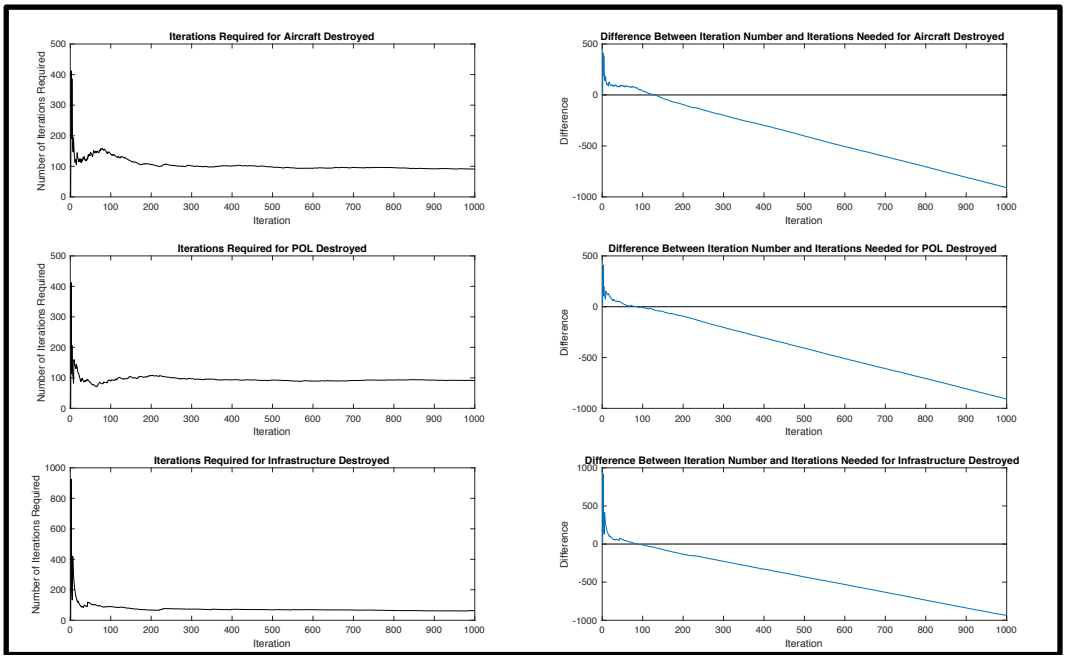

Figure 109: Number of Iterations Required for the Mean to be Within 10% of the True Mean With 95% Confidence for the Airfield Damage Simulation: Case 1

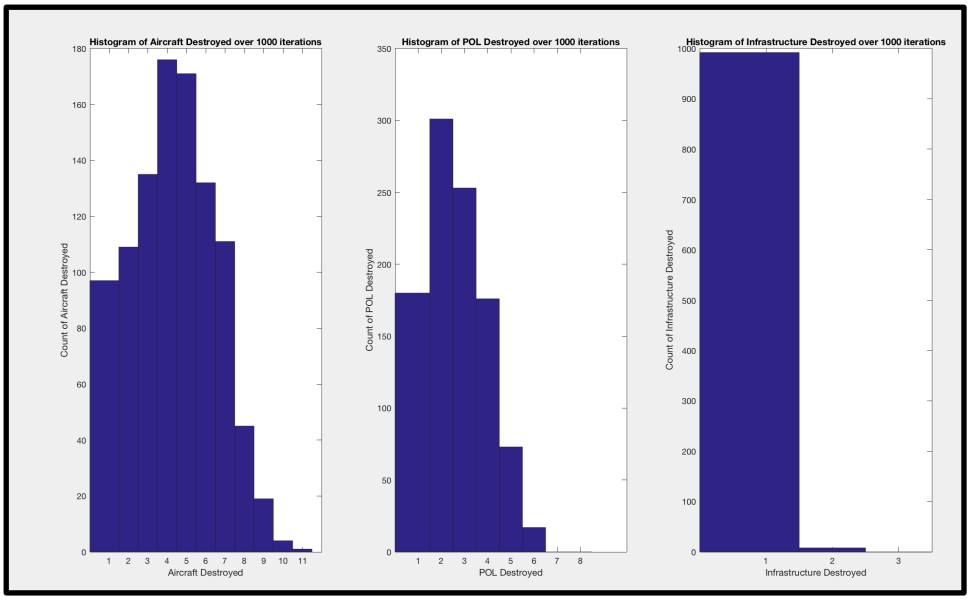

Figure 110: Histograms of Results for Case 1 of Number of Iterations Required for Airfield Attack Simulation

6.5.2. Airfield Damage Surrogate Model DOE

The goal of the next several sections was to develop a predictive model for the shape parameters of the binomial distribution of the number of assets damaged in an attack of the hypothetical airfield described previously. This simulation used the missiles previously described in 6.3. These weapons are summarized below in Table 35. Note that TBM2 and CM1 were only used in the runway cratering simulation and not this airfield damage simulation because they contained penetrating submunitions.

Table 35: Airfield Attack Simulation Missile Parameters

Missile	Lethal Radius (m)					CEP (m)	Guided	Prob – Direct Hit (%)	Prob – Fail (%)
	AC 1	AC 2	AC 3	POL	Hangar				
TBM 1	80	100	50	30	20	200	N	NA	NA
TBM 3	60	80	35	20	10	50	N	NA	NA
CM 2	40	50	25	15	8	20	Y	70	3

The DOE used to in this model was a Latin hypercube design that included constraints on some of the variables. The Latin hypercube was used because of the multiple outputs being assessed from the single DOE runs. The Latin hypercube maintains its spacing of points even when certain factors are excluded and the design collapses to a lower dimensional space. There were eight variables used in the DOE and their ranges are summarized in Table 36 below.

Table 36: Airfield Attack Simulation DOE Input Ranges

Input	Min	Max	Units
TBM 1 – Number	0	10	ea
TBM 3 – Number	0	10	ea
CM 2 – Number	0	10	ea
Percent - Aircraft	0	100	%
Percent - POL	0	100	%
Number of AC1 Present	0	24	ea
Number of AC2 Present	0	24	ea
Number of AC3 Present	0	24	ea

In addition to the input variables shown in Table 36, an additional factor, the percentage of missile attacking the infrastructure, was calculated from these inputs and appended to each input vector. This is calculated as 100-(Percent AC + Percent POL). The constraints added to the DOE ensured that the percentages always summed to 100% and that degenerate cases were avoided. These constraints were:

2. Percent AC + Percent POL <= 100
3. (AC1 + AC2 + AC3) > 0
4. (TBM1 + TBM3 + CM2) > 0

The DOE was constructed of 160 test points and 40 validation points. There were eight input factors, and to have a good sampling across the design space, 20 levels per factor were chosen for a total of 160 test points. The DOE was then increased by 40 points (25%) to ensure enough validation points were captured. The points were cast into either test or validation in a random fashion. After initial tests of the DOE, poor fitting in some of the output modules suggested that additional sample points were needed. Fifty additional points were augmented to the original DOE because of this. The final DOE was then comprised of 200 test points and 50 (20%) validation points. The input DOE is summarized in Figure 111 below.

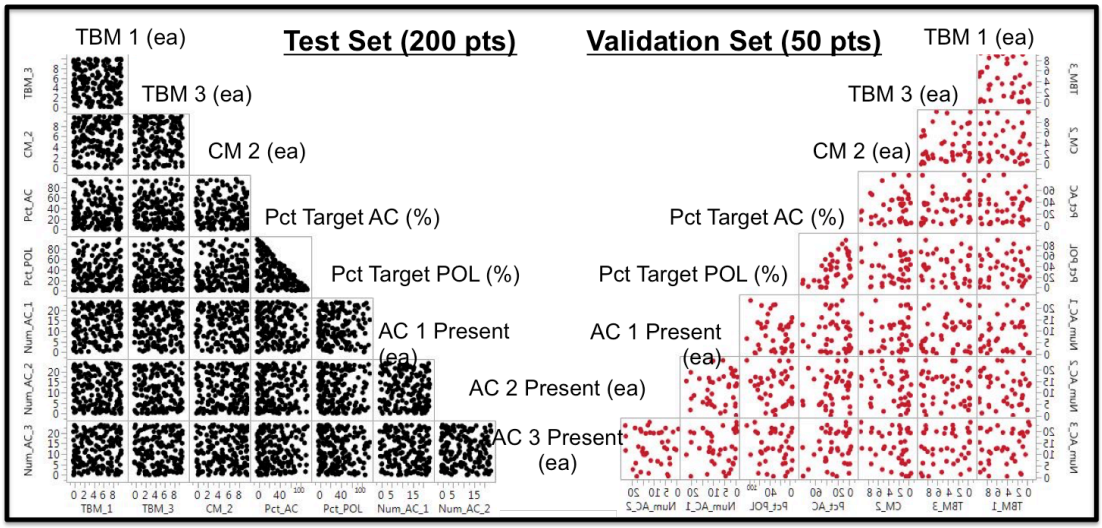

Figure 111: Airfield Attack Simulation Input DOE

Each DOE point from Figure 111 was simulated 300 times (as explained in section 6.5.1) before assessing the number of iterations required such that the calculated mean was within 10% of the true mean with 95% confidence. This was done for each output: number of AC1, AC2, AC3 destroyed, number of POL points destroyed, and number of hangars destroyed. The number of iterations required was the maximum of the calculated required iterations for each output variable.

Once the simulation was complete, the outputs were cast into discrete histograms. Then, a binomial distribution was fit to each distribution for each output variable using the method described in section 6.3.3.12. In the fitting program, the number of possible successes, nn, was given by the input DOE. For aircraft types AC1, AC2 and AC3 this was the total number of aircraft of a given type that was present. For the POL points the number of POL points in all simulations was fixed at eight and for the number of hangars that was also fixed at ten.

The output scatter plots for each output variable are shown below. Figure 112 - Figure 114 show the outputs distribution for the binomial distribution shape parameter and summary statistics for the number of aircraft type AC1, AC2, and AC3 destroyed. Figure 115 shows these same parameters for the number of POL points destroyed and Figure 116 shows the parameters for the number of hangars destroyed. In these diagrams, the black points are the test cases and the red points are the validation cases.

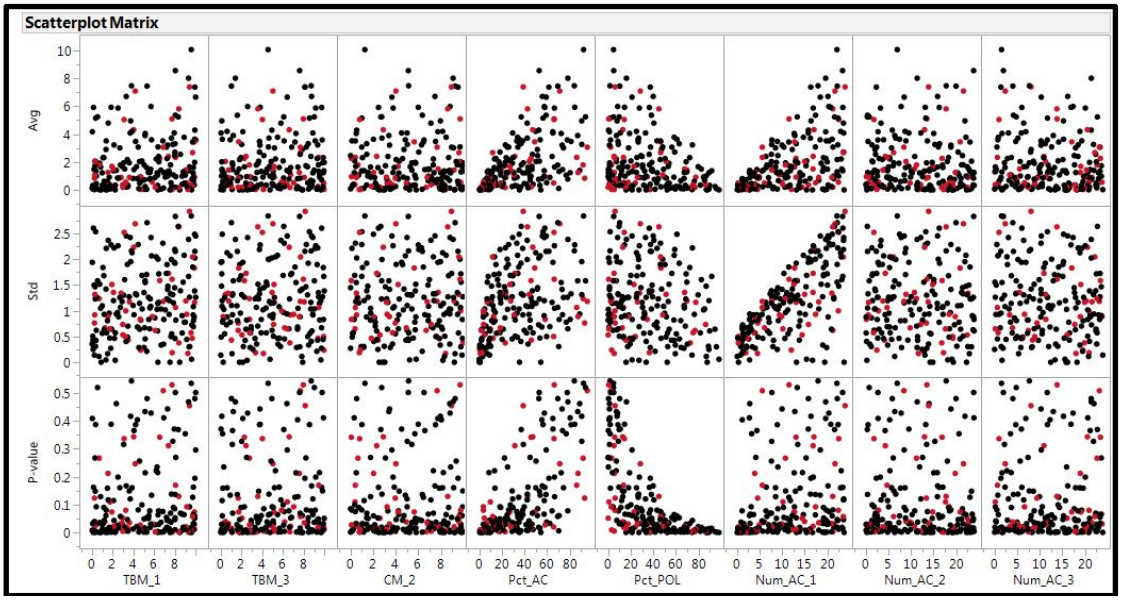

Figure 112: Output Scatterplot for Binomial Shape Parameter and Summary Statistics of Number of AC1 Destroyed in Airfield Attack Simulation

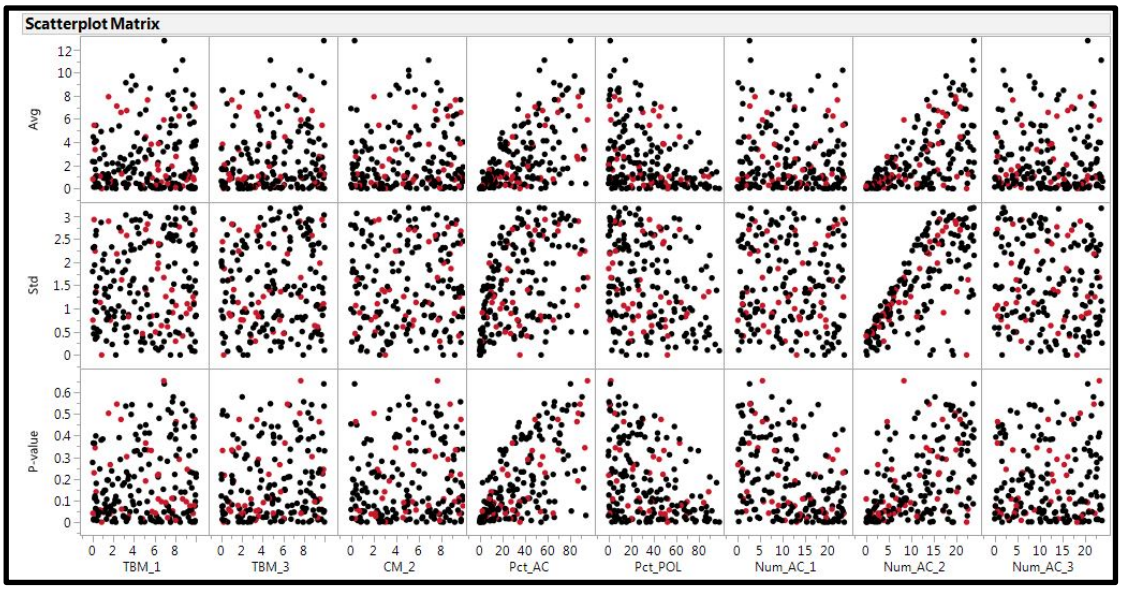

Figure 113: Output Scatterplot for Binomial Shape Parameter and Summary Statistics of Number of AC2 Destroyed in Airfield Attack Simulation

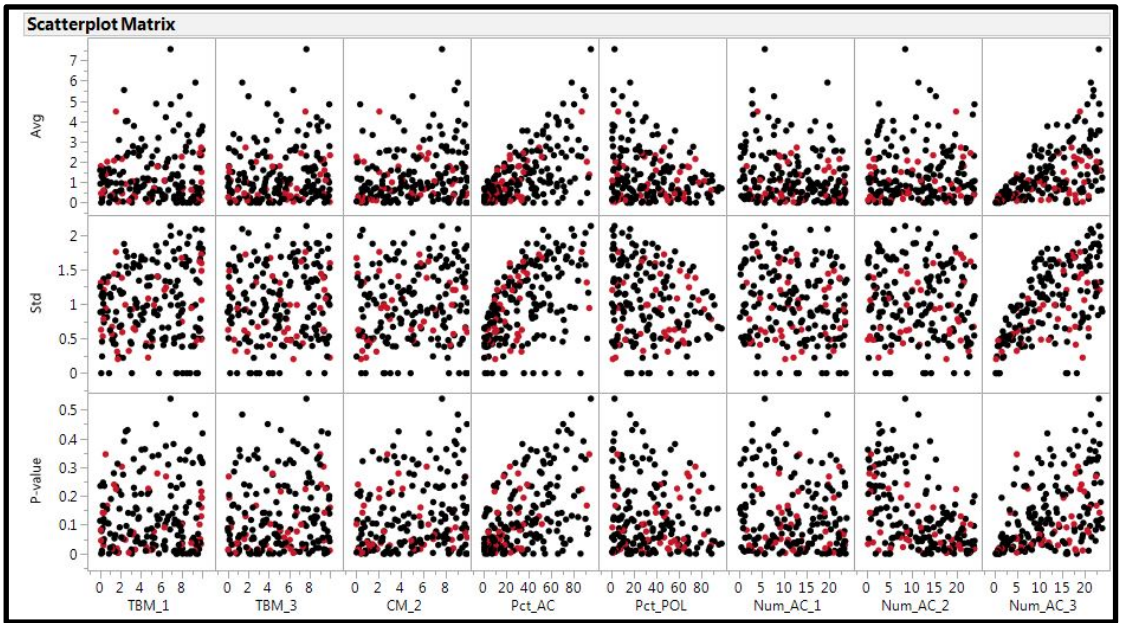

Figure 114: Output Scatterplot for Binomial Shape Parameter and Summary Statistics of Number of AC3 Destroyed in Airfield Attack Simulation

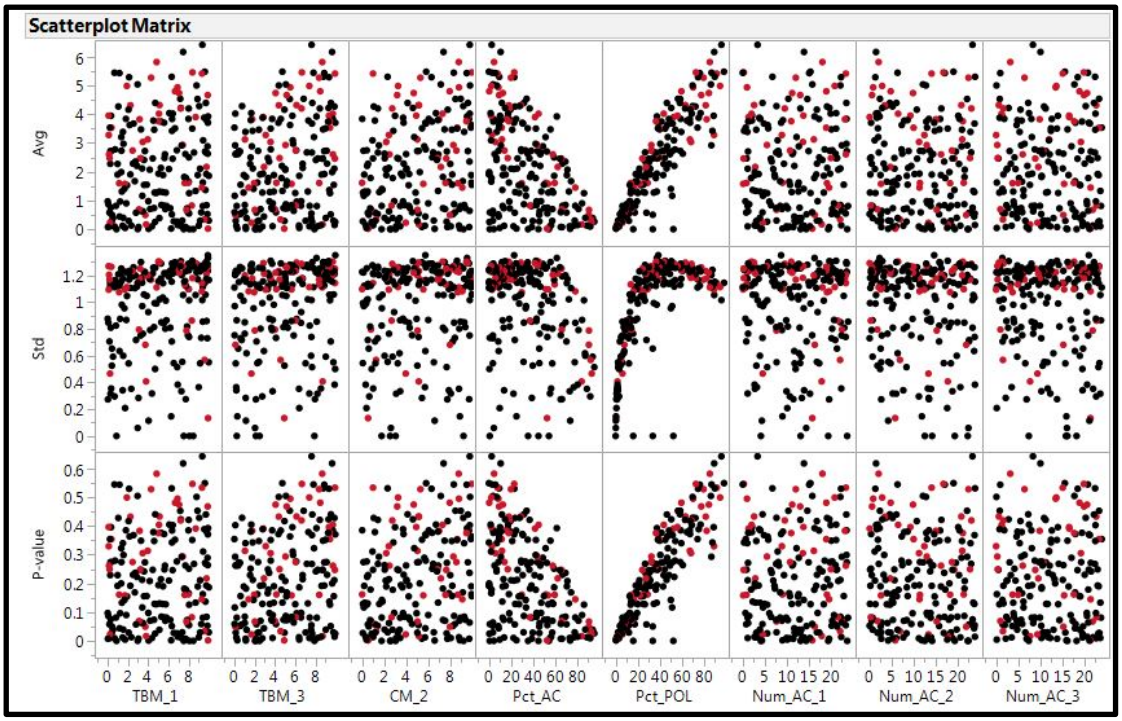

Figure 115: Output Scatterplot for Binomial Shape Parameter and Summary Statistics of Number of POL Points Destroyed in Airfield Attack Simulation

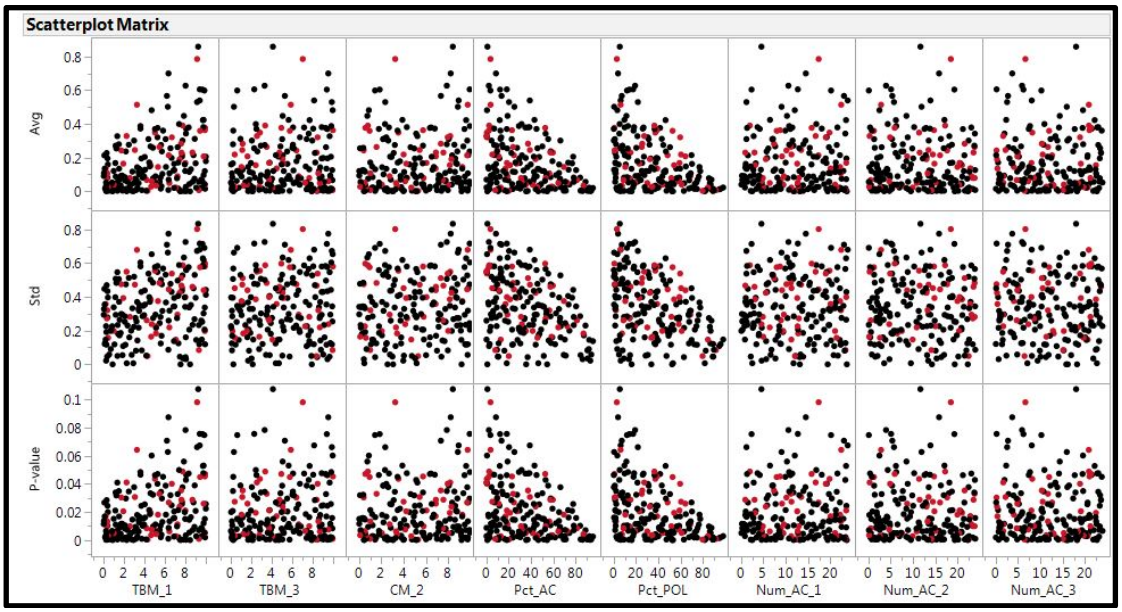

Figure 116: Output Scatterplot for Binomial Shape Parameter and Summary Statistics of Number of Hangars Destroyed in Airfield Attack Simulation

These scatterplots show that the controlling factor in most of the simulations was the percentage of missiles allocated to each target type (i.e. aircraft, POL, or

infrastructure) and the number of incoming missiles, especially TBM2. For the aircraft targets, a dominant factor was also the number of that aircraft type that was present. The next several sections will show the accuracy of the p-value estimate shown in the above scatterplots.

6.5.3. Airfield Damage Surrogate Models

The development procedure of the NN used in the airfield simulation followed a similar procedure as those in the runway cratering simulation. Due to the noisiness of the data, several NN models were created for each output and then the predictions averaged together. In order to ensure a set of points was completely withheld from the development of all models, 20% of the points were initially cast into an overall validation set. The remaining 80% of the points were then used in each fitting but were randomly cast into a training, test, and validation set for each fitting of a particular NN. The number of hidden nodes for a given NN was chosen by increasing the quantity of nodes until a divergence between the test and validation set's R^2 was observed. Once all NN for a given output were created and the results averaged together, that output was compared to the actual observed distribution by randomly choosing the same number of observed points using the predicted binomial shape parameters. The estimated distribution and observed distribution were then compared with a Chi-Squared test as explained in section 6.3.3.11. The results of these models are shown in the next several sections.

6.5.3.1. Distribution Selection for the Airfield Damage Models

The selection of the appropriate discrete distribution (binomial, geometric, or Poisson) followed in a similar manner to that of the Runway Availability model in

section 6.3.3.9. For each distribution, the shape parameters were estimated using the maximum likelihood estimation method (MLE) and then compared to the observed values to calculate the residual sum of squares (RSS). These results are summarized in Table 37. This table shows the number and percent of the 250 DOE points where the given distribution had the lowest RSS. It is clear to see that the binomial distribution had the smallest RSS for all but one output, the number of aircraft type 2 (AC2) destroyed. However, the RSS for many cases was very close between the different distributions for many of the cases. This means that multiple distributions would have fit those test points adequately. To examine this further, the author conducted a second count. This time the number of cases was counted where the given distribution had the lowest RSS or had a RSS that was within 5% of the RSS for the distribution with the lowest RSS. The results of this analysis are shown in Table 37 and Table 38.

Table 37: Maximum Likelihood Residual Sum of Squares Results for Airfield Attack Models

Distribution	AC1		AC2		AC3		POL		Inf	
Binomial	224	49.6%	66	26.4%	122	48.8%	225	90.0%	216	86.4%
Geometric	41	16.4%	77	30.8%	29	11.6%	8	3.2%	14	5.6%
Poisson	85	34.0%	107	42.8%	99	39.6%	17	6.8%	20	8.0%
Table shows number and percent of DOE points where the distribution had the lowest RSS										

Table 38: Maximum Likelihood Residual Sum of Squares or within 5% of lowest RSS for Airfield Attack Models

Distribution	AC1		AC2		AC3		POL		Inf	
Binomial	250	100%	250	100%	250	100%	250	100%	250	100%
Geometric	187	74.8%	213	85.2%	196	78.4%	71	28.4%	235	94.0%
Poisson	238	95.2%	238	95.2%	245	98.0%	250	100%	250	100%
Table shows number and percent of DOE points where the distribution had the lowest RSS										

From Table 38, it can be seen that the binomial distribution was either the distribution that best fit the data (lowest RSS) or was a good enough fit (RSS within 5% of distribution with lowest RSS). Having a single distribution for all the outputs simplified the analysis. Therefore, the binomial distribution was used for all the outputs of the Airfield Attack models.

6.5.3.2. Number of Aircraft Type 1 Destroyed

A total of 30 NNs were built to estimate the shape parameter of the binomial distribution (p-value) and their results averaged together. Each NN had 25 hidden nodes with a hyperbolic tangent activation function. The output was also estimated with a square-root transform to stabilize the variance. The results of the estimate of the p-value are shown below in Figure 117 and the residuals of the estimate are shown in Figure 118. The R^2 value for both the test and validation sets was over 0.92 and the root-mean squared error (RMSE) was only about 2.5%. Also, 100% of the overall validation points passed the chi-squared test indicating that the test could not reject the null hypothesis, that the two distributions were the same, with a 99% confidence level.

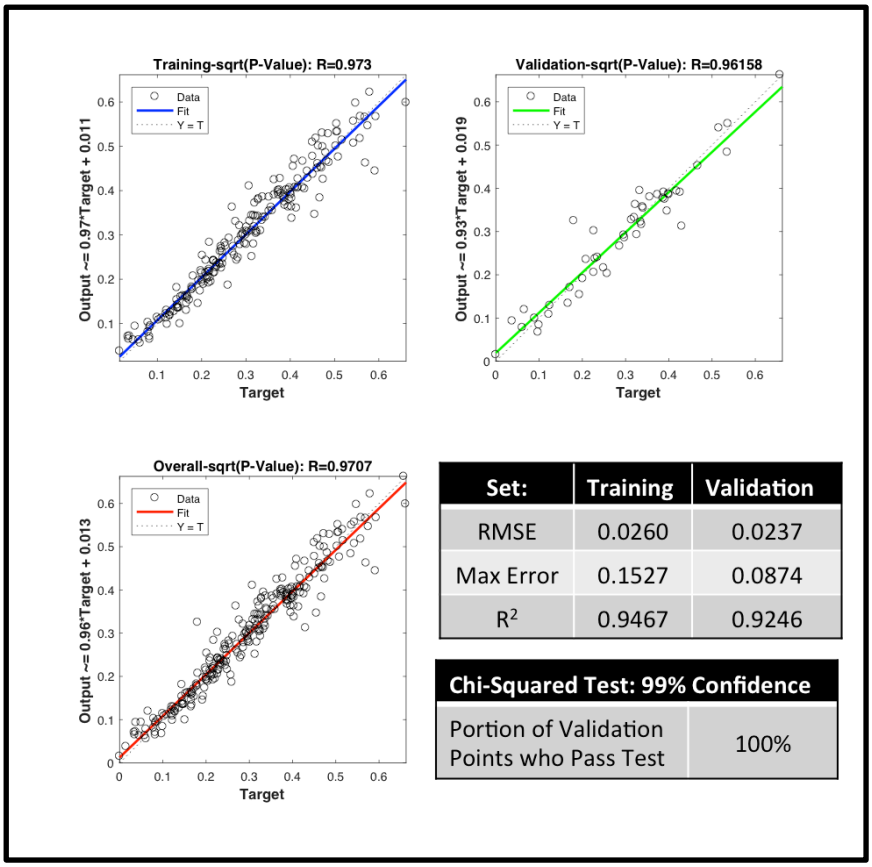

Set:	Training	Validation
RMSE	0.0260	0.0237
Max Error	0.1527	0.0874
R^2	0.9467	0.9246

Chi-Squared Test: 99% Confidence	
Portion of Validation Points who Pass Test	100%

Figure 117: Results of the Binomial P-Value Neural Net Model for Number of Aircraft Type 1 Destroyed from Airfield Damage Model

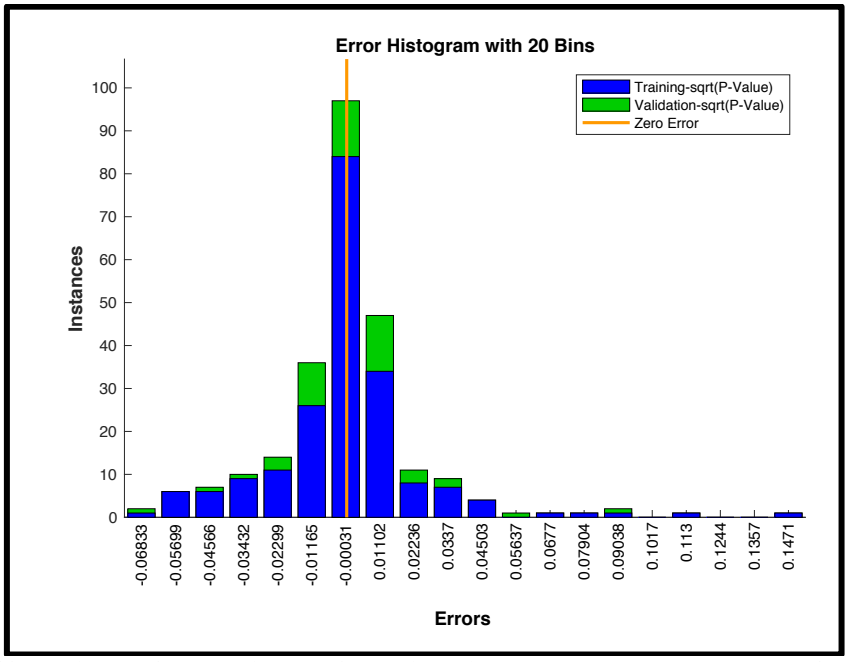

Figure 118: Residuals from Estimate of the Binomial P-Value Neural Net Model for Number of Aircraft Type 1 Destroyed from Airfield Damage Model

6.5.3.3. *Number of Aircraft Type 2 Destroyed*

The geometry of the NN used to estimate of the binomial shape factor for the number of aircraft type two destroyed was similar those used for aircraft type 1. A total of 30 NNs were used and their results averaged together. Each NN had 80 hidden nodes with a hyperbolic tangent activation function and a square-root transform was used to stabilize the variance. The results are shown below in Figure 119 and the residuals of the binomial shape factor estimate are shown in Figure 120. Just as in the case of aircraft type 1, the R^2 value for both the test and validation sets was over 0.98 and root-mean squared error (RMSE) was only about 4%. Also, the chi-squared test for aircraft type 2 failed to reject the null hypothesis, that both distributions were the same, for over 98% of the overall validation points.

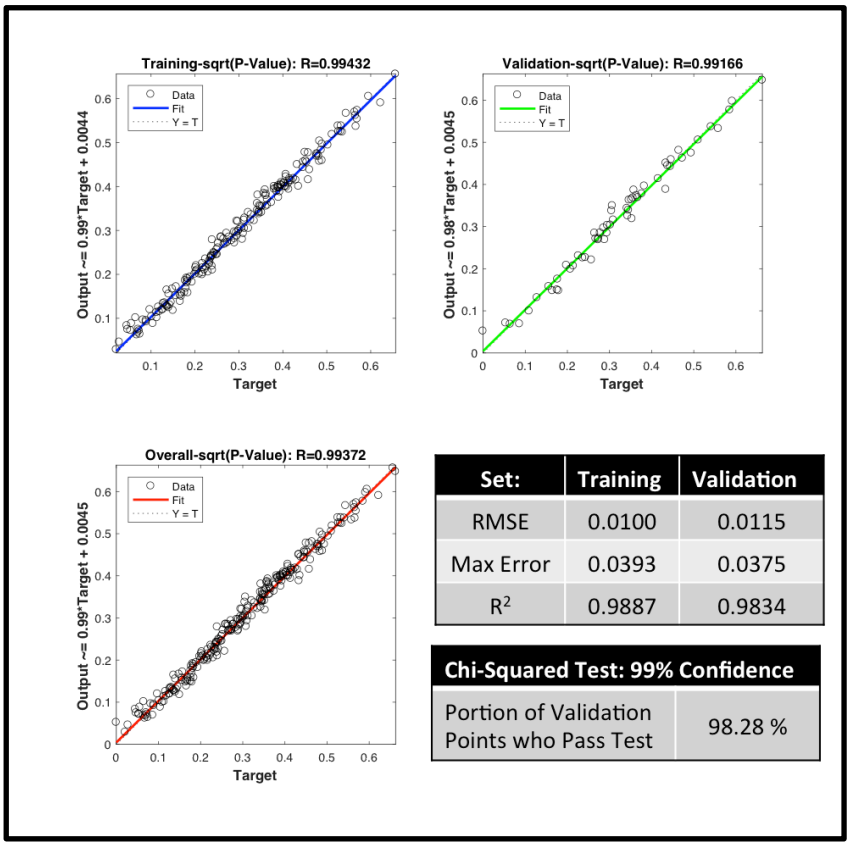

Set:	Training	Validation
RMSE	0.0100	0.0115
Max Error	0.0393	0.0375
R^2	0.9887	0.9834

Chi-Squared Test: 99% Confidence	
Portion of Validation Points who Pass Test	98.28 %

Figure 119: Results of the Binomial P-Value Neural Net Model for Number of Aircraft Type 2 Destroyed from Airfield Damage Model

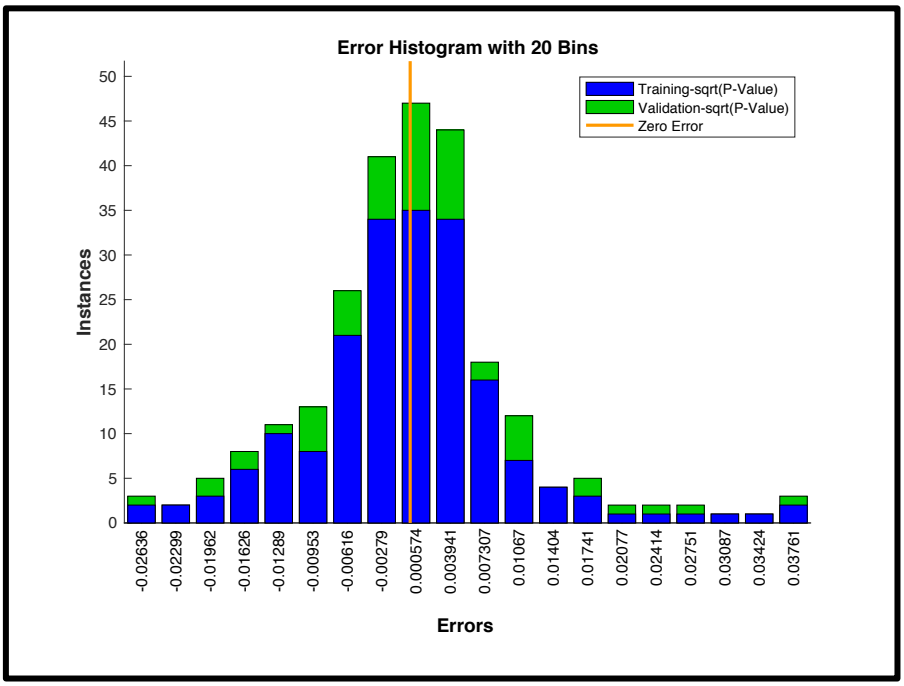

Figure 120: Residuals from Estimate of the Binomial P-Value Neural Net Model for Number of Aircraft Type 2 Destroyed from Airfield Damage Model

6.5.3.4. Number of Aircraft Type 3 Destroyed

The geometry of the NN used to estimate the binomial shape factor for the number of aircraft type 3 destroyed was similar those used for aircraft types 1 and 2. A total of 30 NNs were used and their results averaged together. Each NN had 100 hidden nodes with a hyperbolic tangent activation function and a square-root transform was used to stabilize the variance. The results are shown below in Figure 121 and the residuals of the binomial shape factor estimate are shown in Figure 122. The R^2 value for both the test and validation sets was over 0.93 and the root-mean squared error (RMSE) was only about 3% for the training points and only 4% for the validation points. Also, the chi-squared test for aircraft type 3 failed to reject the null hypothesis, that both distributions were the same, for 100% of the overall validation points.

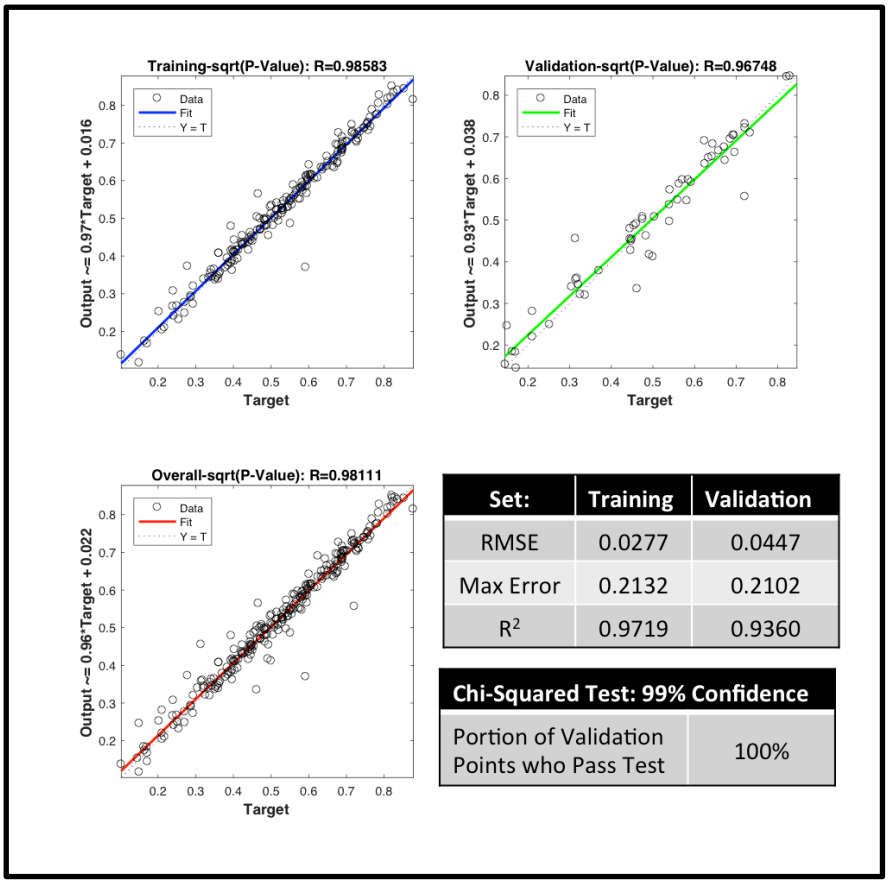

Figure 121: Results of the Binomial P-Value Neural Net Model for Number of Aircraft Type 3 Destroyed from Airfield Damage Model

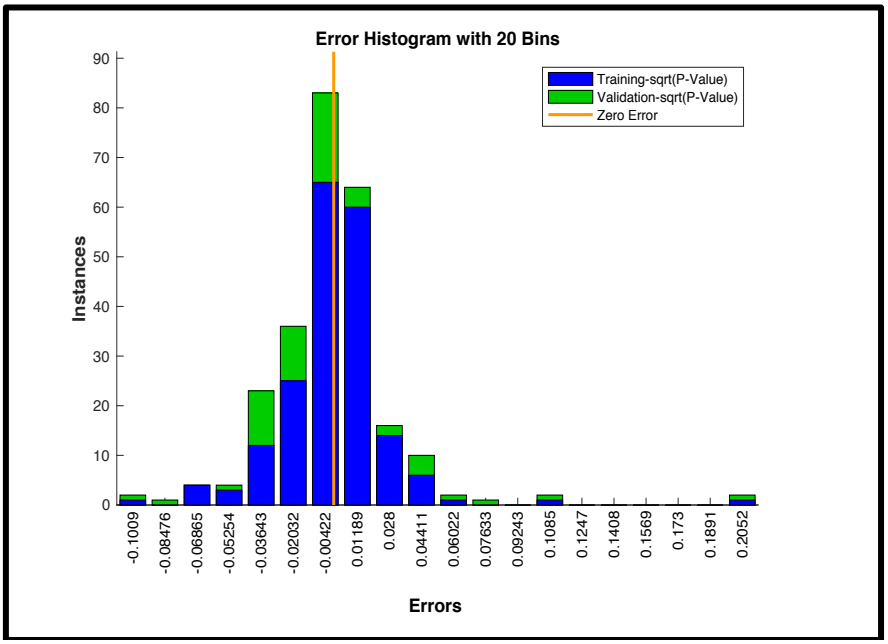

Figure 122: Residuals from Estimate of the Binomial P-Value Neural Net Model for Number of Aircraft Type 3 Destroyed from Airfield Damage Model

6.5.3.5. Number of POL Points Destroyed

The geometry of the NN used to estimate the binomial shape factor for the number of POL points destroyed differed from those used for the number of aircraft destroyed. The main difference was the number of hidden nodes that could be used before a divergence was observed between the R^2 value of the validation and test sets. A total of 30 NNs were used and their results averaged together. Each NN had 20 hidden nodes with a hyperbolic tangent activation function and a square-root transform was used to stabilize the variance. The results are shown below in Figure 123 and the residuals of the binomial shape factor estimate are shown in Figure 124. The R^2 value for both the test and validation sets was over 0.99 and the root-mean squared error (RMSE) was only about 1% for both the training and validation points. The max error foe both the training and validation sets was about 3.6%. Also, the chi-squared test for the number of POL points destroyed failed to reject the null hypothesis, that both distributions were the same, for every one of the overall validation points.

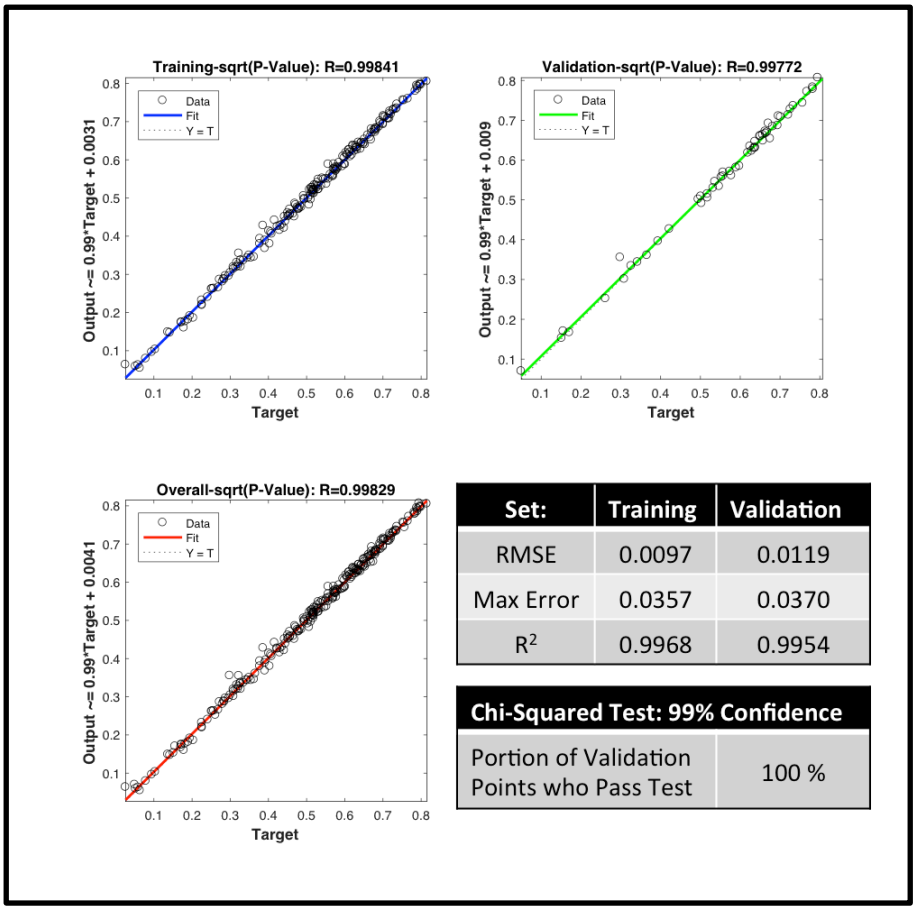

Set:	Training	Validation
RMSE	0.0097	0.0119
Max Error	0.0357	0.0370
R^2	0.9968	0.9954

Chi-Squared Test: 99% Confidence	
Portion of Validation Points who Pass Test	100 %

Figure 123: Results of the Binomial P-Value Neural Net Model for Number of POL Points Destroyed from Airfield Damage Model

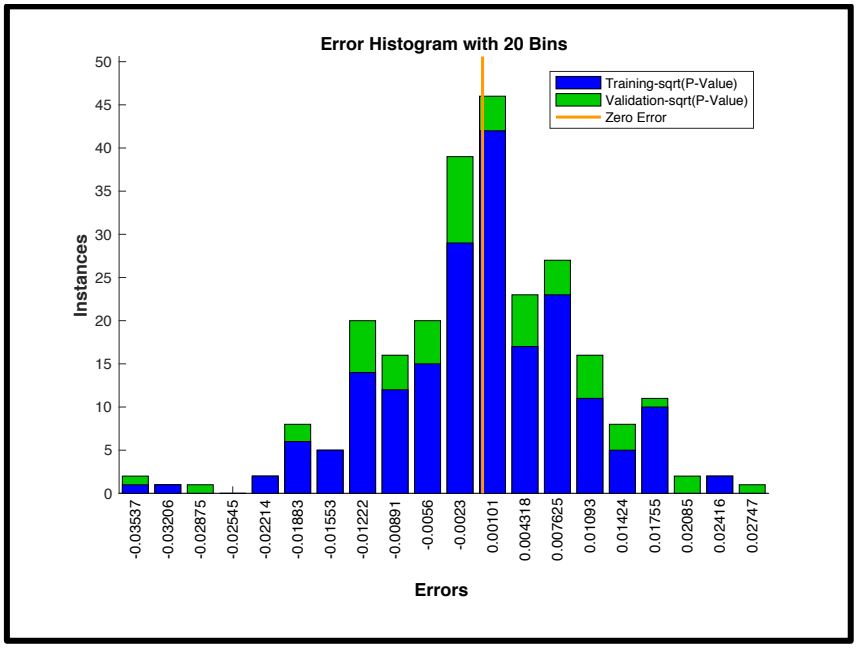

Figure 124: Residuals from Estimate of the Binomial P-Value Neural Net Model for Number of POL Points Destroyed from Airfield Damage Model

6.5.3.6. Number of Hangar Buildings Destroyed

The geometry of the NN used to estimate the binomial shape factor for the number of POL points destroyed was similar to that of the number of POL points destroyed. A total of 30 NNs were used and their results averaged together. Each NN had 30 hidden nodes with a hyperbolic tangent activation function and a square-root transform was used to stabilize the variance. The results are shown below in Figure 125 and the residuals of the binomial shape factor estimate are shown in Figure 126. The R^2 value for both the test and validation sets was over 0.97 and the root-mean squared error (RMSE) and max error was less than 1% for both the training and validation points. Also, the chi-squared test for the number of buildings destroyed failed to reject the null hypothesis, that both distributions were the same, for every one of the overall validation points.

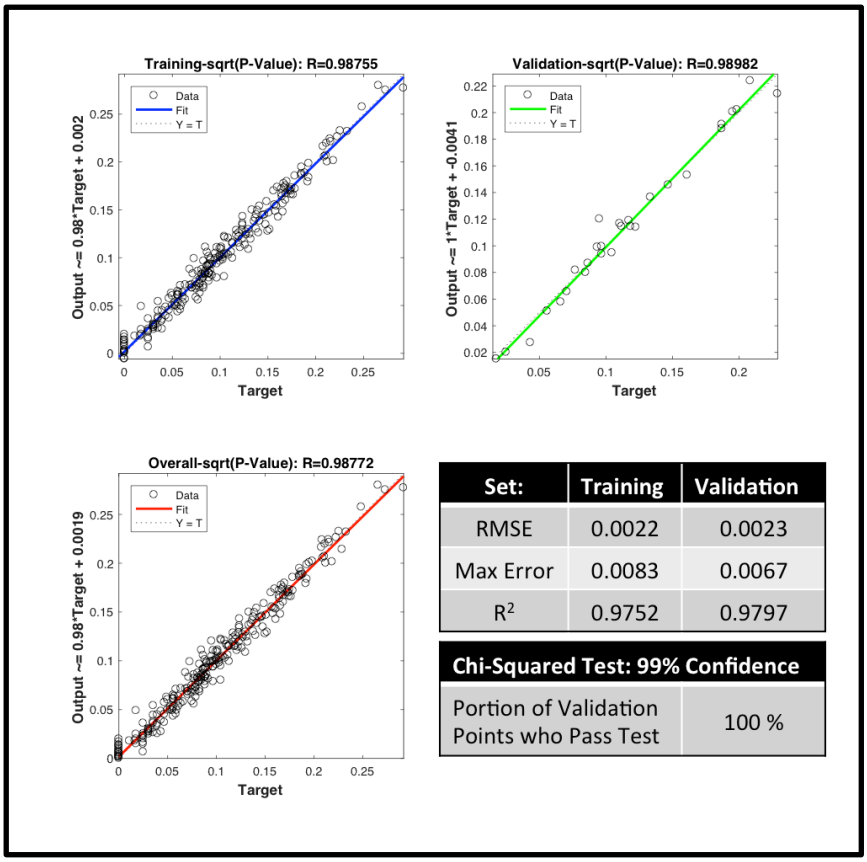

Set:	Training	Validation
RMSE	0.0022	0.0023
Max Error	0.0083	0.0067
R^2	0.9752	0.9797

Chi-Squared Test: 99% Confidence	
Portion of Validation Points who Pass Test	100 %

Figure 125: Results of the Binomial P-Value Neural Net Model for Number of Hangar Buildings Destroyed from Airfield Damage Model

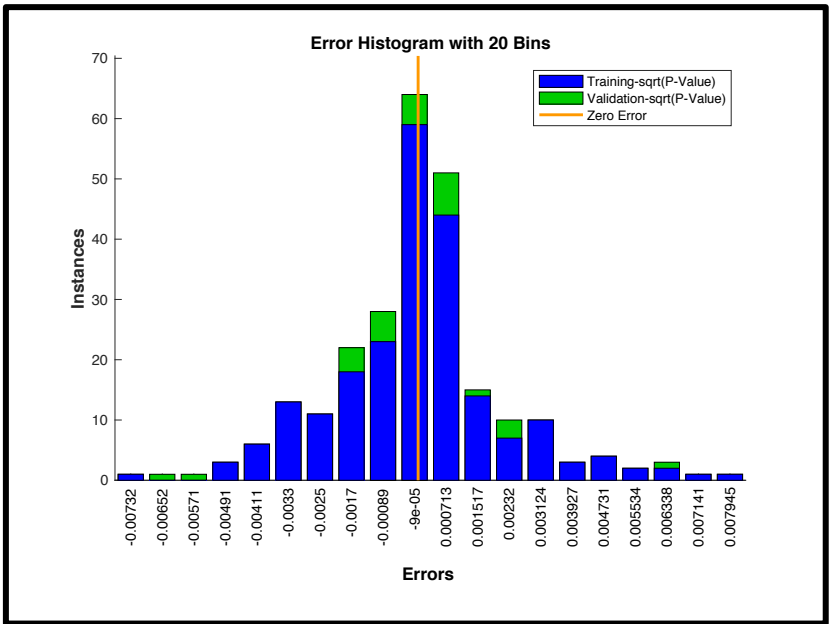

Figure 126: Residuals from Estimate of the Binomial P-Value Neural Net Model for Number of Hangar Buildings Destroyed from Airfield Damage Model

6.5.3.7. Airfield Damage Surrogate Models Assessment

The NNs for all cases of the airfield damage model showed very good prediction capabilities. All but the infrastructure model had R^2 values for both the test and validation cases over 0.99 and the infrastructure had R^2 values over 0.98. This helped to keep the RMSE for the predicted probability of success (p-value) to between 1% and 4% error, even for the validation sets. This contributed to the success of the chi-squared tests, where the test failed to reject the null hypothesis, that the distributions were sampled from the same overall distribution, in every case, except for 1.75% of the validation points in AC2 at 99% confidence level. This helps to answer research question number 3. This research question asked if the accuracy of the surrogate models would be as high as that of the actual model. The hypothesis was that the more than 95% of the validation set of each model would pass the chi-squared test with a 99% confidence level. This was shown to be true for the airfield damage models.

Just as in the runway cratering case, as an additional check, the author produced plots of the actual v. predicted PMFs, CMFs, Q-Q and P-P plots for both the training and validation sets. These points were chosen a random from within each set. While not an exhaustive test of the prediction capability, they do offer an additional check of the results. These results are seen below in Figure 127 and Figure 128 for the test and validation cases of the number of AC1 destroyed (AC2 and AC3 showed similar results), Figure 129 and Figure 130 for the test and validation cases of the number of POL, and Figure 131 and Figure 132 for the test and validation cases of the infrastructure destroyed.

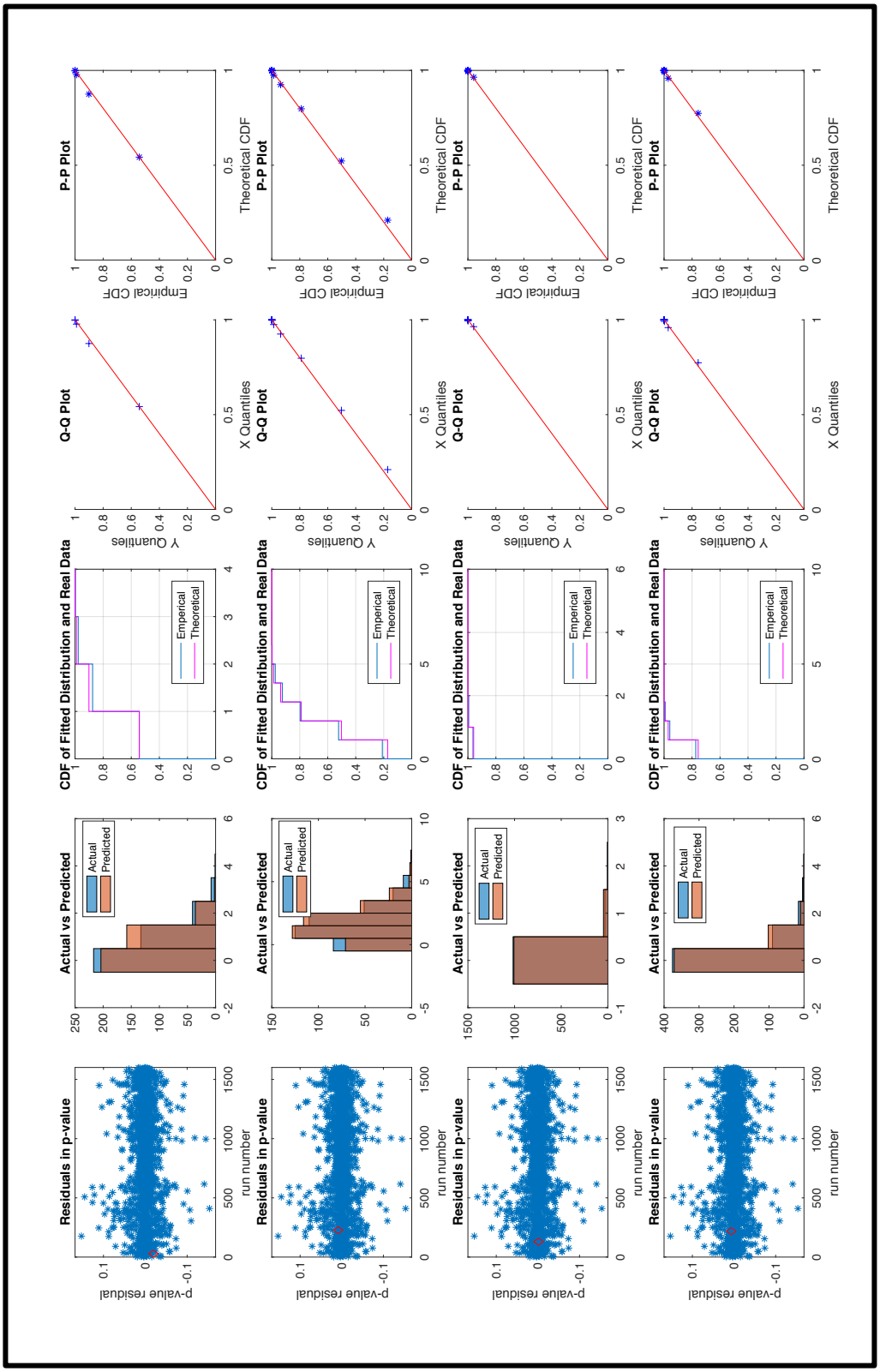

Figure 127: Binomial distribution prediction sample results - Test Set – Amount of Aircraft Type 1 (AC1) Destroyed

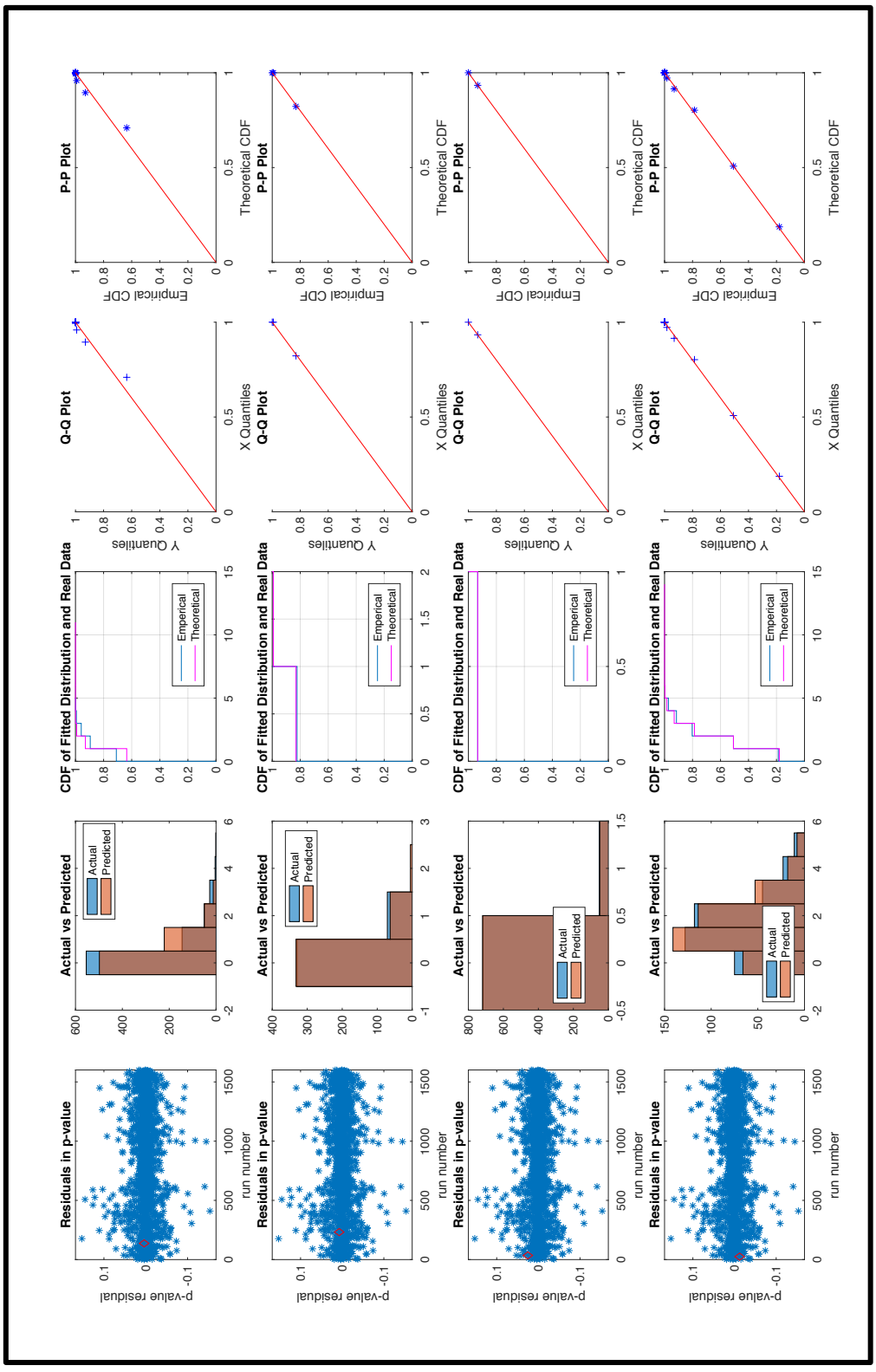

Figure 128: Binomial distribution prediction sample results - Validation Set – Amount of Aircraft Type 1 (AC1) Destroyed

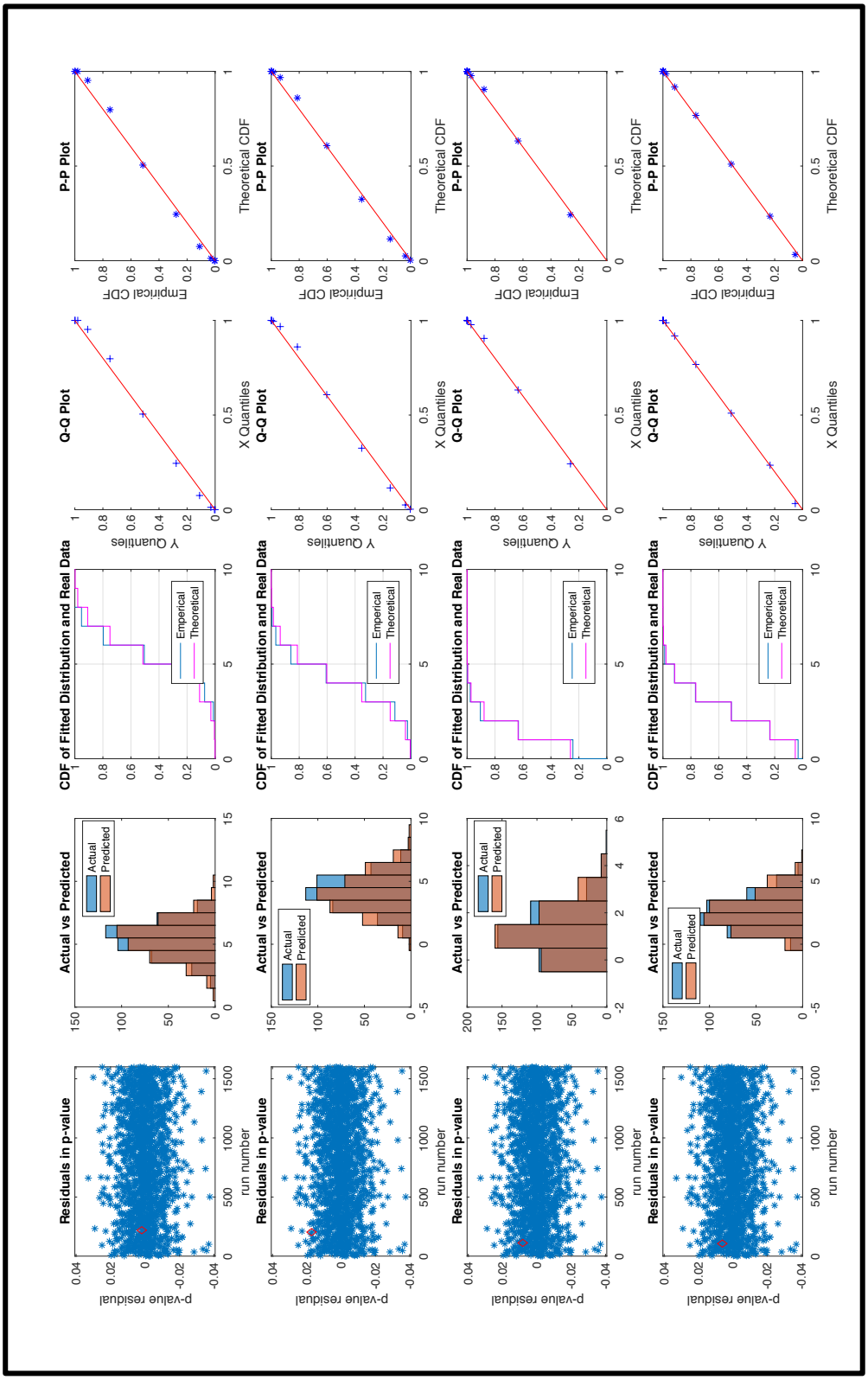

Figure 129: Binomial distribution prediction sample results - Test Set – Amount of POL Points Destroyed

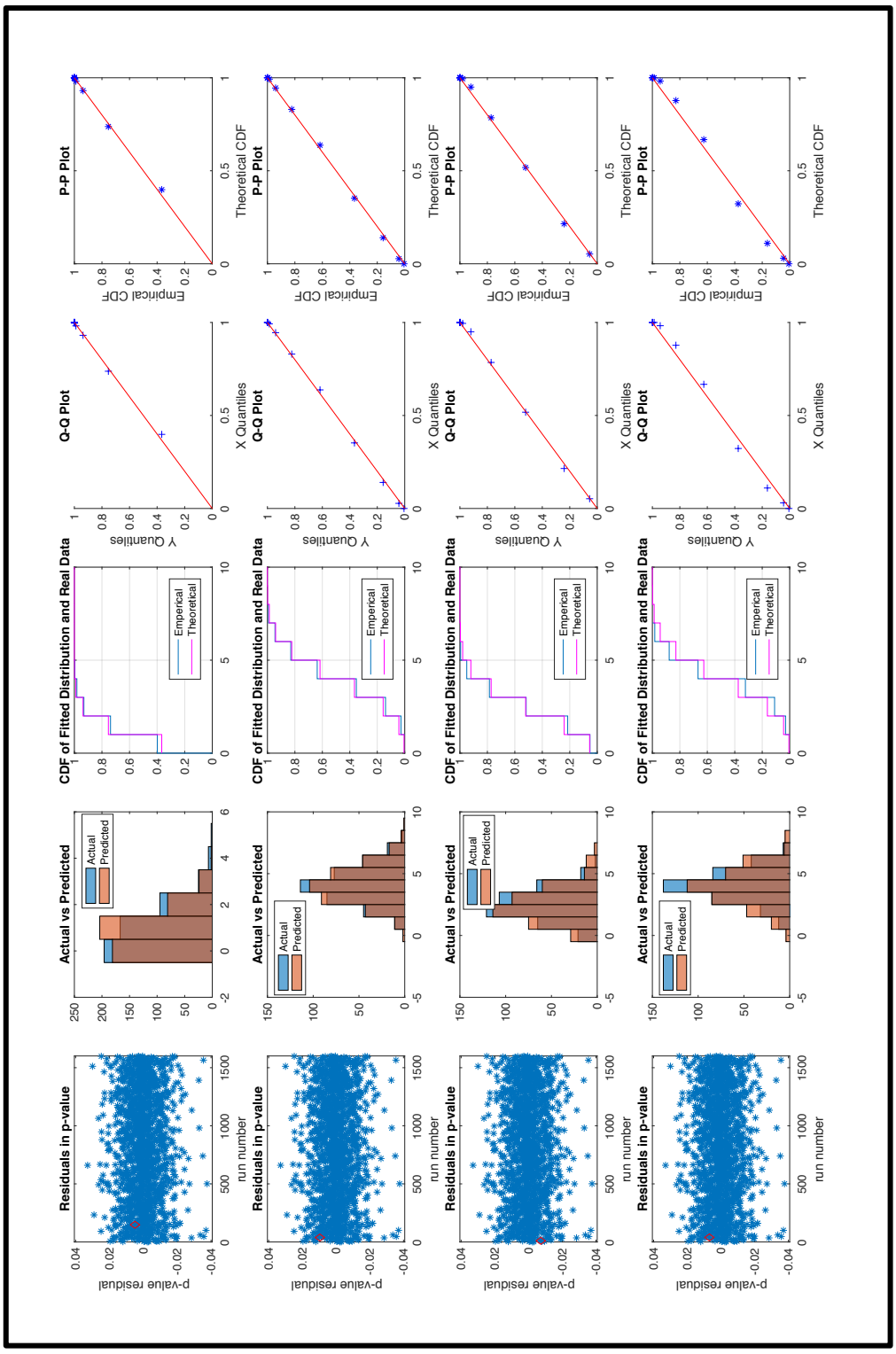

Figure 130: Binomial distribution prediction sample results - Validation Set – Amount of POL Points Destroyed

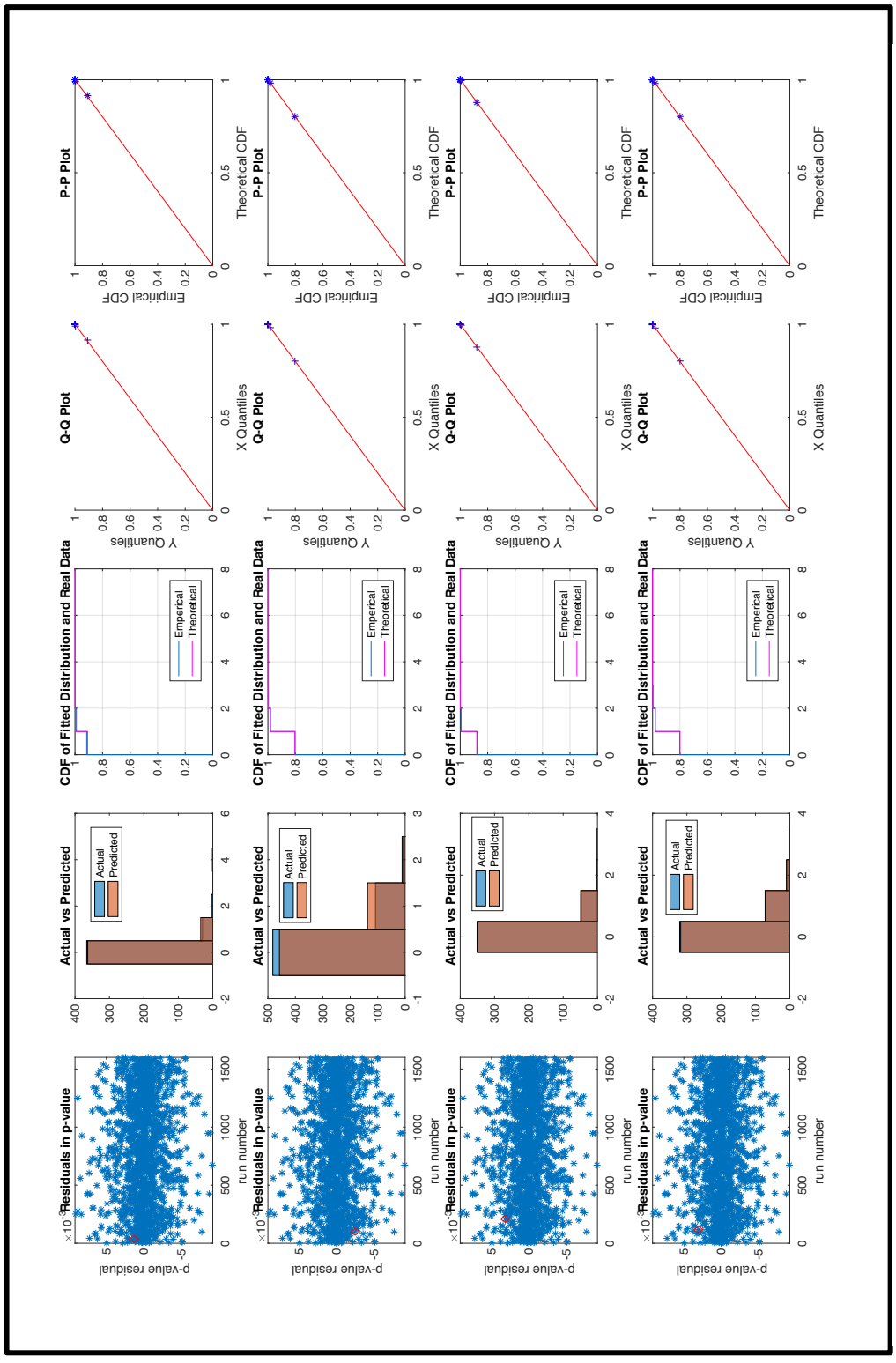

Figure 131: Binomial distribution prediction sample results - Test Set – Amount of Infrastructure Points Destroyed

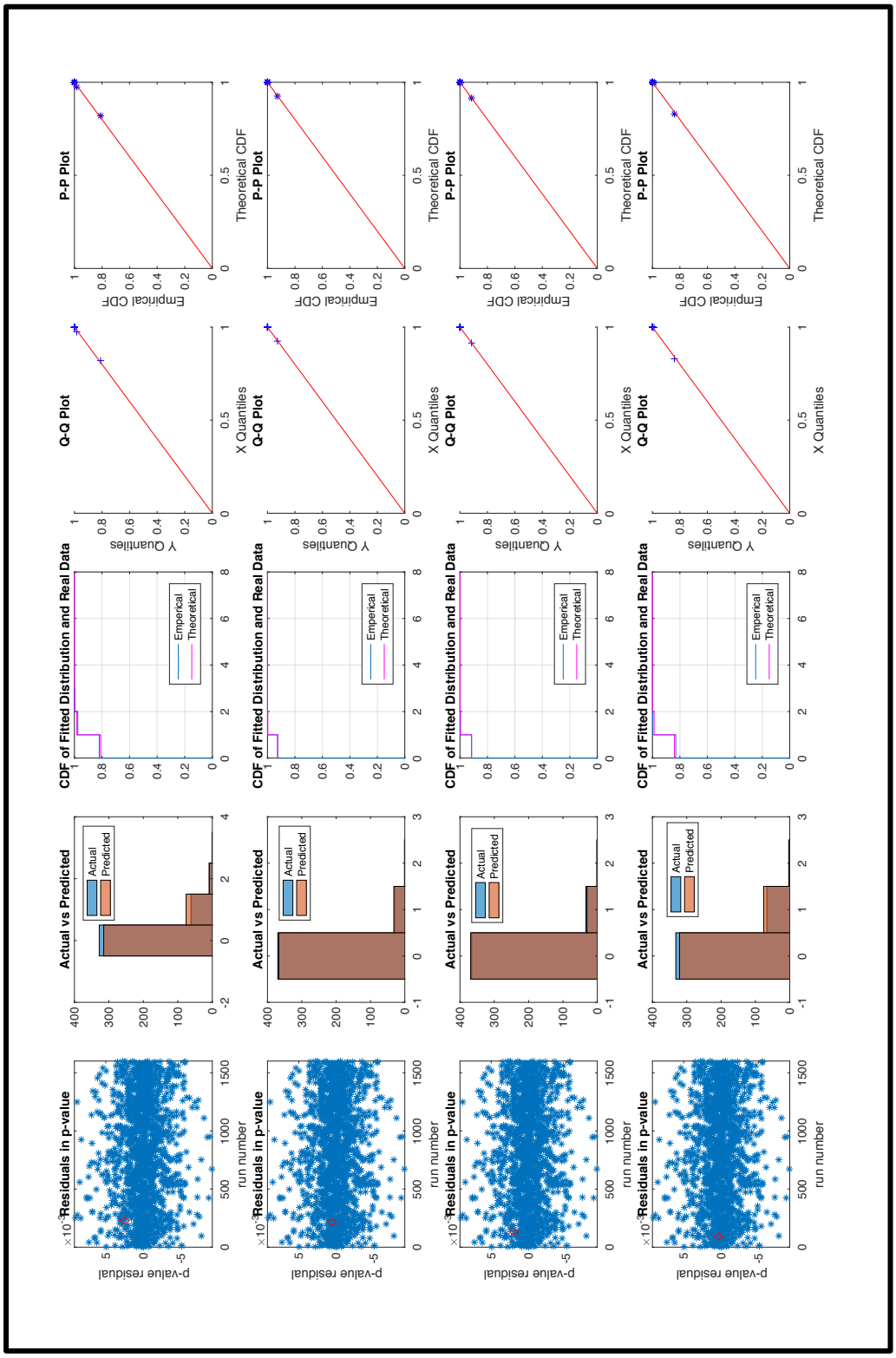

Figure 132: Binomial distribution prediction sample results - Validation Set – Amount of Infrastructure Points Destroyed

7. AIR DEFENSE SIMULATION MODEL

"To be prepared for war is one of the most effective means of preserving peace."
- George Washington

The last chapter developed several models to describe the damage created from missiles that impact an airfield. The current research, as explained in the literature review, is missing these models to describe the effect of missiles that are not destroyed by air defense assets, commonly called leakers. This next section will look at Air Defense Artillery (ADA) simulations. These simulations will determine the number of inbound threats that are destroyed and the number that are leakers. To maintain the highest level of accuracy, this work will consider only high fidelity computer ADA simulations. Many of these high fidelity simulations maintain their accuracy at the cost of a high complexity to setup, a large amount of time for runtime, and a large amount of storage and detail in the outputs. These disadvantages make these platforms poor choices for design space exploration where many runs are required with different combinations of inputs in order to determine the optimum input combination. This work will explore ways to overcome some of these disadvantages while still maintaining a relatively high accuracy simulation.

7.1. Air Defense Model Selection

The high fidelity model will provide the necessary accuracy and precision that should inform major policy and acquisition decisions. This high level of detail, however, is offset by some marked disadvantages. Typically these models will require large run times, storage requirements, and setup times due to the level of detail they are simulating. These disadvantages make them poor environments to do trade-off analysis and optimization due to the large number of simulation runs required. For this reason, the

results from the high level model is carried forward to a faster running tradeoff environment that will maintain nearly the same level of fidelity, but allow trades and optimization.

The main criteria needed for a high level model in a missile defense analysis primarily focuses on the radar and flight dynamic aspect of the model. Missile defense systems are highly dependent on detection and tracking of threats through a radar system. Therefore, the high fidelity model must have a good radar model, as well as a good flight dynamics model. Due to the nature of this study where systems, doctrine, and organizational structure will be varied, the model should allow these aspects to be changed relatively easily without much reprogramming between each change. In addition, the program should run fairly quickly with a small storage requirement and should be available to the researcher at the smallest cost possible. These criteria are summarized below:

a. Accurate radar models
b. High fidelity flight dynamics models
c. Ease of adjustments of systems, tactics, and organization
d. Availability
e. Speed
f. Ease of setup

After initial research, the high fidelity simulation environments were narrowed to four possible programs: EADSIM, Netlogo, the Synthetic Theater Operations Research Model (STORM), and the Joint Integrated Contingency Model (JICM). EADSIM, STORM, and JICM are used throughout the DoD for war-simulations ranging from

engagements to full campaigns. Netlogo was developed and is primarily used throughout academia. STORM and Netlogo are agent-based models. JICM is fully deterministic, but has inputs from another model called the Combat Sample Generator (COSAGE), which is stochastic. EADSIM is stochastic and has independent agents, but operates much more scripted than a fully agent based model. Each of these tools is explained below with the exception of EADSIM. EADSIM was discussed earlier section 2.4.

7.1.1. Agent Based Models

Agent based models are time-stepped simulations where each entity in the program is individually programmed to sense its immediate environment, not the entire environment, and make decisions based off those observations and the observations communicated to it from other agents [156]. This bottom-up approach is fundamentally different than the traditional top-down simulations and is extremely useful for observing emergent behavior or complex dynamics, which can evolve from agent interactions [157, 158]. Naturally, this type of simulation is good for warfare modeling since each military unit naturally acts as an agent. The main difficulty with these types of programs is the extensive time required to program the agents and their interaction rules.

Netlogo is an agent based software environment maintained by Northwestern University. It is an open-source program that is downloadable from a web site and has been used in a wide array of applications from military problems, to social dynamics problems, and biological simulations [159]. The code is written in Scala with some parts in Java [160]. The main advantage of Netlogo is its availability. There is not a pre-preprogrammed flight dynamics or radar model available, so these models would need to be programmed manually. Additionally, the nature of agent-based simulation means that

as doctrine or organization changed, the agent rule sets may need to be reprogrammed which may be cumbersome.

STORM is another agent-based program that is used throughout the DoD. The Air Force originally developed STORM in the 1990's and fully implemented it in 2004. It is written primarily in C++ and today it is the primary campaign model for the Air Force, Navy, and Marine Corps. STORM is a fully agent based simulation and primarily focuses on air-to-air, surface-to-air, and maritime engagements [161]. It does have a land-based model available, however, that has not been developed nearly as well as the air model. The main advantages of STORM are that there is a fairly good radar and flight dynamics model built into the program. The main disadvantages are its availability and the harder setup and adjustment problems as described with Netlogo.

7.1.2. Non-Agent Based Models

The two models considered that are not fully agent-based are EADSIM and JICM. EADSIM does have some characteristics of an agent-based model in that certain elements can sense portions of the environment and make decisions. However, much of the simulation is scripted around these elements. JICM is a fully deterministic model in which all aspects are scripted in advance.

EADSIM is explained in the literature review section above. The main advantages are its radar and flight dynamics models and its availability. Since it is government owned, it is available to any US citizen with a legitimate modeling need. Its main disadvantages are its long setup requirements and runtimes. JICM was developed by the RAND Corporation and operates in a UNIX environment. JICM is a high level campaign tool or a "many-on-many" simulation tool where individual elements are

division or brigade sized [162, 163]. The inputs to JICM come from COSAGE which is a stochastic "few-on-few" tool. The inputs to COSAGE come from individual actual material engagement tests conducted by the Army Material System Analysis Activity (AMSAA). JICM is the primary campaign tool of the Army due to its fast running nature and the ability to rapidly simulate the effects of environmental variables, such as terrain and weather, as well as force size variables. The main advantages of JICM are its ease of adjustments, run speed, and availability. The main weaknesses of JICM lie in its detection and flight dynamics models.

7.1.3. Model Selection

After investigating each model, they were all compared against each other for each criterion listed above. The comparison of each model is subjective, but is based on the author's direct experience and research for all four models. The results of this comparison are shown in Figure 133.

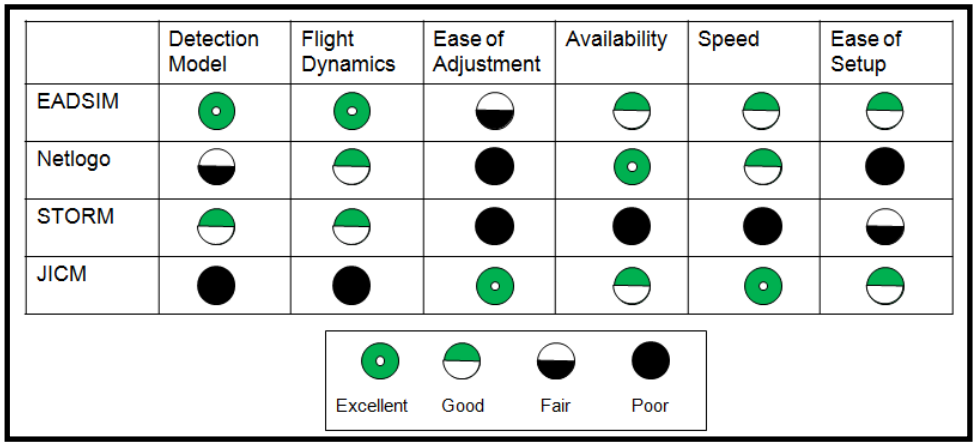

Figure 133: High Fidelity Model Selection

EADSIM proved to be the best high fidelity model mainly due to its robust radar and flight dynamics model. It also scored relatively high for availability, speed, and ease of setup. It scored in the middle of all models for ease of adjustment. Other models were

better in some categories, but overall EADSIM was fairly good across all categories. With the high fidelity model selected, the next step is to determine a suitable lower fidelity model that will allow the required tradeoffs between systems, organization, and doctrine.

7.2. Air Defense Model Setup

EADSIM, like many other high fidelity simulations, requires a high number of inputs due to the complexity of its calculations. This next section will address the basic setup of both the friendly (blue) and enemy (red) forces. In order to maintain an open classification and to speed up the setup process, the scenario used in this work was adapted from the "Demo300" scenario that is shipped with all EADSIM setup disks. This demo has unclassified versions of many ADA and missile systems and is meant to show the capabilities of EADSIM. All systems used in this work are modified versions of the systems in Demo300 using the values expressed in the sections below. These values for various inputs are not meant to represent any known system, but instead are round-number inputs within acceptable and possible ranges in order to make the simulation work as intended. All inputs were fabricated by the author and do not represent any real system.

7.2.1. Blue ADA Forces Setup

The friendly defensive ADA forces are known as the blue forces. The blue ADA forces in this work will be made up of three different systems: an Upper Tier (UT) system, a Lower Tier (LT) system, and a Point (PT) system. The UT system has a single interceptor type that has the largest range and can engage TBM threats only. The LT system is the most versatile. It has three different interceptor types: Interceptor A, B, and

C and can engage both TBMs and CMs/UASs. The PT system has only one interceptor type and can engage only CMs/UASs.

Engagements in EADSIM are geometry dependent. Both the detection and engagement subroutines take into account the angles between systems as well as the cross range, down range, and altitude between systems [65]. This geometry dependency is strongest for closer engagements then for further ones. Therefore, the PT and LT system were setup with explicit launchers. This means that the radar, control station, and launchers were each their own platform with communication links between them. Because the UT system engagements were much further away, it was setup as an implicit system with the radar and launchers in a single platform.

The launchers for the LT and PT system were arrayed around the central launcher, each facing outward with overlapping coverage. All three systems were aligned around a protected airfield. The radar for the PT system is a 360-degree radar while the PT and UT system each has a phased-array radar that has only a 120-degree field of view (FOV). Because the PT is 360-degrees and can only engage CMs, it was arrayed in front of the airfield relative to the attack. The LT and UT systems were each placed behind the airfield to ensure that the airfield was within their 120-degree radar coverage. A screen-shot of the ADA setup is shown below in Figure 134. Additionally, a screen-shot of a test engagement is shown in Figure 135.

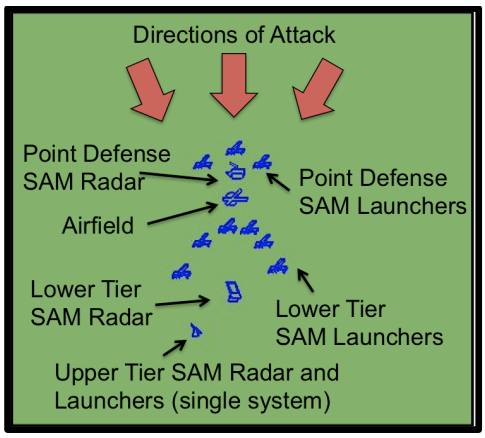

Figure 134: Blue Force ADA Setup (Screen Shot from EADSIM Scenario Generation)

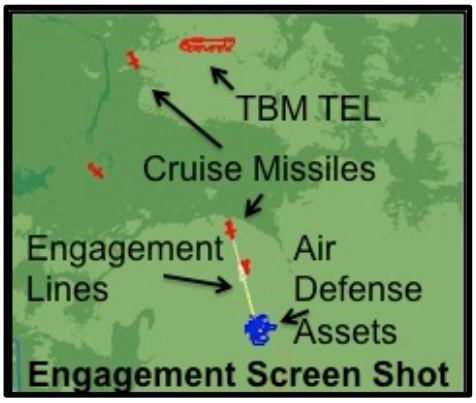

Figure 135: Screen Shot from EADSIM Test Scenario Playback

7.2.2. Blue ADA Weapon and System Characteristics and Setup

Each of the systems, UT, LT, and PT, described above has its own unique interceptors available to it. Each interceptor has a different range and altitude-operating band. These bands overlap each other in order to ensure mutual coverage. The weapon systems show a progression of technology just as real-world systems would. The UT system is the newest and most advanced, since a deployable exo-atmospheric TBM defense system is a relatively new addition to most of the world's militaries. The LT system is a relatively older system and has been through a progression of upgrades. This gives it three different interceptors with increasing levels of capability and different specializations. The PT system is the oldest system and relies on infrared acquisition

with radar cuing as opposed to radar guidance. Finally, for the cost of each interceptor, this work will use a relative cost index number. This is mainly because the systems are fictional, but also because cost figures for military equipment is difficult to obtain. In this work, all costs will be relative to the most capable LT interceptor, Interceptor A.

The UT system is the first layer of defense against incoming TBMs. It is designed to engage only TBMs and not CMs. Because the engagements take place very far away from the radar, and reflected radar energy is inversely proportional to the radius to the target raised to the fourth power, the interceptor must use an active seeker. The ground-based radar provides in flight updates to the missile but the internal interceptor seeker conducts the intercept. Additionally, because of the far distances, the radar must use much more of its resources in terms of power and dwell time to map the incoming targets and provide updates to the outgoing missile. This limits the number of missiles to which the radar can simultaneously provide updates. Thus, the maximum number of simultaneous interceptors allowed in flight was set to six. Additionally, the active seeker, large size and fuel requirements, and the relative newness of the UT interceptor make it extremely expensive. Thus, the cost for each interceptor will be four times that of the LT Interceptor A.

The LT system has a suit of interceptors that are optimized for different engagements. Each LT interceptor has overlapping altitude and range coverage with each other. All of the interceptors can engage both TBMs and CMs, but Inceptor B is optimized primarily for CMs. The least capable, but least expensive interceptor is Interceptor C. This interceptor uses a semi-active seeker that receives reflected energy from the main ground-based radar. It is designed to engage both TBMs and CM/UAVs.

Due to the relative age of the seeker, hardware, and software of the missile, the radar system can only guide up to five simultaneous interceptors in flight at a time. Its age, however, makes it a relatively affordable interceptor that costs only 40% compared to the LT Interceptor A.

Interceptor B for the LT system is an upgraded version of Interceptor C. It still uses a semi-active seeker, but with improved hardware. These improvements allow the radar to guide twice as many interceptors in flight as compared to Interceptor C, but the cost is greater at 70% of the cost of Interceptor A. Additionally it was optimized for ABT targets as opposed to TBMs thus its average velocity is slower, but it is more maneuverable resulting in a greater probability of kill (Pk) against ABT targets. Finally, LT Interceptor A is the most advanced LT interceptor with a combined active and semi-active seeker. This means that the LT system can support a greater number of interceptors in flight at once. It also has a more advanced propulsion system that enables it to reach a higher average velocity. LT Interceptor A and the UT Interceptor have overlapping altitude coverage against TBMs.

The PT interceptor is designed only to engage ABT targets. It has a relatively low maximum range because it uses an infrared seeker system. The system is cued to an engagement by a radar system, but the missile seeker must acquire the target before launch. Additionally, because it is optimized to engage ABTs it has a relatively low average velocity, but is extremely maneuverable. Its smaller size also makes it extremely affordable at only 20% that of LT Interceptor A. The PT interceptor overlaps in range coverage with all the LT interceptors. All of these values are summarized in Table 39 and Table 40 below.

Table 39: Blue Interceptor Characteristics

System	Missile	Interceptors per launcher	Max # in Flight	Average Velocity (m/s)	Seeker	Target Set	Relative Cost
Lower	Interceptor A	12	12	1,400	Active	TBM/CM	1.0
	Interceptor B	8	10	1,000	Semi-Active	TBM/CM	0.7
	Interceptor C	4	5	1,200	Semi-Active	TBM/CM	0.4
Upper	UT Interceptor	8	6	2,000	Active	TBM	4.0
Point	Pt Interceptor	10	NA	900	Infrared	CM	0.2

Table 40: Blue Interceptor Range and Altitude Operating Bands

Interceptor		TBM				CM			
Missile		Range (m)		Altitude (m)		Range (m)		Altitude (m)	
		min	max	min	max	min	max	min	max
Lower	Interceptor A	1,000	30,000	2,000	30,000	500	60,000	50	20,000
	Interceptor B	1,000	25,000	2,000	25,000	500	80,000	50	20,000
	Interceptor C	1,000	20,000	2,000	20,000	500	60,000	50	20,000
Upper	UT Interceptor	1,000	60,000	25,000	60,000	NA	NA	NA	NA
Point	Pt Interceptor	NA	NA	NA	NA	100	20,000	0	30,000

7.2.3. Blue ADA Weapon System Probability of Kill

The probability of kill (Pk) for a single engagement is a single number that represents a complicated kill-chain. In order to destroy an incoming missile with an ADA interceptor, the radar must detect the threat, have enough detection updates to create a track, develop a fire solution, and launch the interceptor. That interceptor must hit the target. If it hits the target, it must do so in a manner to disable the incoming missile. These linked probabilities can be expressed as:

$$P_k = P_D P_{T|D} P_{FS|T} P_{L|FS} P_{H|L} P_{K|H}$$

where
P_D = Probability of Detection
$P_{T|D}$ = Probability of track given detection

$P_{FS|T}$ = Probability of fire solution given track
$P_{L|FS}$ = Probability of launch given fire solution
$P_{H|L}$ = Probability of hit given launch
$P_{K|H}$ = Probability of kill given hit

In EADSIM, the detection algorithm explicitly calculates the probability of detection. Multiple detections within a given time then lead to the establishment of a track. This track must then be maintained with additional detections within a given time span within the predicted location to lead to a fire solution. The rest of the kill chain, however, is calculated implicitly from a set of three-dimensional Pk lookup tables. These tables are expressing the probability of launch, hit, and kill in a single number. They give the probability of kill for a given interceptor-missile combination for the intercept down-range, cross-range, and altitude from the launch point.

Most ADA interceptors are designed to operate efficiently within a given altitude and range band. If the engagement occurs at too close of an altitude or range the interceptor may not have enough time to maneuver to the optimal position prior to impact. If the engagement occurs too far in either range or altitude, the ground-based radar may not be able to provide enough guidance input due to the reduced effectiveness of the radar at extended ranges. In practice, the three-dimensional tables are produced from a combination of hardware in the loop simulations and actual system-on-system test engagements. These tables are typically classified and not available to the public.

In this work, the optimal engagement bands will be simulated with a simplified formula. Each interceptor was assigned a Pk at the minimum altitude/range of the system, given above in Table 40. It was also assigned a Pk at the optimal operating altitude/range and an altitude/range set where this band began and ended. Finally, each interceptor was also assigned a Pk at the maximum operating altitude/range, given in

Table 40. For engagements that occurred within the optimal band between the minimum and maximum altitude/range, the Pk was the optimal Pk. These values are given below in Table 41 and Table 42.

Table 41: Probability of Kill Values for Interceptor-TBM-Altitude Combinations

Probability of Kill (Pk) for TBMs									
Tier	Missile	Pk-Low Alt		Pk-Mid Alt		Pk-High Alt		Alt Low-Mid (ft)	Alt Mid-High (ft)
		TBM 1/2	TBM 3	TBM 1/2	TBM 3	TBM 1/2	TBM 3		
Lower	Int A	60	50	80	70	60	55	10,000	25,000
	Int B	50	40	60	50	30	20	10,000	20,000
	Int C	40	40	60	60	35	25	50,000	15,000
Upper	Upper	60	60	85	85	80	80	30,000	50,000

Table 42: Probability of Kill Values for Interceptor-CM-Range Combinations

Probability of Kill (Pk) for CMs									
Tier	Missile	Pk-Low Range		Pk-Mid Range		Pk-High Range		Range Low-Mid (m)	Range Mid-High (m)
		CM1	CM2	CM1	CM2	CM1	CM2		
Lower	Int A	65	75	80	75	65	60	1,500	40,000
	Int B	70	75	85	80	80	60	1,500	60,000
	Int C	65	75	75	75	75	50	1,500	40,000
Point	Point	70	60	85	70	70	70	500	20,000

For engagements that occurred between the minimum operating range/altitude and the minimum range/altitude of the optimal band, the Pk was calculated as a linearly increasing function that started at the Pk of the minimum range/altitude and ended at the Pk of the optimal engagement band. For engagements that occurred beyond the maximum range/altitude of the optimal engagement band, the Pk was also calculated as a linearly decreasing function that started at the Pk of the optimal band and ended at the Pk

of the maximum engagement range/altitude. Engagements that occurred before the minimum operating range/altitude or after the maximum range/altitude, had a Pk of zero. The Pk calculations are best illustrated in Figure 136 below.

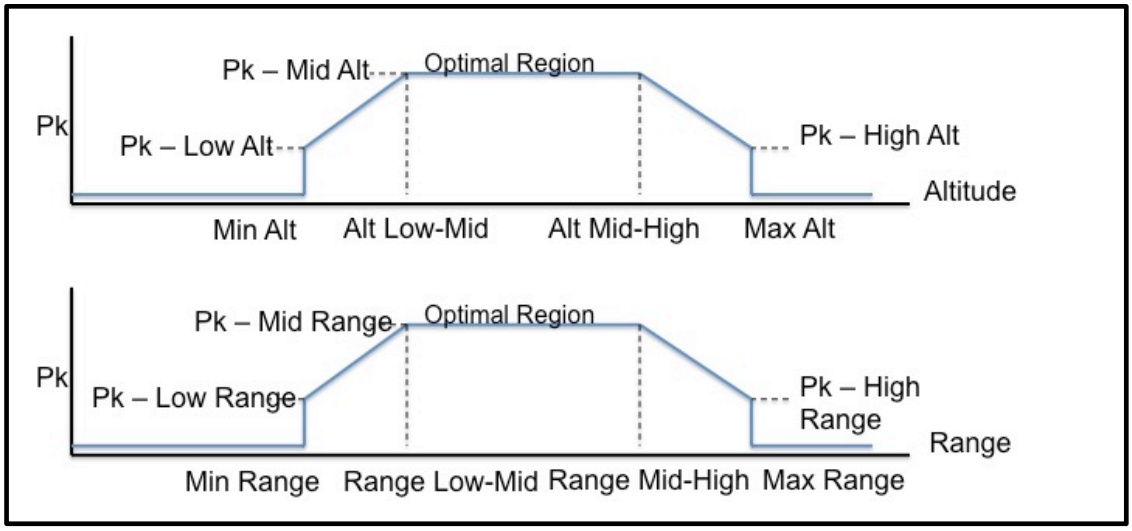

Figure 136: Pk Calculation Method

7.2.4. Blue ADA Radar Characteristics

The blue ADA radar systems were designed to match the above weapon and system descriptions. The UT and LT radar were each a phased-array type radar. This radar system is optimal for tracking a multitude of threats and for giving radar updates for interceptors in flight since the detection beam is electronically steered. This allows it to reposition at a much higher speed than a mechanically steered beam [164]. In radar systems, generally the lower the frequency, the greater the probability of detecting a smaller radar cross-section object. This occurs with a reduction in the precision of the radar and an increased physical size. Lower frequency radars are also more susceptible to clutter. The higher the frequency of the radar, the greater the atmospheric attenuation, which reduces the range. Higher frequency radars also have increased accuracy and smaller physical size of the radar system [164].

Because of these factors, the UT radar operated under the lowest frequency, because it faced only TBMs at a great distance. This meant that it had to be very sensitive and did not have to worry about clutter as much as the other systems that were pointed closer to the horizon. To combat the effects of atmospheric clutter, the signal-to-noise (SNR) threshold was set at the highest of the three radar systems.

The LT system was the most versatile radar that operated against both CM and TBMs. To ensure that it had the sensitivity to detect threats against the ground clutter, it operated at the greatest frequency of the three radar systems but had the lowest SNR threshold. The PT operated in between these two other radar systems. This data is summarized in Table 43.

Table 43: Radar System Characteristics

Radar System	Frequency (GHz)	Power (dbW)	SNR Threshold (db)
Point Defense (PT)	7.5	45	10
Lower Tier (LT)	10	50	5
Upper Tier (UT)	5	35	15

Radar systems are also susceptible to terrain. The terrain plays a much larger role for CM engagements than for TBM engagements due to the engagement angles. To ensure that each system was placed in an optimal position, a set of line-of-site (LOS) checks was conducted for each TBM. During these checks, the position of the radar was adjusted within an area of about 200-meter radius from the original location in order to find the position that resulted in the greatest uninterrupted LOS. A screen shot of these LOS checks is shown below in Figure 137. For these checks, the LOS is plotted in 5-degree increments at three different altitudes above ground level (AGL) shown in different colors. The lines terminate at the point where the radar's LOS is obscured by terrain. In many cases, this occurs at the radar's horizon due to the curvature of the

Earth. Once an optimal location was found, the radar was assigned this location in the simulations. In this figure, the 360-degree field-of-view (FOV) for the PT system is evident verses the 120-degree FOV of the LT and UT systems.

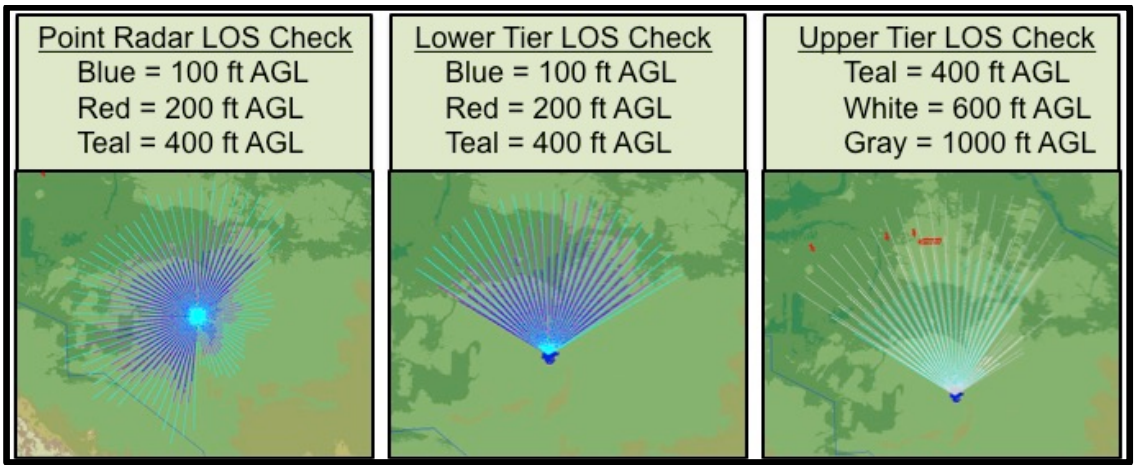

Figure 137: Line-of-Site (LOS) Checks for Radars

7.2.5. Red Forces Setup

In this fictional scenario, the enemy forces, known as the red forces, are arrayed to the North of the blue forces and are targeting the airfield with a variety of TBMs and CMs. The flight, guidance, and warhead characteristics of these missiles have been described in previous sections (Table 23, Table 25, Table 26, Table 27, Table 28, Table 29, Table 30, and Table 31). This section will explain the setup of these missiles within the scenario.

In practice, TBMs operate with a set of Ballistic Missile Operations Areas (BMOAs). This is because the TBMs must be launched from a limited number of Transporter, Erector, and Launch (TEL) vehicles. Because the TELs are a high value asset, when not in use they are hidden in hide sites to prevent their detection and destruction. Upon a launch order, the TELs move to a site where the TBMs are mated to the TEL. This is also where the TEL operators receive their target and all necessary data

for the launch. The TEL and TBM is then driven from the hide site to a launch site. These launch sites are generally pre-surveyed locations that are open areas and relatively flat. Once at the launch site, the TEL erects the TBM, performs all the pre-launch checks, and aligns the internal gyros. Once set, the TBM is launched towards the target, and the TEL returns to a hide site to start the process again.

The nature of the above process limits a TBM unit to operate with a designated BMOA. In this scenario, the classes of TBMs used, TBM1, TBM2, and TBM3, operated each from two BMOAs. TBM1 and TBM2 are longer range TBMs, so their BMOAs are further away then the BMOAs of TBM3. These BMOAs are shown below in Figure 138. This graphic shows the location of the center of each BMOA relative to the target airfield. Each of these BMOAs is 100km in diameter and the TBMs were launched from a random location within the BMOA (uniformly distributed angle and radial distance from center of BMOA). Since each missile had two different BMOAs, each BMOA had an equal chance of boing used for each missile.

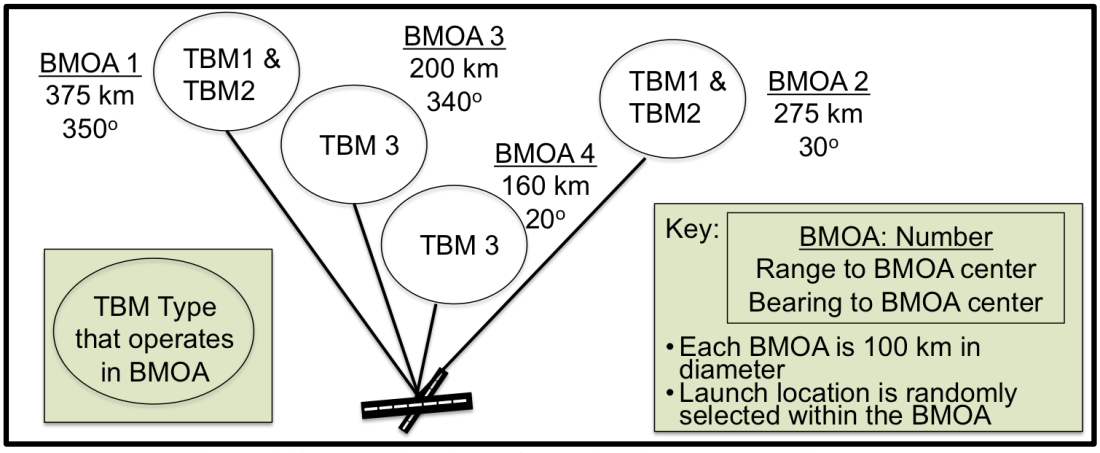

Figure 138: Ballistic Missile Operating Areas Used in Simulation

The number of incoming TBMs and CMs that are destroyed is strongly correlated to the time between the incoming missiles. ADA systems have very limited time

windows to engage the fast moving TBMs. Thus, the blue ADA forces are saturated easier with missiles spaced closely together. This means that the red forces try to launch their TBMs and CMs in such a way that they all approach the target at the same time. This is a difficult operation since different missiles have different flight characteristics, different distances to travel, and different atmospheric conditions they fly through. This means that there is usually a small delay between incoming missiles. This delay is variable and depends on the skill of the operators and the level of advancement in the control and guidance systems. Intelligence reports can generally estimate the likely time between incoming missiles.

For this work, the assumed average rate of the incoming TBMs and CMs was one per second. Because the time is variable, the actual time between each individual missile was estimated with the exponential distribution. The exponential distribution describes the inter-arrival time of a memory-less process [146]. In this application, this means that the time between any two missiles is independent of the time between previous missiles. The cumulative distribution function (CDF) of the exponential distribution is shown below for three different values of average arrival times, one second between events, three seconds between events, and five seconds between events. For any given set of incoming TBMs, the launch time between any two TBMs was calculated using the following formula to ensure that the arrival times between any two TBMs followed the exponential distribution.

$$T_{launch_j} = \max\left(T_{flight}\right) - T_{flight_j} + round(exprnd(\lambda))$$

where,
$T_{launch\text{-}j}$ is the launch time of the jth missile
$Max(T_{flight})$ is the maximum time of flight for the set of missiles
$T_{flight\text{-}j}$ is the time of flight for the jth missile

exprnd(λ) is a random number from the exponential distribution with inter-arrival time given by λ

In the above equation, the random number from the exponential distribution was rounded to the nearest whole second because the smallest time differential that EADSIM can operate with is one second [65].

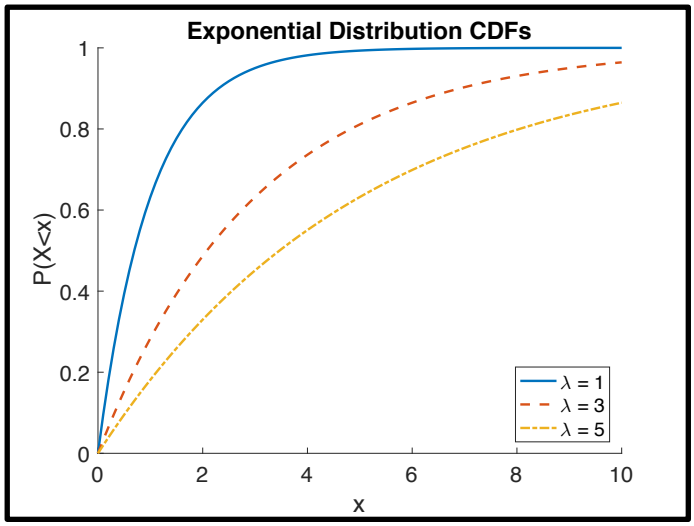

Figure 139: Exponential Distribution Cumulative Density Function

The CMs were assumed to be air launched CMs as opposed to ground launched CMs. The launch characteristics and initial flight patterns do not matter in this scenario since this would occur beyond the radar horizon for all the radars in this scenario. Once the CMs crested the radar horizon, they would all be in their cruise configuration no mater their launch origin. Thus, in this scenario, the CMs were injected into the scenario at the cruise altitude and speed with an initial location dictated by the maximum time of flight for all TBMs in the scenario. Once the launch location was randomly chosen from within the BMOAs, the maximum time of flight for all missiles was calculated. Using this maximum time of flight, the launch distance for the CM could be calculated by the following formula:

$$D_{launch_j} = \left(\max\left(T_{flight}\right) + round\left(exprnd(\lambda)\right)\right) V_{CM_j} \quad if\ j\ is\ odd$$

$$D_{launch_j} = \left(\max\left(T_{flight}\right) + 1\right) V_{CM_j} \quad if\ j\ is\ even$$

where,
$D_{launch\text{-}j}$ is the launch distance of the jth cruise missile
$Max(T_{flight})$ is the maximum time of flight for the set of ballistic missiles
$exprnd(\lambda)$ is a random number from the exponential distribution with inter-arrival time λ
$V_{CM\text{-}j}$ is the cruise speed of the jth CM

In the above equations, it is assumed that the CMs are launched from aircraft that each carry two cruise missiles and that the time between launching of subsequent missiles from the same aircraft is one second. This is why one second is added to the times for the even missiles. For the odd missiles, the aircraft must coordinate their shots and thus, they are subject to random variation.

For detection characteristics, radar cross section (RCS) values were assigned based on average values for TBMs and CMs [165]. Since TBM1 and TBM2 are longer range TBMs in this scenario, it was assumed they were larger and thus have a larger RCS. Additionally TBM1 and TBM2 were assumed to have separating warheads. This means that they are more uniformly shaped and do not have a dominate scatter orientation. They also reenter the atmosphere at very high speeds and thus have pulse-to-pulse decorrelation as opposed to scan-to-scan decorrelation. This makes TBM1 and TBM2 a swirling type 2 target (see appendix A for a description of swirling targets). TBM3 was assumed to have a non-separating warhead. This gives the missile body a dominant scatter along the missile long-axis. The missiles are still traveling fast and experiencing pulse-to-pulse decorrelation. This makes TBM 3 a swirling type 4 target. The CMs each have a long axis giving them a dominant scatter orientation. They are also traveling slow enough to have scan-to-scan decorrelation but not pulse-to-pulse

decorrelation at far distances. This makes them a swirling type 4 target. These values are summarized in Table 44 below.

A relative cost calculation was used comparing all missiles to TBM1 just as in the blue interceptor costs. TBM2 has a more expensive and complicated warhead, since it contains a set of individual runway penetrating munitions with a carrying mechanism that disperses the penetrators at a predetermined altitude. In this work, it was assumed to be 30% more expensive then the same missile with a unitary warhead (TBM1). TBM3 is a smaller and faster TBM with a flatter trajectory. Although it also has a unitary type warhead, its increased accuracy and flatter trajectory make it more advanced and thus more expensive. In this work, it was assumed to the twice as expensive as TBM1. CMs are generally orders of magnitude less expensive than TBMs [18]. Thus, CM1 with a unitary warhead was assumed to be 20 times less expensive than TBM1. CM2 with a submunition warhead was assumed to be 10 times less expensive. These values are summarized in Table 44 below.

Table 44: Red Missile Radar Cross-Section and Cost

Missile	RCS (m^2)	Swerling Target Type	Relative Cost
TBM 1	2.0	2	1
TBM 2	2.0	2	1.3
TBM 3	1.6	4	2
CM 1	1.3	4	0.05
CM 2	1.0	4	0.1

7.3. Air Defense Model Wrapper Function

EADSIM runs by reading a set of input text files, running an executable, and writing results to a large file called the C3Ilog. From this C3Ilog, the user can query the

output with a separate program within the EADSIM executable called the non-graphical post processor (NGPP). This process is called a stats query. This will generate text files that summarize important information [65]. When run with a pre-generated stats query, EADSIM and NGPP read text files and produce text files. This makes it relatively easy to implement a "wrapper" function to run and populate a design of experiments table. From the design of experiments table, a predictive Neural Net (NN) model of the outputs can then be generated. This process is summarized in the figure below.

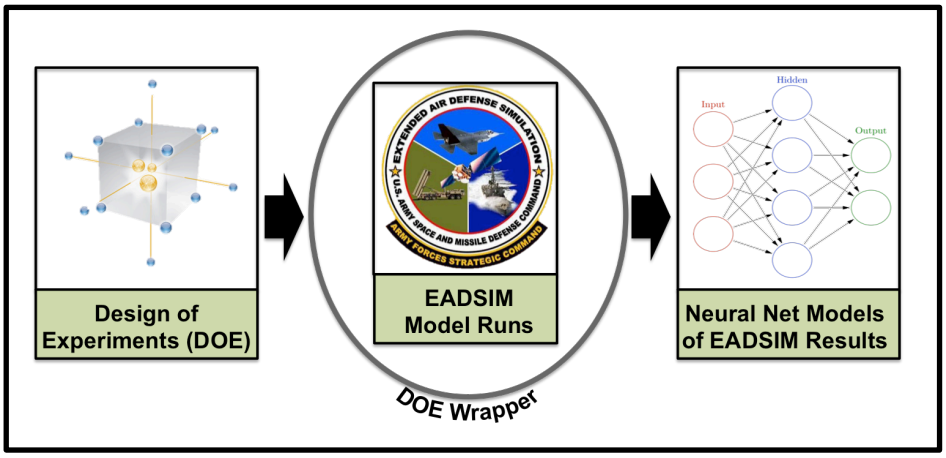

Figure 140: Simulation MetaModel Setup

A summary of Design of Experiments (DOE) and Neural Net (NN) models are covered in appendix B and C. The wrapper function is the link between the DOE and the NN model. The wrapper function reads inputs from the DOE table. Then it must translate the input DOE values into necessary inputs for the EADSIM files. For example, if for a particular run, the DOE specifies 8 TBM1 missiles are to be launched then the wrapper function must set 8 TBM1 platforms to "alive" and the rest of the TBM 1 platforms to "dead."

Once the wrapper function has all the necessary inputs for the files, it then writes these input values to the appropriate locations in the input files while leaving the rest of

the input file unchanged. When all input files are constructed, the wrapper function runs the EADSIM program by specifying the location of the new inputs files and specifying a location for the output files. It then reads the outputs files, collects the necessary output values, and writes those values to the DOE table. Finally, it deletes the input and output files to conserve disk space and moves to the next DOE line. This process is summarized in Figure 141 below. For this work, the wrapper function was implemented with MATLAB running on a Linux cluster, the DoD High Power Computer (HPC) network [166]. The HPC allowed the author to run up to 320 computer cores each day to execute the necessary runs.

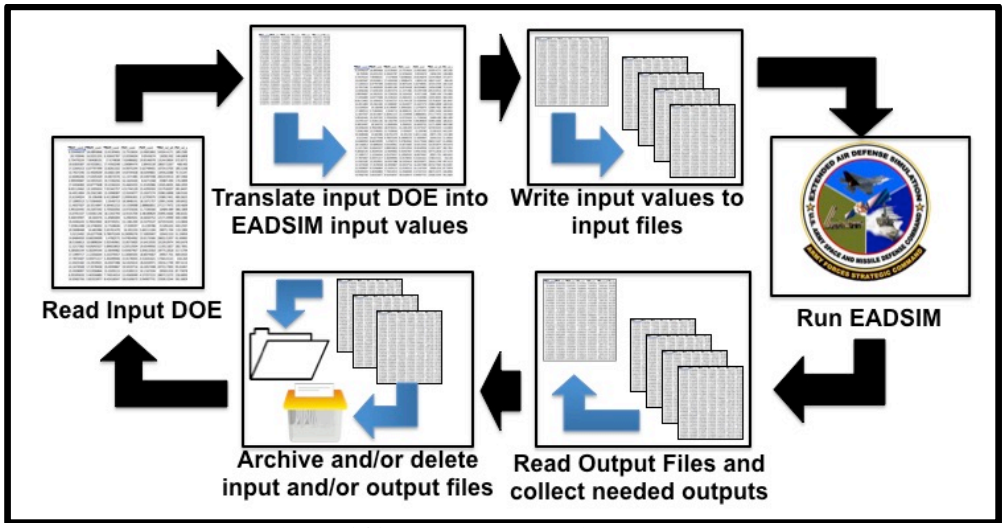

Figure 141: Wrapper Function Process

7.4. Air Defense Model Screening Test

EADSIM has a large input variable set. The focus of this work is on optimization of the ADA doctrine, the rules for how the systems engage threats. To develop the input DOE, the author leveraged his past knowledge of EADSIM and the EADSIM manuals to develop a set of input variables that best represented the variables that a real ADA system would have control over. These included the beginning and ending engagement altitude

and ranges, shot doctrine (number of interceptors shot in volley at each threat), the priority of each weapon to each threat, and the number of launchers of each missile type. In addition, the red forces had control over the number of missiles of each type fired, the release altitude for the missiles that carried submunitions, and the percentage of each missiles type that was shot at each target. These values are summarized below.

Table 45: Input DOE Variables and Ranges

Input Variable	Min	Max	Unit	Input Variable	Min	Max	Unit	Input Variable	Min	Max	Unit
Number of TBM1	0	20	ea	LT Msl C Max Altitude	2,000	20,000	m	PT Shot Doctrine	1	2	ea
Number of TBM2	0	20	ea	LT Msl C Min Altitude	2,000	20,000	m	LT Pri - Msl A - TBM	1	3	ea
Number of TBM3	0	20	ea	UT Shot Doctine	1	2	ea	LT Pri - Msl A - CM	1	3	ea
Number of CM1	0	20	ea	LT Shot Doctrine - TBM	1	2	ea	LT Pri - Msl B - TBM	1	3	ea
Number of CM2	0	20	ea	LT Shot Doectrine - CM	1	2	ea	LT Pri - Msl B - CM	1	3	ea
TBM Release Altitude	10,000	30,000	m	LT Msl A Max Ranage	1,500	60,000	m	LT Pri - Msl C - TBM	1	3	ea
CM Release Altitude	50	500	m	LT Msl A Min Range	1,500	60,000	m	LT Pri - Msl C - CM	1	3	ea
UT Max Altitude	35,000	60,000	m	LT Msl B Max Range	1,500	80,000	m	LT A Num Launchers	1	6	ea
UT Min Altitude	25,000	60,000	m	LT Msl B Min Range	1,500	80,000	m	LT B Num Launchers	1	6	ea
LT Msl A Max Altitude	2,000	30,000	m	LT Msl C Max Range	1,500	60,000	m	LT C Num Launchers	1	6	ea
LT Msl A Min Altitude	2,000	30,000	m	LT Msl C Min Range	1,500	60,000	m	UT Num Launchers	1	6	ea
LT Msl B Max Altitude	2,000	25,000	m	PT Max Range	1,200	20,000	m	PT Num Launchers	1	3	ea
LT Msl B Min Altitude	2,000	25,000	m	PT Min Range	1,200	20,000	m				

The input DOE for this work contained thirty-seven input variables and measured ten output variables. In an attempt to reduce the size of the input DOE, the author conducted a screening test. This screening test identified those input variables that contributed the greatest to the variance of each output variable. If there were input variables that caused little variance for all the output variables, then that input variable could be ignored with little effect on the output prediction NNs.

To run this screening test, the author developed a resolution III DOE that tested the inputs at the extreme minimum and maximum values specified in the table above. The author then used the JMP software to create Pareto plots for each of the ten outputs. The Pareto plots show the relative contribution of each input variable to the variability of the output variable. The plot orders the inputs from the one that causes the most variability to the one that causes the least variability. It also shows a line with the cumulative variability. An example of a Pareto Plot is shown below in Figure 142 for the number of LT B missiles fired during the screening test. The red vertical line is drawn at the 80% cumulative variability line. This plot shows that all variables from the TBM release altitude (TBM_rel_alt) and above contribute to 80% of the cumulative variability for the number of LT missiles of type B that are shot.

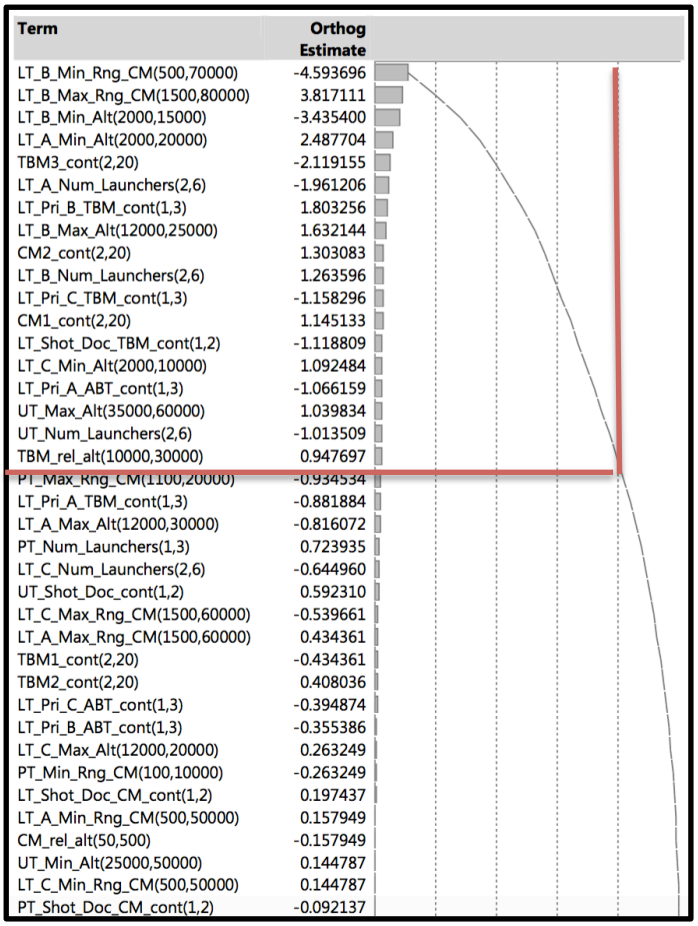

Figure 142: Pareto Plot for Number of LT B Missile Fired

Using the cumulative variability, all the input variables that cause 80% of the cumulative variability in each output were collected. The summary of this analysis is shown below in Table 46. This table shows that all thirty-seven input values were influential in the variability of at least one of the ten output variables. This meant that all thirty-seven variables were included in subsequent analysis.

Table 46: ADA Simulation Screening Test Results

Input / Output	Leakers					Launches				
	TBM1	TBM2	TBM3	CM1	CM2	LT A	LT B	LT C	PT	UT
Number of TBM1	x	x	x							x
Number of TBM2	x	x	x			x			x	x
Number of TBM3	x	x	x	x	x		x		x	x
Number of CM1	x			x	x	x	x	x	x	
Number of CM2			x		x		x	x	x	x
TBM Release Altitude	x	x		x			x			
CM Release Altitude			x		x	x			x	
UT Max Altitude	x	x	x	x			x			x
UT Min Altitude	x	x	x					x	x	x
LT A Max Altitude		x			x	x	x	x		
LT A Min Altitude			x		x	x		x		
LT B Max Altitude			x			x	x	x	x	
LT B Min Altitude						x	x	x	x	
LT C Max Altitude		x			x	x		x		
LT C Min Altitude						x	x	x		
UT Shot Doctrine	x	x								x
LT Shot Doctrine v. TBM	x	x	x	x		x	x			
LT Shot Doctrine v. CM				x	x					
LT A Max Range				x	x	x		x	x	x
LT A Min Range		x		x	x	x				
LT B Max Range				x	x	x	x	x	x	
LT B Min Range	x			x	x		x		x	
LT C Max Range			x	x				x		
LT C Min Range				x				x		
PT Max Range			x			x			x	
PT Min Range			x	x	x		x		x	x
PT Shot Doctrine CM				x		x		x		
LT Priority of A v. TBM		x	x	x			x	x	x	
LT Priority of A v .CM					x					
LT Priority of B v. TBM		x				x	x	x	x	x
LT Priority of B v. CM		x								
LT Priority of C v. TBM							x		x	
LT Priority of C v. CM		x								
LT A Number of Launchers				x			x	x	x	
LT B Number of Launchers							x	x		x
LT C Number of Launchers				x				x	x	
PT Number of Launchers					x				x	
UT Number of Launchers			x				x			x

Table shows input variables that were included in 80% cumulative variability for each output variable.

7.5. Air Defense Model Neural Nets – Failed Tries

This section will explain several failed attempts to model the ADA simulation using neural nets to predict the shape parameters of the output distributions. The

previous section showed that all thirsty-seven input variables had significant contributions to the variability of at least one of the ten outputs. Thus, all variables were included in the input DOE for modeling. The modeling DOE was constructed with a Latin Hypercube design with the variable limits shown in Table 45 and included the following constraints:

1) Minimum Range <= Maximum Range – 1000m for all interceptors
2) Minimum Altitude <= Maximum Altitude – 5000m for all interceptors
3) Number of LT launchers (LTA+LTB+LTC) <= 8.

Initially, each variable was tested at 30 levels for a total of 1,140 design points. The design was then increased by 20% (360 points) to account for validation points. This design is shown below in Figure 143.

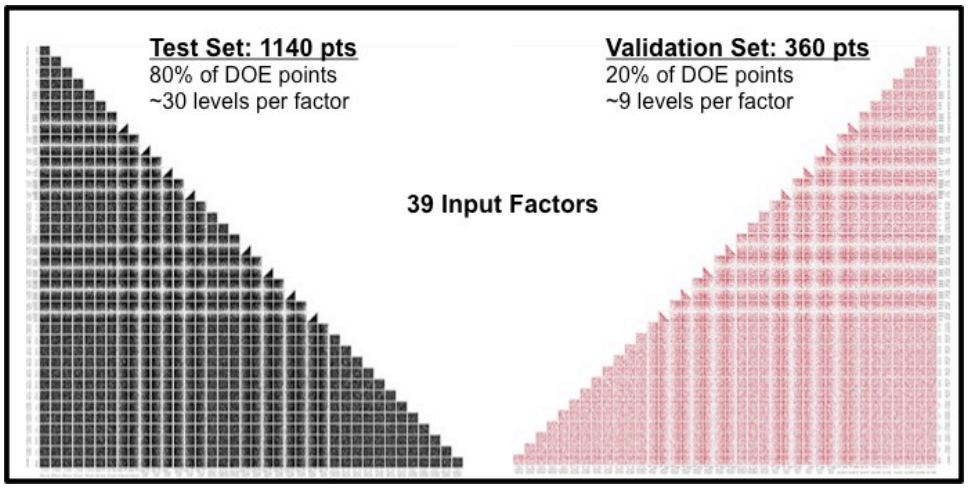

Figure 143: Input DOE for ADA Simulation Model

The above DOE was used in the ADA simulation. Like the damage effect simulations, the simulation was repeated until the number of runs was greater than the number of runs required to ensure that the estimated average was within 10% of the true average. Using these output distributions, the author then tried to fit many different neural nets to predict the outputs. First, shape parameters for the binomial, Poisson, and

geometric distribution were estimated with the most likely estimate (MLE). This allowed the author to estimate the fit error of the estimated distributions in order to determine which of the three distributions best fit the data. Once the correct distribution was determined, the optimization program described in section 6.3.3.12 was used to adjust the shape parameter values until the error of the P-P and Q-Q plot was minimized. This will minimize the sum of squares of the error. Once the optimization was complete, the estimated shape factor was tested using the validation set of data. In all cases the R^2 of the fit was less than 0.8.

In order to improve the fit, the author attempted many transforms of the data to include a log, square root, inverse, squared, and Box-Cox transform. Typically the square root transform was best, but still failed to improve the fit better than an R^2 of 0.8. The author also attempted to use a stacked neural net (NN). This concept is shown in Figure 144. A stacked NN uses the output estimates of some parameter from other NN as an additional set of inputs, beyond the original input vectors, in order to improve the fit of a given parameter. In this case, the author created three NNs stacked on top of each other. The first NN used the input matrix to estimate the average of each case. Then in a feed-forward fashion, the input matrix was combined with the estimate of the average as the input for the second NN who estimated the standard deviation. This output was then combined with the previous input as the full input for the third NN who estimated the shape parameter of the output distribution. However, in a majority of the cases, this method also failed to produce a R^2 greater than 0.8.

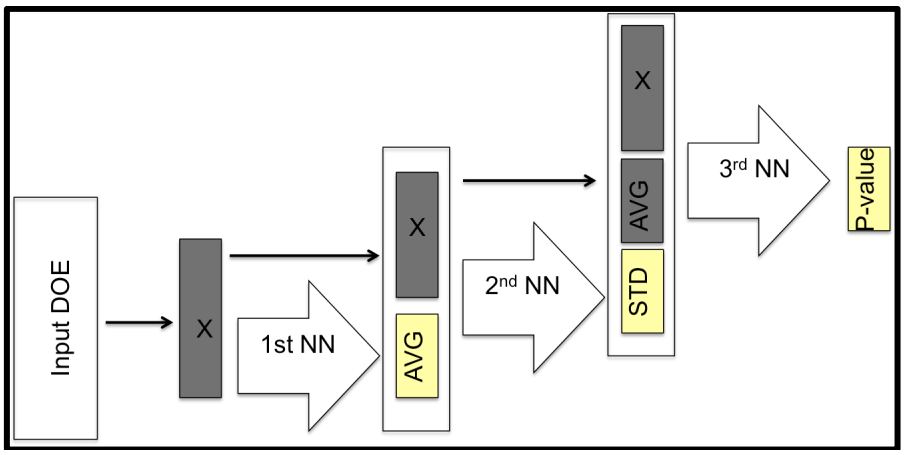

Figure 144: Stacked Neural Net Concept

7.6. Air Defense Model – New Setup

Attempting to model all outputs at once revealed that the interactions between each layer cause too much noise in the overall model. To help solve this, a new setup was created that separated the systems into layers. This allowed each layer to be modeled individually. In the actual simulation, this layering also occurs. A lower layer does not engage until the upper layer is complete. By separating the simulation into layers, however, all but the active layer could be switched off in the simulation. This prevented lower level layers from affecting the outputs of higher-level layers for modeling purposes. In the final simulation, each part of each layer was recombined such that the leakers from one layer were passed as the input for the subsequent layers. A diagram of this layered approach is shown below in Figure 145.

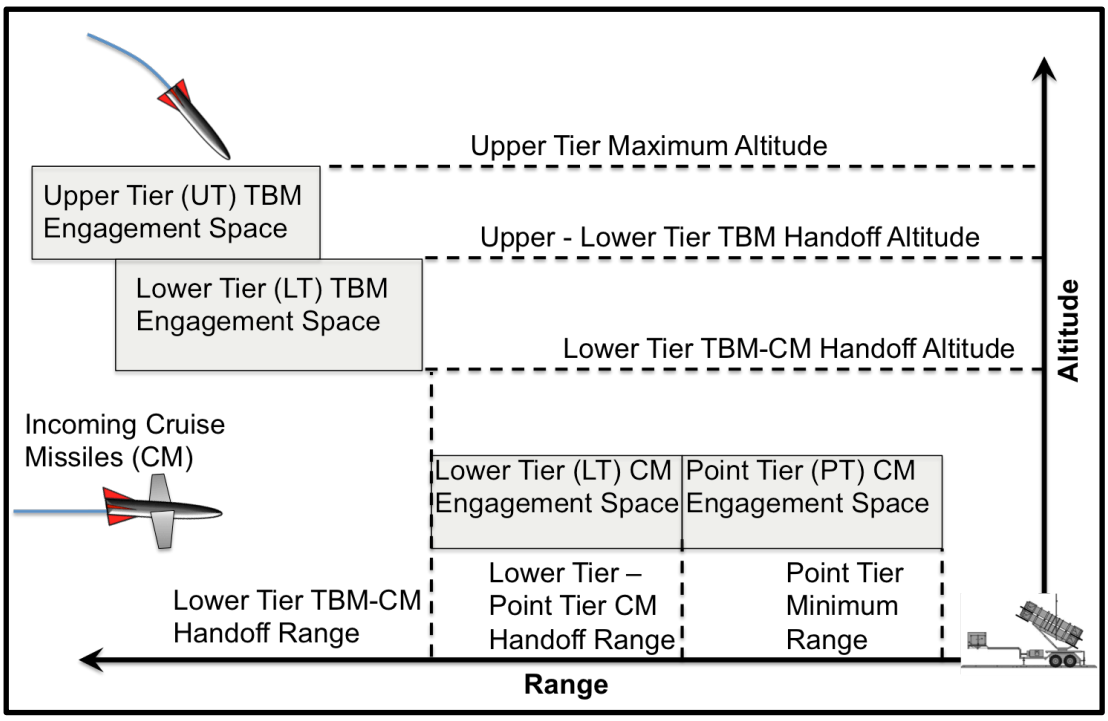

Figure 145: ADA Simulation Shown as Layers

In Figure 145, TBMs are first engaged by the Upper Tier (UT) system. The engagements begin at the UT system's maximum altitude and continue until its minimum altitude. Any TBMs that are not destroyed by the UT system are passed to the Lower-Tier system (LT). There is a delay before the LT systems can begin to engage the TBMs that allow for the system to track the results of any low-level engagements made by the UT just prior to handing off the targets. To account for this, the LT maximum altitude was restricted to 5,000 meters below the UT minimum altitude. This makes the LT maximum altitude a dependent variable on the UT minimum altitude. The LT system engages the TBMs until its minimum altitude. At that point, any TBMs that are not destroyed are passed to the damage model since there is no system below the LT for TBMs.

Once the TBMs pass the LT system's minimum altitude, the LT system then shifts to CM engagements. It begins engaging CMs at its maximum range; however, this maximum range depends on the LT minimum altitude for TBMs. Therefore, a function is required that translates the TBM's altitude into range. Because the TBMs and CMs are designed to arrive at the target simultaneously and the CMs travel at a constant cruise speed, it is possible to create this function from the TBMs flight profile. The profiles generated in section 6.2.1 map the TBMs' flight by calculating the range to the target and altitude above the target for each second of flight. Using this data, a best-fit, three-degree spline was created to predict the time to impact for any given altitude. An example of this is shown below in Figure 146. Because the CMs are traveling at a constant speed, it is then possible to calculate their distance from the target such that they arrive at the given time. This calculated range is the maximum possible range for the LT engagements. However, to account for the time to switch modes and acquire targets, the LT maximum engagement range was limited to 500 meters less than this calculated range.

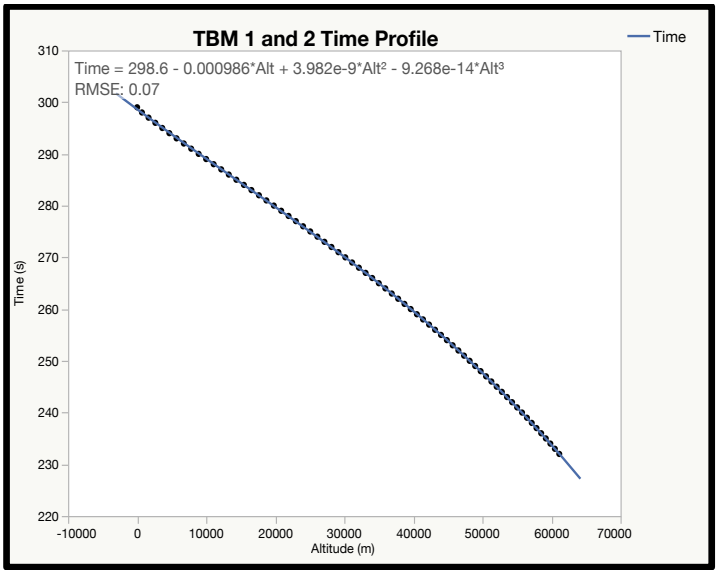

Figure 146: TBM Flight Profile to Predict the Time to Impact for a Given Altitude

The LT system then engages the CMs until its minimum range. At that point any surviving CMs are passed to the point defense (PT) system. The PT system is then delayed from shooting for 500 meters to account for hand-off coordination. This makes the PT system's maximum range a function of the LT system's minimum range minus 500 meters. The PT system then attacks until the CMs reach its minimum range. Any CMs that survive were then passed to the damage calculations functions.

7.7. Air Defense Model Neural Nets – New Setup

A simulation was created using the setup explained in the previous section along with the missiles and interceptor parameters explained in section 7.2. This setup demanded many different DOEs and predictive models to include one model to predict the number of leakers (# leakers), or threats not destroyed, for each blue interceptor and red missile combination. In addition, the new simulation setup requires a model for the number interceptors shot (# Interceptor Shot) by the blue systems against either TBMs or CMs. A summary of all the required predictive models for the simulation is explained below in Table 47.

Table 47: ADA Simulation Predictive Models Required

Blue System	Red System	Model	Blue System	Red System	Model
UT Interceptor	TBM 1	# Leakers	PT Interceptor	CM 1	# Leakers
	TBM 2	# Leakers		CM 2	# Leakers
	TBM 3	# Leakers	LT Type C Interceptor	TBM 1	# Leakers
LT Type A Interceptor	TBM 1	# Leakers		TBM 2	# Leakers
	TBM 2	# Leakers		TBM 3	# Leakers
	TBM 3	# Leakers		CM 1	# Leakers
	CM 1	# Leakers		CM 2	# Leakers
	CM 2	# Leakers	UT Interceptor	TBM	# Interceptor Shot
LT Type B Interceptor	TBM 1	# Leakers	LT Type A Interceptor	CM	# Interceptor Shot
	TBM 2	# Leakers		TBM	# Interceptor Shot
	TBM 3	# Leakers	LT Type B Interceptor	CM	# Interceptor Shot
	CM 1	# Leakers		TBM	# Interceptor Shot
	CM 2	# Leakers	LT Type C Interceptor	CM	# Interceptor Shot
PT Interceptor	CM	# Interceptor Shot		TBM	# Interceptor Shot

This simulation used a wrapper function similar to the one outlined in section 7.3 in order to run the desired DOEs. Due to the stochastic nature of the simulations, many simulation runs were required for each input vector (DOE line) of the DOE. Similar to the previous sections for the stochastic damage effects models, each DOE was repeated until the estimated mean was within 10% of the true mean with 95% confidence (see section 6.3.3.2).

Once the simulation was completed the results were compiled together. The ADA simulation took approximately 1-5 minutes to run on a 3.0 GHz computer. Considering the many different models and DOEs explained in Table 47, runs within each DOE, and repetitions of each run, the run time required to create all these models was too long for a single computer. Therefore, the Department of Defense (DoD) High Performance Computer (HPC) network was utilized to complete the simulations [166]. The HPC allowed the use of between 108 and 320 computer cores per day in order to run

all the DOEs in a massively parallel fashion. This work would have been exponentially slower without the use of the DoD HPC network. Even with the large number of parallel computations, the execution of all the DOEs took several weeks to complete.

After all computations were complete, a neural net (NN) fitting program was developed to predict the average of the response for each DOE input line. Each of these NN models was created with a routine that slowly increased the size of the hidden layer and calculated the R^2 of the k-fold cross-validation of the training set at each step. This continued until the calculated R^2 showed a decrease of 10% from its peak value.

Once the number of hidden nodes was calculated, the net was trained on the full set of training data using both a pure linear and radial basis function as the activation function of the output nodes. The final activation function was chosen based on the largest R^2 of the training set. The NNs were then trained five times over the training set and the final output was an average of these five outputs. Once the network architecture was determined, the net was tested against the validation set (20% of the data chosen at random). Because there were so many models, the full results of the fitting for each model are shown in Appendix A, and a summary of the fit is show below in Table 48.

Table 48: Summary of Neural Net Fit Parameters for ADA Simulation Models

Model	System		Training Set			Validation Set		
	Blue System	Red System	RMSE	Max Error	R Squared	RMSE	Max Error	R Squared
Number of Red Missiles that leak through the defense	LT_A	TBM1	0.039	0.396	0.987	0.100	0.622	0.972
		TBM2	0.031	0.213	0.991	0.082	0.533	0.970
		TBM3	0.053	0.366	0.979	0.176	1.086	0.942
		CM1	0.201	1.594	0.947	0.422	2.760	0.898
		CM2	0.109	0.802	0.976	0.228	0.821	0.942
	LT_B	TBM1	0.017	0.149	0.994	0.106	0.037	0.995
		TBM2	0.017	0.183	0.992	0.065	0.627	0.986
		TBM3	0.035	0.317	0.989	0.043	0.261	0.982
		CM1	0.184	1.334	0.956	0.224	1.196	0.935
		CM2	0.147	1.544	0.969	0.210	0.775	0.942
	LT_C	TBM1	0.009	0.080	0.997	0.020	0.186	0.996
		TBM2	0.005	0.046	0.999	0.012	0.065	0.996
		TBM3	0.010	0.103	0.997	0.010	0.119	0.994
		CM1	0.053	0.399	0.984	0.119	0.821	0.973
		CM2	0.023	0.258	0.994	0.120	0.813	0.978
	UT	TBM1	0.029	0.319	0.992	0.121	1.080	0.983
		TBM2	0.170	0.116	0.993	0.071	0.647	0.987
		TBM3	0.021	0.130	0.993	0.143	1.417	0.981
	PT	CM1	0.073	0.502	0.981	0.157	0.643	0.951
		CM2	0.063	0.770	0.989	0.111	0.695	0.972
Number of Interceptors Shot Against Red Incoming Missiles	LT_A	TBM-All	0.056	0.278	0.955	0.207	1.083	0.873
		CM-All	0.318	3.164	0.962	0.514	2.737	0.931
	LT_B	TBM-All	0.035	0.223	0.980	0.076	0.466	0.953
		CM-All	0.329	2.784	0.996	0.396	3.248	0.995
	LT_C	TBM-All	0.026	0.380	0.986	0.088	0.585	0.940
		CM-All	0.072	0.560	0.984	0.525	3.331	0.904
	UT	TBM-All	0.029	0.489	0.975	0.033	0.190	0.951
	PT	CM-All	0.443	3.990	0.951	0.496	3.366	0.926

8. OPTIMIZATION RESULTS

"For since the fabric of the universe is most perfect and the work of a most wise Creator, nothing at all takes place in the universe in which some rule of maximum or minimum does not appear."

- Leonhard Euler, Mathematician

The preceding sections outlined the ADA simulation and damage effects models and their associated predictive models that are needed for the proposed optimization methodology originally outlined in section 5.1 and shown again in Figure 147. This next chapter will use these models within the proposed optimization methodology to show how the damage that results from an enemy attack can be reduced from adjusting the tactics used by the ADA system. Should this reduction not be sufficient, it will also show how the damage can be further reduced by incorporating new systems into the ADA arsenal.

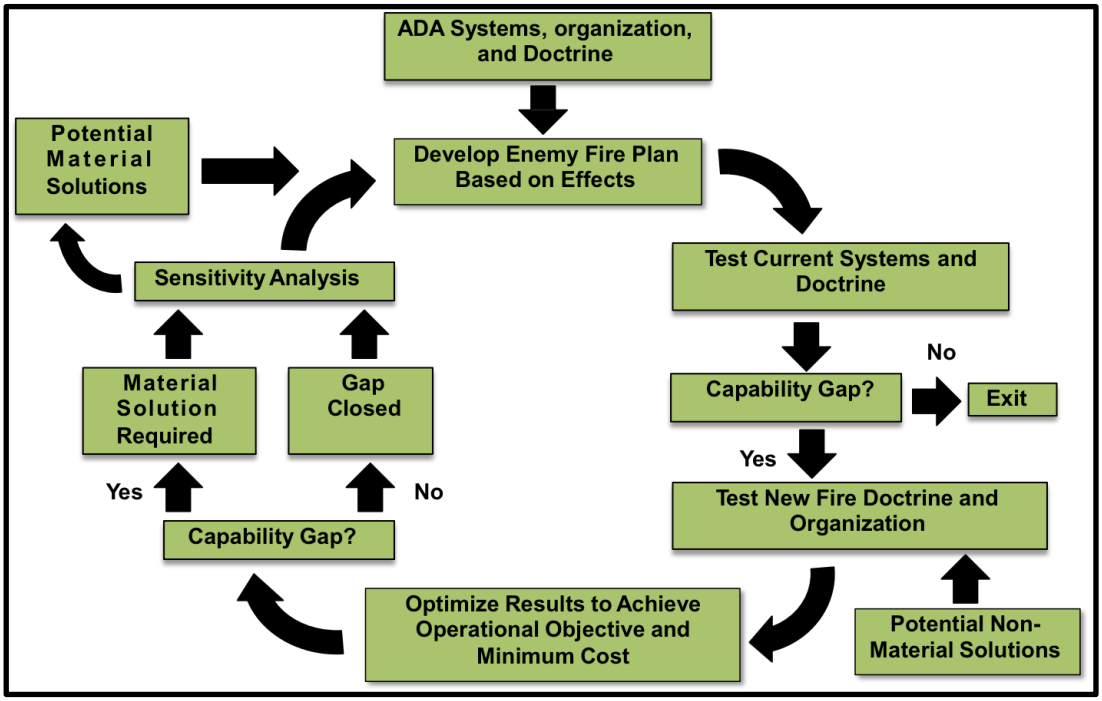

Figure 147: Overall ADOSO Framework Methodology

8.1. Enemy Fire Plan Test Sets

The first step in the optimization process is to develop an optimized enemy fire plan. A fire plan is the number and type of missiles that will be shot at the airfield along with the flight parameters (cruise altitude, release altitude for submunitions, etc.) and the individual targets that each missile will seek (aircraft, runway, POL sites, etc.). By starting with an optimized fire plan, the user is ensured that when the blue tactics are optimized, they are optimized against the worst possible threat.

In order to scope this work, three different fire plans are used in this test case. A small attack made up of 5 TBMs and 5 CMs impacting the target simultaneously. These TBMs and CMs can be of any type (TBM1, TBM2, TBM3, or CM1 and CM2). This represents the current capability of most enemy forces today. The second fire plan is a medium sized attack made up of 15 TBMs and 15 CMs, of any type, impacting the target at the same time. This represents the current state- of-the art capability of some modern missile forces, or the capability that could be obtainable in the next 10 years for most missile forces. Finally, the last fire plan will be a large attack made up of 30 TBMs and 30 CMs, or any type, impacting the target simultaneously. This represents the future capability of many missile forces.

8.2. Blue ADA Tactics for Base Case

In order to optimize the red fire plan, the blue tactics has to be set. These will later be optimized against the optimal red fire plan. The base case for the blue tactics is characterized as “shoot early and shoot often.” This strategy maximizes the use of far reaching systems over closer range/altitude systems. The logic behind this tactics set is

to destroy more threats at a further distance so that there are more shot opportunities and thus, reducing the number of leakers.

The blue ADA systems were explained in section 7.2.1, but are summarized again here. The Upper Tier (UT) system is designed to engage TBMs only and is the furthest range shooter for TBMs. Under, but overlapping, the engagement space for this system is the Lower Tier (LT) system. The LT system is capable of engaging both TBMs and CMs with three different types of interceptors (interceptors A, B, and C). For CMs, the LT system is the furthest range system. In the base case, it is also the only CM engagement system. Later, when a new system is introduced as a material solution it will be a Point Defense (PT) system that engages CMs only and shoots behind, but overlapping, the engagement space of the LT system. A summary of the systems and tactics for the blue system is shown below in Table 49.

In this table, all launchers start with their full complement of interceptors. The shot doctrine is the number of interceptors that are shot in rapid succession at a single inbound threat. The UT system's engagement space, defined by its maximum and minimum engagement altitude, was set to the largest possible value by setting the maximum and minimum altitudes to their limits. This shrinks the engagement space for the LT system since it can only begin to engage targets 5,000 meters below the UT systems (see section 7.6). The LT's minimum altitude is set to an intermediate value to allow some engagement space for CMs, since the maximum engagement range for LT is a function of the minimum engagement altitude for LT (see section 7.6). Finally, the priority interceptor, the interceptor the LT system will initially use against the given

threat, was set for the best, but most expensive, interceptor against TBMs and the least accurate and least expensive interceptor against CMs.

Table 49: Base Case Blue ADA Values

System	Variable	Set Value
Upper Tier	Number of Launchers	6
	Maximum Engagement Altitude	60,000 meters
	Minimum Engagement Altitude	25,000 meters
	Shot Doctrine	1
Lower Tier	Number of Interceptor A Launchers	2
	Number of Interceptor B Launchers	2
	Number of Interceptor C Launchers	4
	Maximum Engaging Altitude - TBMs	20,000 meters
	Minimum Engagement Altitude - TBMs	10,000 meters
	Maximum Engagement Range - CMs	5,000 meters
	Minimum Engagement Range - CMs	2,000 meters
	Shot Doctrine – TBMs	2
	Shot Doctrine - CMs	1
	Priority Interceptor – TBMs	A
	Priority Interceptor – CMs	C

8.3. Optimization Program

The optimization for both the red fire plan and the blue defense is a complex task. Because a large section of the multi-dimensional design space is being explored, there is no guarantee that the design space will be convex. Many of the typical gradient based optimizers may not work if the design space is not convex [147]. Without knowing this about the design space, there is no guarantee that an optimum is the global optimum [147]. Therefore a stochastic optimizer is needed. Good examples of stochastic optimizers are genetic algorithms and particle swarms. Typically, a genetic algorithm works better for models with discrete values, while a particle swarm works better for continuous models [147]. In either case, it is important that the algorithm maintain the spread of the test points for as long as possible in order to identify the Pareto frontier, or

frontier of optimal points. This is the set of all points that are not dominated in at least one dimension. Dominated in this context means that no other point is better in a given dimension than the non-dominated point.

This work used an optimization software called OptDef, made by a company called OptTek [167]. This software was selected due to the author's extensive experience with this software's capabilities. The latest version of the OptDef software includes a basic integration layer that allows a user to run any program with the OptDef optimizer. The integration layer is similar to the wrapper function explained in section 7.3. The user supplies the program input variables and ranges and output variables in a comma separated (.csv) file. The OptDef program then uses its internal optimization routines to calculate the next needed design runs. It writes these inputs to a file and calls the user's integration program. This integration program takes the OptDef supplied input file, writes the appropriate inputs to the correct location on the program's inputs and then runs the program. OptDef then reads the outputs and repeats the process. The main interface for the OptDef program is shown below in Figure 148.

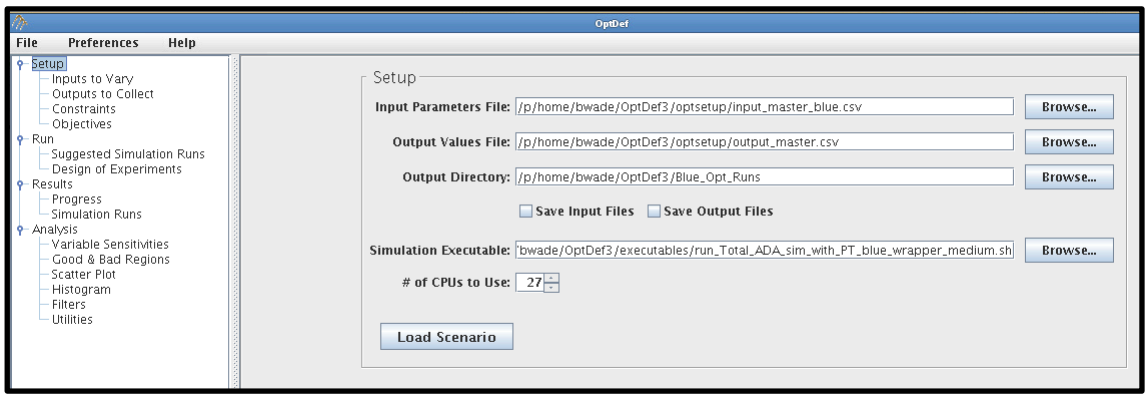

Figure 148: OptDef Optimization Software Screen Shot

8.4. Optimization of Red Fire Plan for Base Case

The three test cases for the red fire plan, small, medium, and large, were each optimized independently. The optimization criteria was to maximum the fraction (percentage) of aircraft destroyed, maximize the fraction of POL sites destroyed, and minimize the fraction of available MOSs that were destroyed. This multi-objective optimization created a frontier of non-dominated solutions for each fire plan. Each point on the frontier represents a combination of inputs that achieves a non-dominated solution in at least one of the optimization goals.

Each fire plan included an identical setup for the input variables. The only difference was that each included a constraint that ensured that the number of missiles in the fire plan matched the correct size (small, medium, and large). Additionally, there was a constraint to ensure that the percent of missiles aimed at aircraft and POL sites did not exceed 100%. The inputs and ranges for those inputs are shown below in Table 50.

Table 50: Red Fire Plan Optimization Variables

Input Variable	Type	Minimum	Maximum
Number of TBM1	Integer	0	20
Number of TBM2	Integer	0	20
Number of TBM3	Integer	0	20
Number of CM1	Integer	0	20
Number of CM2	Integer	0	20
TBM1 – Percent Aimed At Airfield	Float	0	100
TBM2 – Percent Aimed At Airfield	Float	0	100
TBM3 – Percent Aimed At Airfield	Float	0	100
CM1 – Percent Aimed At Airfield	Float	0	100
CM2 – Percent Aimed At Airfield	Float	0	100
TBM Release Altitude for Submunitions	Float	10,000 m	30,000 m
CM Release Altitude for Submunitions	Float	50 m	500 m
Percent of Airfield Missiles Aimed at Aircraft	Float	0	100
Percent of Airfield Missiles Aimed at POL sites	Float	0	100

The results of the optimization for the small, medium, and large fire plans are shown below in Figure 149, Figure 150, and Figure 151. These images show the optimal frontier of non-dominated solutions. The optimal frontier is further illustrated in Figure 152, which shows all the test points for the large attack, to include the dominated test points, along with the optimal frontier of points. All points in grey in Figure 152 are dominated in at least one output dimension be the points on the frontier. The two horizontal axis are the fraction of aircraft destroyed and fraction of POL sites destroyed. The vertical axis is the fraction of MOSs available on the runway for use. The red force is trying to maximize the fraction of aircraft and POL sites destroyed and minimize the fraction of MOSs available.

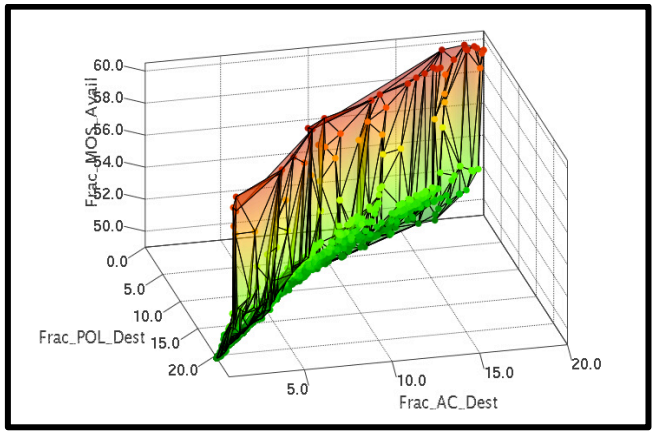

Figure 149: Optimal Frontier for Small-Sized Fire Plan

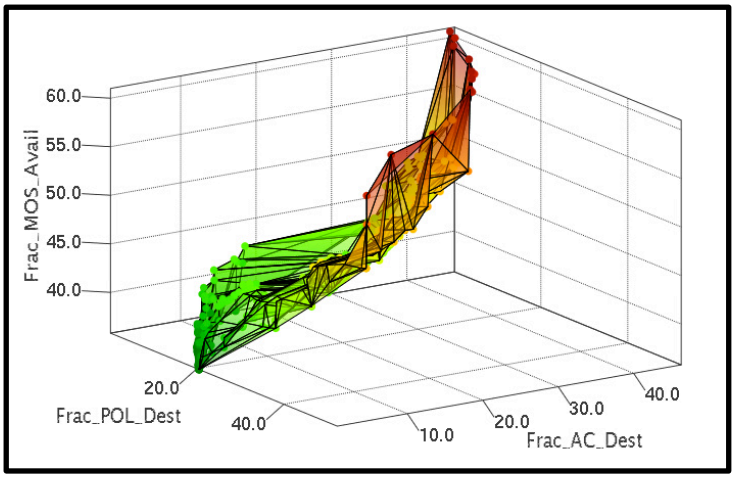

Figure 150: Optimal Frontier for Medium-Sized Fire Plan

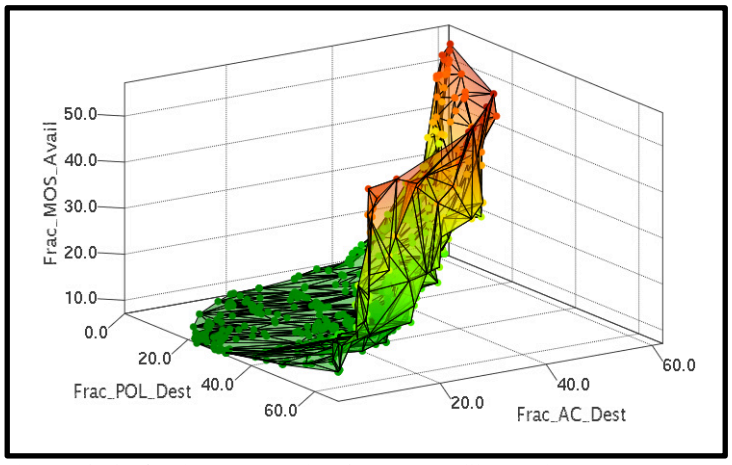

Figure 151: Optimal Frontier for Large-Sized Fire Plan

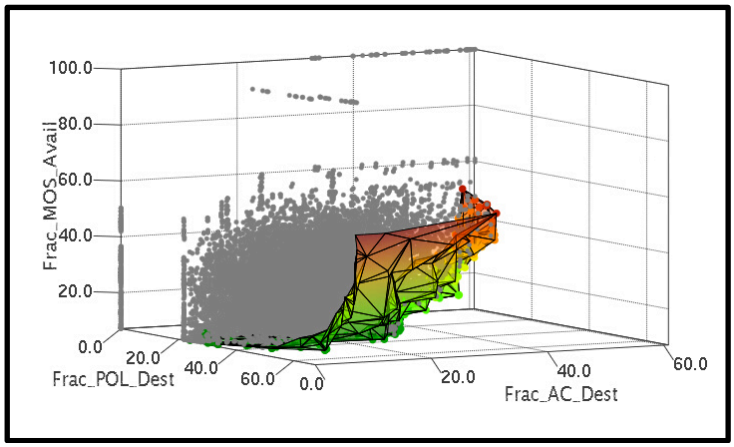

Figure 152: Large Fire Plan with Both Dominated and Frontier Test Points

8.5. Analysis of Optimized Red Fire Plan for Base Case

Examining the optimal frontier for each enemy fire plan shows why the optimal points achieved greater damage than the non-optimal points. This also answers the first research question: Will a fire plan optimized to achieve a given effect (destruction of aircraft, POL sites, or runway) be the fire plan with the greatest number of leakers? The hypothesis for this research question was such that: a fire plan weighted with CMs, as opposed to TBMs, will destroy more point targets such as POL sites and aircraft and a fire plan weighted with TBMs, as opposed to CMs, will destroy more area targets such as the runway. These will not necessarily be the fire plans with the most leakers. The analysis below will show that this hypothesis is mostly true; however, there is discrepancy for which targets are classified as point targets.

The point targets in this scenario were originally thought to be the POL sites and the aircraft on the airfield. The POL sites were fixed in place, but the aircraft changed position on every test iteration as explained in section 6.4.1. This made a difference in the results. The stationary POL targets were much more susceptible to the higher accuracy of the CMs. The CMs have a CEP much smaller than that of the TBMs. Because the aim points are planned near the targets and the POL sites cannot move away from those aim points, any leakers that were aimed at the POL tended to destroy at least one POL site. This is illustrated in Figure 153 using contour plots generated in JMP. The red area of the three fire plans shown in the images is the cases with greater numbers of the POL sites destroyed. The x and y axis are the number of CM and TBM leakers respectively.

All three sized fire plans showed that the greatest number of POL sites destroyed occurred when the number of CM leakers was greatest. A greater number of TBM leakers also helped to destroy more POL sites. Meaning that in this case, the greatest number of leakers equated to the greatest damage. This is why the greatest number of POL sites destroyed (darkest red color in the figure) is in the upper right. However, in all three cases, a high number of CMs resulted in a greater number of POL sites destroyed for a given number of TBM leakers. This is especially evident in the large attacks. In a medium sized attack, the effect is the least pronounced. In this attack a greater number of TBMs or CMs seems to result in a greater number of POL sites destroyed.

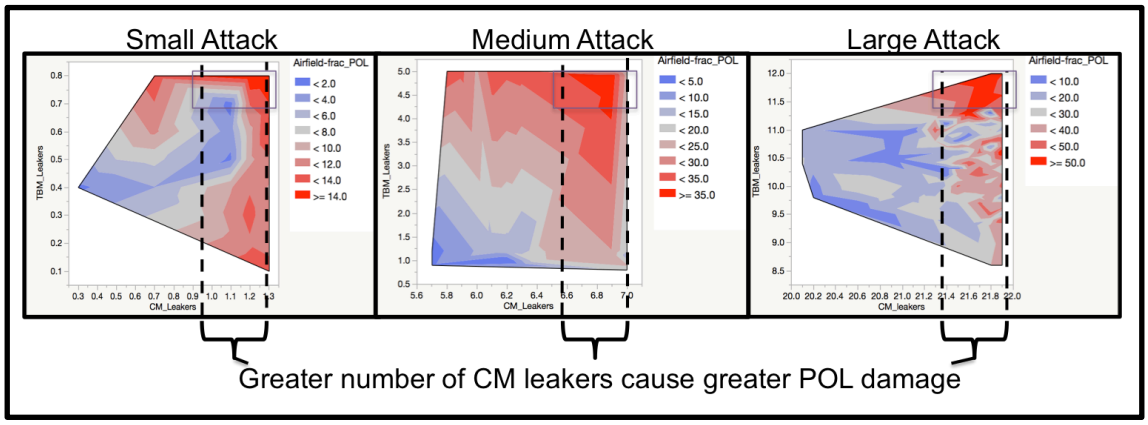

Figure 153: POL Damage Analysis From Three Red Fire Plans

It was originally thought that the aircraft on the airfield were also point targets; however, their mobility makes them different from the POL sites. Very few aircraft were destroyed in any of the optimal fire plans for the small sized attack, so that that attack is not addressed below. The results for the medium and large sized attacks are shown in Figure 154. In this figure, the red areas show the attacks with a larger number of aircraft destroyed. The x and y axis are the number of CM and TBM leakers that impacted the airfield. The largest number of aircraft destroyed came from fire plans that did not have

the largest number of leakers. This was due to the increased blast radius of TBMs and the fact that the aircraft were actually an area target, which will be further explained below.

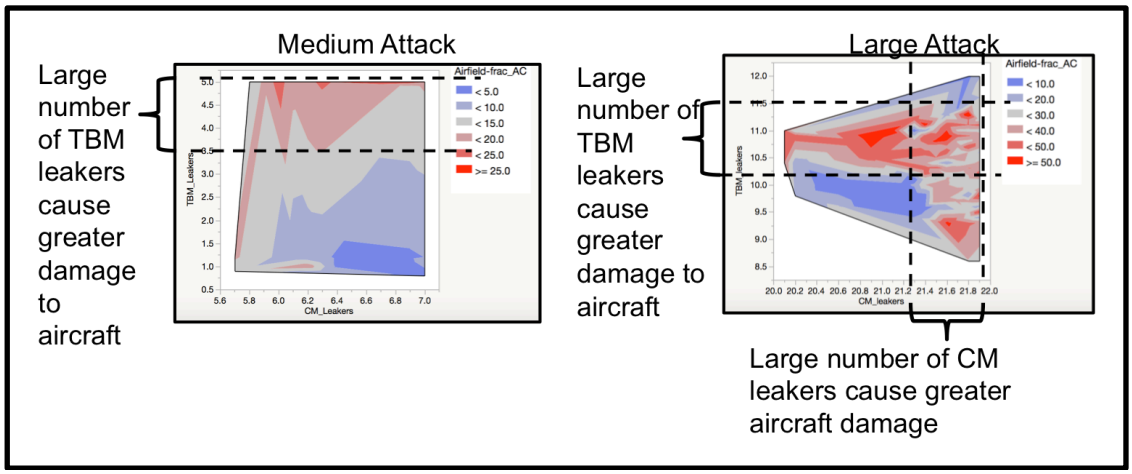

Figure 154: Aircraft Damage Analysis for the Medium and Large-Sized Fire Plans

The aim points for the red missiles were distributed evenly around the known parking locations on the airfield. However, on each trial run, the first aircraft was randomly placed, but then each subsequent aircraft was placed to maximize the minimum distance between points. This meant that for each trial run the aircraft were in new locations. If an aircraft happened to be located near one of the randomly chosen targeted aim points, then there was a high probability that it was destroyed. So, even if an aim point was hit accurately, such as would be the case with CMs since they have a smaller CEP, there might not be aircraft within the lethal radius of that aim point. This resulted in TBMs, with their larger lethal area, being more effective.

To further illustrate this point, the medium sized attack contour plot and its associated leaker distributions are shown in Figure 155. From the distribution plot on the right side of this figure, it is evident that a large number of TBM1 and TBM3 leakers resulted in a greater number of aircraft destroyed. TBM1 and TBM3 were the two TBMs

with unitary warheads. This meant that they had the largest blast radius. Note that CM1 was also prevalent in these fire plans. CM1 was the CM armed with runway penetrating munitions. These munitions had no effect against aircraft. The reason that the optimal fire plans included a larger number of CM1 missiles was that these fire plans were constructed with an equal number of CMs and TBMs. Since the TBMs were more effective against aircraft rather than the CMs, the optimal solution included TBMs aimed at aircraft. This meant that the CMs included in the fire plan were dedicated to the runway. This helped achieve a balanced effect of destruction of aircraft and the runway. Overall, this meant that the fire plans with the greatest number of leakers did achieve a large number of aircraft destroyed, but so did raids that maximized just the number of TBM leakers alone as viewed in the upper portion of the contour plot on the left side of Figure 155.

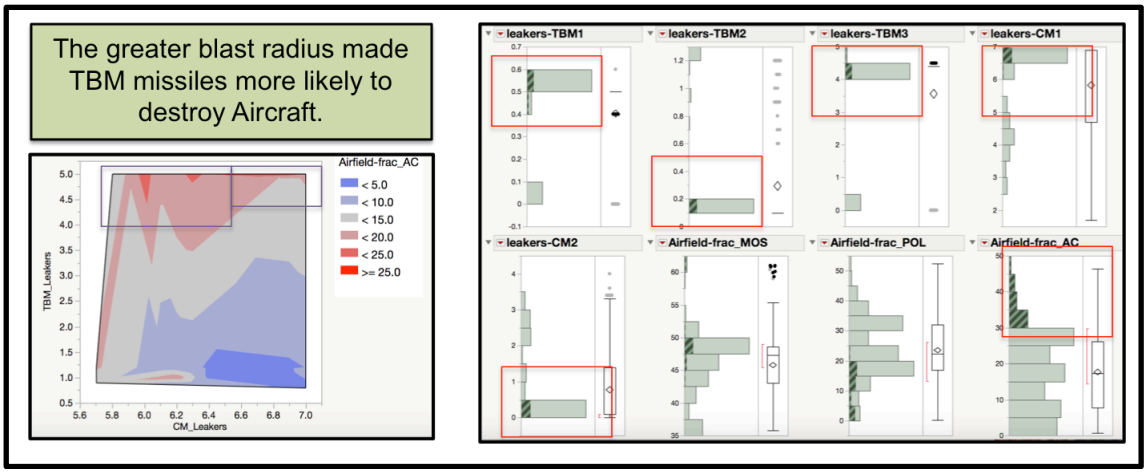

Figure 155: Damage Analysis of Attacks on Aircraft from Medium-Sized Raids

This same logic holds for the larger fire plan. From the contour plot on the left side of Figure 156, it is evident that the fire plans with the greatest number of leakers (upper right corner) are not the fire plans that resulted in the greatest damage to aircraft (dark red areas). From the distributions on the right side of the figure it is again evident

that the greatest damage to aircraft occurred with fire plans that had a large number of TBM1 and TBM3 leakers. With more leakers, a greater number of aim points could be targeted and because of the higher accuracy of the TBM3, the fire plans the included more TBM3 missiles achieve greater effects.

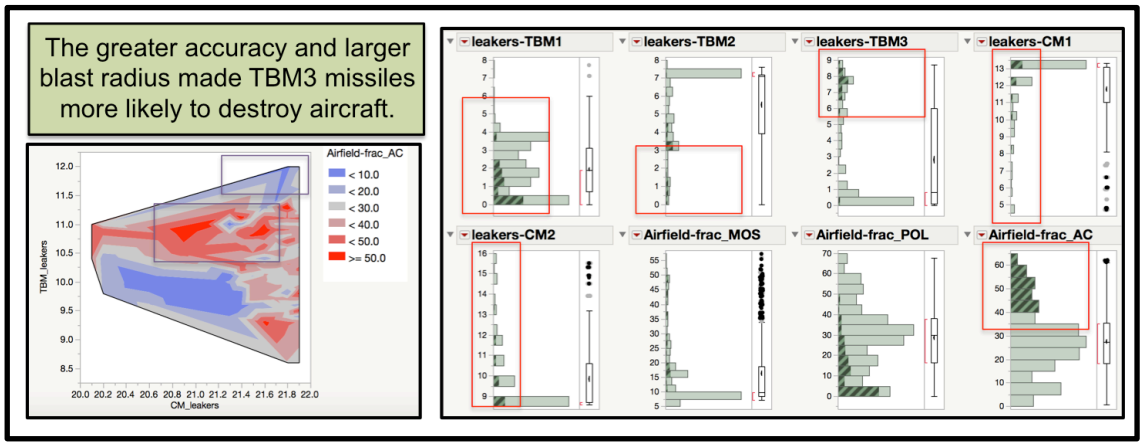

Figure 156: Damage Analysis of Attacks on Aircraft from Large-Sized Raids

The runway in this scenario is 10,000 feet long and 500 feet wide. This makes it an area target as opposed to a point target. An area target is a target that covers a large amount of space, making it much more likely to be struck by a missile. Missiles are aimed at the vicinity of the target area as opposed to individual targets. This analysis also included a special class of munitions called runway-penetrating munitions. These munitions are able to tunnel into the concrete of the runway before exploding in order to cause greater damage (see section 6.2). Because of this, those missiles that carried the runway penetrating munitions (TBM2 and CM1) were more likely to cause greater damage to the runway. This is especially evident in the large-sized attack as shown in Figure 157. The most damage to the runways did not come from the raids with the largest number of leakers (upper right corner of the contour plot). It came from raids

with the greatest number of TBM2 and CM1 missiles, the missiles that carried the runway penetrating munitions.

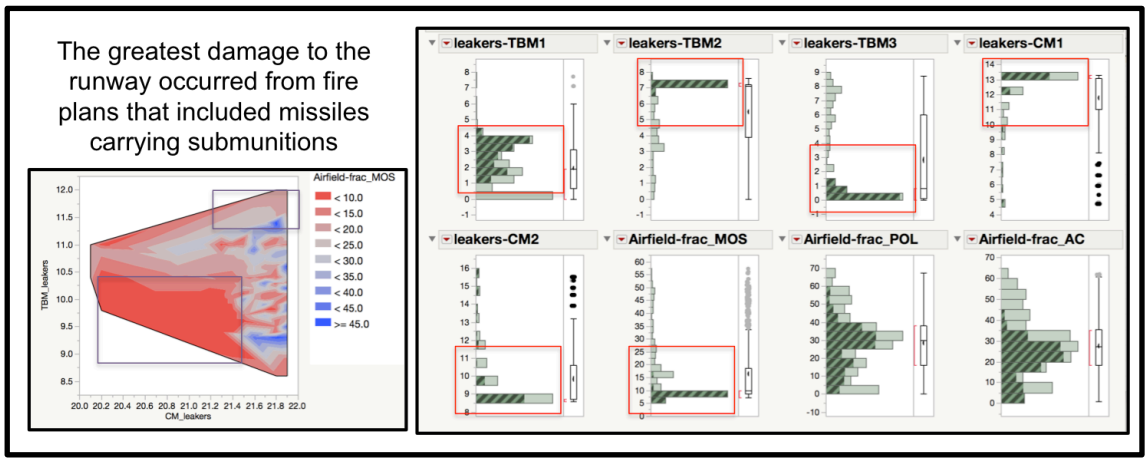

Figure 157: Damage Analysis of Attacks on the Runway from Large-Sized Raids

The same trend is also seen in the medium-sized attack shown below in Figure 158. Again, the raids with the largest number of leakers did not result in the greatest damage to the runways. Instead, the raids with the largest leakers of the missiles carrying the runway penetrating munitions (CM1 and TBM2) resulted in the greatest damage to the runway.

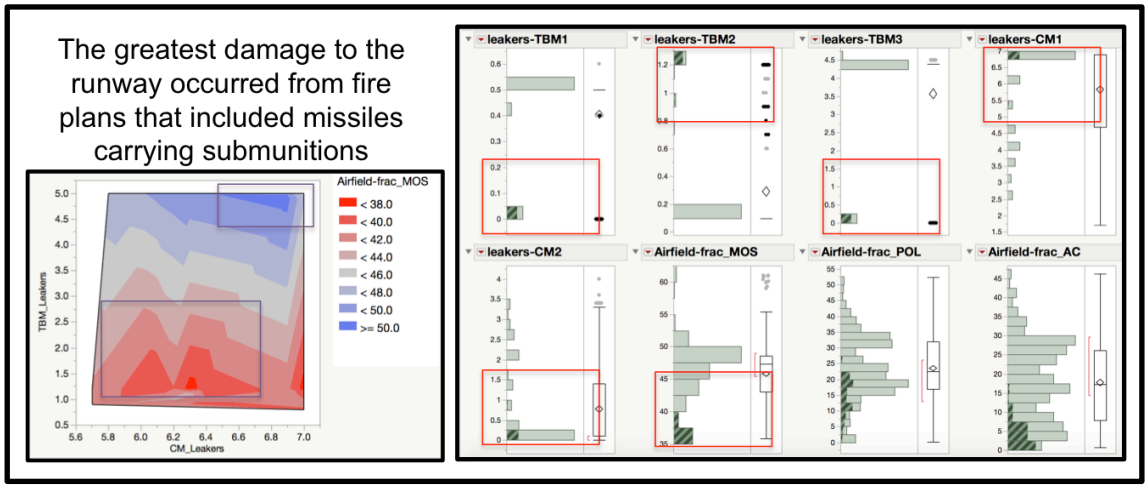

Figure 158: Damage Analysis of Attacks on the Runway from Medium-Sized Raids

Interestingly, this trend did not necessarily carry through to the small raids. The analysis of these sized raids is shown in Figure 159. The contour plot on the left side of this figure again suggests that the raids with the greatest number of leakers did not result in the most damage to the runway, However, an examination of the size of each axis will show that the overall change in the number of leakers for all raids was less than 1 missile and the change in the fraction of MOSs was less than 5% (less than one MOS). This is because the small sized raid only included 5 CMs and 5 TBMs, so there were not many missiles to leak through the defenses. This makes is difficult to draw any definitive conclusions about the cause of the changes since those changes were extremely small.

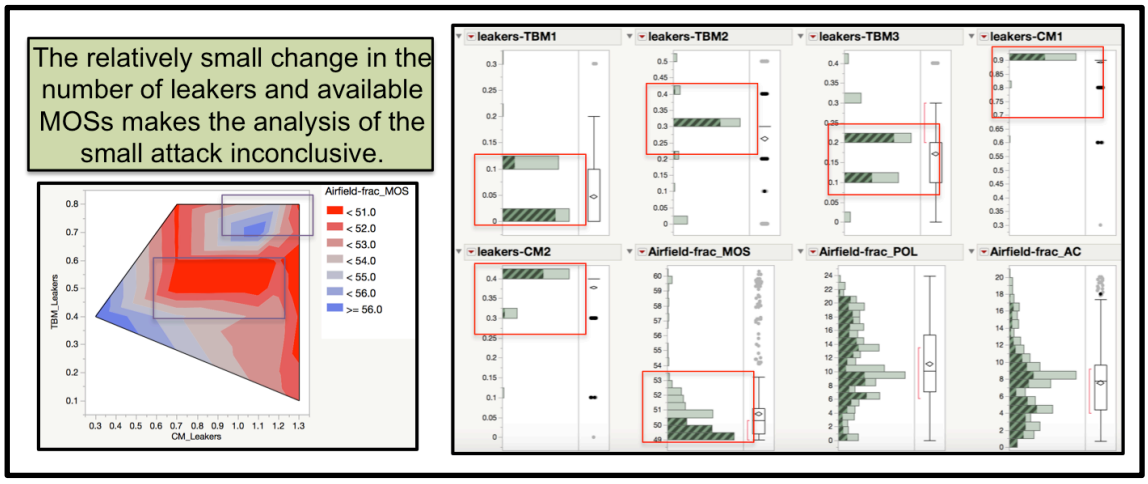

Figure 159: Damage Analysis of Attacks on the Runway from Small-Sized Raids

This analysis of the optimal red fire plans for the base case answers the first research question. The optimal fire plans for a given effect are not necessarily the fire plans with the greatest number of leakers. Instead, the optimal fire plans are those fire plans that maximize the number of leakers of a particular type of munition that is itself optimized to achieve a certain effect. If the desired effect is to destroy fixed-point targets such a POL sites, then the fire plans that maximize accuracy with a greater number of CMs are optimal. If that desired effect is to destroy mobile assets such as aircraft, then

fire plans that maximize the number of TBM leakers, especially TBM leakers with a smaller CEP, are the optimal. Finally, if the desired effect is to destroy the runway, then the fire plans that maximize the number of leakers carrying submunitions are the optimal fire plans.

8.6. Optimization of Blue Tactics Only Against the Optimized Fire Plans

The last section showed how the enemy fire plan could be optimized to maximize different effects such as destruction of aircraft, runways, or fuel sites. No single fire plan was able to maximize all effects simultaneously. The enemy force must tailor each strike package to achieve their desired effect. Unfortunately, the ADA units do not know what this effect is beforehand. Thus, the ADA tactics must be optimized to minimize the damage from any one of the optimal enemy fire plans.

The main decision variables available to the ADA units are when to begin engaging each type of threat, how many interceptors to shoot at each missile, known as the shot doctrine, and which interceptor to target against which missile. These decision variables and their associated ranges are listed in Table 51.

Table 51: ADA Tactics Inputs Variables

System	Variable	Value Range	Units
Upper Tier (UT)	Maximum Engagement Altitude - TBM	25,000-60,000	meters
	Minimum Engagement Altitude - TBM	25,000-60,000	meters
	Shot Doctrine - TBM	1 or 2	each
Lower Tier (LT)	Minimum Engagement Altitude - TBM	10,000-30,000	meters
	Minimum Engagement Range - TBM	2,000-80,000	meters
	Shot Doctrine - TBM	1 or 2	each
	Shot Doctrine – CM	1 or 2	each
	Priority Interceptor – TBM	A, B, or C	n/a

Engagements against TBMs are altitude dependent and engagements against CMs are range dependent. Within the simulation, a constraint was imposed for both the LT

and UT systems that caused the minimum engagement altitude to be less than the maximum engagement altitude by at least 5,000 meters. This 5,000-meter buffer ensured that the engagement space was large enough that the simulation would shoot at least one interceptor. In a similar fashion the minimum engagement range was restricted to at least 500 meters less than the maximum engagement range.

The layered defense structure explained in section 7.6 caused the LT system's maximum range and altitude to be dependent variables. This is because the LT system could not begin to engage TBMs until those TBMs were below the UT system's minimum altitude and the LT system could not engage CMs (maximum engagement range of CMs) until it stopped engaging TBMs (minimum engagement altitude of TBMs). Thus, the LT system's maximum altitude was calculated as the minimum of either the LT priority interceptor's maximum altitude or the 5,000 meters less than the UT's minimum engagement altitude. The LT system's maximum range was calculated using the TBM profile, CM cruise speed, and method explained in section 7.6.

These decision variables were tested and optimized using the OptDef software described in section 8.3. During the optimization for each set of blue decision variables, all fire plans on the optimal frontier were tested. This meant that each test case of ADA decision variables was tested against several hundred optimal fire plans. Once all fire plans were tested against the set of decision variables, the damage to the runway, fuel, or aircraft was averaged so that the output was the mean effect from all the optimal fire plans.

The results of this optimization are shown below in Figure 160, Figure 161, and Figure 162 for the small, medium, and large-sized attacks. In each image, there are two

graphs. In both graphs, the vertical axis is the average cost of the ADA interceptors shot using the relative costs explained in section 7.2.2. All costs are relative to the LT interceptor type A, which has a cost of one unit. The x and y-axis of the left graph of each figure shows the average fraction of MOSs available and the average number of POL sites destroyed. The graphs on the right of each figure show the average number of MOSs again and the average number of aircraft destroyed. In these simulations, the ADA defenses are trying to minimize cost, maximize the number of MOSs available, and minimize the number of fuel sites (POL) and aircraft (AC) destroyed.

The optimal frontier for the blue ADA systems against a small-sized optimal attack is shown below in Figure 160. This simulation shows the results of 33,259 design points. Each of these design points is a combination of the decision variables from Table 51. There are 1,327 optimal points on the frontier.

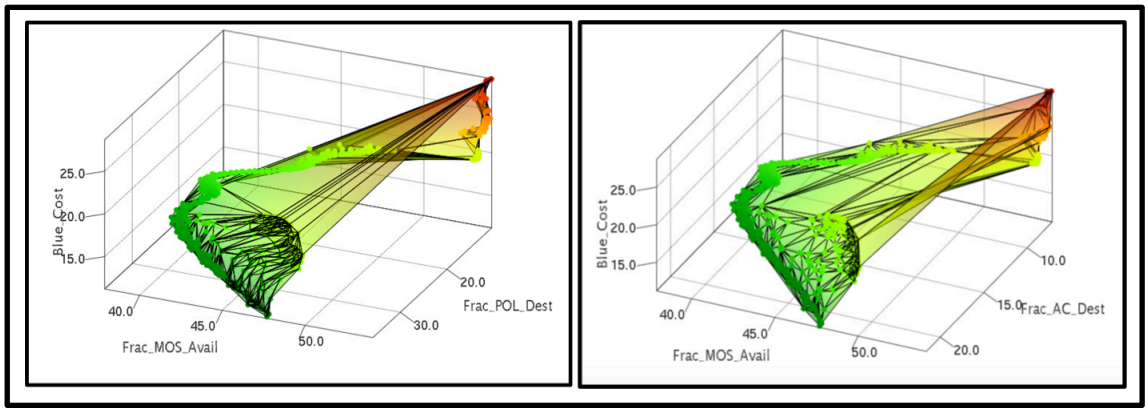

Figure 160: Optimal Frontier for ADA Optimization Against a Small-Size Attack

The optimal frontier for the medium-sized attack is shown in Figure 161 and for a large-sized attack in Figure 162. The optimization against the medium sized attack consisted of 41,217 test combinations of which 2,179 were on the optimal frontier. For the optimization against the large attack, 36,719 combinations were tested and 1,327 were on the optimal frontier.

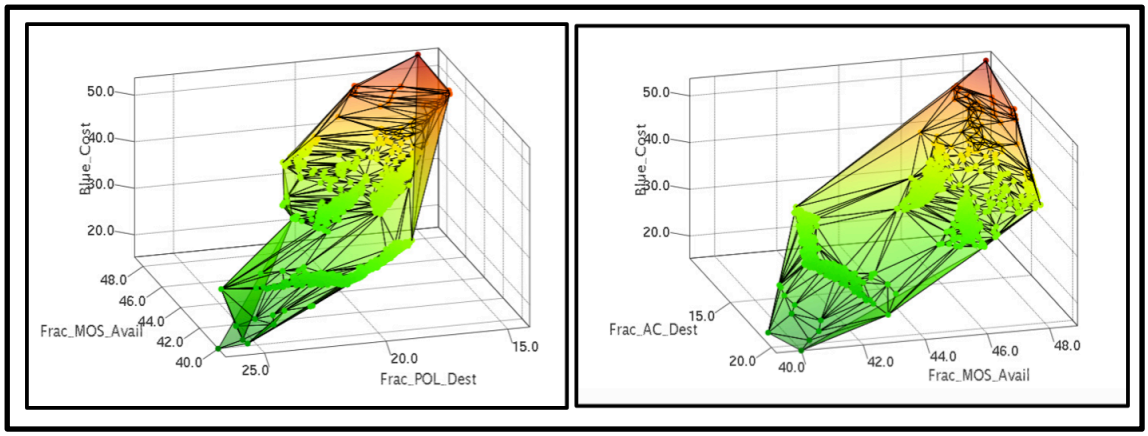

Figure 161: Optimal Frontier for ADA Optimization Against a Medium-Size Attack

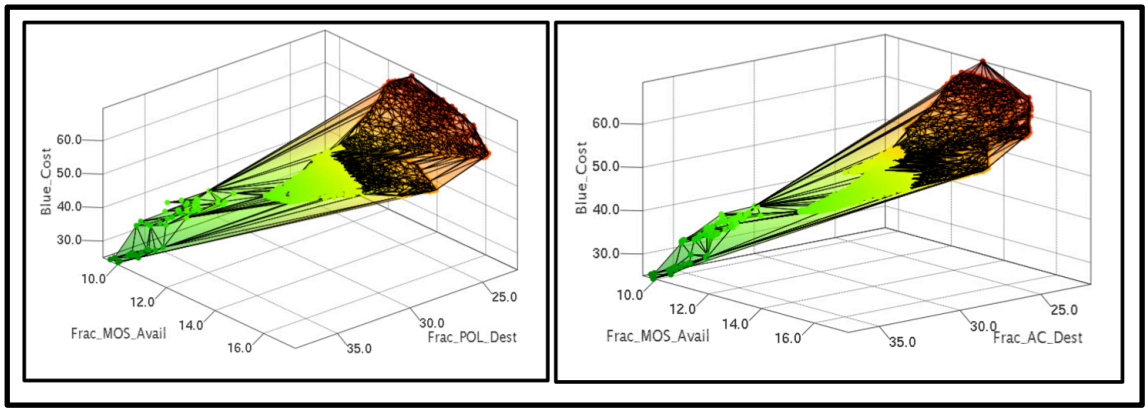

Figure 162: Optimal Frontier for ADA Optimization Against a Large-Size Attack

8.7. Selection of an Alternative on the Optimal Frontier - TOPSIS

Each point on the optimal frontiers described in the previous section represents a combination of blue tactics (i.e. altitudes to begin and end engagements, number of interceptors to shoot, which interceptors to shoot, etc.). Each of these combinations is optimal in that it achieves a non-dominated solution meaning that at least one objective (lowest cost, lowest fraction of aircraft destroyed, lowest fraction of POL destroyed, or greatest fraction of MOSs available) is optimal. The ADA systems can only execute one of these optimal sets of tactics. Therefore, a single point (set of tactics) on the optimal frontier must be chosen.

The selection of the optimal set of tactics is a multi-objective problem. The goal is to simultaneously maximize or minimize several objectives and the chosen set of tactics will represent a compromise between these goals. Each goal, however, is not equally important. Some goals such as minimization of the number of aircraft destroyed might be more important than the cost of the interceptors fired or the amount of runway damaged since the runway is easily repaired. Therefore a multi-attribute decision making (MADM) tool that includes a weighted goal matrix is needed. The Technique for Ordered Preference by Similarity to the Ideal Solution (TOPSIS) fits all these criteria.

The idea for TOPSIS originated from Hwang and Yoon. They proposed selection of the optimal solution based on the closeness to the ideal positive solution and the furthest from the ideal negative solution [168]. This idea forms the basis of TOPSIS which can be best summarized as a decision making tool that uses weighted criteria to measure the Euclidean distance of each alternative to the ideal positive and ideal negative solutions. The selected alternative has the closest distance to the ideal positive solution and the furthest distance from the ideal negative solution. The ideal positive solution is a fictitious solution that, for each criteria, contains the best value (maximum for criteria that are maximized or minimum for criteria that are minimized) from all the sets of alternatives. The ideal negative solution contains the worst value from any alternative. In other words, both the positive and negative ideal solutions combine different values from different alternatives to form the hypothetically best possible alternative. This is illustrated in Figure 163.

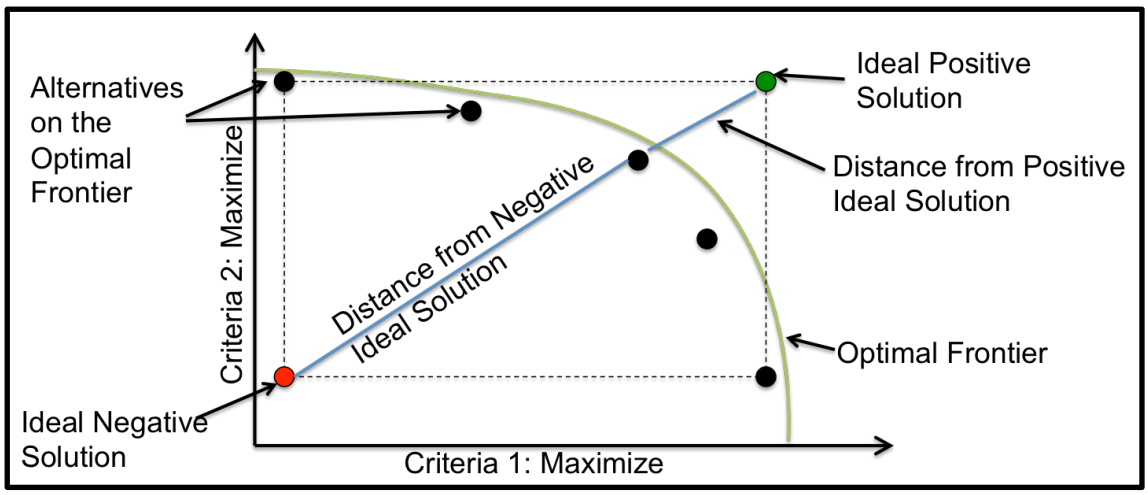

Figure 163: TOPSIS Methodology

TOPSIS begins with an decision matrix (DM). This is a MxN matrix made up of M criteria (C_m) with N alternatives (A_n). In this context, the DM is made up of all the points on the optimal frontier. This decision matrix is shown below with the weights (W_j) shown next to the associated criteria [169].

$$DM = \begin{array}{c} \\ W_1\ C_1 \\ W_2\ C_2 \\ \vdots\ \ \vdots \\ W_m C_m \end{array} \begin{array}{c} \begin{array}{cccc} A_1 & A_2 & \dots & A_n \end{array} \\ \begin{bmatrix} x_{11} & x_{12} & \dots & x_{1n} \\ x_{21} & x_{22} & \dots & x_{2n} \\ \vdots & \vdots & \ddots & \vdots \\ x_{m1} & x_{m2} & \dots & x_{mn} \end{bmatrix} \end{array}$$

Each criteria will have its own scale based on the attributes of that criteria. Therefore, the first step of TOPSIS is to normalize the criteria to a scale of 0-1 in order to form the normalized decision matrix (NDM). Without this step, the criteria with the largest scale or largest range would dominate the decision process. Each criteria (row in the DM) is normalized by dividing the score (x_{ij}) by the root-sum of squares (RSS) for that criteria (row in the DM):

$$NDM = R_{ij} = \frac{x_{ij}}{\sqrt{\sum_{i=1}^{m} x_{ij}^2}}$$

This will form the NDM.

$$NDM = \begin{matrix} . \\ C_1 \\ C_2 \\ \vdots \\ C_m \end{matrix} \begin{matrix} \begin{matrix} A_1 & A_2 & \dots & A_n \end{matrix} \\ \begin{bmatrix} R_{11} & R_{12} & \dots & R_{1n} \\ R_{21} & R_{22} & \cdots & R_{2n} \\ \vdots & \vdots & \ddots & \vdots \\ R_{m1} & R_{m2} & \dots & R_{mn} \end{bmatrix} \end{matrix}$$

The next step is to incorporate the weights for each criteria. These weights can be formed from a survey of the decision makers from another MADM technique such as the analytical hierarchy process (AHP) [169]. These weights should be normalized so that they sum to a total of one. Using these normalized weights, the value of each alternative is found by:

$$V_{ij} = W_j * R_{ij}$$

Incorporating the weights forms the value decision matrix (VDM). Each alternative has been normalized and weighted. The next step is to use the VDM to select the positive ideal solution (PIS) and the negative ideal solution (NIS). This is done by selecting the best and worst value for each criteria from amongst all the alternatives [169]:

$$PIS = A^+ = [V_1^+, V_2^+, \dots, V_n^+] \ where \ V_j^+ = \left\{\left(\max\left(V_{ij}\right) if \ j \in J\right), \left(\min\left(V_{ij}\right) if \ j \in J'\right)\right\}$$

$$NIS = A^- = [V_1^-, V_2^-, \dots, V_n^-] \ where \ V_j^- = \left\{\left(\min\left(V_{ij}\right) if \ j \in J\right), \left(\max\left(V_{ij}\right) if \ j \in J'\right)\right\}$$

where *J* is the set of criteria that are to be maximized and *J'* are the set of criteria to be minimized.

The final step in the TOPSIS methodology is to calculate the Euclidean distance between each alternative and the PIS and NIS. Here S^+ is the distance to the PIS and S^- is the distance to the NIS [169].

$$S_i^+ = \sqrt{\sum_{j=1}^{n} \left(V_j^+ - V_{ij}\right)^2} \quad i = 1,2, \ldots m$$

$$S_i^- = \sqrt{\sum_{j=1}^{n} \left(V_j^- - V_{ij}\right)^2} \quad i = 1,2, \ldots m$$

The relative closeness (C) to the PIS of each alternative is then found by the following equation [169]:

$$C_i = \frac{S_i^-}{S_i^+ + S_i^-}$$

Once the relative closeness for all alternatives has been calculated, these closeness values are rank ordered from largest to smallest for comparison. The alternative with the largest value of relative closeness is the best alternative.

8.8. Selection of the Optimal Set of Blue Tactics - TOPSIS

The previous section explained the TOPSIS methodology for selecting an alternative based upon weighted criteria. This methodology was used to select the set of ADA tactics that would achieve the best compromise of all the criteria based upon the weight matrix. There were four criteria in this selection, the fraction of aircraft destroyed, the fraction of POL sites destroyed, and the fraction of MOSs available on the runway, and the cost of the blue interceptors fired against incoming missiles. All criteria were to be minimized except the fraction of MOSs available, which was to be maximized.

The weights for these criteria are expressed below in Table 52. The fraction of available MOSs was weighted the lowest mainly because only a small number of MOSs are required to support most operations and many airfields now have rapid runway repair kits that can repair damaged MOSs in a very short amount of time [106, 170]. This

criterion was the basis of comparison for the other three. The aircraft are the most expensive and critical asset on the airfield. Therefore, they were weighted as five times more important than preventing damage to the runway. The next most important criteria was the fraction of POL sites destroyed. There are a limited number of these fuel sites and if too many are destroyed then operations on the airfield could be hindered until the sites are repaired. Defending the POL sites was weighted as three times more important than defense of the runway. Finally, the cost of the blue interceptors was the next most important criteria since a long-term conflict would require a defense that conserves resources. Reducing the cost of the defense was weighted as twice as important as defense of the runway.

Table 52: Decision Matrix for ADA Tactics Optimization

Criteria	% AC Destroyed	% POL Destroyed	% MOS Available	Relative Cost
Weight	5	3	1	2
Normalized Weight	0.455	0.273	0.090	0.182
Direction of Optimization	Min	Min	Max	Min

Using the weigh matrix with the TOPSIS methodology resulted in a set of optimized tactics for each sized attack. This optimized tactics set is shown below in Table 53 and graphically depicted in Figure 164 and Figure 165. The maximum altitude and maximum range are starred because these are calculated values and not true decision variables. The maximum altitude for the LT system is the smaller of either 5,000 meters below the UT system's minimum altitude or the LT system interceptor's maximum capable altitude. The maximum range for the LT system is calculated based on the equation in Figure 146.

Table 53: Optimized ADA Tactics from Base Case

System	Lower Tier								Upper Tier		
Attack Size	Altitude		Range		Shot Doctrine		Priority Interceptor		Altitude		Shot Doctrine
	Max*	Min	Max*	Min	CM	TBM	CM	TBM	Max	Min	
Small	20,000	9,090	4,552	500	1	1	C	C	53,711	38,129	1
Med	25,000	12,236	6,172	500	1	1	C	B	53,090	34,886	1
Large	30,000	24,830	11,923	500	1	1	C	A	57,677	43,677	1

The TBM engagements are altitude dependent. Figure 164 below shows the engagement altitudes of the UT and LT system for the base case and the optimized engagements altitudes for the three attack sizes. In addition, each interceptor's full engagement space and probability of kill (pk) is also plotted for reference (see section 7.2.3 for a description of the weapon pk values). The dark band within the pk diagram is the engagement window for each interceptor. This is the area between the maximum and minimum engagement altitude. In the base case, the UT system uses its interceptor's full engagement space. This crowds out the LT system, which must begin engagement well within its operating envelope.

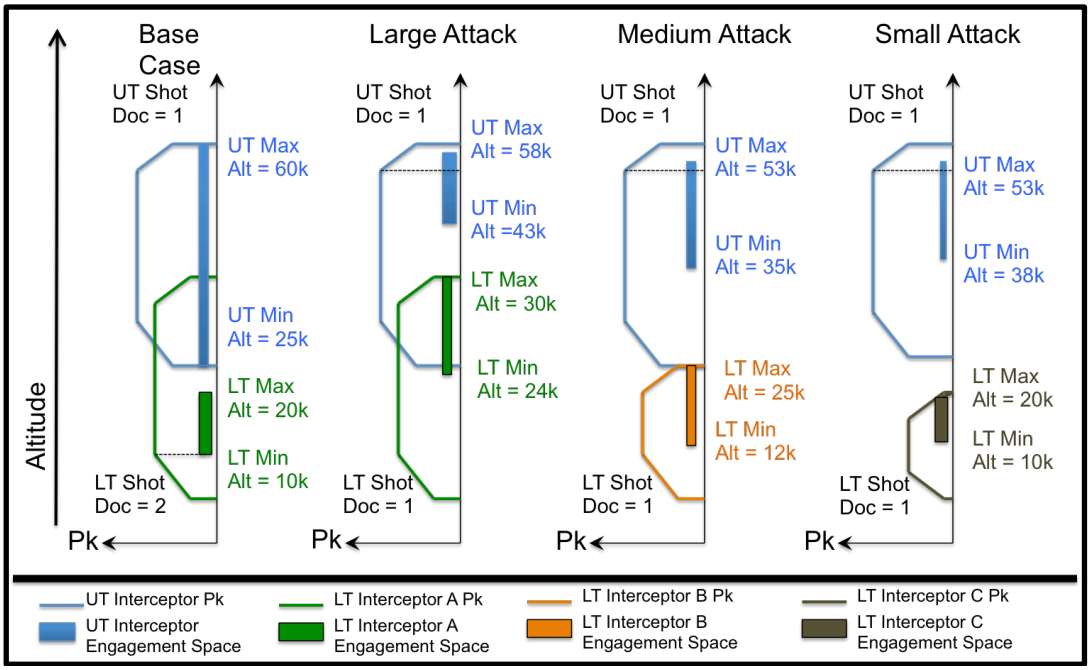

Figure 164: TBM Engagement Altitudes for Optimized Tactics

For the optimized cases, the UT systems all begin their attacks at an altitude where the pk value is greatest. This is shown as the dotted line in each of the three attack size cases. The lower limit of the engagement space is also well within the UT interceptor's envelope. This caused the number of possible engagements for the UT interceptor to remain at one. This is likely due to the high cost of the UT interceptor.

In all three cases, the optimized tactics have the LT interceptor beginning its engagements at the very top of its engagement envelope. This is because the CM engagements cannot begin until after the TBM engagements (see Figure 165 for CM engagement space). The medium attack case had the largest engagement window for the LT system. For the large attack, the interceptor used was interceptor A. This interceptor can have 12 interceptors in flight at once and travels the fastest of the three LT interceptors. This large number meant that the engagement space could be smaller since the interceptors would reach their targets faster and a larger number interceptors could be used in that space. This gave more engagement space for defense against the CMs (see Figure 165).

For the medium attack case, the interceptor used was interceptor B. With 15 missiles inbound and only 16 interceptor B missiles on the rails, the LT system was saturated. This meant that all interceptors had to be used. Interceptor B is limited to 10 in flight at once and travels 40% slower than interceptor A, so it required a larger engagement window to complete all its interceptors. This left only a small window for CM intercepts.

In the small-sized attack size case, there were more than enough LT interceptor C missiles to address the five inbound threats of each type. Interceptor C can also have five

interceptors in flight and the engagements occurred at a lower altitude since the LT interceptor C has the smallest engagement envelope. Also, interceptor C traveled at a speed between that of A and B (20% slower than interceptor A). This meant that the time from launch to intercept was very short so one or two intercepts could occur in the small window. This left more time for the CM engagements.

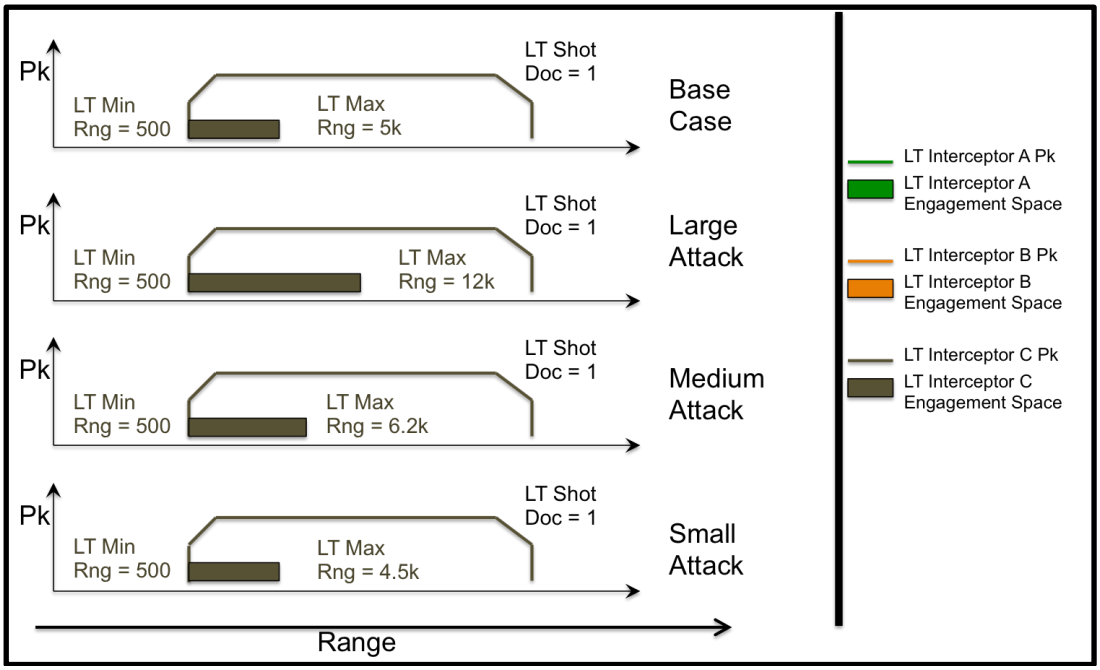

Figure 165: CM Engagement Ranges for Optimized Tactics

The results of these new tactics are shown below in Figure 166. In this figure, the yellow bars show the predicted average outcomes of the base case for each the evaluation criteria for each the three attack sizes. Three of the criteria are minimization criteria, fraction of aircraft destroyed, fraction of POL sites destroyed, and cost of the blue interceptors shot. The fraction of MOSs available is a maximization criterion. The blue bars show the predicted average outcomes using the prediction calculations. The largest difference between the base case and the optimized case occurs for the small attack size.

In the medium and large attack size, there is a large decrease in the average cost of the defense, but there is only a small improvement in the other criteria.

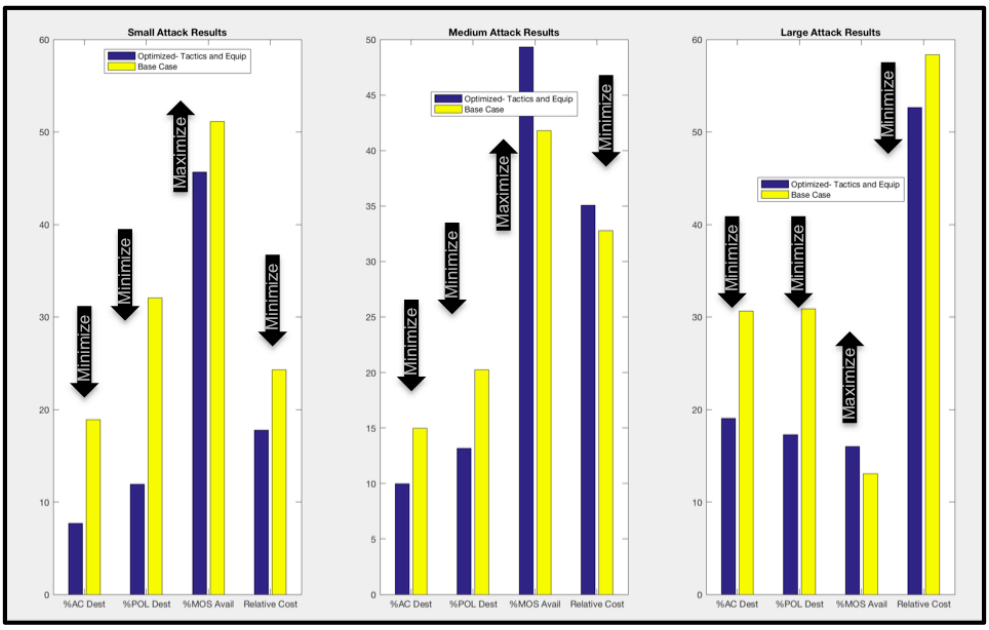

Figure 166: Predicted Average Outcomes for Base and Tactics Optimized Cases

8.9. Test the Optimal Set of Blue Tactics in High Fidelity Models

The optimization in the previous section used predictive models that estimated the average outcome of the high fidelity models. In order to validate the results, the base case and optimized case must be tested in the higher fidelity models. For both the base case and the optimized case, the inputs were coded into the EADSIM input files using a wrapper function similar to that described in section 7.3. For each sized fire plan, the optimized set of tactics was tested against all the fire plans on the red optimal frontier. The leakers from these simulations were then passed to the runway cratering and airfield effects models described in sections 6.2 and 6.4. Each of these simulations is stochastic, so this process was repeated 10-20 times. Because each sized attack contained 500-1,500 optimized fire plans on the optimal frontier, this meant that the process observed 5,000-30,000 results from the high fidelity simulations. The results of this test are shown below

in Figure 167. In this figure the red line is a cumulative distribution function (CDF) of the stochastic outcomes of the base case. The blue line is the CDF of the outcomes for the optimized case.

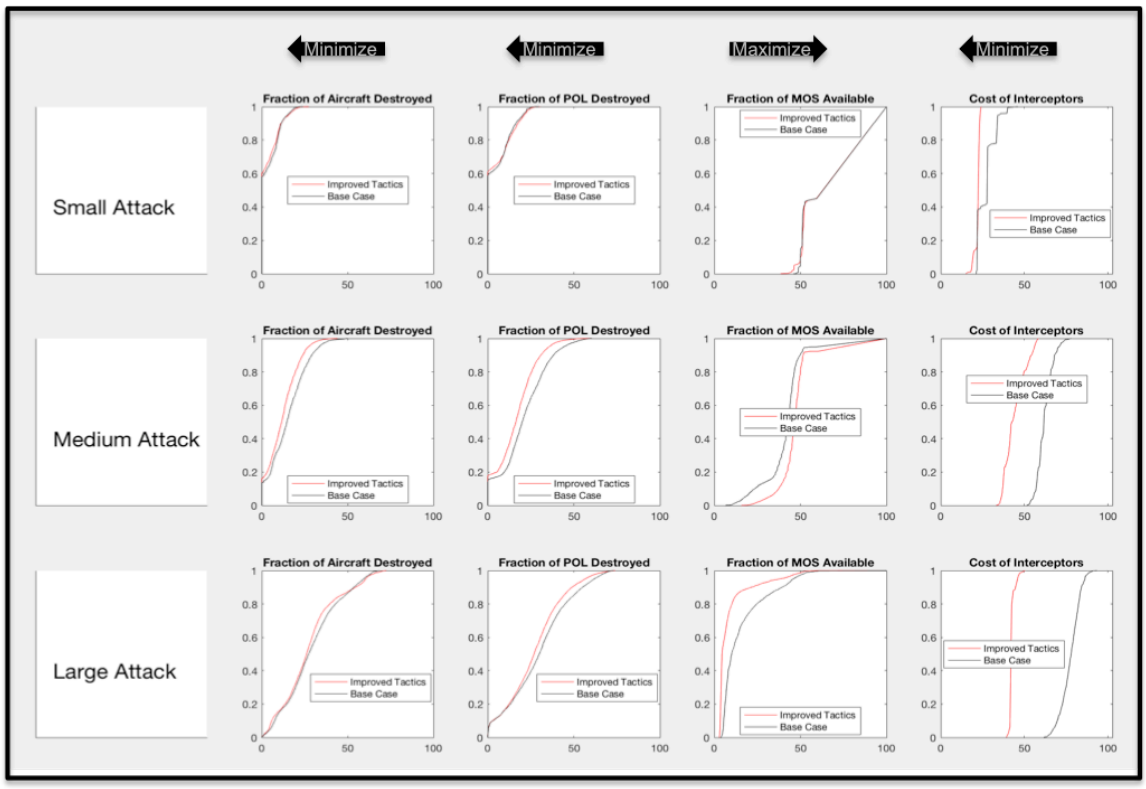

Figure 167: Simulation Results of the Base Case and Tactics Only Optimization

The results confirm those seen with the average outcome in Figure 166. The only major change from the predicted averages to the actual CDFs was that the small attack did not realize the reduction in damage to aircraft, POL sites, or the runway that was predicted from the TOPSIS results. Instead, the actual simulation results showed that the amount of damage was the same for both the base case and the optimized case. The small case, however, did realize the cost savings that was predicted by the TOPSIS results. For the medium and large-sized attack cases, there was a small improvement in the fraction of aircraft and POL destroyed and a large improvement in the cost of the

defense. Looking at the number of MOSs available, the medium-sized attack showed only a small improvement and the large-sized attack actually showed a reduction in the amount of runway available. This is the opposite of what the optimization was supposed to achieve; however, this is not surprising since that criteria was weighted the least.

Even though the optimized tactics appear to improve the defenses, the results are stochastic, so the improvement could be due to random chance. To show that this is not the case, a statistical test, the Student's T-Test of the means, can be preformed.

The Student's T-Test is a hypothesis test to determine if two sample means are different [133]. In the most formal sense, Student's original T-Test assumed equal variance among the test samples. The more general test is called the Welch's T-Test, where the sample variances are not necessarily equal; however, most sources refer to all forms of the hypothesis test as the Student's T-Test [171]. This general form typically falls under the header: Equal or Unequal sample sizes, unequal variances and is the most general form of Student's T-Test. Here, the test statistic is given by [133]:

$$t = \frac{\bar{X}_1 - \bar{X}_2}{\sqrt{\frac{s_1^2}{n_1} - \frac{s_2^2}{n_2}}}$$

The degrees of freedom, df, for this test is given by [133]:

$$df = \frac{\left(\frac{s_1^2}{n_1} + \frac{s_2^2}{n_2}\right)^2}{\frac{\left(\frac{s_1^2}{n_1}\right)^2}{n_1 - 1} + \frac{\left(\frac{s_2^2}{n_2}\right)^2}{n_2 - 1}}$$

In these two equations:
t= t-statistic to test if the populations means are different
X_n= Sample mean of sample group n
S_n = Standard deviation of group n
n_n = Number of samples in group n

This t-statistic calculated above is then compared to standard t-test probability tables. These tables tell the P-value needed to confirm the hypothesis for a given number of degree of freedom, *df*, number of tails, and confidence interval. The confidence interval is how confident the researcher desires the prediction to be. Typically, this is 0.05 or 0.01 meaning 95% or 99% confident respectively. In this case, a 95% confidence test (p=0.05) was preformed. A two-tail test means that the mean of the test sample could be above or below the control sample. A one-tailed test means that the test sample's mean will be only above or below the control's mean. The t-statistic is then compared to the P-value. If the t-test statistic is greater than the P-value then the researcher rejects the null hypothesis, that the two means are the same, and finds evidence that the two sample means are from two different populations with different means, with the confidence used to select the P-value.

The results of the t-test are shown below in Table 54. In this table, all tests rejected the null hypothesis, that the two means were the same, except for the small-sized raid for the fraction of POL sites destroyed and the fraction of MOSs available. These values are shown in red. This validates that the optimized cases did improve the outcomes for the medium and large attacks and the small attack only realize a reduction in the cost, but the same amount of damage to the airfield.

Table 54: T-Test for Optimized Tactics vs Base Case

P-value from T-test	%AC	%POL	%MOS	Cost
Small	0.001	0.90	0.37	0
Medium	3.4E-106	3.9E-78	4.0E-128	0
Large	2.0E-7	3.6E-23	0	0

8.10. Sensitivity Analysis

The previous section revealed that the small-sized attack did not see an improvement in the amount of damage to the airfield, but it did realize a reduction in the cost of the defense. For the medium and large-sized attacks, there was an improvement in all areas except for the amount of undamaged runway following a large-sized attack. If the optimized tactics do not achieve the required results, then a material solution is required. In order to determine the best material solution, a sensitivity analysis is required based on the now optimized tactics. A sensitivity analysis will show what changes in the tactics yields the largest changes to the outcomes. The new material solution could then be tailored to help facilitate this adjustment.

The sensitivity analysis is a computationally intense activity that requires many function calls. This would be inefficient and cumbersome to do with the high fidelity simulations. Instead, it is better if the sensitivity analysis uses the predictive models. The input variables for the optimized tactics included both continuous and discrete variables. For each continuous input variable, the analysis will examine the effects of increasing and decreasing the input variable by 10%, while holding all other variables constant [172]. If 10% above or below the optimal input causes the variable to exceed a limit, then the analysis will only go until that limit. For discrete variables, each setting of the discrete variable is tested.

The results of the small attack are shown below. Figure 168 is the sensitivity of the UT input variables and Figure 169 is the sensitivity of the LT input variables. In each figure, the outcomes are shown vertically (fraction of aircraft damages, fraction of POL destroyed, fraction of MOSs available, and cost of the defense). The continuous

variables are shown in each column and the discrete variables are shown as different lines within each graph.

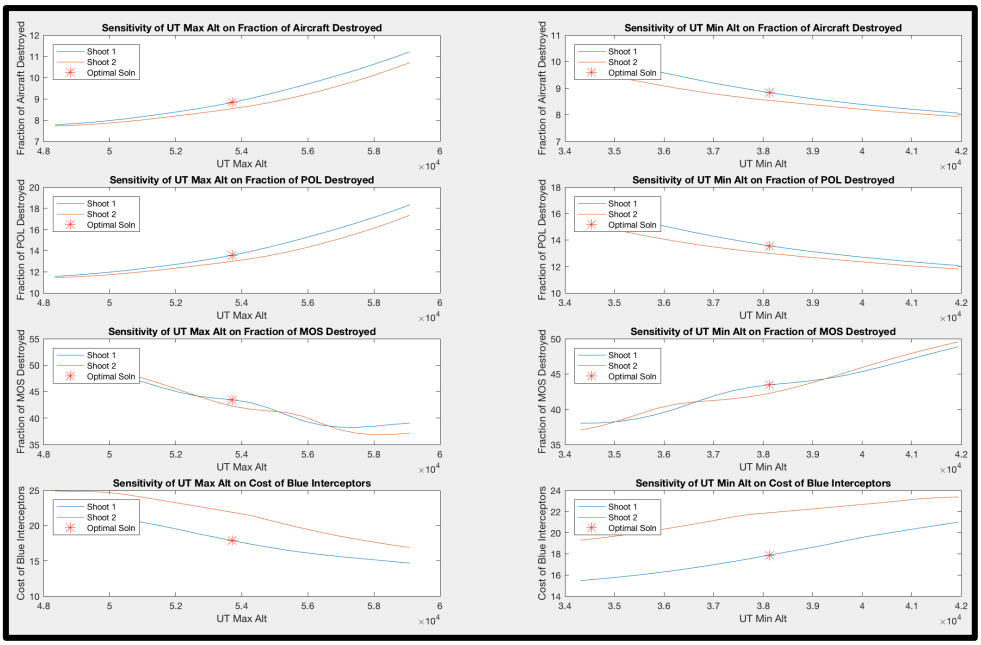

Figure 168: Sensitivity of UT Variables for Small-Sized Attack

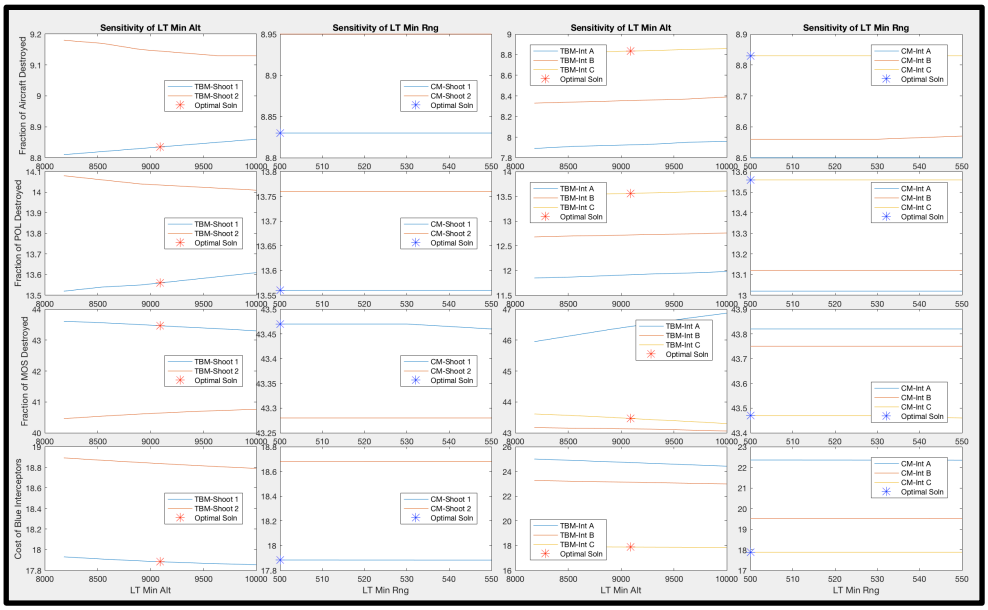

Figure 169: Sensitivity of LT Variables for Small-Sized Attack

For the small-sized attack, all outputs are most sensitive to the UT maximum and minimum altitude. This indicates that the size of the UT engagement space is critical to

maintain. Most variables, other than cost, were insensitive to the shot doctrine of the UT system. For the LT input variables, all outcomes were insensitive to the minimum range of the interceptors, but were highly sensitive to the shot doctrine, interceptor choice, and to a lesser degree the minimum altitude. It is important to remember that the minimum altitude is linked to the maximum range for CM engagements, since CM engagements cannot start until after the TBM engagements. This will be important when selecting a new system in the following steps. The medium-sized attack showed similar trends. The sensitivity of UT variables for the medium-sized attack are shown in Figure 170 and the sensitivity for the LT variables for the medium-sized attack are shown in Figure 171.

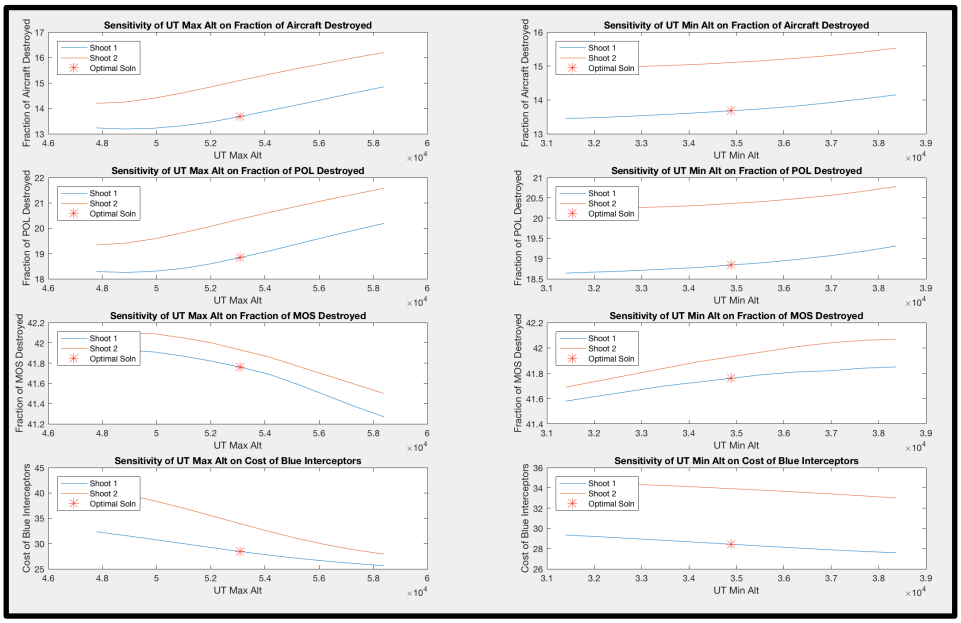

Figure 170: Sensitivity of UT Variables for a Medium-Sized Attack

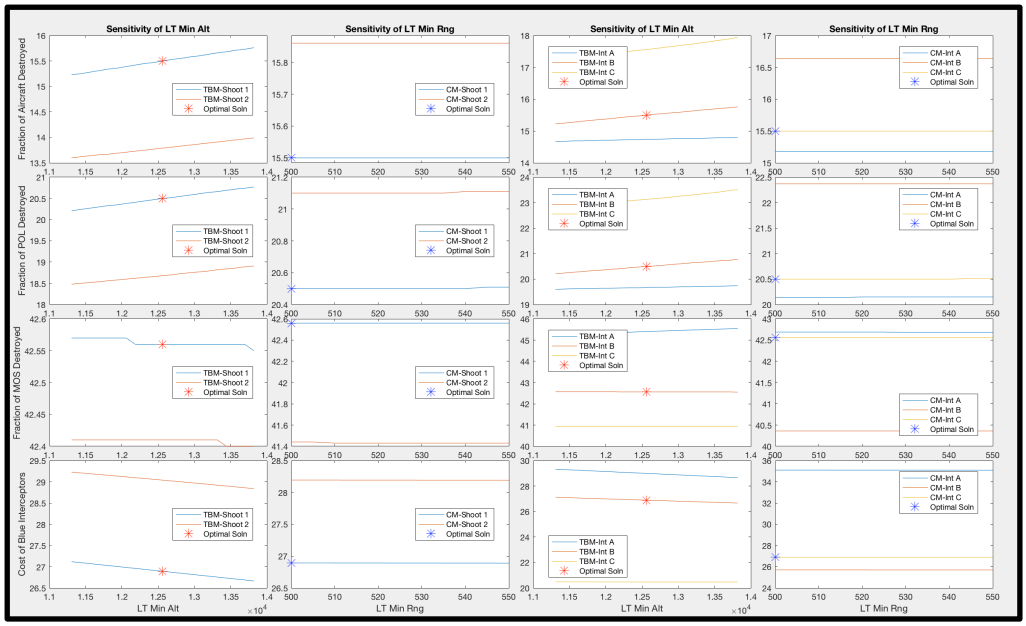

Figure 171: Sensitivity of LT Variables for a Medium-Sized Attack

The optimal solution for a medium sized attack is most sensitive to the UT maximum and minimum altitudes. The outcomes for the medium-sized attack are also more sensitive to the shot doctrine used than were the outcomes for the small-sized attack. The outcomes of the medium-sized attack were not very sensitive to the minimum range of the LT system. They were slightly sensitive to the minimum altitude. Additionally, all outcomes were highly sensitive to the choice of interceptor and shot doctrine. Similar trends hold for the large-sized attack. The results of the large-sized attack sensitivity analysis for the UT input variables is shown in Figure 172 and for the LT input variables in Figure 173.

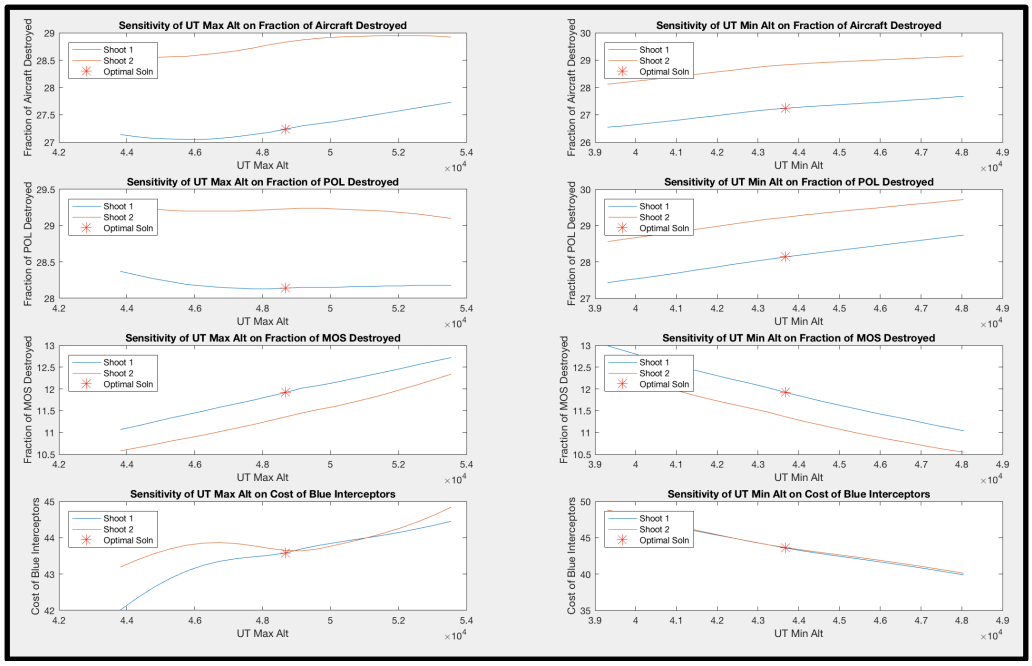

Figure 172: Sensitivity of the UT Variables for a Large-Sized Attack

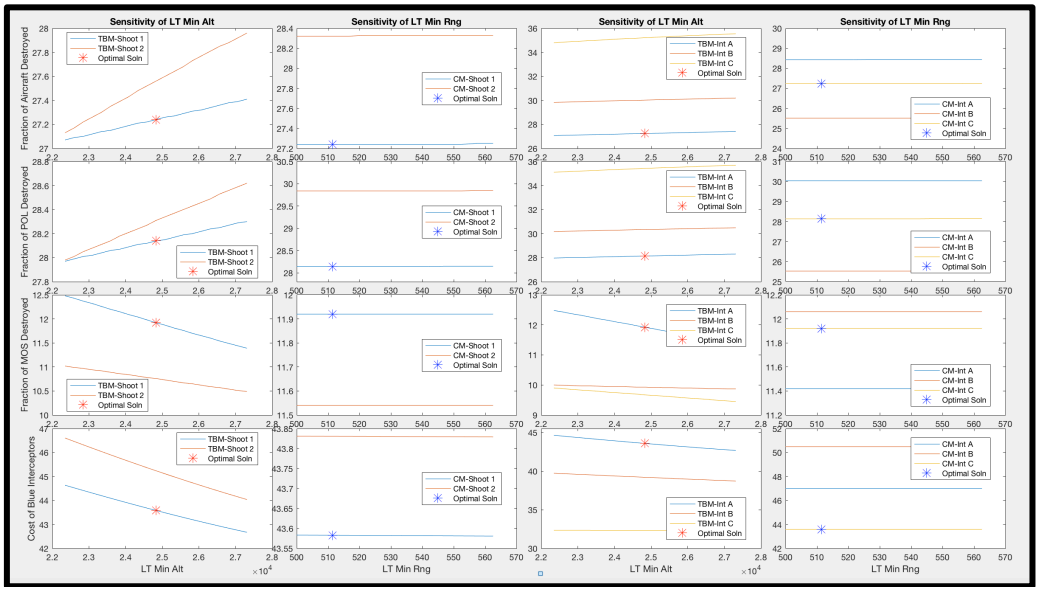

Figure 173: Sensitivity of the LT Variables for a Large-Sized Attack

The sensitivity of variables in the large-sized attack shows a similar trend to that of those same variables in the medium-sized attack. The outcomes are highly sensitive to the UT shot doctrine and engagement altitudes. The outcomes are also highly sensitive to the LT minimum altitude, shot doctrine, and interceptor choice.

8.11. Selection of a Material Solution

The initial optimization looked at changes to the tactics used by the blue systems. These changes in tactics caused a shift in the output CDFs of the simulation showing an increased likelihood of a more favorable outcome for each output variable except for the damage to the runway in the large attack case. This was especially true for the medium and large sized attack, but the small-sized attack only showed marginal improvement. Should a commander decide that the optimized ADA tactics do not change the outcomes enough, a new material solution is needed. The sensitivity analysis is an important step to determining how to close the capability gaps with a material solution.

All attack sizes revealed that the outputs were sensitive the LT minimum altitude. This variable is key in the engagements because it controls both the LT TBM engagement window and the CM engagement window since the maximum range of the CM engagements is a function of the minimum altitude of the TBM engagements. Although there is also a high sensitivity to the UT input variables, there are already two systems engaging TBMs. Therefore, the new point defense (PT) system will be investigated. This PT system is capable of defending against CMs only. By relieving the LT of the full responsibility of defeating the CMs, the LT system should be able to engage more TBMs.

A summary of the PT system's decision variables is shown below in Table 55. The PT system has three launchers each with 10 interceptors each (30 interceptors total).

When integrated into the engagement que, the PT system will defend against CMs behind the LT system. This means that the PT systems' maximum range is dependent on the LT system's minimum range. In order to account to target coordination during the handoff from the LT system, the PT system's maximum range is set to either 500 meters less than the LT system's minimum range, or the maximum range of the PT interceptor (20,000m), whichever is less.

Table 55: Point Defense System Input Variables

System	Variables	Value Range	Units
Point Defense (PT)	Minimum Engagement Range –CM	500-20,000	Meters
	Shot Doctrine - CM	1 or 2	each

8.12. Optimization of the Red Tactics with New Equipment

The selection of a new material solution completes the first iteration of the design cycle of the new proposed methodology (see Figure 12). Now, with the new ADA system organization that includes the PT system, the methodology starts again from the top. The first step in this process is to optimize the red fire plans again so that they are now optimized to do the most damage, recognizing that the blue forces has a new ADA system. For the new base case, the PT system operated with the tactics described below in Table 56. All other blue ADA system tactics were the same, as described in Table 49.

Table 56: PT System Default Tactics for New Base Case

System	Variable	Set Value
Point Defense (PT)	Number of Launchers	3 ea.
	Maximum Engagement Range	1500 meters
	Minimum Engagement Range	100 meters
	Shot Doctrine	1 interceptor

The default maximum engagement range for the PT system is 500 meters less than the default minimum engagement range of the LT system. The minimum

engagement range of the PT system is set to its lower limit in order to maximize the PT system's engagement window. Finally, the PT system shot doctrine is the same as the LT system's shot doctrine against CMs.

The optimization process for the new red fire plans was similar to that described for the base case in section 8.4. The optimization software OptDef was used for the optimization (see section 8.3). The resulting optimal frontier of red missile numbers and tactics for this optimization are shown below in Figure 174, Figure 175, and Figure 176. The shapes of the optimal frontiers are similar to those of the original base case, however, they are shifted on each axis indicating a small reduction in the amount of damage to the airfield due to the new PT system.

The new optimal frontier for the small sized attack is shown in Figure 174. This frontier contains 832 points. The optimization program tested 34,170 points to find this optimal frontier. Similarly, the new optimal frontier for the medium-sized fire plan is shown in Figure 175. For the medium-sized fire plan, the frontier contains 851 points and the program tested 53,498 points. Finally, the large-sized fire plan is shown in Figure 176. This frontier contains 769 points and the program tested 33,488 points.

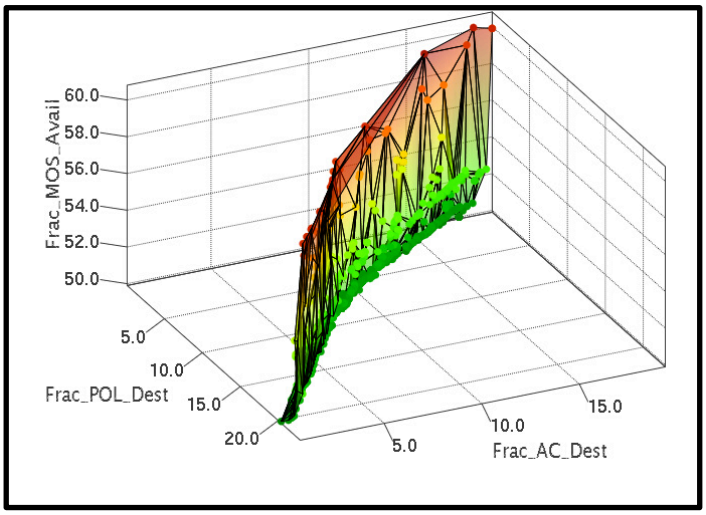

Figure 174: Optimal Frontier for Small-Sized Attack with PT System Included

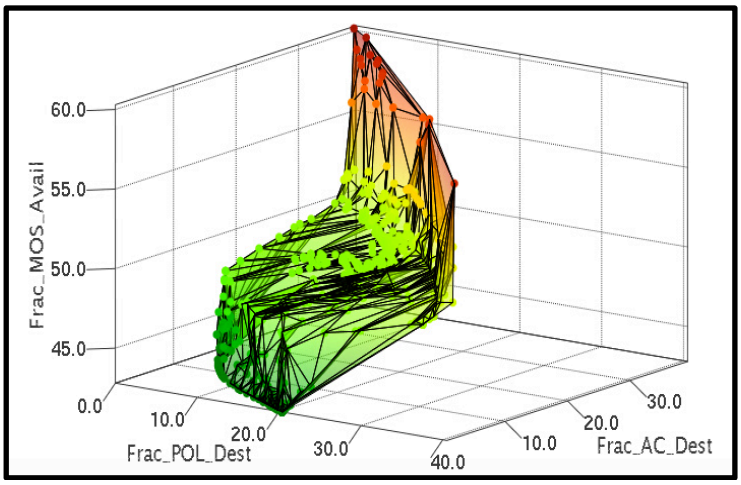

Figure 175: Optimal Frontier for Medium-Sized Attack with PT System Included

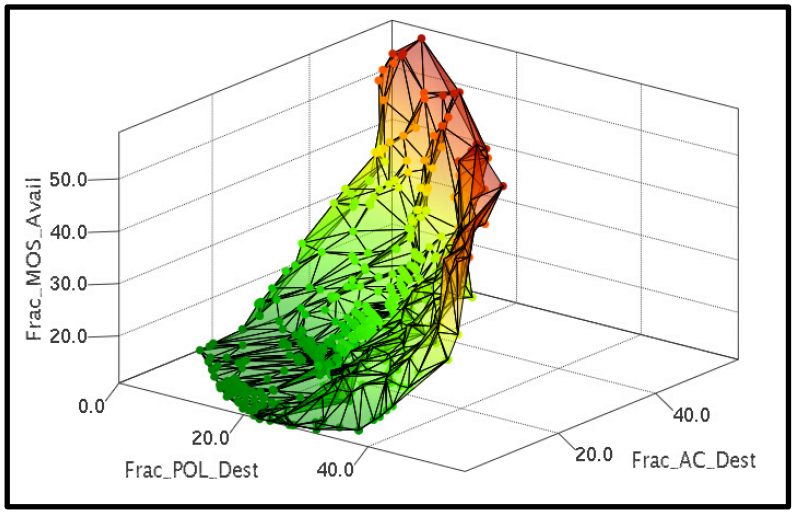

Figure 176: Optimal Frontier for Large-Sized Attack with PT System Included

8.13. Optimization of the Blue Tactics with New Equipment

With the new optimized fire plans, the blue tactics can once again be optimized, now with the PT system, in order to minimize the damage to the airfield at the lowest cost. This optimization was done in a similar manner to that explained in section 8.6, but included the PT system with the variable ranges explained in Table 55. The optimization also had an added constraint that the minimum engagement range PT system had to be less than its maximum engagement range minus 500 meters. The maximum engagement

range was not a decision variable and was instead calculated as 500 meters less than the minimum engagement range of the LT system.

Similar to the optimization of the tactics only case, for each set of blue decision variables, all optimal fire plans on the new frontier were tested for the given raid size. This meant that each test case of the ADA decision variables was tested against several hundred optimal fire plans. Once all fire plans were tested against the set of decision variables, the damage to the runway, fuel, or aircraft was averaged, so that the output was the mean effect from all the optimal fire plans.

The results of this optimization are shown below in Figure 177, Figure 178, and Figure 179. Just as in the tactics only optimization from section 8.6, there are two graphs in each image. In both graphs, the vertical axis is the average cost of the ADA interceptors shot using the relative costs explained in section 7.2.2. All costs are relative to the LT interceptor type A, which has a cost of one unit. The x and y-axis of the left graph of each figure shows the average fraction of MOSs available and the average number of POL sites destroyed. The graphs on the right of each figure show the average number of MOSs again and the average fraction of aircraft destroyed. In these simulations, the ADA defenses are trying to minimize cost, maximize the number of MOSs available, and minimize the number of fuel sites (POL) and aircraft (AC) destroyed. For each sized fire plan, the new optimal frontier of points shows a different shape than those from the original base case. This indicates that the tactics with the new system are different and that the new PT system caused a change in the amount of damage to the airfield.

The optimal frontier for the blue ADA system's tactics with the new PT system included against a small-sized optimal raid is shown in Figure 177. This frontier has 1,580 optimal tactics combinations and the program tested 58,029 design points. The optimal frontier against the medium-sized raid is shown in Figure 178. This frontier has 978 points and the program tested 46,176 design points. Finally, the optimal frontier against the large-sized attack is shown in Figure 179. This frontier has 1,914 optimal points and the program tested 58,096 design points.

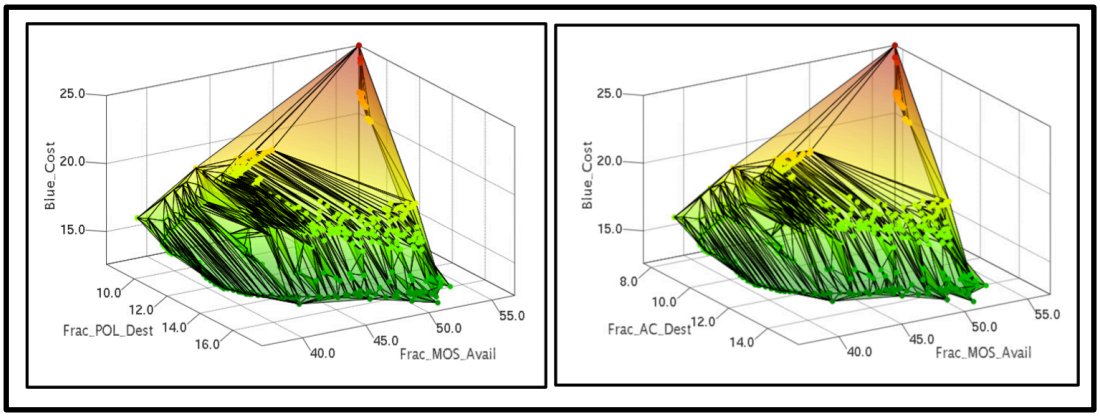

Figure 177: Optimal Frontier for ADA Optimization with PT System Against a Small-Size Attack

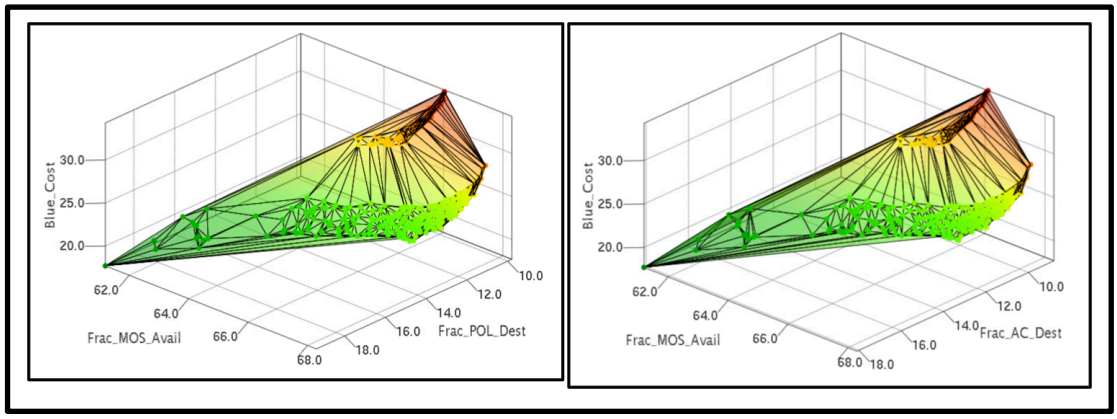

Figure 178: Optimal Frontier for ADA Optimization with PT System Against a Medium-Size Attack

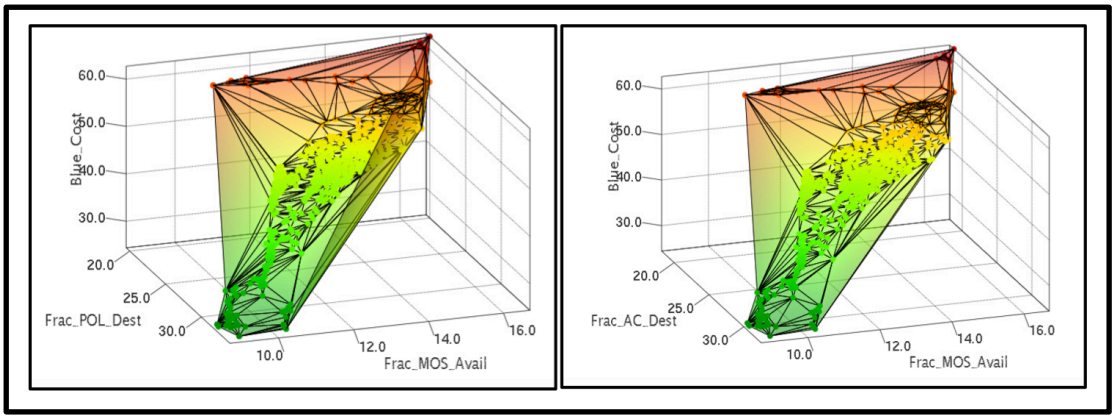

Figure 179: Optimal Frontier for ADA Optimization with PT System Against a Large-Size Attack

8.14. Selection of the Optimal Set of Blue Tactics with PT System - TOPSIS

Each point on the optimal frontiers, found in the previous section, represents a combination of tactics that minimized the damage to the airfield at the lowest cost. In a similar manner to the optimization of tactics alone, TOPSIS was used to select the single set of tactics that now include the PT system, which represents the best compromise of all the criteria based upon the weight matrix. The PT system was introduced in order to close a capability gap that the original set of equipment and optimized tactics could not close alone. These objectives have not changed so the weight matrix is the same as what was used in the original optimization (see Table 52).

There were four criteria in this selection, the fraction of aircraft destroyed, the fraction of POL sites destroyed, and fraction of MOSs available on the runway, and the cost of the blue interceptors fired against incoming missiles. All criteria were to be minimized except the fraction of MOSs available, which was to be maximized. The set of tactics selected for each raid size is summarized in Table 57 and shown graphically in Figure 181 for the decision variables relating to TBM engagements and in Figure 180 for the decision variables related to CM engagements. In the table, the values with stars (*)

indicate a calculated value and not a true decision variable. The LT maximum altitude was the minimum of either the maximum altitude for the LT interceptor or the UT minimum engagement altitude minus 5,000 meters. The LT max range was based on the LT minimum altitude and given by the equation in Figure 146. Finally, the PT system's maximum range was the minimum of the PT system interceptor's max range or the LT system's minimum range minus 500 meters.

Table 57: Optimized ADA Tactics with PT System Included

System	Lower Tier							
Attack Size	Altitude		Range		Shot Doc		Interceptor	
	Max*	Min	Max*	Min	CM	TBM	CM	TBM
Small	20,000	8,951	4,487	3,882	1	1	C	C
Medium	30,000	24,390	11,712	11,113	1	1	C	A
Large	30,000	24,866	11,940	11,397	1	1	C	A

System	Upper Tier			PT Defense		
Attack Size	Altitude		Shot Doc	Range		Shot Doc
	Max	Min	TBM	Max*	Min	CM
Small	47,150	42,150	1	3,382	100	2
Medium	53,842	34,839	1	10,613	100	1
Large	48,183	43,177	1	10,897	100	1

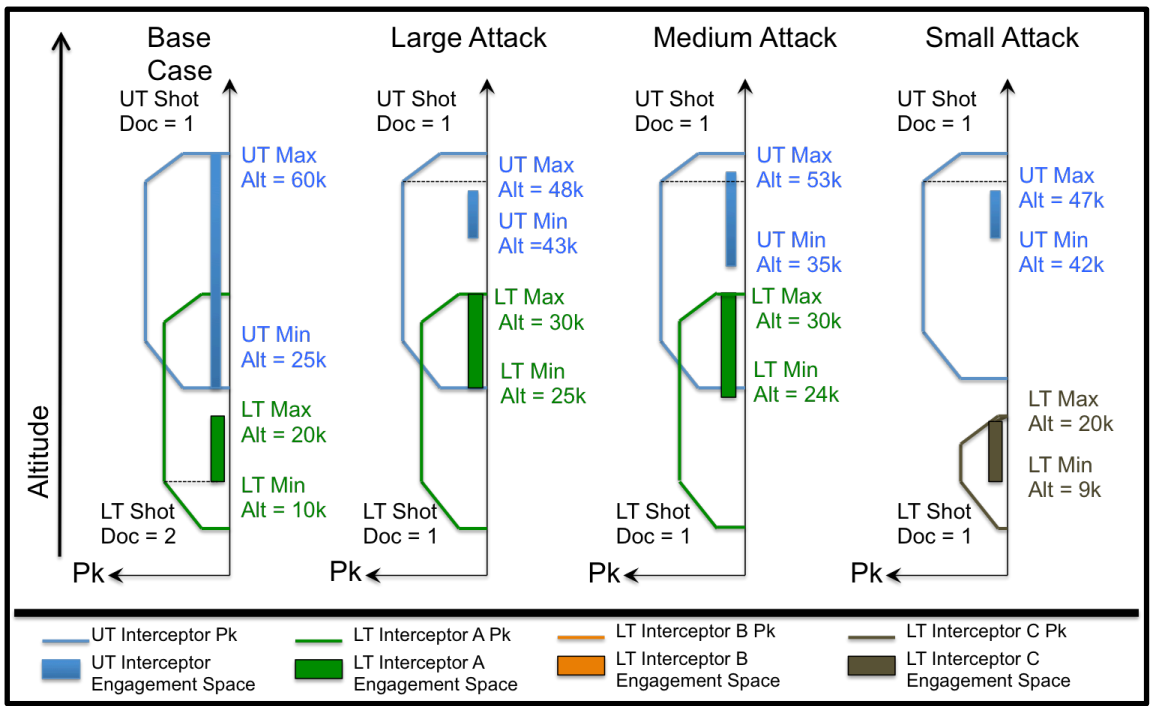

Figure 180: TBM Engagement Altitudes for Optimized Tactics with PT System

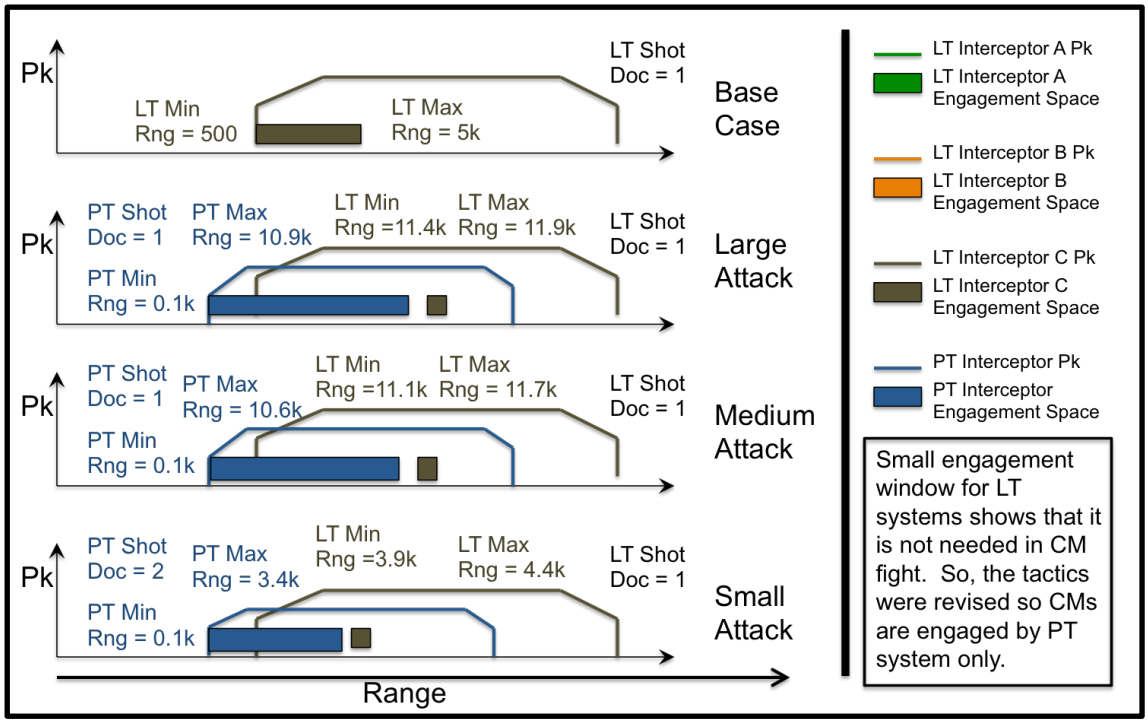

Figure 181: CM Engagement Ranges for Optimized Tactics with PT System

The introduction of the PT system helped the ADA systems defeat CMs. There was little change in the engagement windows for both UT and LT. The one exception was with a medium sized attack, the optimized tactics changed from the LT type B interceptor to the LT type A interceptor. Because the LT type A interceptor has a higher maximum altitude, the engagement altitude increased and the engagement window increased as well.

The largest change in the tactics was in the LT system's engagement window against CMs. This makes sense since the PT system is a CM only system, so it can only help in the CM fight. Just as in the original base case, the lower end of the CM engagement window was at the minimum range of the system, the PT system in this case as opposed to LT system. In all three sizes of attacks, the LT CM engagement window was very small. It was only large enough to take a few shots with the LT type C interceptor and not enough to engage all threats. Instead, the PT system was the primary weapon used against the CMs. This make sense since the Pk of the PT system is only slightly lower than the LT interceptor C system, but the PT system has twice as many available interceptors in the launchers. Additionally, the PT interceptors are half the cost of the LT type C interceptors.

The small size of the LT system's engagement window against CMs indicates that it is not needed in the CM fight. The overall program setup required that CMs were engaged by the LT system first, followed by the PT system (see section 7.6 and Figure 140). The PT system's maximum range was a dependent variable calculated as the LT minimum range minus 500 meters. In the same manner, the LT system's maximum range was also a dependent variable and was a function of the LT system's minimum

engagement altitude against TBMs. These two dependencies coupled the CM and TBM engagements together.

The PT system was not able to engage CMs until the LT system was complete and the LT system could not engage CMs until it was complete against TBMs. Because the LT system's engagement window was so small, it can be removed from the CM engagements. This will decouple the TBM and CM engagements, meaning that they can take place simultaneously with different systems. The UT and LT system will engage TBMs while the PT system engages CMs.

Since the PT system is engaging CMs alone, it can begin those engagements at its maximum range. Likewise, since the LT system does not have to transition from TBM engagements to CM engagements, it can continue to engage TBMs all the way to its minimum engagement altitude (2,000 meters). These revised optimized tactics are shown below in Table 58. The entries in red are the revised values based on the decoupled TBM and CM engagements. The LT maximum altitude is starred in the table because this value was a dependent variable, just as in previous cases. The LT maximum altitude was the larger of the UT system's minimum engagement altitude minus 5,000 meters of the maximum altitude of the LT system's interceptor. This data is also shown graphically for TBM engagements in Figure 182 and graphically for CM engagements in Figure 183.

Table 58: Revised ADA Tactics with PT System Included (Entries in Red Are New Based on Decoupled CM and TBM Engagements)

System	Lower Tier							
Attack Size	Altitude		Range		Shot Doc		Interceptor	
	Max*	Min	Max	Min	CM	TBM	CM	TBM
Small	20000	2000	NA	NA	1	1	C	C
Medium	30000	2000	NA	NA	1	1	C	A
Large	30000	2000	NA	NA	1	1	C	A

System	Upper Tier			PT Defense		
Attack Size	Altitude		Shot Doc	Range		Shot Doc
	Max	Min	TBM	Max	Min	CM
Small	47150	42150	1	20000	100	2
Medium	53842	34839	1	20000	100	1
Large	48183	43177	1	20000	100	1

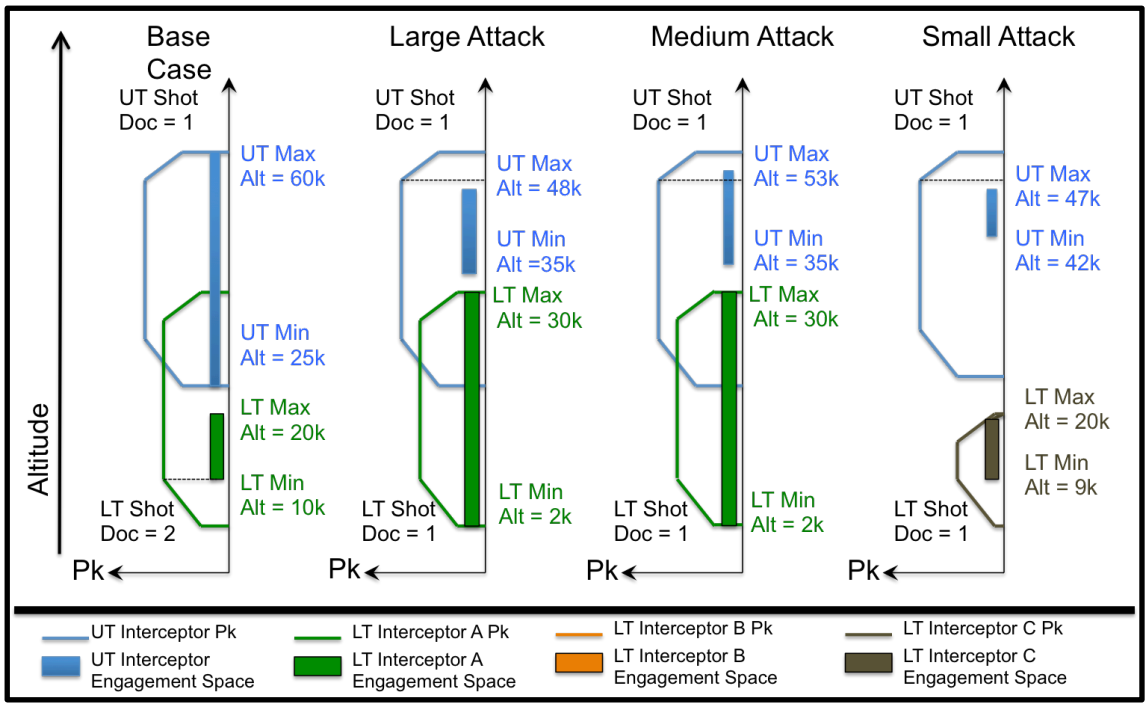

Figure 182: TBM Engagement Altitudes for Revised Tactics with PT System

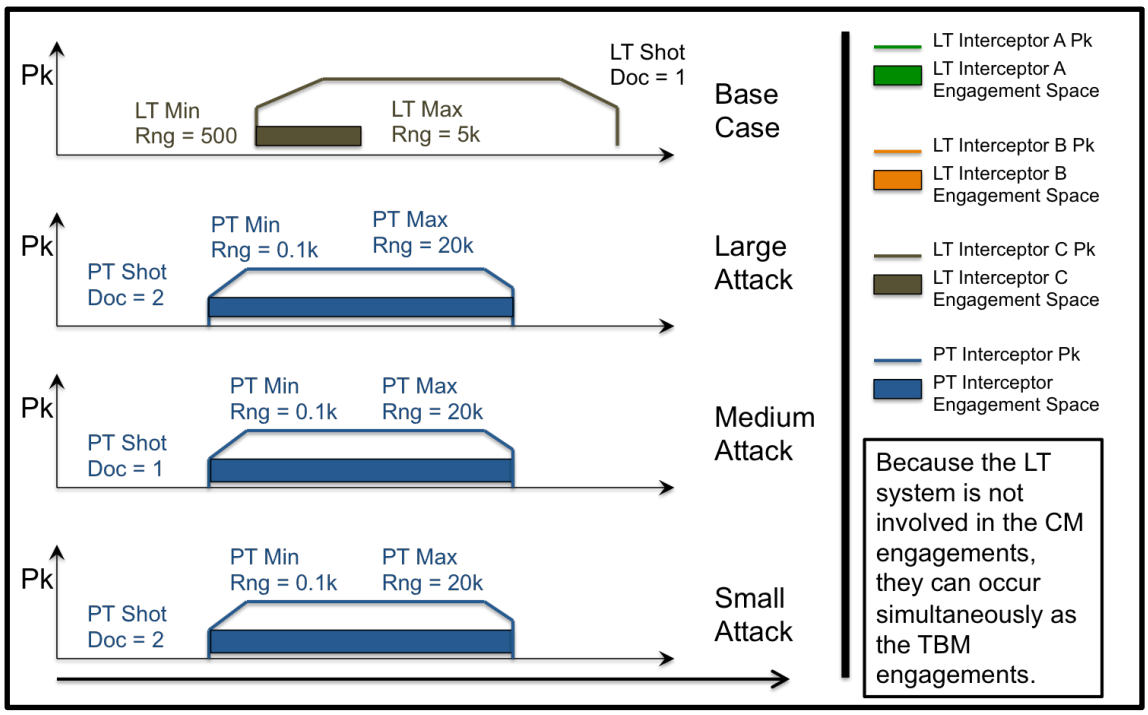

Figure 183: CM Engagement Ranges for Revised Tactics with PT System

These revised tactics were tested with the predictive models before being used in the high fidelity model. The predictive models only estimate the average values for each of the four outcomes. The results of this test is shown in Figure 184. This graph shows that the new tactics with the PT system included should reduce the damage to the aircraft and POL sites and increase the number of MOSs available for all attack sizes. The cost, however, will likely increase from what it was in the tactics only optimization and will likely be comparable to the base case.

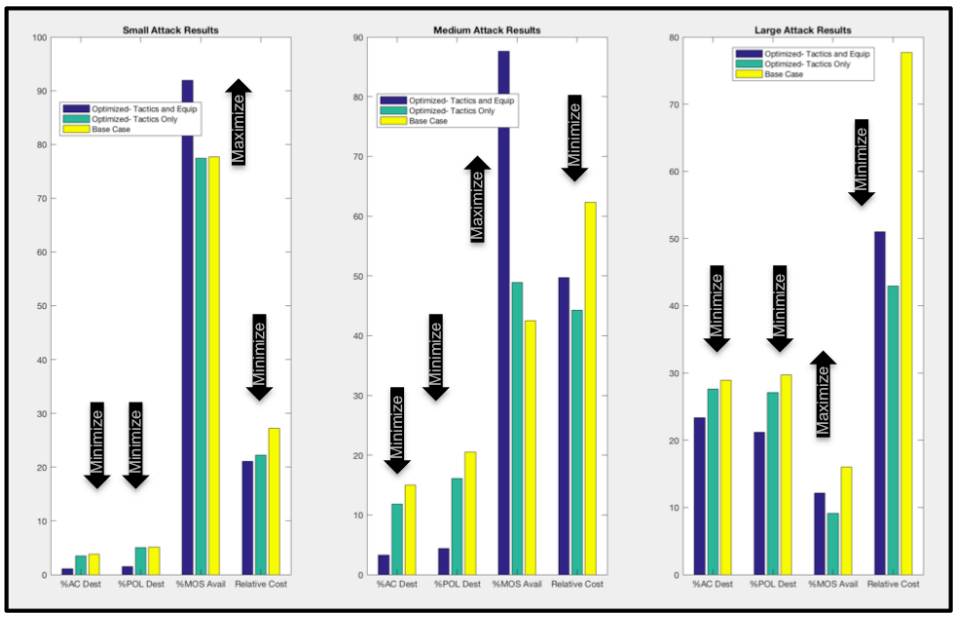

Figure 184: Predicted Average Outcomes for Base and Revised Optimized Cases with PT System

8.15. Test the Optimal Blue Tactics, with PT system, in High Fidelity Model

Just as in the optimization of the tactics only, the optimized solution must be tested in the high fidelity simulations, since the optimization made use of predictive models that sacrifice a small amount of accuracy for speed. The new optimized input tactics, now with the PT system included, were coded into the EADSIM input files using a wrapper function.

For each sized attack, the single optimized set of ADA tactics was tested against all the fire plans on the red optimal frontier. The leakers from these simulations were then passed to the runway cratering and airfield effects models described in sections 6.2 and 6.4. In each attack size, the optimized tactics were tested against 500-1,500 optimized fire plans. Because the programs were stochastic, this process was repeated 10-20 times creating an array of 500-30,000 observations of each outcome. The results of this test are shown below in Figure 185. In this figure, the red line is a cumulative

distribution function (CDF) of the stochastic outcomes of the base case. The blue line is the CDF of the outcomes for the optimized case.

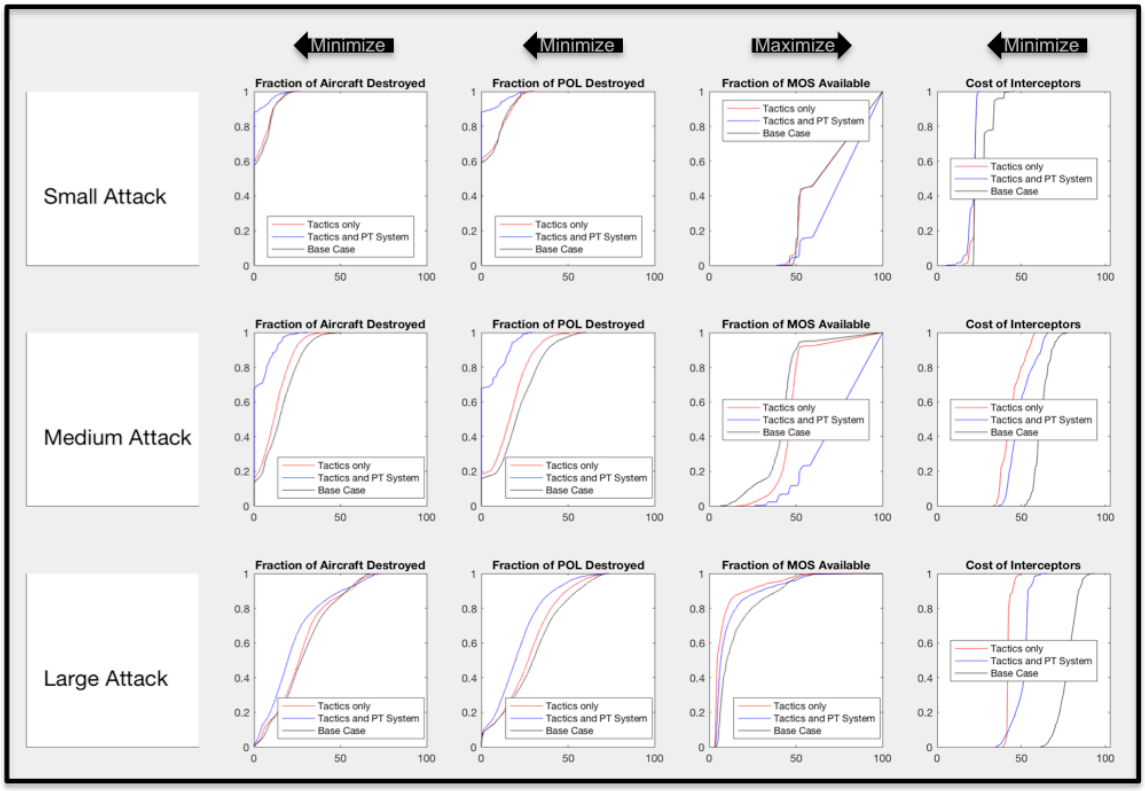

Figure 185: Simulation Results of the Base Case, Tactics Only Optimization, and Optimization with new PT System Included

Each graph in Figure 185 includes the CDF of base case as the black line, the CDF of tactics only optimization as the red line, and the CDF of optimization of tactics with the PT system as the blue line. For the small-sized attack, the additional PT system reduced the amount of damage to aircraft and POL sites from both the base case and the tactics optimization only case. The PT system also increased the amount of useable runway slightly as compared to the base case all for, approximately, the same cost as the optimization of the tactics alone.

For the medium-sized attacks, the addition of the PT system resulted in approximately the same probability of damage for the aircraft and POL sites as compared

to the tactics only optimization, but a small increase in the probability of available runway. The probability of the cost was slightly greater than that of the tactics only case, but less than the base case.

For the large-sized attack, the addition of the PT system reduced the probability of damage to both the aircraft and POL sites and also increased the probability of available runway. The cost, however, was slightly greater than the optimization of tactics alone, but still less than the base case.

Because the simulations were stochastic, the changes to the outcomes outlined above could have been due to random chance and not because there was an overall change in the process. In order to verify that the changes are statistically significant, a Student's T-Test of the means was conducted with a 95% confidence level for the base case and the optimized tactics with the PT system. The results of this test are shown below in Table 59.

Table 59: T-Test Results for Base Case and Optimized Tactics with PT System

P-value from T-test	%AC	%POL	%MOS	Cost
Small	0	0	0	0
Medium	0	0	0	0
Large	2.7E-164	4.6E-277	2.5E-125	0

The results of the T-Test help to answer the second research question: Will the proposed method allow for rapid optimization tactics against a complex attack that is reproducible in the high fidelity system? The hypothesis for this research question was that the optimized result from the proposed method will show an equal amount or a reduction in the damage to the airfield for a lower or equal cost over the base case, with a 95% confidence level, for both the case with and without the new system. In both the

tactics only case (Table 54) and the tactics with a new system (Table 59), the results show that the new method will optimize the results of the high fidelity simulations.

The optimized results show that the two highest weighted criteria, which were reduced damage to aircraft and reduced damage to the POL sites, both showed a reduction in the probability of damage. All cases also showed a decrease in the probability of the cost. The lowest weighted priority, damage to the runway, showed a very small (less than one MOS), but statistically significant, increase in the probability of damage.

9. CONCLUSIONS

"You cannot escape the responsibility of tomorrow by evading it today."
- Abraham Lincoln

Oftentimes, military planners view airbases and seaports far from the front lines as sanctuaries that are beyond the reach of the enemy forces. This is especially true during the last decade and a half of war against a low-tech enemy while we have vulnerable, large, open bases. There will come a time in future conflicts when this will not be the case due to the growing proliferation and stock piling of TBMs and CMs. Even in previous conflicts that did involve TBMs and CMs, the raids were relatively small and easily handled by our current systems and doctrine. The proliferation of technology will increase the number and complexity of these missile systems and the current systems and doctrine will not be able to manage these large and complex strikes. This research demonstrated a methodology to optimize ADA tactics and organization against such overwhelming attacks.

The conclusions from this work fall into one of two categories: conclusions about the proposed methodology and conclusions about ADA analysis in general. For the proposed methodology, this work demonstrates that machine learning and optimization plays an important role in ADA system's tactics and organization analysis. Once built, the predictive models run in fractions of a second compared to the minutes or hours required for the higher fidelity ADA and weapons effects simulations. This is especially true given that both these simulations are stochastic; so many runs of a particular input set are required to produce meaningful results.

Secondly, before any analysis of the friendly ADA tactics and organization, it is necessary to optimize the enemy fire plan. In any ADA analysis, the most controlling variables of the simulation are the enemy fire plan. In military graphics, the enemy forces are drawn in red and friendly forces in blue. If there is not considerable thought and analysis that goes into the red fire plan first, then any analysis of the blue ADA systems is dubious at best. All new officers in the Army are taught: "Pick up the red pen first." This emphasizes to young officers the value of creating a template of the enemy position and then developing the most likely enemy course of action, before planning any mission or course of action by the friendly forces. This same thought process applies to ADA system's analysis. The proposed analysis starts first with an optimization of the enemy fire plan before moving to the ADA system's own tactics optimizations.

Looking at ADA analysis in general, one of the most important conclusions is that ADA tactics should be optimized based on weapons effects analysis and not simply trying to minimize the number of leakers. This work proposed and demonstrated a method to tie together existing research for weapons cratering and weapons blast analysis in order to create an effects model for an airfield. A similar process could be used for an effects model for other likely missile targets such as seaports, assembly areas, and command and control nodes.

The airfield damage effects model allows the analyst to articulate the damage caused by the leakers, which goes beyond knowing merely that there were leakers. This is important because the damage done by the leakers can cause a change in the ability of the friendly force to accomplish their mission. This analysis also showed that different types of leakers cause different damage. Therefore, if some damage is more critical to

reduce, such as damage to the aircraft, as opposed to the runway, the weapons effect models allows the analyst to tailor the tactics and systems to meet these goals.

9.1. Review of Objectives

The three major objectives of this work and their status are listed below in Table 60. All of the research objectives were achieved.

Table 60: Review of Research Objectives

Number	Objective	Met?
1	Determine a method to merge existing tools for ballistics, cratering in concrete, and weapons effects to create a program that will optimize the enemy fire plan to create the most damage to runways, POL sites, and aircraft for a set number of cruise and ballistic missiles as opposed to simply maximizing the number of leakers.	Yes
2	Determine a method to close existing ADA capability gaps through changes to organization and/or doctrine against a given set of complex threats, at a given location, and for a given a set of ADA systems, that will optimize the defense at the lowest cost.	Yes
3	Determine a method that combines ADA simulations and weapons effect simulations such that the method maintains the same accuracy as high-fidelity models but runs at least an order of magnitude faster.	Yes

The first research objective sought to develop a weapons effects tool for an airfield. This work developed a weapons cratering program that uses a six-degree of freedom model to propagate munitions to the ground, it then evaluated three different concrete penetration models and selected the one that best matched new experimental data. Finally, it uses best-fit curves from experimental data for explosive cratering in concrete. For damage to targets, this work uses weaponeering guided and unguided impact accuracy methods to determine where munitions impacted on the airfield. Then a lethal area analysis is implemented to determine the damage caused by different weapons.

The second objective was to determine a method to close a capability gap in an ADA system's defenses in order to defeat a complex threat, raid made up of both TBMs and CMs, for the lowest cost. The cost element is sometimes overlooked in other capability gap analyses. Adding more capability should always increase the probability of achieving a certain objective, but any added capability must be economically feasible. In this work, all of the ADA interceptors were assigned a cost, relative to one of the missiles. This cost was based not only on the actual purchase price of the interceptor, but also on its existing inventory and how easy it is to obtain more during a wartime situation.

The final objective was to find a method to speed up the ADA and weapons effects simulations, while still maintaining the same level of accuracy. This is needed because the ADA and weapons effects simulations used in the methodology of objective two can take minutes to hours for a single run and the stochastic nature of the simulations requires a large number of runs for a single input set. This work made use of designs of experiments and machine learning to develop predictive models for both the ADA and weapons effects simulations. These predictive models can run on a computer in a fraction of a second and maintain enough accuracy to allow them to be used in an optimization process as opposed to the higher fidelity simulations. In order to ensure that the optimized solution is better than the base case, it is then run in the high fidelity simulations and compared to the base case.

This methodology of objective two was demonstrated by optimizing an ADA system to defend an airfield at the lowest cost. This demonstration also made use of the damage effects tool and predictive models of objectives one and three. This

demonstration began by optimizing the enemy fire plan to maximize the effects the enemy force would want to achieve. Following the red optimization, the second part of the new methodology was demonstrated by optimizing the tactics of the ADA system without any new equipment in order to try to close the gap through tactics alone. When this was not possible, this work demonstrated the last part of the methodology by selecting and testing a new material solution. It used a sensitivity analysis to identify the characteristics of a new ADA system that would be the most beneficial. It then optimized the tactics with the new system in order to determine if the operational goals were met.

9.2. Review of Research Questions and Hypothesis

Each of the above research objectives had a corresponding research question and hypothesis. These are shown below in Table 63 along with a very brief statement about the outcome of the outcome of the hypothesis. A more detailed explanation of the results for each research question and hypothesis is described in the remainder of this section.

Table 61: Results of the Research Questions and Hypothesis

Objective	Research Question	Hypothesis	Outcome
1	Will a fire plan optimized to achieve a given effect (destruction of aircraft, POL sites, or runway) be the fire plan with the greatest number of leakers?	A fire plan weighted with CMs, as opposed to TBMs, will destroy more point targets such as POL sites and aircraft and a fire plan weighted with TBMs, as opposed to CMs, will destroy more area targets such as the runway. These will not necessary be the fire plans with the most leakers.	Mostly true. If the aircraft are not stationary, then they are an area target and TBMs are more effective against them.
2	Will the proposed method allow for rapid optimization tactics against a complex attack that is reproducible in the high fidelity system?	The optimized result from the proposed method will show an equal amount or a reduction in the damage to the airfield for an equal or lower cost over the base case, with a 95% confidence level, for both the case with and without the new system.	True for small and medium sized attacks. Large sized attacks saw reduced damage and cost, except for the damage to the runway.
3	Can machine learning accurately predict stochastic high fidelity air defense and weapons effects simulation outputs?	Space filling designs of experiments coupled with predictive models will be able to the shape factors for the distributions of the outputs of higher fidelity models to such an extent that more than 95% of validation cases pass the chi-squared test at a 99% confidence level and will run at least an order of magnitude faster.	True for the weapons effects models. ADA models used predictions of averages only.

The first research question corresponds to the first research objective about building a weapons effect model from existing research. This question asked if a fire plan optimized to achieve a certain effect such as destruction of the aircraft or destruction of the runway be the fire plan with the most number of leakers. Before beginning the research, it was hypothesized that the greater accuracy of CMs would make them more

effective against smaller targets such as the parked aircraft or the POL sites. Conversely, the greater blast damage and size of the resulting craters and the larger spread of the submunitions would make TBMs more effective against the area targets such as the runway. This hypothesis turned out to be mostly true. The TBMs were more effective against the runway and the CMs were more effective against the POL sites. However, instead of CMs being more effective against the aircraft, the TBMs were slightly more effective.

This is mainly due to the mobile nature of the parked aircraft. The friendly forces understand that the parked aircraft are a lucrative target for missile attacks. It is wise to not park them close together where a single missile has a greater chance of destroying multiple aircraft. However, for ease of maintenance and logistics, each aircraft type generally has a specified parking area on the airfield. In this simulation there were three types of aircraft (aircraft A, B and C). Each aircraft type had a parking area with multiple parking locations. When placing the aircraft, they were restricted to their own parking area, unless that parking area was completely full. At which point, the remaining aircraft could be parked anywhere on the airfield.

In order to spread the aircraft out as much as possible and to simulate the random nature of aircraft coming and going from the airfield, the aircraft were parked on the airfield such that they maximized the minimum distance between aircraft while still parking in their designated locations. This meant that for a given number of each aircraft type, the first aircraft was randomly assigned a location within its designated parking area. The subsequent aircraft were placed at the location that maximized the minimum distance between all aircraft already placed. This continued until all aircraft were parked.

Because the location of the aircraft changes throughout the day, the aim points of the missiles were based on the parking locations and not necessarily the occupied locations. Each leaker then randomly targeted a given aim point which may or may not happen to be near aircraft, depending on the random draws of that particular simulation run.

The fact that the missiles were aimed at a large area and not at a specific target made the aircraft more of an area target than a point target. Because they were aimed at the general area of the aircraft, the larger damage radius of the TBMs made them more effective. Thus, the logic of the hypothesis was true, that TBMs would be more effective against area targets and CMs more effective against point targets. But the initial characterization of aircraft as point targets was incorrect.

The second research objective was about using the proposed methodology to conduct a trade study for changes in doctrine (tactics) and organization for an ADA unit. The research question asked if the proposed method would allow for rapid optimization of tactics against a complex attack that is reproducible in a higher fidelity simulation. The proposed method would only be valuable if the results were reproducible in the accredited higher fidelity simulations. The hypothesis for this question was that when the optimized results were tested with the higher fidelity simulations the optimized results would have a lower amount of damage for an equal or lower cost as compared to the base case. This hypothesis was shown to be true for the small and medium sized attacks. For the large sized attack, the optimized case reduced the damage to the aircraft and POL sites and reduced the cost. However, the damage to the runway was increased for both the optimization of the tactics only and the optimization of the tactics with the new point defense system. The damage to the runway was the lowest weighted criteria in the

selection of the optimized tactics in both cases. This meant that the optimized solution favored reduced damage to the aircraft and POL sites and a lower cost, over reduced damage to the runway. A different arrangement of weights would show different results. The increased damage to the runway for the large sized attack can be attributed to the reduced engagement space for the UT system in both cases.

The optimized solution included a reduced engagement shape to limit the number of UT interceptors that would be fired. The UT interceptor was the most expensive interceptor at four times the cost of the LT interceptor type A. Reducing the UT engagement space reduced the cost of the defense, but allowed more TBM leakers through that layer. The large sized attack included 30 TBMs. The LT system was limited to either 20 interceptor A missiles or 16 interceptor C missiles depending on the chosen missile type. The optimal Pk for these missiles was around 80%, so the LT system was only expected to destroy 16 TBMs with interceptor A or 13 TBMs with interceptor C. The remainder of the incoming TBMs had to be destroyed by the UT system. Therefore, as the UT system's engagement space was reduced, the number of unchallenged TBMs increased. If the LT system included additional interceptors, then the results would have been much closer to that of the base case and most likely at a lower cost. An additional iteration of the optimization process with the proposed methodology could prove this to be true.

The final objective was to find a way to combine the weapons effects and ADA simulations, but use predictive models in order to make the models run faster on a given computer. This was needed because stochastic optimization processes require many function calls. If these function calls are too long, then the optimization process can

become so long that it is impractical. This is especially true since the random nature of the ADA and weapons effect simulations requires many runs for each input vector in order to understand the range of possible outcomes. Therefore, the research question was designed to see if machine learning and design of experiments could create a fast running predictive model of the outputs from the higher fidelity simulations. It was hypothesized that the output ranges of each input could be modeled with a known distribution so that the predictive model only had to calculate the shape parameters of that distribution in order to predict the range of results.

This hypothesis was correct for the weapons effects model, but could not be shown as correct for the ADA simulation models. For the two weapons effects models, the runway damage model and airfield damage model, the predictive models were able to predict the shape factors of the validation set (a random set of 20% of the data that was not used to train the predictive model) to such an extent that visually, the predicted and actual histogram of the data matched, and statistically, the two predicted and actual distributions passed the chi-squared test (test that they were from the same unknown distribution) with 99% confidence level.

This was not the case for the ADA simulations model. The author tried innumerous different prediction models and fitting strategies, but was unable to find an adequate predictive model for the shape factors of the output distributions. Instead, predictive models were created for the average output of each outcome (number of leakers for a particular missile type, or the number of interceptors fired by the ADA system). These predictive models were later used in the optimization process and the solutions found with the predicted average outcomes were superior to the base case using

the higher fidelity models to find the actual outcome distributions, so the models proved adequate. Thus, while the hypothesis was not shown to be true for the ADA simulation, the predictive models that were constructed still met the research objective.

10. CONTRIBUTIONS AND FUTURE WORK

"Effective missile defense—not only homeland defense but also the ability to defend US allies abroad and our friends—must be achieved in the most cost-effective manner that modern technology offers."

- Donald Rumsfeld, Former US Secretary of Defense

This work is critical to the ADA community. Because actual tests of the systems are typically too expensive, the testing and optimization of the systems is done with simulations. These simulations are accredited based on hardware in the loop and the limited actual testing that does take place. This dissertation made use of the DoD accredited software EADSIM. The EADSIM simulation, like many other ADA simulations, is very detailed and requires run times on a modern computer ranging from minutes to hours for a single run. The simulation also does not include a weapons effect model. This work attempts to address these two issues by creating fast running prediction models and designing a weapons effect model based off test data and other validated models.

The cost of ADA systems and interceptors is much greater than the cost of TBMs and CMs. This places the ADA systems on the wrong side of the cost equation. Further proliferation of technology will only increase this problem. The ADA community needs to find new ways to defeat these threats. This dissertation shows a methodology to rapidly examine different tactics and new systems. This research will contribute the following to the greater body of knowledge:

1. Proposed and demonstrated a methodology to optimize ADA tactics and organization that examines non-material solutions first and then new material solutions.

2. Created and demonstrated a weapons effects model for an airfield that enables the creation of optimized fire plans that achieve a certain effect.
3. Demonstrated that the weapons effects model could be used to minimize damage to different parts of the target area as opposed to simply minimizing the number of leakers in the analysis of ADA defensive systems.
4. Showed that the shape parameters of output distributions from damage effects models could be predicted with machine learning tools.

In almost all ADA analysis the most controlling variables are the number of missiles that are inbound to the target. In a majority of the literature, and in a large number of analysis that the author has either taken part in or reviewed, there are only one or two TBM and CM fire plans and they are either assumed or given. This work created and showed a methodology that allows an analyst to quickly develop optimized fire plans to achieve certain effects. The work also showed that there are a large number of optimized fire plans that form a non-dominated frontier of fire plans that each is optimized to maximize certain objectives. ADA analysis can use this methodology to create and validate their fire plans before beginning a new ADA simulation.

In a majority of the literature, the goal of the ADA systems optimization is to minimize the number of leakers. This work showed that minimization of the number of leakers does not necessarily minimize damage. Instead, minimization of different missile system types is essential. In this analysis, the author for demonstration purposes, created the blast and damage data; however, it was well within reasonable bounds of what would be expected from real TBMs and CMs against soft targets like aircraft and POL sites. The

analysis showed that TBMs are more effective against area targets, such as the runway and mobile aircraft while the CMs are more effective against point targets such as the POL sites. Thus, if one of these targets was more critical then the other, then minimization of the missiles that caused the most damage to that target would be easier to achieve than trying to minimize the number of leakers of all missile types.

Once the enemy fire plan is created, this work showed a new methodology to optimize the ADA system's tactics and organization. The long run times and large number of runs required for optimization of a stochastic simulation many times prevents a full exploration of the design space. The proposed methodology, when combined with predictive models of the simulations, allows for this full exploration and later optimization. This dissertation was completed with unclassified sources as a way to document the methodology; however, the results could be easily repeated with classified data and real systems' data.

In order to build on this work, future analysis could include counter measures and jammers on the TBMs and CMs. This work only examined TBMs and CMs without any counter measures besides early release submunitions. The missiles with submunitions were only vulnerable to being intercepted before they released their submunitions. Once these submunitions were released they were too numerous and hard to hit, so the interceptors had no effect on them. Other counter measures that are becoming more prevalent on missiles systems include jammers and decoys.

Jammers are most often installed on CMs since their effect is diminished at longer ranges. There are two common missile jammers: noise jammers and digital radio frequency memory (DRFM). A noise jammer emits a large amount of random returns

within a specific frequency band in order to cause the background noise to increase. The hope is that the background noise will increase enough to hide the true return signal. A DRFM records the incoming signal and then emits a false return signal that will mimic the true return. This creates a line of false targets on the radar. The operator must then choose one of these targets to shoot at and if the false targets are spaced far enough apart the true target will be outside the interceptor's seeker field of view when it reaches the location of the false target.

Another way to improve upon this work would be to look at a larger number of TBM and CM launch points. Section 7.2.5 described how the TBMs were limited to a specific area, called a ballistic missile operations area (BMOA), based on the hide sites of the launchers (TELs). However, there could be many more of the BMOAs than what was used in this work. Additionally, CMs are not as limited, so they can be launched from many different locations to include approaches that are out of the sector of the phased-array radars. The out-of-sector CMs would help to highlight the benefits of a 360-degree radar system, such as the one used on the PT system.

Not only could this analysis be repeated with more TBM and CM launch locations, it could be repeated for multiple targets being guarded by multiple ADA systems. This type of analysis would help to highlight trades in organization since the total number of launchers and interceptors could be fixed, but these launchers and interceptors moved from one location to another in order to tailor the organization of the ADA defense at each defended asset. The effects analysis could also be extended to other likely targets such as seaports, assembly areas, and command and communications hubs.

This could also be extended in time so that, as opposed to looking at a single raid like what was done in this analysis, multiple raids could be examined over a long campaign in order to identify times and places where the ADA system's tactics and organization need to change in order to ensure that different areas of the asset are more defended based on the needs of the rest of the campaign.

Finally, the rapid calculations of the prediction models make them good candidates for use as the adjudication tool in wargames. Wargames require that the adjudication tool determine combat losses and weapons effects quickly, so that the pace of the game is not significantly slowed. An ADA centric wargame would allow the enemy force to choose their optimized fire plan based on the effects that are required at a particular time and place, based on the needs of the rest of the campaign. This would be an improvement since this analysis assumed that all the optimized fire plans were equally likely. On the friendly side, a wargame would help the ADA system analyst optimize the organization of the ADA systems defense in order to achieve the required protection of key assets that enable the rest of the campaign plan for the blue forces.

Overall, this dissertation helps the ADA community by fixing some of the problems that the author has experienced with the ADA system's analysis. The analysis of ADA systems will increase in complexity in the coming years due to the rapid proliferation of arms. The number of TBMs and CMs that the ADA systems will have to contend with will increase every year. New ways are needed to explore different methods of dealing with this growing problem.

APPENDIX A: RADAR BASICS

The radar is the heart of the air defense system and it is the device that detects and tracks the TBM, CM, and other targets. RADAR is an acronym for **RA**dio **D**etection **A**nd **R**anging; however, the acronym has become so common that most people generally accept it as a common usage word. A radar is an electrical system that transmits electromagnetic (EM) waves toward a region of space and receives (and subsequently detects) the EM waves "reflected" from any objects in that region [164]. EM waves are actually absorbed by a target and then new EM waves are re-radiated outward in all directions to include back towards the radar system and are therefore detectable. While this explanation is more technically correct, most people prefer to think of the EM waves simply bouncing off the target and returning to the radar similarly to a sound echo off a canyon wall. Each model is applicable in different situations. Generally the reflection model works well, except in cases where one is investigating the actual energy re-radiated by a target.

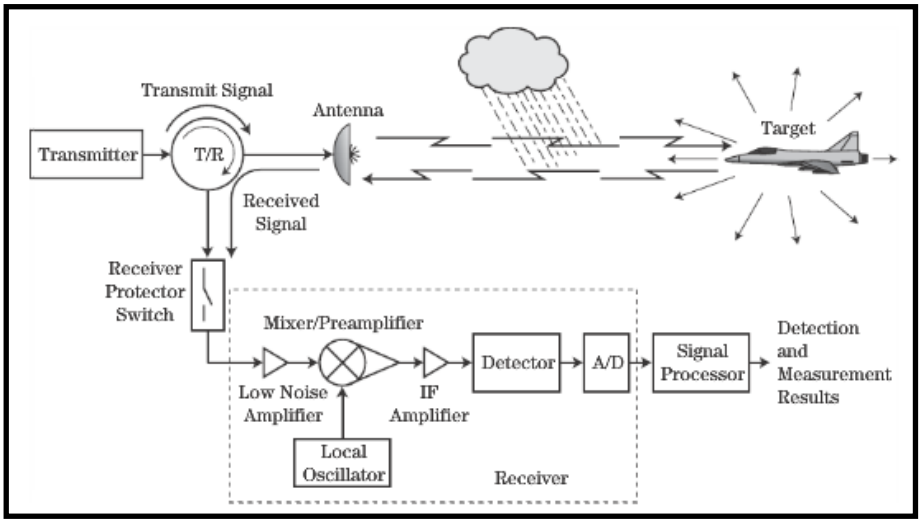

Figure 186: Radar System Components and EM Radiation Reflected Off a Target (Image From [164])

The ability of the radar to detect a target is governed by the Radar Range Equation (RRE). This equation is derived from the diffusion principles of the EM waves as they spread out across an ever-growing sphere as they propagate outwards. The general form of the RRE is given by [164]:

$$SNR = \frac{P_t G_t G_r \lambda^2 \sigma n_p}{(4\pi)^3 R^4 k T_0 F B L_s}$$

SNR = Signal-to-Noise Ratio
P_t = Power of the transmitter in watts
G_t = Gain of the transmitter (unitless)
G_r = Gain of the receiver (unitless)
λ = Wave length of carrier wave in meters
σ = Mean Radar Cross Section (RCS) in square meters
n_p = Number of pulses that are coherently integrated (unitless)
R = Range to the target in meters
k = Boltzmann's constant (1.38×10^{-23} watt-sec/K)
T_0 = Standard Temperature (290 K)
F = noise figure of the receiver (unitless)
B = instantaneous receiver bandwidth in Hz
L_s = Radar system loss (unitless)

SNR is used because the both RCS and noise are random variables. They will change from scan-to-scan and pulse-to-pulse. Thus, in order to detect a target, the signal from that target must be sufficiently greater than the noise of the system. This noise is a result of thermal noise in the receiver, clutter (unwanted wave returns), EM interference from other EM sources, and possibly jamming from an enemy system. Figure 187 below shows a detection system in the presence of random noise. The radar is able to detect the signal if that signal crosses a certain threshold value. The bin index in the x-axis of Figure 187 is a reference to range bins or a discreet range set. The signal amplitude shows the resultant amplitude of the received signal from all reflections in that range bin to include a target, clutter, and the signal noise.

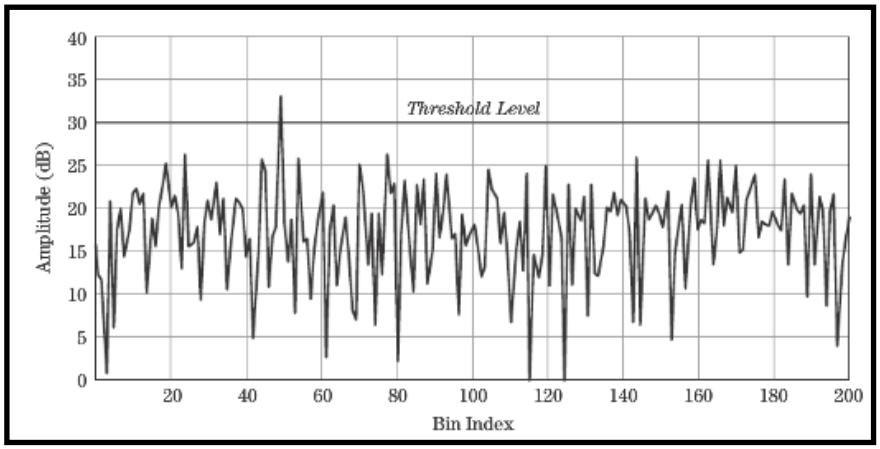

Figure 187: Radar Detection in the Presence of Noise (Image From [164])

The amount of energy re-radiated by an object is quantified as its Radar Cross Section (RCS). Most literature sources use the Greek letter "σ" to represent RCS. RCS has units of square meters, but it is not governed by size alone. Generally, larger objects will have larger RCS values, but the RCS also depends on the material and the complex reflection pattern with the associated constructive and destructive interference pattern from EM waves being re-radiated in all directions by all the different parts of an object. Metallic objects re-radiate EM waves better than carbon based material such as wood or living tissue. Typical RCS values range from 10^{-5} m^2 for insects to 10^6 m^2 for large Navy ships [164]. Due to this large span, a logarithmic power scale is often used with a reference value of one square meter.

$$\sigma(dBsm) = \sigma(dBm^2) = 10log_{10}(\sigma)$$

The RCS of an object is typically shown on a radar diagram. This diagram shows the expected calculated or measured RCS of an object from various aspect angles. These angles start from 0 degrees with the radar looking directly down an aircraft or missile's nose to 90 degrees where the radar is looking directly at a broadside view of the aircraft or missile. This continues to 180 degrees where the radar is viewing the object from the

rear and then around to 270 degree where the radar is looking at the opposite broadside view of the missile or aircraft. An example of an RCS plot is shown in Figure 188. The left side of Figure 188 shows a computer generated RCS plot of a simple aircraft model made of triangles, cones, and cylinders. This can be compared to the right side of Figure 188, which shows the measured values from a full scale A7C Corsair aircraft. Note that the RCS value can vary drastically depending on the aspect angle. In the simulate model the RCS changes from -38 dB to +14 dB. This represents a linear range of 0.000158 m^2 to 25.12 m^2 or a change of a factor is 5. The A7C is even more dynamic changing from -52 dB to +45 dB or a change of a factor of 11.

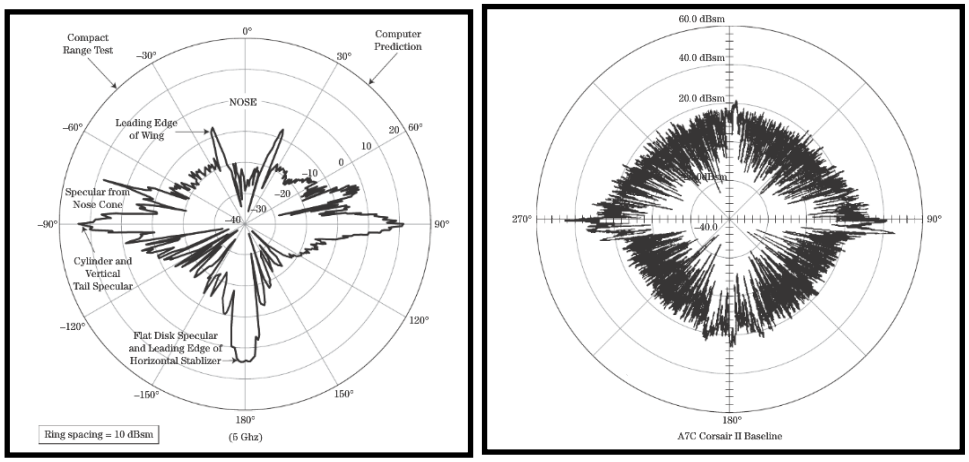

Figure 188: Radar Diagram of RCS from Simulated Aircraft (Left) and from Actual A7C Aircraft (Right) (Images From [164])

These diagrams clearly show that RCS is not constant. Even a radar scanning an object several times a second may get changing returns if the object is moving fast enough or has high speed components such as propellers. Thus, RCS is typically represented as a random variable. At distant ranges, an object will naturally go through intermittent detections as its changing RCS produces larger and smaller SNR values in

the RRE shown at the beginning of this section and the target return signal moves above and below the detection threshold shown in Figure 187.

The large variations in RCS for a target necessitate the need for a detection model that uses random variables for the RCS. These models are called Swerling Radar Models, named after their inventor Peter Swerling. Swerling models are the basis for modern radar detection models [164]. There are five basic Swerling models. A Swerling 0 model is one where the RCS does not change with aspect angle. For most real-world targets, this is not the case. Swerling 1 and 2 models, are used when the target does not have a dominate scatterer [173, 174]. The radar diagram of a target of this type will have an approximately circular shape. These targets are modeled with an exponential distribution. Swerling 3 and 4 models have a dominate scatterer [173, 174]. The radar diagram will have an oval shape where the RCS values tend to enlarge in one direction and tend to shrink 90 degrees from that orientation. These targets are modeled with a chi-squared distribution [174]. Swerling extended his models into probability of detection tables. A derivation and an explanation of these is located in [164].

Swerling models 1 and 3 differ from 2 and 4 in how fast the RCS values change compared to subsequent "pings" of the radar. This is primarily a function of the targets speed and range to the radar. If the target-radar angle is changing faster than the decorrelation angle, or the change in aspect angle where the radar will have significantly different returns, then there will be scan-to-scan decorrelation and the Swerling models 2 and 4 need to be used. Otherwise a Swerling 1 or 3 model is used [173]. A summary of these models is given below in Table 62.

Table 62: Swerling Models (From [173])

Scatter Orientation	Probability Density Function of RCS	Decorrelation	
		Block-to-Block	Pulse-to-Pulse
No Dominant Scatter	Exponential	Swerling 1	Swerling 2
One Dominant Scatterer	Chi-Square, degree 4	Swerling 3	Swerling 4

Because CMs are generally long and narrow with shorter wings, they will have a dominant scatterer along the fuselage. They also generally travel at high speeds and will have a higher likelihood of pulse-to-pulse decorrelation so they are typically modeled with as a Swerling 4. Most SRBMs do not have a separating Reentry Vehicle (RV) and thus have a dominant scatterer. They also travel extremely fast and making them ideally modeled with a Swerling 4. Most MRBMs do have a separating RV. This RV is cone shaped and usually does not have a dominant scatter, but will be moving at extremely high speed. Thus, MRBMs are typically be modeled with a Swerling 2.

APPENDIX B: DESIGN OF EXPERIMENTS OVERVIEW

There are many advantages of current high fidelity ADA models such as EADSIM. These models have good radar representation and flight dynamics models built in that will allow the analysis to include the critical detection component. In addition, they are designed to handle several different types of threats all flying at different profiles. Their main disadvantage, however, is time and computation space. A typical campaign-length simulation of EADSIM with thirty Monte Carlo runs can take 10-30 hours to run on a standard desktop computer and will produce 2 gigabytes of data. In order to be useful in evaluating the entire design space of tactics and fire doctrine, this run time must be sped up and the data storage requirement reduced.

A Design of Experiments (DOE) is a method to quickly sample the design space in the most efficient manner possible. It was first developed for experiments in agriculture during the 1920s. In the 1950s, its use expanded to other fields including engineering [175]. There are three main types of DOEs: Screening, Optimization, and Modeling [176]. The purpose of a screening model is to determine which factors have the largest effect on variability of the outcome. This is meant to focus the experimenter on those factors that have the largest "control" over the process and reduce the dimensionality of the problem [177]. In Figure 189, the 2-level screening test in the upper left is an example of a screening model. The purpose of an optimization model is to determine the factor settings that will either minimize or maximize an objective. In Figure 189, Box-Behnken and Face-Centered Central Composite designs on the lower left and lower right are optimization designs. Finally, the purpose of the modeling design is to sample the design space in such a way that an efficient "meta-model" or a model of

a model can be fit to the process so the outcome can be predicted for any given combination of inputs. Each of these DOEs is meant to help the experimenter understand the underlying process that leads to the outcome, but they do so in different ways. They are also designed to help the experimenter understand the underlying processes with fewer experiments or model runs than a full-factor experiment, where all possible combinations of factors are tested as shown in the upper right of Figure 189.

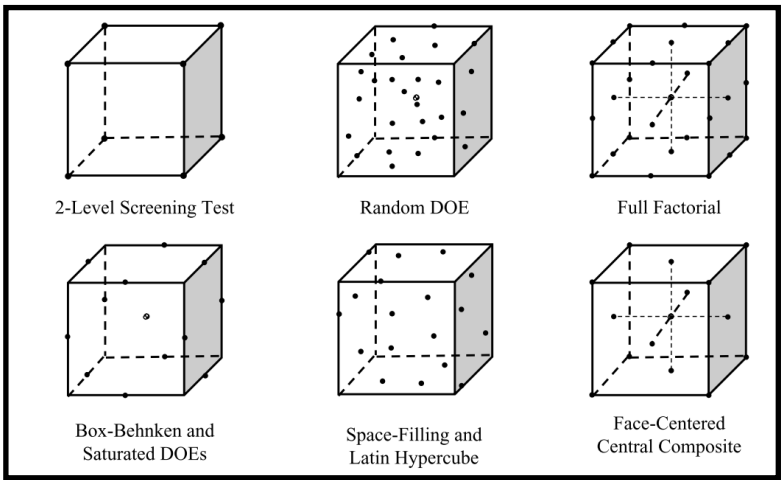

Figure 189: Types of Designs of Experiments (Image From [156])

Design of Experiments Principals

In order to understand how these designs help the experimenter to understand the design space and the underlying process, it is important to cover several principles behind DOEs and their subsequent use in regression modeling. One of the first principles needed is that interactions between factors can play a large role in the outcome of a process. In many processes, the synergistic effect between two or more factors can have an impact that must be considered beyond just looking at the factors operating independently. For example, consider an experiment of the best combinations of ingredients to bake bread. The amount of flour, yeast, and water is important but there is

likely to be a strong relationship between the amount of yeast and water. This relationship will manifest itself in the form of an intersection term.

The second major principle is called the scarcity-of-effects. This principle states that the variability in the outcome of the process is likely driven by only a couple of the design variables. This is also commonly called the Pareto principle [178] after an Italian economist Vilfredo Pareto [179]. It is also sometimes known as the 80-20 Rule meaning that 80% of the outcome is controlled by 20% of the variables [156, 179, 180]. Although the actual numbers are rarely exactly 80% and 20%, the principle has been shown true in many real-life applications [178].

Related to the principle of interactions is the principle of hierarchy. This states that in a regression model, the largest source of variability will be from the first-order terms (main effects) followed by the 2-level interaction terms, then the 3-level interaction terms, etc [178]. This is the main principle behind screening designs. These designs are meant to only test for the main effects since they will have the largest influence on the variability of the outcome.

Finally the heredity principle is related to all the principles mentioned. This principle is also related to modeling and it states that if a second order interaction is deemed important meaning that it has a strong influence on the variability of the outcome, then the main effects factors that make up that 2-level interaction are also important and should be included in the model [178].

DOEs can be used for both "real-world" models and for computer experiments. The main difference is that real-world processes are subject to noise and error. That is

$$y = y_{actual} + \epsilon$$

where y is the output of the process and ε is the error or noise in the result. This means that real-world DOEs must be designed and conducted taking into account this noise. To do this there are several key strategies.

The first strategy for dealing with noise is replication of trials [135, 178]. Typically the noise is assumed to have a normal distribution with a mean of zero and some standard deviation, N(o,σ). From the central limit theorem, if the outcome is sampled an adequate number of times then the results will form a normal distribution with a mean of y_{actual} and a standard deviation of σ [133]. Replicating the design runs will allow the experimenter to estimate the effect of the noise.

A second strategy for dealing with noise is blocking [135, 178, 181]. Blocking is when the experiments are arranged into relatively homogenous groups. This will help to eliminate some of the random error within the blocks since the experiments are similar. The subsequent analysis can then explore the variability between blocks to help isolate the true effects from the random noise [135].

A third strategy that helps somewhat with noise, but is mostly used to control bias, is randomization. By randomizing many of the experiment aspects under the control of the experimenter, the effect of uncontrollable factors can be reduced when the outputs are averaged. This helps to eliminate systematic effects of random and uncontrollable effects [135]. For example, if an experiment is conducted on the ballistic flight of projectile, the winds aloft may not be able to be accurately measured during the actual experiment even though these will affect the flight of the projectile. By running the experiments in a random order, when the results are averaged, the overall effect of the wind will not bias the end results.

In computer models, random noise and uncontrollable variables are typically not an issue. If the model is deterministic than there will never be a difference between runs using the same inputs. So blocking, replication, and randomization do not really apply. In stochastic simulations that rely on a random number generation tool, replication is needed to compute summary statistics, but blocking and randomization is not needed because the error source is known. There is no unknown noise like what occurs in real-life experiments.

In both computer models and real-world models, there are several other key principles that effect the choice of DOE and later the choice of regression. The first is called aliasing or confounding. A DOE is designed to assess the most information with the fewest trials, or at least fewer trials than a full-factorial design. This reduction in trials, however, comes with a cost. The cost is that the experimenter will not be able to discern the cause of some of the variability from different factors. This is called aliasing or confounding [135, 178]. The amount of aliasing increases as the number of independent trials decrease. For example, in a screening design the main effects are confounded with 2-level interactions and higher, but not with other main effects. This means that the experimenter cannot determine how much the outcome changed as a result of just the main effects or because of interactions between those main effects.

The amount of confounding is quantified by the resolution of the design. A resolution III DOE confounds the main effects with 2-level and higher interactions, but does not allow the main effects to be confounded with each other. A resolution IV DOE does not have any confounding between the main effects or two-factor interactions, but does allow confounding between the two-factor and higher interactions. A resolution V

DOE does not confound the main effects or two-factor interactions with each other, but does confound the three-factor and higher interactions [175, 176, 182].

Another key principle is that of orthogonally and specifically orthogonal DOEs. In many experiments, both real world and computer experiments, the experimenter wants to study the effects of several input variables. If these variables or trials themselves are correlated then it will be difficult to determine if the change in the outcome was from one factor or the other [135]. This can be overcome with orthogonal DOEs. Orthogonal DOEs have no correlation between design trails. This helps to maintain the independence of the independent variables [176] and allows the outcome of each trial to be individually and uniquely identified. For computer models, aliasing and orthogonally must be considered [182].

Typically, DOEs and surrogate modeling will be used on complex computer models that require long run times. The experimenter wants to estimate the outputs or optimize the outputs using the fewest design trials, since those trials are computationally expensive. Typically, these computer programs have many input parameters. In DOEs, the number of trials needed is correlated to the number of input factors and the number of levels of those factors. Thus, it is typically advisable to reduce the number of input factors under investigation. This can be done through intelligent selection and/or through statistical selection.

In intelligent variable selection, the experimenter selects input parameters based on experience and judgment. These input parameters should be the ones that have the most effect on the outputs under study. The experimenter then fixes the other input parameters at a certain value. This value could be an average value or a set given value.

For example, in the design of an airplane, the experimenter could set the parameters of the atmosphere to a standard value (the standard atmosphere). In addition, if the experimenter knows that the engine has already been selected, it would be appropriate to set the computer model's engine parameters to the known values of the chosen engine. When doing intelligent selection, the experimenter must acknowledge that there could be interactions between the set variables and the variables under test that will not be captured and thus, not included in the analysis.

In statistical variable selection, the experimenter uses a screening DOE followed by an Analysis of Variance (ANOVA) to select the critical input variables (the input variables that have the most effect on the variability of the response) [178]. For a good introduction to ANOVA see Hines, et al. [133], or Rushing et al. [181]. Screening DOEs are orthogonal level III resolution DOEs. This means that each run is independent from the other and the main effects are not confounded; however, the 2-level and higher interactions are confounded with the main effects. Thus, the screening DOE and ANOVA analysis will show the relative contribution on the variability of the outcome for only the first order terms (main effects) for each of the input variables under study. Typically, the Pareto principle will apply, which states that most of the variability of the output is controlled by only a few input variables. Again, this is normally called the 80-20 Rule meaning the 80% of the variability is controlled by 20% of the inputs. After the ANOVA, the experimenter will identify the critical variables and will set the other variables not chosen to a set value, typically an average value.

Once the number of input variables has been scoped down to a reasonable size, the experimenter must choose the type of DOE to use for the main analysis. The type of

DOE used should correspond to the type of analysis that the experimenter plans to use. Both of these are tied to the shape of the underlying function under investigation [135, 177, 183, 184]. The selection of the correct DOE for the given problem and regression is called optimal design [135, 178]. Screening DOEs are useful when tied to ANOVA because they give a minimum variance estimate of the slope of the response as a function of the inputs [135]. Other orthogonal optimization DOEs such as the Box-Behken and Central Composite designs are useful for low order polynomial regression such as Response Surface Equations (see following section). These types of orthogonal DOEs attempt to minimize some function of the covariance matrix of the least squares estimates of the parameters. These designs can be grouped into three main groups based on which function they use: D-optimal designs minimize the determinate of the covariance matrix, A-optimal designs minimize the average variance of the trace of the covariance matrix, and I-optimal designs minimize the average variance of the predicted response(s) over the design region [135].

Design of Experiments for Computer Models

While DOEs were originally designed for real-world experiments, they have evolved into an efficient tool for computer experiments as well. There are, however, some key differences in a computer experiment as compared to a real-world experiment and these differences change the criteria for selection or design of a DOE.

Many times in computer experiments, the goal is to predict the output from computationally expensive computer programs. This type of experiment does not lend itself well to optimization DOEs. For predicting the output of a computer experiment for

any given set of inputs a non-orthogonal design is needed. This DOE should sample the interior of the design space in such a manner that it will have a high predictive power that accurately estimates the process under scrutiny. [176, 185]. These models are called space-filling designs. Of the DOE models in Figure 189, the only space-filling designs are the random DOE and the Latin Hypercube.

The Random DOE shown in Figure 189 can be used in computer experiments since it does sample the interior of the design space, but because it is random, there is no systematic spread of the sample points. Some areas of the design space will naturally be sampled more than others. This can be countered, to an extent, through the use of stratification where the design space is separated into n distinct regions and one point is randomly populated within each region [135]. This is useful if the experimenter knows *a priori* where the output will change rapidly since the size of the regions can be independently controlled to sample these areas more than others.

If the experimenter does not know the shape of the output he or she may want to ensure that the sampling points are spread uniformly throughout the design space. Also, more specifically, the projection of the input points into the design region for each of the variables is spread evenly. Therefore, a design with widespread points distributed evenly across the range of each of the input variables is desirable. This feature is sometimes referred to as stratified sampling [177]. A design that does this is in a systematic manner is called Latin Hypercube Design (LHD). LHD DOEs were first proposed by McKay, et al. in 1979 [186]. Fang, et al. generalized the LHD notation and design methodology by denoting a LHD design of n runs of S input factors as LHD (n,S), and representing the design as a n x S matrix in which each column is a random permutation of [1,2,…,n]

[187]. The LHD divided each of the s variables into n regions, each with a size of 1/n, and ensures that a single point is placed inside each of the n divisions such that the one-dimensional projection onto each of the s variables is uniformly spaced. Because each LHD is a random permutation, it is a natural extension of the random design with the additional constraint that the one-dimensional projection into each input variable must be uniformly distributed [135, 137, 188]. The random nature of a LHD, however, can lead to designs that do not fill the entire design space well, such as the design on the left of Figure 190. Both designs in Figure 190 project evenly into each of the two design variables, but the design on the left clearly does not sample the upper left and the lower right region of the design space well. Therefore, a LHD generally needs additional constraints to ensure even sampling.

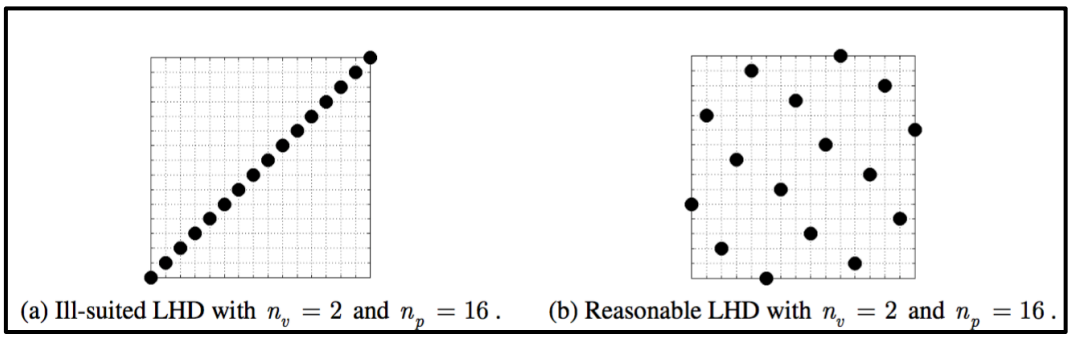

Figure 190: Examples of Two Latin Hypercube Designs (Image From [184])

There have been many methods proposed to help ensure that the LHDs are more space filling. The easiest way, as suggested by Fang, is to generate a LHD and then examine its bivariate scatter plot. If the plot does not look reasonably uniform, than generate a new LHD. While this is certainly easy, it is time consuming and subject to the judgment of the experimenter [137]. A more methodical approach that is easy to implement is called cascading LHD. In a cascading LHD, the experimenter starts with a LHD across the entire design space. Then at each point in the LHD, the experimenter

defines a smaller design space and generates a new LHD. This is repeated as many times as necessary. By developing ever smaller LHDs within each original LHD, the final design is still guaranteed to be orthogonal and maintain the projection properties of the normal LHD design [135]. A second method to ensure adequate space filling properties is to maximize the minimum distance between points. This type of LHD is called maximini (Mm LHD) or φ_p LHD where φ_p is the root-sum of the distances between points. The general distance between points can be found by:

$$d_{ij} = d(\vec{x}_i, \vec{x}_j) = \left[\sum_{k=1}^{n_p} |x_{ik} - x_{jk}|^t\right]^{1/t}, t = 1 \text{ or } 2$$

where xi and xj are any pairs of point in the design space, and n_p is the total number of points in the LHD. The variable t is selected based on the type of distance the experimenter chooses, 1 for rectangular distance and 2 for Euclidian distance [135, 184]. The root-sum of the distances between points is:

$$\varphi_p = \left[\sum_{i=1}^{n_p-1} \sum_{j=i+1}^{n_p} d_{ij}^{-p}\right]^{1/p}$$

Minimizing φ_p is equivalent to maximizing the distance between points in the LHD. The general idea is to generate a number of LHDs and once all the designs are generated, calculate φ_p for each design and select the one with the smallest φ_p. It has been shown that this is equivalent to the D-optimal criteria (minimizing the determinate of the information matrix: $(X'X)^{-1}$) and is thus one class of optimal design [188]. Many methods have been proposed on how to select the LHDs and an excellent summary is in Viana, et al. and Kennedy [137, 184]. The main advantage of LHD is that when any dimension is removed, the remaining points project into the lower dimensional space and

still maintain their uniform stratification [138]. That means that no design points are lost because two points project on top of one another. This makes LHD good for experiments where multiple responses are estimated and each input may not influence every output.

In general, maximizing the minimum (Mm) distance between points seems like a good way to fill the space. The Mm LHD adds the constraint that the 1-D projection into any design input should be uniform, but what if that constraint is removed? One of the most common DOEs that simply spreads the points throughout the design space as best as possible is called "sphere-packing". This DOE can be visualized as arranging the design points so as to pack as many spheres into the cube as possible [185]. Figure 191 below shows an example of the sphere-packing scheme. The main difference between the sphere-packing scheme and the Latin Hypercube is that the Latin Hypercube compromises some of the spread of points to help ensure more uniform spacing. Generally, sphere-packing designs fill the design space better than LHDs [183], but typically the designs are not orthogonal and will not uniformly project into each design variable uniformly [137].

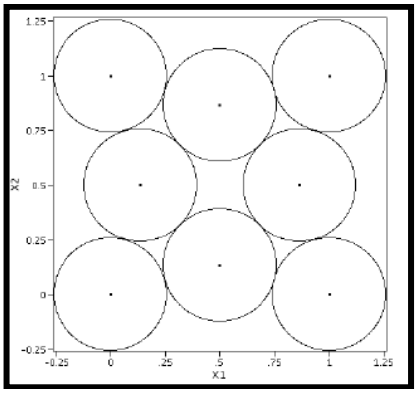

Figure 191: Sphere-Packing Schemes (Image From [185])

In general, pure space-filling designs will result in a larger minimum distance between points, but LHD will ensure that each dimension has an equal number of points

uniformly spread though the design space. This uniform spread of points is desirable since it ensures a good sampling of all dimensions; however, when a histogram is constructed of a LHD, generally there is good sampling of the interior points, but the number of points at the extremes is smaller. This is due to the nature of how the various n-dimensional points project into each dimension. Therefore, another set of designs measure how close the resulting histogram of each dimension is to the uniform distribution. These designs are aptly named uniform designs. Because the uniform design samples each level in an systematic fashion, they are useful for obtaining a good estimate that involves the integral of the unknown function [185]. In fact, the uniform design has been shown to minimize the upper bound on the absolute error of a point estimator, such as the mean, of an unknown function. However, in computer models the experimenter is generally concerned with predicting the overall function output and not just a point estimate of that output [135]. The points of the uniform design are also not guaranteed to be evenly spaced across each dimension and generally takes much longer to generate than space-filling designs of LHD [185].

DOE Wrapper Functions

The process of populating the DOE with outputs from the computer model involves a series of steps. These steps are executed by a computer code called the wrapper function. The wrapper function serves as the interface between the DOE and the actual computer code that we are trying to model as illustrated in Figure 192.

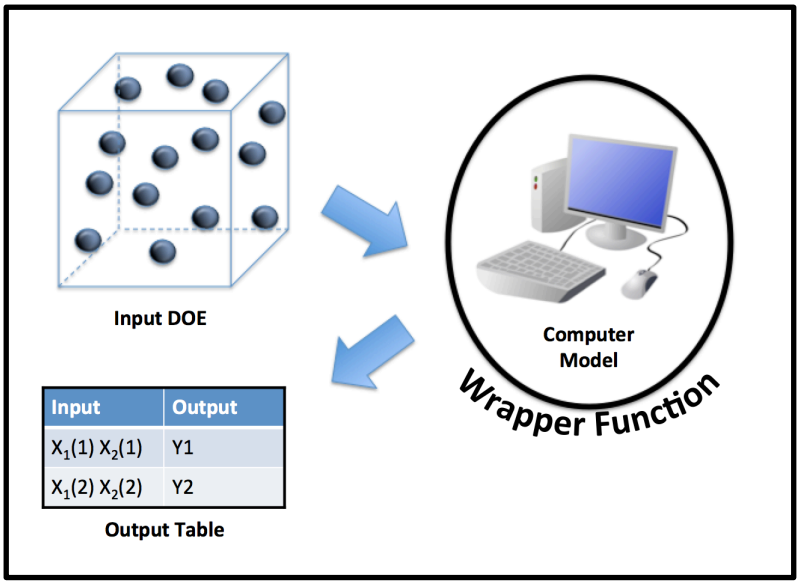

Figure 192: Wrapper Program and its Function

The wrapper function reads the inputs from the i^{th} line of the DOE input table. It writes these input values to the correct locations on the input files for the computer model. It then runs the computer model and opens the output files. It locates the specific outputs we are truing to model and writes these values to the output portion of the DOE table. If file size and computer space is a concern, it can also delete the output files once the needed values have been extracted. It then repeats this process for all i lines in the DOE. Once the DOE is populated with outputs from the wrapper function, the next step is to develop a surrogate model that correctly predicts the outputs from the computer model. The creation and selection of surrogate models is explained in the next appendix.

APPENDIX C: SURROGATE MODELS OVERVIEW

A surrogate model is a model of a model. It is generally used as a faster running predictive model of the higher fidelity, but longer run time, computer model. This surrogate model should be highly accurate (able to correctly predict outputs) and faster to run than the actual computer model. All of the surrogate models that will be introduced are equation type models. The equations are typically very complex, but a computer is able to calculate them in a fraction of a second. This allows us to very quickly estimate the output from a computer model that may take minutes to days to execute. Because the surrogate model is predicting any input vector, the model needs to be trained using points that cover the entire input space. To do this efficiently, designs of experiments (DOEs) are typically used for the training and validation sets of these models. DOEs are explained in the previous appendix.

There are many different types of surrogate models. The ones that are used in this work are introduced below and include a Response Surface Equation (RSE), an Artificial Neural Net (ANN or NN), and Gaussian Kriging. In general, it is difficult to know beforehand which surrogate model will best predict a given output. The general approach is to build several models for each output and evaluate each to select the one that best predicts the output of a test set the best with minimum bias.

Response Surface Equations

A Response Surface Equation (RSE) is a mathematical function that links the input variables to some desired output variable via a polynomial function. It was originally developed by Box and Wilson [189] to examine real-world experiments, yet it

has been found that it is also a good approximation for computer experiments whose output does not drastically change over the input space. A second order RSE is one of the most widely used because it is very flexible, can take on a wide variety of forms, is relatively easy to use, and has proved useful in solving a wide variety of problems [187, 190]. The general form of a second order RSE is given below [190]:

$$y = \beta_0 + \sum_{j=1}^{k} \beta_j x_j + \beta_{jj} x_j^2 + \sum_{i=1}^{k-1} \sum_{j=i+1}^{k} \beta_{ij} x_i x_j + \varepsilon$$

Where
y =Output response
β_i = Regression coefficients of first degree terms
β_{ii} = Regression coefficients of pure quadratic terms
β_{ij} = Regression coefficients of cross-product terms
$x_{i,j}$ = independent variables
ε = error

In the RSE, the x_{ij} terms are the independent variables from the DOE and the y term in the dependent variable from the DOE. The β terms are the unknowns. The goal of finding an RSE is to solve for all the β terms using a least squares methodology such that the x_{ij} terms are mapped to the y terms with the smallest amount of error, ε; meaning that the sum of the squares of the error is minimized. This is expressed in the equation below:

$$L = \sum_{i=1}^{k} \varepsilon_i^2 = \sum_{i=1}^{k-1} \left(y_i - \beta_0 - \sum_{j=1}^{k} \beta_j x_{ij} \right)$$

Where
L =Sum of the square of the error
ε_i = error terms
y_i = output (dependent) terms
β_i = Regression coefficients of first degree terms
$x_{i,j}$ = input (independent) terms

Linear algebra has fortunately found relatively simple expressions to solve for the regression coefficients, β. The above equations can be rewritten in matrix form as [190]:

$$\mathbf{y=X\,\beta+\varepsilon}$$

Where
y = output (dependent) variable vector
X = input (independent) variable matrix
β = regression coefficient variable matrix
ε = error vector

$$y=\begin{bmatrix} y_1 \\ y_2 \\ \vdots \\ y_n \end{bmatrix} \qquad X=\begin{bmatrix} 1 & x_{11} & \dots & x_{1k} \\ 1 & x_{21} & \dots & x_{2k} \\ \vdots & \vdots & \ddots & \vdots \\ 1 & x_{n1} & \dots & x_{nk} \end{bmatrix} \qquad \beta=\begin{bmatrix} \beta_1 \\ \beta_2 \\ \vdots \\ \beta_n \end{bmatrix} \qquad \varepsilon=\begin{bmatrix} \varepsilon_1 \\ \varepsilon_2 \\ \vdots \\ \varepsilon_n \end{bmatrix}$$

If the kernel of the matrix **X** is zero, meaning that it is invertible and full rank, then the sum of squares of the error of the above equation is minimized by the following equation [191]:

$$\widehat{\boldsymbol{\beta}}=(\mathbf{X^T X})^{-1}\mathbf{A^T\,y}$$

Using this equation, the regression coefficients in the original RSE equation can be solved for in such a manner that the sum of the square of the error is minimized.

The RSE formulation has many advantages. From the coefficients, one can determine the importance of a factor. A large coefficient means that the corresponding factor has a large influence on the overall variability of the result. The sign of the coefficient also indicates the direction of this influence (positive or negative). Also, the process explained above for solving the coefficient values is relatively easier and computationally faster than the other surrogate methods that will be introduced. The main disadvantage of RSEs occurs with highly nonlinear, discontinuities, or other

irregular behavior of the response. The smooth nature of the RSE has difficulty modeling rapidly and irregularly changing outputs.

The RSE also has difficulty if the variance of the output changes over the range of the inputs. When this happens the residual plots will exhibit a characteristically funnel like shape. Afterwards, the variance can attempt to be smoothed by applying a transform to the inputs. The most common transforms are a log transform or a square-root transform. These transforms are special cases of the more general Box-Cox power transform. The Box-Cox power transform is given by:

$$Y_\lambda = \begin{cases} \frac{Y^\lambda - 1}{\lambda(Y^{\lambda-1})} \; if \; \lambda \neq 0 \\ \bar{y} ln(y) \quad if \; \lambda = 0 \end{cases}$$

In order to determine which value of lambda (λ) to use, a Box-Cox test can also be applied. The Box-Cost test tries different values of lambda from -5 to +5 and plots the resulting sum of squares of the error (SSE) against these lambdas. The value of lambda that minimizes the SSE is then chosen as the transform.

Artificial Neural Nets

Artificial Neural Nets (ANN) attempt to mimic how neurons in the brain function and process information. It approximates a function from a set of inputs via weighted summations into different activation functions. The general form or architecture of an ANN is shown in Figure 193. Each input is assigned an input node and each output (response) is assigned an output node. Therefore, there will be as many input nodes as input variables in the input layer and as many output nodes as the number of responses we are approximating in the output layer. Note in Figure 193 that each input node is

connected to each hidden node via an edge. Also, each hidden node is connected to each output node via another edge. A weight value is applied to each of these edges and an ANN works by multiplying each input by the edge weight, summing all those weighted inputs together and then applying an activation function inside the hidden node. In some ANN architectures, a basis is also added to the inputs after they are multiplied by the weights. The output from each activation function in each hidden node is then multiplied by the output edge weight and the weighted outputs are summed together at the output node.

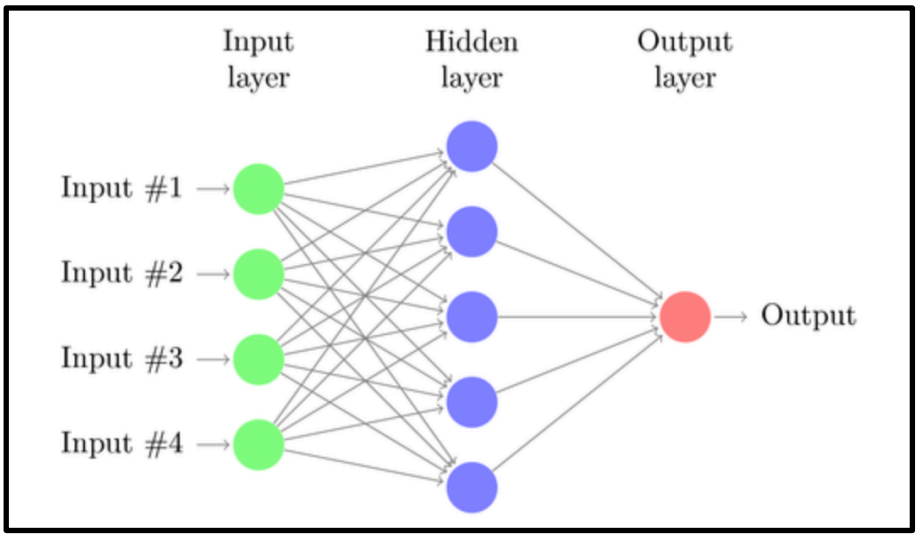

Figure 193: General Neural Net Architecture (Image From [192])

The goal of training the ANN is to evaluate which edge weights lead to outputs that most closely match the training responses. The architecture decisions that are left up to the user are the number of hidden layers, the number of nodes in each hidden layer, and the type of activation function to apply in each hidden node. In general the number of hidden nodes is limited by the size of the training data set and the complexity of the underlying function it is tying to approximate. Too few hidden nodes and the ANN may not have enough degrees of freedom to fit complex functions. The upper limit is dictated

by the size of the training set and again the complexity of the function. Too many hidden nodes can lead to over fitting. Also, each hidden node has an input weight and an output weight that must be determined. If there are too few training points, then the weight matrix can become underdetermined. A general rule of thumb for the number of hidden nodes is:

$$N_h = \frac{N_S}{\alpha(N_i + N_O)} \qquad where\ 2 \leq \alpha \leq 10$$

where:
N_h = Number of hidden nodes
N_S = Number of sample points in the training set
N_i = Number of input variables
N_o = Number of responses

The general form of the ANN can be expressed in matrix format. This makes the data manipulation much easier. Figure 194 shows the same ANN as Figure 193, but in a condensed form that allows us to build the matrix format of the ANN. Here, it is assumed that there are R inputs and these can be arranged into an input vector **P** that is Rx1. It is also assumed that there are S hidden nodes. This makes the matrix of edge weights is a SxR matrix. If there are basis to be added to each hidden node, that bias matrix, **b**, is Sx1.

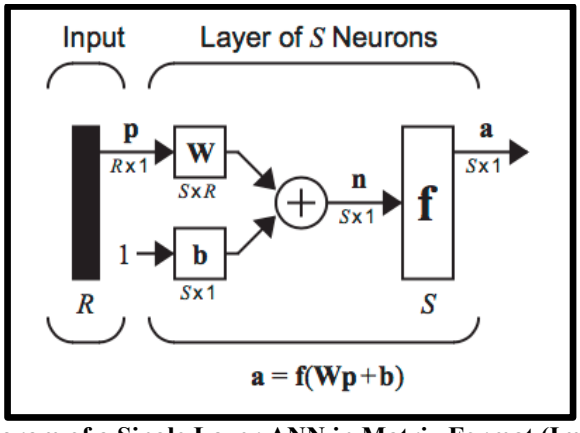

Figure 194: Diagram of a Single Layer ANN in Matrix Format (Image From [193])

In matrix form, the inputs vector, weight matrix, and bias vector can be expressed as:

$$P = \begin{bmatrix} P_1 \\ P_2 \\ \vdots \\ P_R \end{bmatrix} \qquad W = \begin{bmatrix} W_{11} & W_{12} & \dots & W_{1R} \\ W_{21} & W_{22} & \dots & W_{2R} \\ \vdots & \vdots & \ddots & \vdots \\ W_{S1} & W_{S2} & \dots & W_{SR} \end{bmatrix} \qquad b = \begin{bmatrix} b_1 \\ b_2 \\ \vdots \\ b_S \end{bmatrix}$$

The evaluation of an ANN multiplies the input vector by the weight vector and adds the bias. These results are then added together so the resulting matrix expression is:

$$H_j = \sum_{i=1}^{R} (\boldsymbol{WP} + \boldsymbol{b})_{ij} \qquad for\ j = 1,2, \dots S$$

where
H_j is the input to the j^{th} hidden node of the S total hidden nodes
$\mathbf{W_i}$ is the input weight matrix
P is the input vector
b is the bias vector
$(WP+b)_i$ is the i^{th} element of the weighted input vector
R is the total number of input variables

The input vector **H**, will be a Sx1 matrix. The activation function in each node (which can be the same of different for each node) is applied, element wise, to each element in **H** vector. There are many choices for this activation function. A good list of activation functions from [193] is shown below in Table 63.

Table 63: Artificial Neural Net Activation Functions (Image From [193])

Name	Input/Output Relation	Icon	MATLAB Function
Hard Limit	$a = 0 \quad n < 0$ $a = 1 \quad n \geq 0$		hardlim
Symmetrical Hard Limit	$a = -1 \quad n < 0$ $a = +1 \quad n \geq 0$		hardlims
Linear	$a = n$		purelin
Saturating Linear	$a = 0 \quad n < 0$ $a = n \quad 0 \leq n \leq 1$ $a = 1 \quad n > 1$		satlin
Symmetric Saturating Linear	$a = -1 \quad n < -1$ $a = n \quad -1 \leq n \leq 1$ $a = 1 \quad n > 1$		satlins
Log-Sigmoid	$a = \frac{1}{1+e^{-n}}$		logsig
Hyperbolic Tangent Sigmoid	$a = \frac{e^{n}-e^{-n}}{e^{n}+e^{-n}}$		tansig
Positive Linear	$a = 0 \quad n < 0$ $a = n \quad 0 \leq n$		poslin
Competitive	$a = 1$ neuron with max n $a = 0$ all other neurons		compet

These transformed inputs are then multiplied by the exit edge weights and summed together in the output node. If there are T output nodes, the matrix notation for the output is:

$$O_j = \sum_{i=1}^{S} (\boldsymbol{WP} + \boldsymbol{b})_{ij} \qquad for\ j = 1,2,\ldots T$$

where
H_j is the input to the j^{th} hidden node of the S total hidden nodes
W is the output weight matrix (different than the input weight matrix)
P is the input vector
b is the bias vector
$(WP+b)_i$ is the i^{th} element of the weighted input vector
S is the total number of hidden nodes

Once the architecture, number of hidden layers, number of nodes in each layer, and activation function in each hidden node are chosen, the goal of training the ANN is to adjust the weight and basis values to minimize the error between the resulting prediction and the training output. The training set is a subset of the total DOE that is used to train the ANN. The ANN uses the inputs from the DOE as test cases and attempts to match the predicted output to the actual output from the DOE by minimizing the squared error terms:

$$error = (y_i - \hat{y}_i)^2$$

where y_i is the i^{th} response and $\hat{y}_i$ is the i^{th} estimate of that response. Typically some form of gradient decent algorithm is used on the weight function to minimize this error. This general form of training is called back propagation and is the most common way to train ANN.

The main advantages of ANNs are when the design space exhibits discontinuities or rapidly changing behavior [46, 194, 195]. A single or double layer ANN has been shown to solve just about any non linear problem [149]. In fact, they have been called universal approximators [196]. The main disadvantage of ANN is that the resulting function approximation is a "black box." Unlike a RSE where the size is the coefficient on a given term explains its influence on the output, there is no such value in an ANN. Neural nets are also very easy to over fit the data and instead model the underlying process plus noise. This results in a model that can easily predict the training data, but fails to generalize to other data sets [197]. This can be prevented by using a good validation set and a process called k-fold cross validation. In k-fold cross validation, the data is divided evenly into a series of bins, such as into fifths. The first bin is withheld

and the model is fit to the remaining data. This fitted model is then tested with the withheld bin and the error is stored. This process is then repeated with a different withheld set until a model has been created with all bins withheld. After all models have been created, the model with the smallest error is used [195, 198].

Gaussian Krigging

Kriging is an n-dimensional interpolation method developed by South African geologist D.G. Krige in his a master's thesis for interpolation of mining data [199]. All interpolation methods use some correlation function with distance to describe the influence of known points around the prediction of an unknown point. Typically, the closer (in Euclidian space) that a known point is from the unknown point, the more weight the known point's value has on the prediction of the unknown point. The magic of kriging is that the value of surrounding points are weighted according to their spatial covariance, as opposed to their distance only [177, 200]. For deterministic experiments, this is extremely attractive because the error shrinks to zero around known points, so those points are predicted exactly [137, 175, 187]. The general form of the kriging equation is given as [177, 187]:

$$\hat{y} = \sum_{j=1}^{k} \beta_j f_j(x) + Z(X)$$

In this equation, f is a chosen basis function over the entire experimental domain, typically chosen as the Gaussian correlation function [177]. The error term, z, is a stochastic process, but unlike other interpolation methods that assume the error at each point is independent and identically distributed, the kriging model assumes that it is has spatial correlation of [177, 201]:

$$Cov\left[Z(x_i), Z(x_j)\right] = \sigma^2 \psi(x_i x_j)$$

where σ^2 is the variance and $\Psi(x_i\ x_j)$ is the correlation function between two points given as [187]:

$$\psi(\theta; x_i, x_j) = exp\left(-\sum_{j=1}^{k} \theta_j \left|x_i - x_j\right|^{p_j}\right) \quad \text{where } 0<p\leq 2$$

The θ term is a local "influence" term and the p term is a correlation parameter. These terms can be individually chosen for each estimate and thus form a vector of inputs. In general, for a constant value of p, the correlation function, ψ, approaches zero as the distance between points increases and approaches one as the distance decreases. The amount of correlation adjacent points have is controlled by the changing the value of p. This is demonstrated below in Figure 195. As the value of p is decreased from 2 to 0.1, the correlation curve changes from a smooth Gaussian curve to a sharp discontinuous peak.

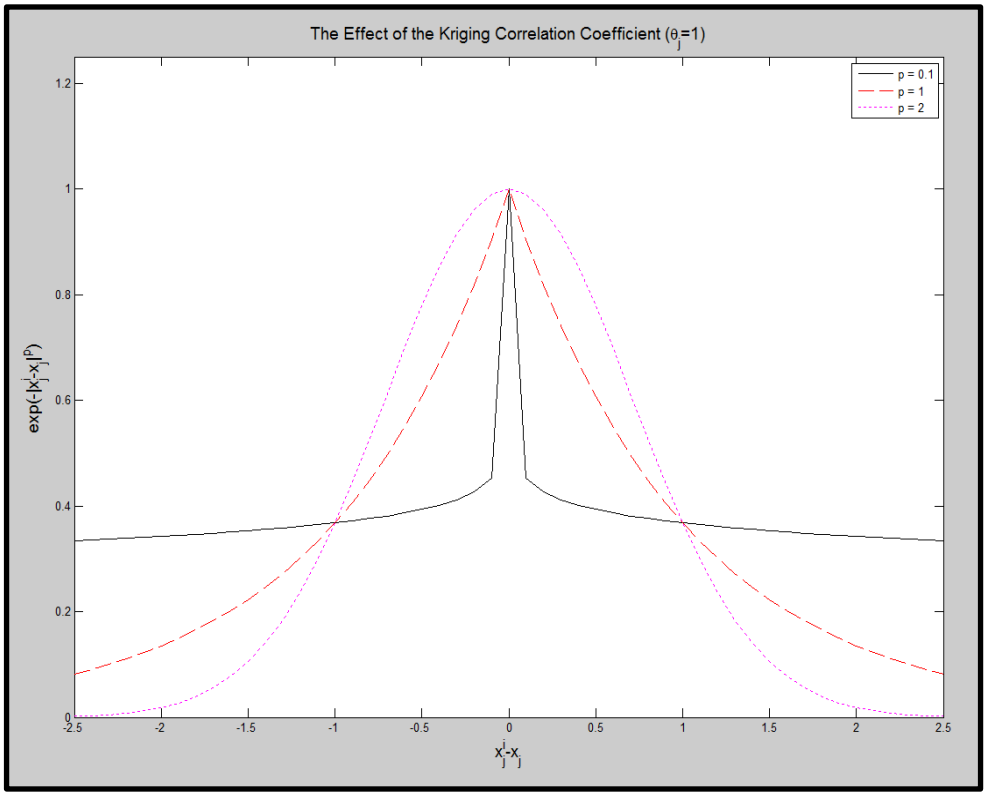

Figure 195: The Effect of Changes in p on Correlation. (Adopted From Image in [188])

A similar plot can be created for the θ, or influence term. This is done below in Figure 196. With a θ value of 0.1, the correlation between neighbors is high as indicated by the large smooth solid curve. As the influence term is increased to 10, the correlation between points decreases, as demonstrated by the sharper dotted line.

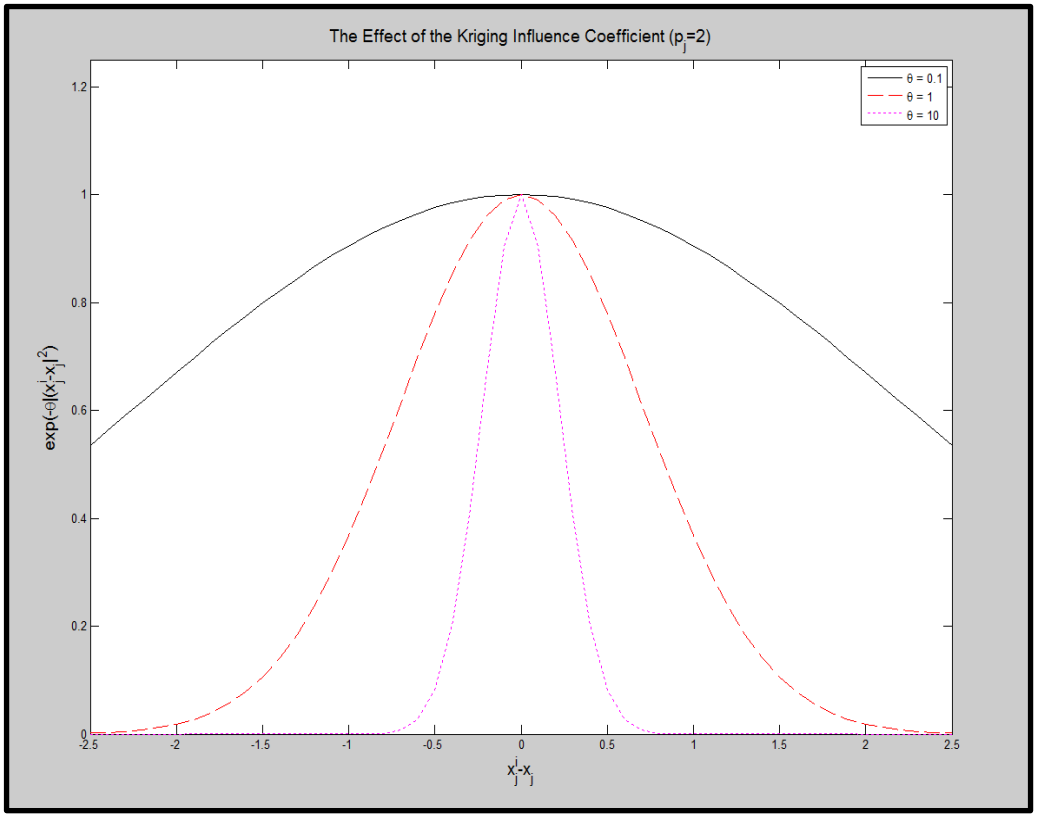

Figure 196: The Effect of Changes in θ on Correlation. (Adopted From Image in [188])

The values of θ and p are chosen to minimize the generalized error in the model. The maximum likelihood estimates (MLEs) for the mean and variance of the error (μ,σ^2) is given by [188]:

$$\hat{\mu} = \frac{1^T \Psi^{-1} y}{1^T \Psi^{-1} 1}$$

$$\widehat{\sigma^2} = \frac{(y - 1\mu)^T \psi^{-1} (y - 1\mu)}{n}$$

These can then be substituted into the concentrated log-likelihood function [188]:

$$\ln(L(Y^1, Y^2, \dots, Y^n)|\mu, \sigma) = -\frac{n}{2}\ln(\hat{\sigma}^2 - \frac{1}{2} ln|\psi|)$$

This function is not differentiable, so the values of θ and p are typically solved for with a stochastic optimizer, such as a genetic algorithm, particle swarm, or simulated annealing.

Surrogate Model Selection

Each of the surrogate models described above, RSE, ANN, and kriging have their own advantages and disadvantages. In practice, it is typically not known beforehand which will produce the best predictor for a given process. Therefore the best practice is to fit several models of different types and evaluate each to see which produces the best fit and more importantly, which predicts an unknown point with the least error. The error is measured as the root mean sum of squares of the prediction error (RMSE) [133, 190]:

$$RMSE = \sqrt{\frac{\sum_{i=1}^{n}(y_i - \hat{y}_i)^2}{n}}$$

Here, y_i is the ith response and $\hat{y}_i$ is the ith estimate of that response and n is the number of test points. Another measure of the goodness of fit is the coefficient of determination, also known as R^2:

$$R^2 = \frac{SS_R}{SS_y} = \frac{\sum_{i=1}^{n}(y_i - \hat{y}_i)^2}{\sum_{i=1}^{n}(y_i - \bar{y}_i)^2}$$

where SS_R is the sum of squares of the residuals, SS_y is the total sum of squares, $\hat{y}$ is the estimate of y and $\bar{y}$ is the mean of y.

The fit or prediction capability of a surrogate model can also be measured graphically by examining the actual v. predicted plot and the residual v. predicted plots. A sample actual by predicted plot for both a good fit (or prediction) and a poor fit (or prediction) is shown below in Figure 197. For a perfect fit, the predicted points would exactly match the actual points from the validation set, so the points in the plot would fall on a 45-degree line. In practice, this rarely happens, as there is normally some amount of prediction error. This causes the points to randomly fall above and below the 45-degree line. The closer the points are to this 45 degree line, the better the prediction or modeling capability of the surrogate model.

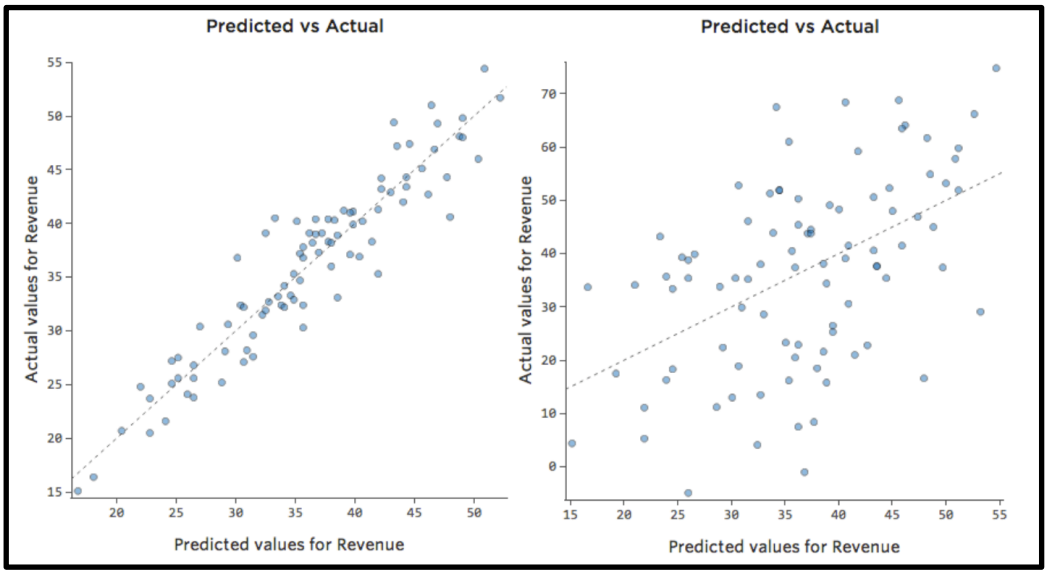

Figure 197: Sample Actual v. Predicted Plot for a Good Fit (Left) and a Poor Fit (Right) (Image From [202])

Ideally, the model should be unbiased such that the error in the prediction is random with a mean of zero. If this is true, the predicted points are equally likely to have a positive error as a negative error (over verse under predict). This is best examined in a plot of the residuals v. predicted values. A sample residual plot is shown below in Figure 198. For a good fit and an unbiased model, the points should be randomly scattered both

above and below zero error. The model should also not show any tendency to over or under predict for any subset of the points. This would be indicated if the residuals were smaller for low values of x, but were large for larger values of x (or vise-versa). The residuals for the plot on the right of Figure 198 show a bias to over predict the values.

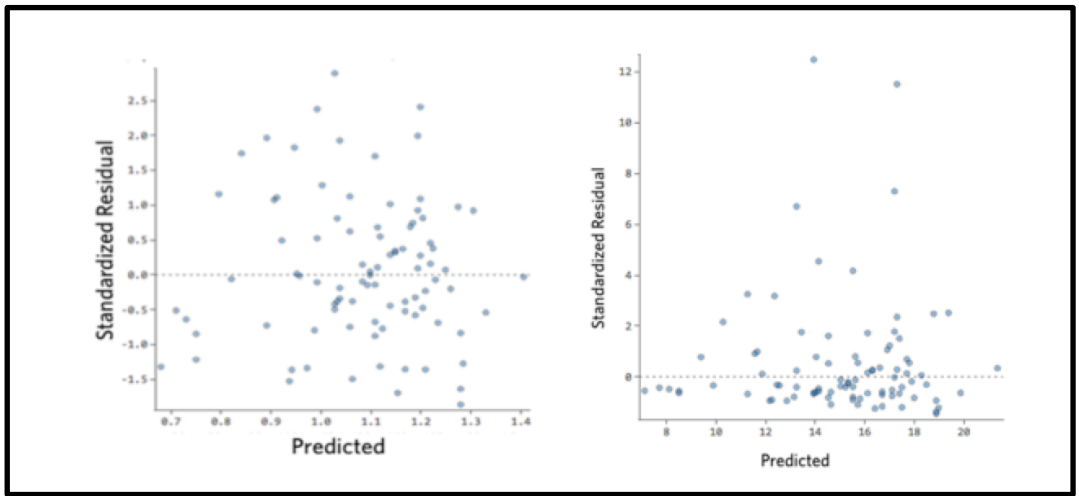

Figure 198: Sample Residual v. Predicted Plot for a Good Fit (Left) and a Poor Fit (Right) (Image From [202])

To determine a model's prediction capability, the test points are divided into two groups: a fit set and a validation set. The general rule is to initially divide your design set so that a random 80% of the design points are in the fit set and 20% are in the validation set [135, 187]. The model is then fitted to the fit set (holding the validation set completely independent) and then the fitted model is tested against the validation set to measure its prediction capability.

The best way to build the fit set and validation set is to design a DOE with the needed number of points to fit a model (the initial number of points is generally recommended as ten times the number of design points), and then augment the DOE with an additional set of points to form the validation set. In practice, the validation set could be random points within the design space or an augmentation to the validation set space-

filling design. By using an augmented space-filling design the experimenter is assured that the validation points are spread throughout the design space and placed at an optimal distance from all the points in the fit set. In addition, if the model shows a poor prediction capability, these points can be added to the original fit set and a new validation set generated.

The process of creating a surrogate model begins when the model is fitted to the fit set. This is done without any influence from the validation set. If the fitting of the model is a stochastic process (as in ANN and kriging) the fit set can be further divided into a fit set and a validation set. This is typically done through a process known as k-fold cross validation. In a k-fold cross validation, the model is fitted k times to a subset of n-k points in the fit set (where n is the total number of points in the set). The model is then evaluated for the k points that were held out of the fit set. This is repeated k times with new points each time and the model with the best fit for the k hold out points is chosen as the surrogate model.

Once the model is trained with the fit set, it is then used to predict the values of the design points in the validation set. In both the fit set and the validation set, the R-squared and the RMSE are calculated and the actual v. predicted plot and residual v. predicted plot are created. The accuracy of the model to predict the fit set is called the model fit error (MFE) and the accuracy of the model to predict the validation set is called the model representation error (MRE).

A good model must not only predict well, it should also be unbiased in its prediction. This means that it should not systematically under or over predict. To test for this bias, it is common to create a histogram of the residuals. This histogram should be

centered at zero, be unimodel, and appear to have a normal distribution. By ensuring that the distribution is centered at zero, we ensure that the residuals are equally positive and negative meaning that the model equally over and under predicts. By ensuring that the model has a normal distribution shape, we ensure that the model has mostly smaller residuals with occasional large under or over predictions. In fact, the construction of a response surface equation demands that the residuals be normally distributed. A neural net and kriging model do not require the residuals be normally distributed, but it is good when they are because it helps to ensure the model is unbiased. Once the histogram is created, a normal quantile plot can also be created to visualize how different the histogram is from a theoretical normal distribution. This is shown below in Figure 199.

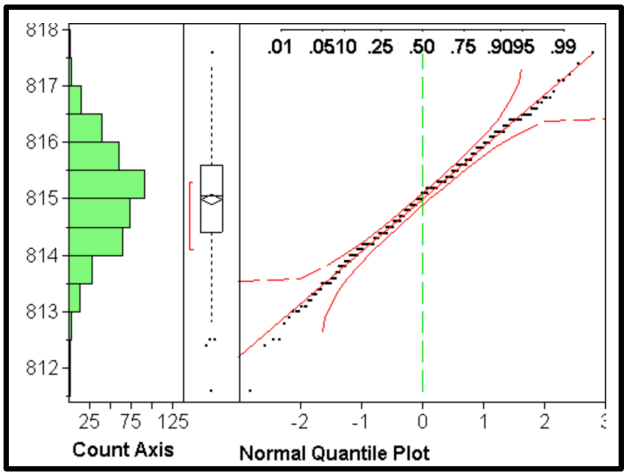

Figure 199: Sample Residual Histogram and Normal Quantile Plot (Image From [203])

Ideally, all points in a normal quantile plot would fall on the 45-degree line y=x. If the normal quantile plot exhibits a nonlinear shape, then the data is probably not linear. A statistical test to determine if the data is from a normal distribution is called the Shaprio-Wilk Test [204]. This test has the null hypothesis that the data is normally distributed. Thus, for a given alpha value, say 0.05, the null hypothesis is rejected if the p-value statistic from the test is less than this value (0.05) indicating that the evidence

suggests the data is not normally distributed. If the p-value is greater than the chosen alpha value, then there is not sufficient evidence to suggest that it is not from a normal distribution.

APPENDIX D: NEURAL NET FIT GRAPHS FOR ADA SIMULATION

This section will show the fit quality for the neural nets (NN) created from the ADA simulation explained in sections 7.6 and 7.7. Each of these NN models was created using a routine that slowly increased the size of the hidden layer and calculated the R^2 of the k-fold cross-validation of the training set at each step. This continued until the calculated R^2 showed a decrease of 10% from its peak value. Once the number of hidden nodes was calculated, the net was trained on the full set of training data using both a pure linear and radial basis function as the activation function of the output nodes. The final activation function was chosen based on the largest R^2 of the training set. The NNs were then trained five times over the training set and the final output was an average of these five outputs. Once the network architecture was determined, the net was tested against the validation set (20% of the data chosen at random).

The results below show the actual verse predicted graphs for both the training and validation sets and the histogram of the fit error with the training and validation sets stacked on top of each other. A good fit will show a linear relationship between the actual and predicted values and a histogram that is approximately normal.

Upper Tier (UT) System against Theater Ballistic Missiles (TBMs) Type 1

This section shows the fit of the neural net that predicted the number of TBM type 1 missiles that leaked through the defenses when faced against the UT system.

Table 64: TBM1 Leakers for Upper Tier System

Neural Net Architecture			Fit Data		
Data Transform		Square Root	Set	Training	Validation
Number of Hidden Nodes		5	RMSE	0.029	0.121
Activation Function	Output Layer	Hyperbolic Tangent	Max Error	0.319	1.080
	Hidden Layer	Radial Basis	R^2	0.992	0.983

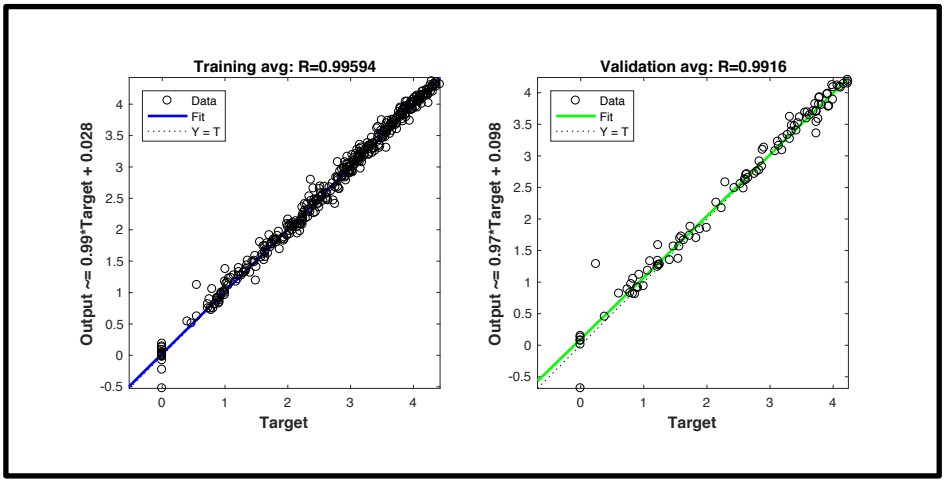

Figure 200: Upper Tier System Fit v. TBM1 for Training and Validation Set

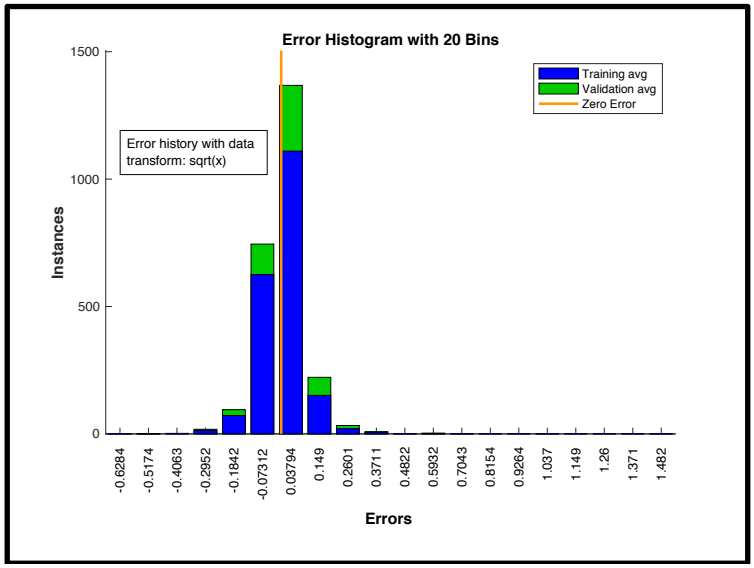

Figure 201: Error Histogram of Fit Error for TBM1 Leakers v. UT System

Upper Tier (UT) System against Theater Ballistic Missiles (TBMs) Type 2

This section shows the fit of the neural net that predicted the number of TBM type 2 missiles that leaked through the defenses when faced against the UT system.

Table 65: TBM2 Leakers for Upper Tier System

Neural Net Architecture			Fit Data		
Data Transform		Square Root	Set	Training	Validation
Number of Hidden Nodes		5	RMSE	0.017	0.071
Activation Function	Output Layer	Hyperbolic Tangent	Max Error	0.116	0.647
	Hidden Layer	Radial Basis	R^2	0.993	0.987

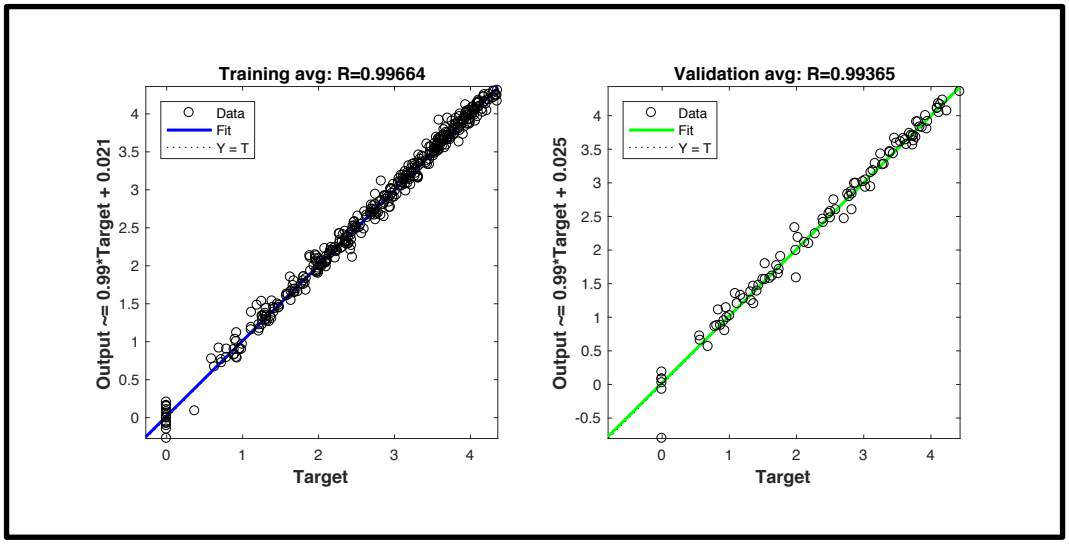

Figure 202: Upper Tier System Fit v. TBM2 for Training and Validation Set

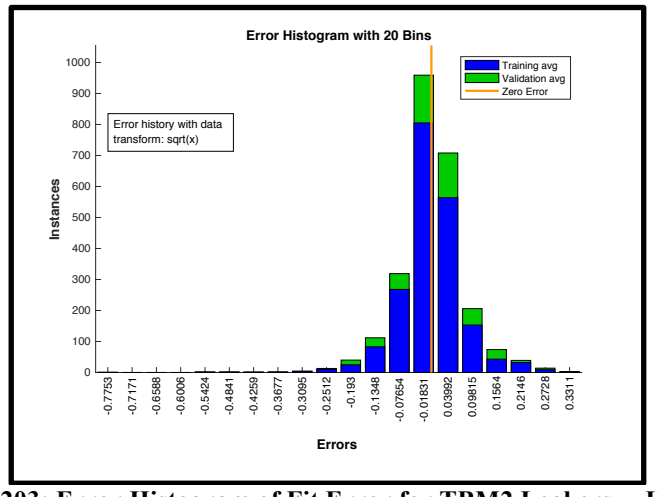

Figure 203: Error Histogram of Fit Error for TBM2 Leakers v. UT System

Upper Tier (UT) System against Theater Ballistic Missiles (TBMs) Type 3

This section shows the fit of the neural net that predicted the number of TBM type 3 missiles that leaked through the defenses when faced against the UT system.

Table 66: TBM3 Leakers for Upper Tier System

Neural Net Architecture			Fit Data		
Data Transform		Square Root	Set	Training	Validation
Number of Hidden Nodes		5	RMSE	0.021	0.143
Activation Function	Output Layer	Hyperbolic Tangent	Max Error	0.130	1.417
	Hidden Layer	Pure Linear	R^2	0.993	0.981

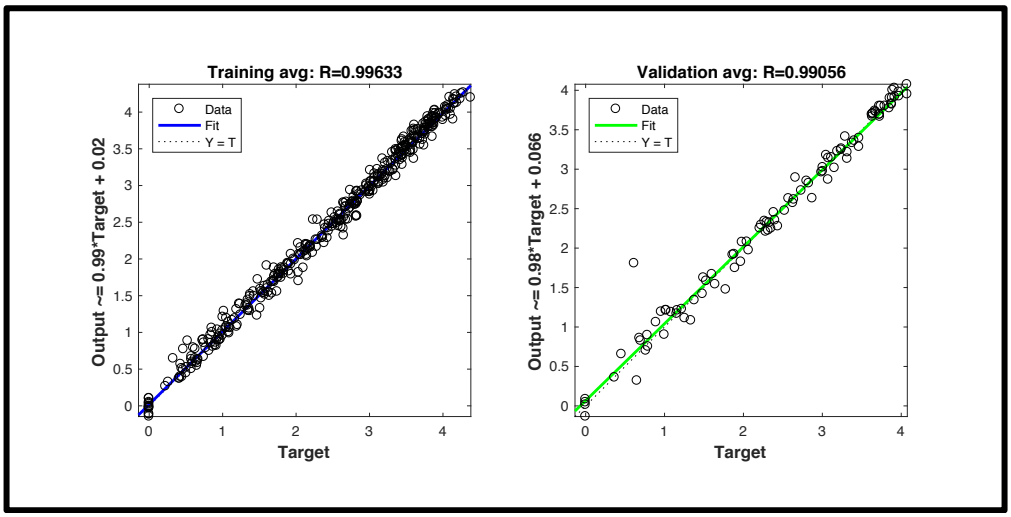

Figure 204: Upper Tier System Fit v. TBM3 for Training and Validation Set

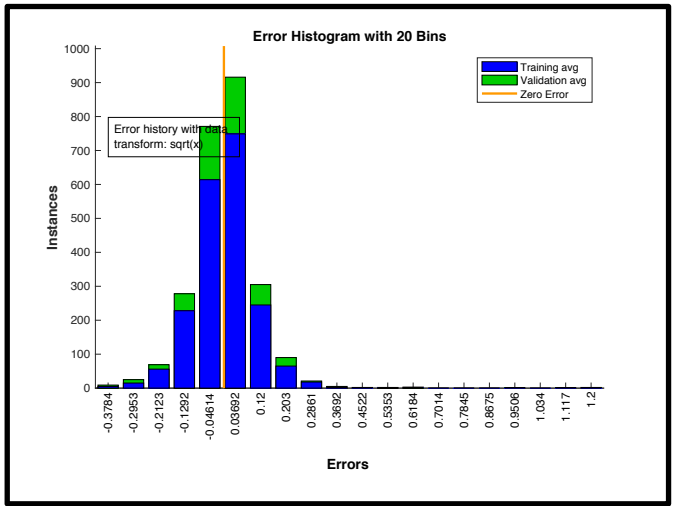

Figure 205: Error Histogram of Fit Error for TBM3 Leakers v. UT System

Upper Tier (UT) System against Theater Ballistic Missiles (TBMs) – Interceptors Shot

This section shows the fit of the neural net that predicted the number of UT interceptors that were shot against incoming TBM missiles.

Table 67: Interceptors Shot for Upper Tier System

Neural Net Architecture			Fit Data		
Data Transform		Square Root	Set	Training	Validation
Number of Hidden Nodes		5	RMSE	0.029	0.033
Activation Function	Output Layer	Hyperbolic Tangent	Max Error	0.489	0.190
	Hidden Layer	Radial Basis	R^2	0.975	0.951

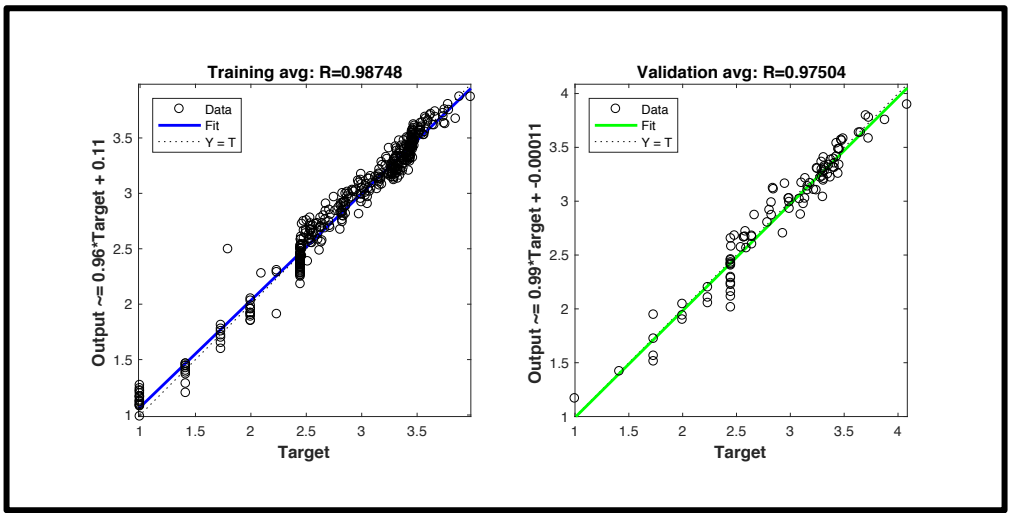

Figure 206: Upper Tier System Fit for Number of Interceptors Shot for Training and Validation Set

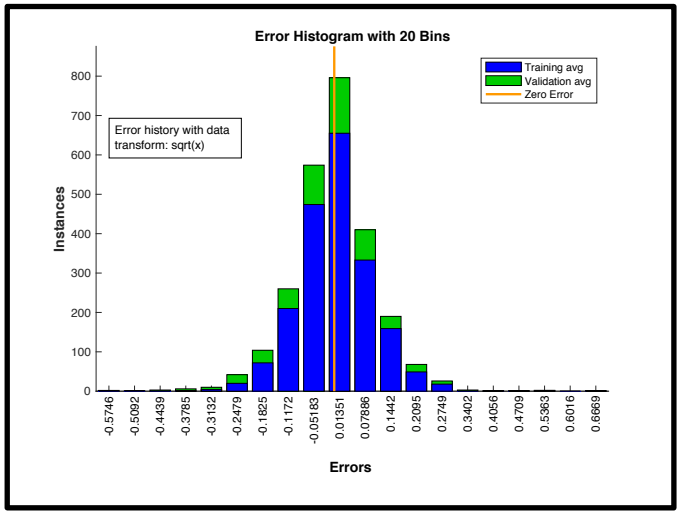

Figure 207: Error Histogram of Fit Error for Number of Interceptors Shot for UT System

Lower Tier System with Interceptor A against Theater Ballistic Missiles (TBMs) Type 1

This section shows the fit of the neural net that predicted the number of TBM type 1 missiles that leaked through the defenses when faced against the LT system with interceptor A.

Table 68: TBM1 Leakers for Lower Tier System with Interceptor A

Neural Net Architecture			Fit Data		
Data Transform		Square Root	Set	Training	Validation
Number of Hidden Nodes		5	RMSE	0.039	0.100
Activation Function	Output Layer	Hyperbolic Tangent	Max Error	0.396	0.622
	Hidden Layer	Radial Basis	R^2	0.987	0.972

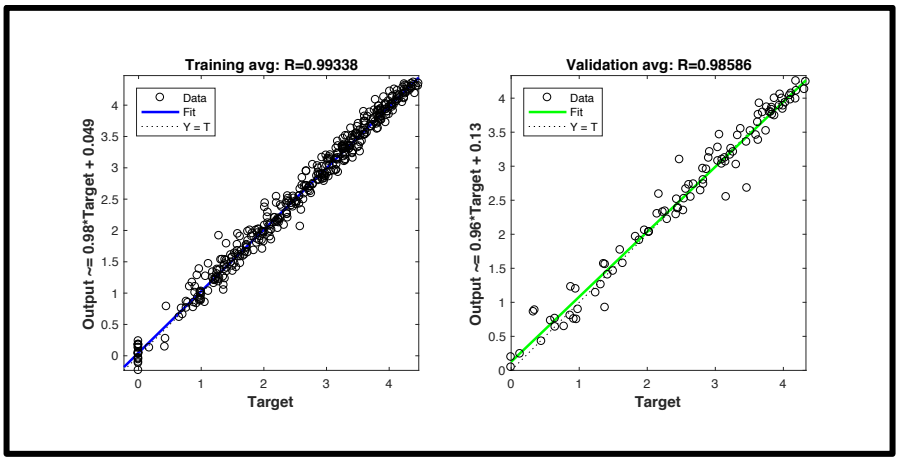

Figure 208: Lower Tier System with Interceptor A Fit v. TBM1 for Training and Validation Set

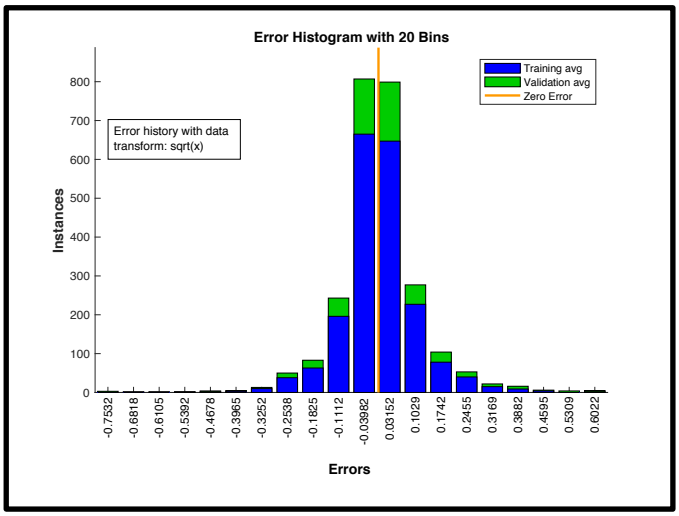

Figure 209: Error Histogram of Fit Error for TBM1 Leakers v. LT System with Interceptor A

Lower Tier System with Interceptor A against Theater Ballistic Missiles (TBMs) Type 2

This section shows the fit of the neural net that predicted the number of TBM type 2 missiles that leaked through the defenses when faced against the LT system with interceptor A.

Table 69: TBM2 Leakers for Lower Tier System with Interceptor A

Neural Net Architecture			Fit Data		
Data Transform		Square Root	Set	Training	Validation
Number of Hidden Nodes		10	RMSE	0.031	0.082
Activation Function	Output Layer	Hyperbolic Tangent	Max Error	0.213	0.533
	Hidden Layer	Radial Basis	R^2	0.991	0.970

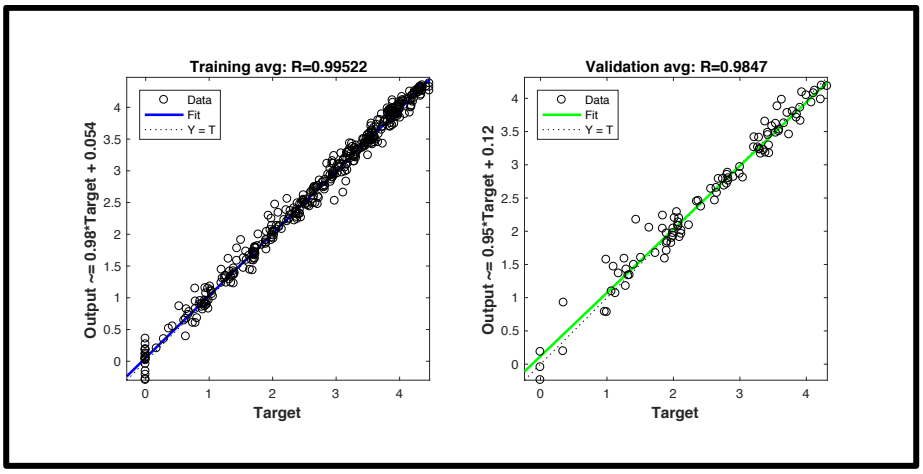

Figure 210: Lower Tier System with Interceptor A v. TBM2 for Training and Validation Set

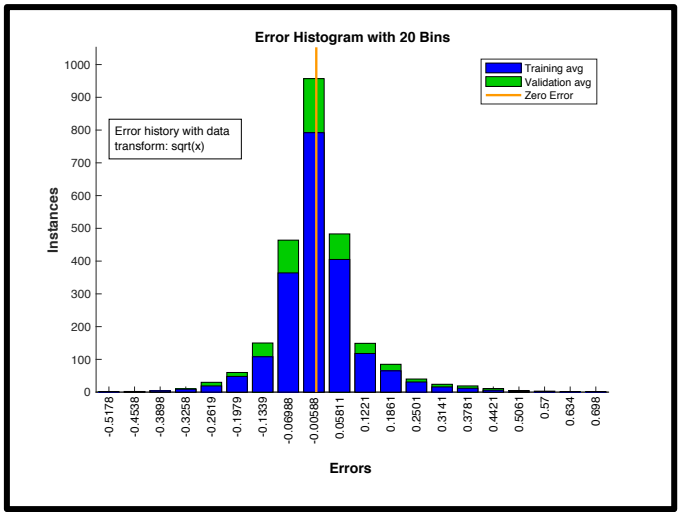

Figure 211: Error Histogram of Fit Error for TBM2 Leakers v. LT System with Interceptor A

Lower Tier System with Interceptor A against Theater Ballistic Missiles (TBMs) Type 3

This section shows the fit of the neural net that predicted the number of TBM type 3 missiles that leaked through the defenses when faced against the LT system with interceptor A.

Table 70: TBM3 Leakers for Lower Tier System with Interceptor A

Neural Net Architecture			Fit Data		
Data Transform		Square Root	Set	Training	Validation
Number of Hidden Nodes		10	RMSE	0.053	0.176
Activation Function	Output Layer	Hyperbolic Tangent	Max Error	0.366	1.086
	Hidden Layer	Pure Linear	R^2	0.979	0.942

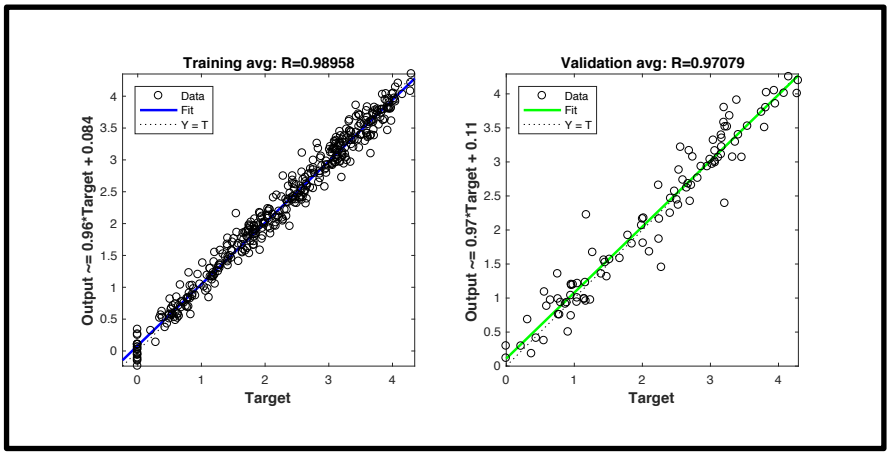

Figure 212: Lower Tier System with Interceptor A v. TBM3 for Training and Validation Set

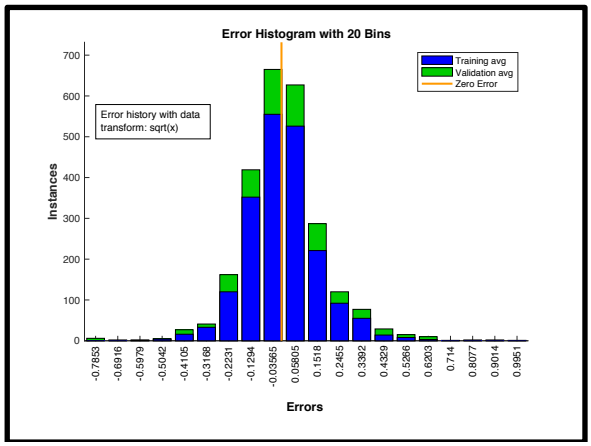

Figure 213: Error Histogram of Fit Error for TBM3 Leakers v. LT System with Interceptor A

Lower Tier System with Interceptor A against Ballistic Missiles – Interceptors Shot

This section shows the fit of the neural net that predicted the number of LT type A interceptors that were shot against incoming TBM missiles.

Table 71: Interceptors Shot for Lower Tier System Interceptor A Against TBMs

Neural Net Architecture			Fit Data		
Data Transform		Square Root	Set	Training	Validation
Number of Hidden Nodes		5	RMSE	0.056	0.207
Activation Function	Output Layer	Hyperbolic Tangent	Max Error	0.278	1.083
	Hidden Layer	Radial Basis	R^2	0.955	0.873

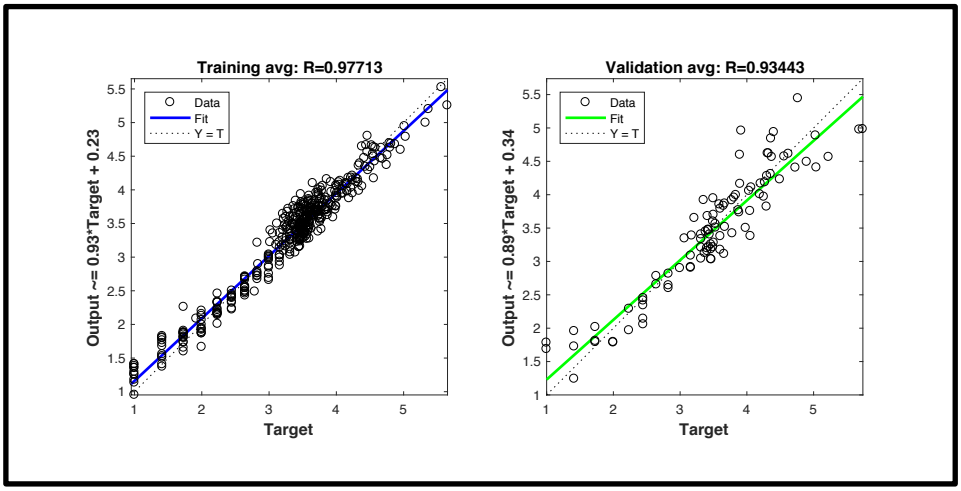

Figure 214: Lower Tier System Fit for Number of Interceptor A Missiles Shot Against TBMs for Training and Validation Set

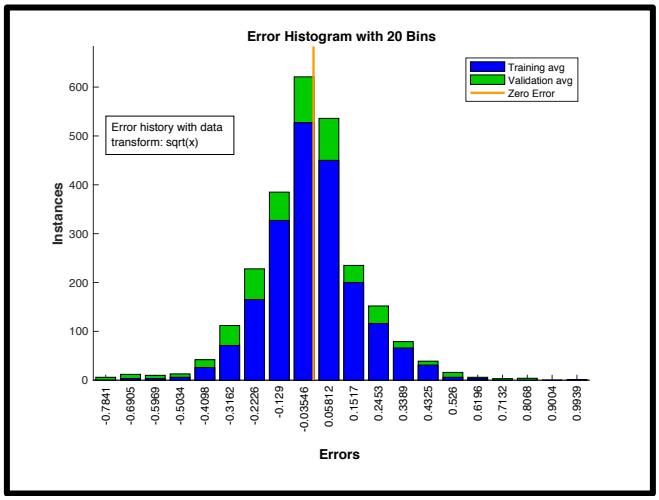

Figure 215: Error Histogram of Fit Error for Number of Interceptor A Missiles Shot Against CMs for LT System with Interceptor A

Lower Tier System with Interceptor A against Cruise Missiles (CMs) Type 1

This section shows the fit of the neural net that predicted the number of CM type 1 missiles that leaked through the defenses when faced against the LT system with interceptor A.

Table 72: CM1 Leakers for Lower Tier System with Interceptor A

Neural Net Architecture			Fit Data		
Data Transform		Square Root	Set	Training	Validation
Number of Hidden Nodes		10	RMSE	0.201	0.422
Activation Function	Output Layer	Hyperbolic Tangent	Max Error	1.594	2.706
	Hidden Layer	Radial Basis	R^2	0.947	0.898

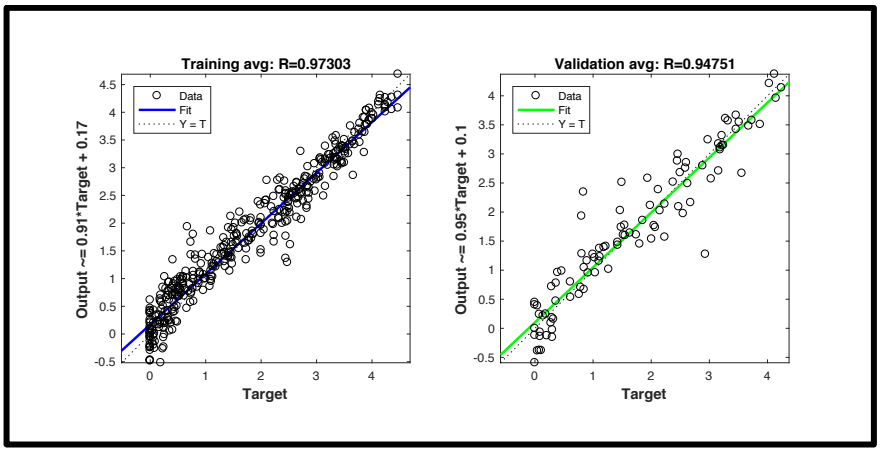

Figure 216: Lower Tier System with Interceptor A v. CM1 for Training and Validation Set

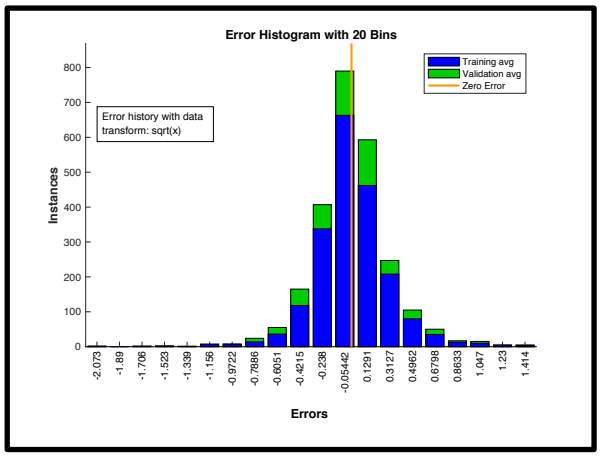

Figure 217: Error Histogram of Fit Error for CM1 Leakers v. LT System with Interceptor A

Lower Tier System with Interceptor A against Cruise Missiles (CMs) Type 2

This section shows the fit of the neural net that predicted the number of CM type 2 missiles that leaked through the defenses when faced against the LT system with interceptor A.

Table 73: CM2 Leakers for Lower Tier System with Interceptor A

Neural Net Architecture			Fit Data		
Data Transform		Square Root	Set	Training	Validation
Number of Hidden Nodes		15	RMSE	0.109	0.228
Activation Function	Output Layer	Hyperbolic Tangent	Max Error	0.802	0.821
	Hidden Layer	Pure Linear	R^2	0.976	0.942

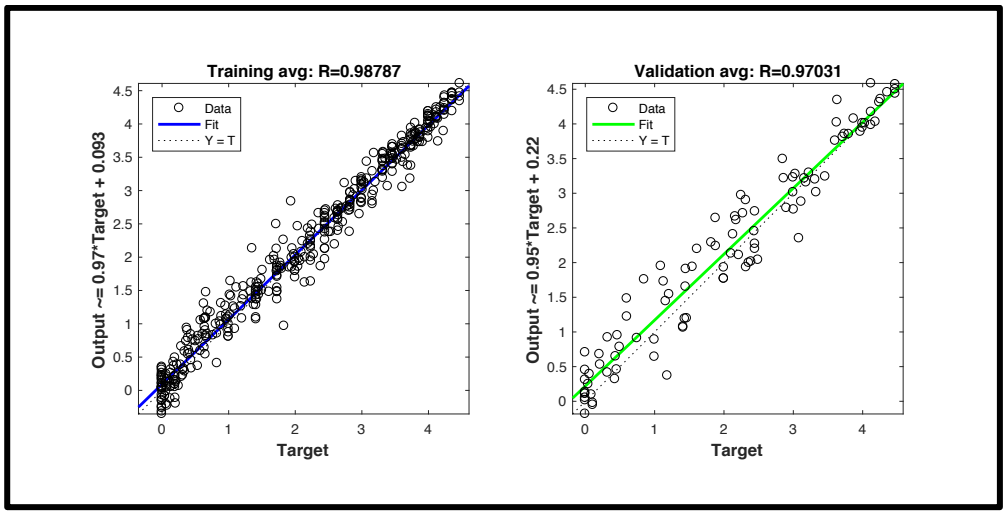

Figure 218: Lower Tier System with Interceptor A v. CM2 for Training and Validation Set

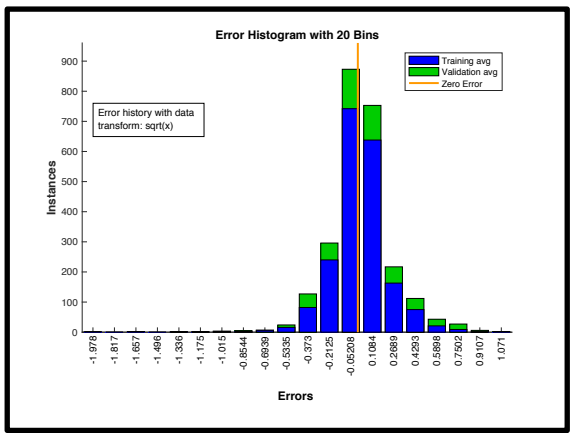

Figure 219: Error Histogram of Fit Error for CM2 Leakers v. LT System with Interceptor A

Lower Tier System with Interceptor A against Cruise Missiles – Interceptors Shot

This section shows the fit of the neural net that predicted the number of LT type A interceptors that were shot against incoming CM missiles.

Table 74: Interceptors Shot for Lower Tier System Interceptor A Against Cruise Missiles

Neural Net Architecture			Fit Data		
Data Transform		Square Root	Set	Training	Validation
Number of Hidden Nodes		5	RMSE	0.318	0.514
Activation Function	Output Layer	Hyperbolic Tangent	Max Error	3.164	2.737
	Hidden Layer	Radial Basis	R^2	0.962	0.931

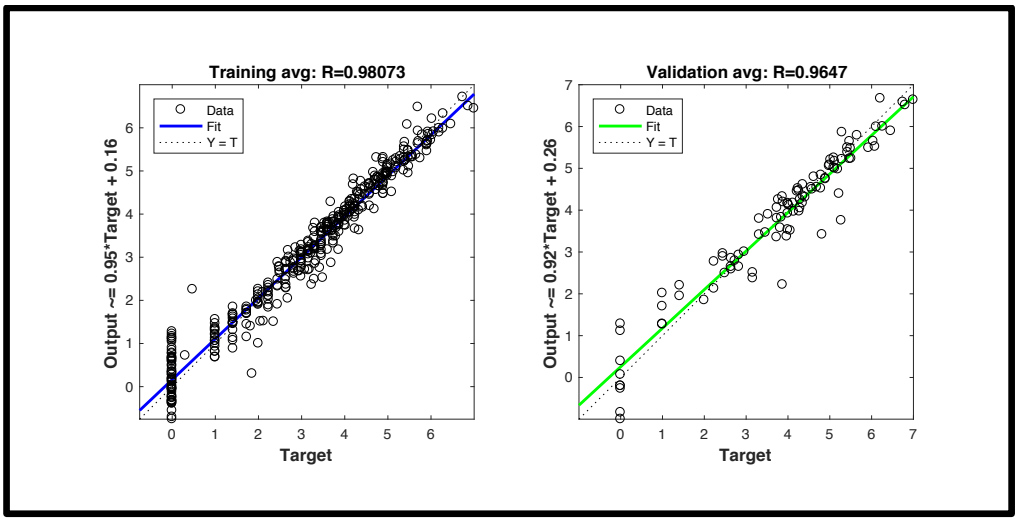

Figure 220: Lower Tier System Fit for Number of Interceptor A Missiles Shot Against CMs for Training and Validation Set

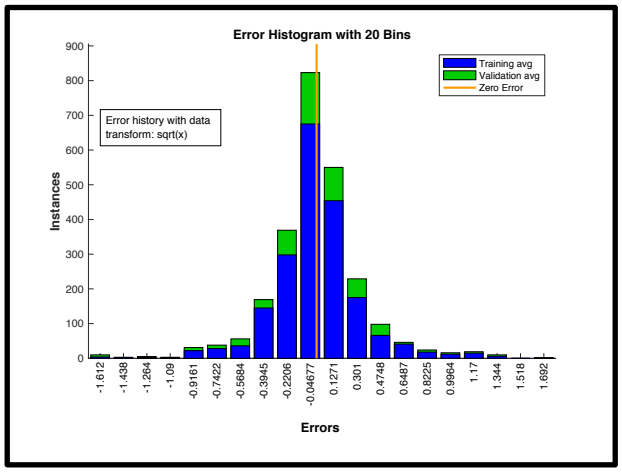

Figure 221: Error Histogram of Fit Error for Number of Interceptor A Missiles Shot Against CMs for LT System with Interceptor A

Lower Tier System with Interceptor B against Theater Ballistic Missiles (TBMs) Type 1

This section shows the fit of the neural net that predicted the number of TBM type 1 missiles that leaked through the defenses when faced against the LT system with interceptor B.

Table 75: TBM1 Leakers for Lower Tier System with Interceptor B

Neural Net Architecture			Fit Data		
Data Transform		Square Root	Set	Training	Validation
Number of Hidden Nodes		5	RMSE	0.017	0.106
Activation Function	Output Layer	Hyperbolic Tangent	Max Error	0.149	0.037
	Hidden Layer	Pure Linear	R^2	0.994	0.995

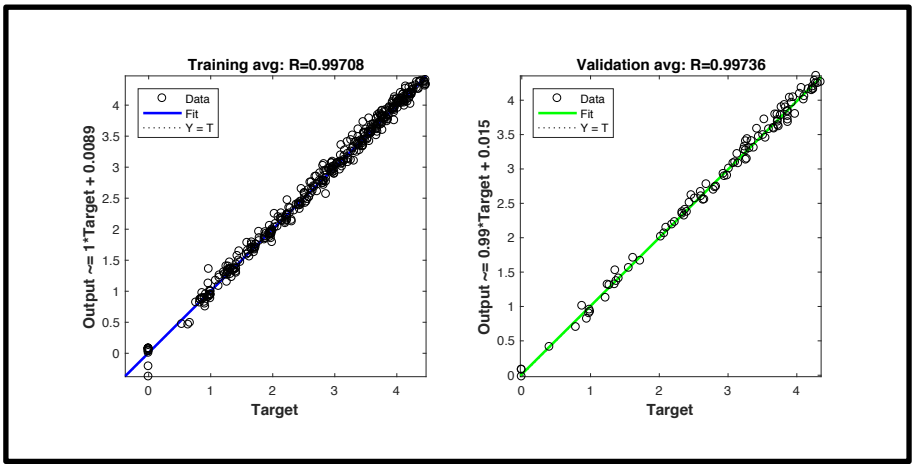

Figure 222: Lower Tier System with Interceptor B Fit v. TBM1 for Training and Validation Set

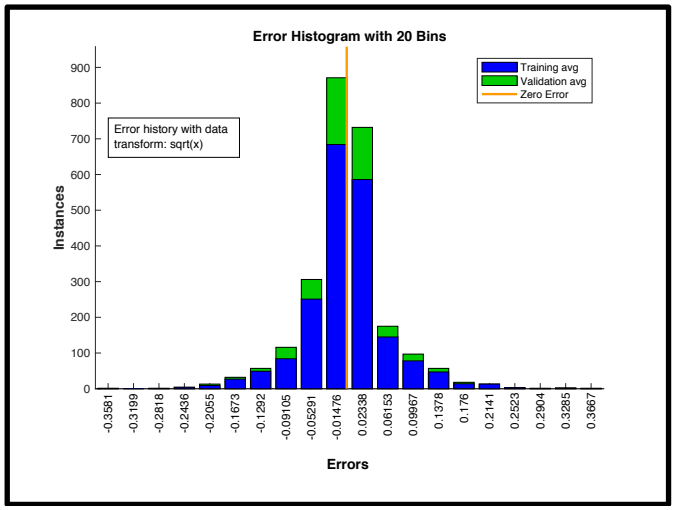

Figure 223: Error Histogram of Fit Error for TBM1 Leakers v. LT System with Interceptor B

Lower Tier System with Interceptor B against Theater Ballistic Missiles (TBMs) Type 2

This section shows the fit of the neural net that predicted the number of TBM type 2 missiles that leaked through the defenses when faced against the LT system with interceptor B.

Table 76: TBM2 Leakers for Lower Tier System with Interceptor B

Neural Net Architecture			Fit Data		
Data Transform		Square Root	Set	Training	Validation
Number of Hidden Nodes		5	RMSE	0.017	0.065
Activation Function	Output Layer	Hyperbolic Tangent	Max Error	0.183	0.627
	Hidden Layer	Pure Linear	R^2	0.992	0.986

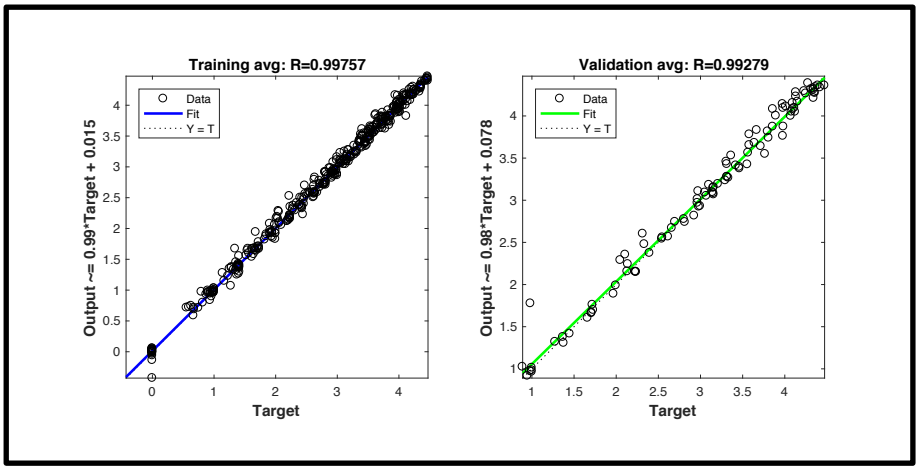

Figure 224: Lower Tier System with Interceptor B v. TBM2 for Training and Validation Set

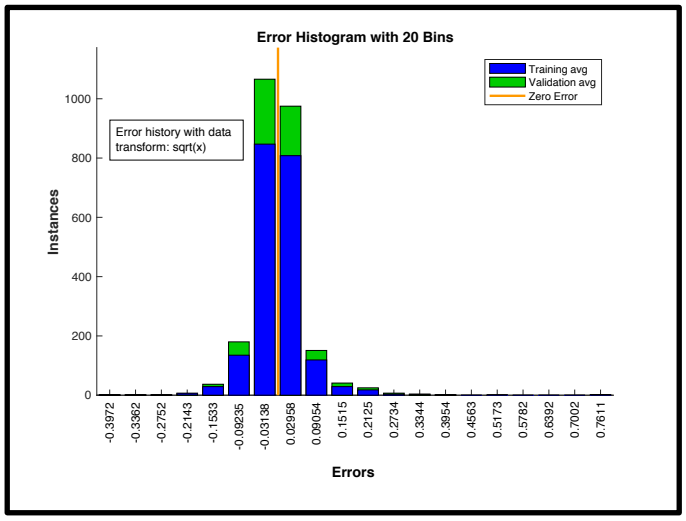

Figure 225: Error Histogram of Fit Error for TBM2 Leakers v. LT System with Interceptor B

Lower Tier System with Interceptor B against Theater Ballistic Missiles (TBMs) Type 3

This section shows the fit of the neural net that predicted the number of TBM type 3 missiles that leaked through the defenses when faced against the LT system with interceptor B.

Table 77: TBM3 Leakers for Lower Tier System with Interceptor B

Neural Net Architecture			Fit Data		
Data Transform		Square Root	Set	Training	Validation
Number of Hidden Nodes		5	RMSE	0.035	0.042
Activation Function	Output Layer	Hyperbolic Tangent	Max Error	0.317	0.261
	Hidden Layer	Pure Linear	R^2	0.989	0.982

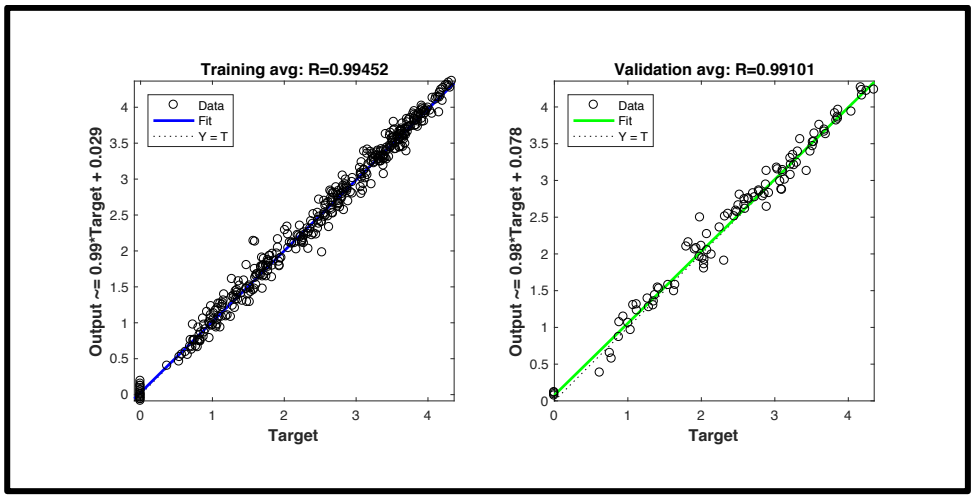

Figure 226: Lower Tier System with Interceptor B v. TBM3 for Training and Validation Set

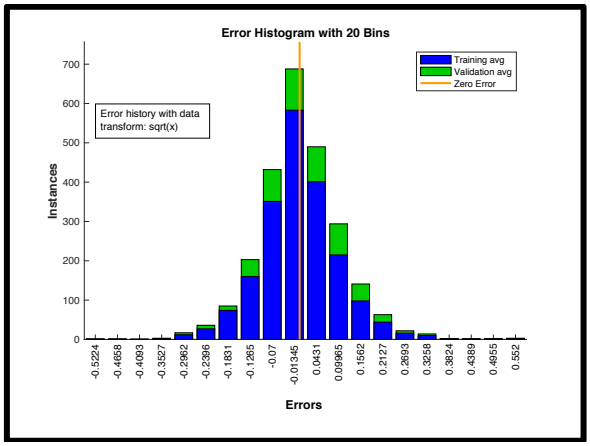

Figure 227: Error Histogram of Fit Error for TBM3 Leakers v. LT System with Interceptor B

Lower Tier System with Interceptor B against Ballistic Missiles – Interceptors Shot

This section shows the fit of the neural net that predicted the number of LT type B interceptors that were shot against incoming TBM missiles.

Table 78: Interceptors Shot for Lower Tier System Interceptor B Against TBMs

Neural Net Architecture			Fit Data		
Data Transform		Square Root	Set	Training	Validation
Number of Hidden Nodes		5	RMSE	0.035	0.076
Activation Function	Output Layer	Hyperbolic Tangent	Max Error	0.223	0.466
	Hidden Layer	Radial Basis	R^2	0.980	0.953

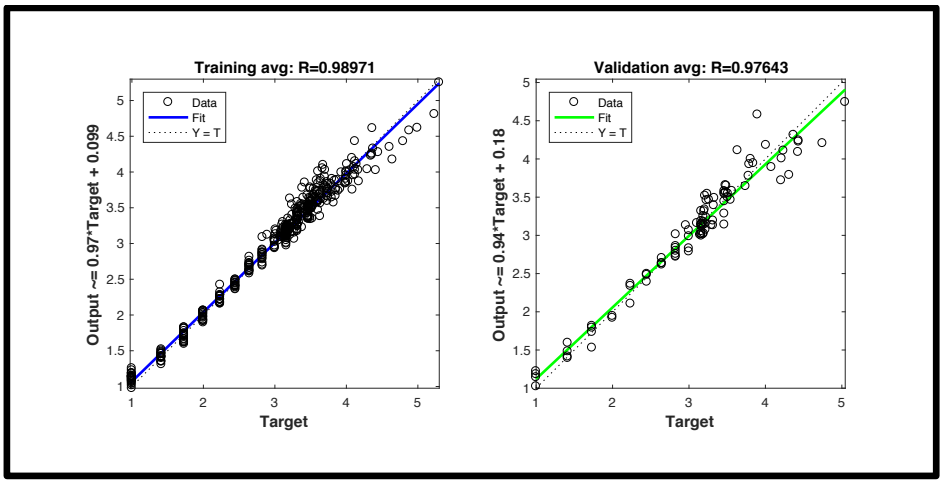

Figure 228: Lower Tier System Fit for Number of Interceptor B Missiles Shot Against TBMs for Training and Validation Set

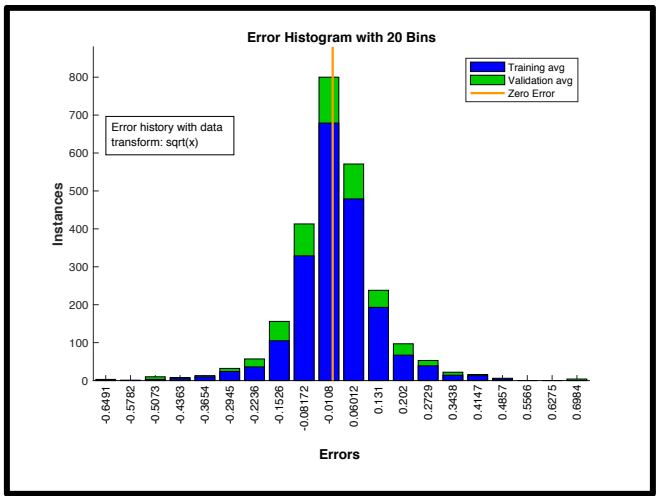

Figure 229: Error Histogram of Fit Error for Number of Interceptor B Missiles Shot Against CMs for LT System with Interceptor B

Lower Tier System with Interceptor B against Cruise Missiles (CMs) Type 1

This section shows the fit of the neural net that predicted the number of CM type 1 missiles that leaked through the defenses when faced against the LT system with interceptor B.

Table 79: CM1 Leakers for Lower Tier System with Interceptor B

Neural Net Architecture			Fit Data		
Data Transform		Square Root	Set	Training	Validation
Number of Hidden Nodes		10	RMSE	0.184	0.244
Activation Function	Output Layer	Hyperbolic Tangent	Max Error	1.334	1.196
	Hidden Layer	Pure Linear	R^2	0.956	0.935

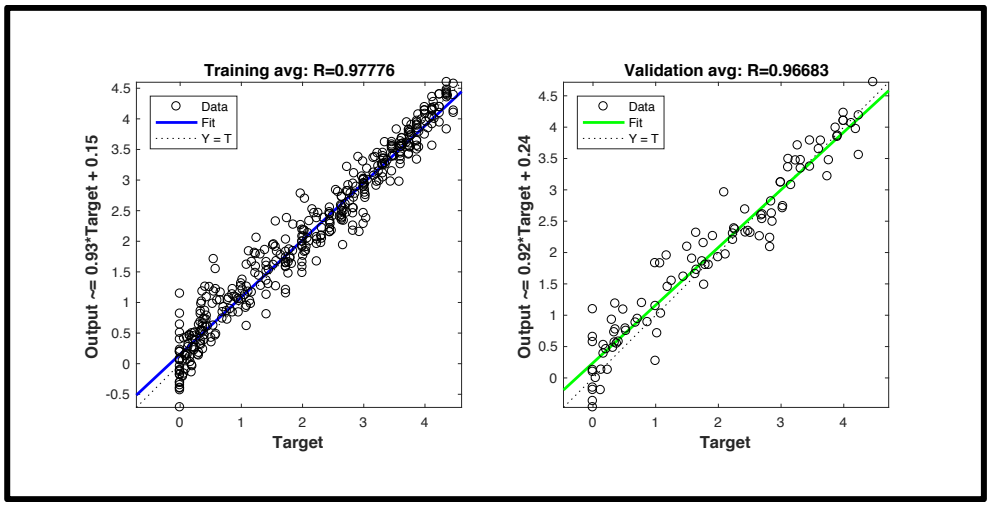

Figure 230: Lower Tier System with Interceptor B v. CM1 for Training and Validation Set

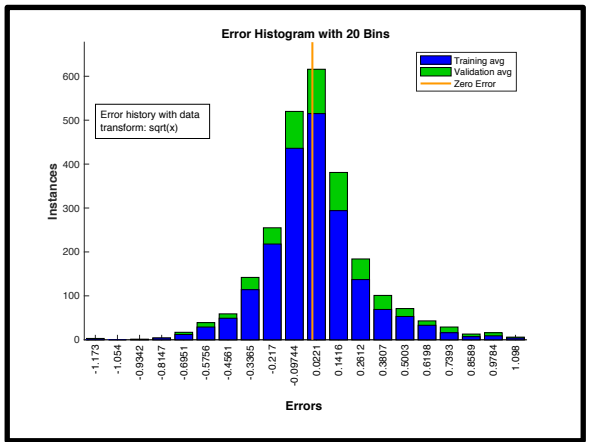

Figure 231: Error Histogram of Fit Error for CM1 Leakers v. LT System with Interceptor B

Lower Tier System with Interceptor B against Cruise Missiles (CMs) Type 2

This section shows the fit of the neural net that predicted the number of CM type 2 missiles that leaked through the defenses when faced against the LT system with interceptor B.

Table 80: CM2 Leakers for Lower Tier System with Interceptor B

Neural Net Architecture			Fit Data		
Data Transform		Square Root	Set	Training	Validation
Number of Hidden Nodes		5	RMSE	0.147	0.210
Activation Function	Output Layer	Hyperbolic Tangent	Max Error	1.544	0.775
	Hidden Layer	Pure Linear	R^2	0.969	0.942

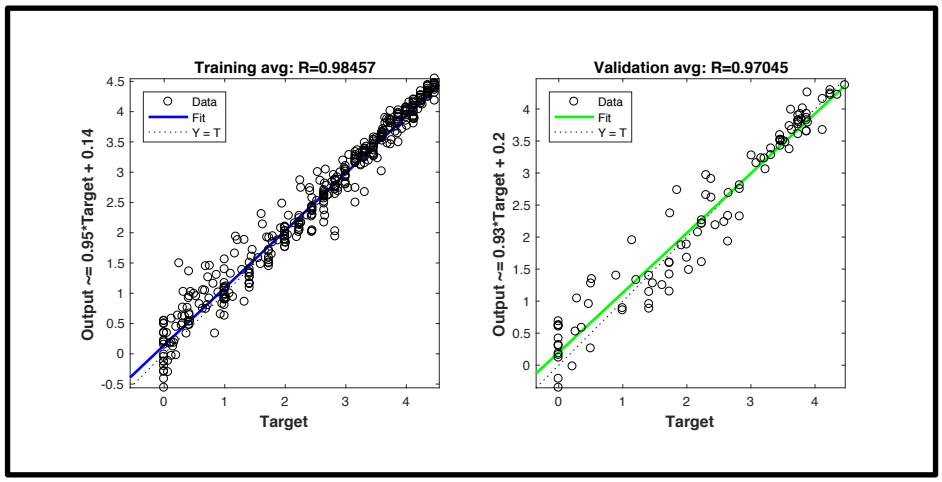

Figure 232: Lower Tier System with Interceptor B v. CM2 for Training and Validation Set

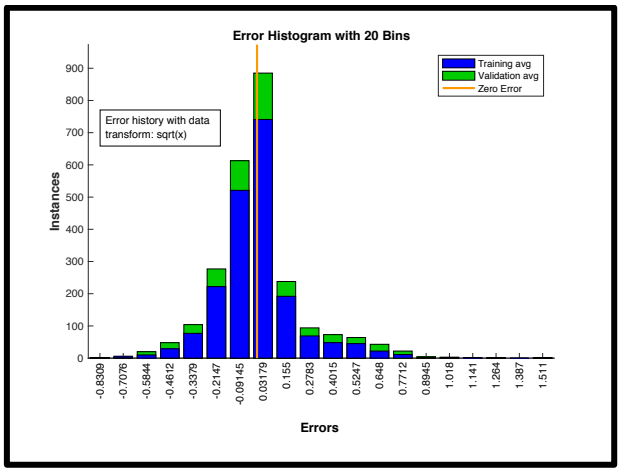

Figure 233: Error Histogram of Fit Error for CM2 Leakers v. LT System with Interceptor B

Lower Tier System with Interceptor B against Cruise Missiles – Interceptors Shot

This section shows the fit of the neural net that predicted the number of LT type B interceptors that were shot against incoming CM missiles.

Table 81: Interceptors Shot for Lower Tier System Interceptor B Against Cruise Missiles

Neural Net Architecture			Fit Data		
Data Transform		Square Root	Set	Training	Validation
Number of Hidden Nodes		10	RMSE	0.329	0.395
Activation Function	Output Layer	Hyperbolic Tangent	Max Error	2.783	3.248
	Hidden Layer	Radial Basis	R^2	0.996	0.995

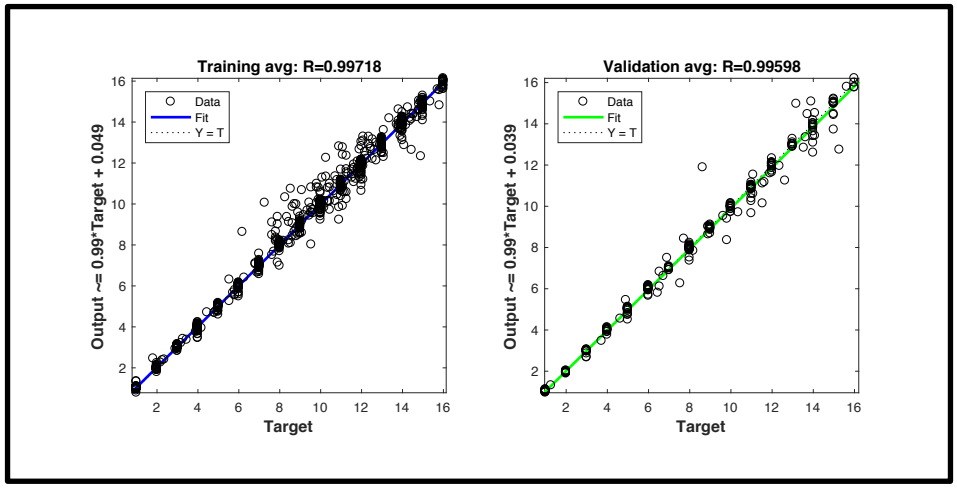

Figure 234: Lower Tier System Fit for Number of Interceptor B Missiles Shot Against CMs for Training and Validation Set

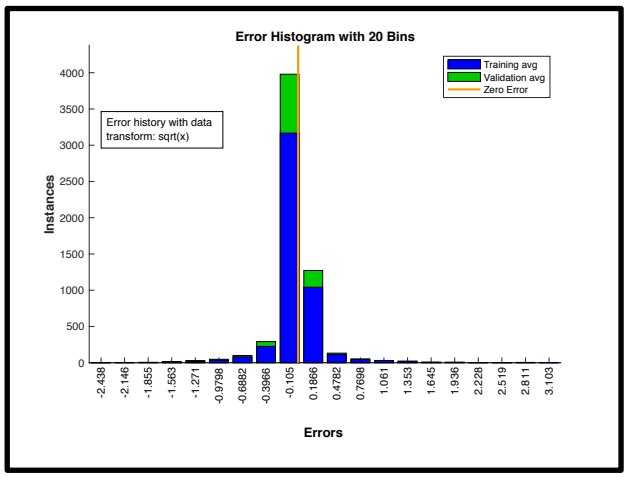

Figure 235: Error Histogram of Fit Error for Number of Interceptor B Missiles Shot Against CMs for LT System with Interceptor B

Lower Tier System with Interceptor C against Theater Ballistic Missiles (TBMs) Type 1

This section shows the fit of the neural net that predicted the number of TBM type 1 missiles that leaked through the defenses when faced against the LT system with interceptor C.

Table 82: TBM1 Leakers for Lower Tier System with Interceptor C

Neural Net Architecture			Fit Data		
Data Transform		Square Root	Set	Training	Validation
Number of Hidden Nodes		5	RMSE	0.009	0.020
Activation Function	Output Layer	Hyperbolic Tangent	Max Error	0.080	0.186
	Hidden Layer	Radial Basis	R^2	0.997	0.996

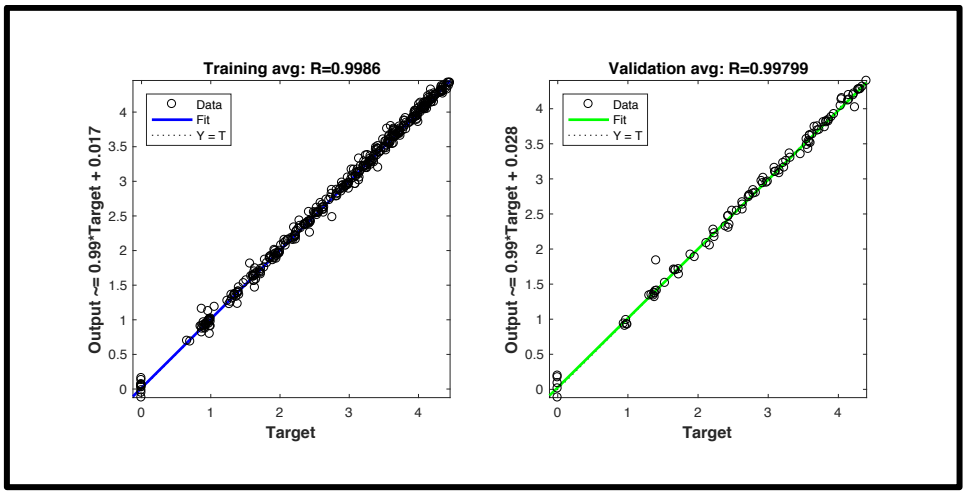

Figure 236: Lower Tier System with Interceptor C Fit v. TBM1 for Training and Validation Set

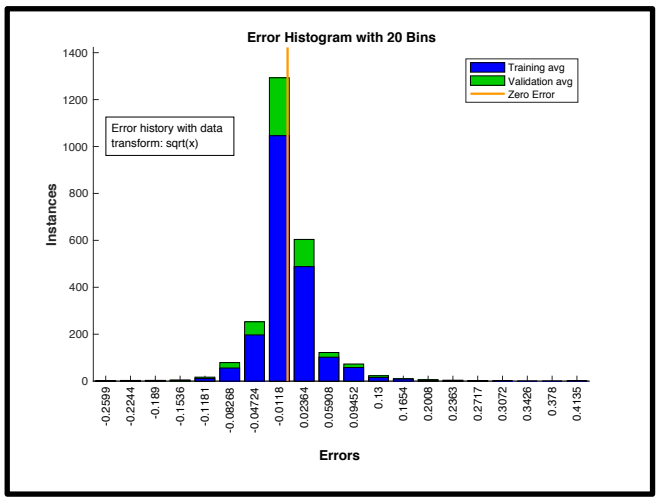

Figure 237: Error Histogram of Fit Error for TBM1 Leakers v. LT System with Interceptor C

Lower Tier System with Interceptor C against Theater Ballistic Missiles (TBMs) Type 2

This section shows the fit of the neural net that predicted the number of TBM type 2 missiles that leaked through the defenses when faced against the LT system with interceptor C.

Table 83: TBM2 Leakers for Lower Tier System with Interceptor C

Neural Net Architecture			Fit Data		
Data Transform		Square Root	Set	Training	Validation
Number of Hidden Nodes		5	RMSE	0.005	0.012
Activation Function	Output Layer	Hyperbolic Tangent	Max Error	0.046	0.065
	Hidden Layer	Radial Basis	R^2	0.999	0.996

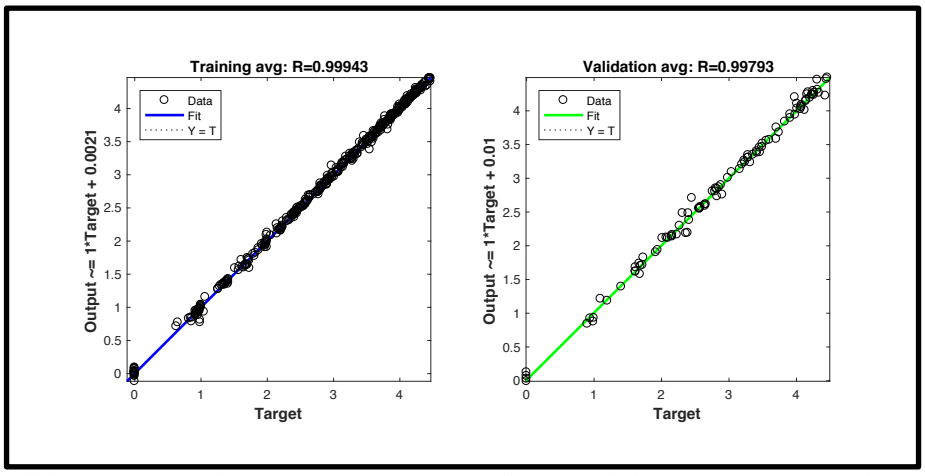

Figure 238: Lower Tier System with Interceptor C v. TBM2 for Training and Validation Set

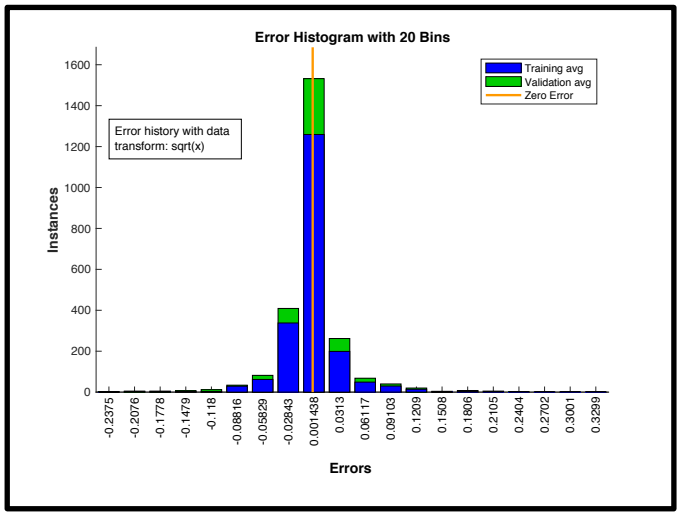

Figure 239: Error Histogram of Fit Error for TBM2 Leakers v. LT System with Interceptor C

Lower Tier System with Interceptor C against Theater Ballistic Missiles (TBMs) Type 3

This section shows the fit of the neural net that predicted the number of TBM type 3 missiles that leaked through the defenses when faced against the LT system with interceptor C.

Table 84: TBM3 Leakers for Lower Tier System with Interceptor C

Neural Net Architecture			Fit Data		
Data Transform		Square Root	Set	Training	Validation
Number of Hidden Nodes		5	RMSE	0.010	0.010
Activation Function	Output Layer	Hyperbolic Tangent	Max Error	0.103	0.119
	Hidden Layer	Pure Linear	R^2	0.997	0.994

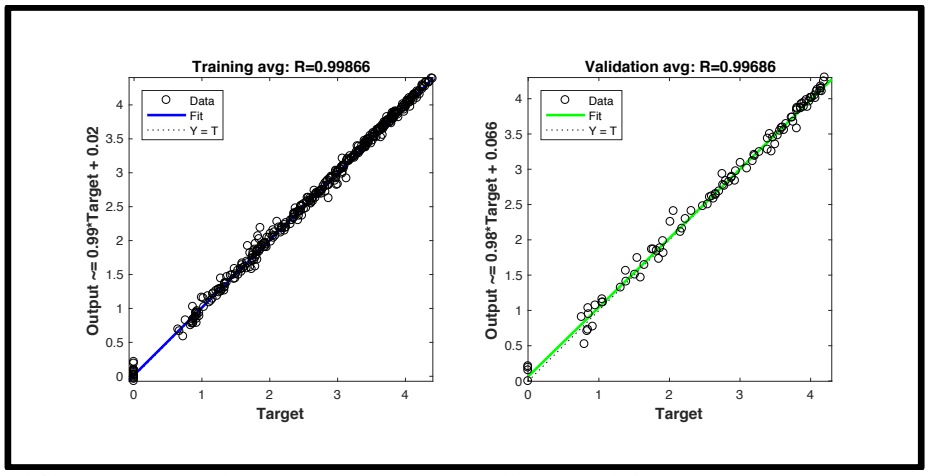

Figure 240: Lower Tier System with Interceptor C v. TBM3 for Training and Validation Set

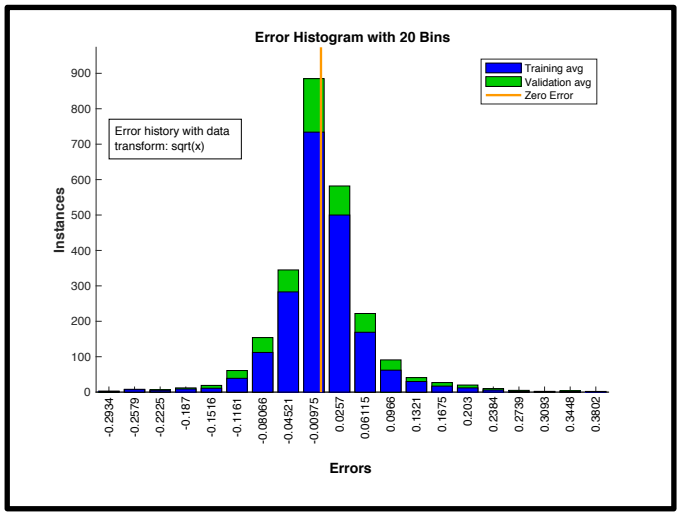

Figure 241: Error Histogram of Fit Error for TBM3 Leakers v. LT System with Interceptor C

Lower Tier System with Interceptor C against Ballistic Missiles – Interceptors Shot

This section shows the fit of the neural net that predicted the number of LT type C interceptors that were shot against incoming TBM missiles.

Table 85: Interceptors Shot for Lower Tier System Interceptor C Against TBMs

Neural Net Architecture			Fit Data		
Data Transform		Square Root	Set	Training	Validation
Number of Hidden Nodes		15	RMSE	0.026	0.088
Activation Function	Output Layer	Hyperbolic Tangent	Max Error	0.380	0.585
	Hidden Layer	Pure Linear	R^2	0.986	0.940

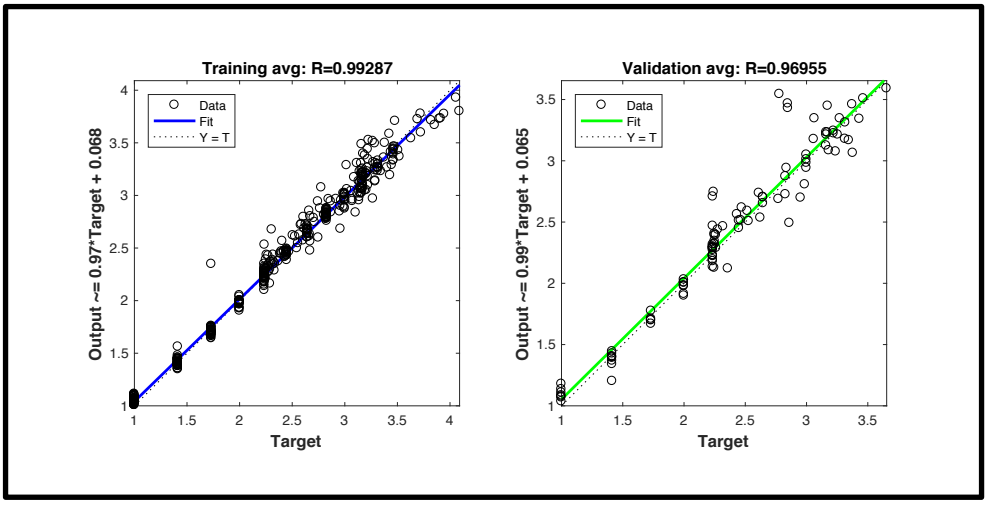

Figure 242: Lower Tier System Fit for Number of Interceptor C Missiles Shot Against TBMs for Training and Validation Set

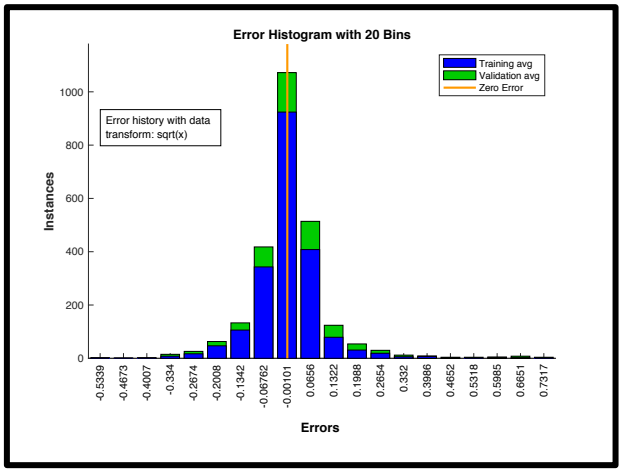

Figure 243: Error Histogram of Fit Error for Number of Interceptor C Missiles Shot Against CMs for LT System with Interceptor C

Lower Tier System with Interceptor C against Cruise Missiles (CMs) Type 1

This section shows the fit of the neural net that predicted the number of CM type 1 missiles that leaked through the defenses when faced against the LT system with interceptor C.

Table 86: CM1 Leakers for Lower Tier System with Interceptor C

Neural Net Architecture			Fit Data		
Data Transform		Square Root	Set	Training	Validation
Number of Hidden Nodes		15	RMSE	0.053	0.119
Activation Function	Output Layer	Hyperbolic Tangent	Max Error	0.399	0.821
	Hidden Layer	Radial Basis	R^2	0.984	0.973

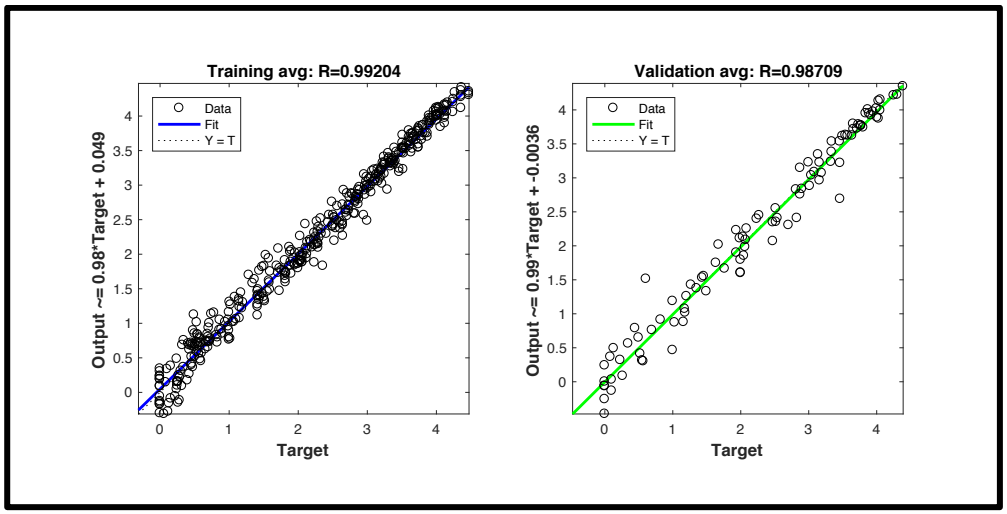

Figure 244: Lower Tier System with Interceptor C v. CM1 for Training and Validation Set

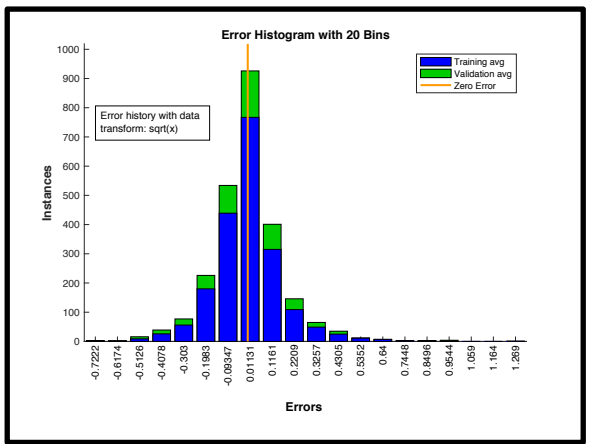

Figure 245: Error Histogram of Fit Error for CM1 Leakers v. LT System with Interceptor C

Lower Tier System with Interceptor C against Cruise Missiles (CMs) Type 2

This section shows the fit of the neural net that predicted the number of CM type 2 missiles that leaked through the defenses when faced against the LT system with interceptor C.

Table 87: CM2 Leakers for Lower Tier System with Interceptor C

Neural Net Architecture			Fit Data		
Data Transform		Square Root	Set	Training	Validation
Number of Hidden Nodes		15	RMSE	0.023	0.127
Activation Function	Output Layer	Hyperbolic Tangent	Max Error	0.258	0.813
	Hidden Layer	Radial Basis	R^2	0.994	0.978

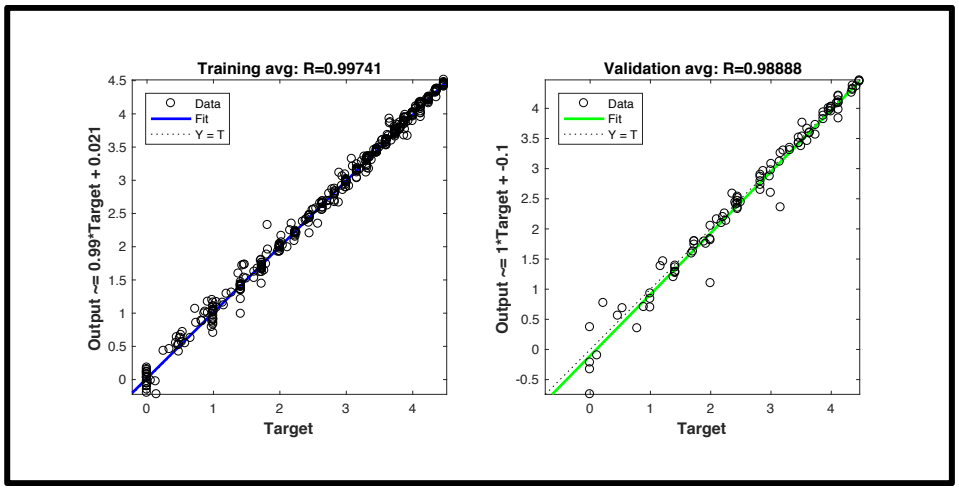

Figure 246: Lower Tier System with Interceptor C v. CM2 for Training and Validation Set

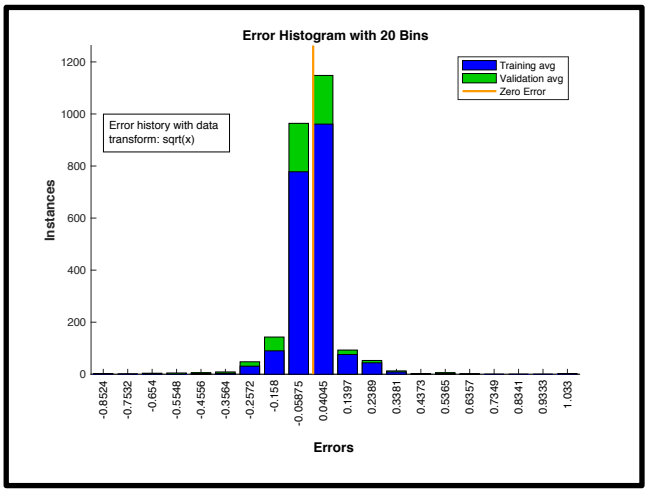

Figure 247: Error Histogram of Fit Error for CM2 Leakers v. LT System with Interceptor C

Lower Tier System with Interceptor C against Cruise Missiles – Interceptors Shot

This section shows the fit of the neural net that predicted the number of LT type C interceptors that were shot against incoming CM missiles.

Table 88: Interceptors Shot for Lower Tier System Interceptor C Against Cruise Missiles

Neural Net Architecture			Fit Data		
Data Transform		Square Root	Set	Training	Validation
Number of Hidden Nodes		10	RMSE	0.072	0.525
Activation Function	Output Layer	Hyperbolic Tangent	Max Error	0.560	3.331
	Hidden Layer	Radial Basis	R^2	0.984	0.904

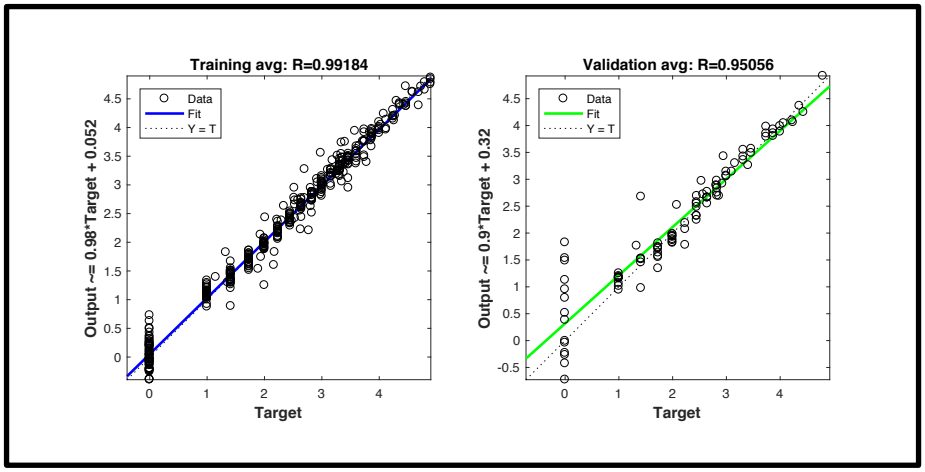

Figure 248: Lower Tier System Fit for Number of Interceptor C Missiles Shot Against CMs for Training and Validation Set

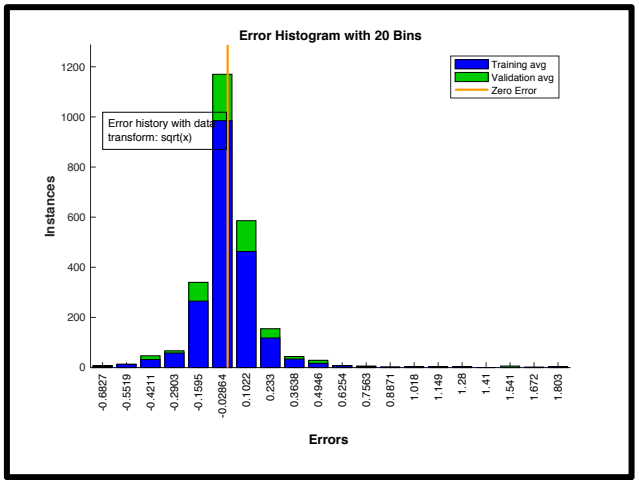

Figure 249: Error Histogram of Fit Error for Number of Interceptor C Missiles Shot Against CMs for LT System with Interceptor C

Point Defense (PT) System against Cruise Missiles (CMs) Type 1

This section shows the fit of the neural net that predicted the number of CM type 1 missiles that leaked through the defenses when faced against the PT system.

Table 89: CM1 Leakers for Point Defense System

Neural Net Architecture			Fit Data		
Data Transform		Square Root	Set	Training	Validation
Number of Hidden Nodes		10	RMSE	0.073	0.157
Activation Function	Output Layer	Hyperbolic Tangent	Max Error	0.502	0.643
	Hidden Layer	Pure Linear	R^2	0.981	0.951

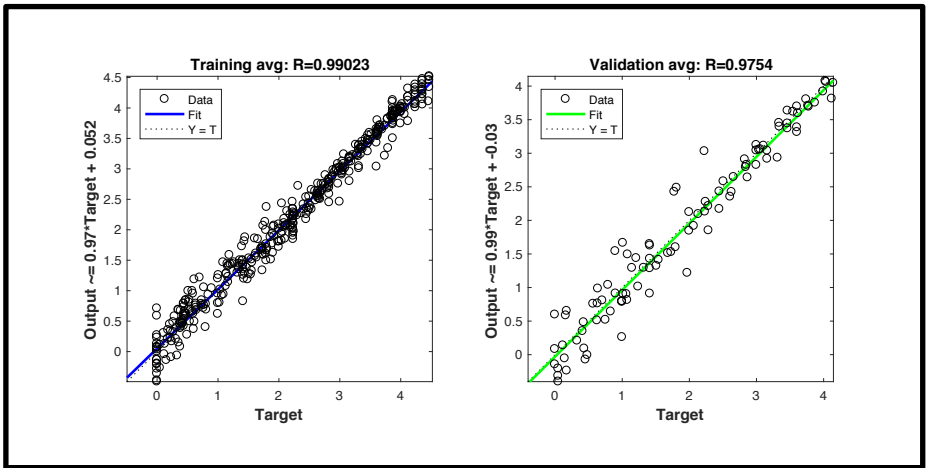

Figure 250: Point Defense System Fit v. CM1 for Training and Validation Set

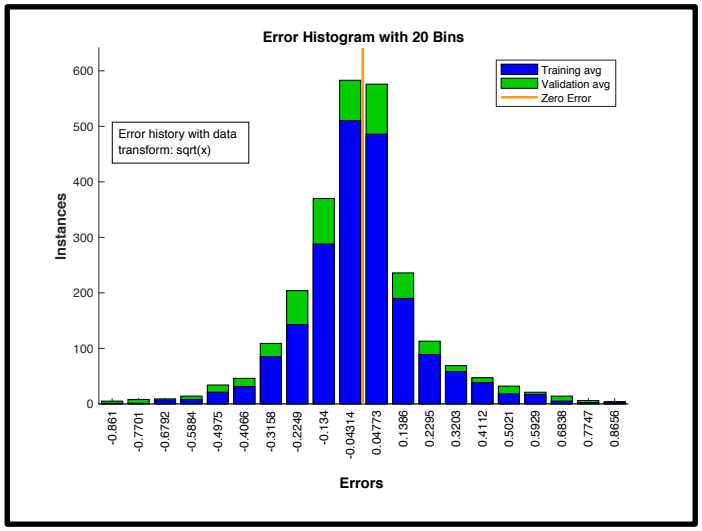

Figure 251: Error Histogram of Fit Error for CM1 Leakers v. PT System

Point Defense (PT) System against Cruise Missiles (CMs) Type 2

This section shows the fit of the neural net that predicted the number of CM type 2 missiles that leaked through the defenses when faced against the PT system.

Table 90: CM2 Leakers for Point Defense System

Neural Net Architecture			Fit Data		
Data Transform		Square Root	Set	Training	Validation
Number of Hidden Nodes		15	RMSE	0.063	0.111
Activation Function	Output Layer	Hyperbolic Tangent	Max Error	0.770	0.695
	Hidden Layer	Radial Basis	R^2	0.989	0.972

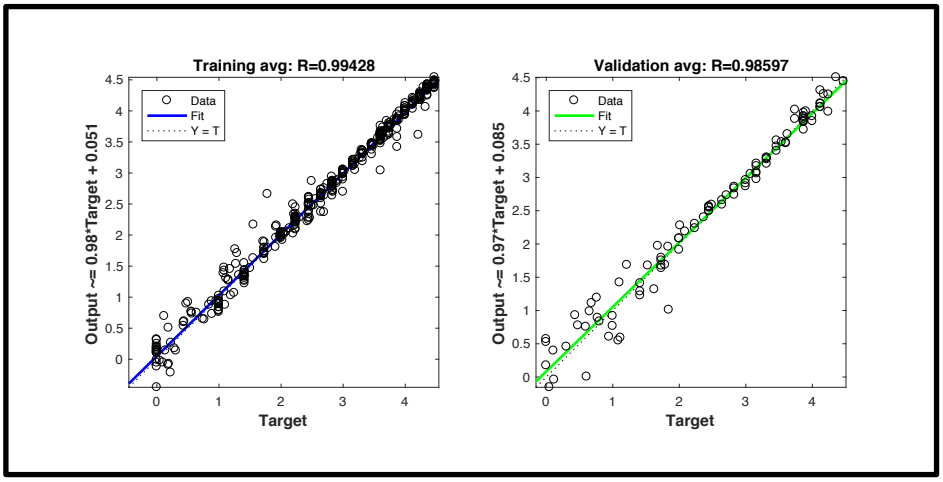

Figure 252: Point Defense System Fit v. CM2 for Training and Validation Set

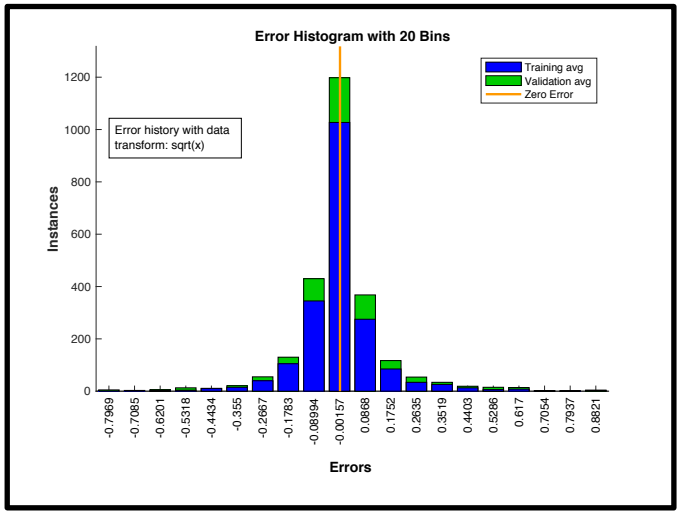

Figure 253: Error Histogram of Fit Error for CM2 Leakers v. PT System

Point Defense (PT) System against Cruise Missiles (CMs) – Interceptors Shot

This section shows the fit of the neural net that predicted the number of PT interceptors that were shot against incoming CM missiles.

Table 91: Interceptors Shot for Point Defense System

Neural Net Architecture			Fit Data		
Data Transform		Square Root	Set	Training	Validation
Number of Hidden Nodes		15	RMSE	0.029	0.033
Activation Function	Output Layer	Hyperbolic Tangent	Max Error	0.489	0.190
	Hidden Layer	Radial Basis	R^2	0.975	0.951

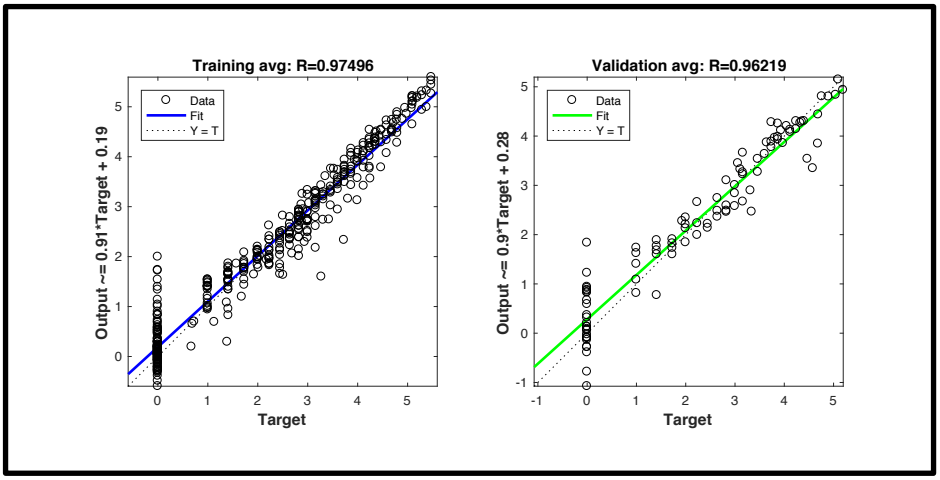

Figure 254: Point Defense Fit for Number of Interceptors Shot for Training and Validation Set

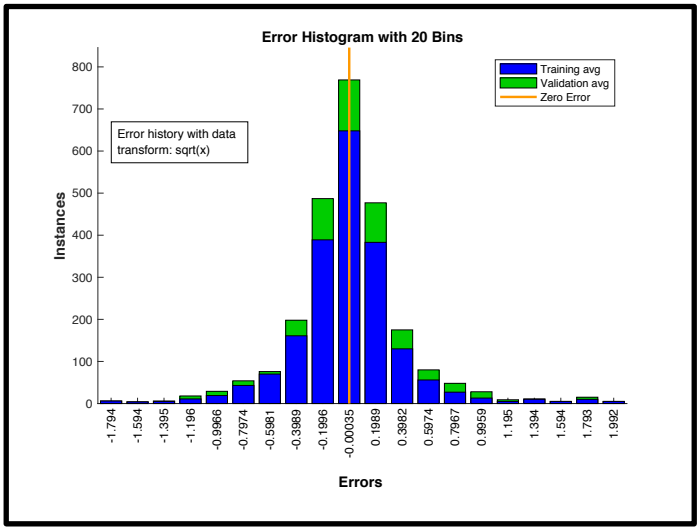

Figure 255: Error Histogram of Fit Error for Number of Interceptors Shot for PT System

REFERENCES

1. *Ballistic Missile Basics*. [cited 2014 March 7]; Available from: https://www.fas.org/nuke/intro/missile/basics.htm.

2. Davenport, K. *Worldwide Ballistic Missile Inventories*. 2012 [cited 2014 March 7]; Available from: https://www.armscontrol.org/factsheets/missiles.

3. *FY98 Air and Missile Defense Master Plan*. 1998, Headquarters, Department of the Army: Washington DC.

4. *Minuteman Weapon System History and Description*, I.S.P. Office, Editor. 2001: Hill AFB, UT.

5. *Cruise Missiles*. Special Weapons Primer [cited 2014 February 20]; Available from: http://www.fas.org/nuke/intro/cm/.

6. *Land Attack Cruise Missiles*. [cited 2014 March 11]; Available from: http://www.fas.org/irp/threat/missile/naic/part07.htm.

7. Kopp, C. *Cruise Missiles*. 2005 [cited 2014 March 8]; Available from: http://www.ausairpower.net/TE-Cruise-Missiles-1985.html.

8. Gormley, D.M., *The Neglected Dimension: Controlling Cruise Missile Proliferation.* The Nonproliferation Review, 2002. **9**(2).

9. *Missile Technology Control Regime (MTCR)*. [cited 2014 February 15]; Available from: http://www.mtcr.info/english/objectives.html.

10. Rosett, C. *The Iran-North Korea Axis of Proliferation*. 2013 [cited 2017 30 January]; Available from: https://www.forbes.com/sites/claudiarosett/2013/03/09/the-iran-north-korea-axis-of-proliferation/ - 6d53c4c96036.

11. Waterman, S., *China Missile Fear: U.S. Vulnerable to Nuclear-Tipped Submarine-Launched Missiles, Pentagon Warns*, in *The Washington Times*. 2014: Washington DC.

12. *Ballistic Missiles and Missile Defense*. [cited 2014 March 7]; Available from: http://www.publications.parliament.uk/pa/cm200809/cmselect/cmfaff/222/22208.htm.

13. Gormley, D.M., *Survival: Global Politics and Strategy.* Global Politics and Strategy, 2008. **50**(4): p. 137.

14. Gormley, D.M. and K.S. McMahon, *Controlling the Spread of Land-Attack Cruise Missiles*. 1995, Marina del Rey, CA.: American Institute for Strategic Cooperation.

15. Feicket, A., *Cruise Missile Proliferation*. 2005, Congressional Research Service, The Library of Congress: Washington DC.

16. Speier, R.H., G. Nacouzi, and K.S. McMahon, *Cruise Missile Penaid Nonproliferation*. 2014, RAND Corporation: Santa Monica, CA.

17. Gormley, D.M., *Missile Contagion: Cruise Missile Proliferation and the Threat to International Security*. 2008, Annapolis, MD: Naval Institute Press.

18. Gormley, D.M. *Winning on Ballistic Missiles but Losing on Cruise: The Missile Proliferation Battle*. 2009 [cited 2014 February 20]; Available from: https://www.armscontrol.org/act/2009_12/Gormley.

19. Erwin, S. *Proliferation of Cruise Missiles Sparks Concern About U.S. Air Defenses*. 2013 [cited 2014 February 20]; Available from: http://www.nationaldefensemagazine.org/archive/2013/February/Pages/ProliferationofCruiseMissilesSparksConcernAboutUSAirDefenses.aspx.

20. Lewis, G.N., S. Fetter, and L. Gronlund, *Casualties and Damage From Scud Attacks in the 1991 Gulf War*. 1993, Massachusetts Institute of Technology.

21. Lin, H., *Rationalized Speed/Altitude Thresholds for ABM Testing.* Science & Global Security, 1990. **2**: p. 87-101.

22. *Hypersonic Versions of Brahmos Missile on the Way*. 2011 [cited 2014 March 7]; Available from: http://articles.economictimes.indiatimes.com/2011-10-09/news/30260244_1_air-version-stealth-supersonic-cruise-missile-india-s-defence-research.

23. *Missile Threat*. 2012 [cited 2014 August 15]; Available from: http://missilethreat.com/missiles-of-the-world/.

24. Cali, C.M. *UAV Proliferation and the Challenge of Change*. 2013 [cited 2014 February 15]; Available from: http://journal.georgetown.edu/2013/10/09/uav-proliferation-and-the-challenge-of-change-by-c-michael-cali/.

25. Wade, B.M. and P. Chang, *New Measures of Effectiveness for the Air and Missile Defense Simulation Community.* Phalanx: The Magazine of National Security Analysis, 2015. **Vol 48**(No. 4): p. 49-53.

26. Wu, L., et al. *An Anytime Algorithm Applied to Dynamic Weapon-Target Allocation Problem with Decreasing Weapons and Targets*. in *2008 IEEE Congress on Evolutionary Computation*. 2008.

27. Burr, S.A., J.E. Falk, and A.F. Karr, *Integer Prim-Read Solutions to a Class of Target Defense Problems.* Operations Research, 1985. **33**(4): p. 726-745.

28. Amerault, J.F., *A Computerized Algorithm for the Determination of the Optimal Allocation of Two Weapons Systems Against N Targets*. 1972, Monterey, California. Naval Postgraduate School.

29. Parnell, G.S., et al., *Multiobjective Decision Analysis of Theater Missile Defense Architectures.* Systems Engineering, 2001. **4**(1): p. 24-34.

30. Brown, G., et al., *A Two-Sided Optimization for Theater Ballistic Missile Defense.* Operations Research, 2005. **53**(5): p. 745-763.

31. Garrett, R.K., et al., *Managing the Interstitials, a System-of-Systems Framework Suited for the Ballistic Missile Defense System.* Systems Engineering, 2011. **14**(1): p. 87-109.

32. Larson, E.V. and G.A. Kent, *A New Methodology for Assessing Multilayer Missile Defense Options*. 1994, Santa Monica, CA.: RAND Corporation.

33. Menq, J.-y., P.-c. Tuan, and T.-s. Liu, *Discrete Markov Ballistic Missile Defense System Modeling.* European Journal of Operational Research, 2007. **178**(2): p. 560-578.

34. Wilkering, D.A., *A Simple Model for Calculating Ballistic Missile Defense Effectiveness.* Science & Global Security, 1999. **8**(2): p. 183-215.

35. Park, S. and L. Rothrock, *Systematic Analysis of Framing Bias in Missile Defense: Implications Toward Visualization Design.* European Journal of Operational Research, 2007. **182**(3): p. 1383-1398.

36. Cheng, C.-H., *Evaluating Naval Tactical Missile Systems by Fuzzy AHP Based on the Grade Value of Membership Function.* European Journal of Operational Research, 1997. **96**(2): p. 343-350.

37. Ahuja, R.K., et al., *Exact and Heuristic Algorithms for the Weapon-Target Assignment Problem.* Operations Research, 2007. **55**(6): p. 1136-1146.

38. Eckler, A.R. and S.A. Burr, *Mathematical Models of Target Coverage and Missile Allocation*. 1972, Military Operations Research Society.

39. Singh, U.K. and V. Padmanabhan. *Training and Classification of Ballistic Missiles Using Hidden Markov Model*. in *2013 Sixth International Conference on Contemporary Computing*. Noida, India: IEEE.

40. Singh, U.K., V. Padmanabhan, and A. Agarwal, *A Novel Method For Training and Classification of Ballistic and Quasi-Ballistic Missiles in Real-Time*, in *International Joint Conference on Neural Networks*. 2013: Dallas, TX. p. 13.

41. Wacholder, E., *A Neural Network-Based Optimization Algorithm for the Static Weapon-Target Assignment Problem.* ORSA Journal on Computing, 1989. **1**(4): p. 232.

42. Holland, O.T. and S.E. Wallace, *Using Agents to Model the Kill Chain of the Ballistic Missile Defense System.* Naval Engineers Journal, 2011. **123**(3): p. 141-151.

43. Chicher, C. and M.S. Obaidat. *ARBALET: An Aid for Ballistic Threat Analysis and ATBM Defense Design*. in *Proceedings of the 1997 Summer Computer Simulation Conference Simulation and Modeling Technology for the Twenty-First Century*. 1997. Arlington, VA.: Society for Computer Simulation

44. Brofos, A.M. and M.S. Obaidat. *Use of a System-of-System Simulation to Determine Asset Deployment for USMC Air Defense Missions*. in *Proceedings of the 1997 Summer Computer Simulation Conference Simulation and Modeling Technology for the Twenty-First Century*. 1997. Arlington, VA.: Society for Computer Simulation.

45. Gupta, R., *Defense Positioning and Geometry: Rules for a World with Low Force Levels*. 1993: Washington, D.C. : Brookings Institution.

46. Ender, T., et al., *Systems-of-Systems Analysis of Ballistic Missile Defense Architecture Effectiveness Through Surrogate Modeling and Simulation.* IEEE Systems Journal, 2010. **4**(2): p. 156-166.

47. *DOTmLPF-P Analysis*. Available from: https://dap.dau.mil/acquipedia/Pages/ArticleDetails.aspx?aid=d11b6afa-a16e-43cc-b3bb-ff8c9eb3e6f2.

48. *Manual for the Operation of the Joint Capabilities Integration and Development System*. JCIDS Manual. 2012, Washington DC: Joint Interoperability Test Command.

49. *Generic Acquisition Process (Pre-Tailoring): Acquisition Decision Points and Phases*. 2014 [cited 2017 March 24]; Available from: http://www.acqnotes.com/wp-content/uploads/2014/09/Generic-Acquisition-Process-Pre-Tailoring-Chart.pdf.

50. *How the Army Runs: A Senior Leader Reference Handbook*. 2014, Carlisle, PA: U.S. Army War College.

51. *JCIDS Process: DOTMLPF-P Change Recommendation (DCR)*. [cited 2014 March 7]; Available from: http://www.acqnotes.com/Acquisitions/DOTMLPF Change Recommendation (DRC).html.

52. Sydney Freedberg, J. *Army Explores New Missile Defense Options*. Breaking Defence, 2015.

53. E.D. Woolsey, R., *An Analysis of a Model of the MPS MX Missile System Using Geometric Programming.* Applied Mathematical Modeling, 1991. **15**(9): p. 493-495.

54. Jian-Jun, D., et al. *Reliability Allocation of Anti-Air Missile Weapon System Based on Ant Colony Algorithm*. in *2013 International Conference on Quality, Reliability, Risk, Maintenance and Safety Engineering*. 2013. Chengdu, China.: IEEE.

55. *EADSIM Introduction*. 2010, Teledyne Brown Engineering: Huntsville, AL.

56. O'Meara, N.T. and R.M. Soland, *Optimal Attack Against an Area Defense Protecting Many Targets.* INFOR, 1990. **28**(1): p. 40-52.

57. *Manual for the Operation of the Joint Capabilities Integration and Development System*. [cited 2017 March 1]; Available from: http://www.acqnotes.com/Attachments/JCIDS Manual - 31 July 2009.pdf.

58. Anderson, C.M., *Generalized Weapons Effects Modeling*, in *Department of Mechanical Engineering*. 2004, Naval Post Graduate School: Monterey, CA. p. 129.

59. *Joint Targeting Applications Course Syllabus*. 2014, Joint Targeting School: Virginia Beach, VA.

60. Clark, B., *Commanding the Seas: A Plan to Reinvigorate the US Navy Surface Warfare*. 2014, Center for Strategic and Budgetary Assessments: Washington DC.

61. Gourley, S.R., *PAC-3 Missile*, in *Army*. 2006, Association of the US Army: Washington DC.

62. Driels, M.R., *Weaponeering: Conventional Weapon System Effectiveness*. AIAA Education Series. 2004, Reston, VA.: American Institute of Aeronautics and Astronautics.

63. Przemieniecki, J.S., *Mathematical Methods in Defense Analyses*. 3rd ed. AIAA education series. 2000, Reston, VA: American Institute of Aeronautics and Astronautics.

64. *Capabilities-Based Assessment (CBA) User's Guide, Version 2*. Joint Staff Manual. 2006, Washington, DC: Joint Chief of Staff: Force Structure, Resources, and Assessments Directorate (JCS J-8).

65. *EADSIM User Manual*. 2015, Teledyne Brown Engineeing: Huntsville, AL.

66. *Movable Type Scripts: Calculate Distance, Bearing and More Between Latitude/Longitude Points*. [cited 2015 July 21]; Available from: http://www.movable-type.co.uk/scripts/latlong.html.

67. *Turnpoint Discrepancies in Competition Scoring*. 2008 [cited 2015 July 19]; Available from: http://www.flytec.comSupportDistance_discrepancies.pdf.

68. *Excel Formula to Calculate Distance*. 2007 [cited 2015 July 21]; Available from: http://bluemm.blogspot.com/2007/01/excel-formula-to-calculate-distance.html.

69. *Department of Defense World Geodetic System 1984: Its Definition and Relationships with Local Geodetic Systems*. 2000, National Imagery and Mapping Agency.

70. Vincenty, T., *Direct and Inverse Solutions of Geodesics on the Ellipsoid With Application of Nested Equations*. 1975, Directorate of Overseas Surveys: Surrey, England.

71. McCoy, R.L., *Modern Exterior Ballistics: The Launch and Flight Dynamics of Symmetric Projectiles*. 2nd ed. 2012, Atglen, PA: Schiffer Military History.

72. Miller, D.G., *Typographical Errors in Robert L. McCoy, "Modern Exterior Ballistics" Schiffer Publishing Ltd, Atglen, PA, 1999*. 2010, Donald G Miller: Livermore, CA.

73. Carlucci, D.E. and S.S. Jacobson, *Ballistics: Theory and Design of Guns and Ammunition*. 2014, Taylor & Francis Group: Boca Raton, FL.

74. *120-mm MORTAR, M120*. [cited 2015 October 9]; Available from: http://www.globalsecurity.org/military/library/policy/army/fm/23-90/ch7.htm.

75. Gkritzapis, D.N., et al., *Prediction of the Impact Point for Spin and Fin Stabilized Projectiles.* Information Science and Applications, 2008. **5**(12).

76. Harkins, T.E., *Understanding Body-Fixed Sensor Output From Projectile Flight Experiments*. 2003, Army Research Laboratory: Aberdeen Proving Ground, MD.

77. Siouris, G.M., *Missile Guidance and Control Systems*. 2004, New York, NY.: Springer.

78. Senan, N.A.F., *A Brief Introduction to Using ODE45 in MATLAB*. Department of Mechanical Engineering, University of California at Berkeley: Berkeley, CA.

79. Stengel, R.F., *Flight Dynamics*. 2004, Princeton, NJ.: Princeton University Press. xvii, 845 p.

80. Li, Q.M., et al., *Local Impact Effects of Hard Missiles on Concrete Targets.* International Journal of Impact Engineering, 2005. **32**: p. 224-284.

81. Dancygier, A.N. and D.Z. Yankelevsky, *High Strength Concrete Response to Hard Projectile Impact.* International Journal of Impact Engineering, 1996. **18**(6): p. 583-599.

82. Haldar, A. and H.A. Hamieh, *Local Effect of Solid Missiles on Concrete Structures.* Journal of Structural Engineering, 1984. **110**(5): p. 948-960.

83. Yu, R., P. Spiesz, and H.J.H. Brouwers, *Numerical Simulation of Ultra-High Performance Fibre Reinforced Concrete (UHPFRC) Under High Velocity Impact of Deformable Projectiles*, in *15th International Symposium on Interaction of the Effects of Munitions with Structures*. 2013: Potsdam, Germany.

84. Li, Q.M. and X.W. Chen, *Dimensionless Formula for Penetration Depth of Concrete Target Impacted by A Non-Deformable Projectile.* International Journal of Impact Engineering, 2003. **01**(2003): p. 93-116.

85. Longcope, D., T.L. Warren, and H. Duong, *Aft-Body Loading Function for Penetrators Based on the Spherical Cavity-Expansion Approximation*. 2009, Sandia National Laboratories: Albuquerque, NM.

86. Wang, Z.-l., Y.-C. Li, and J.G. Wang, *Numerical Study on Craters and Penetration of Concrete Slab by Ogive-Nose Steel Projectile.* Computers and Geotechnics, 2007. **34**(1): p. 1-9.

87. Shan, Y., et al., *On the Inertia Term of Projectile's Penetration Resistance.* Advances in Materials Science and Engineering, 2013. **2013**(1): p. 6.

88. Ben-Dor, G., A. Dubinsky, and T. Elperin, *Ballistic Impact: Recent Advances in Analytical Modeling of Plate Penetration Dynamics - A Review.* Applied Mechanics Review, 2005. **58**: p. 355-370.

89. Yankelevsky, D.Z., *Local Response of Concrete Slabs to Low Velocity Missile Impact.* International Journal of Impact Engineering, 1997. **19**(4): p. 331-343.

90. Kennedy, R.P., *A Review of Procedures for the Analysis and Design of Concrete Structures to Resist Missile Impact Effects.* Nuclear Engineering and Design, 1975. **37**: p. 183-203.

91. *Effects of Impact and Explosion, Summary Technical Report of Division 2*. 1946, National Defense Research Committee: Washington, D.C.

92. Bangash, M.Y.H., *Concrete and Concrete Structures: Numerical Modeling and Applications*. 1989, London; New York: Elsevier Applied Science;.

93. Kar, A.K., *Local Effects of Tornado-Generated Missiles.* Journal of the Structural Division, 1978. **104**(5): p. 809-816.

94. Young, C.W., *Penetration Equations*, S.N. Laboratories, Editor. 1997, Applied Research Associates, Inc.: Albuquerque, NM.

95. DiGiulian, T. *Calculating CRH*. 2004 [cited 2015 April 29]; Available from: http://www.navweaps.com/index_tech/tech-094.html.

96. Kumaran, U.S., et al., *Effect of Diffrent Nose-Shaped Projectiles on The High Speed Perforation of Concrete*, in *Shock Compression of Condensed Matter*, M.D. Furnish, L.C. Chhabilidas, and R.S. Hixson, Editors. 1999, American Institute of Physics. p. 1233-1236.

97. Forrestal, M.J., et al., *Penetration of Grout and Concrete Targets with Ogive-nose Steel Projectiles.* International Journal of Impact Engineering, 1996(18): p. 465--476.

98. Cargile, J.D., *Development of a Constitutive Model for Numerical Simulation of Projectile Penetration into Brittle Geomaterials*, in *Applied Mechanics|Engineering, Civil*. 1999, Purdue University: West Lafayette, Indiana.

99. Canfield, J.A. and I.G. Clator, *Development of a Scaling Law and Techniques to Investigate Penetration in Concrete*. 1966, US Naval Weapons Laboratory: Dahgren, VA.

100. Luccioni, B., et al., *Craters Produced by Underground Explosions.* Computational Structures, 2009. **87**(21-22): p. 1366-1373.

101. Bening, R.G. and M.K. Kurtz, *The Formation of a Crater as Observed in a Series of Laboratory-Scale Cratering Experiments*. 1967, US Army Engineer Nuclear Cratering Group: Livermore, CA.

102. Knox, J.B. and R.W. Terhune, *Calculation of Explosion-Produced Craters-High Explosive Sources.* Journal of Geophysical Research, 1965. **70**(10): p. 2377-2393.

103. Sublette, C. *The Effects of Underground Explosions*. 2001 [cited 2014 April 23]; Available from: http://nuclearweaponarchive.org/Library/Effects/UndergroundEffects.html.

104. Bull, J.W. and C.H. Woodford, *The Effect of Large Subgrade Voids on the Fatigue Life of Runways.* Computers and Structures, 2001. **79**(2001): p. 2431-2441.

105. Bull, J.W. and C.H. Woodford, *Camouflets and Their Effect on Runway Support.* Computers and Structures, 1998. **69**(1998): p. 695-706.

106. *Unified Facilities Criteria (UFC) Airfield Damage Repair*. 2002, US Air Force, US Government Printing Office: Washington DC.

107. Baker, W.E., *Modeling of Large Transient Elastic and Plastic Deformations of Structures Subjected to Blast Loading.* Journal of Applied Mechanics, 1960. **27**(3): p. 521-527.

108. Chock, J.M.K., *Review of Methods for Calculating Pressure Profiles of Explosive Air Blast and its Sample Application*, in *Aerospace Engineering*. 1999, Virginia Polytechnic Institute: Blacksburg, VA.

109. Lampson, C.W., *Effects of Impact and Explosion*, in *Explosions in Earth*. 1946, Office of Scientific Research and Development: Washington DC. p. 110.

110. Morrey, C.B., *Underground Explosion Theory*, in *Operation Jangle*. 1952, Office of Technical Services, Department of Commerce: Washington DC.

111. Chabai, A.J., *On Scaling Dimensions of Craters Produced by Buried Explosives.* Journal of Geophysical Research, 1965. **70**(20): p. 5075-5098.

112. Bulson, P.S., *Explosive Loading of Engineering Structures: a History of Research and a Review of Recent Developments*. 1997, E & FN Spon: London ; New York.

113. Maienschein, *Estimating Equivalency of Explosives Through A Thermochemical Approach*, in *12th International Conference Symposium*. 2002: San Diego, CA.

114. *Compendium of Crater Data*, in *Cratering from High Explosive Charges*. 1960, US Army Engineer Waterways Experiment Station: Vicksburg, MS.

115. Needham, C.E. and SpringerLink (Online service), *Blast Waves*, in *Shock Wave and High Pressure Phenomena*. 2010, Springer-Verlag: Berlin, Heidelberg.

116. Chabai, A.J., *Scaling Dimentions of Craters Produced by Buried Explosions*. 1965, Sandia Laboratory: Albuquerque, NM.

117. Kiger, S.A. and J.P. Balsara, *A Review of the 1983 Revision of TM 5-855-1 "Fundamentals of Protective Design" (Nonnuclear)*. USAE Waterways Eperiment Station: Vicksburg, MS.

118. Ross, A.C. and P.L. Rosengren Jr., *Expedient Nonlinear Analysis of Reinforced Concrete Structures*, in *Second International Symposium on the Interaction of Nonnuclear Munitions with Structures*. 1985: Florida University, Graduate Research Center.

119. Metwally, a.a.A.e., *Compressive Strength Prediction of Portland Cement Concrete with Age Using a New Model.* Housing and Building National Research Center Journal, 2014. **2014**(10): p. 145-155.

120. *Portland Cement Compressive Strength*. 2007 [cited 2015 May 19, 2015]; Available from: http://www.pavementinteractive.org/article/Protland-Cement-Compressive-Strength.

121. Oluokun, F.A., *Prediction of Concrete Tensile Strength from Its Compressive Strength: Evaluation of Existing Relations for Normal Weight Concrete.* ACI Materials Journal, 1991. **88**(3): p. 302-209.

122. *Density of Concrete*. [cited 2015 May 19]; Available from: http://www.everything-about-concrete.com/density-of-concrete.html.

123. *Steelworker Nonresident Training Course*. 1996, US Navy: Pensacola, FL.

124. Inc., J.a.C. *Rebar*. [cited 2015 May 19]; Available from: http://www.jettandcompanyinc.com/Documents/Rebar.pdf.

125. Krause, H.H., *New Energetic Materials*, in *Energetic Materials*, U. Teipel, Editor. 2005, Wiley-VCH Verlag GmbH & Co. KGaA: Weinheim, Germany. p. 1-25.

126. Smith, A.C. and M. Sapko, J., *Detonation Wave Propagation in Underground Mine Entries*. National Institute of Occupational Safety and Health, USA.

127. *Air Base Damage Repair (Pavement Repair)*. 1988, Department of the Army: Washington, DC.

128. *Airfield Damage Repair Operations*. 2008, Department of the Air Force: Washinton DC.

129. Anderson, J.D., *Aircraft Performance and Design*. 1999, Boston, MA.: McGraw-Hill.

130. Halliday, J.M., *Tactical Dispersal of Fighter Aircraft: Risk, Uncertainty, and Policy Recommendations*. 1987, Santa Monica, CA.: RAND Corporation.

131. *Engineering Technical Letter (ETL) 13-3: Minimum Airfield Operating Surface Selection and Repair Quality Criteria*. 2013, US Air Force Civil Engineering Center: Tyndall Air Force Base, FL.

132. Priddy, L.P., *Evaluation of Precast Portland Cement Concrete Panels for Airfield Pavement Repairs*. 2015, Geotechnical and Structures Laboratory, Engineering Research and Development Center: Vicksburg, MS.

133. Hines, W.W., et al., *Probability and Statistics in Engineering*. 4th ed. 2003: Hoboken, NJ : Wiley.

134. Przemieniecki, J.S., *Mathematical methods in defense analyses*. 3rd ed. AIAA education series. 2000, Reston, VA: American Institute of Aeronautics and Astronautics. xx, 398 p.

135. Santner, T.J., B.J. Williams, and W.I. Notz, *The Design and Analysis of Computer Experiments*. Springer Series in Statistics, ed. Springer. 2010, New York, NY: Springer-Verlag New York, Inc. 283.

136. Donnelly, T., *Basic Design of Experiments Using Custom DOE Platfom*. 2015, SAS Institute Inc.: Rockville, MD.

137. Kennedy, K., *Bridging the Gap Between Space-Filling and Optimal Designs: Design for Computer Experiments*. 2013, Arizona State University: Tempe, AZ.

138. Viana, F.A.C., *Things You Wanted to Know About Latin Hypercube Design and Were Afraid to Ask*, in *10th World Cogress on Structural and Multidisciplinary Optimization*. 2014: Orlando, FL.

139. Qian, P.Z.G., *Nested Latin Hypercube Designs.* Biometrika, 2009. **96**(4): p. 957-970.

140. Donnelly, T. *Efficient Simulation Using Design of Experiments (DOE)*. in *82nd MORS Symposium*. 2014. Alexandria, VA.

141. *Advisory Circular: Airport Pavement Design and Evaluation*. 2009, Federal Aviation Administration, US Department of Transportation.

142. Forden, G., *GUI Missile Flyout: A General Program for Simulating Ballistic Missiles.* Science and Global Security, 2007. **15**: p. 133-146.

143. Law, A.M., *Simulation Modeling and Analysis*. 5th ed. 2015, New York, NY: McGraw Hill Education.

144. Driels, M.R. and Y.S. Shin, *Determining the Number of Iterations For Monte Carlo Simulations of Weapon Effectivness*. 2004, Naval Postgradute School: Monterey, CA.

145. Lacey, M. *The Binomial Distribution*. [cited 2016 August 20]; Available from: http://www.stat.yale.edu/Courses/1997-98/101/binom.htm.

146. Devore, J.L., *Probability and Statistics for Engineering and the Sciences*. 5th ed. 2000, Pacific Grove, CA.: Duxbury.

147. Vanderplaats, G.N., *Multidiscipline Design Optimization*. 2007, Colorado Springs, CO.: Vanderplaats Research and Development, Inc.

148. AbouRizk, S. and D.W. Halpin, *Fitting Beta Distributions Based on Sample Data.* Journal of Construction Engineering and Management, 1994. **120**(2): p. 288-305.

149. Karsoliya, S., *Approximating Number of Hidden Layer Neurons in Multiple Hidden Layer BPNN Architecture.* International Journal of Engineering Trends and Technology, 2012. **3**(6): p. 714-717.

150. Rajkumar, T. and J. Bardina, *Training Data Requirment for a Neural Network to Predict Aerodynamic Coefficients*. NASA Ames Research Center: Moffett Field, CA.

151. Keiner, K. *Data Transformations*. [cited 2016 June 6]; Available from: http://faculty.ycp.edu/~kkleiner/ecology/labimages/Statistics/Data Transformations.pdf.

152. Jarnagin Jr, M.P. and A.R. DiDonato, *Damage to a Circular Target by a Guassian Distributed Warhead with Uniformly Distributed Bomblets.* Operations Research, 1966. **14**(6): p. 1014.

153. Macke, R.C., *A Proposed Method for Defining and Measuring Weapon System Accuracy*, in *Department of Operations Research and Administrative Sciences*. 1972, Naval Post Graduate School: Monterey, CA. p. 69.

154. Peterson, K.A., *Numerical Simulation Investigations in Weapons Delivery Probabilities*, in *Department of Mechanical Engineering*. 2008, Naval Post Graduate School: Monterey, CA. p. 85.

155. Elek, P. and S. Jaramaz. *Size Distribution of Fragments Generated by Detonation of Fragmenting Warheads*. in *23rd International Symposium on Ballistics*. 2007. Tarragona, Spain.

156. Biltgen, P.T., *A Methodology for Capability-Based Technology Evaluation for Systems-of-Systems A Methodology for Capability-Based Technology Evaluation for Systems-of-Systems*, in *Department of Aerospace Engineering*. 2007, Georgia Institute of Technology: Atlanta, GA. p. 512.

157. Macal, C.M. and M.J. North, *Tutorial on Agent-Based Modeling and Simulation.* Journal of Simulation, 2010. **4**(3): p. 151-162.

158. Borshchev, A. and A. Filippov, *From System Dynamics and Discrete Event to Practicle Agent Based Modeling: Reasons, Techniques, Tools*, X. Technologies, Editor., St. Petersburg Technical University: St. Petersburg, Russia.

159. Tangen, S.A., *A Methodology for the Quantification of Doctrine and Materiel Approaches in a Capability-Based Assessment A Methodology for the Quantification of Doctrine and Materiel Approaches in a Capability-Based Assessment*, in *Department of Aerospace Engineering*. 2009, Georgia Institute of Technology: Atlanta, GA.

160. Wilensky, U., *NetLogo itself*, in *NetLogo*. 1999, Center for Connected Learning and Computer-Based Modeling, Northwestern University: Evanston, IL.

161. Sweeney, R.L., J.P. Hamman, and S.M. Biemer, *The Application of Systems Engineering to Software Development: A Case Study.* Johns Hopkins APL Technocal Digest, 2011. **29**(4).

162. Wilson, B.A. and D.B. Fox, *Ground Combat in JICM*, ed. N.D.R. Institute. 1959, Santa Monica, CA.: RAND Corperation.

163. Fox, D.B. and C.M. Jones, *JICM 3.0: Documentation and Tutorial*, ed. N.D.R. Institute. 1998, Santa Monica, CA: RAND Corporation.

164. Richards, M.A., J.A. Scheer, and W.A. Holm, *Principles of Modern Radar, Volume I - Basic Principles*. 2010, Raleigh, NC: SciTech Publishing.

165. *Radar Cross Section (RCS)*. [cited 2014 February 11]; Available from: http://www.globalsecurity.org/military/world/stealth-aircraft-rcs.htm.

166. *The Depatment of Defense High Performance Computing (HPC) Environment*. [cited 2017 January 31]; Available from: https://centers.hpc.mil.

167. *OptTek Systems*. [cited 2017 March 3]; Available from: http://www.opttek.com.

168. Hwang, C. and K. Yoon, *Multiple Attribute Decision Making: Methods and Applications: A State-of-the-Art Survey* 1981, Berlin; New York: Springer-Verlag.

169. Srikrishna, S., R.A. Sreenivasulu, and S. Vani, *A New Car Selection in the Market using TOPSIS Technique.* International Journal of Engineering Research and General Science, 2014. **2**(4): p. 177-181.

170. *Air Force Pamphlet 10-219: Airfield Damage Repair Operations*. 2012, US Air Force: Washington, DC.

171. Ruxton, G.D., *The Unequal Variance t-test is an Underused Alternative to Student's t-test and the Mann–Whitney U test.* Behavioral Ecology, 2006. **17**(4): p. 688-690.

172. Pannell, D.J. *Sensitivity Analysis: Strategies, Methods, Concepts, and Examples*. [cited 2017 February 5]; Available from: http://dpannell.fnas.uwa.edu.au/dpap971f.htm.

173. Richards, M.A., *Target Model Fluctuations and Detection*, in *Principles of Modern Radar Class Briefing*. 2014, Georgia Institute of Technology: Atlanta, GA.

174. Swerling, P., *Probability of Detection for Fluctuating Targets*. 1954, US Air Force Project RAND, Rand Corporation: Santa Monica, CA.

175. Kleijnen, J.P.C., *Design and Analysis of Simulation Experiments*. 2008, New York ; London: Springer.

176. Mavris, D., *Technical Feasibility and Economic Viability Gap Analysis Lecture Notes*. 2009, Georgia Institute of Technology: Atlanta, GA.

177. Simpson, T.W., D.K.J. Lin, and W. Chen, *Sampling Stategies for Computer Experiments: Design and Analysis.* International Journal of Reliability and Applications, 2001. **2**(3): p. 209-240.

178. Goos, P. and B. Jones, *Optimal Design of Experiments: A Case Study Approach*. 2011, West Sussex, UK: John Wiley and Sons, Ltd. 287.

179. Kirby, M.R., *A Methodology for Technology Identification, Evaluation, and Selection In Conceptual and Preliminary Aircraft Desgin*, in *Department of Aerospace Engineering*. 2001, Georgia Institute of Technology: Atlanta, GA.

180. Robinson, S.B., *A Modeling Process to Understand Complex System Architectures*, in *Department of Aerospace Engineering*. 2009, Georgia Institute of Technology: Atlanta, GA. p. 347.

181. Rushing, H., A. Karl, and J. Wisnowski, *Design and Analysis of Experiments by Douglas Montgomery: A Supplement for Using JMP*. 2013, SAS Institute,: Cary, N.C.

182. Kleijnen, J.P.C., et al., *A User's Guide to the Brave New World of Designing Simulation Experiments.* INFORMS Journal on Computing, 2005. **17**(3): p. 263-289.

183. Jones, B. and R.T. Johnson, *Design and Analysis for the Guassian Process Model.* Quality and Reliability Engineering International, 2009. **25**(2009): p. 515-524.

184. Viana, F.A.C., G. Venter, and V. Balabanov, *An Algorithm for Fast Optimal Latin Hypercube Design of Experiments.* International Journal for Numerical Methods in Engineering, 2010. **82**(2): p. 135-156.

185. Stall, J., *JMP Design of Experiments, Release 6*. Vol. JMP 6.0.3. 2005, Cary, NC: SAS Institute.

186. McKay, N., W. Conover, and R. Beckman, *A Comparison of Three Methods for Selecting Values of Input Variables in the Analysis of Output From a Computer Code.* Technometrics, 1979. **21**: p. 239-245.

187. Fang, K., R. Li, and A. Sudjianto, *Design and Modeling for Computer Experiments*. 2006, Boca Raton, FL: Chapman & Hall.

188. Forrester, A.I.J., A. Sóbester, and A.J. Keane, *Engineering Design via Surrogate Modeling: A Practical Guide*. Progress in Astronautics and Aeronautics. 2008, Chichester, West Sussex, England ; Hoboken, NJ: J. Wiley.

189. Box, G.E.P. and W.K. B., *On the Experimental Attainment of Optimal Conditions.* Journal of the Royal Statistical Society, 1951. **B**(13): p. 1-38.

190. Myers, R.H. and D.C. Montgomery, *Response Surface Methodology: Process and Product Optimization Using Designed Experiments*. 2nd Edition ed. Wiley series in probability and statistics. 2002, New York, NY.: Wiley.

191. Bretscher, O., *Linear Algebra With Applications*. 5th ed. 2013, Upper Saddle River, NJ: Pearson Prentice Hall.

192. Fauske, K.M. *Example: Neural Network*. 2006 [cited 2015 November 29]; Available from: http://www.texample.net/tikz/examples/neural-network/.

193. Hagan, M.T., H.B. Demuth, and M.H. Beale, *Neural Network Design*. 2 ed., Boulder, CO: Campus Pub. Service, University of Colorado Bookstore.

194. Johnson, C. and J. Schutte, *Basic Regression Analysis for Integrated Neural Networks (BRAINN) Documentation Version 2.3*. 2009, Georgia Institute of Technology: Atlanta, GA.

195. Sung, W.J., *A Neural Network Construction Method for Surrogate Modeling of Physics-Based Analysis*, in *Department of Aerospace Engineering*. 2011, Georgia Institute of Technology: Atlanta, GA.

196. Hornik, K., M. Stinchcombe, and H. White, *Multilayer Feedfoward Networks are Universal Approximators.* Neural Networks, 1989. **2**: p. 359-366.

197. Donnelly, T. *Surrogate Modeling of Stochastic Computer Simulation Data – Identifying Insurgents from a Helicopter Flying Surveillance*. in *82nd MORS Symposium*. 2014. Alexandria, VA.

198. Donnelly, T. *Improving the Prediction of Cyber Attacks Using Ensemble Modeling*. in *82nd MORS Symposium*. 2014. Alexandria, VA.

199. Krige, D.G., *A Statistical Approach to Some Mine Valuations and Allies Problems at the Witwatersrand*. 1951, University of Witwatersrand: Johannesburg, South Africa.

200. Bohling, G., *Kriging*. 2005, Kansas Geological Survey.

201. Crowley, D.R., *An Efficient Approach for High-Fidelity Modeling Incorporating Contour-Based Sampling and Uncertainty*, in *Department of Aerospace Engineering*. 2013, Georgia Institute of Technology: Atlanta, GA.

202. *Interpreting Residual Plots to Improve Your Regression*. Statwing Documentation: Statwing's Approach to Statistical Testing [cited 2015 March 30]; Available from: http://docs.statwing.com/interpreting-residual-plots-to-improve-your-regression/.

203. *Plotting Techniques*. [cited 2016 January 23]; Available from: http://www-stat.wharton.upenn.edu/~buja/mba/plotting-techniques.html.

204. Shaprio, S.S. and M.B. Wilk, *An Analysis of Variance Test for Normality (Complete Samples).* Biometrika, 1965. **52**(3-4): p. 591-611.